R-09-24

Groundwater flow modelling of periods with temperate climate conditions – Laxemar

Steven Joyce, Trevor Simpson, Lee Hartley,
David Applegate, Jaap Hoek, Peter Jackson,
David Roberts, David Swan
Serco Technical Consulting Services

Björn Gylling, Niko Marsic
Kemakta Konsult AB

Ingvar Rhén, SWECO Environment AB

December 2010

Svensk Kärnbränslehantering AB
Swedish Nuclear Fuel
and Waste Management Co

Box 250, SE-101 24 Stockholm
Phone +46 8 459 84 00

ISSN 1402-3091
SKB R-09-24

Groundwater flow modelling of periods with temperate climate conditions – Laxemar

Steven Joyce, Trevor Simpson, Lee Hartley,
David Applegate, Jaap Hoek, Peter Jackson,
David Roberts, David Swan
Serco Technical Consulting Services

Björn Gylling, Niko Marsic
Kemakta Konsult AB

Ingvar Rhén, SWECO Environment AB

December 2010

Keywords: SKBdoc 1267488, Hydrogeology, Groundwater, Modelling, Transport, Temperate, Laxemar.

Abstract

As a part of the license application for a final repository for spent nuclear fuel at Forsmark, the Swedish Nuclear Fuel and Waste Management Company (SKB) has undertaken a series of groundwater flow modelling studies. These represent time periods with different hydraulic conditions and the simulations carried out contribute to the overall evaluation of the repository design and long-term radiological safety.

This report concerns the modelling of a repository at the Laxemar-Simpevarp site during temperate climate conditions as a comparison to corresponding modelling carried out for Forsmark /Joyce et al. 2010/. The collation and implementation of onsite hydrogeological and hydrogeochemical data from previous reports are used in the construction of a Hydrogeological base case (reference case conceptualisation) and then an examination of various areas of uncertainty within the current understanding by a series of model variants. The Hydrogeological base case models at three different scales, 'repository', 'site' and 'regional' make use of a discrete fracture network (DFN) and equivalent continuous porous medium (ECPM) models. The use of hydrogeological models allow for the investigation of the groundwater flow from a deep disposal facility to the biosphere and for the calculation of performance measures that will provide an input to the site performance assessment.

The focus of the study described in this report has been to perform numerical simulations of the hydrogeological system from post-closure and throughout the temperate period up until the receding shoreline leaves the modelling domain at around 15,000 AD. Besides providing quantitative results for the immediate temperate period following post-closure, these results are also intended to give a qualitative indication of the evolution of the groundwater system during future temperate periods within an ongoing cycle of glacial/inter-glacial events.

Sammanfattning

Som en del av en ansökan för ett slutförvar för använt kärnbränsle i Forsmark har Svensk Kärnbränslehantering AB (SKB) genomfört en serie grundvattenflödesmodelleringsstudier. De olika studierna representerar tidsperioder med olika klimatförhållanden och de utförda simuleringarna bidrar till den övergripande bedömningen av förvarsdesign och långsiktig radiologisk säkerhet.

Föreliggande rapport är en modelleringsstudie av grundvattenflödet kring ett förvar i Laxemar-Simpevarp under tempererade klimatförhållanden. Rapporten liknar till sitt innehåll modelleringsstudien av grundvattenflödet kring ett förvar i Forsmark utförd av /Joyce et al. 2010/. Ett hydrogeologiskt basfall (referensfalls-konceptualisering) är definierat baserat på platsspecifika hydrogeologiska och hydrogeokemiska data sammanställda i andra rapporter. Olika typer av osäkerheter givet nuvarande förståelse (beskrivning) undersöks med hjälp av en serie modellvarianter. Det hydrogeologiska basfallet, beskrivet på förvars-, plats- och regionalskala, studeras med kontinuerliga porösa media modeller (CPM), ekvivalenta kontinuerliga porösa media modeller (ECPM) och diskreta sprik-nätverksmodeller (DFN). Användningen av hydrogeologiska modeller gör det möjligt att studera grundvattenflöde från ett djupförvar till biosfär och för att beräkna resultat som går vidare in i säkerhetsanalysen.

Studiens tonvikt ligger på numeriska simuleringar av det hydrogeologiska systemets utveckling från och med förslutning fram till slutet av den temperarade perioden vid ca år 15 000 AD då strandlinjen har passerat modelldomänen. Förutom kvantitativa resultat för den tempererade period som följer direkt efter förvarets förslutning, ger studien kvalitativa indikationer för grundvattensystemets utveckling under kommande tempererade perioder i efterföljande cykler av glacialer och inter-glacialer.

Contents

1 Introduction 7
1.1 Background 7
1.2 Scope and Objectives 8
1.3 Setting 8
1.4 This report 13

2 Hydrogeological model of the Laxemar site 15
2.1 Supporting documents 15
2.2 Systems approach in SDM-Site 16
2.3 Summary of the bedrock hydrogeological model 17
2.3.1 General 17
2.3.2 Hydraulic characteristics of hydraulic conductor domains (HCD) 18
2.3.3 Hydraulic characteristics of hydraulic rock mass domains (HRD) 21
2.3.4 Hydraulic characteristics of the focused volume 24
2.4 Summary of the Quaternary deposits hydrogeological model (HSD) 26
2.5 Groundwater flow simulations and confirmatory testing 30

3 Concepts and methodology 31
3.1 Conceptual model types 31
3.1.1 Continuous porous medium (CPM) representation 31
3.1.2 Discrete fracture network (DFN) representation 31
3.1.3 Equivalent continuous porous medium (ECPM) representation 34
3.1.4 Stochastic continuum representation 36
3.1.5 Embedded CPM/DFN models 37
3.1.6 Particle tracking 39
3.1.7 Requirements for site assessment 40
3.2 Modelling methodology 40
3.2.1 Model scales 40
3.2.2 Representation of deformation zones (DZs) 48
3.2.3 Variable density groundwater flow and salt transport 50
3.2.4 Transport calculations 51
3.2.5 Flow and transport in the repository and EDZ 51
3.2.6 Calculation of performance measures 53
3.2.7 Deposition hole rejection criteria (FPC/EFPC) 57

4 Hydrogeological base case model specification 59
4.1 Regional-scale model 60
4.1.1 Model Description 60
4.1.2 Boundary conditions and initial conditions 65
4.1.3 Calculation of past and future evolution 65
4.1.4 Outputs 68
4.2 Site-scale model 68
4.2.1 Model Description 68
4.2.2 Boundary conditions and initial conditions 71
4.2.3 Calculations 71
4.2.4 Outputs 71
4.3 Repository-scale model 71
4.3.1 Model Description 72
4.3.2 Boundary conditions and initial conditions 75
4.3.3 Calculations 75
4.3.4 Outputs 76

5 Model variants 77
5.1 Elaborated Hydro-DFN 77
5.1.1 Introduction 77
5.1.2 Elaborated Hydro-DFN methodology 78
5.1.3 Main changes compared to the SDM-Site Hydro-DFN 80
5.1.4 Calculations 84
5.2 Elaborated Hydro-DFN model with no Minor Deformation Zones 84
5.2.1 Specification 84
5.2.2 Representation 84
5.2.3 Calculations 84
5.3 Stochastic Continuum model 85
5.3.1 Specification 85
5.3.2 Representation 86
5.3.3 Confirmatory testing 94

6 Results 95
6.1 Presentation of results 95
6.2 Hydrogeological base case model results 96
6.2.1 Distribution of reference waters 96
6.2.2 Evolution of exit locations with time 101
6.2.3 Evolution of performance measures with time 106
6.2.4 Spatial distribution of performance measures 108
6.2.5 The effect of FPC and EFPC 112
6.2.6 Additional realisation 114
6.3 Elaborated Hydro-DFN model results 115
6.4 The Elaborated Hydro-DFN model with no Minor Deformation Zones results 120
6.5 Stochastic continuum model results 122

7 Discussion and conclusions 129

8 References 133

Appendix A Glossary of abbreviations and symbols 137

Appendix B File Formats 139

Appendix C Peformance Measure Plots 141

Appendix D Derivation of Performance Measure Equations 203

Appendix E Elaborated Hydro-DFN model 209

Appendix F Differences between Hydrogeological base case and SDM-Site Laxemar models 263

Appendix G A comparison of inflows to tunnels under open repository conditions between ConnectFlow and DarcyTools 269

Appendix H Using analytic expressions to estimate time for fresh water penetration to repository depths 271

Appendix I Compilation of input files 279

1 Introduction

1.1 Background

The Swedish Nuclear Fuel and Waste Management Company (SKB) has conducted site investigations at two different locations, the Forsmark and Laxemar-Simpevarp areas (Figure 1-1), with the objective of siting a final repository for spent nuclear fuel according to the KBS-3 concept. The Forsmark site has been chosen as the actual location of the repository. In conjunction with the preparatory work for an application of a final repository for spent high-level nuclear fuel, information from a series of groundwater flow modelling studies is evaluated to serve as a basis for an assessment of the repository's design and long-term radiological safety premises. The present report is one of a series of three groundwater flow modelling studies, which together handle different periods of the entire lifetime of a final repository at Laxemar-Simpevarp to provide a comparison to corresponding studies for Forsmark. The three modelling studies are:

- Groundwater flow modelling of the excavation and operation phases – (/Svensson and Rhén 2010/).
- Groundwater flow modelling of periods with temperate climate conditions – Laxemar (this report).
- Groundwater flow modelling of periods with periglacial and glacial climate conditions – Laxemar (/Vidstrand et al. 2010/).

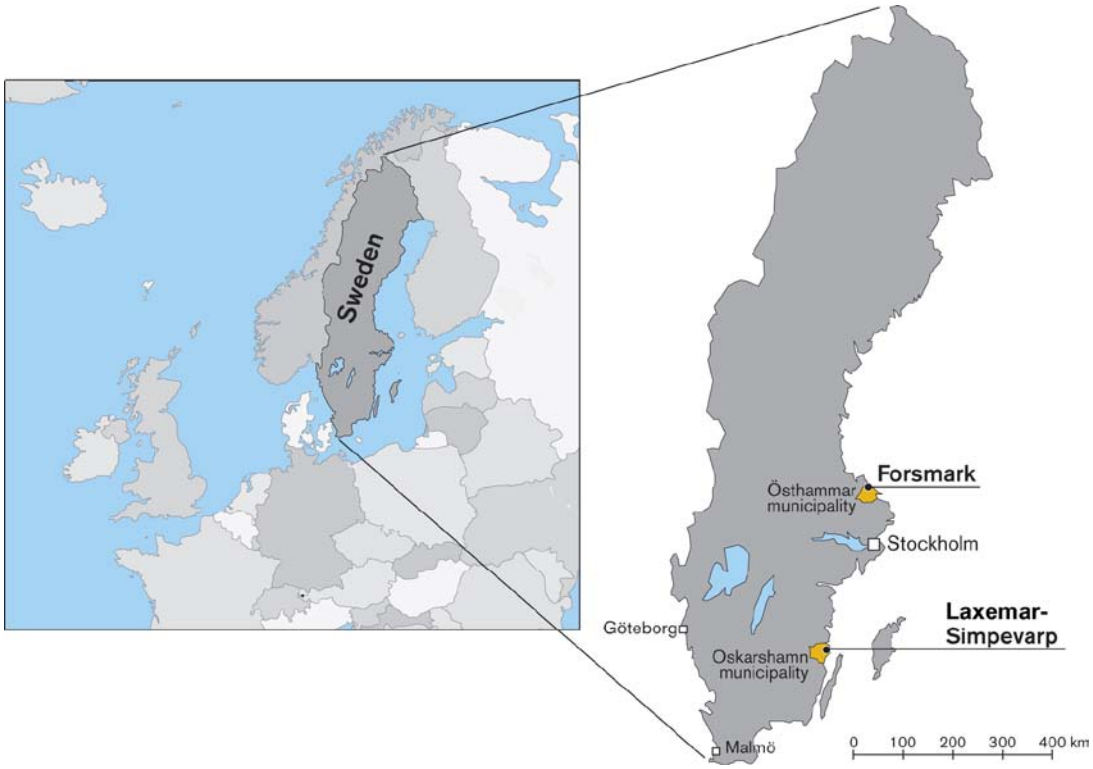

Figure 1-1. *Map of Sweden showing the location of the Forsmark and Laxemar-Simpevarp sites, located in the municipalities of Östhammar and Oskarshamn, respectively. (Figure 1-1 in /SKB 2008a/).*

1.2 Scope and Objectives

The main objective of the modelling work reported here is to model the hydrogeology of the Laxemar-Simpevarp site during the temperate period from 8000 BC to 15,000 AD and to calculate performance measures for the intended repository. The time period 2000 AD to 15,000 AD represents the interval following the closure, backfilling and saturation of the repository.

The main items studied in this work are:

- Exit locations and performance measures for particles released from the canister locations in the repository.
- The effect of stochastically varying the hydraulic properties of the discrete fracture network (DFN).
- The effect of an alternative description of the statistical properties of the flowing fractures (an alternative Hydro-DFN model, called the Elaborated Hydro-DFN).
- The effect of excluding minor deformation zones (MDZs).

The modelling work used the ConnectFlow software /Serco 2010a/, which allowed modelling on different scales to be carried out using both continuous porous medium (CPM) and discrete-fracture network (DFN) concepts, including embedded CPM/DFN models. The use of a DFN concept provides more detailed flow and transport modelling of fractured rock, allowing the tails in the distributions of the performance measures to be captured.

1.3 Setting

The Laxemar-Simpevarp area is located on the Swedish east coast near Oskarshamn and c. 350 km south of Stockholm.

The Laxemar-Simpevarp regional model area is dominated by a geological unit referred to as the Transscandinavian Igneous Belt (TIB). The bedrock is dominated by well preserved c. 1.8 Ga intrusive rocks varying in composition between granite-syenitoid-dioritoid-gabbroid. Although a non-uniformly distributed faint to weak foliation, is present, the most prominent ductile structures at Laxemar are discrete, low-temperature, brittle-ductile to ductile shear zones of mesoscopic to regional character, which are related to the waning stages of the Svecokarelian Orogeny. Subsequently, the rock mass has been subjected to repeated phases of brittle deformation, under varying regional stress regimes, involving reactivation along earlier formed structures. There are indications that the ductile anisotropy, including both larger ductile shear zones as well as the weak to faint foliation, minor shear zones and mylonites, has had an influence on the later brittle deformation. With a few exceptions, the deterministically modelled deformation zones at Laxemar are characterised by brittle deformation although virtually all the zones have their origin in an earlier ductile regime. The brittle history of the Laxemar-Simpevarp area is complex and involves a series of reactivation events that do not allow the construction of a consistent simple model covering their development. /Wahlgren et al. 2008/. /Söderbäck 2008/ provides a detailed description of the geological evolution of the Fennoscanian Shield in south-eastern Sweden from c. 1.91 Ga and to the Quaternary period.

The investigated area is close to the coast, cf. Figure 1-2. The topography is fairly flat (regional topographic gradient in the order of 4%; the topography corresponds to the Sub-Cambrian Peneplain /Fredén 2002/) but with relatively distinct valleys, cf. Figure 1-3 and Figure 1-4. The investigation area is located within a crystalline basement, mostly covered by a rather thin till in the elevated areas and with glaciofluvial sediments in the larger valleys. The site-average annual precipitation and specific discharge are estimated to be on the order of 600 mm and 160–170 mm, respectively /Werner et al. 2008, Larsson-McCann et al. 2002/ and the area is covered with a fairly large number of small streams indicating small local drainage basins within the regional model area, cf. Figure 1-2. The Äspö Hard Rock laboratory is an underground research facility that is located below the Äspö Island, cf. Figure 1-2, and the facility affects the groundwater flow locally in the area. The Simpevarp peninsula hosts the Clab interim facility and the nuclear power plants O1, O2 and O3. At Clab, inflows are observed to the rock caverns near the surface and the shallow shafts surrounding the foundations of the power plants, but it has a very local effect on the groundwater flow. The hydrogeology of the area is described in more detail in /Rhén and Hartley 2009/.

The regional and local model areas employed for model version SDM-Site Laxemar are shown in Figure 1-5. The *Laxemar-Simpevarp regional (scale) model area/volume* (Later in the report referenced as *Regional model area/volume*) for SDM-Site Laxemar is the same as the one used in model version Laxemar 1.2.

Laxemar local (scale) model area/volume (Later in the report referenced as *Local model area/volume*) for model version SDM-Site Laxemar and *Focused area/volume* for the *complete site investigations* is the central, southern and western parts of the local model area, cf. Figure 1-5.

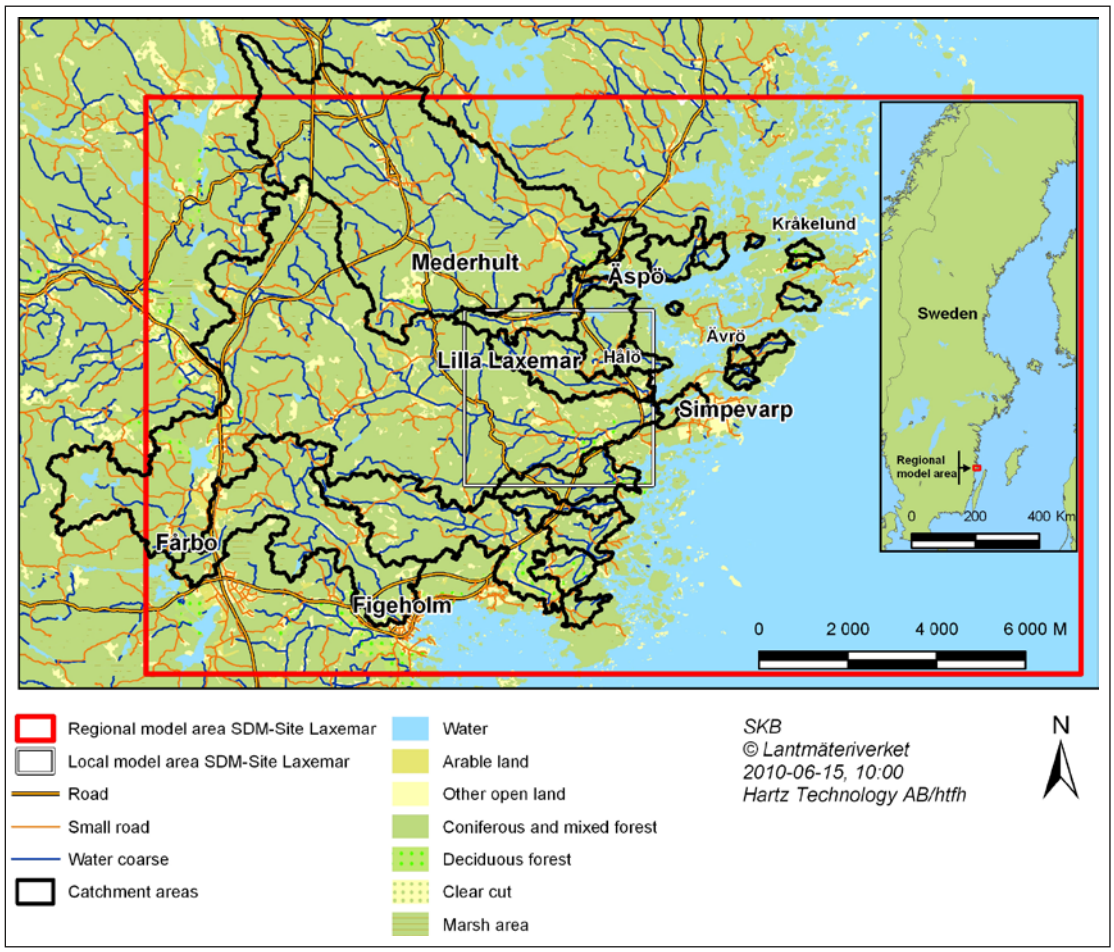

Figure 1-2. *Overview map of the Laxemar-Simpevarp regional model area with the SDM-Site Laxemar local model area indicated. The large number of small streams indicates small local drainage basins within the regional model area. /Rhén and Hartley 2009/.*

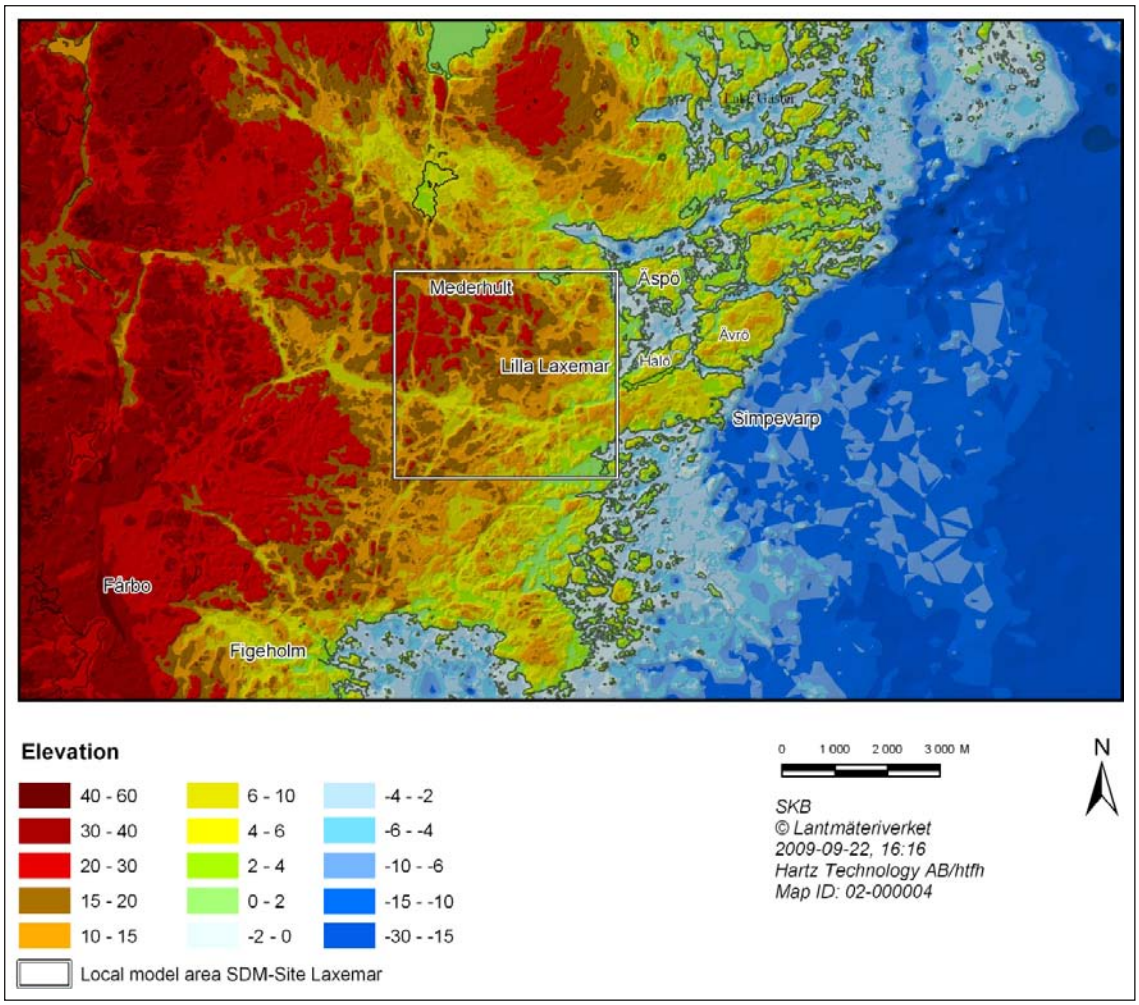

Figure 1-3. *Overview map illustrating the elevation of the ground-surface topography (m.a.s.l.) in an area corresponding to the Laxemar-Simpevarp regional model area, including the bathymetry of lakes and the sea. /Rhén and Hartley 2009/.*

Figure 1-4. *Air photographs showing the flat topography, low gradient near shore situation in the Laxemar-Simpevarp area with shallow bays, a) view from the southeast, Clab facility in the foreground, b) view from the west, drill site KLX05/KLX12A in the centre of the photograph. Both photographs show the outline of the focused area in Laxemar in red, cf. Figure 1-5. /Rhén and Hartley 2009/.*

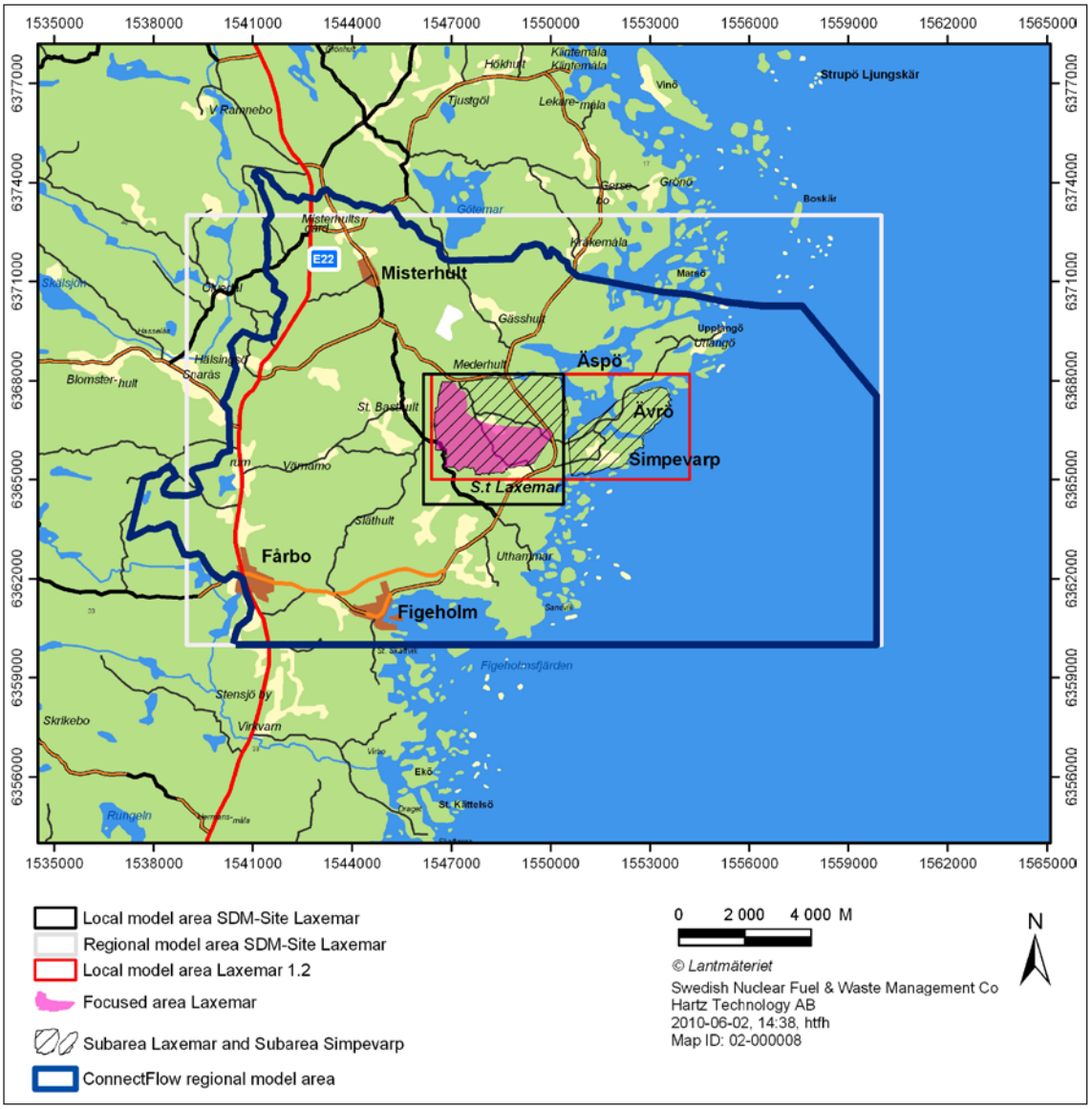

Figure 1-5. *Regional and local model areas used for model version SDM-Site Laxemar. The area coverage of the regional model is the same as that employed in previous model versions, whereas the local model area is significantly reduced compared to that employed in model version Laxemar 1.2. Laxemar subarea and Simpevarp subarea defined the investigation areas during the initial stage of the site investigations. The choice of boundaries used for the SDM-Site regional groundwater flow simulations (using ConnectFlow) based on surface water catchments is also shown. /Rhén and Hartley 2009/.*

1.4 This report

In Chapter 4 of the work reported here, we describe the Hydrogeological base case models used for carrying out the groundwater flow and transport calculations during the temperate period at Laxemar-Simpevarp. These models implement the conceptual understanding derived in SDM-Site, as described in Chapter 2. Chapter 2 is shared by all three modelling reports listed in Section 1.1. Chapter 3 describes the modelling concepts and methodology used. Chapter 5 describes the models used for several variants of the Hydrogeological base case. Chapter 6 presents the main results of the modelling and the overall conclusions are given in Chapter 7.

Appendix A gives a glossary of the abbreviations and symbols used in the report.

Appendix B describes the formats of some of the output files produced.

Appendix C gives the full set of modelling results.

Appendix D gives a derivation of the performance measure equations.

Appendix E presents the details of the Elaborated Hydro-DFN model.

Appendix F presents the changes in the regional-scale palaeo-hydrogeological modelling relative to SDM-Site Laxemar.

Appendix G is a comparison of tunnel inflows under open repository conditions between ConnectFlow and Darcy Tools.

Appendix H is an analysis of the time taken for fresh water to penetrate to repository depths.

Appendix I is a compilation of the input files used for the modelling.

2 Hydrogeological model of the Laxemar site

2.1 Supporting documents

The SDM-Site Laxemar hydrogeological reporting in /Rhén and Hartley 2009/ provides a detailed summary of the work described in /Rhén et al. 2008/ and in /Rhén et al. 2009/, i.e. the field investigations, the data analyses, the conceptual model development and the numerical modelling of groundwater flow and solute transport. The complete SDM-Site Laxemar site-descriptive modelling work is reported in /SKB 2009a/ and the overall confidence assessment associated with the modelling work is detailed in /SKB 2009b/.

Table 2-1 shows the cumulative number of boreholes providing hydraulic information about the bedrock in the Laxemar-Simpevarp area. The number of boreholes is shown in relation to the two investigation stages; Initial Site Investigations and Complete Site Investigations (ISI and CSI), the five model versions (Version 0, Simpevarp 1.1, Simpevarp 1.2 and Laxemar 1.2, and model version SDM-Site Laxemar) carried out during the period 2002–2008. Model version Laxemar 1.2 represents the culmination of the ISI. The current hydrogeological modelling based on data freeze Laxemar 2.3 constitutes the principal contribution to SDM-Site Laxemar, corresponding to the CSI from a hydrogeological point of view. Investigations in ca. 4,000 m of deep cored boreholes (KLX01–04) provided old and new (from ISI) hydraulic data within the Laxemar local model area for model version Laxemar 1.2. After Laxemar Stage 2.3 (CSI) hydraulic data from 16 additional deep cored boreholes within the Laxemar local model area with an approximate total length of 12,800 m were available (KLX05, KLX06, KLX07A, KLX08, KLX09, KLX10, KLX11A, KLX12A, KLX13A, KLX15A, KLX16A, KLX17A, KLX18A, KLX19A, KLX20A, KLX21B).

Table 1-1 also shows references to the major background reports in relation to each model version/ stage /Follin et al. 2004, 2005, 2006, Hartley et al. 2004, 2005, 2006a, b, c, 2007, Holmén 2008, Rhén et al. 1997, 2006a, b, c, 2008, 2009, SKB 2002, 2004, 2005, 2006a, b/.

Table 2-1. The cumulative new (drilled during site investigation) number of boreholes providing hydraulic information about the bedrock in the Laxemar-Simpevarp area at the end of the five model versions carried out during the period 2002 through 2008. Kxx = core-drilled boreholes, Hxx = percussion-drilled boreholes (KLX and HLX: core-drilled boreholes or percussion-drilled boreholes within the Laxemar local model area). The reports listed in italics describe the hydraulic data collected and/or the hydrogeological modelling undertaken. The reports with underlined reference numbers summarise the development of the hydrogeological modelling along with the developments achieved within the other disciplines. /Rhén and Hartley 2009/.

	Initial site investigation (ISI)			Complete site investigation (CSI)	
Desk top exercise	**Training exercise**	**Preliminary SDM**	**Preliminary SDM**	**Feedback and strategy**	**Model verification and uncertainty assessment**
Version 0	**Version 1.1**	**Simpevarp Version 1.2**	**Laxemar Version 1.2**	**Laxemar Stage 2.1**	**Laxemar Stage 2.3 (Version SDM-Site)**
0 Kxx 0 Hxx	0 Kxx [(1)] 0 Hxx	4 Kxx [(2)] 3 Hxx	9 Kxx [(3)] 14 Hxx 3 KLX (7%)[(3)] 9 HLX(26%)	11 KLX (25%)[(4)] 9 HLX (26%)[(4)]	44 KLX (100%)[(5)] 34 HLX (100%)
R-02-35 *TR-97-06*	R-04-25 *TR-97-06* *R-04-63* *R-04-65*	R-05-08 *R-06-20* *R-05-11* *R-05-12*	R-06-10 *R-06-21* *R-06-22* *R-06-23* *R-06-24*	R-06-110 *R-07-57* *R-08-60*	TR-09-01 *R-08-78* *R-08-91* *R-08-92*

[(1)]: Some old data from KLX01 and KLX02 were used besides earlier interpretations from the area.

[(2)]: Old data from KLX01, KLX02, KAV01, KAV02 and KAV03 also used besides the indicated three KSH holes and KAV01 with some new data.

[(3)]: KLX02–04. KLX02 included as some new tests were performed in that borehole. A few data from KLX05 and KLX06 were also available but these boreholes are not included here as the large amount of data became available later. Kxx also includes three KSH holes, KAV01, KAV04A, and KAV04B. Old data from KLX01 also used but not included in the numbers in the table.

[(4)]: KLX02–12 included but data not complete for all these boreholes at this stage. Old data from KLX01 also used. New HLX boreholes were not considered.

[(5)]: 19 core holes longer than 300 m and 25 shorter than 300 m. KLX01 and KLX27A not included.

2.2 Systems approach in SDM-Site

In order to meet the objectives for model version SDM-Site Laxemar /Rhén and Hartley 2009/, the groundwater system is divided into different hydraulic domains. Figure 2-1 illustrates schematically SKB's systems approach as employed in the hydrogeological SDM for Laxemar. The groundwater system consists of three basic hydraulic domain types, namely HSD, HCD and HRD, where:

- HSD (Hydraulic Soil Domain) represents the Quaternary deposits.
- HCD (Hydraulic Conductor Domain) represents deformation zones.
- HRD (Hydraulic Rock mass Domain) represents the fractured bedrock between the deformation zones.

The systems approach constitutes the basis for the conceptual modelling, the site investigations and the numerical simulations carried out in support of the hydrogeological SDM /Rhén et al. 2003/.

Besides the three hydraulic domains shown in Figure 2-1, the groundwater flow (saturated flow) and solute transport modelling consists of three additional elements:

- A solute (salt) transport model for the modelling of advective transport and matrix diffusion.
- Initial conditions for groundwater flow and hydrochemistry.
- Boundary conditions for groundwater flow and hydrochemistry.

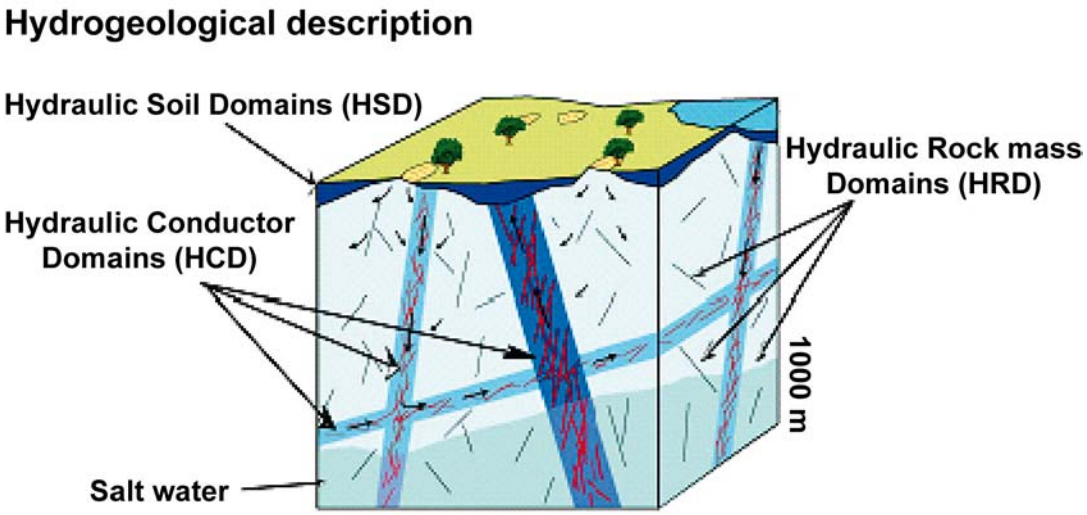

Figure 2-1. *Cartoon showing the division of the crystalline bedrock and the overburden (Quaternary deposits) into hydraulic domains. Within each domain, the hydraulic properties are represented by equivalent values, or by spatially distributed statistical distributions /Rhén et al. 2003/.*

2.3 Summary of the bedrock hydrogeological model

2.3.1 General

Single-hole hydraulic tests, interference tests, groundwater levels and hydrochemical data are the basis for the hydrogeological characterisation, together with the geological model. The PFL-f (f stands for fracture or feature) method is essential for the hydrogeological model. The PFL-f method is a geophysical logging device developed to detect continuously flowing features in sparsely fractured crystalline bedrock by means of difference flow logging, using a 1 m test section that is moved stepwise 0.1 m. The PFL method essentially provides an estimate of the specific capacity (Q/s) [L^2T^{-1}], where s represents the drawdown and Q the flow rate. Transient injection tests with PSS have been performed using 3 different test scales: 5, 20 and 100 m with 5 m tests only being performed in the elevation interval –300 m to –700 m, covering the foreseen repository depth, cf. /Rhén and Hartley 2009/ for details.

The Laxemar-Simpevarp regional model area is in general characterised by an undulating bedrock surface with a thin cover of Quaternary deposits, mainly till on the top of the hills and thicker Quaternary deposits in the valleys made up of till overlain by postglacial deposits. The crystalline bedrock is intersected by a number of deformation zones, denoted Hydraulic Conductor Domains (HCD) in the hydrogeological model, which are mainly steeply dipping, with less fractured bedrock between these zones. The bedrock in between the HCDs is in the hydrogeological model called Hydraulic Rock mass Domains (HRD). Hydraulically, the deformation zones are generally more conductive than the bedrock in between. The general tendency within the Laxemar-Simpevarp regional model volume is that the hydraulic conductivity decreases with depth in both HCDs and HRDs. The Quaternary deposits, called Hydraulic Soil Domains (HSD) in the hydrogeological model are generally more conductive than the bedrock. Figure 2-2 shows a generalised vertical section illustrating the overall hydrological and hydrogeological conceptual model of the Laxemar-Simpevarp area. The hydrogeological characteristics of the HCDs, HRDs and HSDs are further described in sections 2.3.2 through 2.3.4 and details are found in /Rhén et al. 2008/.

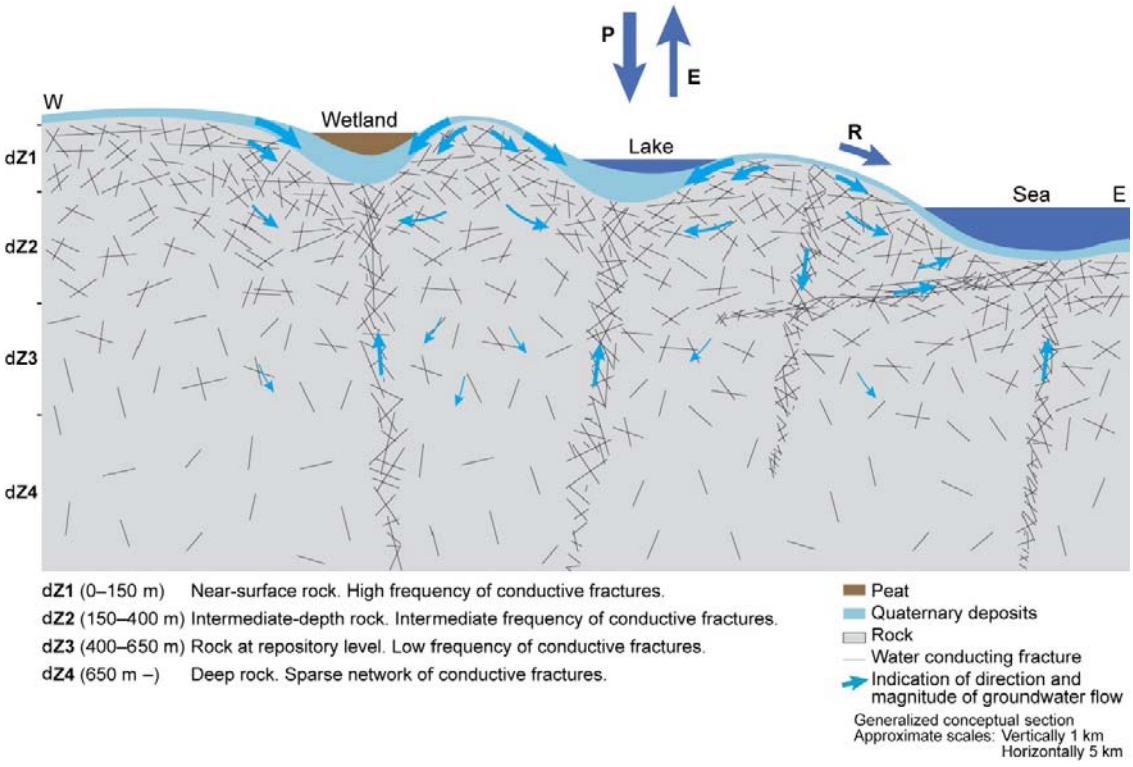

Figure 2-2. *Generalised section illustrating the conceptual model of hydrology and hydrogeology in Laxemar. Note the different horizontal (5 km) and vertical (1 km) scales. Furthermore, the thickness of the Quaternary deposits is exaggerated in the figure. /Rhén and Hartley 2009/.*

2.3.2 Hydraulic characteristics of hydraulic conductor domains (HCD)

The deformation zone model, as implemented in the SDM-Site regional scale flow model, is shown in Figure 2-3.

The key interpreted characteristics are:

- A clear trend of decreasing transmissivity with depth.
- A positive correlation between interpreted deformation zone "size" and transmissivity. Size here corresponds to interpreted trace length on the surface.
- Indications that the transmissivity of HCDs is dependent on the orientation of deformation zones. E-W zones appear more conductive than zones of other orientations.
- Significant horizontal variability with an estimated standard deviation of $\log_{10}(T)$ of 1.4. The standard deviation of $\log_{10}(T)$ of the entire sample of HCD transmissivities is 1.4 and standard deviation of $\log_{10}(T)$ of transmissivities within individual zones is in the range 0.5 to 2. Sample sizes within individual zones were between 2 to 14.

The data and the general models suggested for the initial assignment of hydraulic properties to HCDs in the groundwater flow modelling are presented in Figure 2-4 cf. a detailed account in /Rhén et al. 2008/. The variability in transmissivity is large but considering mean values for depth zones employed in the HRD modelling, see Figure 2-4, the transmissivity decreases with depth, cf. /Rhén et al. 2008/. There is also a tendency that the transmissivity is positively correlated to the interpreted lineament length of the HCD and also that HCDs with E-W orientations are slightly more transmissive than HCDs of other orientations, cf. /Rhén et al. 2008/.

However, some of the HCDs are intersected by several boreholes at a range of depths and it was judged that there was enough data for assessment of zone-specific trend functions for seven of the HCDs, cf. /Rhén et al. 2008/.

An exponential trend model is used for the depth trend of the transmissivity:

$$T(z) = 10^{(a+B\cdot z)} \qquad (2\text{-}1)$$

z: Elevation in m (m.a.s.l.) (z defined positive up). The coefficients *a* and *B* in the exponential trend model are based on a linear regression of $\log_{10}(T)$. See /Rhén et al. 2008/ for details.

Several interference tests have shown that dolerite dykes may act as hydraulic barriers, at least locally. The best example relates to the steep N-S oriented HCD ZSMNS001C just west of the focused area, associated with a core of dolerite, cf. /Rhén and Hartley 2009/. Both interference tests and monitoring data show fairly large differences in hydraulic head on either side of two other HCDs associated with dolerite dykes, ZSMNS059A and the KLX19_DZ5-8_dolerite, are also acting as hydraulic barriers, but probably to a lesser degree where the dykes become thinner. Mapping of the cored boreholes and outcropping deformation zones has shown that fault gouge is present in some deformation zones. This implies that these HCDs can exert some hydraulic barrier effect, most likely highly localised.

The distribution of the mean transmissivity in the HCD for the *base case*[1] is shown in Figure 2-5. For stochastic realisations with horizontal heterogeneity within SDM-Site, these values are used as the mean sampled value for a log-normal distribution with specified standard deviation, but truncated at ± 2 standard deviations. Equivalent plots for one example realisation of the HCD with spatial variability, standard deviation in $\log_{10}(T) = 1.4$, is shown in Figure 2-6. In both cases, the heterogeneous transmissivity field is conditioned to measured values at the intercept with borehole intervals where measurements are available.

[1] *"Base case"* in /Rhén and Hartley 2009/ accounting for the SDM-Site Laxemar modelling corresponds to "*Deterministic base model simulation"* in the SDM-Site Forsmark modelling /Follin 2008/.

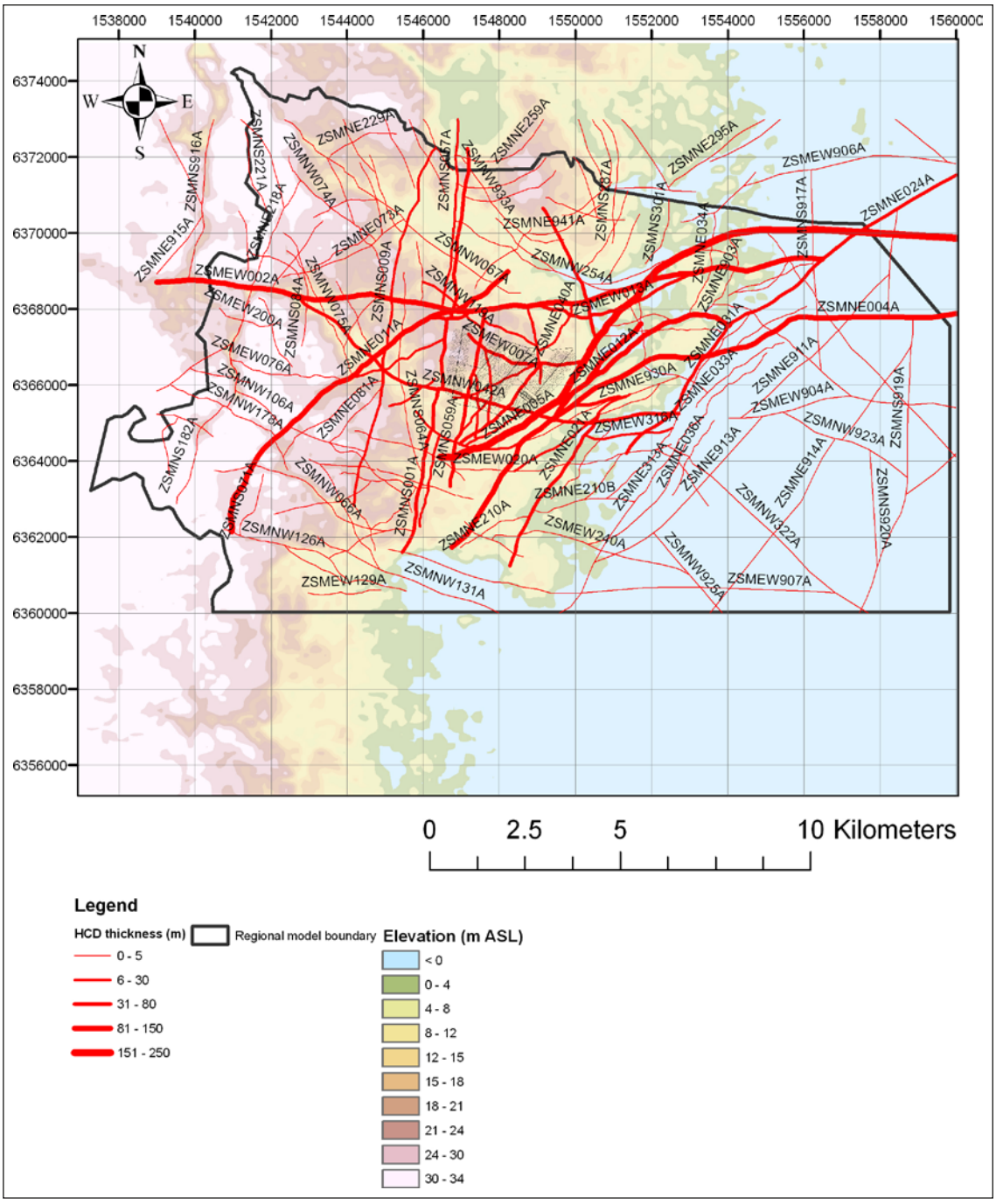

Figure 2-3. *Deformation zones included in the SDM-Laxemar deterministic deformation zone model. Colouring of zones is according to judged thickness.*

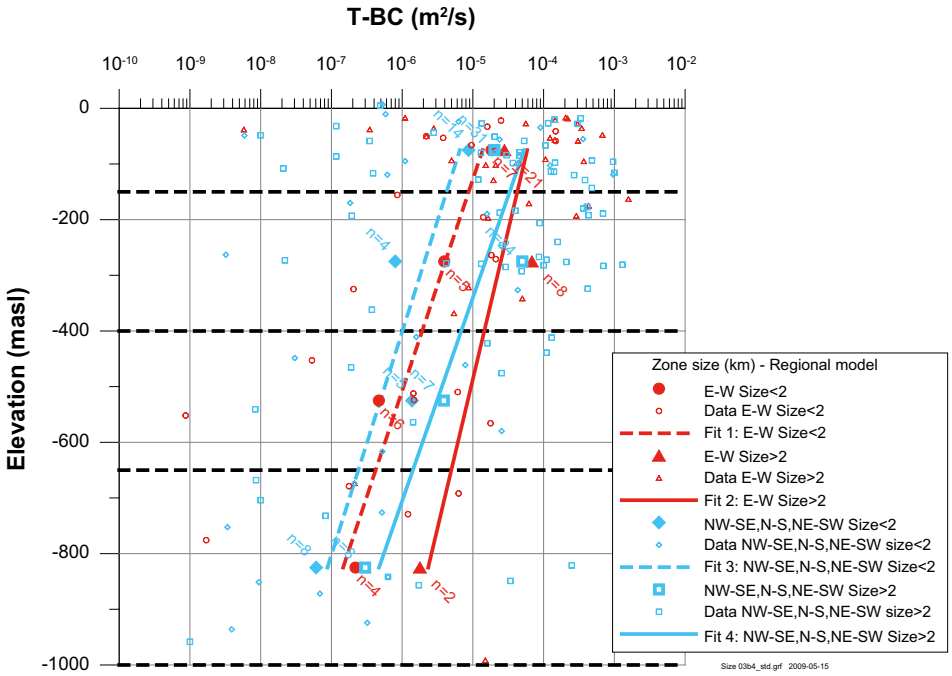

Figure 2-4. *Deformation zone transmissivity (T) related to deformation zone orientations in the horizontal plane and size, versus elevation for the regional model. Mean of $log_{10}(T)$, plotted as well as the number of observations (n). Regression line based on Mean of $log_{10}(T)$ /Rhén and Hartley 2009/.*

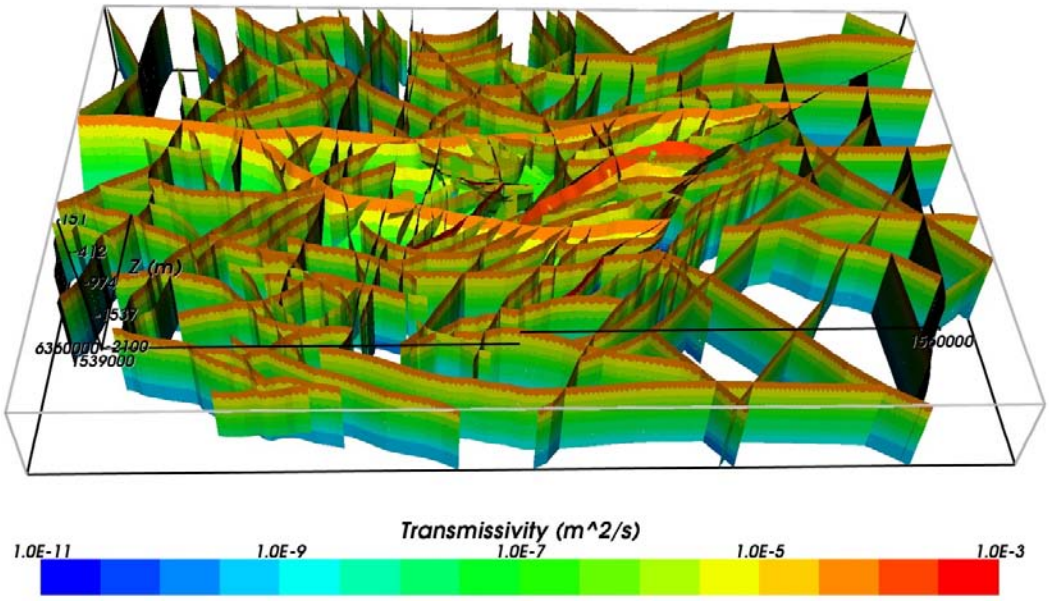

Figure 2-5. *All HCDs and their inferred depth dependent transmissivity for the deterministic base case model. Oblique view looking from the south. /Rhén and Hartley 2009/.*

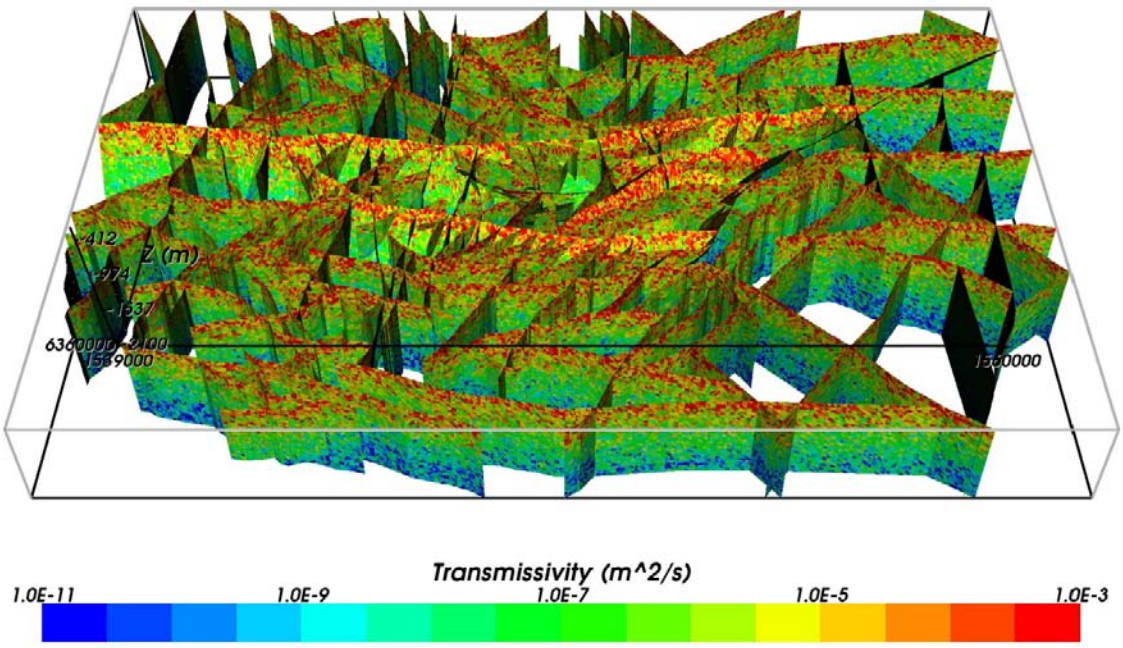

Figure 2-6. *All HCDs and their inferred depth dependent transmissivity for a case with spatial variability and a standard deviation in Log(T) of 1.4. Oblique view looking from the south. /Rhén and Hartley 2009/.*

2.3.3 Hydraulic characteristics of hydraulic rock mass domains (HRD)

The hydraulic rock mass domain model, as implemented in the SDM-Site regional scale flow model, is shown in Figure 2-7 through Figure 2-10. According to /Rhén et al. 2008/, four separate hydraulic rock mass domains (HRD) should be modelled in the local model area; HRD_C, HRD_EW007, HRD_N and HRD_W, that are based on the fracture domains, cf. Figure 2-9, Figure 2-10 and /Wahlgren et al. 2008/.

The key interpreted characteristics are:

- The flowing features (fractures and minor deformation zones) can be grouped in four orientation sets; steep ENE, WNW, N-S and a sub-horizontal set.
- The intensity of flowing features is generally highest for the WNW set (aligned with the principal horizontal stress) with the sub-horizontal set also being important in the upper bedrock.
- A clear decreasing intensity of flowing features with depth but generally with a similar transmissivity distribution of the flowing features for the specific depth interval studied (as measured by difference flow logging; PFL-f).
- As a consequence, a resulting clear trend of decreasing hydraulic conductivity with depth, (injection tests, test scale 100 m) may be observed.
- The hydraulic conductivity is c. 10 times lower in HRDs than that of the HCDs (injection tests, test scale 100 m).

The rock mass in the regional model, outside the defined four HRDs mentioned above, is based on the material property assignments made in model version Laxemar 1.2 /SKB 2006b, Rhén et al. 2006c/ (summarised in /Rhen et al. 2009/) and assessments of similarities between regional HRDs and the newly developed HRDs inside the Laxemar local model volume; HRD_C, HRD_EW007, HRD_N and HRD_W, cf. Table 2-2.

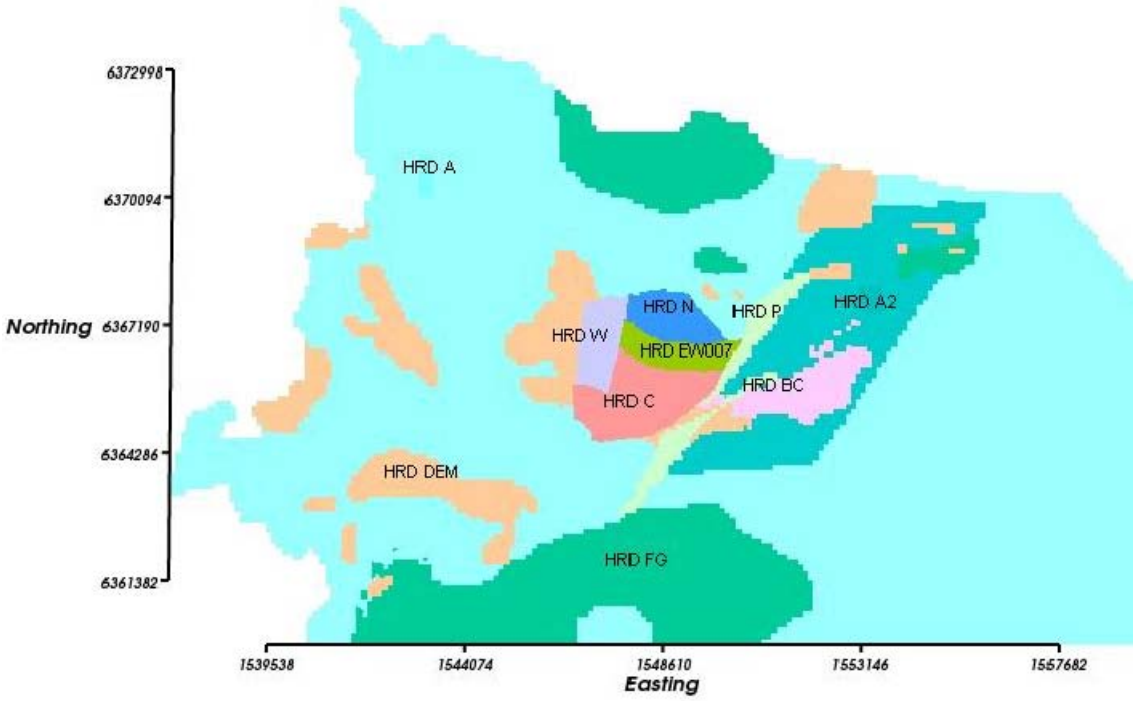

Figure 2-7. *Hydraulic rock mass domains on the top surface of the bedrock in the regional scale hydrogeological model. /Rhén and Hartley 2009/.*

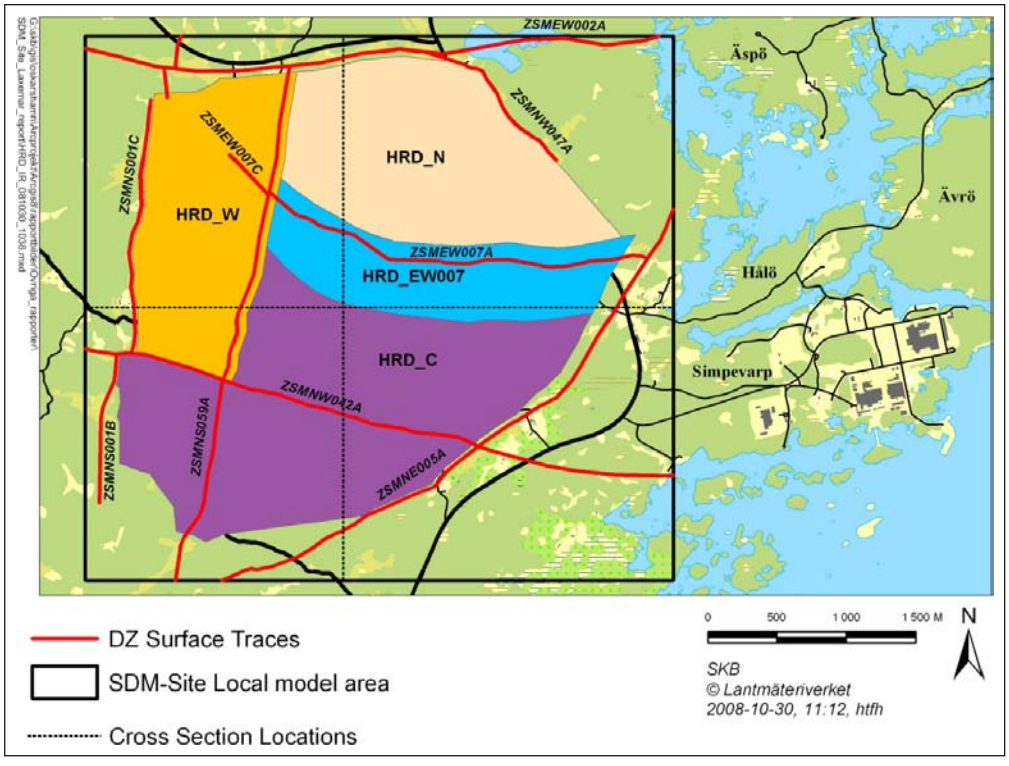

Figure 2-8. *Illustration of the SDM-Site Laxemar Hydraulic Rock mass Domain Model. Horizontal view. /Rhén and Hartley 2009/.*

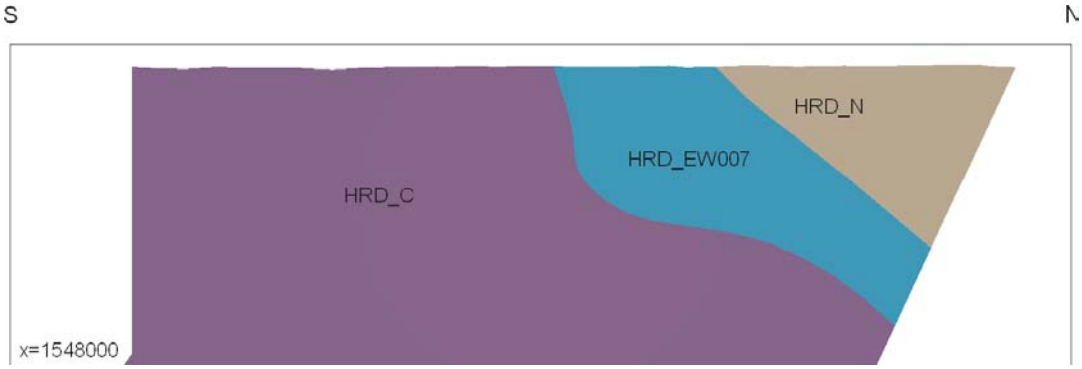

Figure 2-9. *Illustration of the SDM-Site Laxemar Hydraulic Rock mass Domain Model. Top: horizontal view. Vertical section from south (left) to north at Easting's X = 154,800 m, /Rhén and Hartley 2009/.*

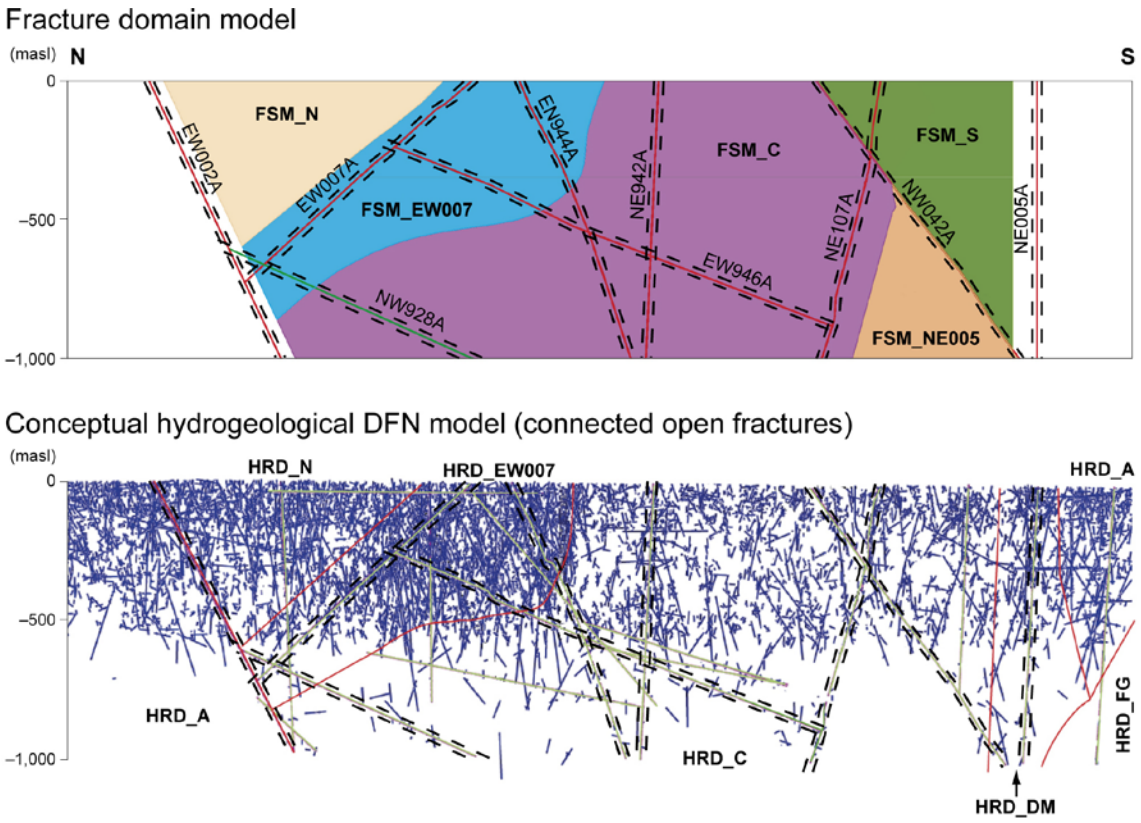

Figure 2-10. *Comparison of conceptual models for fracture domains, hydraulic DFN and associated hydraulic rock mass domains along the N-S section cf. Figure 2-8. The length of the section is ~ 4,300 m. /SKB 2009a/.*

Table 2-2. Proposed hydraulic property assignment of the regional-scale hydraulic rock mass domains to be used in SDM regional groundwater flow modelling /Rhén et al. 2008/.

Regional hydraulic rock mass domain	Suggested hydraulic properties based on hydrogeological DFN
HRD_A	HRD_N
HRD_A2	HRD_N, but rock below –650 m.a.s.l. is the same as –400 m.a.s.l. to –650 m.a.s.l.
HRD_D-E-M	HRD_C
HRD_B-C	HRD_C
HRD_F-G	HRD_N, 10 times higher T
HRD_P	HRD_N

2.3.4 Hydraulic characteristics of the focused volume

The focused volume comprises HRD_C, HRD_W and the southern part of HRD_EW007, cf. Figure 1-5 and Figure 2-8. HRD_EW007 is more conductive compared to HRD_C and HRD_W. An example of data used for the calibration of the hydrogeological DFN model is shown in Figure 2-11. The *base case* for SDM-Site Laxemar assumes a semi-correlated transmissivity model, cf. Table 2-3. The general characteristics of the HRDs are summarised in Table 2-4 and in Table 2-5 an example of hydrogeological DFN parameters is shown.

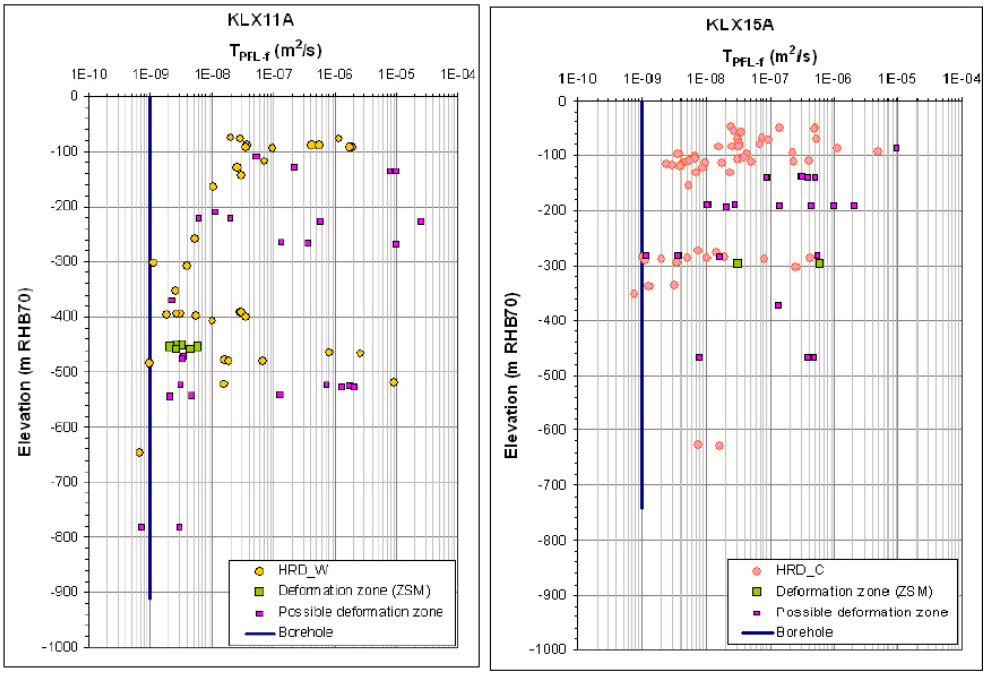

Figure 2-11. *Measured transmissivities(based on PFL-f) in fractures in a) deformation zones and b) in fracture domains in boreholes in the focused volume exemplified with two boreholes; KLX11A (HRD_W) and KLX15A (HRD_C) /SKB 2009a/.*

Table 2-3. Transmissivity parameters used for all sets when matching measured PFL-f flow distributions. (Log base 10) /Rhén et al. 2008/.

Type	Description	Relationship	Parameters
Correlated	Power-law relationship	$\log(T) = \log(a\, r^{b})$	a , b
Semi-correlated	Log-normal distribution about a power-law correlated mean	$\log(T) = \log(a\, r^{b}) + \sigma_{\log(T)}\, N[0,1]$	a , b, $\sigma_{\log(T)}$
Uncorrelated	Log-normal distribution about a specified mean	$\log(T) = \mu_{\log(T)} + \sigma_{\log(T)}\, N[0,1]$	$\mu_{\log(T)}$, $\sigma_{\log(T)}$

Table 2-4. Schematic summary of groundwater flow and solute transport characteristics under the current temperate climate conditions.

Depth zone	General characteristics
dZ1: > –150m	Near-surface rock, characterised by a high intensity of conductive fractures. Sub-horizontal and steeply dipping fractures striking WNW dominate. Advection dominated – high groundwater flow rates with sub horizontal fracturing giving $K_h > K_v$ in many areas. Flushed by post-glacial meteoric water. High fracture intensity implies matrix blocks 1–2 m in size, which gives equilibrium between fracture and matrix on timescales of ~1,000 years.
dZ2: –150m to –400m	Intermediate-depth rock, characterised by an intermediate intensity of conductive fractures. Steeply dipping fractures striking WNW dominate except in HRD_W where no set is clearly dominant and in HRD_N and HRD_C the sub horizontal set is also important beside the WNW set. Some advection, but rock matrix diffusion (RMD) retards post-glacial meteoric penetration. Fracture intensity is generally much lower, reducing groundwater flux and increasing matrix blocks to typically ~5 m in size, such that porewater chemistry lags behind that of the fracture water by 1,000s of years.
dZ3: –400m to –650m	Rock at repository level, characterised by a low intensity of conductive fractures. Steeply dipping fractures striking WNW dominate except for HRD_W where no set is clearly dominant. Low advection. RMD important because advective flow rates are small. Fracture intensity lower still, with typical matrix blocks ~10 m in size, such that porewater chemistry lags behind that of fracture water ~10,000 years.
dZ4: < –650m	Deep rock, characterised by a sparse network of conductive fractures. Steeply dipping fractures striking WNW dominate except for HRD_W where no set is clearly dominant (however rather few data occur within dZ4). Very low advection. RMD dominates Fracture intensity very low, with typical matrix blocks ~100 m in size, such that porewater chemistry lags behind that of fracture water ~100,000 years.

Table 2-5. Description of the calibrated hydrogeological DFN input parameters for HRD_C with fixed r_0 = 0.038 m and intensity of open fractures based OPO (Open and Partly Open fractures). /Rhén et al. 2008/.

Depth zone (m.a.s.l.)	Set	Orientation set pole: (trend, plunge), conc. (°,°,-)	Fracture radius model power-law (k_r, r_0)	Intensity P_{32} (m^2/m^3) of open fractures	Transmissivity model T (m^2/s) (a, b, σ) See Table 2-3.
–150 to 0	ENE	(155.1,3.4), 9.6	(2.6, 0.038)	0.52	SC: ($6\cdot10^{-8}$, 0.5, 0.4) UC: ($2\cdot10^{-7}$, 0.6) C: ($2\cdot10^{-8}$, 0.9)
	WNW	(204,1.6), 12	(2.5, 0.038)	0.95	SC: ($2\cdot10^{-7}$, 0.6, 0.7) UC: ($1\cdot10^{-5}$, 0.9) C: ($5\cdot10^{-8}$, 1.1)
	N-S	(270.2,8.4), 7.8	(2.7, 0.038)	0.54	SC: ($2\cdot10^{-7}$, 0.6, 0.5) UC: ($1\cdot10^{-7}$, 0.7) C: ($6\cdot10^{-8}$, 1.2)
	SubH	(46.3,84.7), 12	(2.7, 0.038)	1.20	SC: ($1.5\cdot10^{-7}$, 0.7, 0.7) UC: ($3\cdot10^{-7}$, 0.8) C: ($6\cdot10^{-8}$, 1.0)
–400 to –150	ENE	(155.1,3.4), 9.6	(2.85, 0.038)	0.47	SC: ($1\cdot10^{-6}$, 0.7, 0.7) UC: ($2\cdot10^{-7}$, 0.7) C: ($5\cdot10^{-8}$, 1.4)
	WNW	(204,1.6), 12	(2.45, 0.038)	0.55	SC: ($8\cdot10^{-8}$, 0.3, 0.1) UC: ($3\cdot10^{-7}$, 0.6) C: ($2\cdot10^{-9}$, 1.3)
	N-S	(270.2,8.4), 7.8	(2.85, 0.038)	0.63	SC: ($1\cdot10^{-7}$, 0.7, 0.7) UC: ($2\cdot10^{-7}$, 0.4) C: ($3\cdot10^{-8}$, 1.0)
	SubH	(46.3,84.7), 12	(2.85, 0.038)	0.71	SC: ($1.5\cdot10^{-7}$, 0.8, 0.9) UC: ($8\cdot10^{-7}$, 1.4) C: ($3\cdot10^{8}$, 1.1)

Depth zone (m.a.s.l.)	Set	Orientation set pole: (trend, plunge), conc. (°,°,-)	Fracture radius model power-law (k_r, r_0)	Intensity P_{32} (m^2/m^3) of open fractures	Transmissivity model T (m^2/s) (a, b, σ) See Table 2-3.
–650 to –400	ENE	(155.1,3.4), 9.6	(2.8, 0.038)	0.38	SC: ($5\cdot10^{-7}$, 0.5, 0.5) UC: ($2\cdot10^{-6}$, 0.8) C: ($3\cdot10^{-8}$, 0.7)
	WNW	(204,1.6), 12	(2.5, 0.038)	0.74	SC: ($2\cdot10^{-8}$, 0.6, 0.4) UC: ($1\cdot10^{-7}$, 0.9) C: ($3\cdot10^{-9}$, 0.9)
	N-S	(270.2,8.4), 7.8	(2.9, 0.038)	0.47	SC: ($1\cdot10^{-8}$, 0.4, 0.4) UC: ($8\cdot10^{-8}$, 0.4) C: ($1\cdot10^{-8}$, 0.5)
	SubH	(46.3,84.7), 12	(2.9, 0.038)	0.58	SC: ($3\cdot10^{-7}$, 0.6, 0.6) UC: ($2\cdot10^{-6}$, 0.9) C: ($1.5\cdot10^{-7}$, 0.9)
–1,000 to –650	ENE	(155.1,3.4), 9.6	(2.9, 0.038)	0.46	SC: ($5\cdot10^{-9}$, 0.6, 0.4) UC: ($1\cdot10^{-8}$, 0.4) C: ($5\cdot10^{-9}$, 0.6)
	WNW	(204,1.6), 12	(2.8, 0.038)	0.73	SC: ($5\cdot10^{-8}$, 0.6, 0.4) UC: ($5\cdot10^{-7}$, 0.4) C: ($5\cdot10^{-8}$, 0.6)
	N-S	(270.2,8.4), 7.8	(2.95, 0.038)	0.25	SC: ($5\cdot10^{-9}$, 0.6, 0.4) UC: ($1\cdot10^{-8}$, 0.4) C: ($5\cdot10^{-9}$, 0.6)
	SubH	(46.3,84.7), 12	(2.95, 0.038)	0.35	SC: ($1\cdot10^{-7}$, 0.6, 0.4) UC: ($2\cdot10^{-7}$, 0.4) C: ($1\cdot10^{-7}$, 0.6)

2.4 Summary of the Quaternary deposits hydrogeological model (HSD)

The stratigraphical distribution of Quaternary deposits in the investigated area is rather uniform. Till is the oldest Quaternary deposit in the area, and is consequently resting directly upon the bedrock surface. The till in the valleys is often overlain by glacial clay, which in many valleys is overlain by a thin layer of sand followed by clay gyttja and peat.

The model developed by /Nyman et al. 2008/ contains six layers of Quaternary deposits, denoted Z1–Z6; Z1 represents the upper layer of the Quaternary deposits. These layers, illustrated in the cross section in Figure 2-12, are defined and described briefly in /Rhén et al. 2009/ and in /Nyman et al. 2008, Sohlenius and Hedenström 2008/.

Figure 2-13 shows the modelled distribution of total overburden depth in the Laxemar-Simpevarp regional model area. Figure 2-14 illustrates the variable depth of the Quaternary deposits along a vertical north-south section across the E-W regional deformation zone in the northern part of the local model domain; the Mederhult zone (ZSMEW002A).

This detailed Quaternary deposit model was simplified in the in the SDM-Site regional groundwater flow modelling representing it by four element layers vertically, each of a constant 1 m thickness, with the horizontal extent of the hydrogeological grid element (40–120 m), to represent the HSD. The same hydraulic conductivity tensor was specified for each element in a vertical stack of 4 grid elements, but varied horizontally from element-to-element, and was anisotropic with regard to horizontal and vertical components in order to represent the effective hydraulic properties of the Quaternary deposit layers. The effective hydraulic conductivity tensor for the soil package was calculated according to the actual modelled thickness of the layers of the Quaternary deposits and the hydraulic conductivities of the soil types at that location. HSD properties used in the SDM-Site *base case model* are described in Table 2-6 and illustrated in Figure 2-15. See /Rhén et al. 2009/ for details of the implementation.

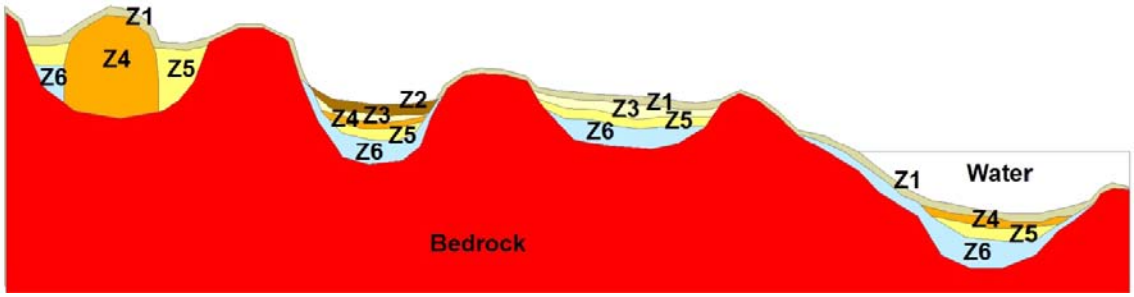

Figure 2-12. *The stratigraphical model which was used for modelling stratigraphy and total depth of Quaternary deposits in the Laxemar-Simpevarp regional model area. /Sohlenius and Hedenström 2008/. Layer Z1–6:*

Layer Z1 represents a thin surface(-affected) layer.

Layer Z2 represents (fen or bog) peat.

Layer Z3 represents postglacial clay, clay gyttja/gyttja clay, gyttja or recent fluvial sediments.

Layer Z4 represents postglacial sand/gravel, glaciofluvial sediments or artificial fill.

Layer Z5 represents glacial clay.

Layer Z6 represents (glacial) till.

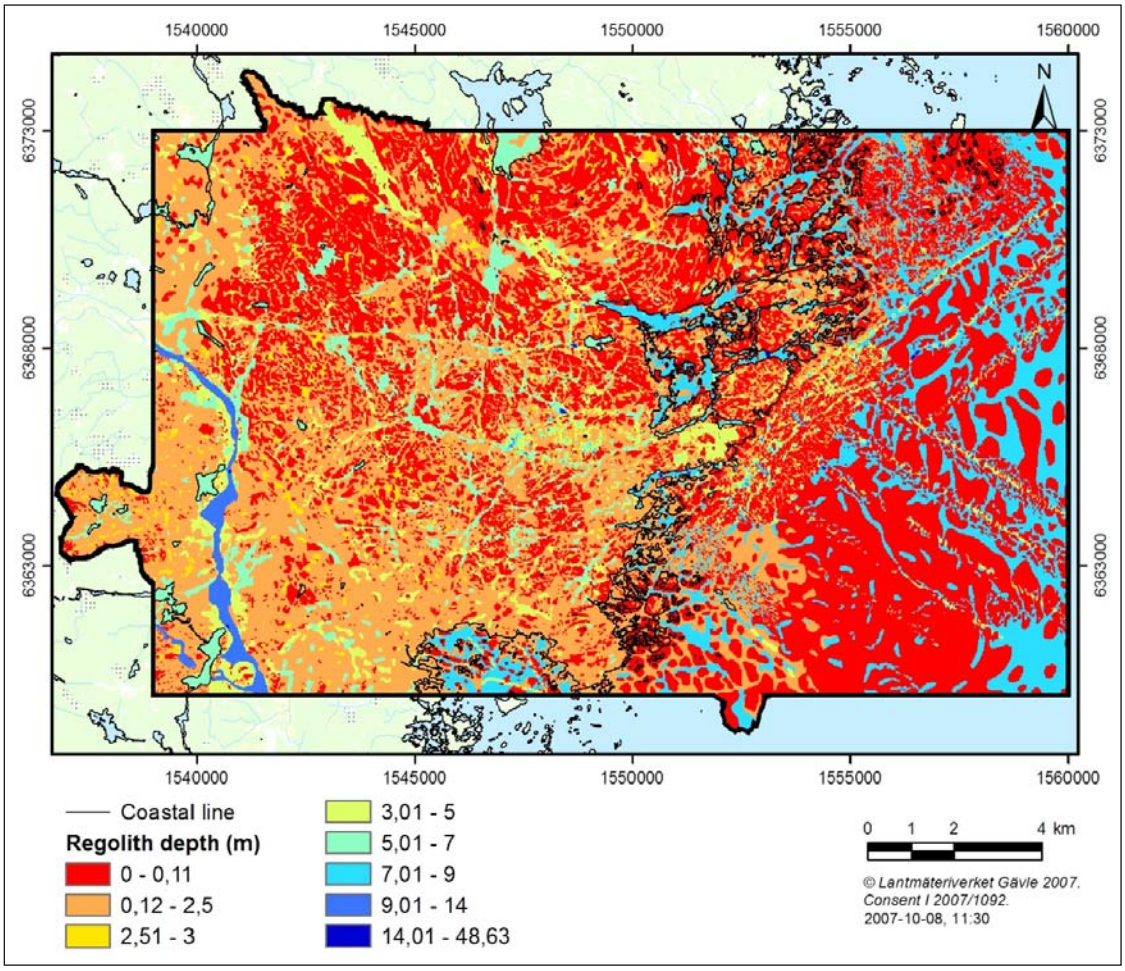

Figure 2-13. *The modelled distribution of total depths of the Quaternary deposits in the Laxemar-Simpevarp area. /Sohlenius and Hedenström 2008/.*

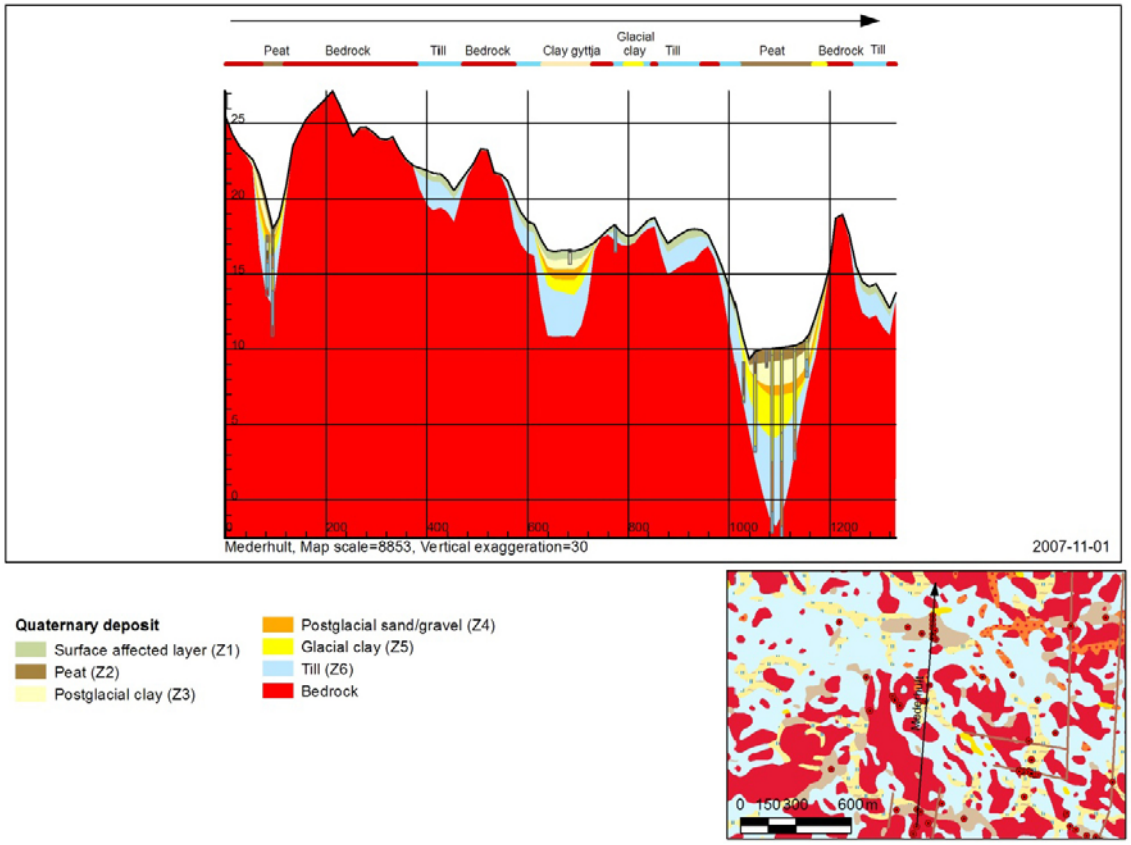

Figure 2-14. *The profile shows the total depth and stratigraphy of the Quaternary deposits in a north-south profile close to Mederhult. The valley in the right part of the profile (between 1000 and 1200 on the horizontal scale) is one of the largest lineaments in the model area (ZSMEW002A , cf. /Rhén et al. 2009, Figure 3-1/), /Sohlenius and Hedenström 2008/.*

Table 2-6. Prescription for hydrogeological properties of Hydraulic soil property domains used in the hydrogeological modelling (based on /Werner et al. 2008/). The relation to the model and description of the Quaternary deposits (QD type and layer) /Nyman et al. 2008, Sohlenius and Hedenström 2008, Werner et al. 2008/ is given in the second column. The modifications relative to the initial HSD assignments are highlighted in bold font, with the main change being to introduce anisotropy. Porosity is derived from specific yield /Werner et al. 2008/. /Rhén and Hartley 2009/.

Hydraulic soil property domain	QD type and layer applied to	*K* (m/s)	Porosity
Surface affected layer	Soil > 5 m thick: QD type: 1, 2, 5, 6, 7, 9, 13, 16, 17, 18, 20, 22, 24, 25, 26, 27 Layer Z1 Domain 2–24 Layer Z6	$\mathbf{K_h = 8{\cdot}10^{-4}}$ $\mathbf{K_h/K_v = 10:1}$ Original: $4{\cdot}10^{-4}$	0.15
Peat	QD type: 11, 12 Layer Z2	$K_h = 3{\cdot}10^{-6}$ $\mathbf{K_h/K_v = 10:1}$	0.24
Glacial clay	QD type: 6, 8, 9, 10, 12 Layer Z3	$K_h = 1{\cdot}10^{-7}$ $\mathbf{K_h/K_v = 10:1}$	0.03
Postglacial sand/gravel	QD type: 6, 7, 8, 9, 10, 12 13, 14, 15, 16, 20, 23, 24, 25, 26 Layer Z4	$K_h = 5{\cdot}10^{-3}$ $\mathbf{K_h/K_v = 10:1}$	0.25
Glacial clay	QD type: 6, 8, 9, 10, 12, 13, 14, 15, 16, 17, 18, 19, 20, 21, 22, 23, 24 Layer Z5	$K_h = 1{\cdot}10^{-8}$ $\mathbf{K_h/K_v = 2:1}$	0.03
Till	Soil < 5 m thick: QD type: 1, 2, 5, 6, 7, 9, 13, 16, 17, 18, 20, 22, 24, 25, 26, 27 Layer Z1 Domain 2–24 Layer Z6	$K_h = 4{\cdot}10^{-5}$ $\mathbf{K_h/K_v = 10:1}$	0.05
Surface affected peat	QD type: 3,8, 21, 23 Layer Z1	$K_h = 3{\cdot}10^{-6}$ $\mathbf{K_h/K_v = 10:1}$	0.24
Surface affected shingle	QD type: 4 Layer Z1	$K_h = 1{\cdot}10^{-2}$ $\mathbf{K_h/K_v = 10:1}$	0.25
Surface affected sand	QD type: 10, 15 Layer Z1	$K_h = 1{\cdot}10^{-2}$ $\mathbf{K_h/K_v = 10:1}$	0.25
Gyttja	QD type: 7 Layer Z3	$K_h = 1{\cdot}10^{-8}$ $\mathbf{K_h/K_v = 2:1}$	0.03
Postglacial fine sand	QD type: 17 Layer Z4	$K_h = 5{\cdot}10^{-4}$ $\mathbf{K_h/K_v = 10:1}$	0.25
Postglacial sand	Domain 18, 19 Layer Z4	$K_h = 1{\cdot}10^{-3}$ $\mathbf{K_{hh}/K_v = 10:1}$	0.25
Postglacial gravel	QD type: 21, 22 Layer Z4	$K_h = 1{\cdot}10^{-2}$ $\mathbf{K_h/K_v = 10:1}$	0.25
Artificial fill	QD type: 27 Layer Z4	$K_h = 4{\cdot}10^{-5}$ $\mathbf{K_h/K_v = 10:1}$	0.05

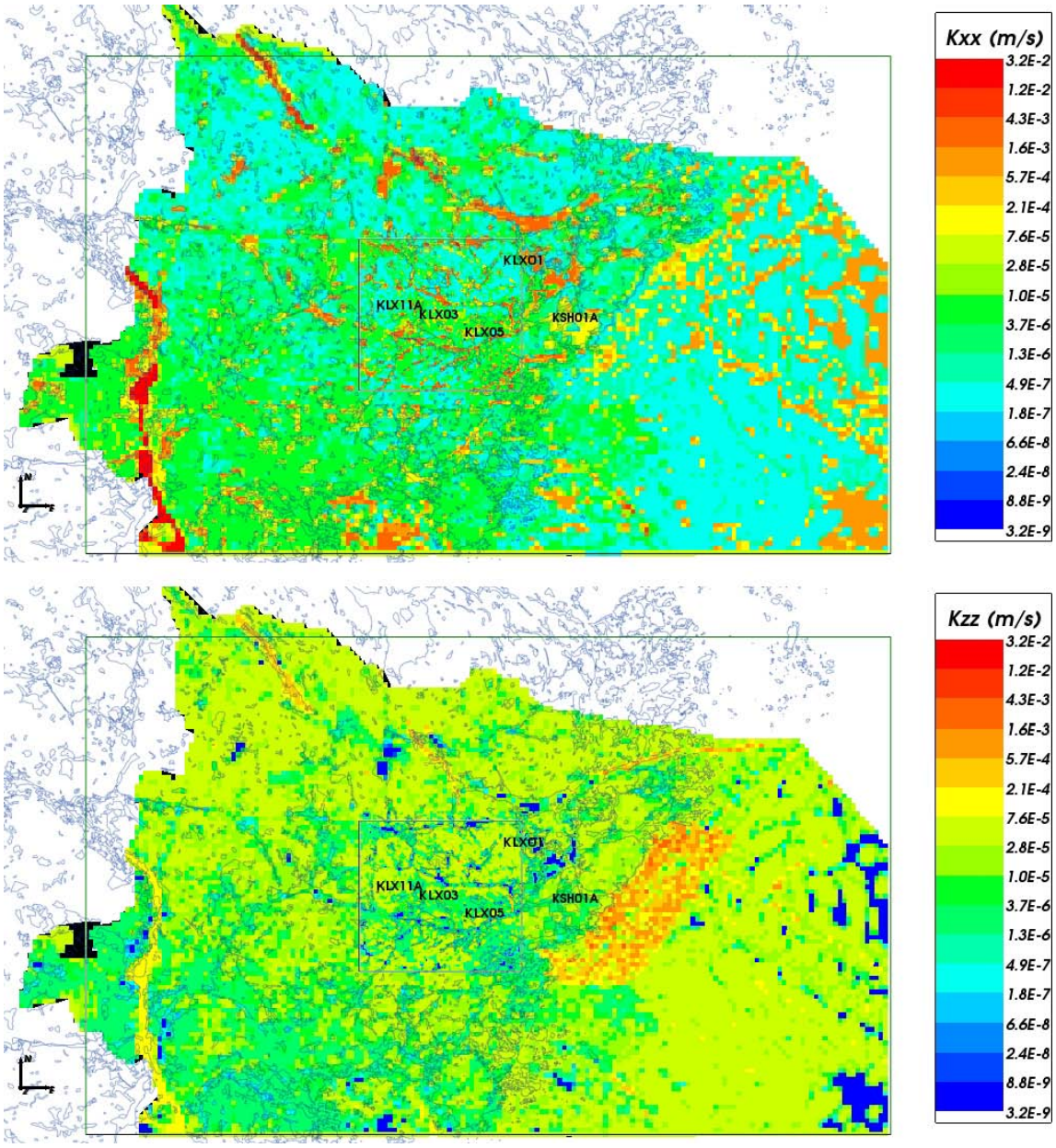

Figure 2-15. *Resulting effective hydraulic conductivity for HSD top layer based on layer thicknesses and hydraulic properties of the Quaternary deposits. Top: E-W horizontal component; Bottom: vertical component. /Rhén and Hartley 2009/.*

2.5 Groundwater flow simulations and confirmatory testing

The SDM-Site regional scale groundwater flow and solute transport simulation tests of palaeohydrogeological evolution, natural head measurements and hydraulic interference test data have confirmed that hydrogeological properties, as given by the SDM-Site hydrogeological DFN model *base case* /Rhén et al. 2008/ (based on all open and partly open fractures and semi-correlated transmissivity model), together with the HCD parameterisation provide an appropriate description of the hydrogeological situation in the bedrock. Only relatively minor modifications were considered necessary to obtain an acceptable match between the regional groundwater flow model results and field data.

3 Concepts and methodology

3.1 Conceptual model types

There are several conceptual model types that can be used to describe the groundwater flow relevant to the granitic bedrock at Laxemar: namely, continuous porous medium (CPM), discrete fracture network (DFN), equivalent continuous porous medium (ECPM), and stochastic continuum. CPM, ECPM and stochastic continuum groundwater flow models treat the rocks as a continuum characterised by quantities defined at all points in a 3D region. DFN models explicitly model the water conducting fractures through which the groundwater flows in fractured rocks, and are characterised by quantities associated with the fractures. Typically, for crystalline hard rocks, groundwater flow generally takes place through an interconnected network of fractures.

3.1.1 Continuous porous medium (CPM) representation

CPM models are considered the appropriate models for certain types of rock, in which flow is predominantly through an interconnected network of pores in the rock matrix, such as for many sandstones, or for soils and unconsolidated deposits. The model assumes continuity in three dimensions and hence a high degree of connectivity between points in the modelling domain. Connectivity is only reduced when very low conductivity layers or flow barriers are incorporated in the model. The flow through such domains is modelled by Darcy's law, which relates specific discharge (Darcy flux) to the driving force, i.e. the pressure gradient and/or buoyancy force. The equations used are specified in /Serco 2010b/.

The CPM representation is less useful for fractured rocks as it can only represent bulk properties over large volumes. However, it can be of use for regions of a model where there is limited data available on fracturing and it is appropriate to use generic rock properties. Where there is sufficient fracture data available an ECPM representation can be used, as described in Section 3.1.3.

3.1.2 Discrete fracture network (DFN) representation

The discrete fracture network (DFN) concept assumes flow through a fractured rock is predominantly through an inter-connected network of flow-conductive fractures, with groundwater moving from one fracture to another at the intersections between them. The equations used are specified in /Serco 2010c/. The properties of the network are usually characterised in terms of:

- Spatial distribution (e.g. Poisson, fractal, clustered around points or lineaments).
- Fracture intensity (and its spatial variation).
- Fracture sets distinguished by orientation.
- Fracture size (e.g. log-normal, power-law distributions).
- Transmissivity-size relationships.

The properties of each fracture are primarily:

- Size.
- Orientation (strike and dip).
- Transmissivity (and possibly spatial variability within the fracture).
- Transport aperture.
- Storativity.

In ConnectFlow, fractures are usually rectangular, but may be right-angled triangles where a complex surface has been triangulated into many pieces. For stochastic fractures, the properties are sampled from probability distribution functions (PDFs) specified for each fracture set. The properties may be sampled independently or correlated with other properties.

The DFN concept is very useful since it naturally reflects the individual flow conduits in fractured rock, and the available field data. However, to model flow and transport on the regional-scale it is often necessary to consider larger-scale bulk properties in the context of an ECPM continuum concept. This requires methods (i) to convert the properties of a network of discrete fractures of lengths less than the continuum blocks into equivalent continuous porous medium (ECPM) block properties, known as upscaling, and (ii) to represent larger scale features such as fracture zones by appropriate properties in a series of continuum blocks (the IFZ method). The implementations of the upscaling and IFZ methods in ConnectFlow are described in Sections 3.1.3 and 3.2.2, respectively.

An example of a DFN model generated on the repository-scale is shown in Figure 3-1. It includes both stochastic fractures, each of which is square, combined with deterministic fracture zones that are defined as more complex non-planar surfaces. Horizontal and vertical slices through the fractures are shown in Figure 3-2.

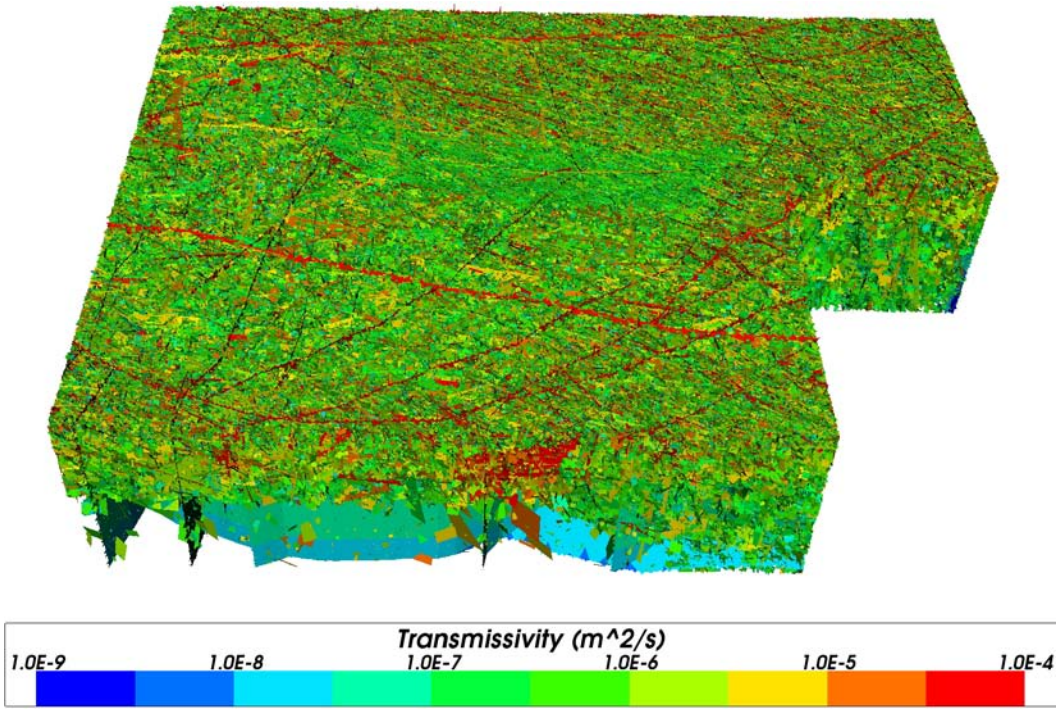

Figure 3-1. *An example of a site-scale DFN model showing stochastic fractures and higher transmissivity deterministic deformation zones, coloured by* $\log_{10}$*(transmissivity).*

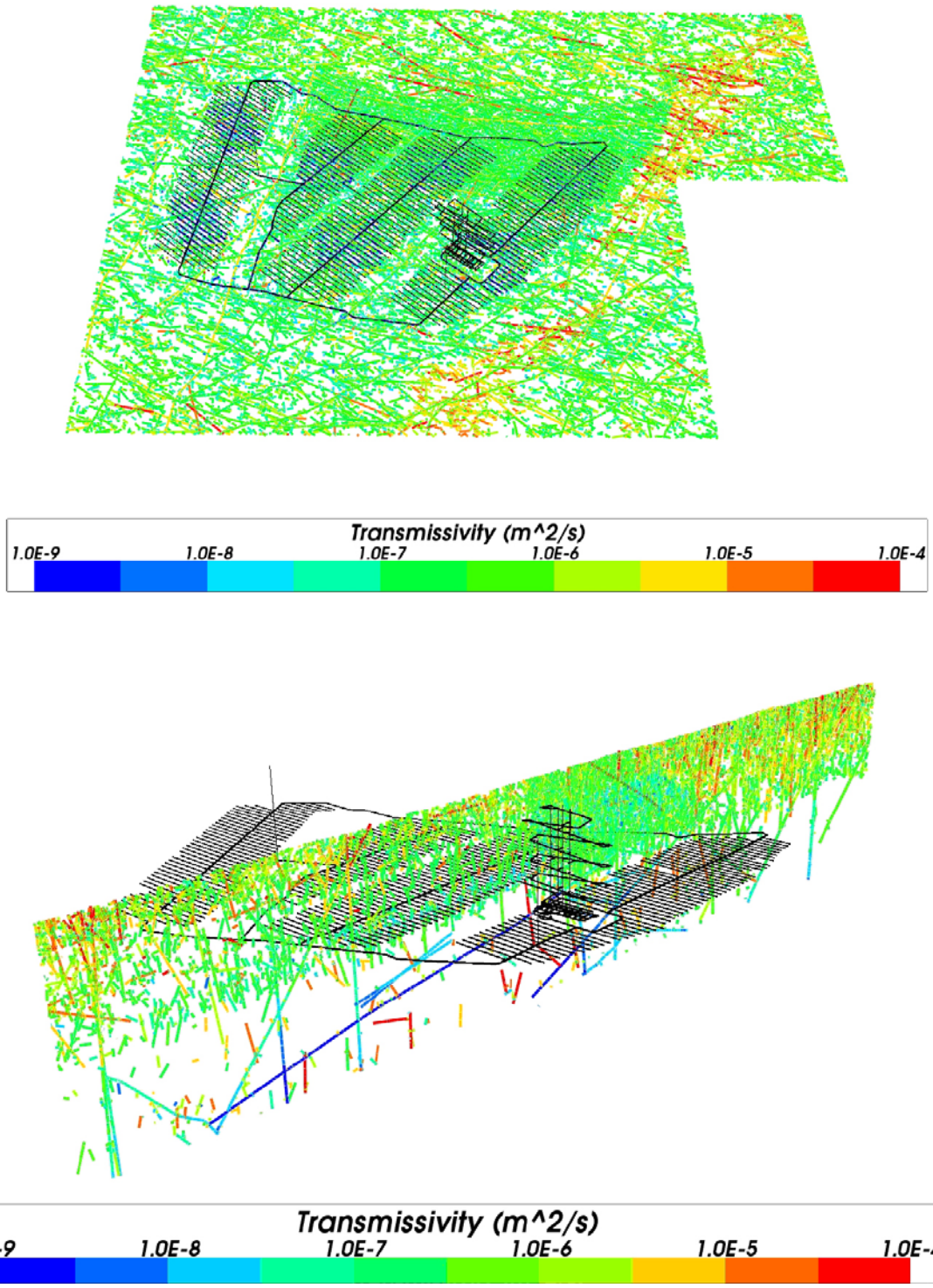

Figure 3-2. *Slices through an example of a site-scale DFN model showing stochastic fractures and higher transmissivity deterministic deformation zones, coloured by $\log_{10}$(transmissivity). Repository structures are shown in black. Top: horizontal slice at z=–510 m; Bottom: Vertical slice.*

3.1.3 Equivalent continuous porous medium (ECPM) representation

In order to assess the implications of the DFN model on flow and transport on the regional-scale, it is often necessary for practical reasons to convert the DFN model to an ECPM model with appropriate properties. The resulting parameters are a directional hydraulic conductivity tensor, fracture kinematic porosity and other transport properties (such as the fracture surface area per unit volume). In ConnectFlow, a flux-based upscaling method is used that requires several flow calculations through a DFN model in different directions.

Figure 3-3 shows an illustration of how flow is calculated in a DFN model (a 2D network is shown for simplicity). To calculate equivalent hydraulic conductivity for the block shown, the flux through the network is calculated for a linear head gradient in each of the axial directions.

Due to the variety of connections across the network, several flow-paths are possible, and may result in cross-flows non-parallel to the head gradient. Cross-flows are a common characteristic of DFN models and can be approximated in an ECPM by an anisotropic hydraulic conductivity.

In 3D, ConnectFlow uses six directional components to characterise the symmetric hydraulic conductivity tensor. Using the DFN flow simulations, the fluxes through each face of the block are calculated for each head gradient direction. The hydraulic conductivity tensor is then derived by a least-squares fit to these flux responses for the fixed head gradients /Jackson et al. 2000/.

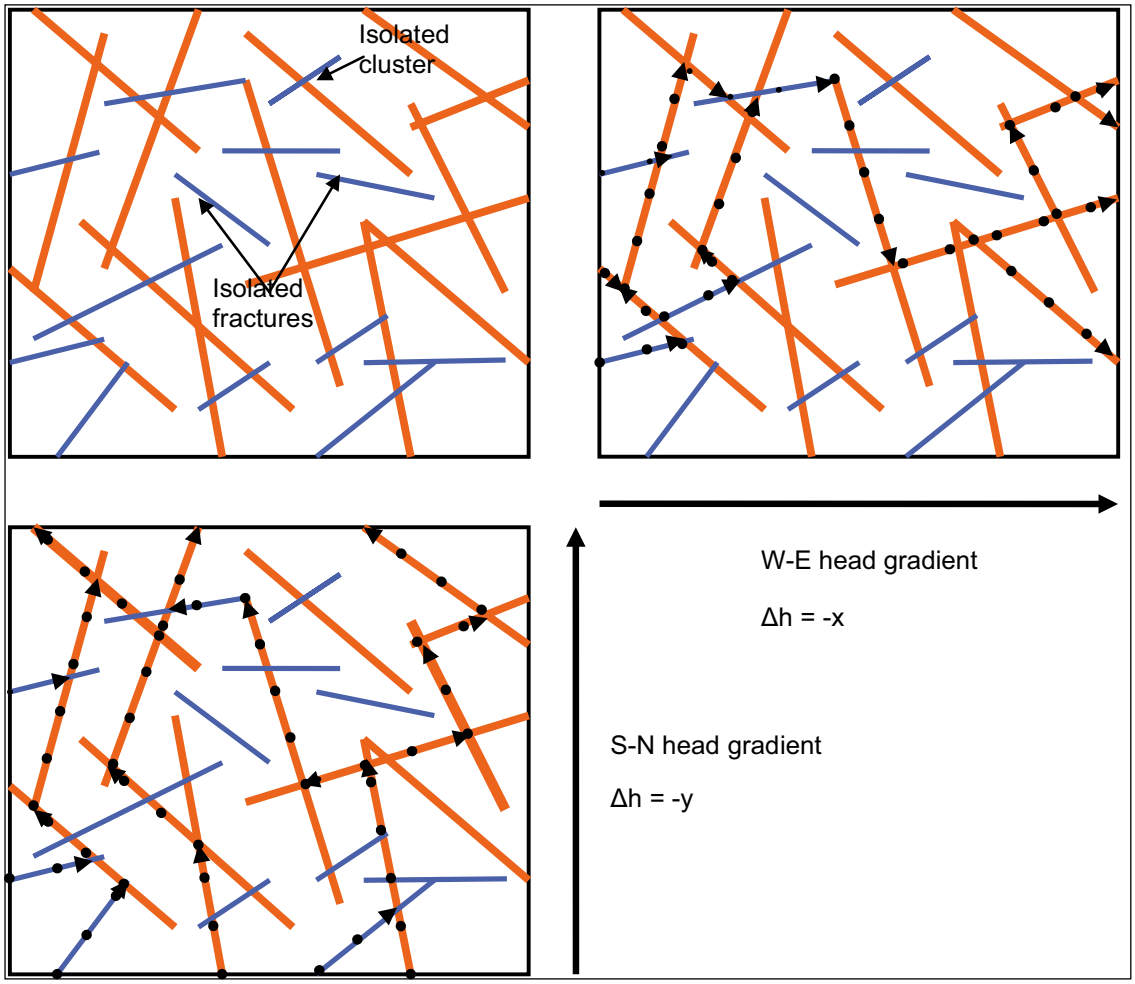

Figure 3-3. *2D illustration of flow through a network of fractures. A random network of fractures with variable length and transmissivity is shown top left (orange fractures are large transmissivity, blue are low). Top right: flow-paths (dotted arrows) for a linear head gradient W-E decreasing along the x-axis. Bottom left: flow-paths through the network for a linear head gradient S-N decreasing along the y-axis.*

Kinematic porosity, ϕ, for each block is calculated as

$$\phi = \frac{\sum_f e_t a_f}{V} \quad (3\text{-}1)$$

where V is the volume of the block, a_f is the area of each fracture in the block and e_t is the transport aperture of the fracture, which, for SDM-Site Laxemar /Rhén et al. 2009/ and this study, is related to fracture transmissivity, T, by

$$e_t = 0.705 T^{0.404} \quad (3\text{-}2)$$

The summation is over all fractures within the block. As for SDM-Site /Rhén et al. 2009/, the porosity was multiplied by five to account for the lower limit on the fracture size truncation.

Flow wetted fracture surface area per unit volume of rock, a_r, is calculated for each block as:

$$a_r = 2P_{32} \quad (3\text{-}3)$$

where P_{32} is the fracture area per unit volume within the block, calculated as

$$P_{32} = \frac{\sum_f a_f}{V} \quad (3\text{-}4)$$

where V is the volume of the block. The a_r value is used in transport calculations to calculate the flow-related transport resistance (F) within the ECPM, as described in Section 3.2.6.

One refinement of the upscaling methodology is to simulate flow through a slightly larger domain than the block size required for the ECPM properties, but then calculate the flux responses through the correct block size. The reason for this is to avoid over-prediction of hydraulic conductivity from flows through fractures that just cut the corner of the block but that are unrepresentative of flows through the in situ fracture network (Figure 3-4). The area around the block is known as a 'guard-zone', and an appropriate choice for its thickness is approximately one fracture radius. The problem is most significant in sparse heterogeneous networks in which the flux through the network of fractures is affected by 'bottlenecks' through low transmissivity fractures, and is quite different to the flux through single fractures.

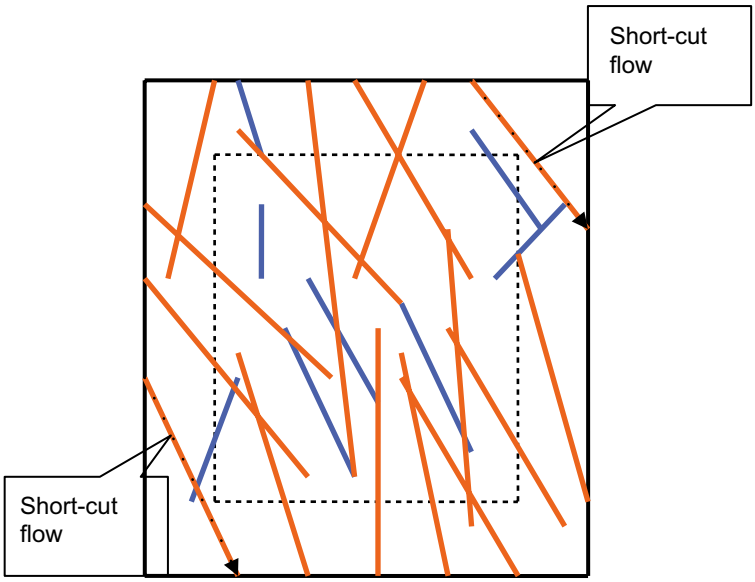

Figure 3-4. *A 2D illustration of how overestimates of block-scale hydraulic conductivity caused by flow short cuts can be corrected by the use of a guard zone (the area outside the dotted line).*

3.1.4 Stochastic continuum representation

The stochastic continuum approach is an alternative to the ECPM representation and assigns properties to the HRD rock that represent the statistical properties of the bedrock derived from Pipe-string System (PSS) measurement data. Not only is it a different conceptual model type, it also uses measured data in a different way, i.e. larger scale PSS measurements rather than smaller scale PFL-f measurements reproduced by individual features. For each HRD and depth zone, geometric mean and standard deviation values for hydraulic conductivity are determined for particular borehole interval scales. Only measurement intevals not crossed by deformation zones are used. In the work reported here, 20 m and 100 m interval scale properties were used, corresponding to 20 m and 100 m PSS measurements resepectively (extracted from Appendix 9 in /Rhén et al. 2008/), and were assumed to be applicable to volumes (cubes) of the corresponding length scale.

The elements at an appropriate scale (for example 20 m or 100 m) are represented in a property grid. For each element in the property grid, an isotropic hydraulic conductivity value is stochastically generated from the geometric mean and standard deviation values for a 20 m or 100 m scale (depending on the size of the element) using a nugget method, i.e. there is no spatial correlation between the properties of neighbouring elements. The hydraulic conductivities are then mapped from the property grid on to the actual model grids used for the simulations using an interpolation or upscaling method, depending on the relative sizes of corresponding elements in the property grid and model grid.

The methodolgy is thus:

1. Generate 20 m and 100 m property grids with stochastically assigned hydraulic conductivities.
2. Map hydraulic conductivity values from each property grid on to regional-, site- and repository-scale model grids.

The mapping from the property grids to the model grids is carried out on an element by element basis as follows:

1. If the property grid element and a model grid element match in size and location then just copy the hydraulic conductivity value.
2. If the model grid element contains a whole number of property grid elements then upscale the hydraulic conductivity values. This is done for each direction (Kxx, Kyy, Kzz) by taking the arithmetic mean of the harmonic means of the hydraulic conductivity values in that direction.
3. Otherwise just use the hydraulic conductivity value of the property grid element that contains the centre of the model grid element (as shown in Figure 3-5).

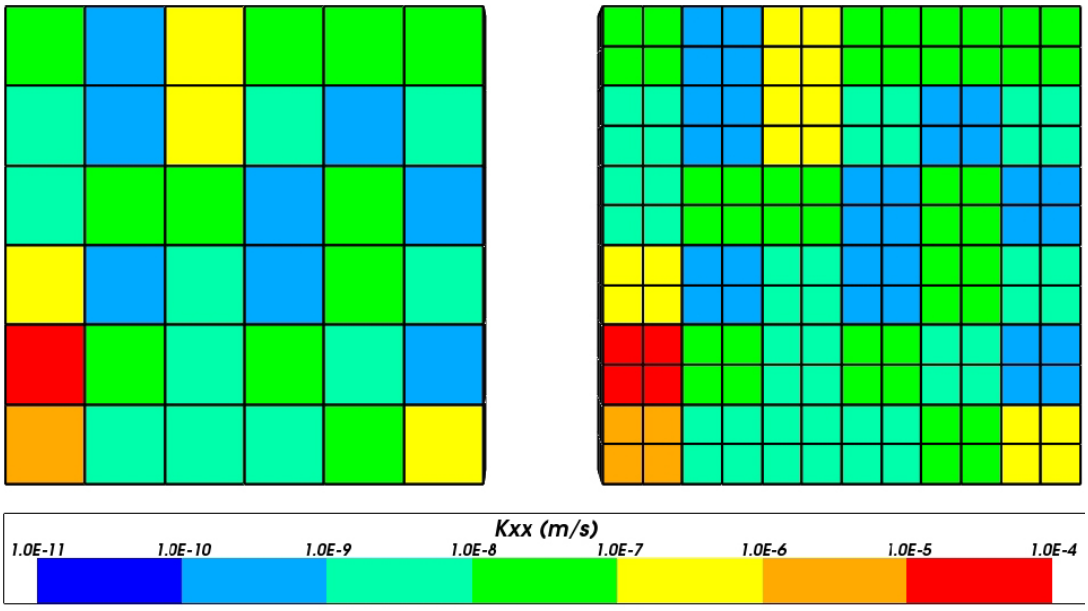

Figure 3-5. *An example of mapping hydraulic conductivity values from a property grid (left) on to a more refined model grid (right) using an interpolation method.*

3.1.5 Embedded CPM/DFN models

In addition to the capability to create distinct models based on the concepts described above, ConnectFlow offers the option to construct embedded models that integrate sub-models of different types. That is, the model can be split into two different domains: one that uses the CPM concept, and one that uses the DFN concept. However, DFN and CPM sub-models have to be exclusive, i.e. the approaches cannot be used simultaneously in any part of the domain. Internal boundary conditions between the domains ensure continuity of pressure and conservation of mass. On the DFN side of the interface, these boundary conditions are defined at nodes that lie along the lines (traces) that make up the intersections between fractures and the interface surface. On the CPM side, the boundary conditions are applied to nodes in finite-elements that abut the interface surface. Thus, extra equations are added to the discrete system matrix to link nodes in the DFN model to nodes in the finite-element CPM model, as shown in Figure 3-6. By using equations to ensure both continuity of pressure and continuity of mass, a more rigorous approach to embedding is obtained than by simply interpolating pressures between separate DFN and CPM models. The equations used are specified in /Serco 2010a/.

In order to construct embedded models of the same fractured rock (mixing DFN and CPM sub-models), the data used for the DFN and CPM models should be self-consistent. For example, if a repository-scale DFN model is embedded within an ECPM model, then flow statistics on an appropriate scale (the size of the elements in the ECPM model) need to be consistent. This is achieved by the fracture upscaling techniques described in Section 3.1.3.

Two quite different examples are included below to illustrate some of the possible models that can be constructed. Figure 3-7 shows an example of a model where a local-scale DFN model is embedded within a larger regional-scale ECPM model. The DFN sub-model is used to provide detailed flow and transport calculations around a repository, while the ECPM sub-model provides a representation of the regional-scale flow patterns that control the boundary conditions on the DFN model. The interface between these two sub-models is on the outer faces of the DFN model.

The converse example is to embed a CPM sub-model within a DFN sub-model as shown in Figure 3-8. In this case, a CPM sub-model is used to represent flow in backfilled main and deposition tunnels, while the surrounding fractured rock is represented by a DFN sub-model. The interface between the two sub-models has a complex geometry corresponding to the outer surface of the tunnel system.

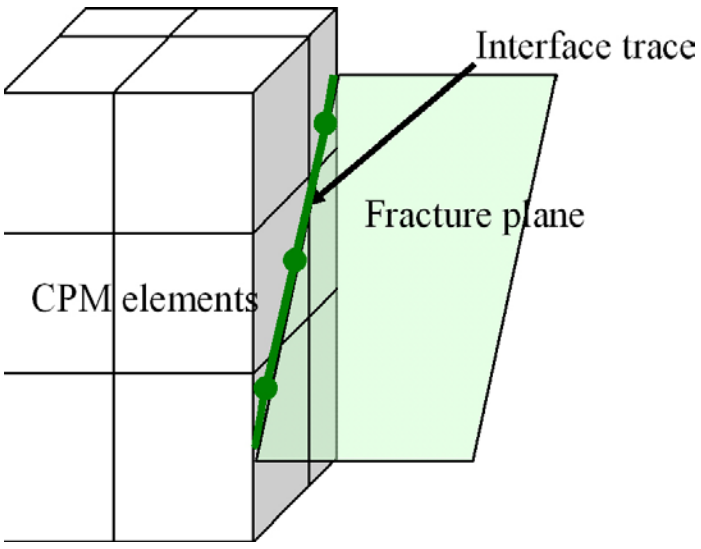

Figure 3-6. *Illustration of embedding between DFN and CPM sub-models. A finite-element CPM mesh is shown on the left. The right hand surface is intersected by a single fracture plane. Extra equations are used to link the DFN to the CPM.*

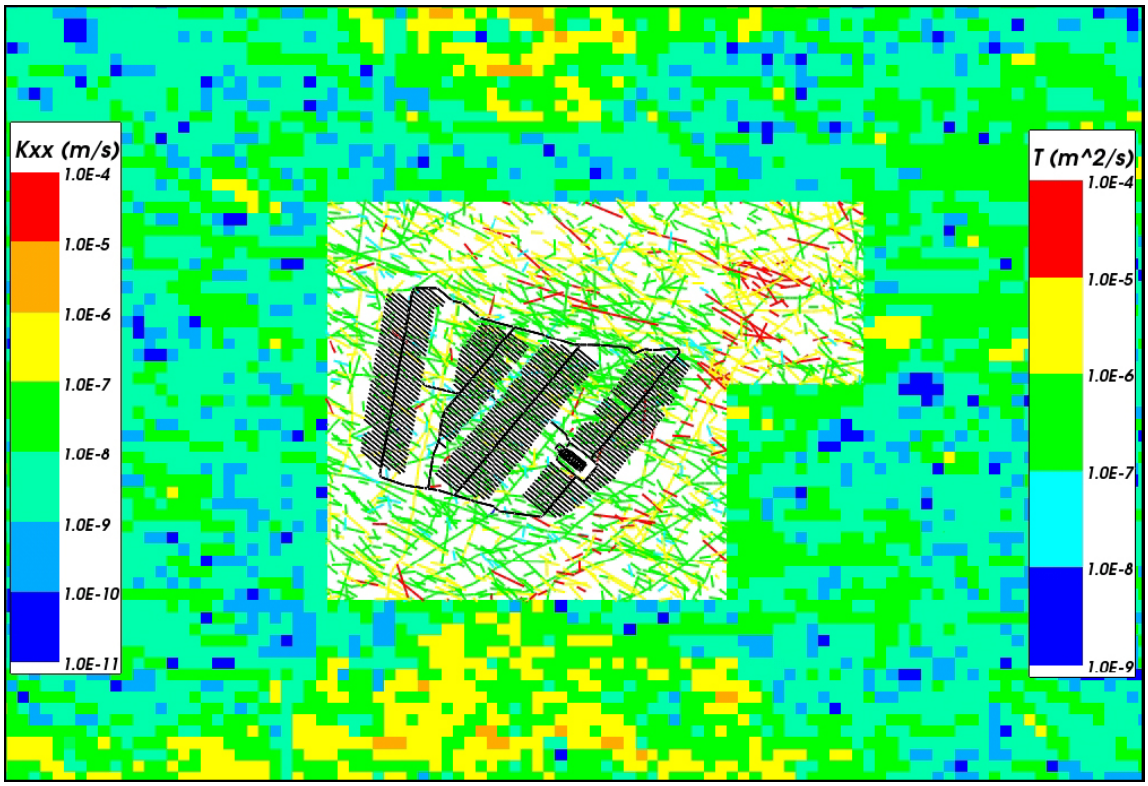

Figure 3-7. *An example of an ECPM/DFN ConnectFlow model using a DFN sub-model to represent the detailed fractures around a repository, and embedded within a larger regional-scale ECPM sub-model as a slice at repository depth. Fractures are coloured by transmissivity and the ECPM is coloured by horizontal hydraulic conductivity. Repository structures are shown in black.*

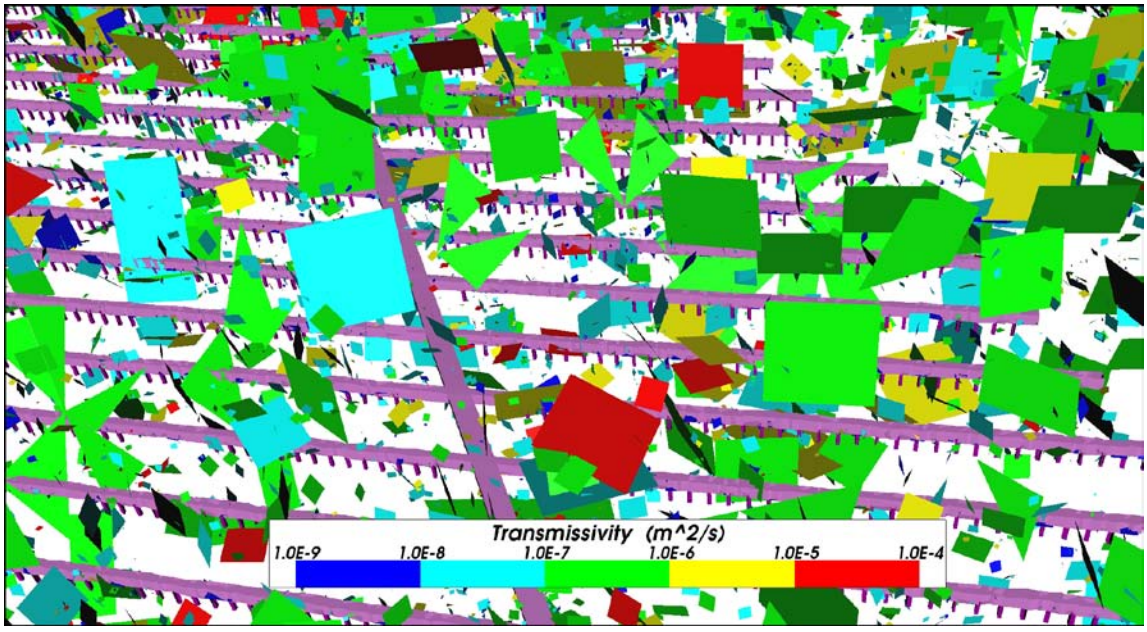

Figure 3-8. *An example of a DFN/CPM ConnectFlow model using a CPM sub-model of deposition and main tunnels embedded within a DFN sub-model. 80% of fractures have been removed to reveal the tunnels. The interface between the two sub-models is on the boundary of the CPM model. The fractures are coloured by transmissivity and the CPM sub-model is pink.*

In summary, embedded models make it possible to represent different regions using different model concepts and then combine the regions into a single model. This is different from the case where discrete fractures co-exist in the same space with a porous medium model of the rock matrix. The interaction between fractures and the rock matrix within the same domain can be represented in ConnectFlow by modelling rock matrix diffusion (RMD) within CPM/ECPM models, but it should be recognised that this is a different situation. It may be noted that RMD of salinity is not represented within the DFN domain, but RMD of radionuclides within the fracture system can be accounted for either in the particle tracking algorithm or later in the far field radionuclide transport calculations.

3.1.6 Particle tracking

A particle tracking algorithm is used to represent advective transport of radionuclides. In CPM models, particles are tracked in a deterministic way by moving along a discretised path within the local finite-element velocity-field.

In DFN models, a stochastic 'pipe' network type algorithm is used. Particles are moved between pairs of fracture intersections stepping from one intersection to another. At any intersection there may be several possible destinations that the particle may move to, as flow follows different channels through a fracture. A random process weighted by the mass flux between pairs of intersections (connected by a 'pipe') is used to select which path is followed for any particular particle. Hence, there is an explicit hydrodynamic dispersion process built into the transport algorithm used in the DFN if more than one particle is released per start point. The time taken to travel between any two intersections, the distance travelled and flow-related transport resistance (described in Section 3.2.6) are calculated for each pipe based on flow rates and geometries.

In an embedded model, particles are traced through both DFN and CPM regions continuously, using the appropriate algorithm for the region currently containing the particle (Figure 3-9). The implication is that particle tracks are deterministic until they enter a DFN sub-model, and are then stochastic afterwards, even if the particle goes back into a CPM sub-model.

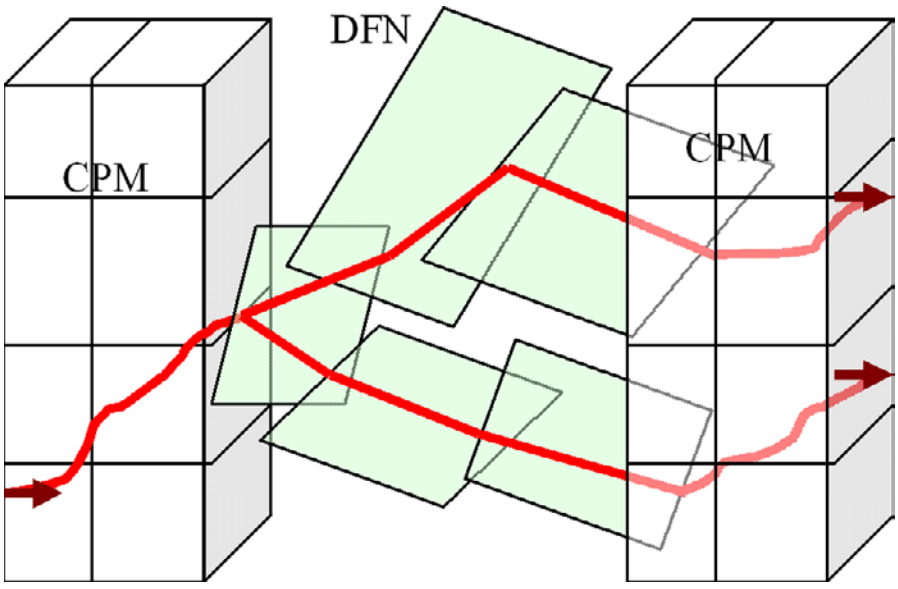

Figure 3-9. *Illustration of particle tracking through an embedded DFN/CPM to show the different particle tracking methods in the two regions: deterministic in CPM, stochastic in DFN.*

3.1.7 Requirements for site assessment

A number of factors are considered when assessing a site, including the performance measures given in Section 3.2.6. Of these, the distributions of equivalent flux at the release point, U_r, and flow-related transport resistance, F_r, are particularly important. Further, it is the tails in these distributions that are key in assessing the suitability of a site. The DFN representations used in the site-scale and repository-scale models for the Hydrogeological base case and Elaborated Hydro-DFN case are well suited to capturing these tails and hence these cases are the main focus of the report.

3.2 Modelling methodology

3.2.1 Model scales

Three different scales of model are used in the temperate period modelling. Each scale of model is chosen to focus in on parts of the model of interest, with consideration to what is computationally feasible and which types of calculations are supported by the ConnectFlow software for different model concepts. By considering these three scales of model a comprehensive and robust study can be made of the issues relevant to groundwater flow and transport and some conceptual uncertainties can be quantified.The models are described fully in Chapter 4, but each scale is summarised below.

Information on variable values and particle transport is passed between the different model scales. Figure 3-10 shows the relationship between the scales, the embedding of the rock representations that they use and how data is passed between them.

Figure 3-11 shows a flowchart that gives the workflow of modelling processes and data transfer. The green boxes represent generation of the fractures in the regional-scale domain. The larger fractures (radius > 5.6 m) are upscaled to provide ECPM properties for the regional-scale model. The full set of fractures are used directly in the site-scale and repository-scale models. The purple boxes represent the regional-scale modelling, involving the upscaling of the DFN and palaeohydrogeological modelling of the transient evolution of groundwater hydrochemistry, including the effects of rock matrix diffusion (RMD). The pressures and densities at selected times are then exported for use in the site-scale modelling (yellow boxes) and the repository-scale modelling (blue boxes). Both of these scales carry out steady-state groundwater flow calculations for the chosen time slices followed by particle tracking calculations for particles released at the repository. The site-scale model also serves to continue particles that have reached the boundaries of the repository-scale model. The orange boxes indicate the final products of the calculations.

Table 3-1 gives a modelling summary for each scale, including the main physical concepts modelled. Table 3-2 shows how each feature within the models is represented at each scale.

Figure 3-12 shows how the domains of the three different scales of model relate to each other. Note that the site-scale DFN covers the repository structures, but is not required to cover the full domain of the repository-scale blocks. Figure 3-13 shows how the repository structures are represented within the site-scale model. Further details on these models are contained in Chapter 4.

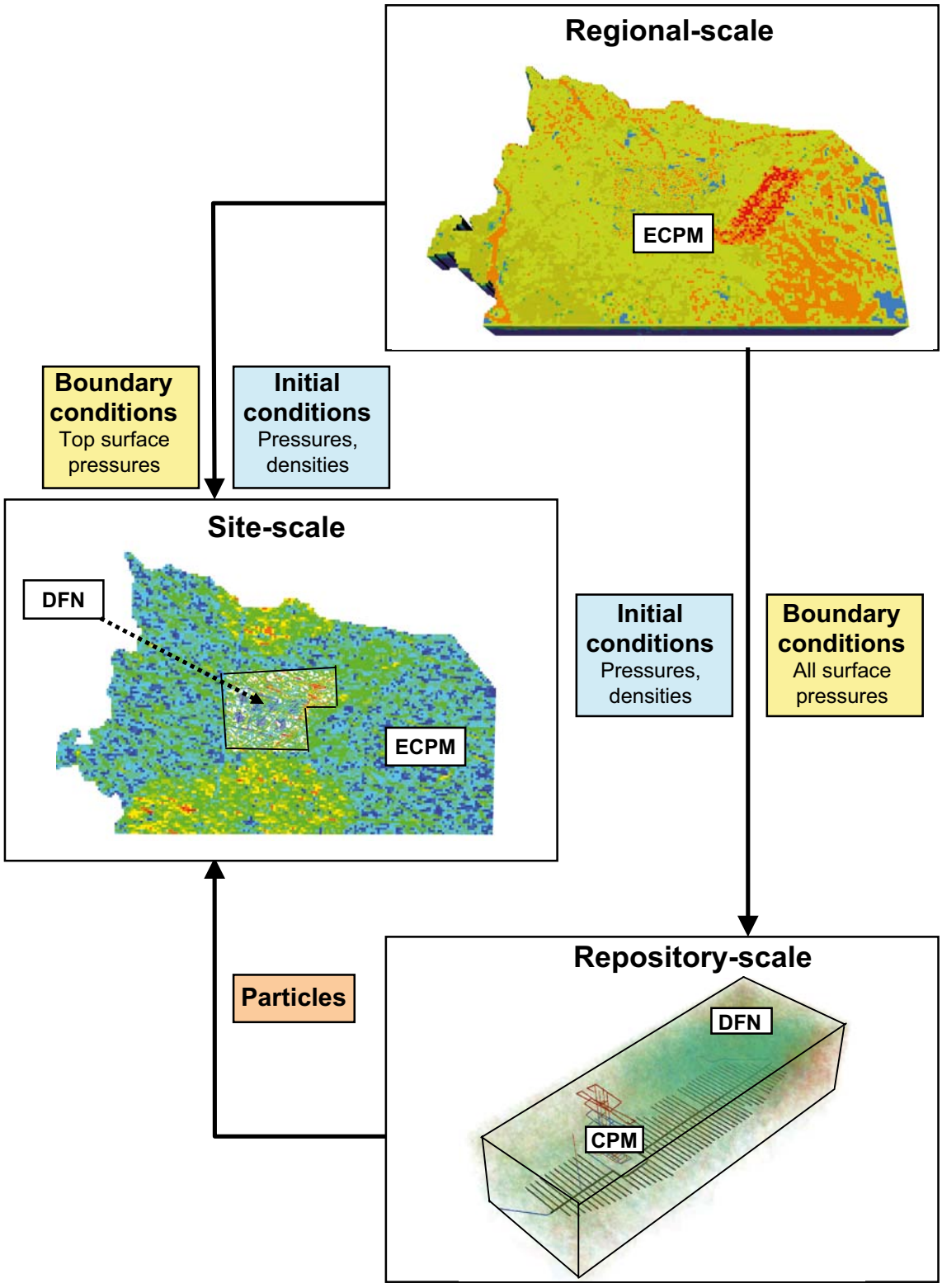

Figure 3-10. *Illustration of the concepts of model scales, embedding, and the transfer of data between scales. Models are coloured by hydraulic conductivity (CPM/ECPM) or transmissivity (DFN).*

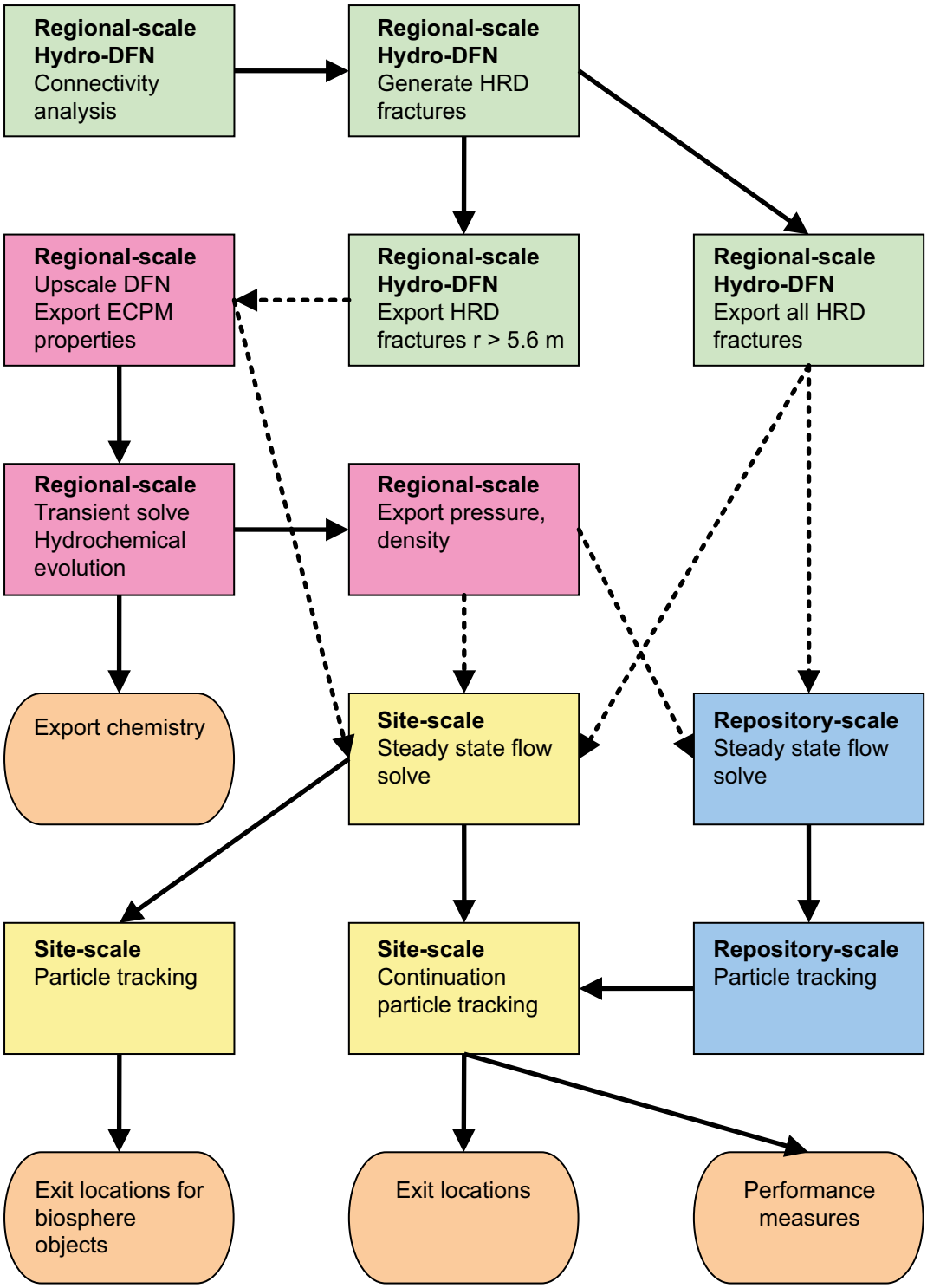

Figure 3-11. *Modelling processes. Fracture generation is shown in green, regional-scale processes in pink, site-scale processes in yellow and repository-scale processes in blue. Outputs are shown in orange. Solid arrows indicate the modelling workflow within a scale and dotted arrows indicate a transfer of data between scales.*

Table 3-1. Modelling summary for each scale.

	Regional-scale	Site-scale	Repository-scale
Earliest time simulated	8000 BC	5000 BC	2000 BC
Latest tme simulated	15,000 AD	15,000 AD	15,000 AD
Flow model	Saturated flow in a porous medium (ECPM/CPM)	Saturated flow at fixed time slices in a porous medium (ECPM/CPM) with an embedded discrete fracture network (DFN)	Saturated flow at fixed time slices in a discrete fracture network (DFN) with an embedded CPM representation of the tunnels
Transport model	Rock matrix diffusion	Single porosity	Single porosity
Fluid properties	Salinity S(x,y,z|t) Temperature T(z) Density ρ(S, T) Viscosity μ(T)	Salinity S(x,y,z|t) Temperature T(const.) Density ρ(S) Viscosity μ(const.)	Salinity S(x,y,z|t) Temperature T(const.) Density ρ(S) Viscosity μ(const.)
Modelling procedure	1. Multiple heterogeneous realisations 2. Transient boundary conditions 3. Solve for flow and transport, with RMD, of reference waters at each time step	1. Multiple heterogeneous realisations 2. Fixed boundary conditions at different time slices 3. Calculate flow at each time slice 4. Fixed flow particle tracking at each time slice	1. Multiple heterogeneous realisations 2. Fixed boundary conditions at different time slices 3. Calculate flow at each time slice 4. Fixed flow particle tracking at each time slice
Primary output	Fluid pressure and density at different time slices	Flow and particle tracking performance measures	Flow and particle tracking performance measures
Secondary output	Hydrochemistry at different time slices	Particle exit locations at different time slices	Particle exit locations at different time slices

Table 3-2. Representation of model features at each scale.

Feature	Regional-scale	Site-scale	Repository-scale
HCD	ECPM	Single fracture surfaces	Single fracture surfaces
HRD	ECPM	DFN/ECPM	DFN
HSD	CPM	CPM	Not present
Main tunnels	Not present	Equivalent fractures	CPM
Deposition tunnels	Not present	Equivalent fractures	CPM
Deposition holes	Not present	Not present	CPM
Other repository structures	Not present	Equivalent fractures	Equivalent fractures
EDZ	Not present	Equivalent fractures	Equivalent fractures

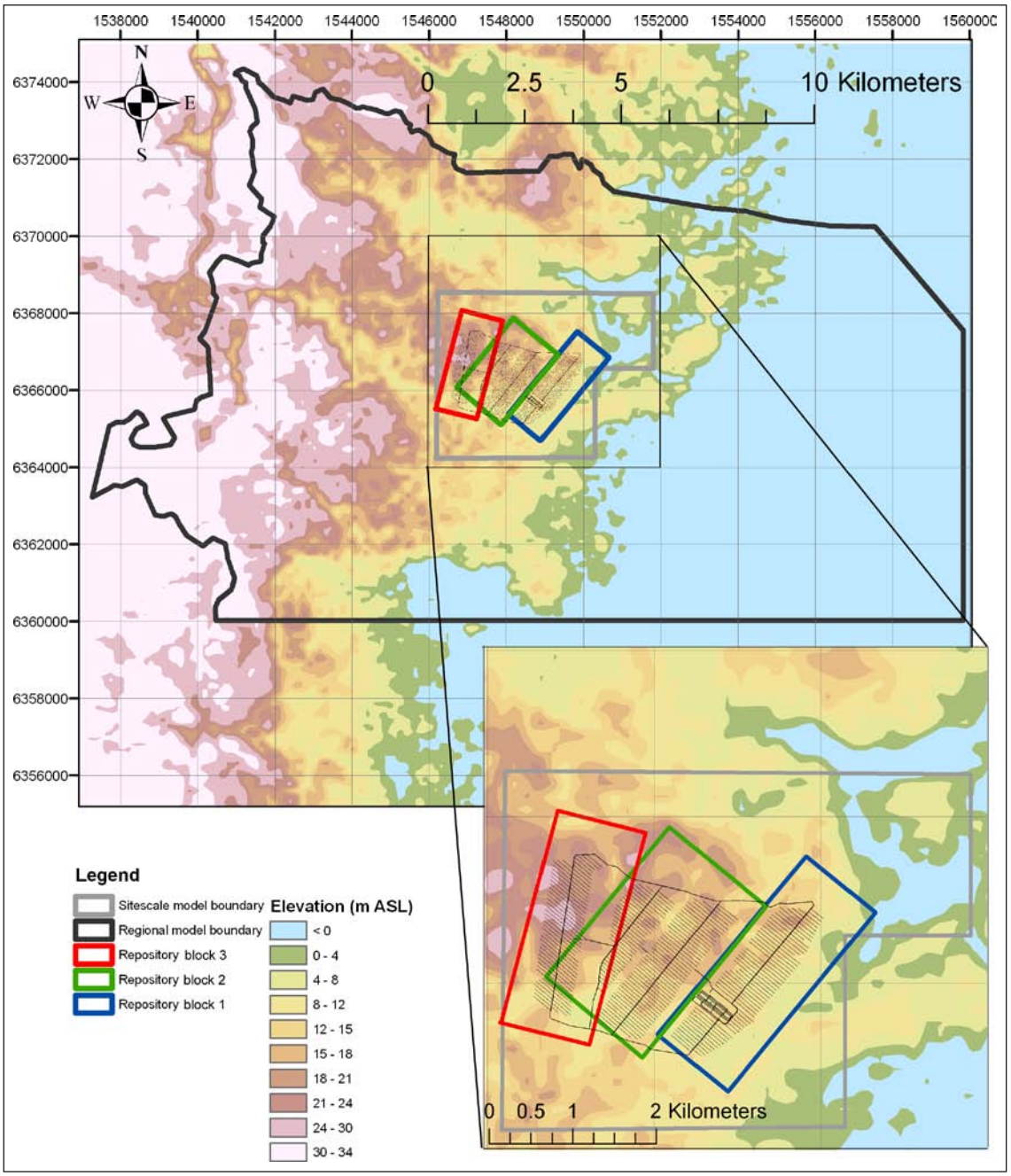

Figure 3-12. *The different scales of model: regional-scale (black); embedded DFN in the site-scale model (grey); repository-scale block models (red, green, blue). Surface topography is coloured by elevation.*

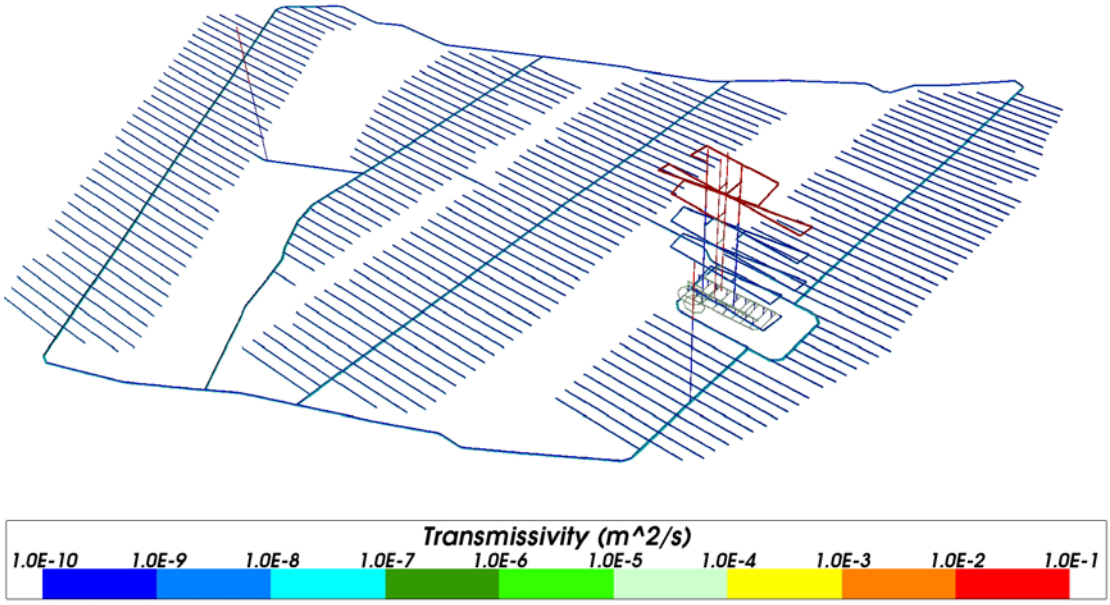

Figure 3-13. *Tunnels and excavation damaged zone (EDZ) in the site-scale model, coloured by transmissivity.*

The regional-scale model corresponds to the SDM-Site model and covers the same domain. The model uses an ECPM representation for the HRD and a CPM representation for the HSD, as illustrated in Figure 3-14. The deformation zones are represented by Implicit Fracture Zone (IFZ) fractures (described in Section 3.2.2). The model is used to calculate the transient evolution of coupled groundwater flow and reference water transport with rock matrix diffusion (RMD) from 8000 BC to 15,000 AD. The calculated pressure and fluid density values are exported from this model for particular times for use by the two other scales.

The site-scale model replaces the part of the regional-scale ECPM model local to the repository area with an explicit embedded DFN representation of the HRD, as shown in Figure 3-15. The DFN region was chosen to encompass all the repository features and to extend from the bottom of the HSD to a depth of a few hundred metres below the repository. The fractures in this region are identical to the ones used to provide the upscaled properties for the ECPM in the regional-scale model. Each deformation zone is represented by a single fracture surface with appropriate hydraulic properties, as described in Section 3.2.2. Fractures with appropriate hydraulic and transport properties are also used to represent the repository structures. Boundary conditions (pressure) and initial conditions (pressure and density) are imported from the regional-scale model. The density is held fixed and the pressure field consistent with the densities and boundary conditions is calculated to give conservation of mass. The site-scale model is primarily used to continue particles from the repository-scale model, but it is also used track particles from the repository to provide exit locations for biosphere objects.

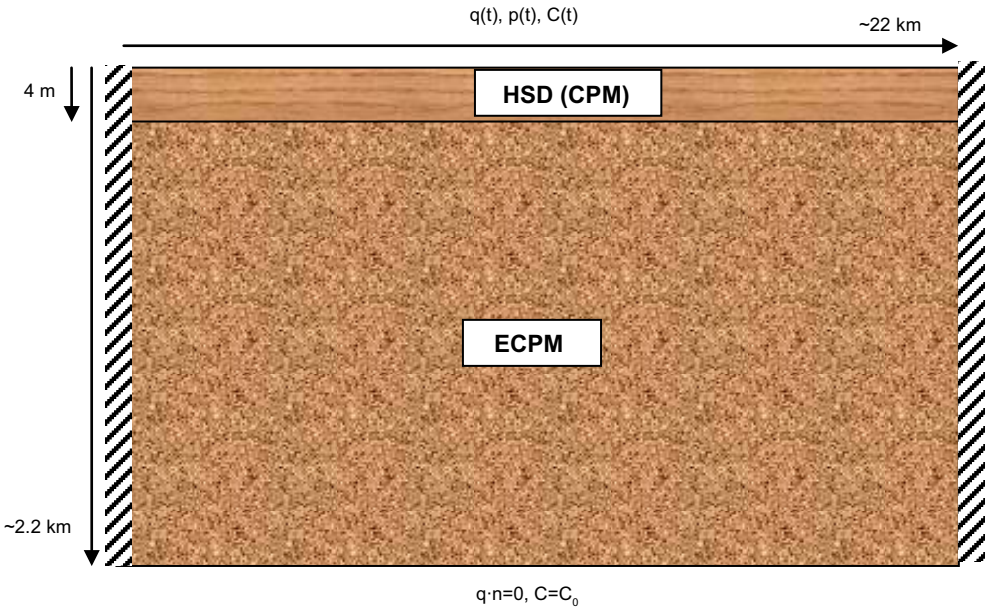

Figure 3-14. *Schematic illustration of the regional-scale model. The bedrock is represented as an ECPM (upscaled DFN). The HSD in the upper layers of the model is represented as a CPM. The hatched lines represent no flow boundaries. The top surface has flux, q, pressure, p, and concentration, C (reference water fractions), boundary conditions that vary with time. The bottom surface has a fixed concentration boundary condition.*

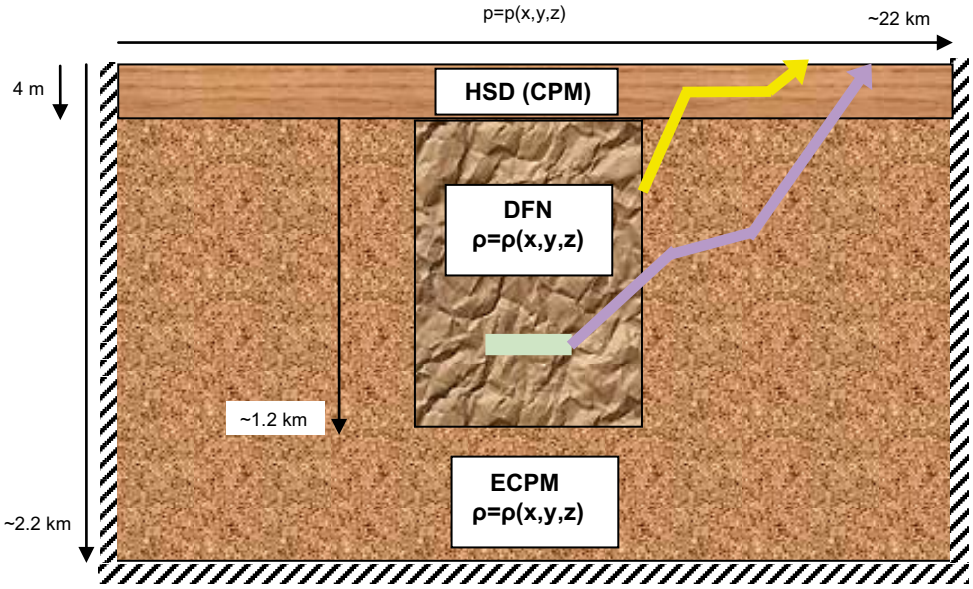

Figure 3-15. *Schematic illustration of the site-scale model. A DFN is embeded within the ECPM of a regional-scale model. The repository location is indicated by the pale green box. The hatched lines represent no flow boundaries. The top surface boundary condition uses specified pressures, p(x,y,z) imported from the regional-scale model for specified time slices. The continuation of a repository-scale particle is shown in yellow. A site-scale only particle tracked from the repository is shown in pale purple.*

The repository-scale model uses a CPM representation of the main tunnels, deposition tunnels and deposition holes in the repository. This provides a suitable representation of the tunnel backfill, which is a porous medium, and allows detailed 3D particle tracking within the tunnels.These structures are embeded within a DFN representation of the HRD. The fractures in this region are identical to the ones used to provide the upscaled properties for the ECPM in the regional-scale model, but with additional smaller-scale fractures added close to the repository structures. These small scale fractures provide more detailed particle tracking for particles released at the repository. These small fractures are on the same scale as the smallest fractures modelled around the boreholes in the calibration to PFL data in SDM-Site. It is not practicle to model these small fractures everywhere, but they provide transport pathways for particles released from deposition holes. Other repository structures (transport tunnels, central tunnels, the ramp and shafts) are represented by fractures with appropriate hydraulic and transport properties in the same way as for the site-scale model. The geometries of these structures are more difficult to model as a CPM and they are less important for particle tracking due to their distance from the deposition holes. The excavation damaged zone (EDZ) and deformation zones (HCD) are represented as fractures in the same way as in the site-scale model. The repository-scale model is divided into 3 blocks for computational efficiency. Boundary conditions (pressure) and initial conditions (pressure and density) are imported from the regional-scale model. The density is held fixed and the pressure field consistent with the densities and boundary conditions is calculated to give conservation of mass. An illustration of a repository-scale block is shown in Figure 3-16.

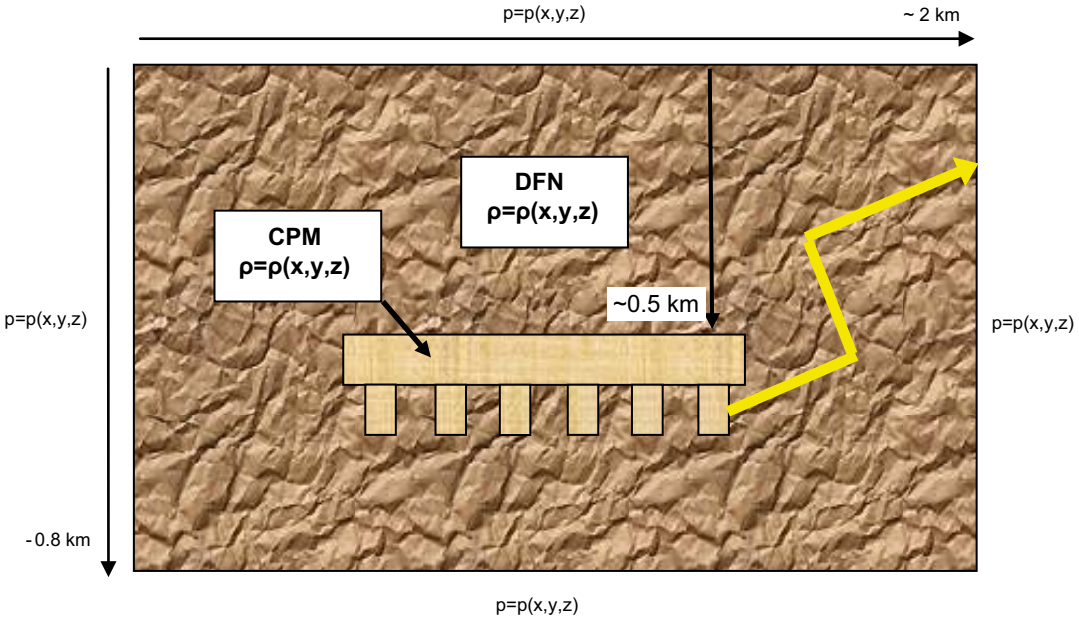

Figure 3-16. *Schematic illustration of the repository-scale model. A CPM representation of the main tunnels, depositon tunnels and deposition holes is embeded within a DFN representation of the HRD. The external surface boundary conditions use pressures, p(x,y,z), imported from the regional-scale model for specified time slices. The top surface elevation corresponds to the bottom of the HSD. The yellow line represents a particle tracked from a single canister location to the boundary of a repository-scale block.*

3.2.2 Representation of deformation zones (DZs)

For SDM-Site Laxemar and this study, the basic concept is that fractures exist on a continuous range of length scales, which motivates a methodology to generate sub-lineament-scale fractures stochastically on scales between a few metres to about 1 km, and then combine this DFN by superposition with the larger scale deterministic deformation zones (DZs) contained within the HCD. The approach used to represent the DZs was different in the DFN and CPM/ECPM models, as described below.

Deformation zones in CPM/ECPM models

In CPM and ECPM models the DZs were represented by modifying the hydraulic properties of any finite-elements intersected by one or more zones to incorporate the structural model in terms of the geometry and properties of zones using the Implicit Fracture Zone (IFZ) method in ConnectFlow, as described in /Marsic et al. 2001/. In a CPM model, properties are homogeneous within a set of defined sub-domains prior to superposition of the DZs. Afterwards, the hydraulic properties vary from element to element if intersected by a DZ. In an ECPM model, the methodology is to first create one or more realisations of the stochastic DFN (including the DZs to provide connectivity) on the regional-scale and then, using the upscaling methods described in Section 3.1.3, to convert this to a realisation of the ECPM model, with the DZs removed. The ECPM model properties are then modified to incorporate the effect of the DZs.

The IFZ method identifies which elements are crossed by a fracture zone and combines a hydraulic conductivity tensor associated with the fracture zone with a hydraulic conductivity tensor for the background stochastic network. For each element crossed by the fracture zone the following steps are performed:

1. The volume of intersection between the fracture zone and the element is determined.
2. The hydraulic conductivity tensor of the background rock is calculated in the coordinate system of the fracture zone.
3. The combined conductivity tensor of the background rock and the fracture zone is calculated in the coordinate system of fracture zone.
4. The effective hydraulic conductivity tensor that includes the effect of the fracture zone is determined in the original coordinate system.

The methodology is illustrated in Figure 3-17. In 3D, the resultant hydraulic conductivity is a 6-component symmetric tensor in the Cartesian coordinate system. The tensor can be diagonalised to give the principal components and directions of anisotropy.

Similarly, combined scalar block-scale porosity is calculated for the element, based on combining the deformation zone porosity and the background block-scale porosity using a weighting based either on the relative volume or on relative transmissibility (total channel flow capacity, which is transmissivity times flow length [m^3s^{-1}]). The latter weighting was used for this study and can be suitable for transport since it weights the combined porosity toward the fracture zone porosity if this is of a relatively high hydraulic conductivity.

The result of this process is to produce a spatial distribution of CPM element properties (hydraulic conductivity tensor, porosity and flow wetted surface) that represent the combined influence of both the deterministic fractures zones and background stochastic fractures.

It may be noted the term “background conductivity” here means the equivalent conductivity of the stochastic fracture network. No extra component for matrix conductivity or micro-fracturing is added. However, the stochastic DFN is necessarily truncated in some way, e.g. based on fracture radius which in consequence means that some elements may not include a connected network of fractures or may only be connected in some directions. To avoid this just being a result of the choice of truncation limit and chance, a minimum block conductivity and porosity is set for any elements that have zero properties following the fracture upscaling and IFZ methods. Appropriate minimum properties were derived in the SDM Hydro-DFN studies by calculating the minimum values seen when the DFN is truncated only at very small fractures relative to the block size, and so are essentially free from the truncation effect.

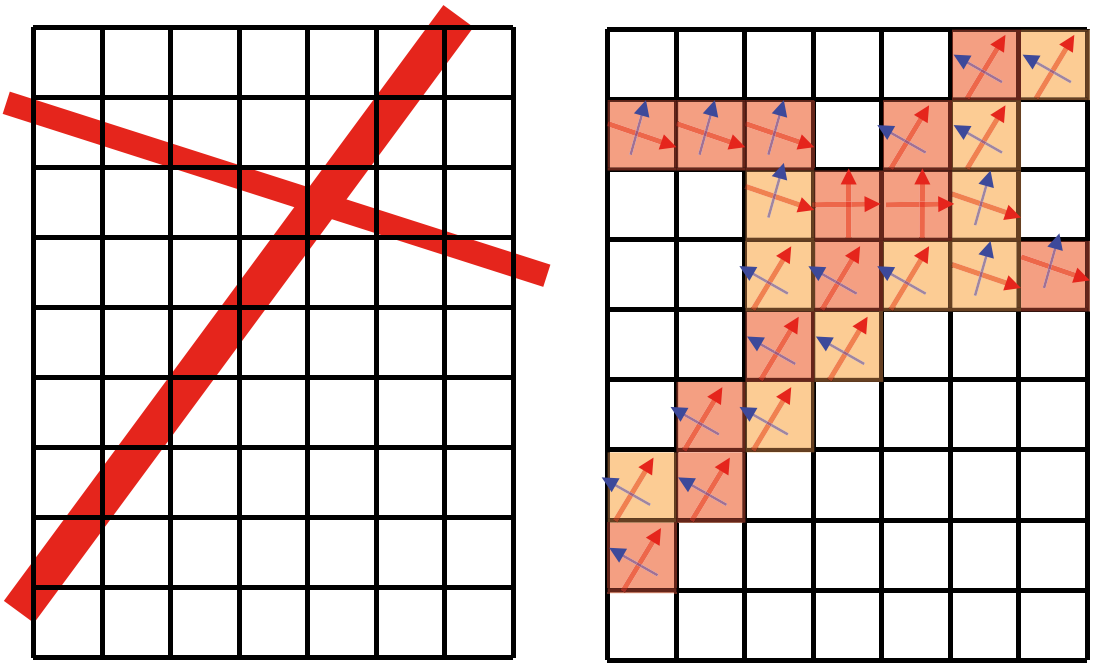

Figure 3-17. *Schematic illustration of the modification of the hydraulic conductivity tensor by the IFZ method. A finite-element grid crossed obliquely by two fracture zones of different thickness (left).*

Deformation zones in DFN models

In DFN models, the deformations zones (DZs) are modelled as planes which are composed of many rectangular or triangular planes that discretise the geometry and hydraulic properties. The site descriptive modelling prescribed a depth dependent transmissivity that decreased significantly with depth and also depended on the dip (gently dipping or vertical) of the zone. Therefore, it was necessary to sub-divide the zones into relatively small sub-fractures to represent the property variations.

The transport aperture, e_t, of each sub-fracture that represents a DZ is calculated as:

$$e_t = \phi b \qquad (3\text{-}5)$$

where ϕ is the porosity and b is the thickness of the deformation zone at that point, as specified by the geologists. The transport aperture is then used in transport calculations and used to calculate performance measures in the same way as for other fractures in the DFN, as described in Section 3.2.6.

Deformation zones in embedded models

To ensure consistency of how larger scale fractures zones are represented when they cross between DFN and CPM models, the fracture zone geometries need to be defined consistently. This is achieved by using the same deformation zone data file for both the DFN and CPM regions of the model. Figure 3-18 illustrates how a large deterministic fracture that crosses between DFN and CPM sub-models can be modelled in such a way as to ensure there is continuity in its representation, and hence in flow between the regions.

A few fractures in the DFN region are shown in red and orange. The red fractures may be stochastic, for example. The orange fracture is a deterministic DZ that crosses the interface. On the DFN side it is shown as a plane, while on the CPM side it is drawn with its actual thickness. The elements crossed by the DZs are coloured yellow. Hydraulic conductivity, porosity and flow wetted surface in these elements is modified by the IFZ method to represent the effect of the DZ on flow and transport.

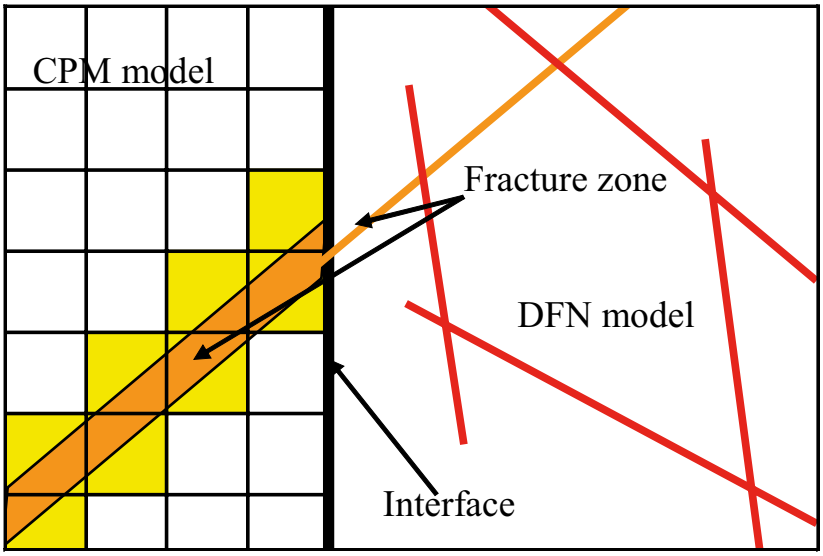

Figure 3-18. *Schematic illustration of continuity of DZs across a CPM/DFN interface in a ConnectFlow model. The DFN region is to the right with a CPM grid to the left.*

3.2.3 Variable density groundwater flow and salt transport

Variations in groundwater composition create variations in groundwater density and hence buoyancy-driven flow that modifies the pattern of groundwater flows. Since gradients in the water table at Laxemar are relatively weak, then buoyancy forces arising from the presence of salt are significant. ConnectFlow has the following capabilities for handling variable-density flow:

1. An option in CPM or ECPM models to simulate flow in a porous medium for groundwater of variable salinity, where the salinity arises from a number of groundwater constituents. This can be modelled either in terms of transport of mass fractions of the basic hydrogeochemical constituents (such as chloride, sodium), which are taken to be conservative, or in terms of transport of fractions of selected reference waters. In both cases the transport equations are coupled with the overall mass conservation equation for groundwater flow. In addition, rock matrix diffusion (RMD) is included in the transport of mass fractions of groundwater constituents, or in the transport of fractions of reference waters respectively. The diffusion of salt into or out of the matrix will continuously change the fluid density at every location and thus change the flow pattern.
2. An option to calculate groundwater flow for specified spatial variations in groundwater density in DFN models and embedded models. That is, the groundwater density has to be interpolated on to the fracture system from another model, but then the consistent pressure distribution and flow-field is calculated with buoyancy forces included. The groundwater density is typically interpolated from a CPM or ECPM model for a selected time slice, thus providing only an instantaneous representation of the flow field. Particle tracking through both DFN and embedded models with the calculated flow field can then be performed.

The RMD capability makes it possible to model diffusion of the reference waters between groundwater flowing in fractures and immobile water in the rock matrix between the fractures. The numerical approach used (/Hoch and Jackson 2004/) is based on a method developed by /Carrera et al. 1998/ and enhanced to enable potentially larger time steps to be taken. The approach combines an approximation that is accurate for small times with one that is accurate for long times, to give a representation of the diffusion into the rock matrix that is accurate for all times. At early times, the diffusion is represented in terms of the inverse of the square root of time, and at long times it is represented as a series of decaying exponentials. The main parameter that controls the rate of RMD is the fracture surface area per unit volume, σ [m^2/m^3].

3.2.4 Transport calculations

A major objective of the modelling is to compute groundwater flow-paths from each deposition hole (there are 8,031 in total) to the surface. The approach taken was to track particles moving with the advective flow from release points around the deposition holes until they reach the top surface. In doing this, two key issues that have to be addressed are how to do this when two scales of model are being used, and how to deal with the transient evolution of the flow-field.

The repository-scale models are very detailed around the repository but have limited extent. Vertically, the model extends from –800 m elevation to the bottom of the HSD that lies on top of the rockhead, but does not extend horizontally far beyond the edge of the repository layout. The vertical path was found to be an important one in the embedded DFN/CPM model, but still some paths exit the vertical sides of the repository-scale model. The solution is to track particles from the release points to the outer boundary of the repository-scale model, and then restart the particle tracking in the corresponding site-scale model from the points where the particles leave the repository-scale model. Performance measures such as travel-time are calculated as the cumulative travel-time along both legs of the path.

It is possible in ConnectFlow to track particles as they move through a flow-field that evolves with time in a CPM model. However, for a DFN model or an embedded CPM/DFN model, fixed instantaneous flow-fields from selected times must be used to obtain a qualitative assessment of the potential impact of releases at different times. The objective is to establish whether flow-paths are sensitive to the retreat of the shoreline, and if so, whether flow-paths stabilise once the shoreline becomes remote from the site. The release times are chosen carefully to represent different phases when the flow-field appears to be either changing significantly, or when there are periods of relative stability. Hence, for the transport calculations reported here, performance measures are calculated based on fixed flow-fields at several selected times.

For the case where the shoreline is retreating away from the site, such that a major discharge area is getting further away in time, then it is expected that flow-paths and travel-times are getting longer, and hence using the instantaneous flow-field at the release time is considered a conservative approximation for the subsequent evolution. However, it is expected that the influence of the shoreline location will decrease at greater distances from the repository location. When travel-times become longer than the temperate climate period due to retention (e.g. due to sorption), then one needs to consider transport in the wider context of the climate evolution, which is outside the remit of the study reported here.

3.2.5 Flow and transport in the repository and EDZ

The repository itself, along with structures such as the transport tunnels, shafts, and their associated excavation damaged zones (EDZs), have a potentially significant impact on the local groundwater flow. In order to account for these effects it is necessary to represent the repository appropriately in the model. The potential conduits for flow within the repository are the deposition tunnels, main tunnels, transport tunnels, ramp and shafts, together with the EDZ around the tunnels created during construction of the repository. The operational and re-saturation phases are not considered here, so it is assumed that only saturated flow needs to be considered. It is assumed that all tunnels have been backfilled to give homogeneous properties. For the EDZ, the design premise is that it will be continuous and the transmissivity will be $1.0 \cdot 10^{-8}$ m^2/s over a thickness of 0.3 m /SKB 2010a/. Although this is the scenario adopted by the Hydrogeological base case as a conservative approach, data suggests that a continuous EDZ would not form at all /SKB 2010a/.

In terms of safety assessment calculations, three potential paths for radionuclides to leave the canister are considered:

1. **Q1**, diffusion into the mobile water in fractures surrounding the deposition hole.
2. **Q2**, diffusion into mobile water in the EDZ.
3. **Q3**, diffusion into a fracture intersecting the tunnel.

In order to study each of these paths, the detailed repository-scale models have to represent the deposition holes, tunnels and EDZ explicitly, and flow-paths have to be computed for a release at three appropriate positions around each canister. Hence, the performance measures (PMs) defined in Section 3.2.6 are calculated for three paths for each canister. It is possible that the three particles may follow very similar trajectories, such that t_r, L_r and F_r are similar, but U_r, U_{EDZ} or U_t will vary, where the subscript r denotes rock and the subscript t denotes the repository structures, primarily tunnels. Further, for each path, the PMs are calculated for portions of the path spent in the rock, tunnels, and EDZ separately. In the work reported here, no retention of radionuclides is assumed within the tunnels and EDZ and so the flow wetted surface (a_r) is assigned a zero value in the tunnels and EDZ, and hence F_{EDZ} and F_t are zero, and therefore only t_{EDZ}, L_{EDZ}, t_t and L_t are calculated. Figure 3-19 shows the three pathways considered.

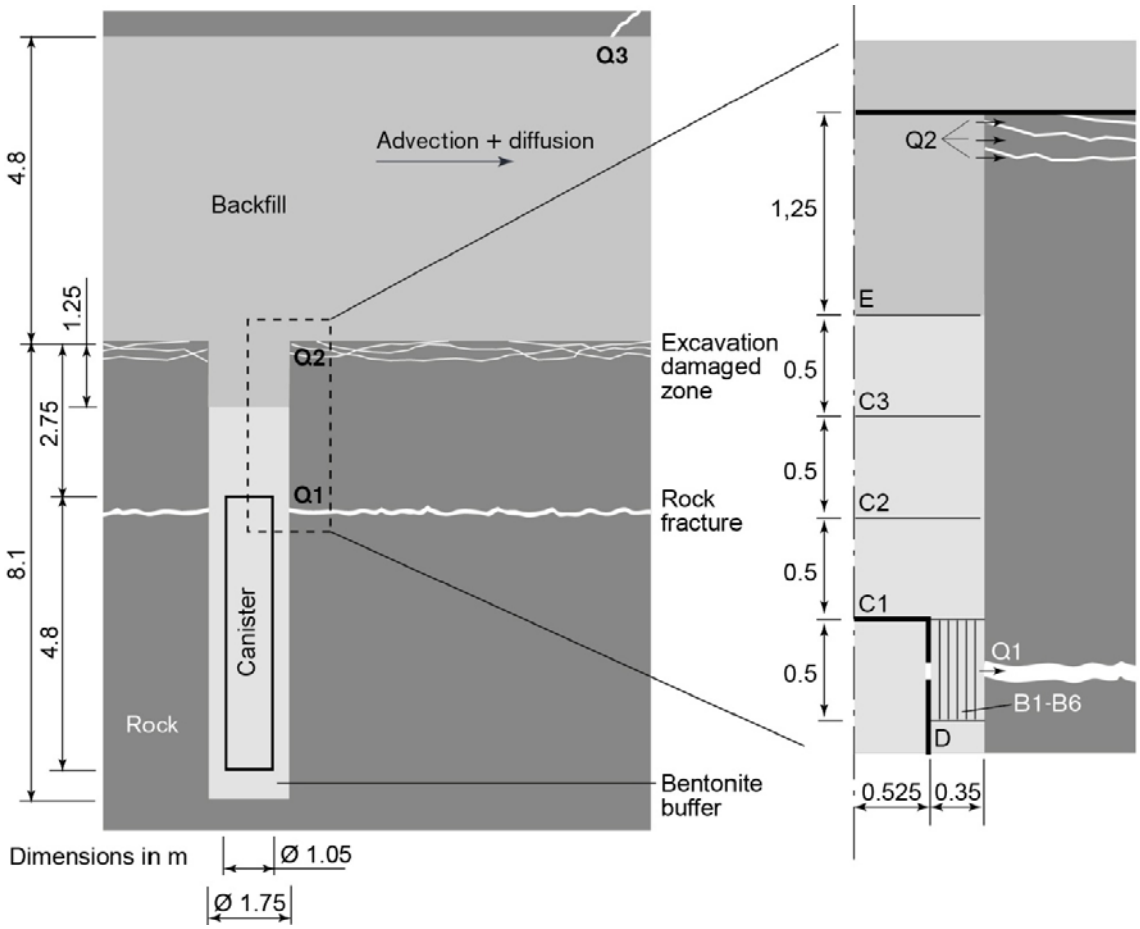

Figure 3-19. *Schematic view of the repository design, showing the small hole in the canister and the location of the various possible transport paths into near-field rock.*

3.2.6 Calculation of performance measures

To provide input to performance assessment (PA) calculations, tables of performance measures are produced for each case using five performance measures (PMs). In a CPM representation these are defined as:

1. Travel-time, $t_r = \sum_l \frac{\phi \delta l}{q}$, where δl is a step length, for example through one finite-element, along a path of l steps, ϕ is the kinematic porosity, and q is the Darcy flux.
2. Equivalent flux at the release point, U_r, described in more detail below.
3. Equivalent flow rate at the release point, Q_{eq}, described in more detail below.
4. Pathlength, $L_r = \sum_l \delta l$.
5. Flow-related transport resistance, $F_r = \sum_l \frac{a_r \delta l}{q}$, where a_r is the flow wetted surface area per unit volume of rock. This is a measure of the potential for retention and retardation of radionuclides within the rock.

The subscript "*r*" indicates that the PM is calculated in the rock. That is, they only represent cumulative PMs for those parts of paths within the rock and exclude parts of flow-paths that pass through the EDZ or tunnel backfill. PMs are calculated for legs of paths within the EDZ and tunnels, but are computed as separate PMs for each path and distinguish by an "*EDZ*" or "*t*" subscript, respectively.

In a DFN representation the PMs are defined as:

1. Travel-time, $t_r = \sum_f \frac{e_{tf} w_f \delta l}{Q_f}$, where δl is a step length along a path of f steps, each between a pair of fracture intersections, e_{tf} is the fracture transport aperture, w_f is the flow width between the pair of intersections, and Q_f is the flow rate between the pair of intersections in the fracture.
2. Equivalent flux at the release point, U_r, described in more detail below.
3. Equivalent flow rate at the release point, Q_{eq}, described in more detail below.
4. Pathlength, $L_r = \sum_f \delta l$.
5. Flow-related transport resistance, $F_r = \sum_f \frac{2 w_f \delta l}{Q_f} = \sum_f \frac{2 t_{rf}}{e_{tf}}$, where t_{rf} is the travel time in a fracture along the path.

The results from the particle tracking are used to produce ensemble statistics for the performance measures, as well as locating the discharge areas. The ensemble is over the set of 8,031 particle start locations, one for each deposition hole and is in total divided over three blocks; block 1 with 2,158 start locations, block 2 with 3,576 start locations and block 3 with the remaining 2,297 start locations (Figure 3-13). Apart from the work done on the repository layout, no further attempt is made to avoid starting particles in either deterministic fracture zones or high transmissivity stochastic fractures. In reality, such features are likely to be avoided during repository construction, and hence the model may tend to see particles start in a wider range of possible fracture transmissivities than might be encountered in reality.

To avoid particles becoming stuck in regions of stagnant flow, they are not started if the initial flow rate per unit width is less than $1 \cdot 10^{-6}$ m^2/y for Q1 and Q2 and the initial Darcy flux is less than $1 \cdot 10^{-6}$ m/y for Q3. For Q1 and Q2, flow rate per unit width, q_f, in a fracture is defined as

$$q_f = e_{tf} v = \frac{Q_f}{\sqrt{a_f}} \qquad (3\text{-}6)$$

where:

- e_{tf} is the transport aperture of the fracture [m].
- v is the velocity [m/y].
- Q_f is the volumetric flow rate in the fracture [m^3/y].
- a_f is the area of the fracture plane [m^2].

For Q3, the Darcy flux, q, is defined as the volumetric flow rate per unit area.

Equivalent flow rate (Q_{eq}) for input to near-field models

The near-field code COMP23 calculates the non-stationary nuclide transport in the near-field of a repository. The system is divided in to compartments, where the only restriction is that a compartment is formed of the same material. The model, which is a very coarsely discretised Integrated Finite Difference Model, embeds analytical solutions at locations where other models require a very fine discretisation, such as entrances and exits from small holes and fractures. In the repository, radionuclides leaking out through a small hole in the canister wall diffuse into the bentonite buffer and may then migrate through various pathways into the flowing water in rock fractures.

For compartments in contact with water flowing in fractures in the rock, the diffusive transport is determined by an equivalent flow-rate, Q_{eq} [m^3/y]. This parameter is a fictitious flow-rate of water that carries a concentration equal to that at the compartment interface. It has been derived by solving the equations for diffusive transport to the passing water by using boundary layer theory /Neretnieks 1979/. The value of Q_{eq} is dependent on the geometry of the contact area, the water flux, the flow porosity or fracture aperture and the diffusivity. As part of the SR-97 assessment formulae were derived for a CPM model /Moreno and Gylling 1998/. The formulae are different for a DFN model as detailed below for the three pathways The derivation of the equations is given in Appendix D.

Q-equivalent release into the fractured rock (Q1) for a repository-scale model

Path Q1 considers release of radionuclides into the fractured rock surrounding the deposition hole, and hence the particle starts within a fracture that intersects the wall of the deposition hole. Several fractures may intersect the deposition hole. For reasons of making a conservative assumption, the flux into all fractures that intersect the deposition hole and contribute to advective flow away from the deposition hole are included in the calculation of Q_{eq}. That is, an effective flow-rate is calculated for all fractures that cut the deposition hole and are connected to at least one other fracture. These equivalent flow-rates are summed for the deposition hole to give the total Q_{eq}. The equivalent groundwater flow rate for Q_{eq1} can be written as:

$$Q_{eq1} = \sum_f \left(\frac{Q_f}{\sqrt{a_f}} \sqrt{\frac{4 D_w t_{wf}}{\pi}} \right) \qquad (3\text{-}7)$$

where $t_{wf} = \dfrac{L_f \cdot e_{tf}}{Q_f / \sqrt{a_f}}$

If there are several fractures intersecting a single deposition hole, then a conservative approach to calculate the equivalent groundwater flow rate requires the flow to be summed across all the fractures, with t_{wf} calculated separately for each fracture. Hence, the average equivalent flux, U_{r1}, for all fractures intersecting the deposition hole is:

$$U_{r1} = \frac{1}{w_c} \sum_f \frac{Q_f}{\sqrt{a_f}} \qquad (3\text{-}8)$$

where:

- D_w is the diffusivity in water, [m^2/y].
- t_{wf} is the time the water is in contact with the deposition hole within each fracture, [y].
- L_f is the length of the fracture intersection with the wall of the deposition hole, [m].
- U_{r1} is the equivalent initial flux in the fracture system averaged over the rock volume adjacent to the deposition hole [m/y].
- Q_f is the volumetric flow rate in the fracture intersecting the deposition hole [m^3/y].
- e_{tf} is the transport aperture of the fracture intersecting the deposition hole [m].
- a_f is the area of the fracture plane intersecting the deposition hole [m^2].
- w_c is the deposition hole height [m].

Here, D_w was set to 0.0316 m^2/y and w_c was set to 5 m, although this is strictly the canister height. All other values were determined in the flow simulations.

Q-equivalent release into the EDZ (Q2) for a repository-scale model

Path Q2 considers the release of radionuclides into the EDZ. Here the particles are released within a fracture used to represent the EDZ that surrounds the top of the deposition hole. The equivalent groundwater flow-rate, Q_{eq2}, is calculated from the flow in the EDZ fractures that cut the deposition hole. These effective flow-rates are summed for the deposition hole to give the total Q_{eq}, with t_{wE} calculated separately for each fracture. The equivalent groundwater flow-rate, Q_{eq2}, can be written as:

$$Q_{eq2} = \sum_E \left(\frac{Q_E}{\sqrt{a_E}} \sqrt{\frac{4 D_w t_{wE}}{\pi}} \right) \tag{3-9}$$

where $t_{wE} = \dfrac{L_E \, e_{tE}}{Q_E / \sqrt{a_E}}$

The equivalent flux, U_{r2}, for flow in the EDZ is:

$$U_{r2} = \frac{1}{w_E} \sum_E \frac{Q_E}{\sqrt{a_E}} \tag{3-10}$$

where:

- D_w is the diffusivity in water, [m^2/y].
- t_{wE} is the time the water is in contact with the deposition hole within each EDZ fracture, [y].
- L_E is the length of the EDZ fracture intersection with the wall of the deposition hole, [m].
- U_{r2} is the equivalent initial flux in the EDZ fracture system averaged over the EDZ fracture cross-sectional area [m/y].
- Q_E is the volumetric flow rate in the EDZ fracture intersecting the deposition hole [m^3/y].
- e_{tE} is the transport aperture of the EDZ fracture intersecting the deposition hole [m].
- a_E is the area of the EDZ fracture plane intersecting the deposition hole [m^2].
- w_E is the EDZ thickness [m].

Here, D_w was set to 0.0316 m^2/y and w_E was set to 0.3 m. All other values were determined in the flow simulations.

Q-equivalent release into the tunnel (Q3) for a repository-scale model

Path Q3 considers the release of radionuclides into a tunnel and then a fracture that intersects the tunnel. It is assumed that diffusive equilibrium of radionuclides is achieved in the tunnel backfill and diffusion takes place into the water flowing in fractures surrounding the tunnel. Hence, an equivalent flow-rate, Q_{eq3}, is required for advective flow in the first fracture encountered along the path after a particle is released in the tunnel backfill above the deposition hole. The equivalent groundwater flow-rate, Q_{eq3} is calculated from the flow-rate in the first fracture the particle enters after leaving the tunnel.

The equivalent groundwater flow-rate, Q_{eq3}, in the fracture intersecting the tunnel can be written as:

$$Q_{eq3} = 2 \sqrt{\frac{4 D_w L e_{tf} \left(Q_f / \sqrt{a_f} \right)}{\pi}} \tag{3-11}$$

The factor 2 indicates that flow can be around either side of the tunnel. For Q1 and Q2 in the repository-scale model, the factor 2 is not necessary as the flows through intersections with each face of the deposition hole are explicitly summed. The initial flux, U_{r3}, for flow in the first fracture intersecting the tunnel is:

$$U_{r3} = \frac{Q_f}{w_T \sqrt{a_f}} \qquad (3\text{-}12)$$

where:

- D_w is the diffusivity in water, [m^2/y].
- L is the half circumference of the tunnel [m].
- Q_f is the volumetric flow rate in the fracture intersecting the tunnel [m^3/y].
- w_T is the fracture width intersecting the tunnel [m].
- a_f is the area of the fracture plane intersecting the tunnel [m^2].
- e_{tf} is the transport aperture of the fracture intersecting the tunnel [m].

Here, D_w was set to 0.0316 m^2/y , L was set to 7 m and w_T was set to 2.5 m. All other values were determined in the flow simulations.

Q-equivalent release (Q1, Q2, Q3) for a site-scale model

For the site-scale model, the repository structures are represented by equivalent fractures rather than as CPM. Therefore, particles are released directly into fractures for Q1, Q2 and Q3. Since the tunnels and deposition holes are not represented with a 3D volume, it is not appropriate to sum over all fractures intersecting the deposition hole or tunnel. Therefore, the Q_{eq} and U_r values are only calculated for the single fracture that the particle enters when it leaves the deposition hole or tunnel. The equivalent groundwater flow-rate, Q_{eq123}, is calculated from the flow in the starting fracture for each released particle. The equivalent groundwater flow rate, Q_{eq123}, can be written as:

$$Q_{eq123} = 2\sqrt{\frac{4D_w L e_{tf} U_{T0}}{\pi}} \qquad (3\text{-}13)$$

This is equivalent to equations (3-7) and (3-9) for a single fracture, with the factor 2 indicating that flow can be around either side of the deposition hole or tunnel. For Q1 and Q2 in the repository-scale model, the factor 2 is not necessary as the flows through intersections with each face of the deposition hole are explicitly summed. The equivalent flux, U_{r123}, for flow in the fracture is:

$$U_{123} = \frac{U_{T0}}{w} \qquad (3\text{-}14)$$

where:

- D_w is the diffusivity in water, [m^2/y].
- L is the half circumference of the deposition hole (Q1 and Q2) or tunnel (Q3), [m].
- U_{T0} is the flow rate in the fracture per unit fracture width [m^2/y].
- e_{tf} is the transport aperture of the fracture [m].
- w is the deposition hole height or fracture width [m].

Here, D_w was set to 0.0316 m^2/y , L was set to 2.8 m for Q1, to 2.8 m for Q2 and to 7.0 m for Q3, w was set to 5.0 m for Q1 (although this is strictly the canister height), to 0.3 m for Q2 and to 2.5 m for Q3. All other values were determined in the DFN flow simulations. This is equivalent to equations *(3-8)* and (3-10) for a single fracture.

Q-equivalent release (Q1, Q2, Q3) for a stochastic continuum model

For a stochastic continuum model the equations for Q_{eq} can be expressed in an equivalent form as:

$$Q_{eq} = 2w\sqrt{\frac{4D_w L \phi U_r}{\pi}} \qquad (3\text{-}15)$$

where:

- D_w is the diffusivity in water, [m²/y].
- L is the half circumference of the deposition hole (Q1 and Q2) or tunnel (Q3), [m].
- ϕ is the kinematic porosity.
- U_r is the initial Darcy flux (Q1 and Q2) or the Darcy flux where the particle leaves the tunnel (Q3) [m/y].
- w is the deposition hole height (Q1), the EDZ thickness (Q2) or the fracture zone thickness (Q3) [m].

Here, D_w was set to 0.0316 m²/y , L was set to 2.8 m for Q1, to 2.8 m for Q2 and to 7.0 m for Q3, w was set to 5.0 m for Q1 (although this is strictly the canister height), to 0.3 m for Q2 and to 2.5 m for Q3. All other values were determined in the CPM flow simulations. For Q1 and Q2, Q_{eq} is calculated at the particle starting location and for Q3 it is calculated at the point where the particle first exits the tunnel. The factor 2 indicates that flow can be around either side of the tunnel or deposition hole. For Q1 and Q2 in the repository-scale model, the factor 2 is not necessary as the flows through intersections with each face of the deposition hole are explicitly summed.

3.2.7 Deposition hole rejection criteria (FPC/EFPC)

During construction of the repository some deposition holes may be excluded due to the presence of transmissive fractures. If such fractures are detected then the deposition hole may not be constructed. There are two criteria for deciding whether or not a hole should be excluded:

1. Full perimeter criteria (FPC) – a deposition hole is excluded if it is intersected by the hypothetical extension of a fracture that intersects the full perimeter of the corresponding deposition tunnel.
2. Extended full perimeter criteria (EFPC) – a deposition hole is excluded if its full perimeter is intersected by a fracture that also intersects the full perimeter of four or more neighbouring deposition holes in the same deposition tunnel.

An algorithm for analysing the deposition holes according to the FPC and EFPC was implemented in ConnectFlow. This was used to flag deposition holes that may be excluded due to these criteria, but they were not actually excluded in the flow or particle tracking calculations. For the purposes of the algorithms, full-perimeter indicated an intersection between a fracture and all four side edges of a deposition tunnel or a deposition hole. Also, in the implementation of the FPC, the fracture was not hypothetically extended when considering intersections with deposition holes, i.e. the fracture needed to actually intersect the deposition hole as well as the full perimeter of the deposition tunnel. This approximation is unlikely to significantly affect the number of deposition holes fulfilling the FPC.

EDZ fractures were not considered for the FPC or the EFPC. Deformation zone fractures were flagged differently for the FPC. Also recorded was the longest length and highest transmissivity of fractures intersecting each deposition hole. This information, along with the FPC and EFPC results, was made available for safety assessment analyses.

4 Hydrogeological base case model specification

The Hydrogeological base case implements the conceptual understanding derived in SDM-Site Laxemar, as described in Chapter 2. However, limited changes were made, as described in Appendix F, to reflect an updated understanding of the site or to address issues of concern for a safety assessment.

The base case model simulation in SDM-Site used a homogeneous HCD and a single realisation of the HRD. In this study, the Hydrogeological base case has the base model (denoted r0) plus one additional realisation (denoted r2):

- r0: Homogeneous HCD + realisation 1 of the HRD.
- r2: realisation 2 of a stochastic HCD + realisation 2 of the HRD.

where r*n* denotes realisation *n*. The extra realisation examines the effect of a stochastic HCD and whether or not r1 of the HRD is unusual in some way.

The Hydrogeological base case was implemented as a set of models at three different scales to focus on the quantities of interest at each scale. However, each model scale is a representation of the same Hydrogeological base case and each is derived from the same set of properties and fractures. The regional-scale model was concerned with the large scale evolution of pressure and reference water distribution over time from 8000 BC to 15,000 AD. The site-scale model used a DFN to provide a more detailed representation of the site for carrying out particle transport calculations. The repository-scale model used a CPM representation of the main tunnels, deposition tunnels and deposition holes within the site-scale DFN to provide detailed performance measures for the initial portions of the particle transport pathways. Each model scale is described in more detail in the following sections.

Since the HRD and, in some cases, the HCD are based on stochastic properties, the Hydrogeological base case was represented as two realisations. Each realisation forms part of the Hydrogeological base case. A summary of the base case and the variant cases covered in chapter 5 is given in Table 4-1.

Table 4-1. Summary of modelling cases.

Case	Description	Report section	Scales	Times	Number of realistions
Hydrogeological base case	The Hydrogeological base case, using the SDM-Site Hydro-DFN, with a semi-correlated transmissivity-size relationship.	4	Regional	8000 BC to 15,000 AD	2
			Site	5000 BC, 2000 BC, 2000 AD, 5000 AD, 10,000 AD, 15,000 AD	2
			Repository	2000 BC, 2000 AD, 5000 AD, 15,000 AD	2
Elaborated Hydro-DFN	Based on an elaborated Hydro-DFN parameterisation, described in Appendix F.	5.1	Regional	8000 BC to 15,000 AD	2
			Site	2000 AD	2
			Repository	2000 AD	2
No minor deformation zones (MDZs)	Based on the elaborated Hydro-DFN parameterisation model with the MDZs not included in the HCD.	5.2	Regional	8000 BC to 15,000 AD	1
			Site	2000 AD	1
			Repository	2000 AD	1
Stochastic continuum	Based on hydraulic conductivity statistics obtained from PSS measurements.	5.3	Regional	8000 BC to 15,000 AD	2
			Site	2000 AD, 15,000 AD	2
			Repository	2000 AD, 15,000 AD	2

4.1 Regional-scale model

The regional-scale model used the same representation as the SDM-Site Laxemar model, but with the changes given in Appendix F. Its purpose was to model the evolution of hydrogeology and hydrochemistry from 8000 BC to 2000 AD, and then into the future temperate period up to 15,000 AD. Periglacial climate conditions are expected at Laxemar before the retreating shoreline reaches the boundary of the model domain at around 15,000 AD.

4.1.1 Model Description

The regional-scale model was constructed from the following domains:

- Hydraulic conductor domain (HCD): deformation zones of generally relatively high transmissivity.
- Hydraulic rock mass domain (HRD): the bedrock between the deformation zones.
- Hydraulic soil domain (HSD): the surface hydrological units.

Each domain is described in the following sections.

As in SDM-Site, the model used 40 m horizontal refinement for the elements in the area local to the repository (an approximately 5.6 km x 4.3 km block with a section cut out to the southeast). Elsewhere, 120 m horizontal refinement was used. The model extended from the ground surface to an elevation of –2,200 m. The upper layers of the model were mapped to be parallel to the surface topography.

Hydraulic Conductor Domain (HCD)

The HCD consists of the deformation zones within the model region. Each deformation zone represents a region of increased fracturing and increased hydraulic conductivity, kinematic porosity and flow-wetted surface area per unit volume of rock. Each deformation zone was included in the regional-scale model as an implicit fracture zone (IFZ), as described in Section 3.2.2. Figure 4-1 shows the deformation zones representing the HCD in the base case model. Each deformation zone was given depth dependent deterministic properties and conditioned on borehole measurements in the regions around the intersections between boreholes and deformation zones.

The IFZs for the HCD were applied to the ECPM representation of the rock using the method given in Section 3.2.2. Within the local domain the element size was 40 m. Within the regional domain the element size was 120 m. These element sizes define the resolution at which the IFZs were applied.

The HCD model also represented the deformation zones as IFZs with stochastic properties to represent heterogeneity. One stochastic realisation of these deformation zones was produced and paired with one realisation of the HRD, to explore the effect of variability in hydraulic properties. This HCD realisation is shown in Figure 4-2.

Hydraulic Rock mass Domain (HRD)

The HRD consists of the bedrock between the deformation zones. For SDM-Site and the regional-scale model this was represented in the model as an ECPM. The properties of the ECPM were generated by upscaling a regional-scale DFN, using the processes described in Section 3.1.3. The ECPM was very similar to that used in SDM-Site, except that the repository structures were considered when determining the connectivity of the HRD fractures. Fractures were generated from 0.4 m to 564 m radius, but only fractures above 5.6 m radius were included for the upscaling as the smaller fractures would not contribute significantly to flow on the block scales considered.

Values of the vertical component of the hydraulic conductivity are shown for slices through the model in each depth zone in Figure 4-3 and Figure 4-4. Values for the kinematic porosity and flow wetted fracture surface area per unit volume of rock are shown for slices through the model at approximately the repository depth in Figure 4-5.

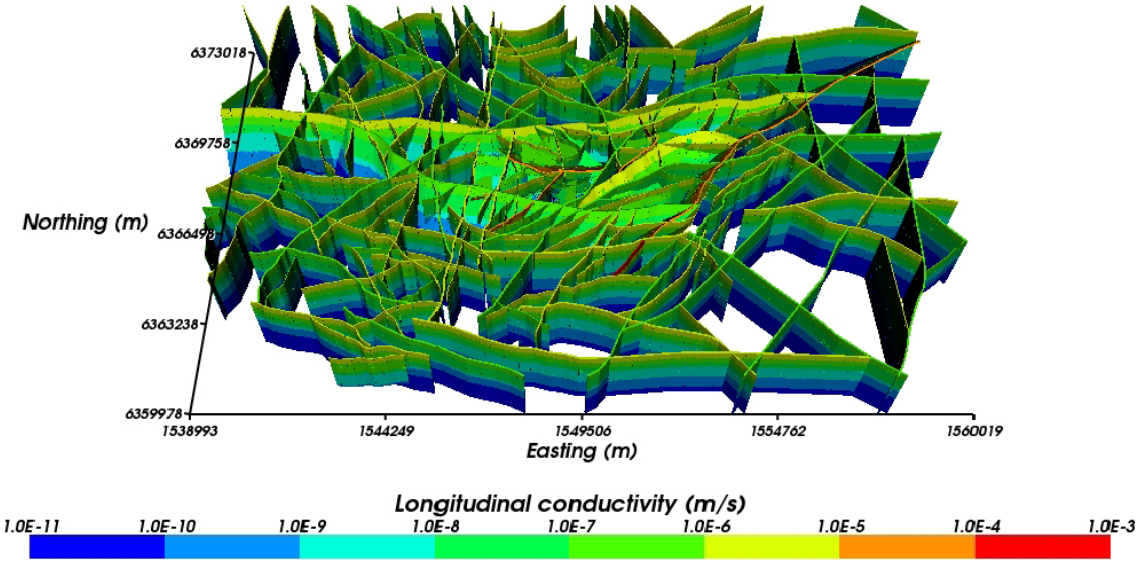

Figure 4-1. *The deformation zones used in the regional-scale Hydrogeological base case model. The deformation zones are coloured by hydraulic conductivity, showing the depth dependency of properties.*

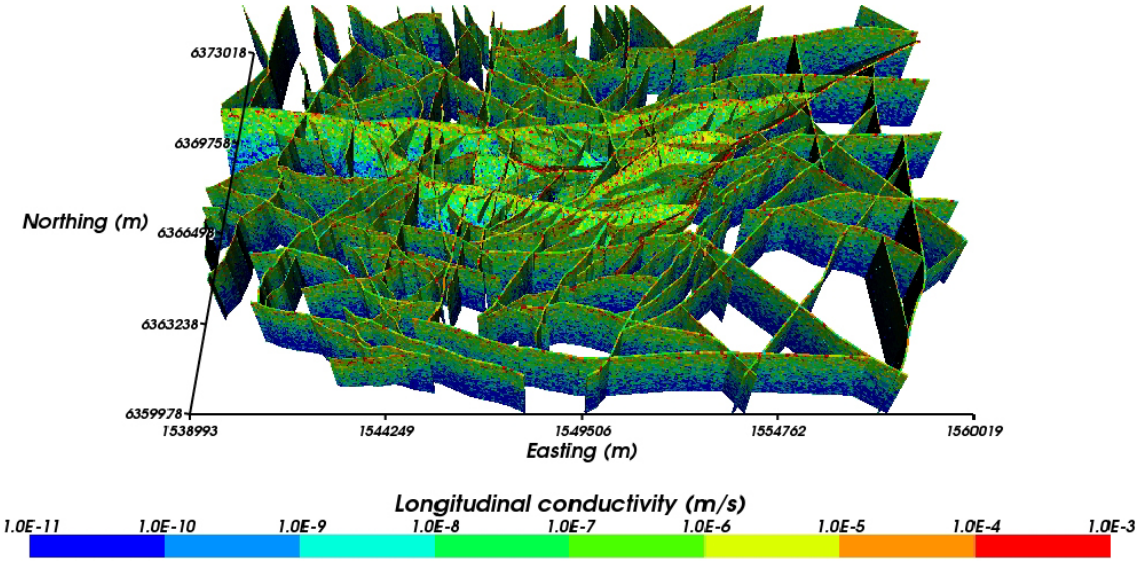

Figure 4-2. *The implicit fracture zones used in one realisation of the HCD. The IFZs are coloured by hydraulic conductivity, which shows the depth dependency of properties. The heterogeneity in hydraulic conductivity within individual IFZs is indicated by the speckled colouration.*

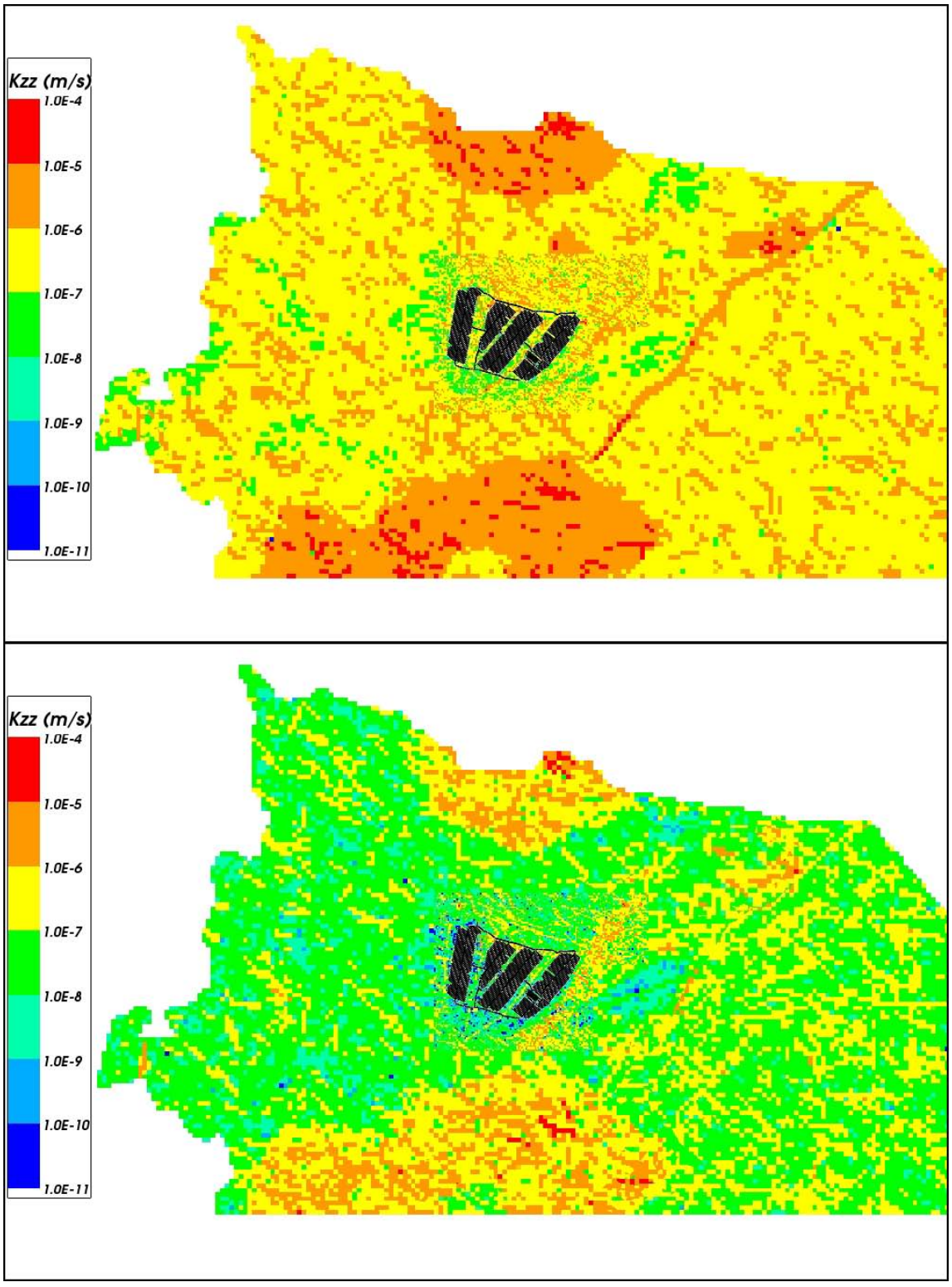

Figure 4-3. *Distribution of vertical hydraulic conductivity on horizontal slices through the regional-scale model. From top to bottom: z = –80 m (in DZ1), z = –250 m (in DZ2).*

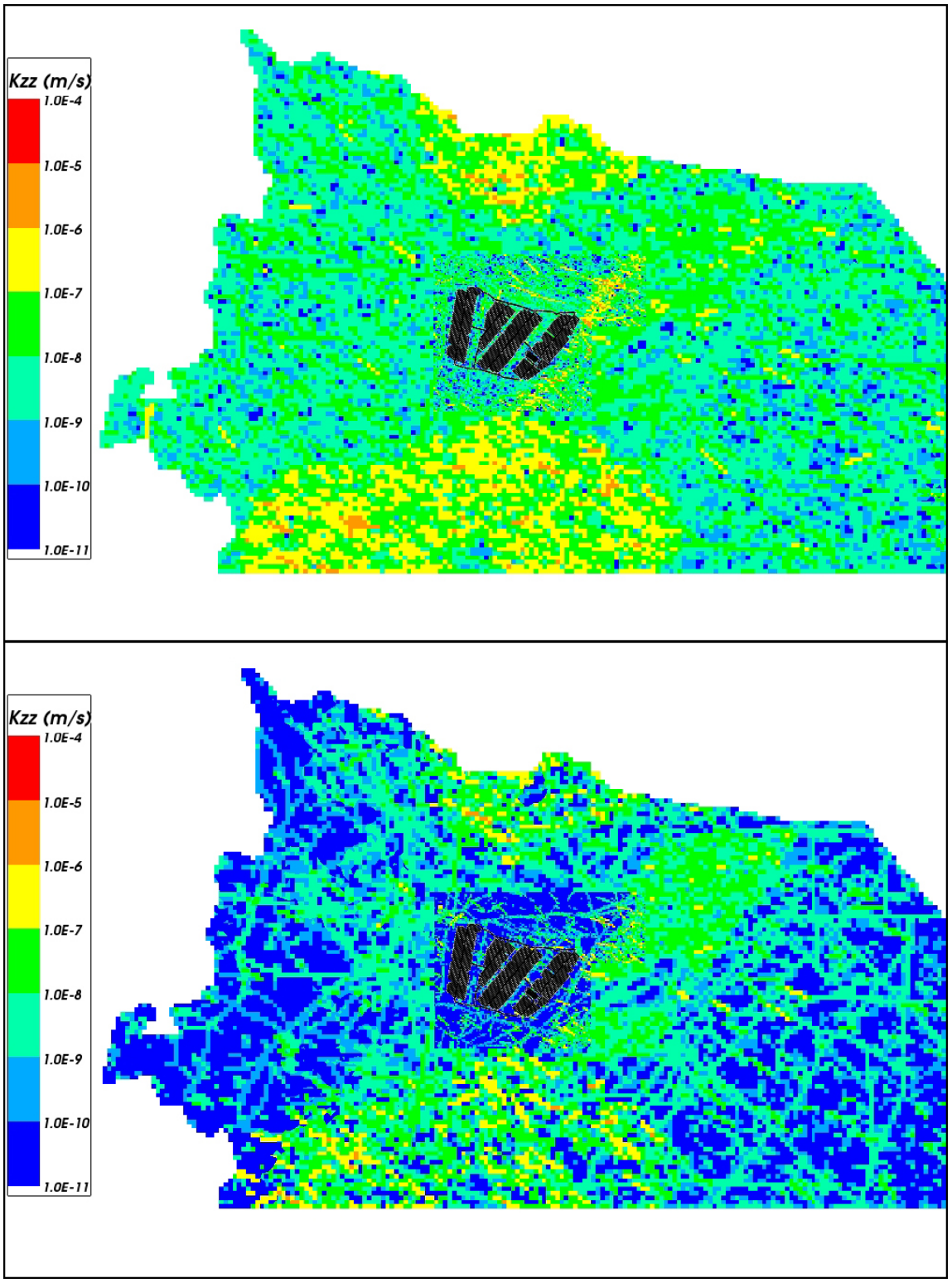

Figure 4-4. *Distribution of vertical hydraulic conductivity on horizontal slices through the regional-scale model. From top to bottom: z = –510 m (repository depth in DZ3), z = –700 m (in DZ4).*

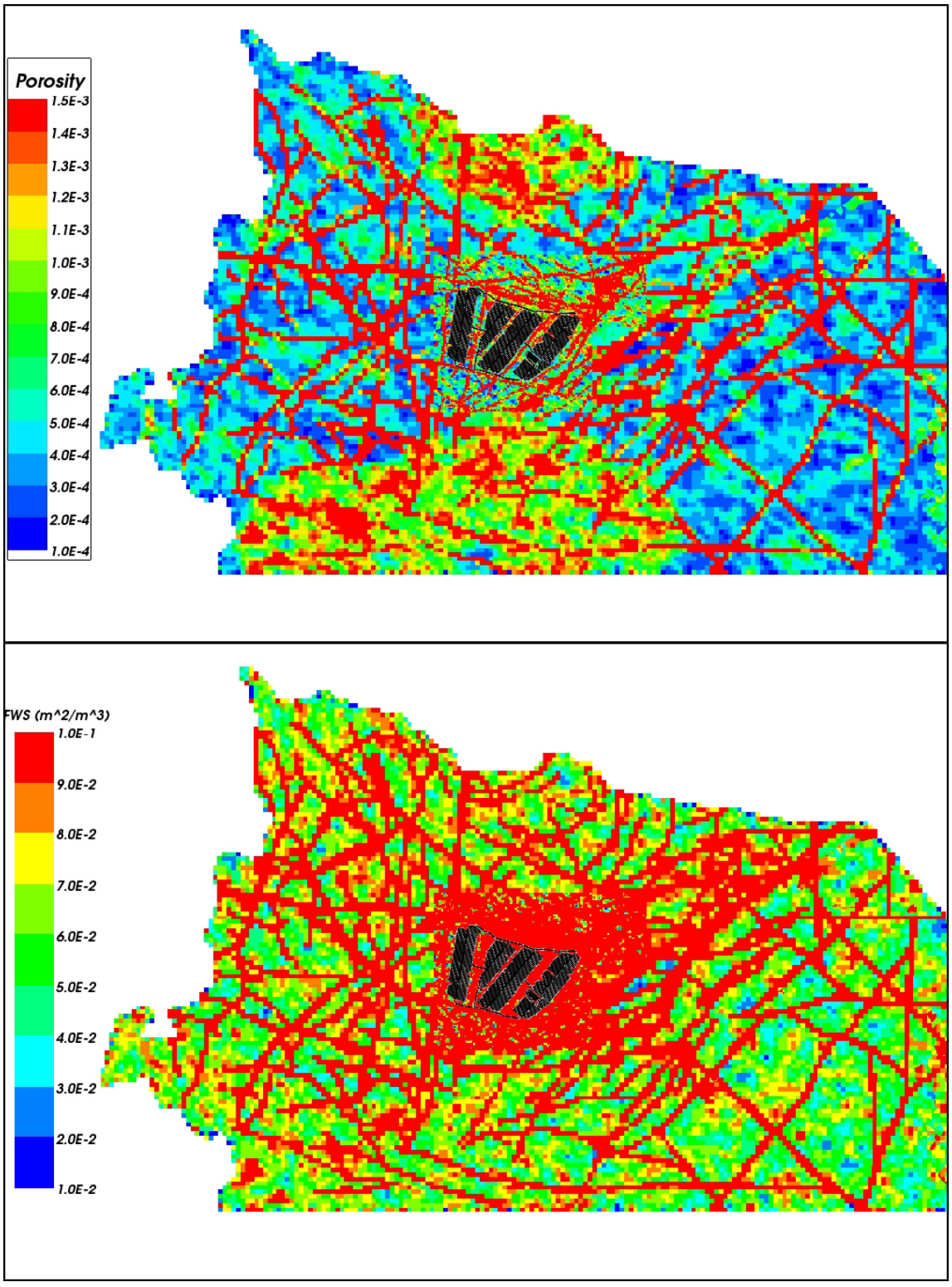

Figure 4-5. *Distribution of kinematic porosity (top) and flow wetted fracture surface area per unit volume of rock (bottom) on a horizontal slice at z = –510 m (repository depth) through the regional-scale model.*

Hydraulic Soil Domain (HSD)

The HSD consists of the surface layers of soil in the top few metres of the regional-scale model. It was modelled using a CPM representation, identical to the HSD used in SDM-Site.

Multiple realisations

To explore the effect of variability in the rock properties, one additional realisation of the regional DFN was generated. This realisation was coupled with the corresponding HCD realisation to construct a model and carry out calculations. The additional realisation will illustrate whether or not spatial variability in HCD properties will affect performance measures and whether or not realisation 1 of the HRD is unusual in some way.

4.1.2 Boundary conditions and initial conditions

The boundary conditions used for this study were the same as those used for SDM-Site. They consisted of a recharge-discharge boundary condition on the top surface and no flow through the sides and bottom of the model. The bottom of the model also had a hydrochemical boundary condition set to the initial values of the reference water fractions. The reference water fractions on the top boundary varied with time according to the elevation of shoreline with regard to the topography of the ground surface.

The initial conditions were also the same as those used in SDM-Site, except as noted in Appendix F.

4.1.3 Calculation of past and future evolution

The past evolution of the regional-scale model was calculated in the same way as for SDM-Site, i.e. the calculation of pressures and reference water fractions for a transient evolution in 20 year time steps from 8000 BC to 2000 AD, including the effects of rock matrix diffusion (RMD). The future evolution continued these calculations to 15,000 AD. The change in the shoreline due to post-glacial land rise was obtained from the curve shown in Figure 4-6. The salinity of the Baltic Sea was obtained from the curve shown in Figure 4-7.

The location of the shoreline at different times is shown in Figure 4-8. It can be seen that the repository area is under the sea until about 2000 BC and by 15,000 AD the shoreline has reached the edge of the model domain.

For the additional realisation of the HCD and HRD, the calculations were carried out from 8000 BC to 2000 AD only.

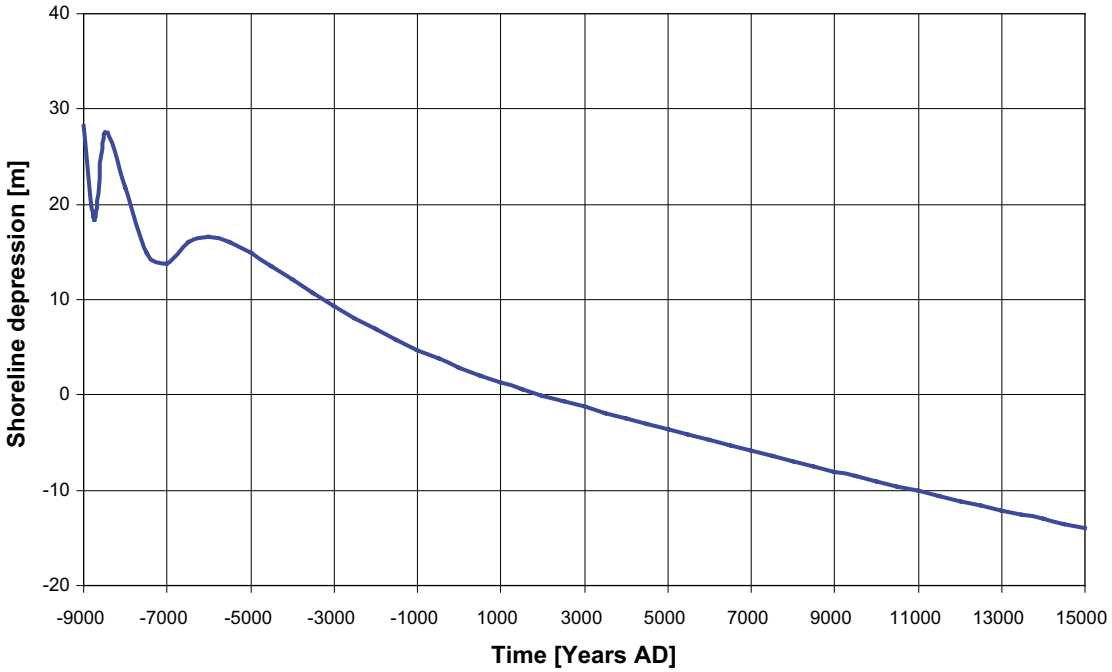

Figure 4-6. *Evolution of the shoreline (/SKB 2010b/).*

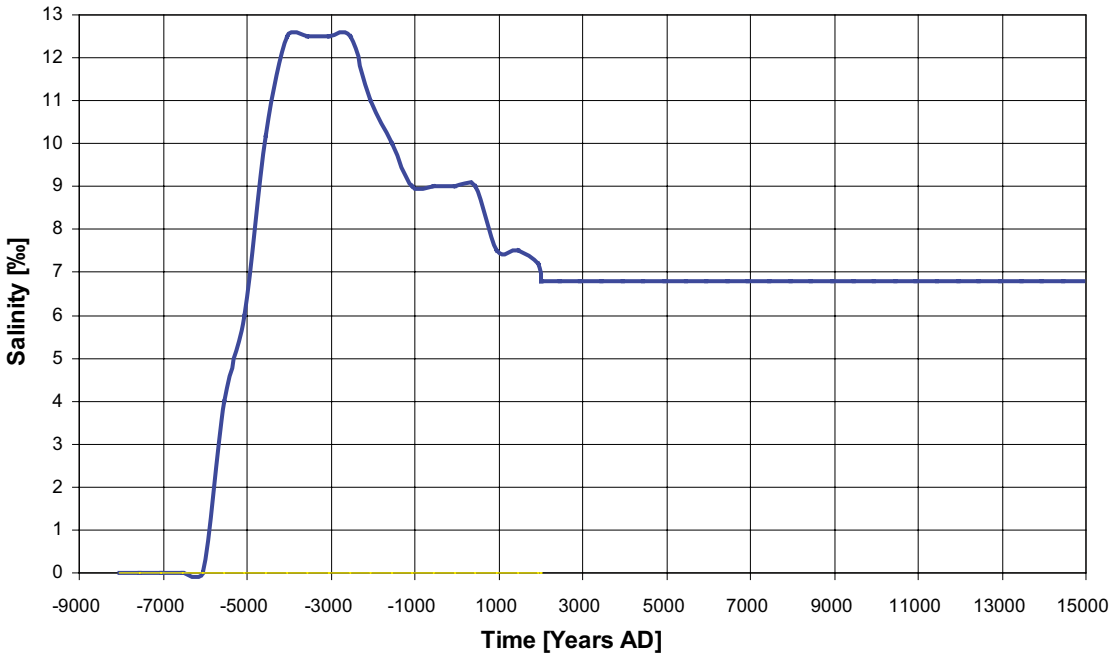

Figure 4-7. *Evolution of the salinity of the Baltic Sea (/Westman et al. 1999, Söderbäck 2008/).*

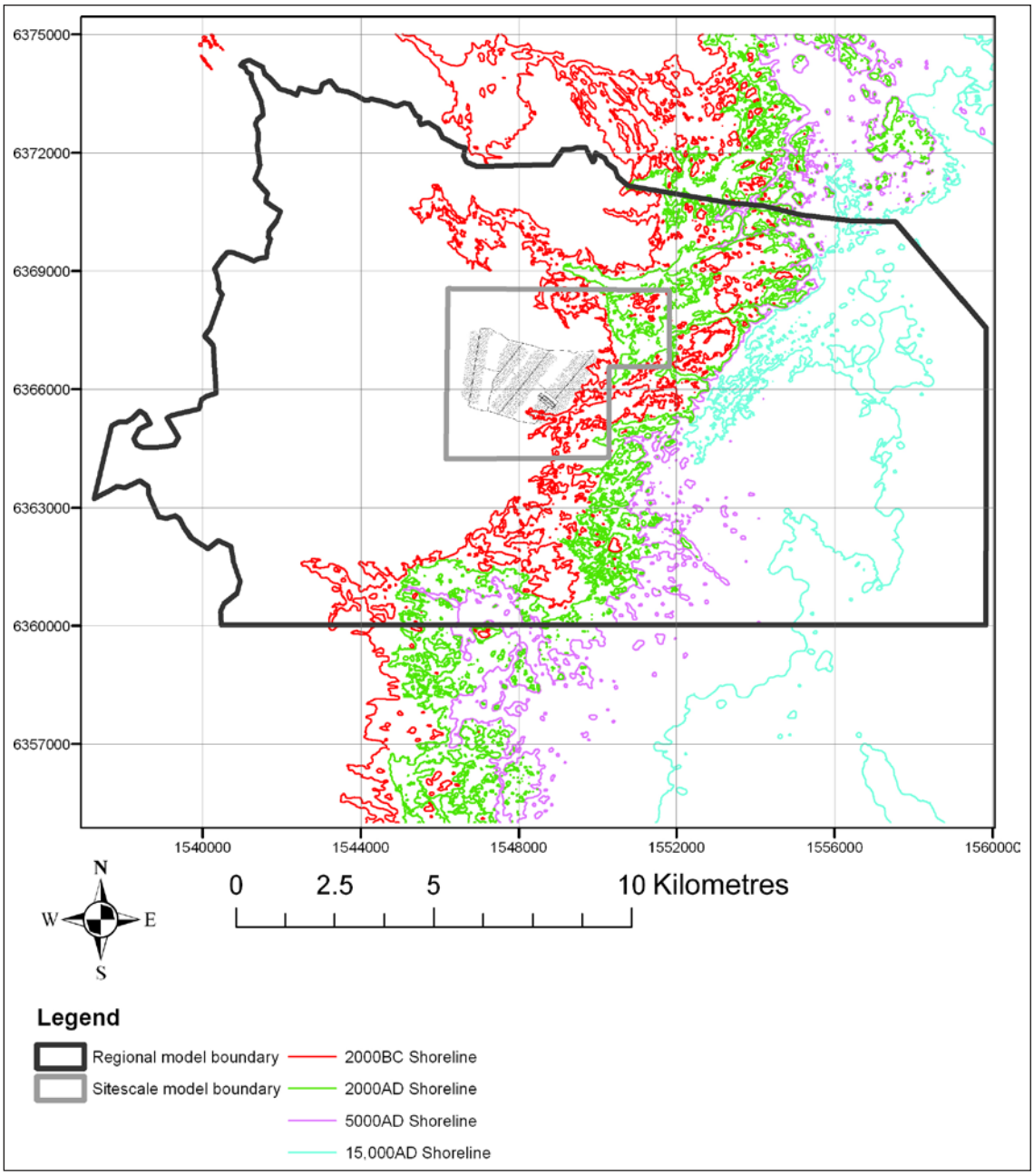

Figure 4-8. *Shoreline location at different times (red = 2000 BC, green = 2000 AD, purple = 5000 AD and blue = 15,000 AD) presented against the regional-scale domain (black). The repository structures are shown in grey.*

4.1.4 Outputs

The principal outputs of the regional-scale model were the fluid density distribution and pressure boundary conditions at chosen times for use in the site-scale and repository-scale models. Also exported were hydraulic conductivity values, salinity values and reference water fractions for use in other studies.

4.2 Site-scale model

The bedrock at Laxemar is of low hydraulic conductivity and it is thought that the primary hydraulic flow pathways are through a network of connected fractures. In order to better represent this system, a discrete fracture network (DFN) model was used in the local domain around the repository location, embedded within the regional-scale ECPM model. Thus the extent of the site-scale model is the same as the regional-scale model, but the local region has been replaced by an explicit DFN, as shown in Figure 4-9. The use of a DFN has implications for particle transport as it constrains the flow pathways available and hence the discharge locations reached. This effect cannot readily be observed using an ECPM model at the grid resolutions available computationally.

The main purpose of the site-scale model is to continue particles from the repository-scale model until they exit in the biosphere. It is also used to determine particle exit locations for pathways calculated entirely within the site-scale model for a greater number of starting times than are computationally feasible using the repository-scale model. These calculations are then used to guide the selection of time slices used for the repository-scale model.

4.2.1 Model Description

The site-scale model was constructed from the following domains:

- Hydraulic conductor domain (HCD): deformation zones of generally relatively high transmissivity.
- Hydraulic rock mass domain (HRD): the bedrock between the deformation zones.
- Hydraulic soil domain (HSD): the surface hydrological units.
- Repository structures.

Each domain is described in the following sections.

Hydraulic Rock mass Domain (HRD)

The site-scale model had the same domain as the regional-scale model, but the local model was replaced with an embedded DFN, as shown in Figure 4-9. The ECPM/CPM part of the model was the same as the equivalent parts of the regional-scale model. The DFN was the same as that used to provide the upscaled properties for the regional-scale model, thus ensuring consistency between the two scales. Fractures were included with radii from 5.6 m to 564 m. Fractures were tessellated to 40 m in length to give a reasonable resolution, i.e. any fracture with a side length larger than 40 m (equivalent to a radius of 22.6 m – see Equation (4-1) where L is fracture side length and r is fracture radius) was divided into square sub-fractures with a side length of 40 m.

$$L = \sqrt{\pi r^2} \tag{4-1}$$

Hydraulic Conductor Domain (HCD)

The same HCD was used as in the regional-scale model. In the ECPM model they were represented implicitly, but in the DFN they were represented as explicit fracture surfaces with appropriate hydraulic properties. The HCD fractures were tessellated to 40 m in length.

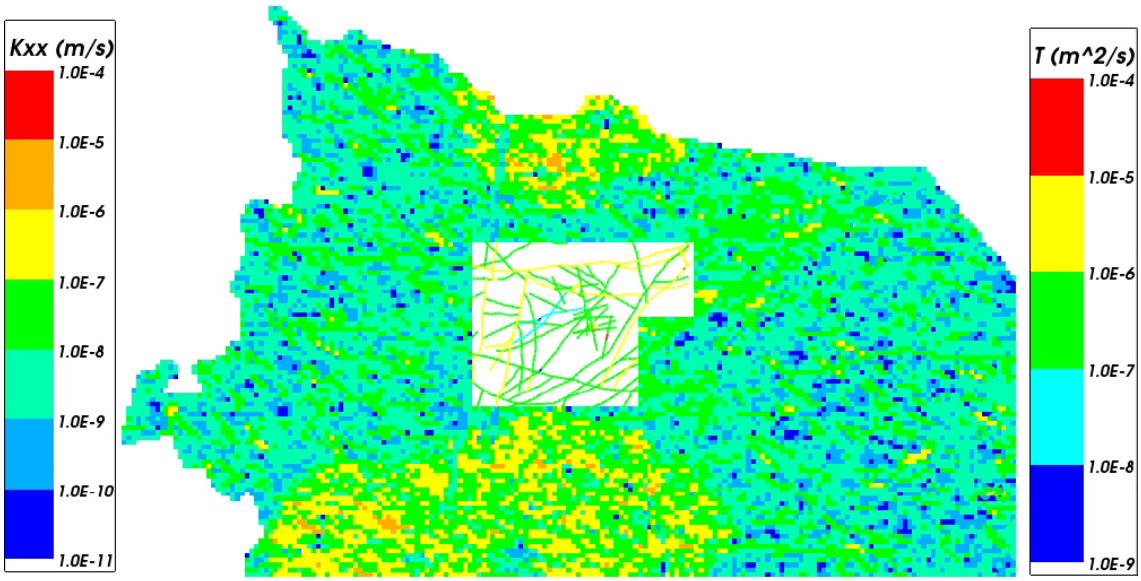

Figure 4-9. *Site-scale model: A horizontal slice at –510 m (repository depth). Only the fractures representing deformation zones are shown. Fractures are coloured by transmissivity and the ECPM is coloured by horizontal hydraulic conductivity.*

Hydraulic Soil Domain (HSD)

The HSD was identical to that used in the regional-scale model.

Repository Structures

The repository was represented by fractures with appropriate hydraulic and transport properties. The modelled repository structures were based on a layout desribed in /SKB 2007/. All tunnels, ramp and shafts were included and were tessellated to 10 m in length. Deposition holes were not represented. Table 4-2 shows the properties of the repository structures used in the site-scale and repository-scale models. The hydraulic conductivity and porosity values correspond to the backfill properties that will be used in each structure. The top sealing hydraulic conductivity was applied to those parts of the repository features that are above an elevation of –200 m, i.e. the upper parts of the ramp and shafts, which correspond to areas of backfill that could be degraded by permafrost.

An excavation damaged zone (EDZ) was also represented in the site-scale model as a set of fractures orthogonal to the repository structure fractures. In the case of the tunnels and ramp, the EDZ fractures were horizontal and intersected the bottom of the tunnel fractures. In the case of the ramp, the EDZ matched the slope of the ramp. For the shafts, the EDZ fractures intersected the centre of the shaft fractures. There was no EDZ included for the central area as it would have little effect given the high conductivity of the backfill (coarsely crushed rock) in those tunnels. The EDZ fractures were the same width as the associated repository structures and tessellated to 6 m in length. Figure 4-10 shows the representation of the repository structures and EDZ.

Multiple realisations

To explore the effect of spatial variability in the rock properties, an additional realisation of the HRD was used. This realisation was coupled with the corresponding HCD realisation to construct a model and carry out calculations.

Table 4-2. Properties of the repository structures used in the site-scale and repository-scale models.

Structure	Height (m)	Width (m)	Hydraulic Conductivity (m/s)	Porosity
Main tunnel	6.0	10.0	$1.0 \cdot 10^{-10}$	0.45
Transport tunnel	6.0	7.0	$1.0 \cdot 10^{-10}$	0.45
Deposition tunnel	6.0	4.0	$1.0 \cdot 10^{-10}$	0.45
Deposition hole	8.0	1.5	$1.0 \cdot 10^{-12}$	0.41
Central area tunnel	6.0	7.0	$1.0 \cdot 10^{-5}$	0.27
Ramp	6.0	5.2	$1.0 \cdot 10^{-10}$	0.45
Elevator shaft	4.34	4.34	$1.0 \cdot 10^{-10}$	0.45
Skip shaft	3.96	3.96	$1.0 \cdot 10^{-10}$	0.45
Air intake shaft	3.32	3.32	$1.0 \cdot 10^{-10}$	0.45
Air exhaust shaft	2.81	2.81	$1.0 \cdot 10^{-10}$	0.45
Deposition area air exhaust shaft	3.07	3.07	$1.0 \cdot 10^{-10}$	0.45
Top sealing	N/A	N/A	$1.0 \cdot 10^{-1}$	N/A
EDZ	0.3	See below	$3.333 \cdot 10^{-8}$	$1.0 \cdot 10^{-4}$

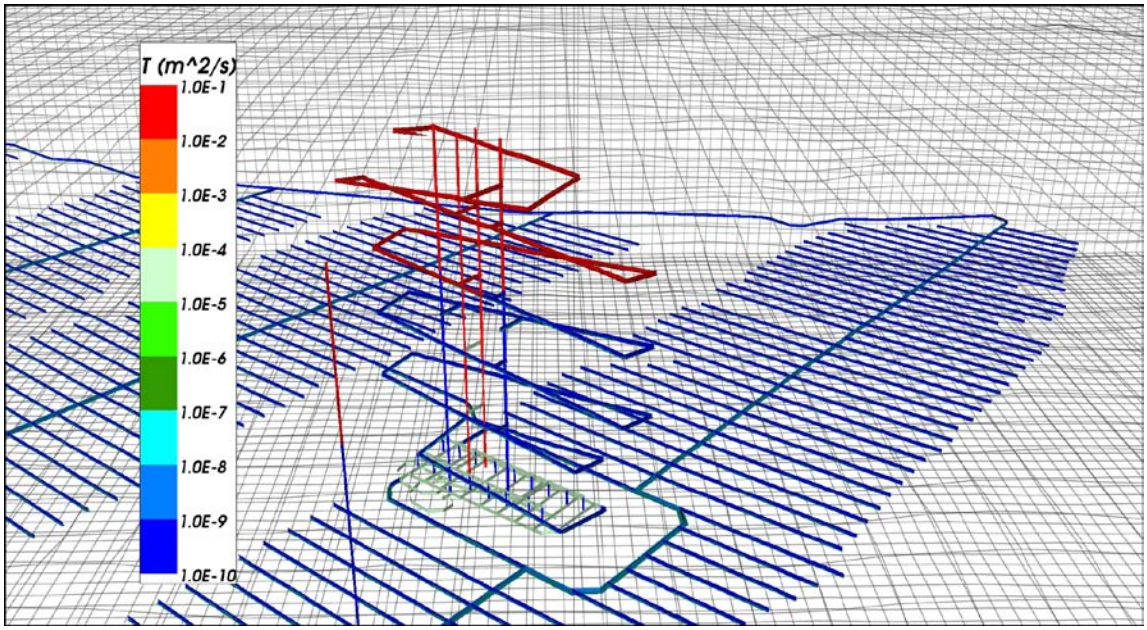

Figure 4-10. *Site-scale model. Fracture representation of tunnels, ramp and shafts. Fractures are coloured by transmissivity.*

4.2.2 Boundary conditions and initial conditions

The pressure boundary condition values on the top surface were imported from the regional-scale model for specified times. No-flow boundary conditions were present on the sides and bottom of the model.

The initial conditions for pressure and fluid density were imported from the regional-scale model for specified times. For the DFN, the pressure and fluid density values were interpolated on to the fracture network. The fluid density values were fixed (but non-uniform in space) during the calculations.

4.2.3 Calculations

The steady state groundwater pressures were calculated consistent with the applied boundary conditions and fluid densities. The calculations were carried out for 5000 BC, 2000 BC, 2000 AD, 5000 AD, 10,000 AD and 15,000 AD for a single realisation of the HRD and the deterministic HCD. The calculations were also carried out for an additional realisation of the HRD and HCD at 2000 AD.

Particle tracking calculations were carried out using the calculated groundwater flow fields for each of the specified times. Since there were no deposition holes present in the model, particles were started from the fracture intersection with the highest flux within a 4 m search radius of each of the Q1, Q2 and Q3 release points. Particles were tracked until they exited the model. These calculations are primarily to provide exit locations for surface modelling. Here the details of the repository representation are less important and the reduced computational cost means that more release times can be considered.

The site-scale model was also used to continue particles from the repository-scale model (see Section 4.3.3). Each particle was started from the fracture intersection with the highest flux within a 4 m search radius of the point it exited the repository-scale model and tracked until it exited the site-scale model. These particle tracking calculations were carried out for each of the times used for the repository-scale model and for the additional realisation of the HRD and HCD at 2000 AD.

4.2.4 Outputs

Performance measures and exit locations were produced from the particle tracking calculations for each of the specified times, both for the site-scale only model and for continuation from the repository-scale model. For continuation from the repository-scale model, the performance measures and exit locations were also produced for the additional realisation of the HRD and HCD at 2000 AD.

4.3 Repository-scale model

The repository-scale model focussed directly on the region around the Laxemar repository tunnels. The main tunnels, deposition tunnels and deposition holes were represented as a continuous porous medium (CPM) in order to better represent the backfill and to model the detailed flow within these features. The other repository structures (transport tunnels, central area, ramp and shafts) were represented as deterministic fractures with appropriate hydraulic and transport properties.

The main purpose of the repository-scale model was to deliver a high resolution of flows and particle releases close to the canister positions.

In order to be computationally feasible, the repository-scale model was divided into three blocks, as shown in Figure 4-11. Block 1 contained the southeastern main tunnel and included the central area, ramp and shafts. Block 2 contained the middle two main tunnels. Block 3 contained the northwestern main tunnel. Each block extended from an elevation of –800 m at the bottom to a top surface mapped to the topography below the HSD layers (4 m below the ground surface). There were was no HSD present in the repository-scale models.

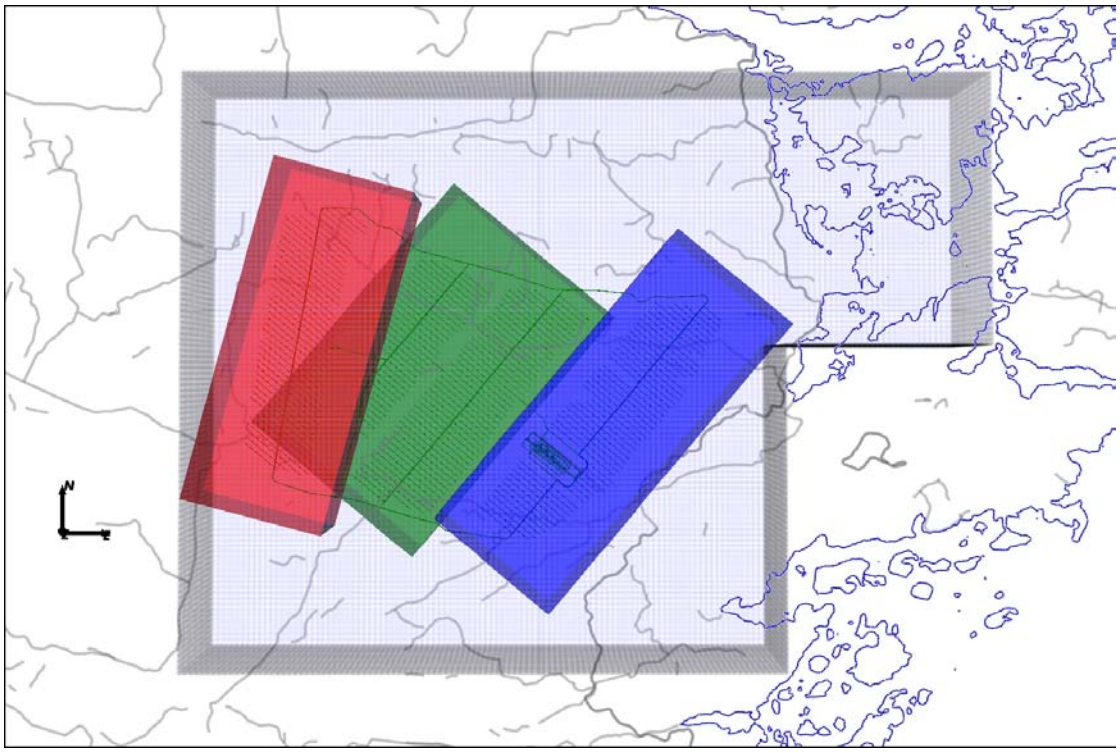

Figure 4-11. *Repository-scale blocks. Block 1 is coloured blue, block 2 is coloured green and block 3 is coloured red. The Site-scale DFN domain is shown in grey. The shoreline at 2000 AD is shown in blue, the repository structures are shown in black and the surface features are shown in grey.*

4.3.1 Model Description

The repository-scale model was constructed from the following domains:

- Hydraulic conductor domain (HCD): deformation zones of generally relatively high transmissivity.
- Hydraulic rock mass domain (HRD): the bedrock between the deformation zones.
- Repository structures.

Each domain is described in the following sections.

Hydraulic Rock mass Domain (HRD)

The same HRD was used as for the site-scale model, but fractures were included with radii from 0.4 m to 564 m. The fractures below 5.6 m in radius were only generated close the repository structures. These additional small fractures may be important in creating local connectivity between the repository structures and the fracture network. For each block, the parts of the fractures outside the boundaries of that block were removed. As with the site-scale model, fractures were tessellated to 40 m in length.

Hydraulic Conductor Domain (HCD)

The same HCD was used as for the site-scale model. For each block, the parts of the HCD fractures outside the boundaries of that block were removed. As with the site-scale model, HCD fractures were tessellated to 40 m in length.

Hydraulic Soil Domain (HSD)

There was no HSD included in the repository-scale model. However, the effect of the HSD on particles was considered during their continuation in the site-scale model.

Repository Structures

The main tunnels, deposition tunnels and deposition holes were represented as a continuous porous medium (CPM) in order to better represent the backfill and to model the detailed flow within these features. The other repository structures (transport tunnels, central area, ramp and shafts) were represented as deterministic fractures with appropriate hydraulic and transport properties. The repository structure fractures were tessellated to 10 m in length. The properties of the repository structures used in the site-scale and repository-scale models are given in Table 4-2.

Figure 4-12 shows the repository structures in each block. The CPM structures are coloured green and the fracture structures are coloured blue. If parts of main tunnels or deposition tunnels from a neighbouring block are included within the domain of a block, then they are represented as fractures with appropriate properties. This ensures the connectivity of repository structures with the boundaries of the block where appropriate.

An excavation damaged zone (EDZ) was also represented in the repository-scale model as a set of fractures with appropriate hydraulic and transport properties. In the case of the main and deposition tunnels, the EDZ was represented as a set of horizontal fractures below each tunnel, with a vertical cross fracture present to provide an intersection with the tunnel floor. For the transport tunnels and ramp, the EDZ fractures were horizontal relative to the structure and intersected the bottom of the tunnel fractures. In the case of the ramp, the EDZ matched the slope of the ramp. For the shafts, the EDZ fractures intersected the centre of the shaft fractures. There was no EDZ included for the central area as it would have little effect given the high conductivity of the backfill in those tunnels. The EDZ fractures were tessellated to 6 m in length. Figure 4-13 shows the EDZ, coloured red, below a main tunnel and some deposition tunnels.

Multiple realisations

To explore the effect of variability in the rock properties, an additional realisation of the HRD was used. This realisation was coupled with the corresponding HCD realisation to construct a model and carry out calculations.

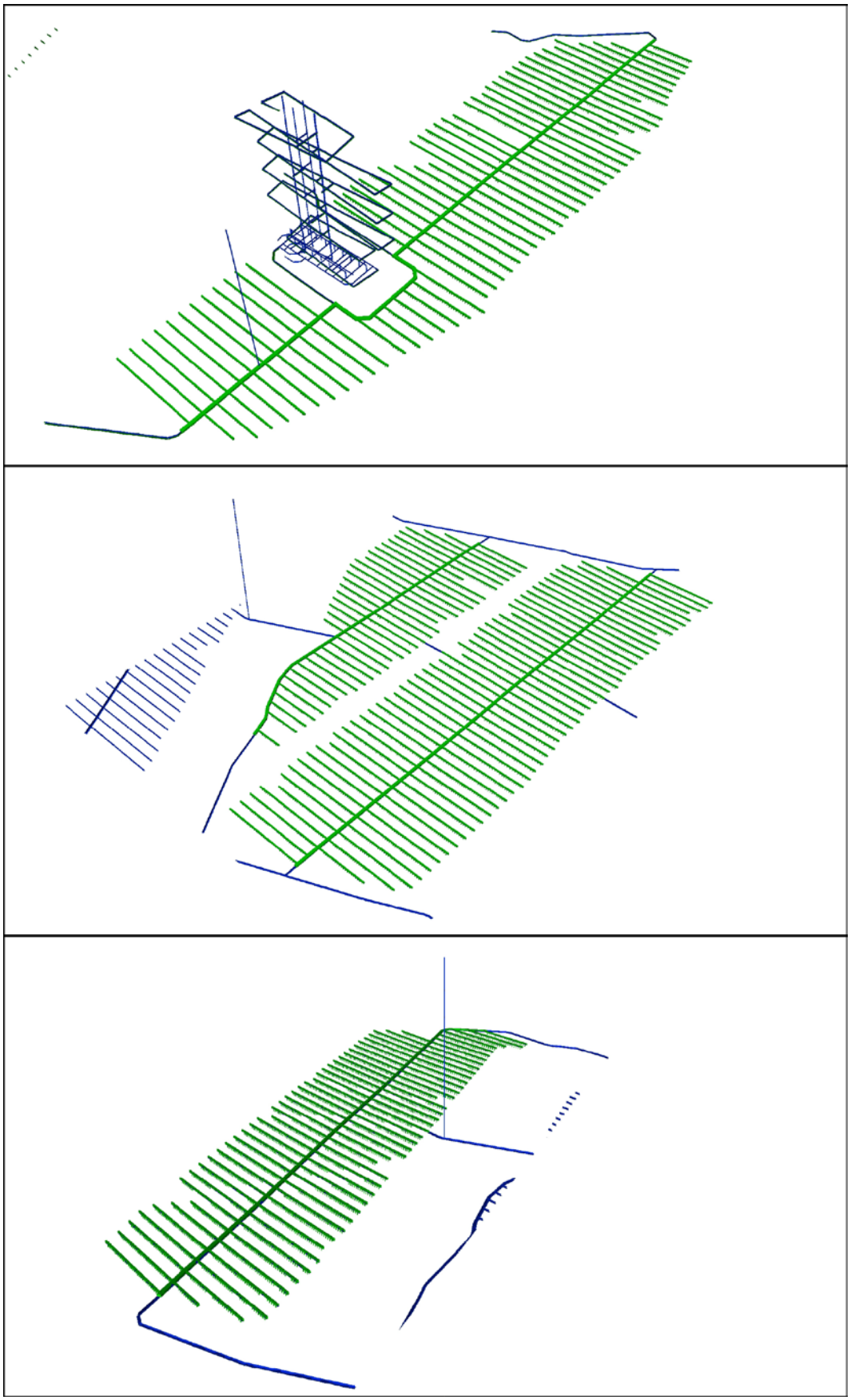

Figure 4-12. *Repository-scale structures. The CPM structures are coloured green and the fracture structures are coloured blue. Top: Block 1. Middle: Block 2: Bottom: Block 3.*

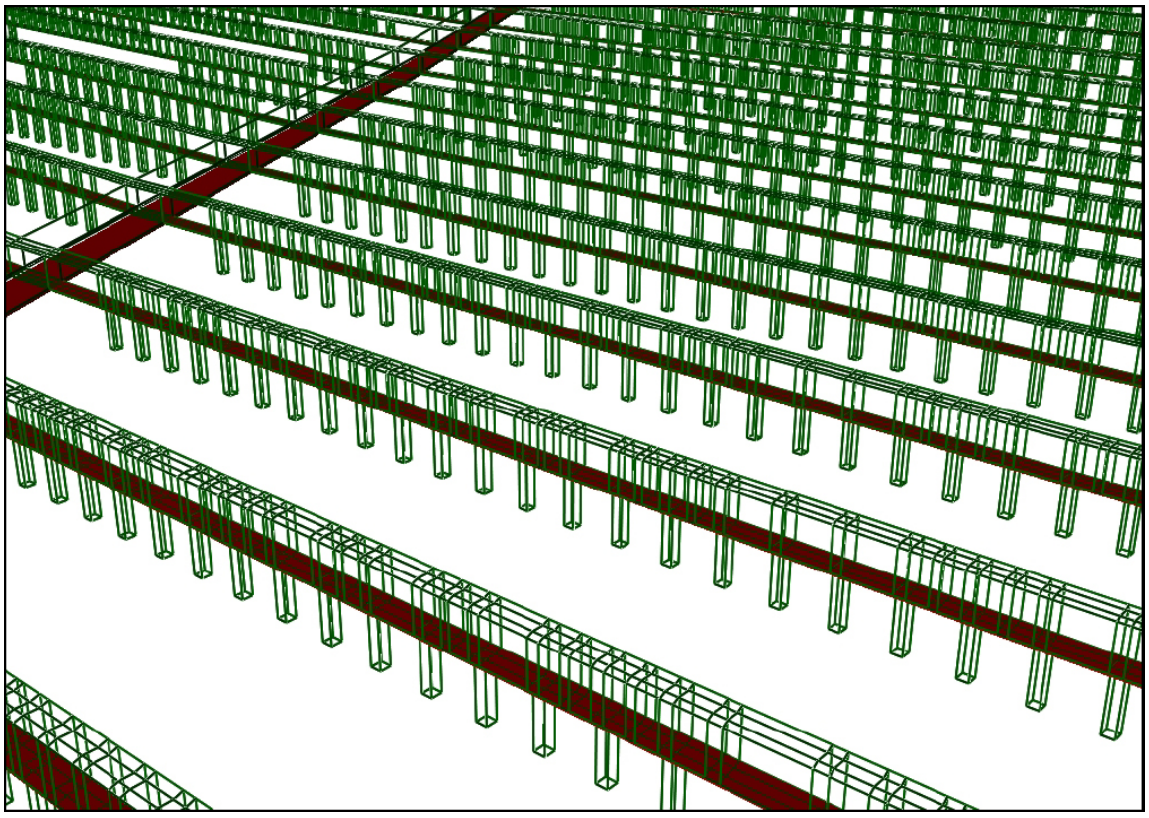

Figure 4-13. *Repository-scale model. Close-up view of block 3 deposition tunnels and part of a main tunnel. Tunnels are shown in green wireframe and the EDZ is coloured red.*

4.3.2 Boundary conditions and initial conditions

The pressure boundary condition values on the external surfaces of each block were imported from the regional-scale model for specified times. The initial conditions for pressure and fluid density were also imported from the regional-scale model for specified times. For the DFN, the pressure and fluid density values were interpolated on to the fracture network. The fluid density values were fixed (but non-uniform in space) during the calculations.

4.3.3 Calculations

The groundwater pressures were calculated consistent with the applied boundary conditions and fluid densities. The calculations were carried out at 2000 BC, 2000 AD, 5000 AD and 15,000 AD for a single realisation of the HRD and the deterministic HCD (the Hydrogeological base case). These times were chosen as being representative of particular periods within the evolution of the site. The calculations also were carried out for an additional realisation of the HRD and HCD at 2000 AD.

Particle tracking calculations were carried out for each block using the calculated groundwater flow fields for each of the specified times or realisations. Q1 particles were started from the fracture intersecting the deposition hole with the highest flux. Q2 particles were started in the EDZ fractures above each deposition hole. Q3 particles were started in the tunnel CPM 1 m above the top of each deposition hole. Particles were tracked until they exited the block, either through the top, bottom or sides, at which point they were continued in the site-scale model. In the case of particles exiting through the top of the model this would correspond to the bottom of the HSD in the site-scale model.

Within the site-scale model each particle was re-started from the fracture intersection with the highest flux within a 4 m search radius of the point it exited the repository-scale model block and tracked until it exited the site-scale model.

4.3.4 Outputs

Performance measures and exit locations were produced from the particle tracking calculations for each of the specified times and realisations. They were produced for the combined repository-scale and site-scale paths.

5 Model variants

5.1 Elaborated Hydro-DFN

5.1.1 Introduction

Modelling of the palaeohydrogeological evolution of the Laxemar site and interference tests undertaken as part of SDM-Site /Rhén et al. 2009/, produced a relatively poor match to data when using the initial uncalibrated model. The initial uncalibrated model was derived from upscaling the SDM-Site Hydro-DFN /Rhén et al. 2009/. This model predicted flushing with meteoric and Littorina waters to greater depths than inferred from measurements. Also very little glacial water was predicted to remain in the model, which was inconsistent with measurements. Reducing the permeabilities of the initial uncalibrated model at elevations below –150 m by a factor of three improved the match to measured values of the various chemical tracers and interference test data. This suggests the values of the ECPM permeabilities derived from SDM-Site could be slightly too high.

The potential consequences of over-estimating the effective permeabilities at repository elevation include over-estimating the equivalent flow rates at deposition holes and over-estimating the inflow rates to deposition tunnels.

Particular properties of the Hydro-DFN which could cause an over-estimate of the permeability when the Hydro-DFN is upscaled include:

- The fracture size distribution, in particular over-estimating the intensity of relatively large fractures. That is, under-estimating the fracture size distribution parameter k_r.
- The fracture size to transmissivity distribution, especially over-estimating the transmissivity of fractures at sizes comparable to the ECPM block size.
- The fractures are too isotropic, i.e. they do not reflect the differences in transmissivities between fracture sets.

In light of these issues, consideration was given to aspects of the methodology used in SDM-Site Laxemar /Rhén et al. 2009/ which could potentially lead to either over-estimating the number of large fractures (i.e. under-estimating the fracture size distribution parameter k_r) or over-estimating the transmissivity of fractures. The issues identified included the following:

- The size of the model domain could potentially influence the calibration of the Hydro-DFN in the following way: The number of flowing fractures intersecting a borehole in the models depends on the connectivity of the fracture network, specifically on whether there is a network of fractures extending from the model boundary to the borehole. If the model domain were reduced in size, the distance to the boundary decreases, and the number of flowing fractures calculated to intersect the borehole increases. If the model domain were reduced, the fracture size distribution derived through the calibration process could be shifted towards smaller fracture size, i.e. higher k_r values. The size of the model domain used in /Rhén et al. 2009/ was based on the average spacing between HCDs, with a model side length of 200 m.
- A further issue with the SDM-Site Hydro-DFN is not a concern with the methodology used, but the observation that certain repository performance measures are particularly sensitive to specific model parameters. This is thought to be due to the orientation of the repository, for the present design, relative to the dominant WNW fracture set. For the present repository layout the deposition tunnels are approximately parallel to the WNW fracture set. This means that a large fracture with high transmissivity belonging to this set can cause high flow rates for a number of deposition holes if these are not rejected by the design criteria. The performance measures relating to equivalent flow rates are therefore particularly sensitive to the fracture size to transmissivity relationship for the WNW set.
- A greater emphasis should be placed on the measured differences in flow rate distributions between sets to better resolve anisotropy in the fracture flows.

- The maximum Terzaghi weighting applied to the count of fracture intersections was set to 7 in SDM-Site Laxemar /Rhén et al. 2008/. This is appropriate for the borehole fracture intersection data where there is a corresponding uncertainty in measuring the angle of the fracture to the borehole. For the model predictions of fracture intersections, a higher maximum Terzaghi weighting is justified by a comparison of the specified areal fracture intensity (P_{32}) with the model predictions of Terzaghi corrected fracture intensity along a borehole. These comparisons show that the matches are improved for higher maximum Terzaghi weighting values. The effect of this parameter is bounded by the difference in the calculated Terzaghi corrected fracture intensity of fractures intersecting a borehole when a maximum Terzaghi correction of 7 is applied, compared to the specified areal fracture intensity. The maximum difference amounts to approximately 20%. Increasing the maximum Terzaghi weighting factor has the effect of increasing the calculated Terzaghi corrected fracture intensity of fractures intersecting a borehole, for the same fracture network. Hence Increasing the maximum Terzaghi correction applied could lead to a larger fracture size distribution parameter k_r and fewer large fractures, particularly for the sub-vertical fracture sets, compared to the SDM-Site Hydro-DFN. Using a higher maximum Terzaghi weighting requires more stochastic model realisations for consistent results.

The Elaborated Hydro-DFN was developed to address the four issues described above.

5.1.2 Elaborated Hydro-DFN methodology

The key changes used for the Elaborated Hydro-DFN methodology compared to the methodology detailed in /Rhén et al. 2009/, as used for SDM-Site, are the following:

- Representative boreholes were modelled explicitly and deformation zones were included in these models.
- Particular care was taken with the fracture size to transmissivity relationship assigned to the WNW set in depth zone 3 (DZ3).
- Particular care was taken to calibrate the fracture sets individually.
- A maximum Terzaghi correction of 100 was used in the modelling, compared to a value of 7 used in the SDM-Site Hydro-DFN calibration /Rhén et al. 2008/.

Generic models without deterministic HCD features and assuming vertical boreholes were used in the SDM-Site Hydro-DFN calibration /Rhén et al. 2009/: this model formed the basis for the Hydrogeological base case model in this report. In the Elaborated Hydro-DFN methodology a set of ‘representative boreholes’ were chosen for each of HRD_C, HRD_W and HRD_EW007. The representative boreholes were chosen to have a significant length of borehole in the relevant HRD. The following boreholes were modelled: KLX11A, KLX17A and KLX19A in HRD_W; KLX03, KLX05, KLX15A and KLX21B in HRD_C; and KLX07A and KLX08 in HRD_EW007. The locations of the representative boreholes, along with a trace of the deformation zones, are shown in Figure 5-1.

The representative boreholes were modelled explicitly, and deterministic HCD features were also included in the models. An example is shown in Figure 5-2. This change to the methodology means that the deformation zones are effectively controlling the distance from the representative borehole to a specified pressure boundary condition. Therefore the number of flowing fractures intersecting the borehole should be less sensitive to the size of the model domain than was the case with the SDM-Site Hydro-DFN calibration models. Since the deformation zones are sometimes closer than the model boundary to the representative boreholes, the calibrated fracture size distribution could be shifted towards smaller fractures.

Further details of the modelling are described in Appendix E. This appendix also shows the match to the calibration targets.

An analysis of the time taken for fresh water to penetrate to repository depths for the Elaborated Hydro-DFN model is given in Appendix H.

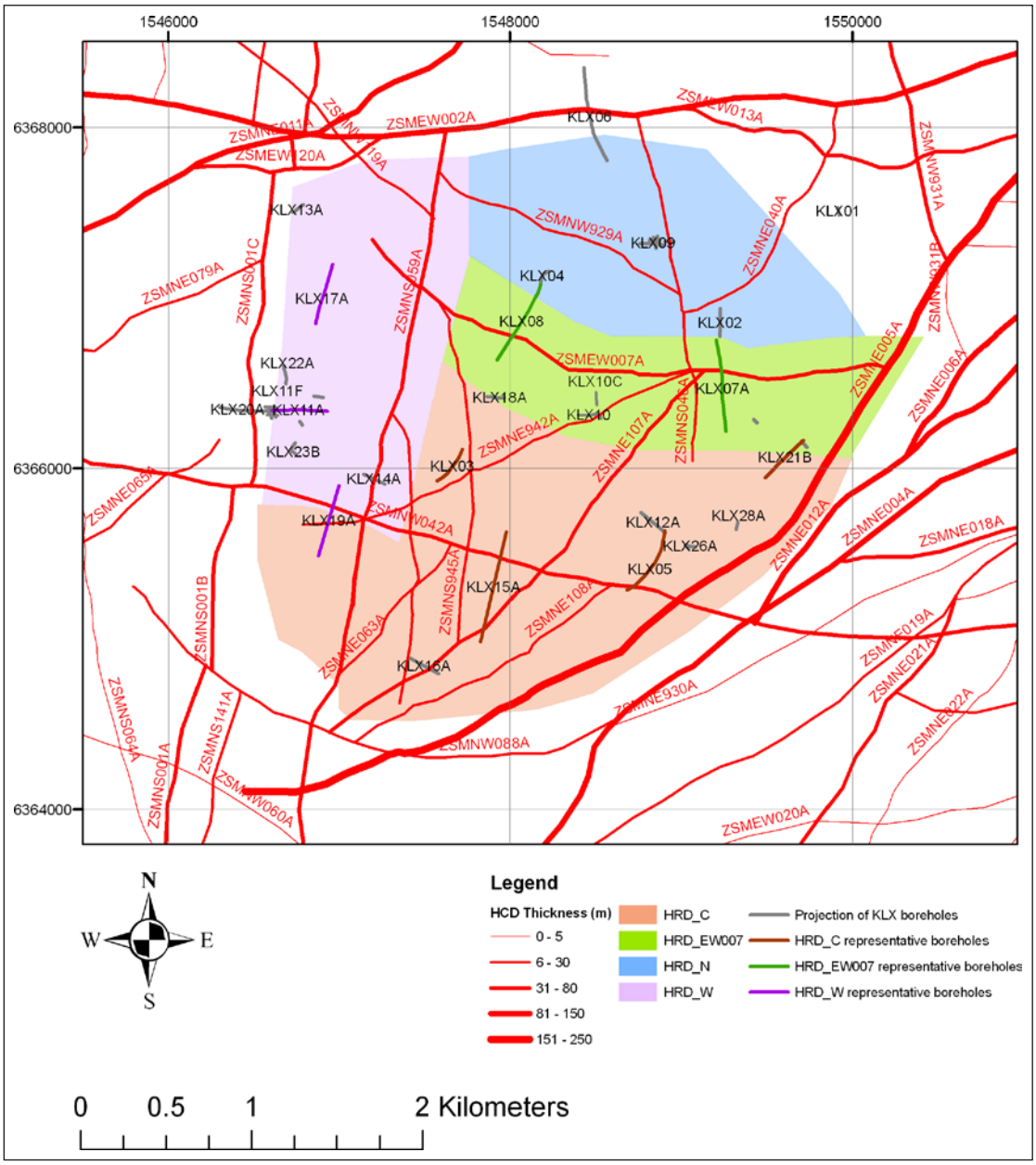

Figure 5-1. *The locations of the representative boreholes used in the Elaborated Hydro-DFN model calibration. A trace of the deformation zones at ground surface is shown in red. The locations of various HRDs at the bedrock surface are indicated.*

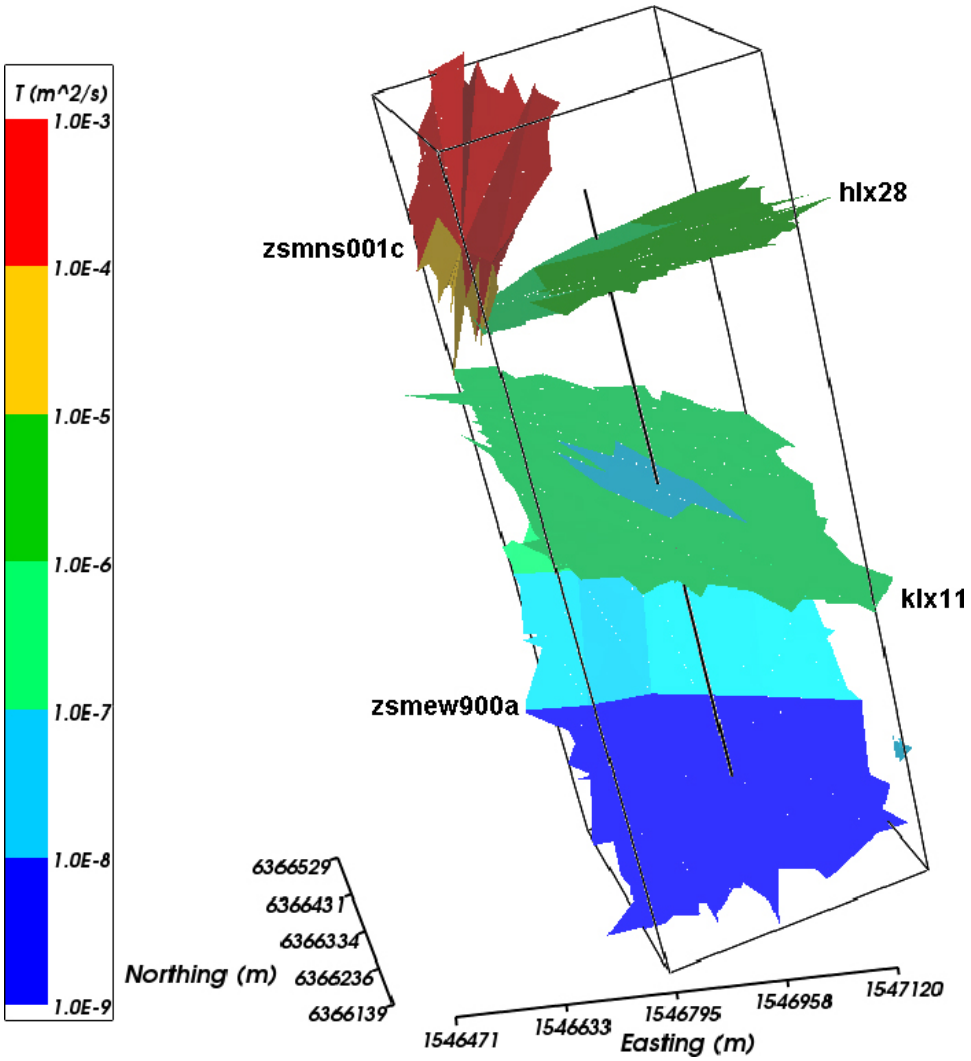

Figure 5-2. *The Elaborated Hydro-DFN calibration model for KLX11A. Only the deformation zones are shown, coloured by transmissivity.*

5.1.3 Main changes compared to the SDM-Site Hydro-DFN

The Elaborated Hydro-DFN parameters for HRD_C, HRD_EW007 and HRD_W are tabulated in Appendix E. In general there is a shift to a slightly larger fracture size slope parameter, k_r, compared to the SDM-Site Hydro-DFN /Rhén et al. 2009/. The effects of the changes to the fracture size to transmissivity relationship are more difficult to predict, however the effects of all of the changes to the methodology on the ECPM effective block scale conductivities are summarised in Figure 5-3. This figure shows that the effective block scale conductivities are reduced at repository elevation in each of the HRDs by around a factor of 3 compared to the SDM-Site model. There are relatively small changes to HRD_EW007 in depth zone 1 (DZ1) and depth zone 2 (DZ2). The largest changes are in HRD_W in depth zone 2 (DZ2) and depth zone 3 (DZ3).

The changes to HRD_W in DZ3 were investigated, as this is the largest change at repository elevation, and serves as an example of the changes in other regions. The total areal intensity of open and partly open (OPO) fractures specified in the two Hydro-DFN parameterisations is shown in Figure 5-4. This figure shows that the Elaborated Hydro-DFN predicts 15% to 25% fewer fractures with radius greater than 10 m and 100 m respectively, compared to the SDM-Site Hydro-DFN.

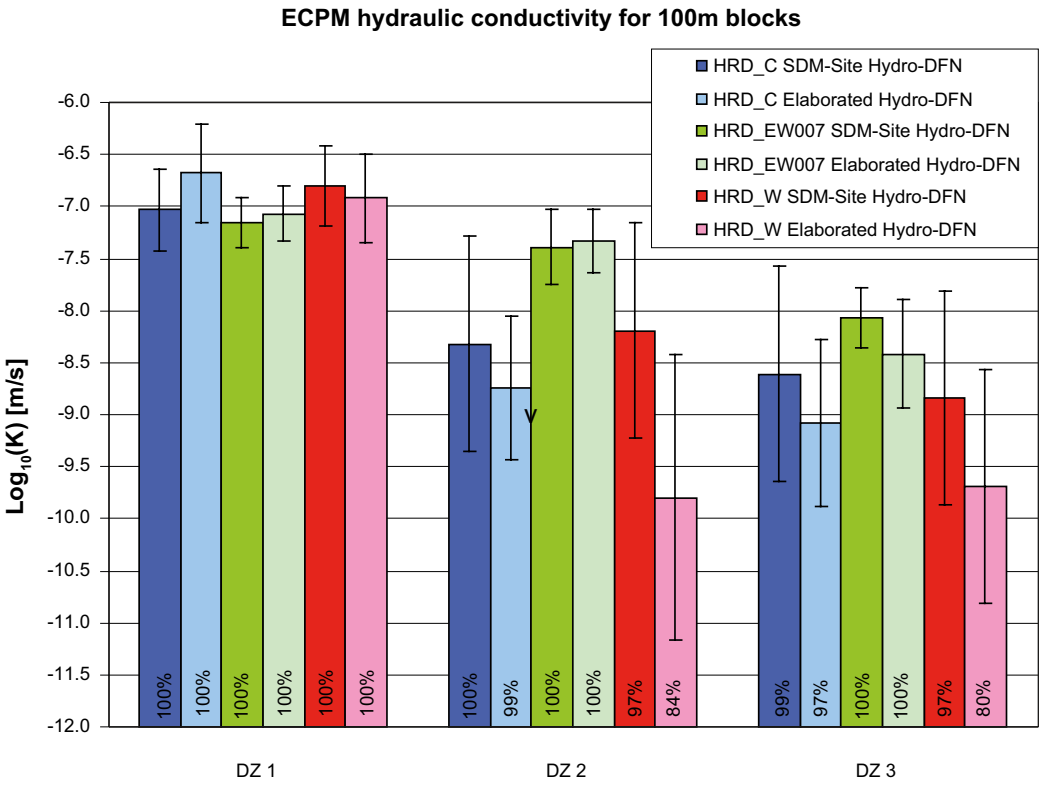

Figure 5-3. A summary of the conductivities of the upscaled Elaborated Hydro-DFN compared to the SDM-Site Hydro-DFN for 100 m ECPM blocks in each local HRD and depth zones 1 to 3 (DZ1, DZ2, DZ3). The columns indicate the median block conductivity. The error bars indicate one standard deviation of $log_{10}(K)$. The percentage in the base of the columns indicates the percentage of the blocks which percolate.

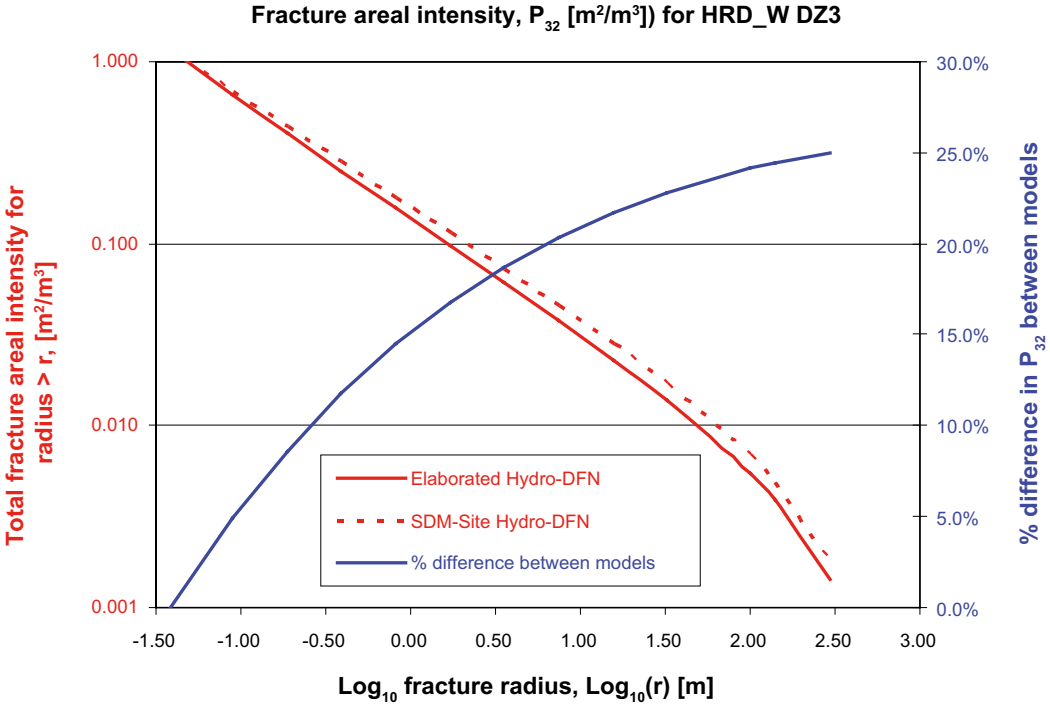

Figure 5-4. Total fracture intensity of open and partly open (OPO) fractures specified for the SDM-Site Hydro-DFN and the Elaborated Hydro-DFN.

The fracture size to transmissivity relationships used for the SDM-Site Hydro-DFN and the Elaborated Hydro-DFN are shown, for the WNW fracture set of DZ3 in HRD_W, are shown in Figure 5-5. These plots shows that, for all fracture radii, the Elaborated Hydro-DFN predicts lower fracture transmissivities, on average, than the SDM-Site Hydro-DFN. The difference amounts to approximately a factor of three in transmissivity, for fractures of radius 100 m.

The match predicted by models using both the SDM-Site Hydro-DFN and the Elaborated Hydro-DFN to PFL_f specific capacity (Q/S where Q is flow-rate and S is drawdown) data for the WNW fracture set of HRD_W in Depth Zone 3 are shown in Figure 5-6. This figure shows that a reasonable match is obtained in both cases, despite the differences to the Hydro-DFN parameters. The SDM-Site Hydro-DFN possibly slightly over-estimates the inflow rates.

The match to hydrochemical data predicted by the Elaborated Hydro-DFN model is shown in Appendix E. The match is improved compared to the uncalibrated SDM-Site Laxemar model. As expected, the fit to the data is comparable to the match achieved by the calibrated SDM-Site Laxemar model, i.e. the model with conductivities below –150 m reduced by a factor of 3 compared to the uncalibrated model. Therefore, the Elaborated Hydro-DFN model gives an ECPM model that requires no adjustments in order to predict hydrochemical results consistent with data.

These results show that the model very successfully matches the inflow statistics of PFL-f and PSS data. Also the model gives a good match to head and hydrochemistry measurements, thus giving confidence in the model.

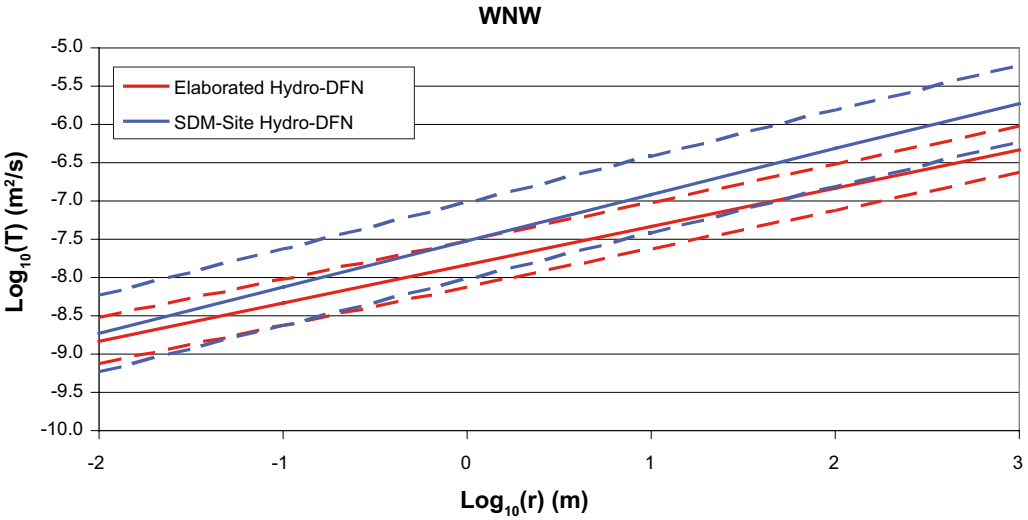

Figure 5-5. *The fracture size to transmissivity relationship for HRD_W Depth Zone 3 for the WNW fracture set specified for the SDM-Site Hydro-DFN (Semi-Correlated model) and the Elaborated Hydro-DFN. The dashed lines indicate one standard deviation (of $\log_{10}(T)$) from the geometric mean transmissivity.*

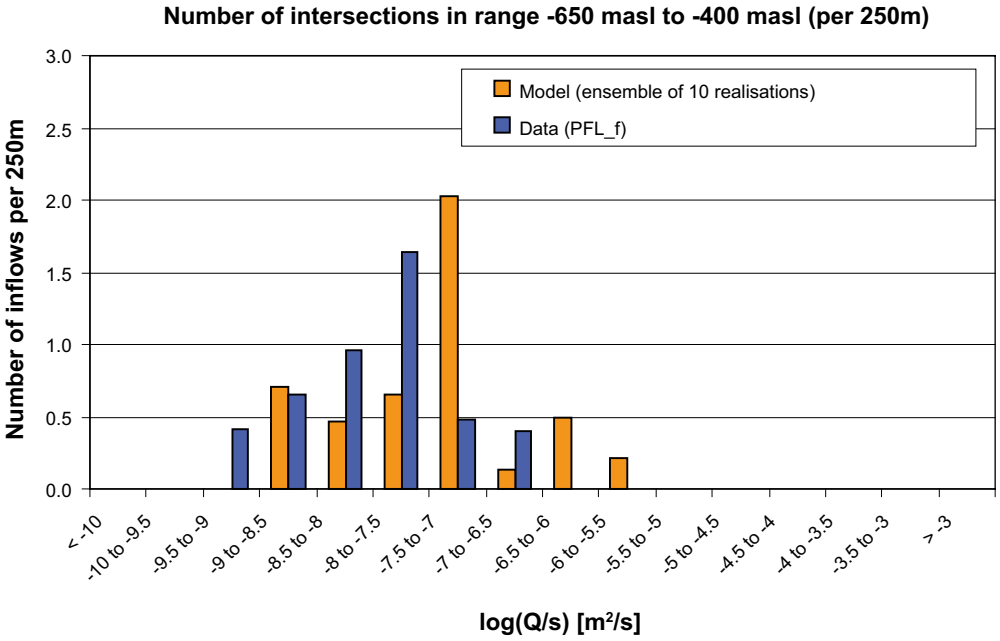

SDM-Site Hydro-DFN

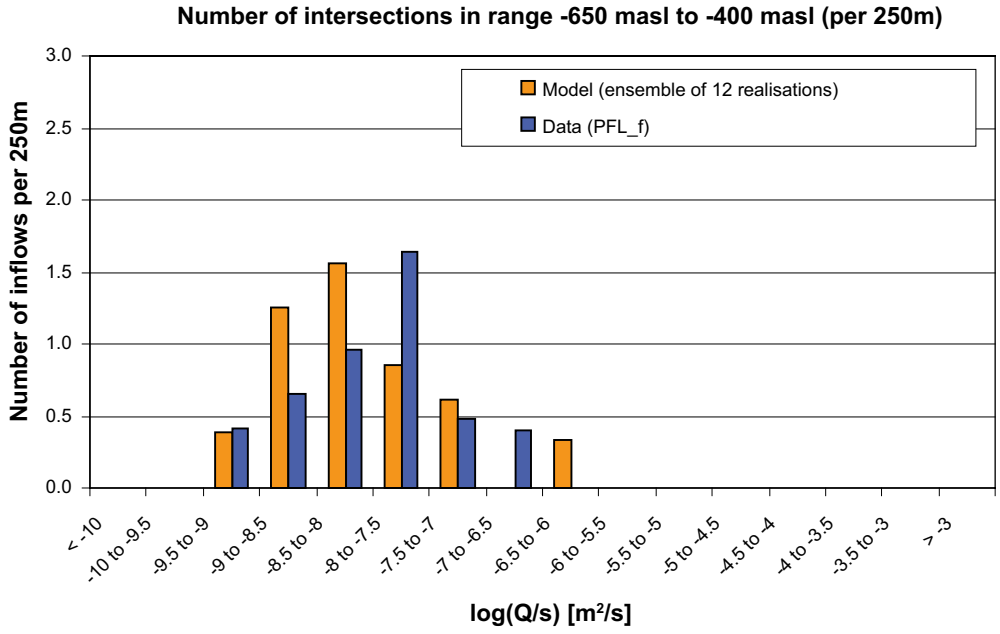

Elaborated Hydro-DFN

Figure 5-6. *The match to PFL_f data for HRD_W, Depth Zone 3, WNW fracture set. The top figure shows the match for the SDM-Site Hydro-DFN, the bottom figure shows the match for the Elaborated Hydro-DFN.*

5.1.4 Calculations

Simulations of the evolution of hydrochemistry and the calculations of performance measures and particle exit locations were carried out at the three different scales in the same way as for the Hydrogeological base case, but using the elaborated Hydro-DFN. A case with a homogeneous HCD and realisation 1 of the HRD (denoted r0) and a case with realisation 2 of a stochastic HCD and realisation 2 of the HRD (denoted r2) were considered. Performance measures and exit locations were only calculated for the 2000 AD time slice.

5.2 Elaborated Hydro-DFN model with no Minor Deformation Zones

5.2.1 Specification

The essential basis for the 3D model of deterministically modelled deformation zones and the statistics of the minor deformation zones (MDZ) is the "extended single-hole interpretation" (ESHI) /Wahlgren et al. 2008/. The local model volume contains 64 deterministically modelled deformation zones, cf. /Rhén and Hartley 2009/. A subset of the deterministically modelled deformation, 25 zones, do not have linked lineaments at ground surface. Two of these, ZSMEW946A and ZSMNW928A are supported by seismic reflector geometries and borehole intercepts. The other 23 of these deterministic zones are interpreted on the basis of only one single borehole intercept. In doing so, only those zones with an interpreted true thickness of 10 m or more in a borehole are interpreted to have a size (length) in excess of 1,000 m. These 23 deformation zones are modelled deterministically as discs with radius 564.2 m (based on an equal area of 1x1 km^2). Based on the hydrogeological evaluation it was decided to add five more HCDs as deterministically modelled deformation zones, modelled as discs with radius 564 m /Rhén and Hartley 2009/. The true size and properties of these modelled discs is considered very uncertain. These 23+5 deformation zones are not considered to be minor deformation zones (MDZ) that are a part of the stochastic features in the HRDs, but their sizes correspond to the assessed maximum size of MDZs /Rhén and Hartley 2009/. As a sensitivity case it is therefore relevant to exclude these 28 uncertain deformations zones with size approximately as expected for MDZs.

5.2.2 Representation

This variant used the Elaborated Hydro-DFN model, but excluded the 28 MDZs described above from the deterministic HCD.

5.2.3 Calculations

Simulations of the evolution of hydrochemistry and the calculations of performance measures and particle exit locations were carried out at the three different scales in the same way as for the Elaborated Hydro-DFN case, but with the MDZs exclued. Only the case with a homogeneous HCD and realisation 1 of the HRD (denoted r0) was considered. Performance measures and exit locations were only calculated for the 2000 AD time slice.

5.3 Stochastic Continuum model

5.3.1 Specification

The Stochastic continuum model provides an alternative model concept and uses the site data in a different way to explore the sensitivity of the results to the model representation and to scope the corresponding range of performance measures that can be obtained. This is achieved by making alternative assignments to the HRD properties based on a stochastic continuum approach (described in Section 3.1.4) rather than a hydrogeological DFN approach. The statistical properties of the hydraulic conductivities in the HRDs of this variant are derived from 20 m and 100 m PSS measurements, shown in Table 5-1 and Table 5-2 respectively. The other HRDs are assigned hydraulic conductivities from this table according to the mapping given in /Rhén et al. 2009, Table 7-5/. Other properties are assigned as for the Hydrogeological base case. Performance measures and exit locations are calculated in the same way as for the Hydrogeological base case at 2000 AD and 15,000 AD, using the modifications required for the Stochastic continuum case described in Section 3.2.6.

Table 5-1. Hydraulic conductivity statistics dervied from 20 m PSS measurements (extracted from Appendix 9 in /Rhén et al. 2008/).

HRD	Depth zone [m.a.s.l.]	Mean $\log_{10}$(K) [m/s]	Std. dev. $\log_{10}$(K) [m/s]
HRD_W	> –150 (DZ1)	–8.36	2.08
	–400 to –150 (DZ2)	–10.41	2.65
	–650 to –400 (DZ3)	–11.10	2.55
	< –650 (DZ4)	–11.40	1.67
HRD_C	> –150 (DZ1)	–7.31	1.34
	–400 to –150 (DZ2)	–9.61	1.82
	–650 to –400 (DZ3)	–10.57	1.75
	< –650 (DZ4)	–11.40	1.67
HRD_N	> –150 (DZ1)	–6.60	1.97
	–400 to –150 (DZ2)	–7.76	1.99
	–650 to –400 (DZ3)	–9.74	1.87
	< –650 (DZ4)	–11.29	2.23
HRD_EW007	> –150 (DZ1)	–6.71	1.09
	–400 to –150 (DZ2)	–7.83	1.93
	–650 to –400 (DZ3)	–8.75	1.51
	< –650 (DZ4)	–10.75	1.67

Table 5-2. Hydraulic conductivity statistics dervied from 100 m PSS measurements (extracted from Appendix 9 in /Rhén et al. 2008/).

HRD	Depth zone [m.a.s.l.]	Mean $\log_{10}$(K) [m/s]	Std. dev. $\log_{10}$(K) [m/s]
HRD_W	> –150 (DZ1)	–6.67	0.59
	–400 to –150 (DZ2)	–9.05	3.00
	–650 to –400 (DZ3)	–9.63	1.64
	< –650 (DZ4)	–10.52	1.40
HRD_C	> –150 (DZ1)	–6.94	1.02
	–400 to –150 (DZ2)	–8.92	1.18
	–650 to –400 (DZ3)	–9.82	1.47
	< –650 (DZ4)	–10.52	1.40
HRD_N	> –150 (DZ1)	–6.41	0.39
	–400 to –150 (DZ2)	–6.28	0.60
	–650 to –400 (DZ3)	–7.83	1.04
	< –650 (DZ4)	–9.52	1.40
HRD_EW007	> –150 (DZ1)	–6.69	1.04
	–400 to –150 (DZ2)	–6.45	1.15
	–650 to –400 (DZ3)	–8.40	1.35
	< –650 (DZ4)	–9.52	1.40

5.3.2 Representation

Two property grids were created, one corresponding to the 20 m scale and one to the 100 m scale. Each grid was the same as the one used for the Hydrogeological base case, except that the 20 m grid used 20 m elements for the local part of the model and the 100 m grid used 120 m elements for the local part of the model. Both property grids used 120 m elements in the regional part of the model. The reason that 120 m elements were used rather than 100 m elements was to provide compatibility with the Hydrogeological base case model and because 120 m is an exact multiple of 40 m, which was the element size used for the local part of the regional-scale model, and will facilitate mapping of properties from the property grids to the model grids. Two stochastic realisations of the properties were generated for each scale. Each hydraulic conductivity value was limited to the range $1 \cdot 10^{-10}$ m/s to $1 \cdot 10^{-4}$ m/s. Values outside of this range were resampled (rather than truncated).

As with the Hydrogeological base case, model grids were created on three scales, regional, site and repository. The different scales were designed to give similar levels of resolution in a CPM model to those in the DFN/CPM/ECPM models of the Hydrogeological base case.

Regional-scale model

Two regional-scale models were constructed, each with the same grid as used for the Hydrogeological base case regional-scale model. This used 40 m elements in the local part and 120 m elements in the regional part. Hydraulic conductivity values from the 20 m property grid were mapped on to the first model, using upscaling (Section 3.1.4) in the local part and direct transfer of values for the regional part. Hydraulic conductivity values from the 100 m property grid were mapped on to the second model, using interpolation (Section 3.1.4) in the local part and direct transfer of values for the regional part. Two realisations of each model were created, the first using the first realisation of the property grid (HRD) and a deterministic HCD (denoted r0) and the second using the second realisation of the property grid (HRD) and the second stochastic realisation of the HCD (denoted r2). The deformation zone properties from the HCD were mapped on to the models using the same IFZ procedure used for the Hydrogeological base case model (Section 4.1.1). The HSD was the same as for the Hydrogeological base case model (Section 4.1.1).

Palaeohydrogeological simulations were carried out using each realisation of each model in the same way as for the Hydrogeological base case (Section 4.1.3), with the same initial conditions and the same boundary conditions. Pressure and density values were exported at selected times for use by the site-scale and repository-scale models.

Site-scale model

Two site-scale models were constructed, each with the same grid as used for the regional-scale model, except that 20 m elements were used for the local part of the model. Hydraulic conductivity values from the 20 m property grid were mapped on to the first model, using direct transfer of values. Hydraulic conductivity values from the 100 m property grid were mapped on to the second model, using interpolation in the local part and direct transfer of values for the regional part. Two realisations of each model were created as for the regional-scale model, using the same HCD and HSD as in the regional-scale model. The properties of the repository structures were the same as in the Hydrogeological base case (Table 4-2) and were assigned using the IFZ method (Section 3.2.2). Slices through realisation r0 of the models in each depth zone, coloured by the vertical component of the hydraulic conductivity are shown in Figure 5-7 to Figure 5-10.

Steady-state groundwater flow calculations were carried out for each model and realisation using the corresponding pressures and densities imported from the regional-scale model for 2000 AD and 15,000 AD. The initial conditions and boundary conditions were applied in the same way as for the Hydrogeological base case site-scale model. Subsequent particle tracking calculations were used to continue particles from the corresponding repository-scale model. Exit locations and performance measures were calculated as for the Hydrogeological base case, using the modifications required for the Stochastic continuum case described in Section 3.2.6.

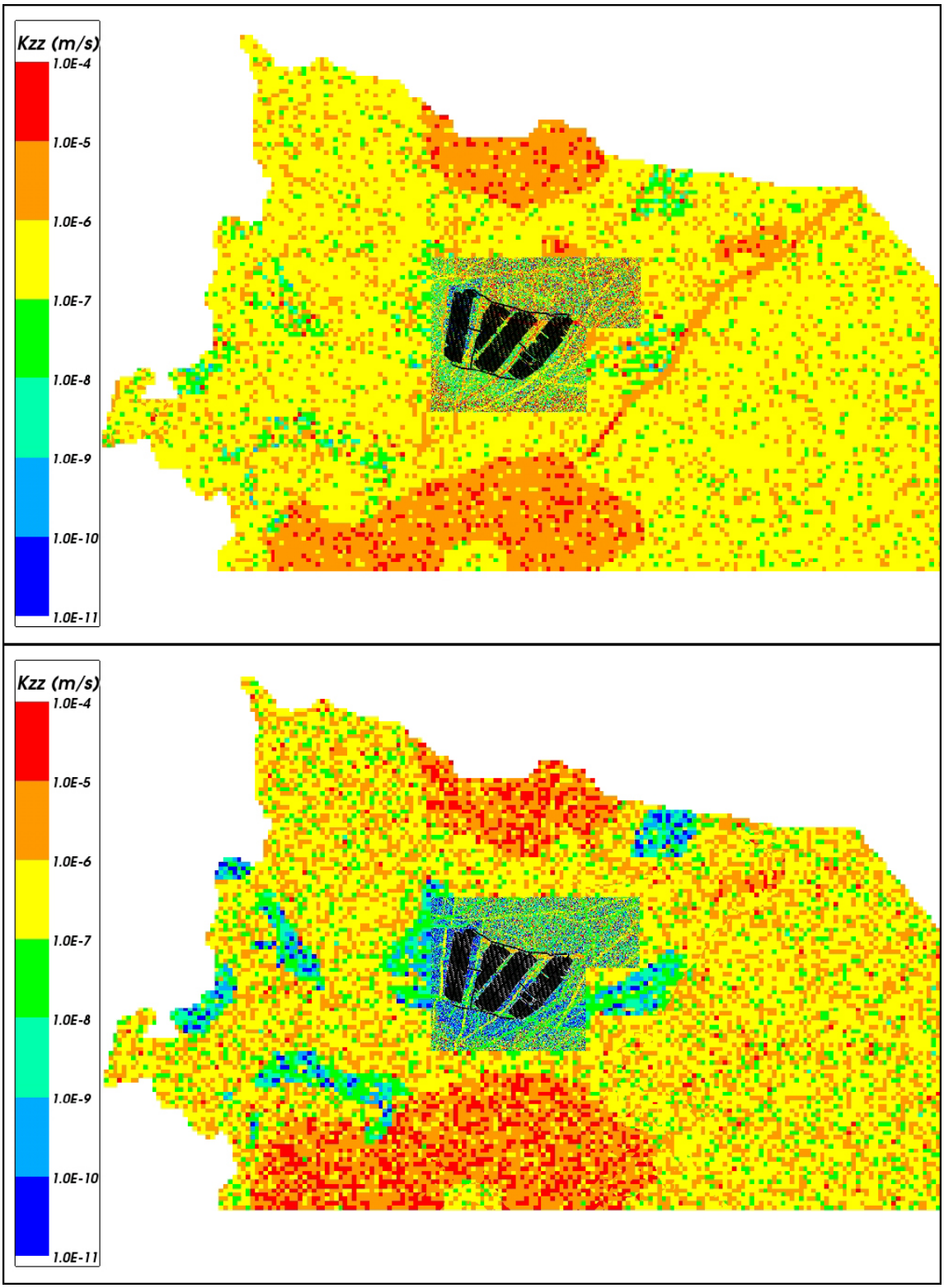

Figure 5-7. *Distribution of vertical hydraulic conductivity on horizontal slices through the 20 m scale Stochastic continuum site-scale model using the deterministic HCD and realisation 1 of the HRD (denoted r0). Repository structures are shown in black. From top to bottom: z = –80 m (in DZ1), z = –250 m (in DZ2).*

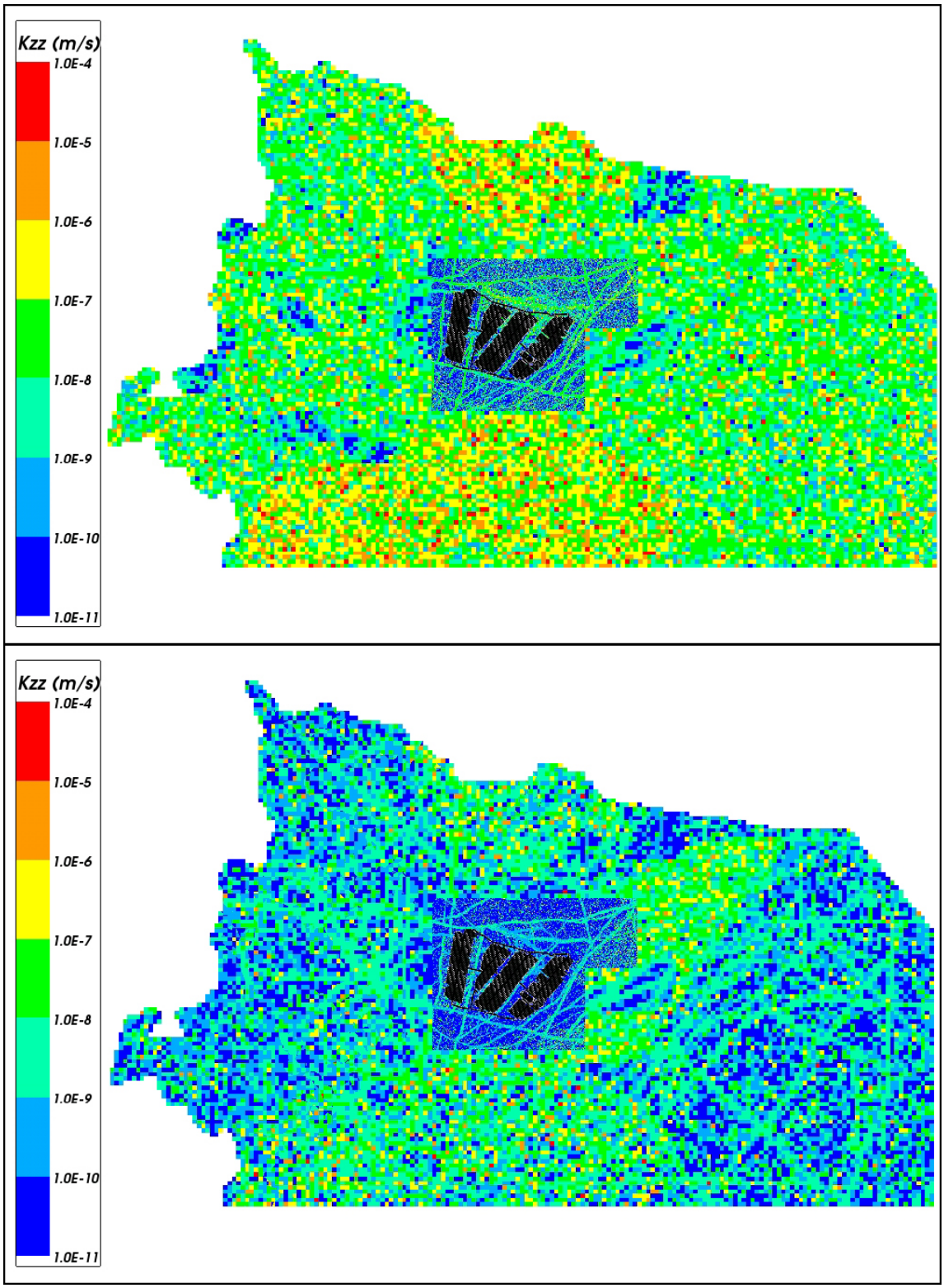

Figure 5-8. *Distribution of vertical hydraulic conductivity on horizontal slices through the 20 m scale Stochastic continuum site-scale model using the deterministic HCD and realisation 1 of the HRD (denoted r0). Repository structures are shown in black. From top to bottom: z = –510 m (in DZ3), z = –700 m (in DZ4).*

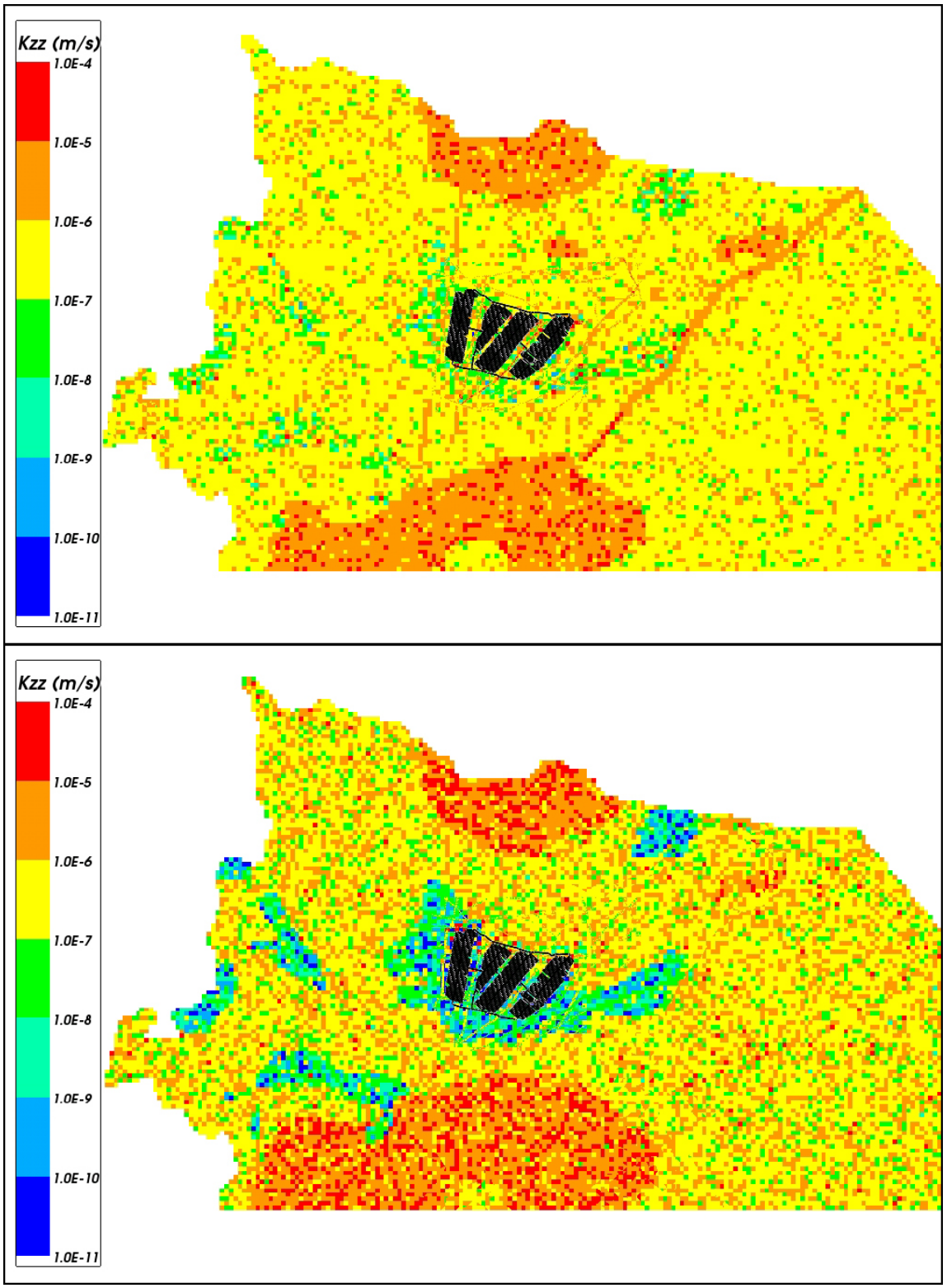

Figure 5-9. *Distribution of vertical hydraulic conductivity on horizontal slices through the 100 m scale Stochastic continuum site-scale model using the deterministic HCD and realisation 1 of the HRD (denoted r0). Repository structures are shown in black. From top to bottom: z = –80 m (in DZ1), z = –250 m (in DZ2).*

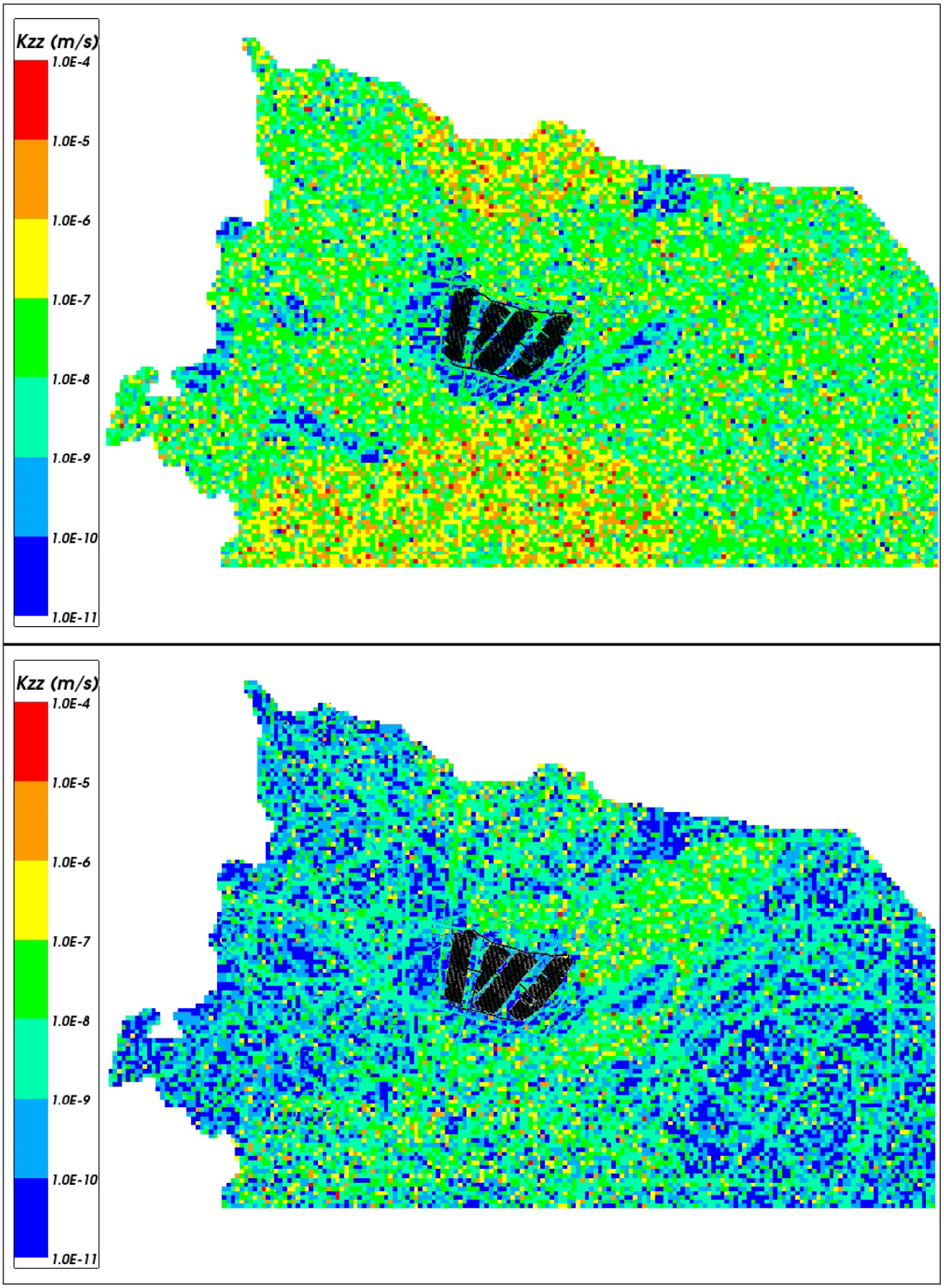

Figure 5-10. *Distribution of vertical hydraulic conductivity on horizontal slices through the 100 m scale Stochastic continuum site-scale model using the deterministic HCD and realisation 1 of the HRD (denoted r0). Repository structures are shown in black. From top to bottom: z = –510 m (repository depth in DZ3), z = –700 m (in DZ4).*

Repository-scale model

Two repository-scale models were constructed, corresponding to the 20 m and 100 m property scales, each sub-divided in to three blocks with the same grids as used for the Hydrogeological base case, except that elements were sub-divided until they were no larger than 20 m in size. Hydraulic conductivity values from the corresponding property grid were mapped on to both models using interpolation. Two realisations of each model were created, the first using the first realisation of the property grid (HRD) and a deterministic HCD (denoted r0) and the second using the second realisation of the property grid (HRD) and the second stochastic realisation of the HCD (denoted r2). The deformation zone properties from the HCD were mapped on to the models using the same IFZ procedure used for the regional-scale model. The properties of the repository structures were the same as in the Hydrogeological base case (Table 4-2). For the main tunnels, deposition tunnels, deposition holes and EDZ these properties were assigned explicitly to the appropriate elements in the model. The properties of the other repository structures were assigned using the IFZ method (Section 3.2.2). Slices through realisation r0 of block 1 of the models at repository depth, coloured by the vertical component of the hydraulic conductivity are shown in Figure 5-11 and Figure 5-12. The repository structures in block 1 are shown in Figure 5-13.

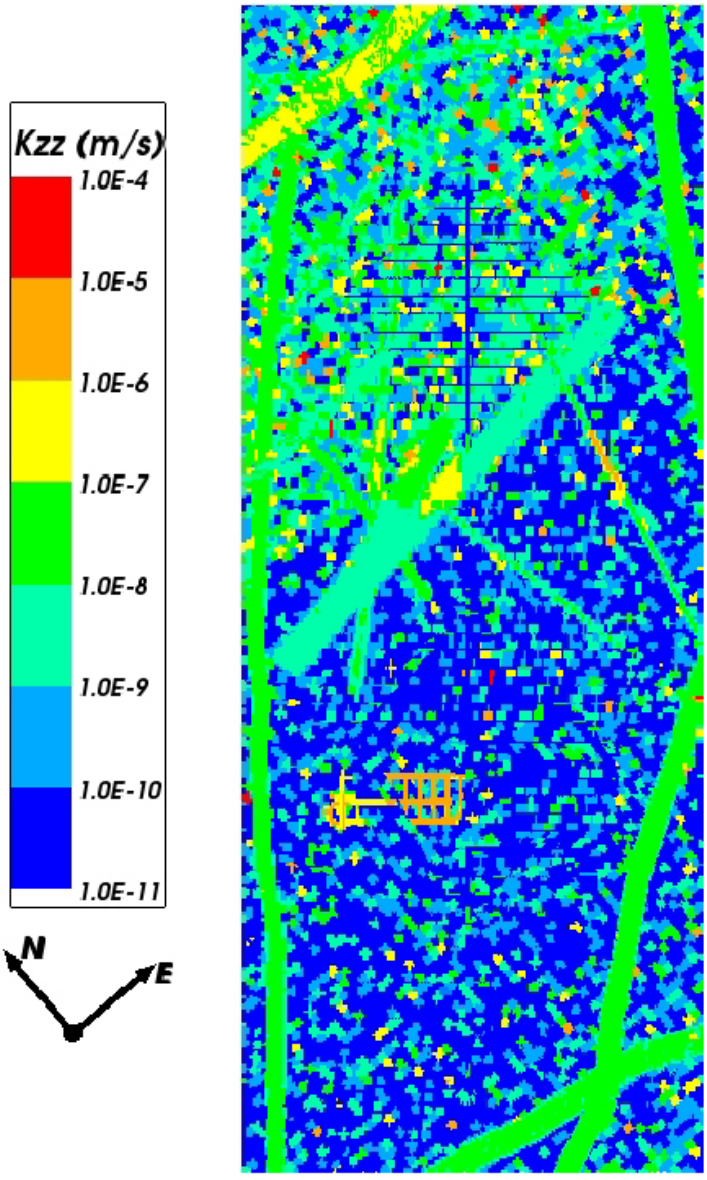

Figure 5-11. *Distribution of vertical hydraulic conductivity on a horizontal slice through the 20 m scale Stochastic continuum repository-scale model using the deterministic HCD and realisation 1 of the HRD (denoted r0) at z = –510 m (repository depth in DZ3).*

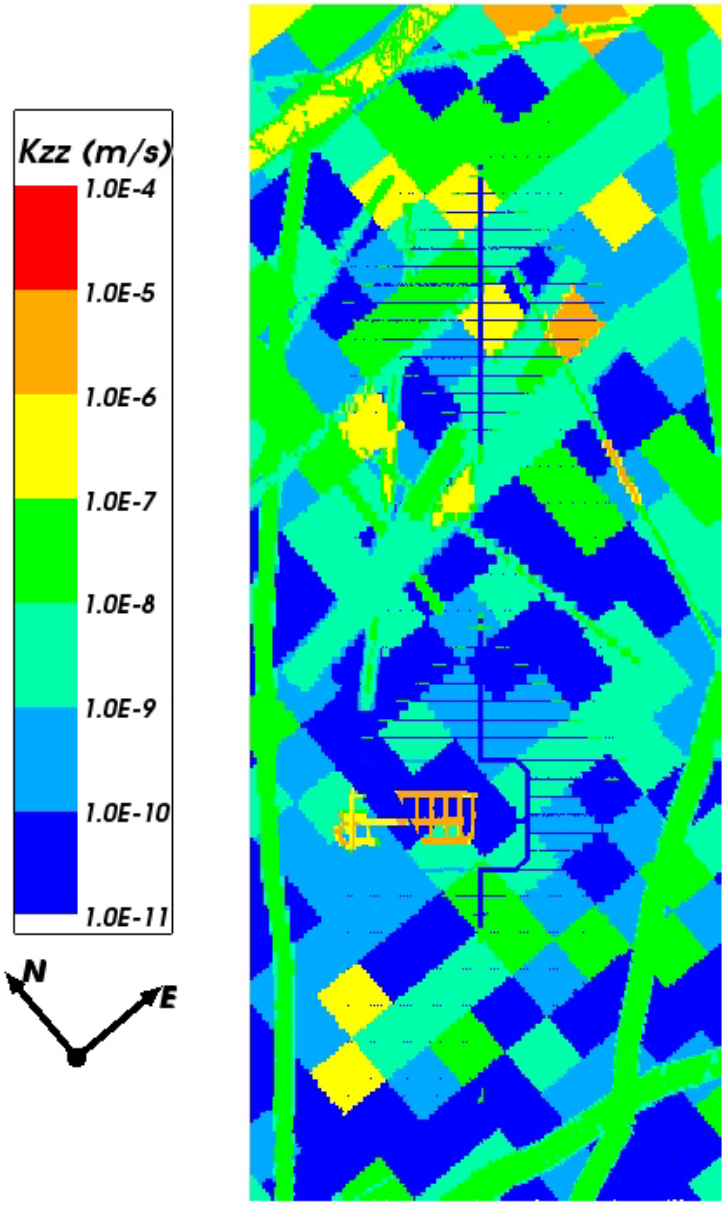

Figure 5-12. *Distribution of vertical hydraulic conductivity on a horizontal slice through the 100 m scale Stochastic continuum repository-scale model using the deterministic HCD and realisation 1 of the HRD (denoted r0) at z = –510 m (repository depth in DZ3).*

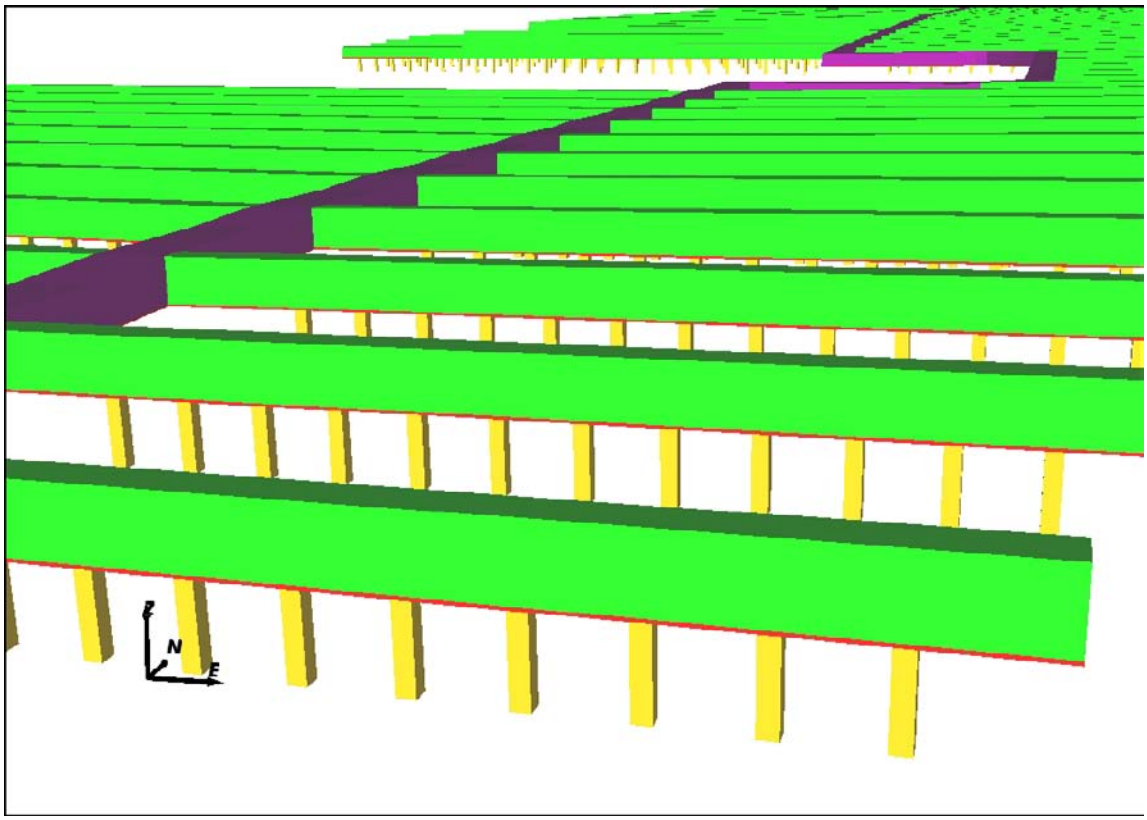

Figure 5-13. *Close up view of the tunnels in block 1 of a Stochastic continuum repository-scale model. The main tunnel is coloured purple, the deposition tunnels are green, the deposition holes are yellow and the EDZ is red.*

Steady-state groundwater flow calculations were carried out for each model and realisation using the corresponding pressures and densities imported from the regional-scale model for 2000 AD and 15,000 AD. The initial conditions and boundary conditions were applied in the same way as for the Hydrogeological base case repository-scale model. Particle tracking calculations were carried out and continued in the corresponding site-scale model. Performance measures were calculated as for the Hydrogeological base case, using the modifications required for the Stochastic continuum case described in Section 3.2.6.

Since the flow velocity can vary around the deposition hole, four particle tracking start points were considered for each Q1 and Q2 location, corresponding to positions 0.1 m away from the centre of each of the four vertical faces of the portions of the deposition hole within the bedrock (Q1) or EDZ (Q2), as shown in Figure 5-14. To be conservative, the particle tracking start point with the highest Darcy flux was chosen for each location.

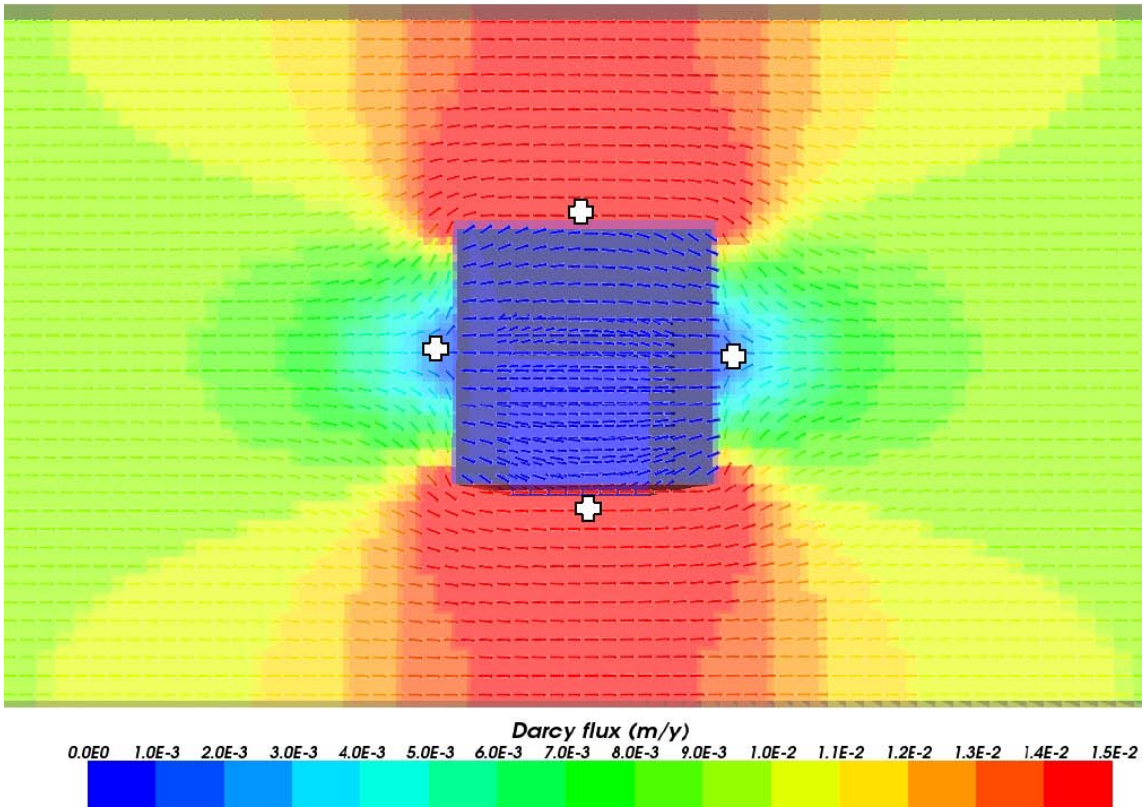

Figure 5-14. *Darcy flux in an idealised model of the EDZ with a head gradient of 0.01 m/m applied from left to right. The repository structure properties and dimensions are the same as in the Stochastic continuum model. The arrows show the direction of flow. The potential particle start points are indicated by white crosses.*

5.3.3 Confirmatory testing

As part of the modelling procedure, regional-scale palaeohydrogeological simulations were performed. These calculated the hydrochemical conditions at present-day which can be compared with the site data as for the other confirmatory tests in SDM-Site (/Rhén et al. 2008/). The results of a comparison with the Elaborated Hydro-DFN case and the site data are given in Appendix C. There is a reasonable match to the hydrochemistry data and the results are generally comparable to those obtained for Elaborated Hydro-DFN model. However, no iterative calibration procedure was carried out and other data, such as interference tests, were not considered. Still, the paeleohydrogeological results seem to suggest the hydrogeological properties give a reasonable representation of regional flow and transport.

6 Results

6.1 Presentation of results

The primary results obtained from this study are particle exit locations and performance measures. The performance measures are described in Section 3.2.6 and, for the rock, include initial equivalent flux, U_r, initial equivalent flow rate, Q_{eqr}, flow-related transport resistance, F_r, travel time, t_r, and path length, L_r. Unless otherwise stated, segments of particle paths in the ECPM and CPM parts of the model do not contribute to the performance measures in the rock, which may be a significant portion of the particle pathways for later times. The initial equivalent flux, U_r, and flow-related transport resistance, F_r, performance measures are particularly important for a site assessment, especially the tails in their distributions.

Particle start or exit locations are displayed as plots of the points overlaid on a representation of the model domain, with location information such as deformation zones and surface features (roads, railways, rivers and streams) added to provide context. The points are coloured either to indicate which case they relate to or to represent a property associated with the particle, such as a performance measure. Start point plots relate particle properties to repository location. Exit point plots relate particle properties to discharge location. Both types of plot only include particles that have successfully reached the top surface of the model.

Cumulative distribution plots (CDF) of performance measures show the cumulative fraction of particles as a function of performance measure value. These plots allow the distribution of performance measure values to be readily seen, including the tails of those distributions. Non-normalised plots consider all particles, but the curves begin (intercept the fraction axis) at the fraction of particles that do not start. In addition, for advective travel time and flow-related transport resistance, the plots end at one minus the fraction of particles that become stuck along the path. Normalised plots filter out particles that do not start and particles that do not reach the top surface of the model and then re-normalise the proportions to the range zero to one. The ranges used for the horizontal axes of the CDF plots were chosen to be consistent with those used in the CDF plots of the corresponding performance measures in the SR-Site Forsmark temperate modelling report /Joyce et al. 2010/ to allow comparisons to be more easily made. The ranges do not indicate the minimum and maximum values of the performance measures, i.e. the minimum and maximum values on the horizontal axis are not the minimum and maximum values of the corresponding performance measure.

Bar and whisker plots are used for comparing the median and spread of performance measures for several cases. The cases are shown side by side and each case has its own bar and whiskers. The median is shown as a red line. The 25th and 75th percentiles are the blue bar (or box) and the 5th and 95th percentiles are the black whiskers. For plots of U_r all particles that successfully start are included. For other plots, particles that fail to reach the top surface of the model are excluded.

When carrying out particle transport calculations not all released particles successfully reach the top surface of the model. Some are discarded before they start, either because there is no available fracture for them to start in (for Q1) or because the initial flow is below a starting threshold. Some particles fail to reach the model boundary because of numerical issues, such as local mass balance problems, and some particles exit from the sides or bottom of the model. The way these unsuccessful particles are handled varies according to the plot used, as described above, but in each case the plot caption will indicate the percentage of particles included. Where several cases are displayed on one plot, either the percentages are given individually or a range is given. The percentages are given separately for Q1, Q2 and Q3 particle releases.

The main results and discussion are presented in this chapter. The full set of results are given in Appendix C.

6.2 Hydrogeological base case model results

6.2.1 Distribution of reference waters

Coupled groundwater flow and solute transport is conceptualised in terms of the evolution through mixing of a number of groundwater constituents, called reference waters. The reference waters have different origins and chemical compositions. The hydrochemical evolution of the groundwater is then calculated from the fractions of reference waters present. In the fractures, water mixing takes place through the processes of advection, dispersion, and diffusion. In addition, there is an exchange with the matrix by rock matrix diffusion. The porewater chemical composition, i.e. the water in the matrix, is assumed to evolve only as a result of rock matrix diffusion (see /Hoch and Jackson 2004/).

Groundwater composition is described in terms of mixtures of five references waters based on the SDM-Site Laxemar hydrochemistry description /Laaksoharju et al. 2009/. The main chemical composition characteristics for the purposes of mixing of the reference waters can be described in terms of chloride, magnesium, bicarbonate and $\delta^{18}O$, as defined reference waters in Table 6-1.

Figure 6-2 to Figure 6-6 show the evolution of each reference waters with time from 5000 BC to 15,000 AD for a vertical slice taken through the regional-scale model. The location of this slice is shown in Figure 6-1.

Figure 6-2 shows that the highest fractions (0.9 to 1.0) of the Deep Saline reference water are predicted to occur at depth. The volumes with high saline fractions are characterised by high chloride content, so that the Deep Saline distribution predicted can be compared to the chloride distributions presented in Figure 9-15 of /Rhén et al. 2009/. The Deep Saline distribution does not significantly change from 5000 BC through to 15,000 AD because other reference waters have a lower density, and thus typically mix at shallower depths.

Table 6-1. The definitions of the various reference waters specified at initial conditions.

Reference water	Description
Deep Saline	Strong saline source implies a high chloride content (> 6,000 mg/L). Non-marine origin implies a low magnesium content (< 20 mg/L). Non-postglacial meteoric implies low bicarbonate content (< 50 mg/L). Enriched $\delta^{18}O$.
Littorina	Brackish saline source implies moderate chloride content (max. ~ 5,500 mg/L). (*Baltic Sea Water* has a present-day chloride content of ~ 3,000 mg/L). Marine origin implies a high magnesium content (max.250–350 mg/L). Non-postglacial meteoric implies low bicarbonate content (< 100 mg/L). Enriched $\delta^{18}O$ (> –10‰ SMOW).
Altered Meteoric	Non-saline source implies a low chloride content (< 200 mg/L). Non-marine origin implies a low magnesium content (< 50 mg/L). Postglacial meteoric implies high bicarbonate content (> 50mg/L). Intermediate $\delta^{18}O$ (–12 to –11‰ SMOW).
Glacial	Non-saline source implies a low chloride content (< 8 mg/L). Non-marine origin implies a low magnesium content (< 8 mg/L). Non-postglacial meteoric implies low bicarbonate content (< 50mg/L). Significantly depleted $\delta^{18}O$.
Inter-glacial porewater	Possible saline source implies a low-moderate chloride content (<5,000 mg/L). Non-marine origin implies a low magnesium content (< 50 mg/L). Non-postglacial meteoric implies low bicarbonate content (< 50 mg/L). Intermediate $\delta^{18}O$ (> –10‰ SMOW).

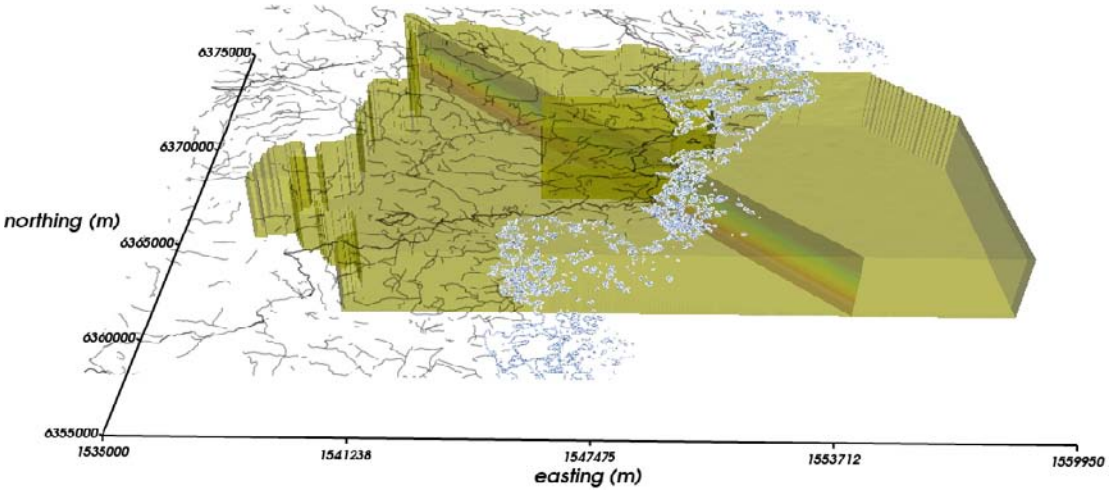

Figure 6-1. *The location of the north west to south east vertical slice used in the fractional distributions plots of various waters for the regional-scale model. The shoreline at 2000 AD is shown in blue. Surface features are shown in grey.*

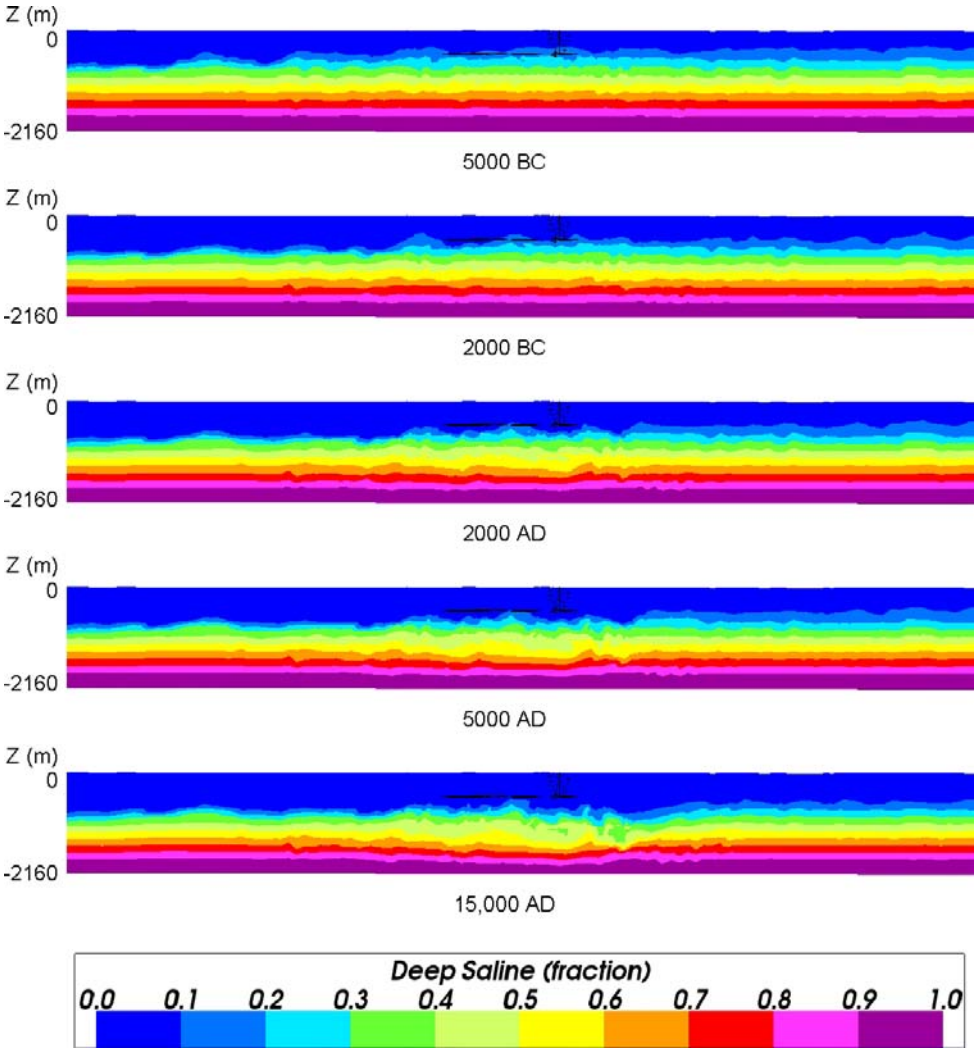

Figure 6-2. *Vertical slices (north west to south east) of the distributions of the Deep Saline reference water for the regional-scale model with the location of the repository (–500 m) shown in black and positioned centrally. From the top: Distributions at 5000 BC, 2000 BC, 2000 AD, 5000 AD and 15,000 AD.*

Figure 6-3 shows that the Littorina reference water is predicted to exist at high fractions at shallow depths over the south eastern part of the model domain at 5000 BC. At 2000 BC the Littorina reference water has reached repository elevation at fractions > 0.3. As the coastline moves south east in time the areas with significant Littorina water fractions also move south east. By 15,000 AD there is predicted to be very little Littorina water within the model domain, as it is replaced by Altered Meteoric reference water, as shown in Figure 6-4.

The distribution of the fractions of the Altered Meteoric reference water is presented in Figure 6-4. At 5000 BC the Altered Meteoric reference water has not yet been specified as a non-zero component of the top-surface boundary condition, but by 2000 BC its inclusion is evident, and the north west of the modelling domain has fractions of 0.9 at repository depth. As time progresses the penetration depth does not significantly increase below repository depth, but volumes containing significant fractions of the Altered Meteoric reference water are predicted to extend south east, following the migration of the coastline until, at 15,000 AD, the penetration depth is approximately uniform throughout the entire modelled domain.

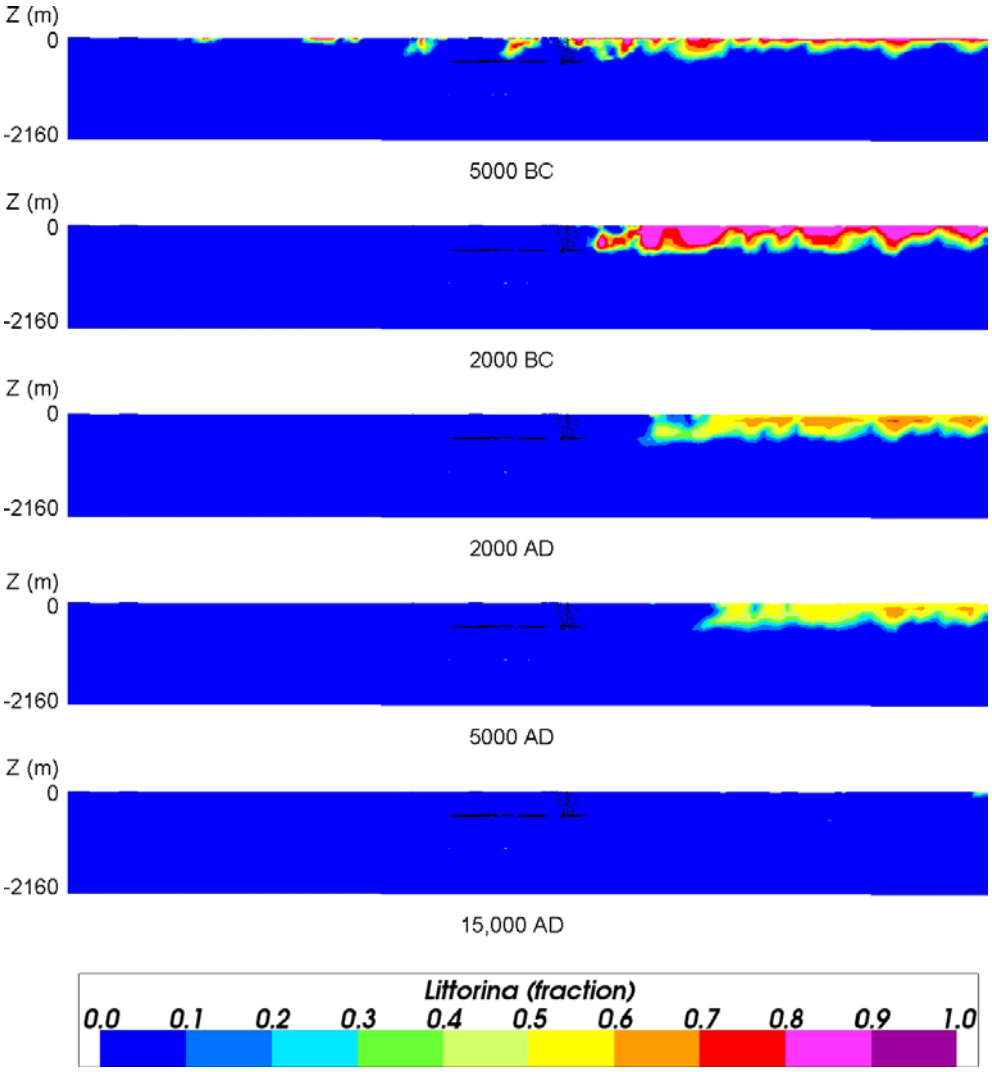

Figure 6-3. *Vertical slices (north west to south east) of the distributions of the Littorina reference water for the regional-scale model with the location of the repository (–500 m) shown in black and positioned centrally. From the top: Distributions at 5000 BC, 2000 BC, 2000 AD, 5000 AD and 15,000 AD.*

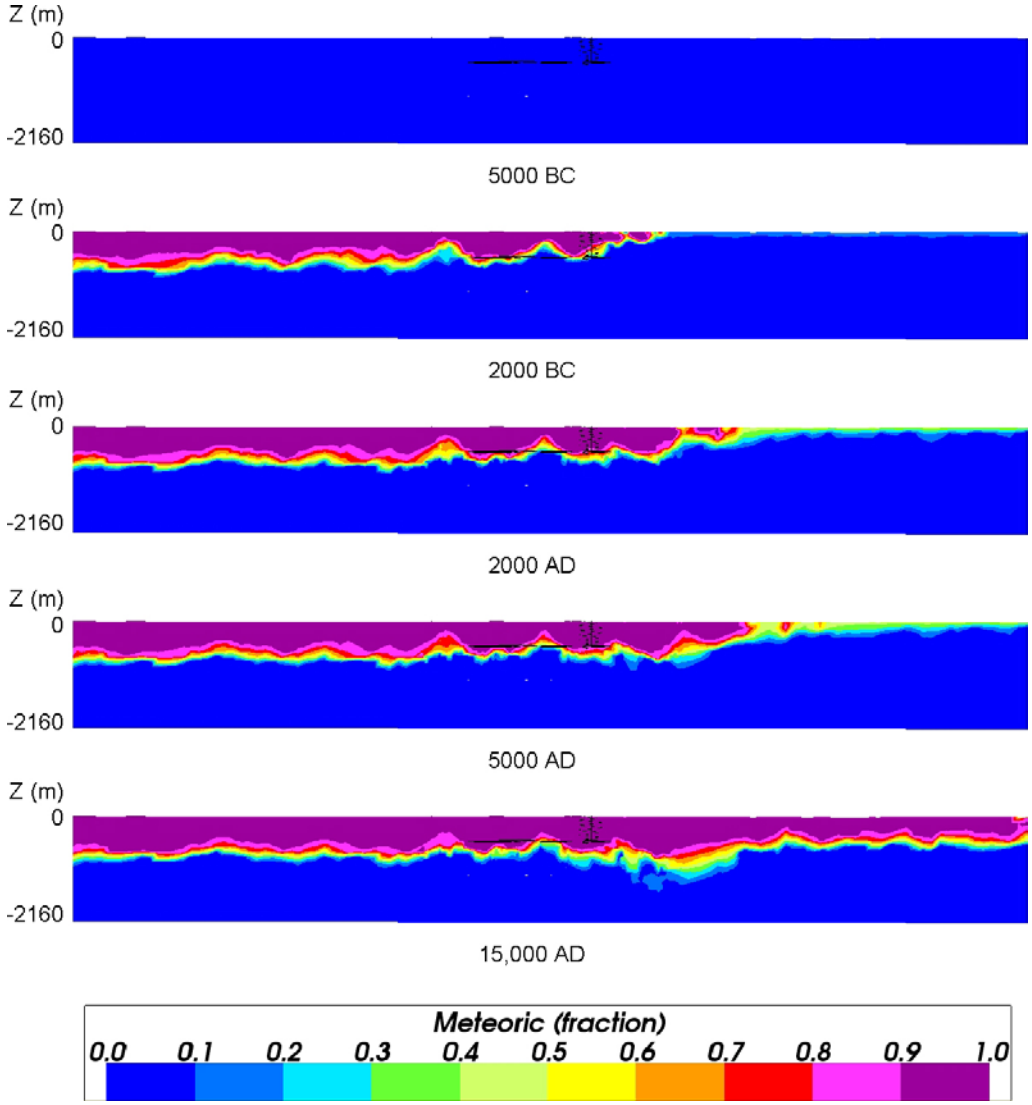

Figure 6-4. *Vertical slices (north west to south east) of the distributions of the Altered Meteoric reference water for the regional-scale model with the location of the repository (–500 m) shown in black and positioned centrally. From the top: Distributions at 5000 BC, 2000 BC, 2000 AD, 5000 AD and 15,000 AD.*

The distribution of the fractions of the Glacial reference water calculated by the model is presented in Figure 6-5. The fractions of the Glacial water at 5000 BC are calculated to be significant to the north west of the repository at depths of up to approximately –500 m. To the south east of the repository the fractions at 5000 BC are relatively high in a horizontal extent but vertically limited to a layer at an elevation shallower than repository depth. No additional Glacial reference water is added to the model, through the top-surface boundary conditions, after 4000 BC. As time progresses the layer with significant Glacial reference water fractions (at approximately –600 m to –1,000 m) is progressively reduced, particularly at the higher elevations.

Figure 6-6 shows the calculated values of the fractions for the Inter-glacial reference water. This figure shows a thick layer from approximately –300 m to –1,000 m with groundwater composed of 20% to 50% Inter-Glacial reference water. Over time there is a gradual increase in the fraction as this reference water diffuses out of the rock matrix.

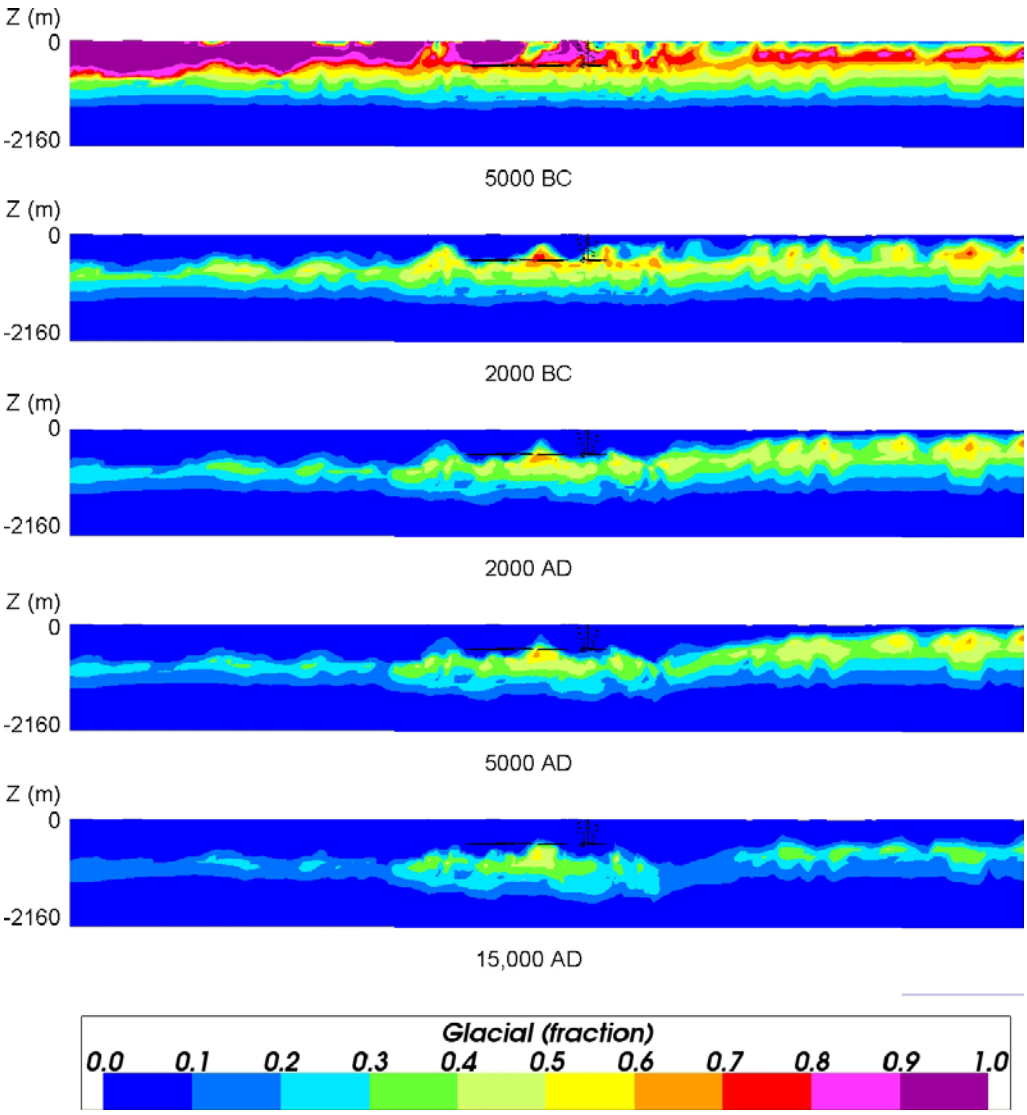

Figure 6-5. *Vertical slices (north west to south east) of the fraction distributions of the Glacial reference water for the regional-scale model with the location of the repository (–500 m) shown in black and positioned centrally. From the top: Distributions at 5000 BC, 2000 BC, 2000 AD, 5000 AD and 15,000 AD.*

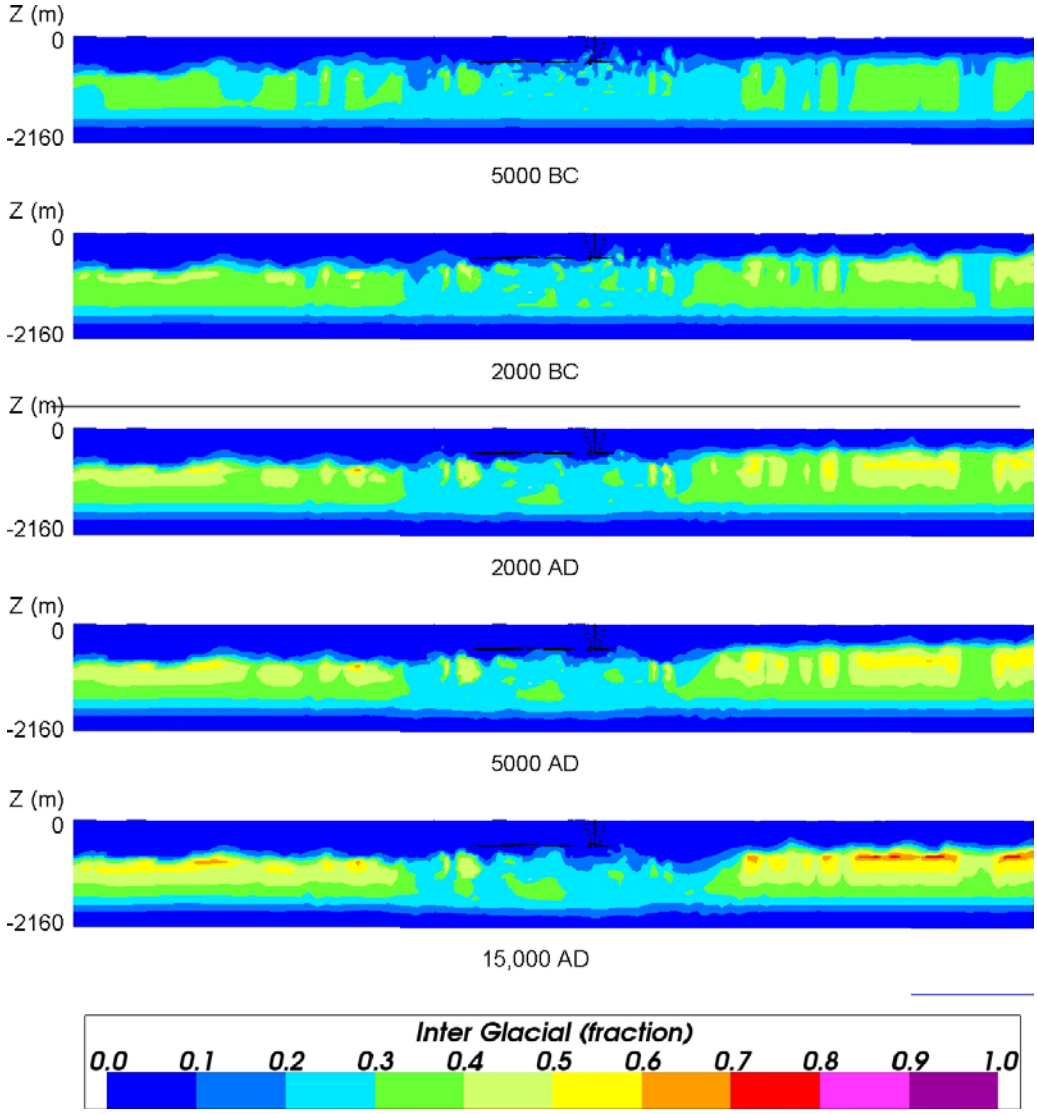

Figure 6-6. *Vertical slices (north west to south east) of the distributions of the Inter-glacial reference water for the regional-scale model with the location of the repository (–500 m) shown in black and positioned centrally. From the top: Distributions at 5000 BC, 2000 BC, 2000 AD, 5000 AD and 15,000 AD.*

6.2.2 Evolution of exit locations with time

The discharge locations of particles released from Q2 locations in the site-scale model are shown, for various discharge times, in Figure 6-8 to Figure 6-10. These figures suggests that the particle discharge locations are strongly influenced by the locations of outcropping deformation zones. There is some variation in the discharge locations with time, as the shoreline recedes to the east, however the influence is less than that of the deformation zones. Also, the influence of the shoreline location will tend to decrease as it moves further from the repository.

Site investigations, summarised in /Rhen et al. 2009/, show a noticeable downward gradient in the upper 200 m of bedrock in about 50% of the core-drilled boreholes, with others showing lower vertical gradients (either upwards or downwards). Regional groundwater flow modelling calculates discharge in the larger valleys and near this sea (reproduced in Figure 6-7), which is in accordance with measured heads and the distribution of surface water. The particle exit locations at 2000 AD shown in Figure 6-9 correspond to some of these discharge locations.

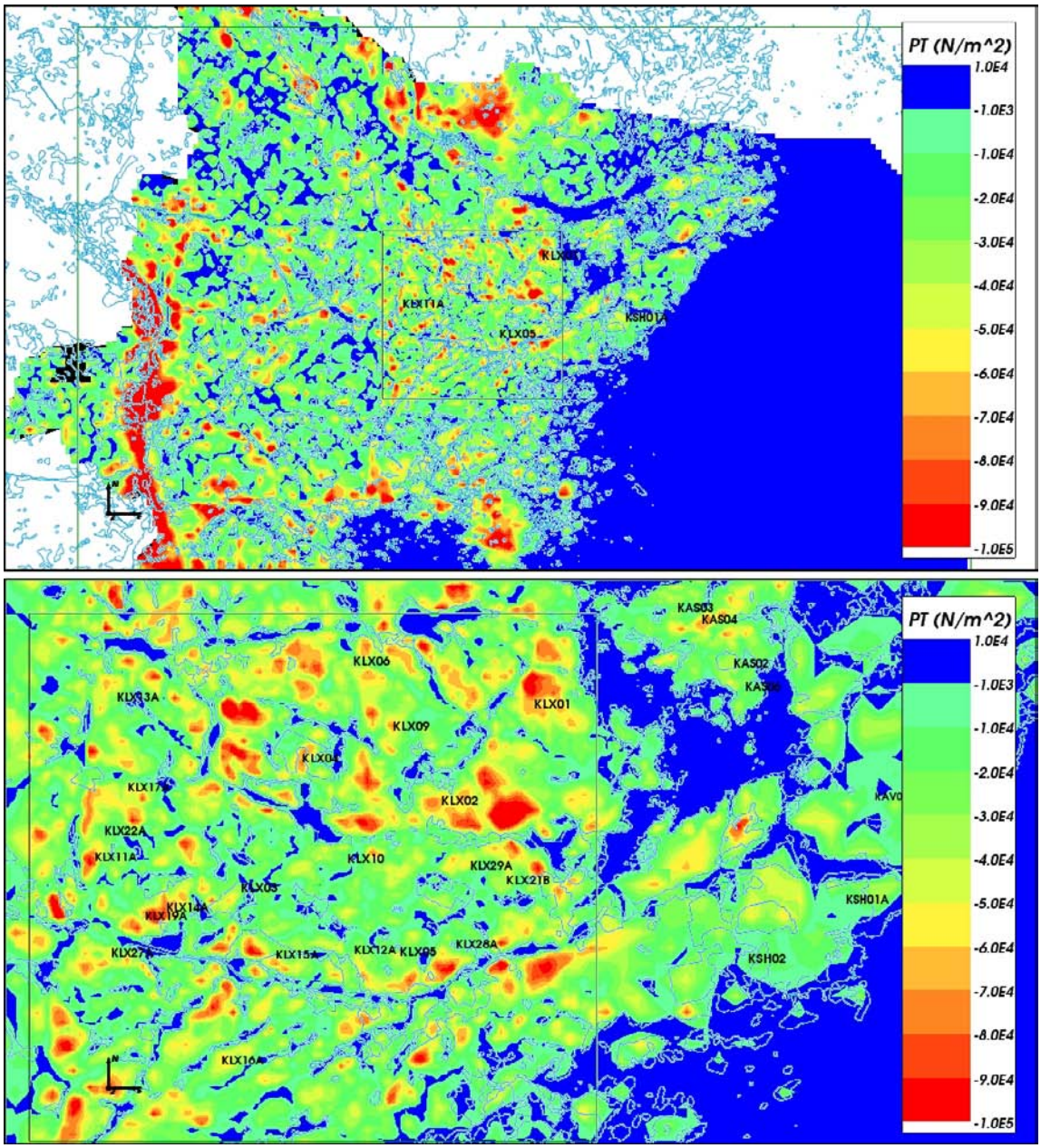

Figure 6-7. *Total pressure (Pa) distribution on the top surface of the base case model on the regional scale (top) and in the Laxemar local model area (bottom) to show the distribution of recharge (red to green) and discharge (dark blue). The outlines of surface waterbodies (including shoreline) and Laxemar local model area (square) are superimposed. Figure 8-7 in /Rhen et al. 2009/.*

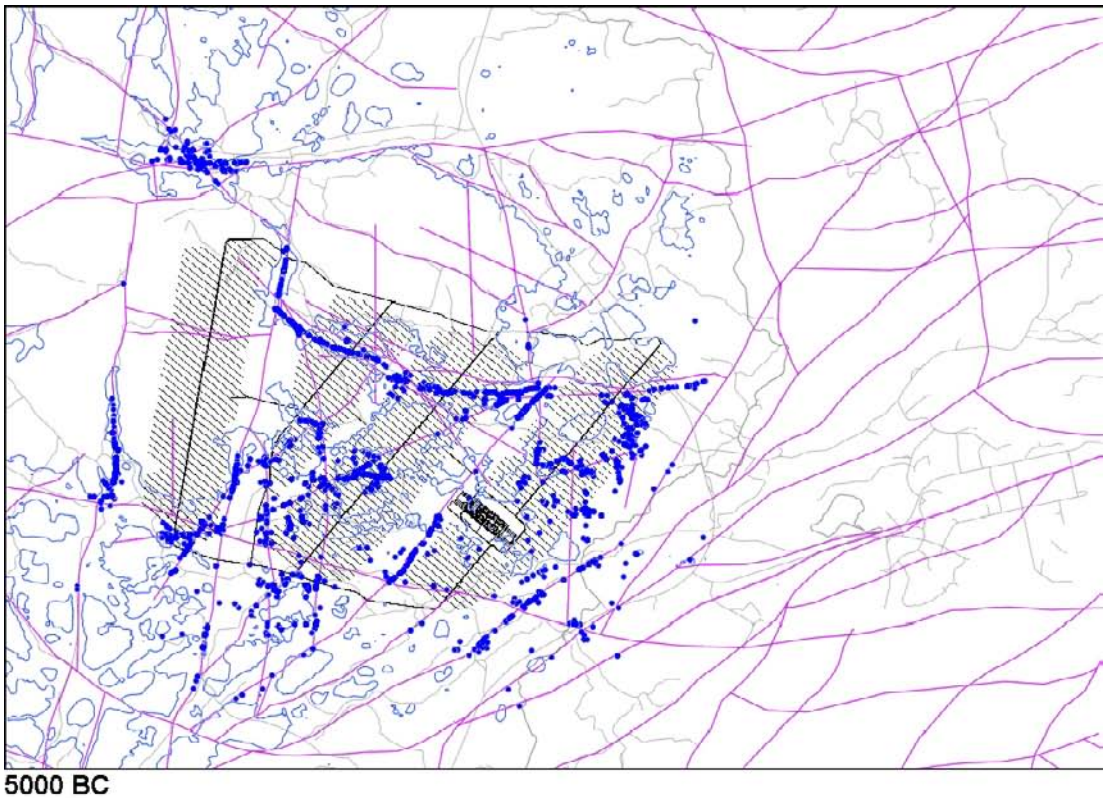

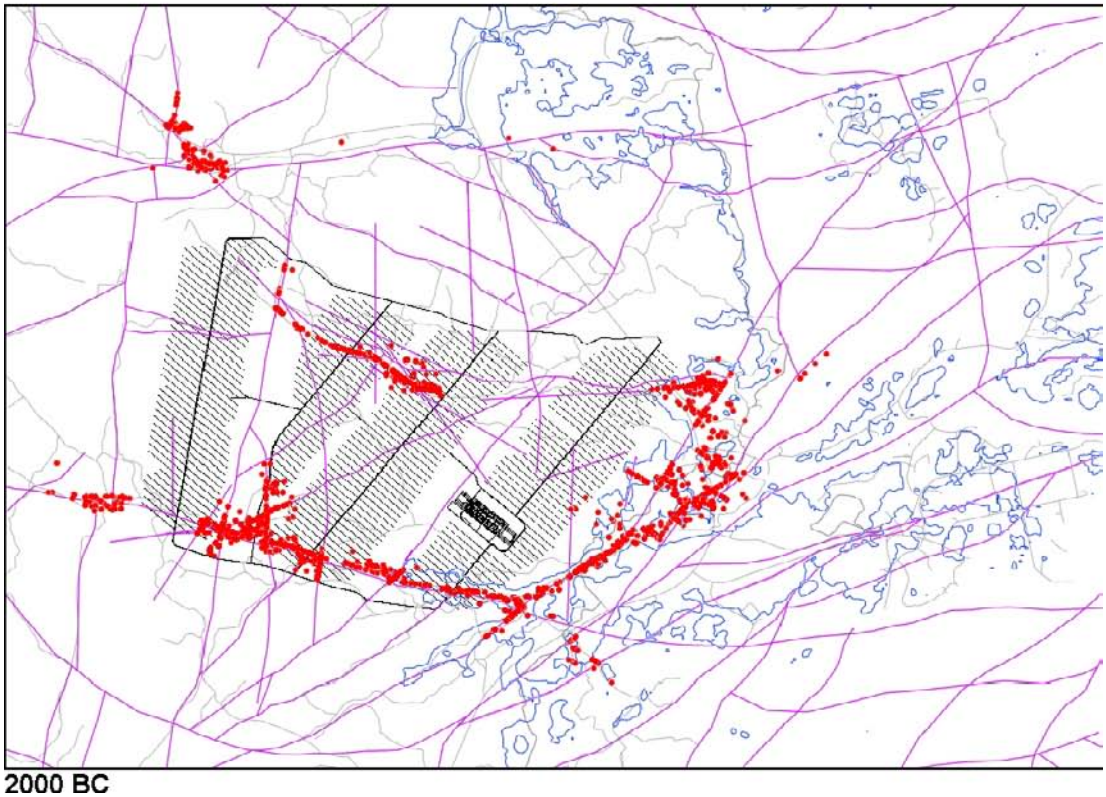

Figure 6-8. *Exit locations for the Q2 particles successfully reaching the top boundary of the site-scale Hydrogeological base case model (96%–98%) for releases at 5000 BC (dark blue) and 2000 BC (red). The shoreline at each time is shown in blue, deformation zones at z = –50 m in purple, repository structures in black and surface features in grey.*

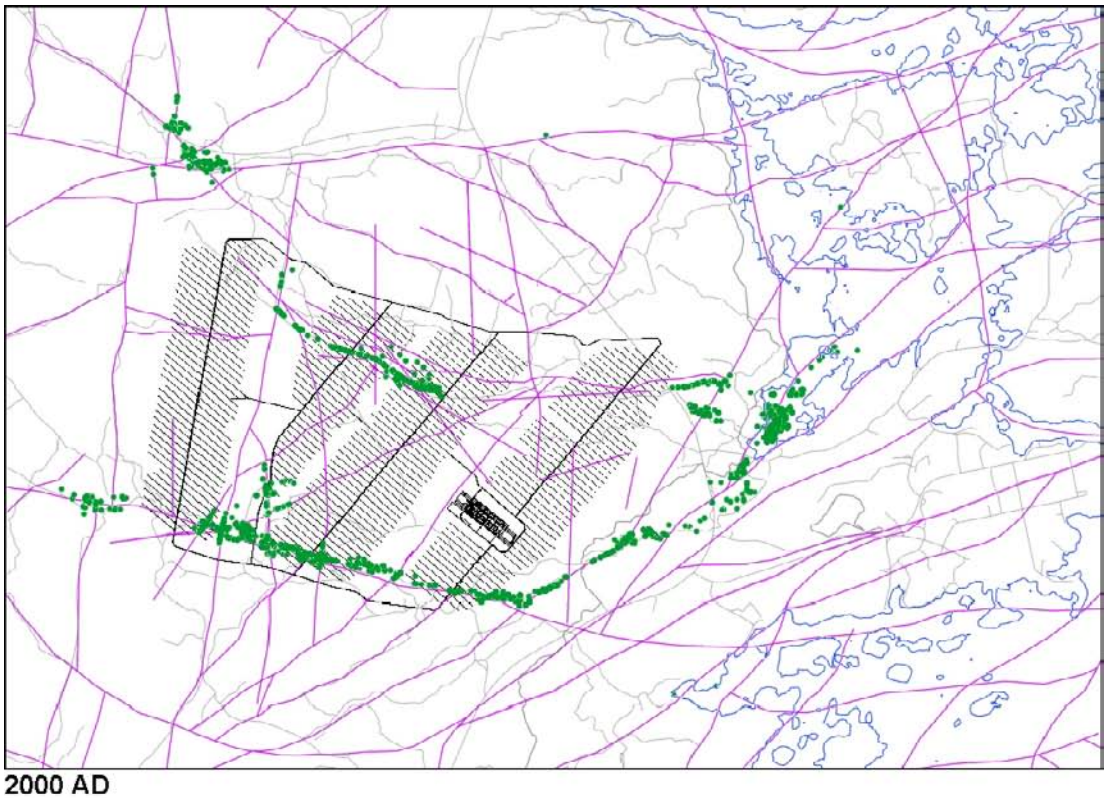

2000 AD

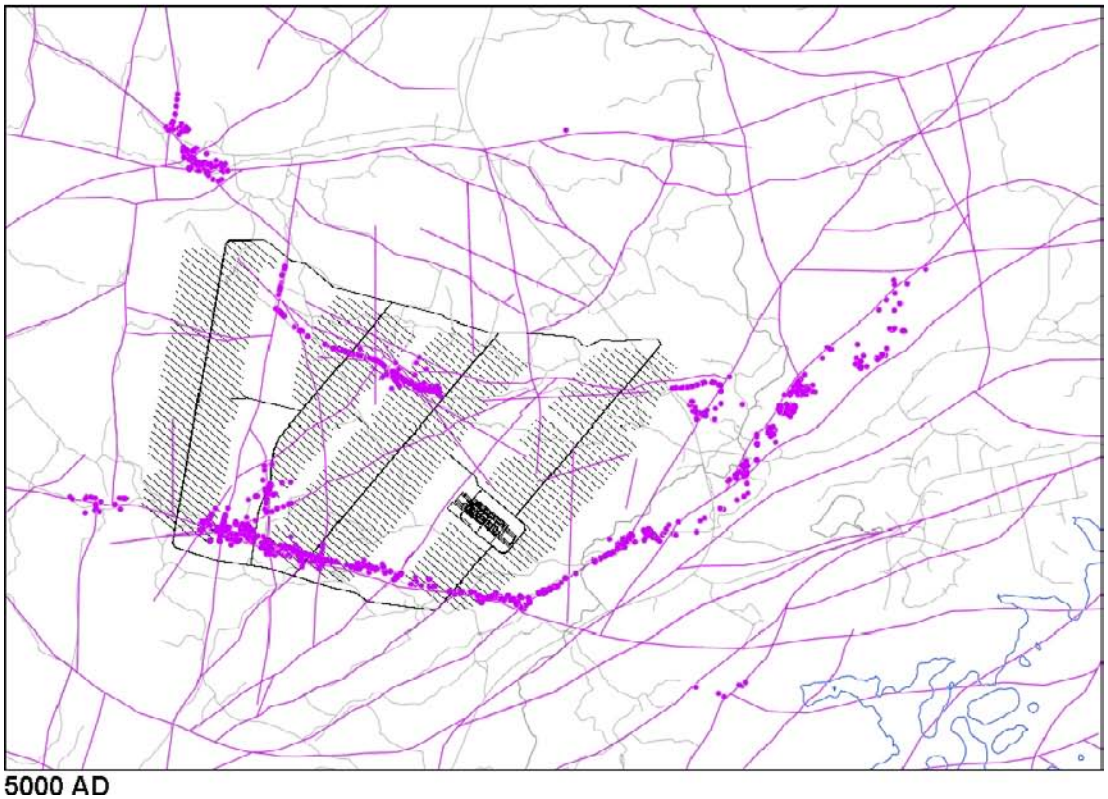

5000 AD

Figure 6-9. *Exit locations for the Q2 particles successfully reaching the top boundary of the site-scale Hydrogeological base case model (96%–98%) for releases at 2000 AD (green) and 5000 AD (purple). The shoreline at each time is shown in blue, deformation zones at z = –50 m in purple, repository structures in black and surface features in grey.*

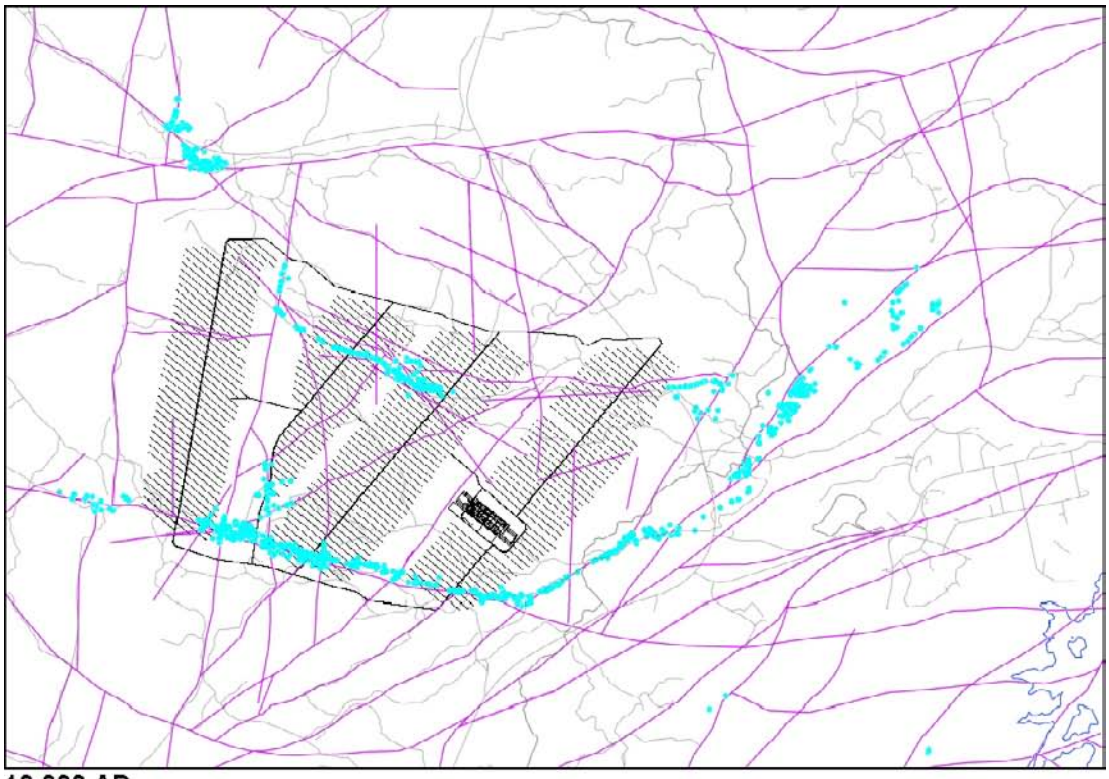

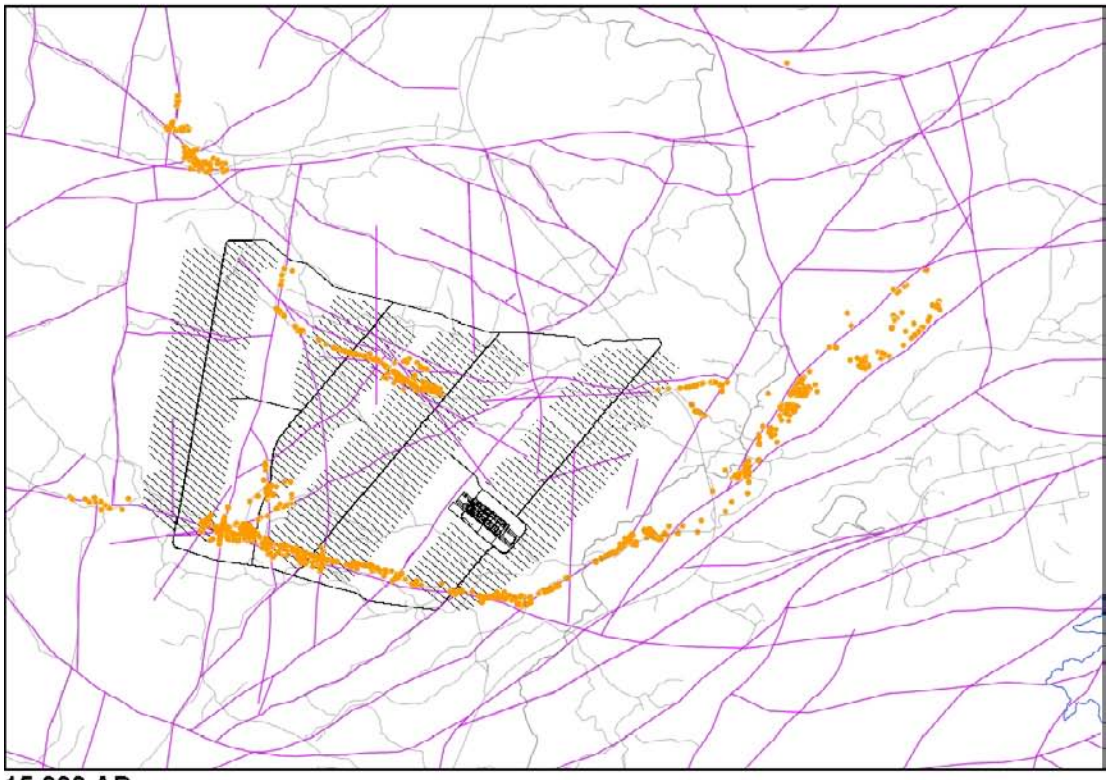

Figure 6-10. *Exit locations for the Q2 particles successfully reaching the top boundary of the site-scale Hydrogeological base case model (96%–98%) for releases at 10,000 AD (light blue) and 15,000 AD (orange). The shoreline at each time is shown in blue, deformation zones at z = –50 m in purple, repository structures in black and surface features in grey.*

6.2.3 Evolution of performance measures with time

Four time slices were chosen, 2000 BC, 2000 AD, 5000 AD and 15,000 AD, for the repository-scale model, based on the results of the site-scale modelling, to give representative exit locations that are progressively distant from the repository as the shoreline recedes.

Normalised CDF plots for the Q1 release locations are shown in Figure 6-11 to Figure 6-13, for the equivalent flux at the release point (U_r), the flow-related transport resistance (F_r) and the travel time (t_r), respectively. For each release time, approximately 24% of particles failed to get started in a fracture with a flow rate per unit width > $1 \cdot 10^{-6}$ m^2/y and a further 7% of particles did not exit the model due to numerical issues. There is very little variation in any of the performance measures in the rock with release time. This is because the particle exit locations are dominated by the deformation zones rather than the location of the retreating shoreline. Also, the contribution from the ECPM to the performance measures is not included, which is likely to be a more significant component for later times as some particle pathways become longer and more horizontal.

The median value of U_r at the release point is approximately 0.003 m/y, with the 90 percentile value approximately 0.1 m/y.

The median value of F_r is approximately 100,000 y/m, with the 10 percentile value approximately 10,000 y/m.

The median value of t_r is approximately 100 years, with the 10 percentile value approximately 20 years.

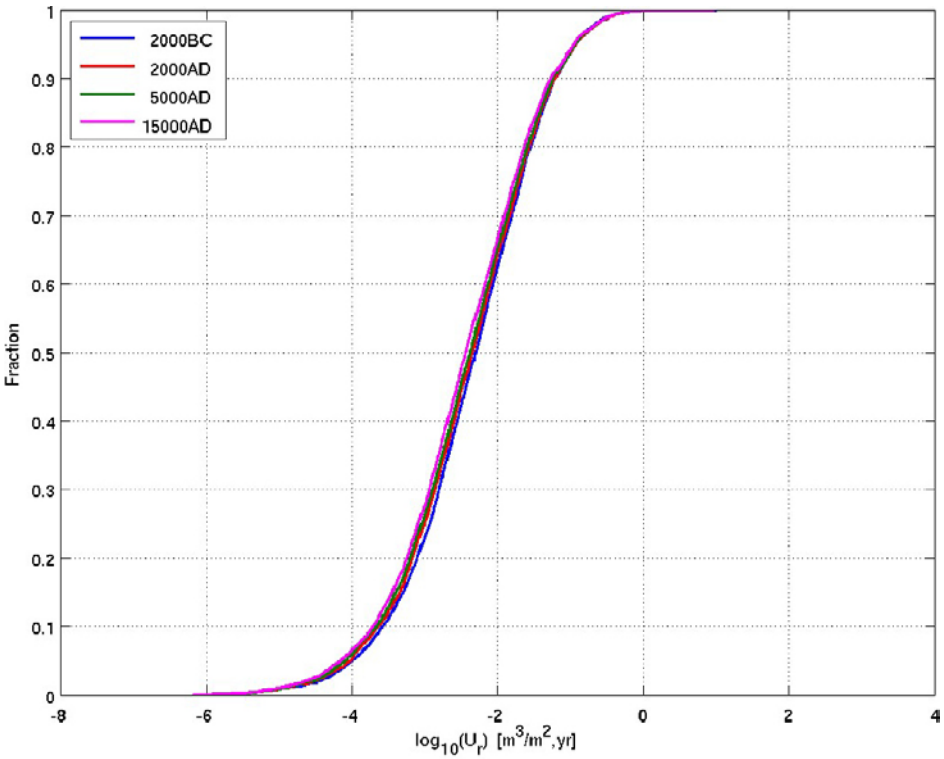

Figure 6-11. *Normalised CDF plots of U_r in the Hydrogeological base case model for the Q1 particles successfully reaching the model top boundary (69%), released at the given times.*

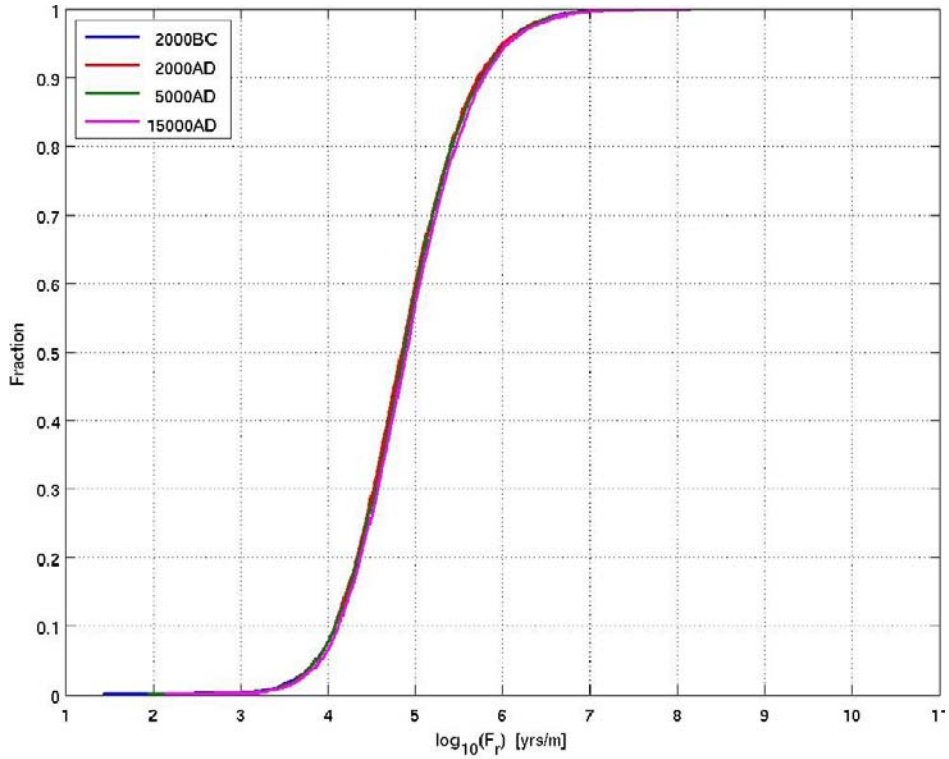

Figure 6-12. *Normalised CDF plots of F_r in the Hydrogeological base case model for the Q1 particles successfully reaching the model top boundary (69%), released at the given times.*

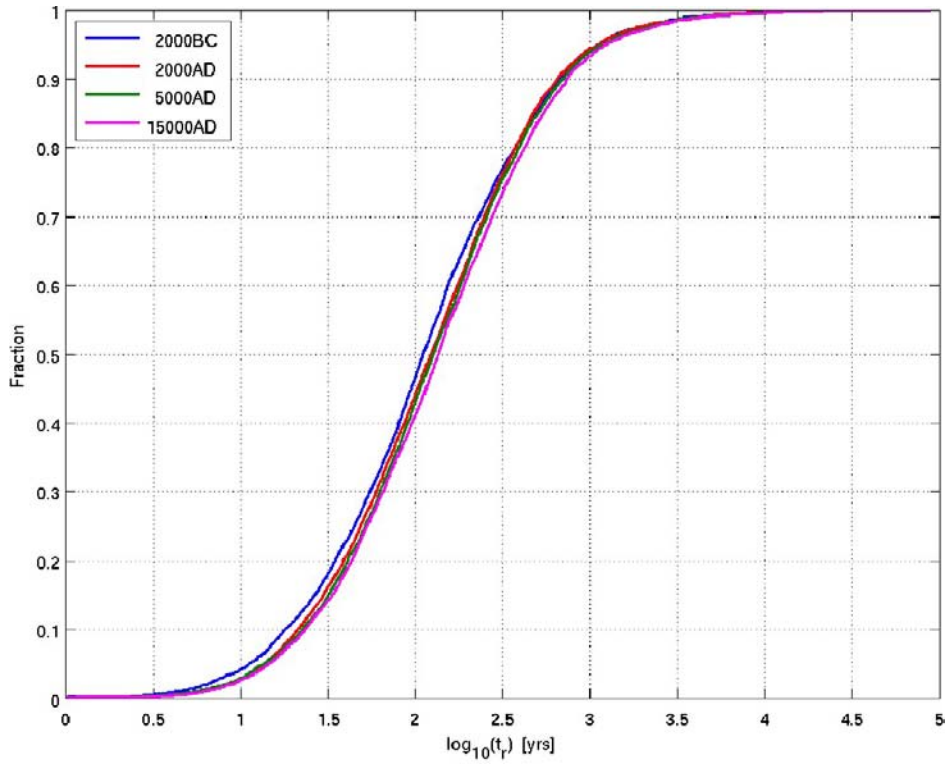

Figure 6-13. *Normalised CDF plots of t_r in the Hydrogeological base case model for the Q1 particles successfully reaching the model top boundary (69%) released at the given times).*

6.2.4 Spatial distribution of performance measures

Figure 6-14 and Figure 6-15 show the Q1 release locations of successful particles (those reaching the model top boundary), coloured by U_r and F_r respectively, for the 2000 AD release time. The U_r and F_r values calculated by the model vary across the repository.

The U_r plot shows that there are several locations within the repository with relatively high fluxes. These often correspond to locations near to deformation zones, suggesting that the U_r values can be strongly influenced by the proximity of major conducting features. The converse, namely that locations near to deformation zones necessarily have relatively high fluxes is not apparent from the figure.

The F_r plot shows that there are several locations within the repository with relatively low flow-related transport resistance, most notably within HRD_EW007. They also correspond to locations near to deformation zones. This suggests that the F_r values are potentially strongly influenced by the proximity of major conducting features. The converse, namely that locations near to deformation zones necessarily have relatively low flow-related transport resistance is not apparent from the figure.

The correlation between deformation zone location and relatively high U_r or relatively low F_r values suggests that avoiding placing deposition holes close to such features may be an important consideration during repository construction. It appears from the figures that there is only weak correlation between high U_r locations and low F_r locations. This is also shown in the scatter plot of F_r against U_r in Figure 6-19, the exception being for U_r values greater than approximately 10^{-2} m/y, which are associated with low F_r values, although the correlation is weak.

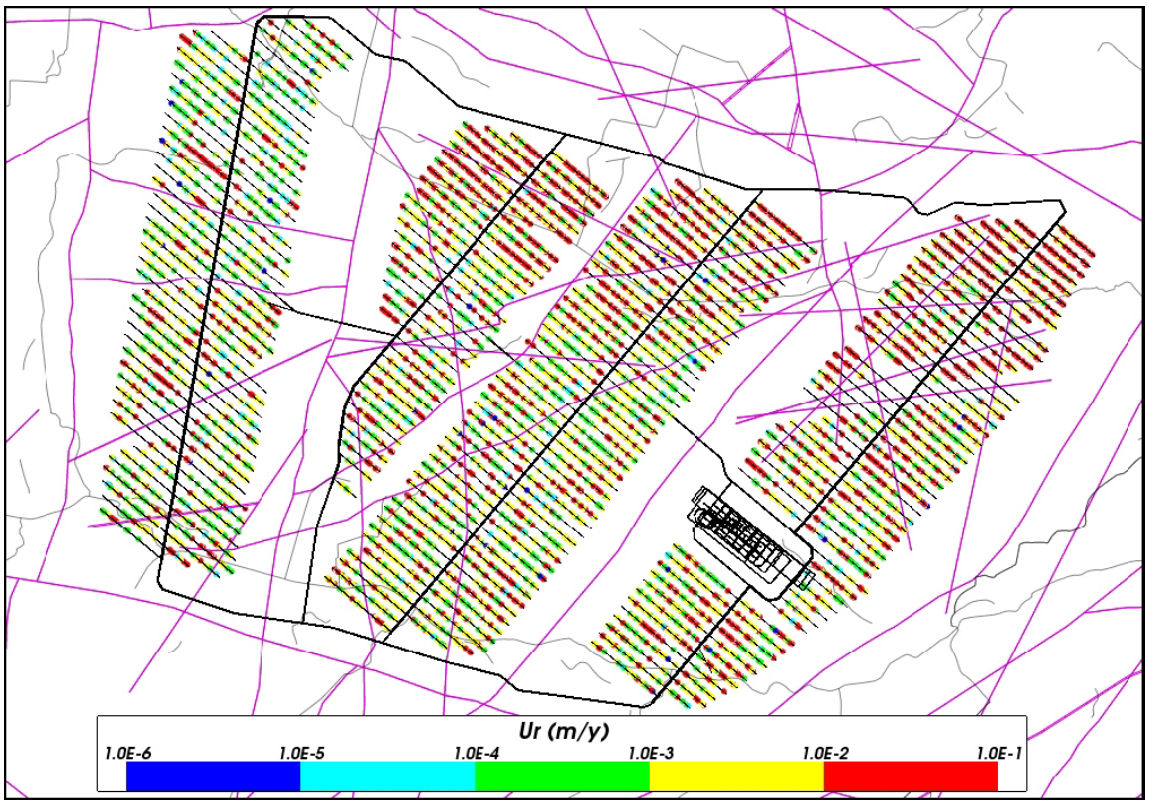

Figure 6-14. *Starting locations coloured by $\log_{10}(U_r)$ for Q1 particles released at 2000 AD and successfully reaching the top boundary of the Hydrogeological base case model (69%). The deformation zones at z = –510 m (purple), repository structures (black) and surface features (grey) are also shown.*

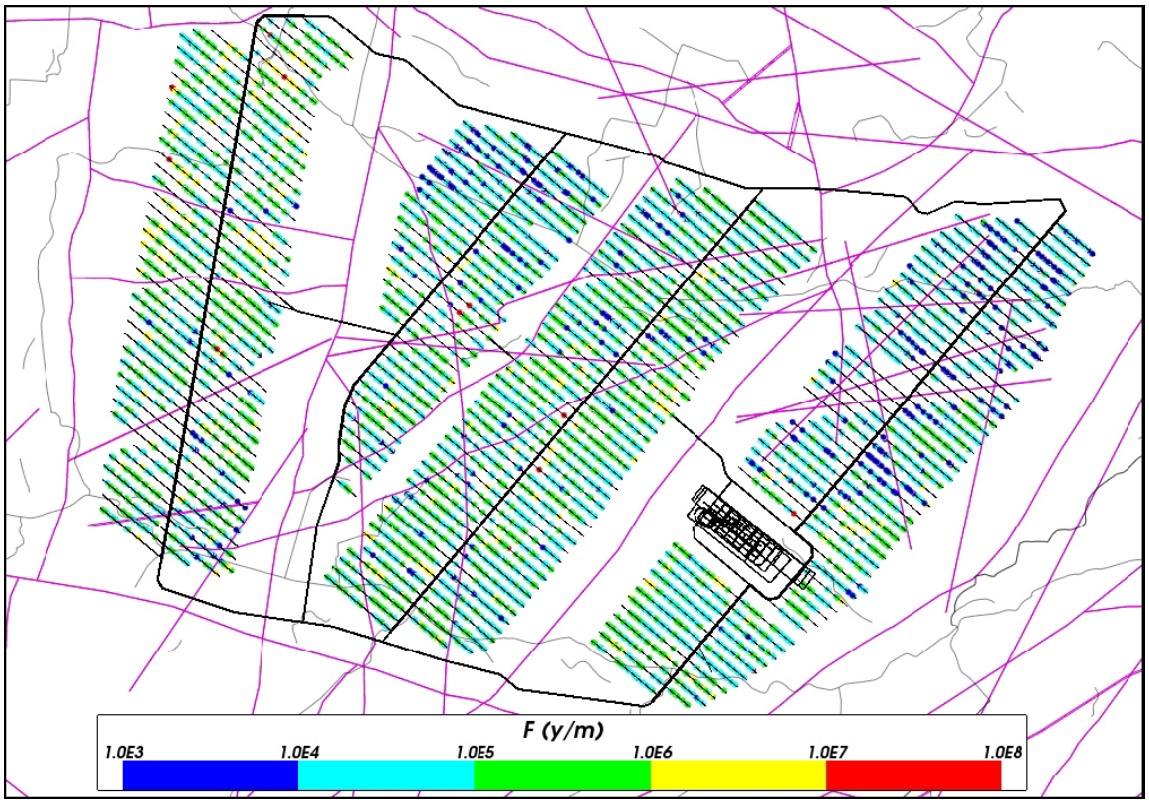

Figure 6-15. *Starting locations coloured by $\log_{10}(F_r)$ for Q1 particles released at 2000 AD and successfully reaching the top boundary of the Hydrogeological base case model (69%). The deformation zones at z = –510 m (purple), repository structures (black) and surface features (grey) are also shown.*

A plot showing discharge locations coloured by flow-related transport resistance is shown in Figure 6-16. This figure does not suggest any discharge regions are particularly associated with low flow-related transport resistance.

The CDF plots of U_r and F_r for Q1 release locations in each of HRD_C, HRD_EW007 and HRD_W are shown in Figure 6-17 and Figure 6-18. These figures suggest that Q1 release locations in HRD_EW007 are associated with higher U_r values and lower F_r values than Q1 release locations in HRD_C or HRD_W. The difference amounts to approximately a factor of 3 in the median value of U_r and F_r compared to (the average of) HRD_C and HRD_W. Of the total number of available deposition holes, approximately 60% are in HRD_C, 30% are in HRD_W and 10% are in HRD_EW007.

Figure 6-20 shows the percentage of Q1 particles entering the HCDs. ZSMEW007A is entered by 23% of particles. Most deformation zones are entered by less than 15% of particles, suggesting that their effect is quite localised.

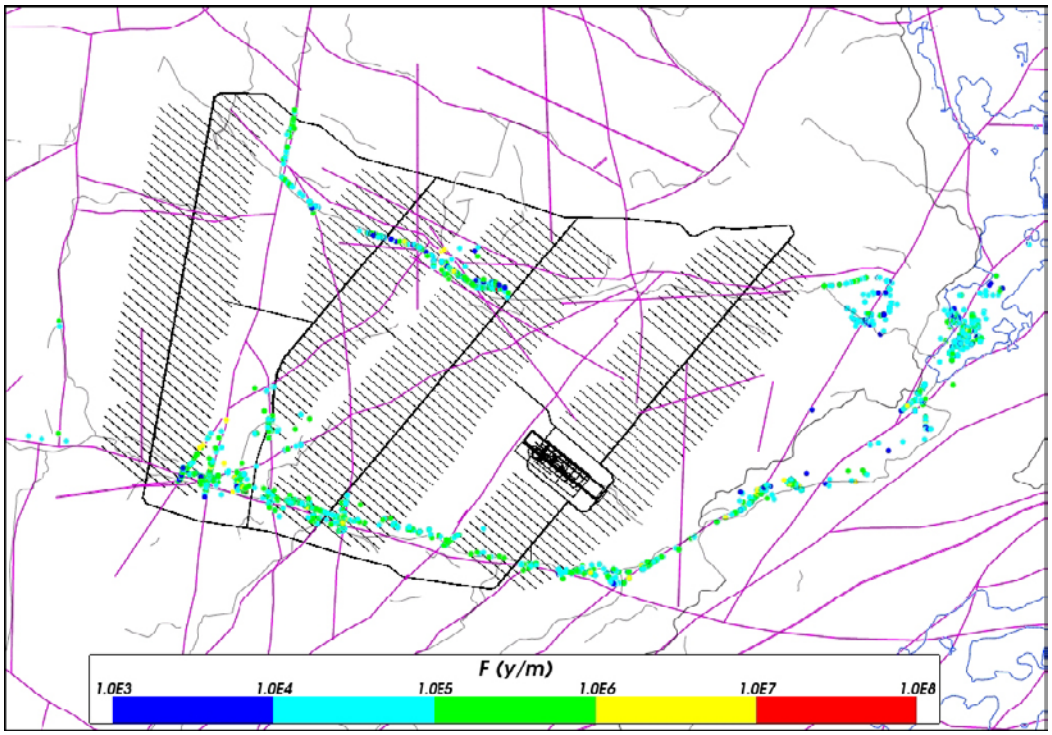

Figure 6-16. *Exit locations coloured by $\log_{10}(F_r)$ for Q1 particles released at 2000 AD and successfully reaching the top boundary of the Hydrogeological base case model (69%). The deformation zones at z = –50 m (purple), the shoreline at 2000 AD (blue) and surface features (grey) are also shown.*

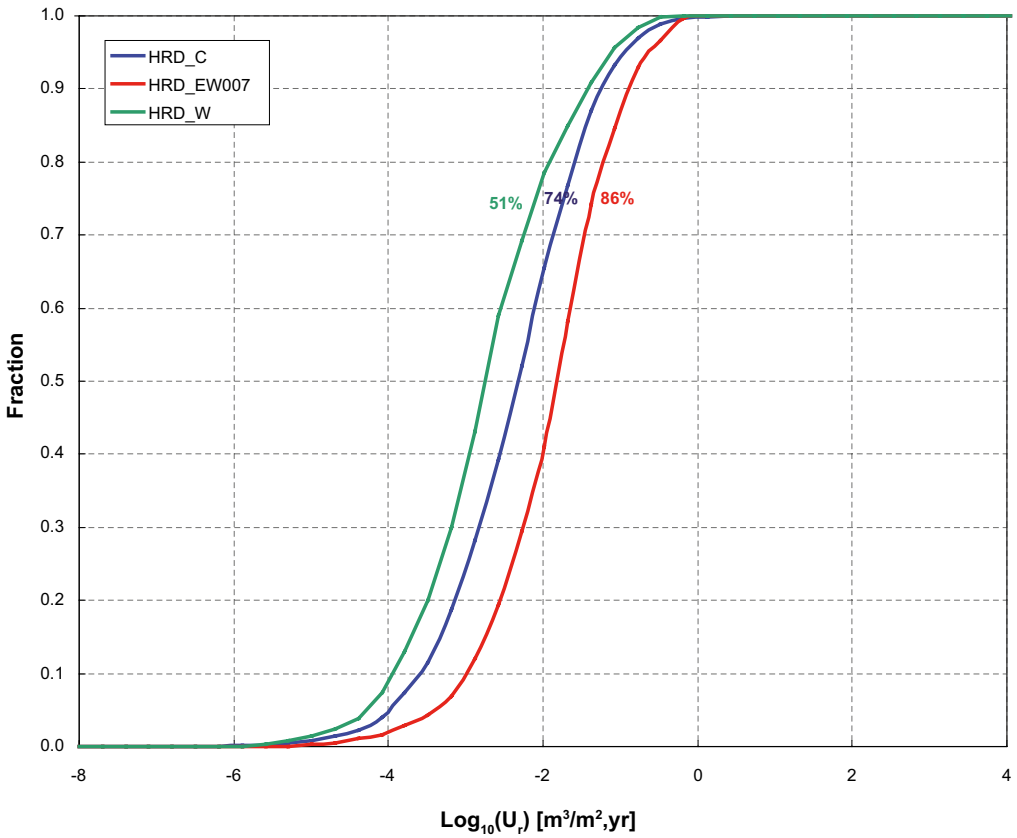

Figure 6-17. *Normalised CDF plots of U_r for Q1 release locations in each local HRD of the Hydrogeological base case model for the particles successfully reaching the model top boundary (indicated by the percentage shown next to each curve), released at 2000 AD.*

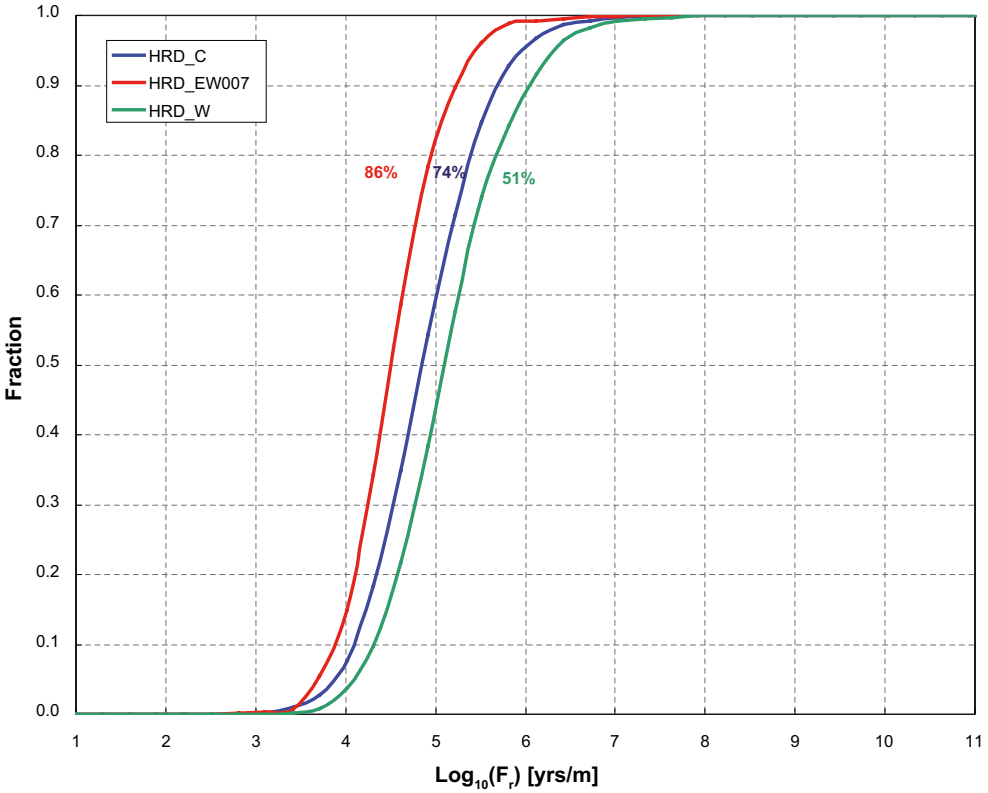

Figure 6-18. *Normalised CDF plots of F_r for Q1 release locations in each local HRD of the Hydrogeological base case model for the particles successfully reaching the model top boundary (indicated by the percentage shown next to each curve), released at 2000 AD.*

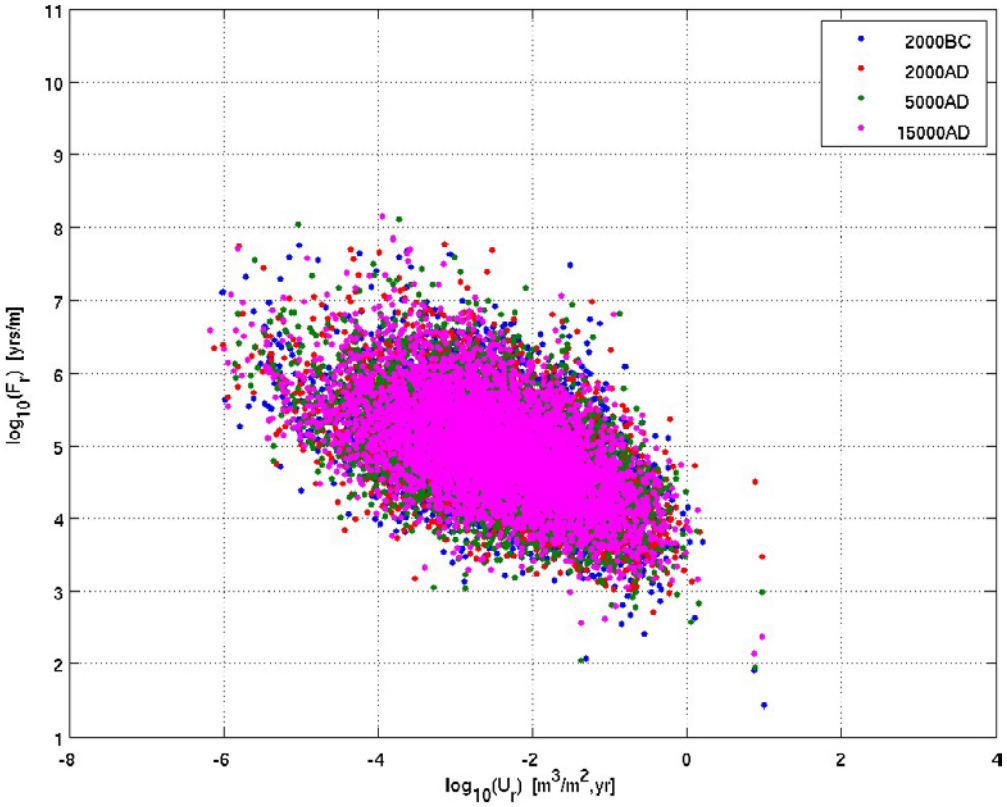

Figure 6-19. *Scatter plot of F_r against U_r for Q1 particles released at 2000 BC, 2000 AD, 5000 AD and 15,000 AD and successfully reaching the top boundary of the Hydrogeological base case model (69%).*

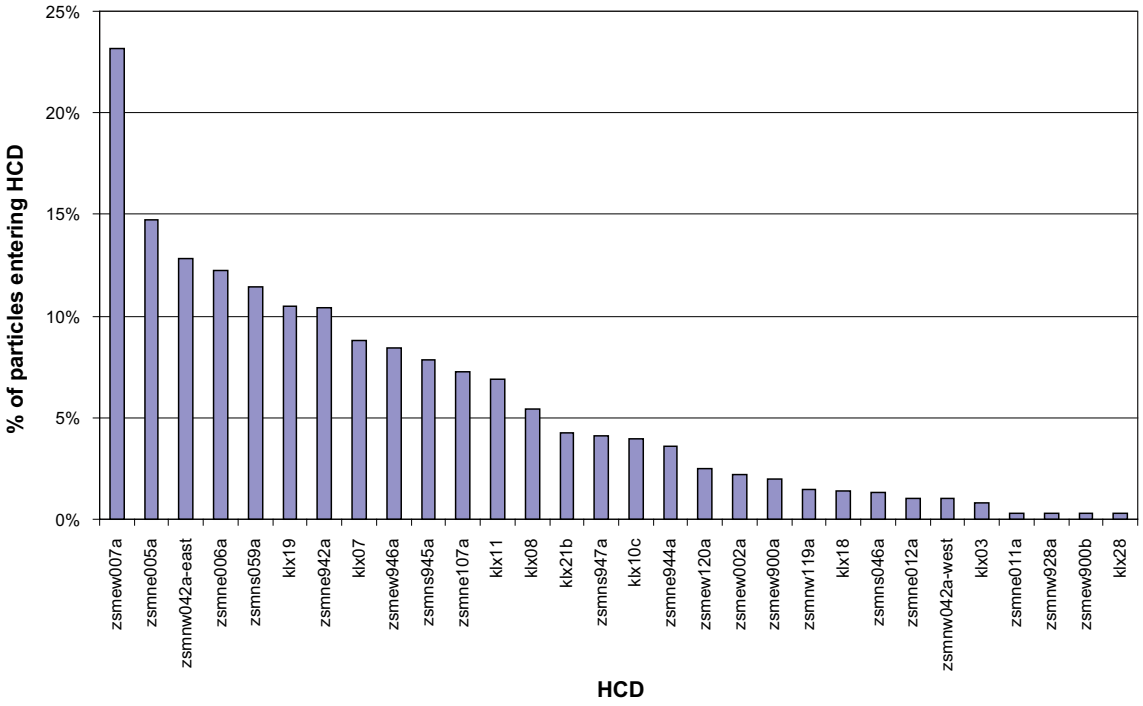

Figure 6-20. *Histogram showing the percentage of particles that enter the HCD for Q1 particles released at 2000 AD and successfully reaching the top boundary of the Hydrogeological base case model (69%). The deformation zones are ordered by descending percentage and the top 30 displayed. A particle may enter several deformation zones and so the percentages sum to over 100%.*

6.2.5 The effect of FPC and EFPC

Figure 6-21 and Figure 6-22 show the non-normalised plots of U_r and F_r respectively for the Hydrogeological base case model with the FPC and EFPC included. In these plots the intersection with the vertical axis represents the proportion of particles that do not get started (blue curve) and/or are excluded by FPC (red curve) or FPC and EFPC (green curve). These plots show that approximately an additional 9% of particles are excluded by FPC and a further 1% by EFPC.

There is little difference in the median value of U_r when FPC and EFPC are applied. The change to the tail of the distribution associated with relatively high U_r values amounts to a reduction from approximately 0.1 m/y to 0.03 m/y at the 10 percentile level.

There is little difference in the median value of F_r when FPC and EFPC are applied. Any change to the tail of the distribution associated with low flow-related transport resistance is minor.

It is reasonable that the application of FPC and EFPC criteria, as tests on the fractures intersecting individual deposition holes, should have more affect on U_r than F_r. This is because the value of U_r depends largely on the fracture network local to the deposition hole, whilst the flow-related transport resistance is a property of the entire particle path, from release to discharge.

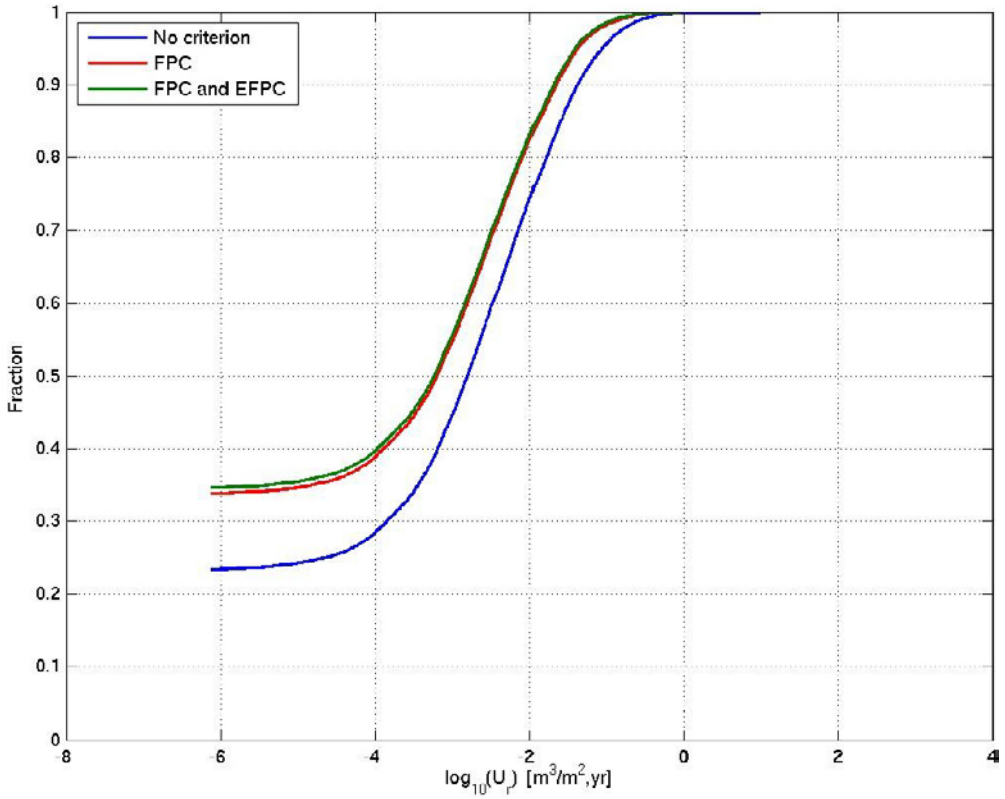

Figure 6-21. *Non-normalised CDF plots of U_r in the Hydrogeological base case model for the 8,031 Q1 particles released at 2000 AD, including FPC and EFPC.*

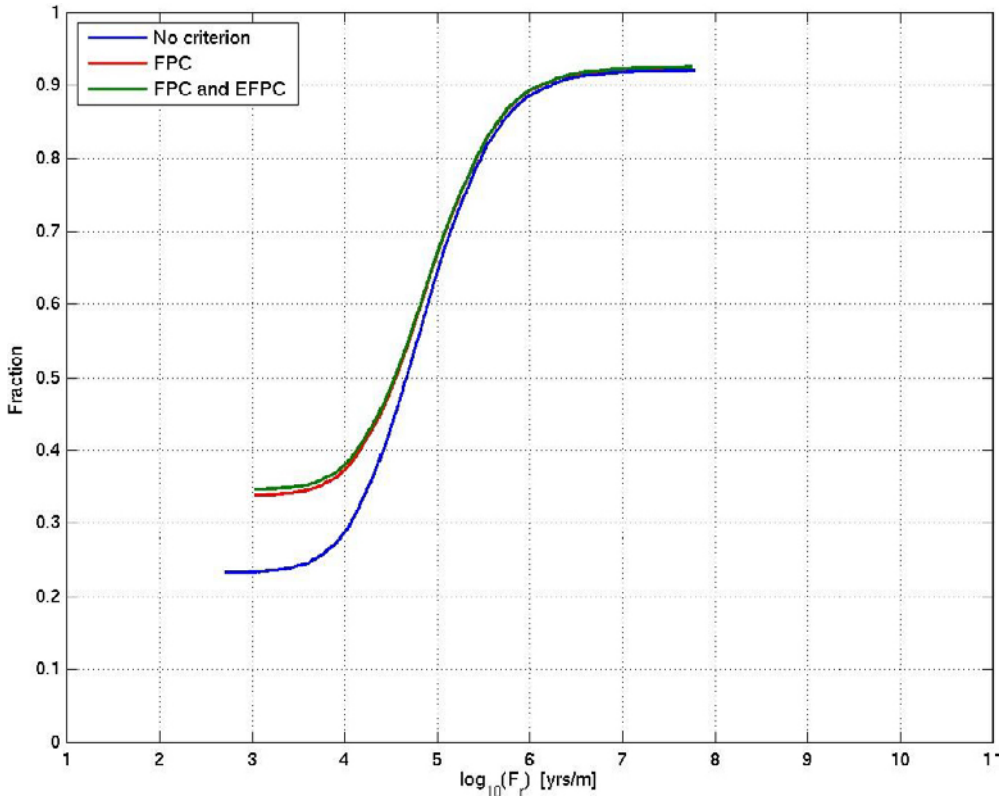

Figure 6-22. *Non-normalised plots of CDF of F_r in the Hydrogeological base case model for the 8,031 Q1 particles released at 2000 AD, including FPC and EFPC.*

6.2.6 Additional realisation

The distributions of U_r and F_r for an additional realisation of the Hydrogeological base case model are shown in Figure 6-23 and Figure 6-24 respectively. The results suggest that the distributions of both performance measures do not change significantly between the two stochastic realisations of the HRD. It also suggests that introducing heterogeneity to the HCD does not have a significant impact on performance measures. This suggests that the flow paths are not dominated by individual stochastic fractures or the localised properties of deformation zones.

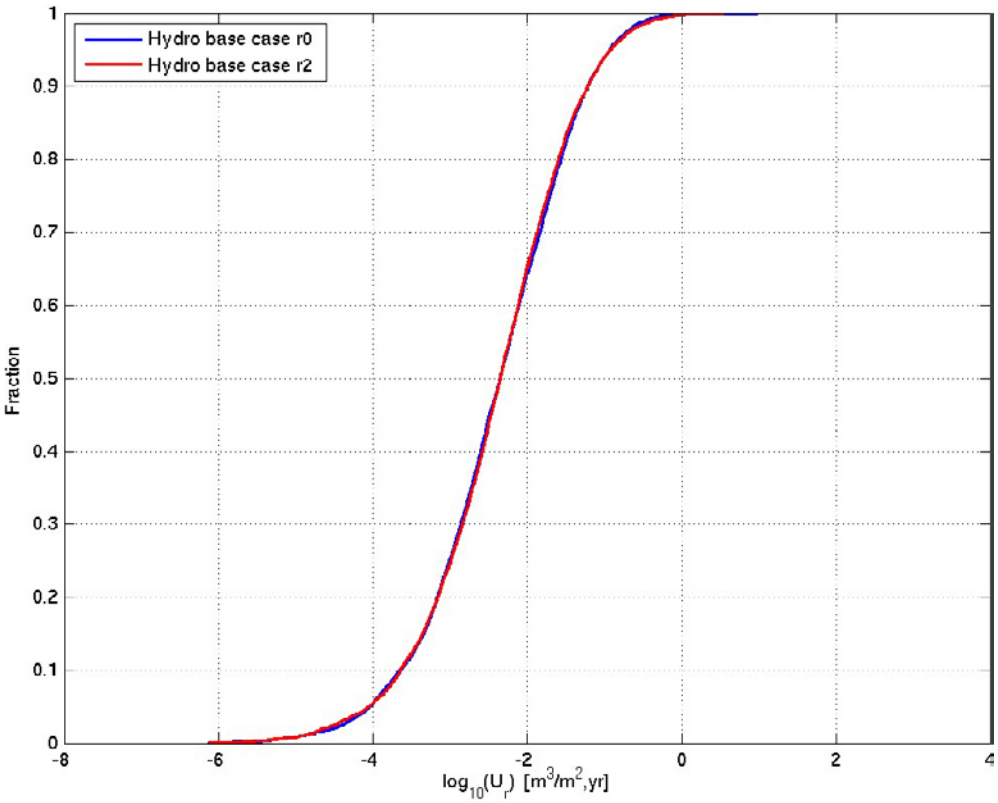

Figure 6-23. *Normalised CDF plots of U_r in the Hydrogeological base case model (r0) and one additional stochastic realisation of the HCD and HRD (r2) for the Q1 particles successfully reaching the model top boundary (~69%).*

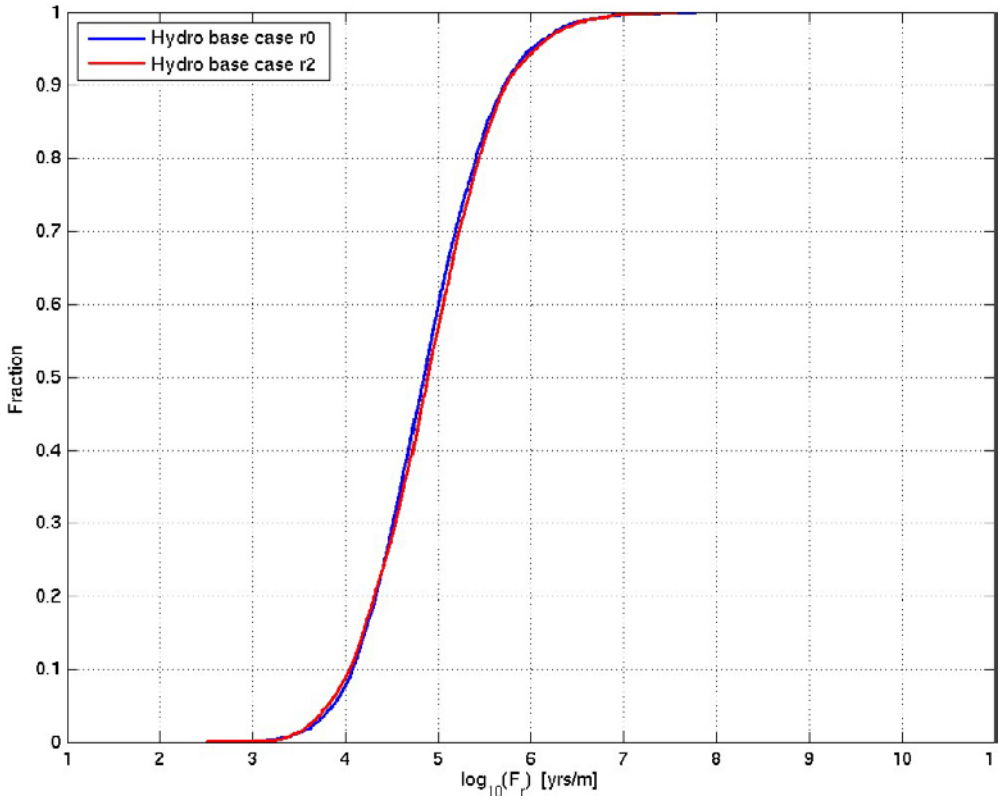

Figure 6-24. *Normalised CDF plots of F_r in the Hydrogeological base case model (r0) and one additional stochastic realisation of the HCD and HRD (r2) for the Q1 particles successfully reaching the model top boundary (~69%).*

6.3 Elaborated Hydro-DFN model results

The results of the calibration and confirmatory testing process for the Elaborated Hydro-DFN model are given in Appendix E. These show that the model very successfully matches the inflow statistics of PFL-f and PSS data. Also the model gives a good match to head and hydrochemistry measurements, thus giving confidence in the model.

Maps of discharge locations for Q2 releases are shown in Figure 6-25 for both realisations of the model, for a release at 2000 AD. These figures show that the discharge locations are similar between realisations, and similar to the results calculated by the Hydrogeological base case. The discharge locations are strongly influenced by the locations of outcropping deformation zones, which are the same for the two cases.

Performance measures for two realisations of the Elaborated Hydro-DFN are shown in Figure 6-26 to Figure 6-28. These figures also show results for both realisations of the Hydrogeological base case for comparison.

The figures suggest that there is no significant difference between the two realisations of the Elaborated Hydro-DFN in terms of the distributions of U_r, F_r, or t_r. There are, however, significant differences between the distributions of the performance measures calculated by the Elaborated Hydro-DFN compared to the Hydrogeological base case.

The proportion of particles successfully entering a fracture from a Q1 release location is ~70% for the Elaborated Hydro-DFN compared to ~76% for the Hydrogeological base case model. The reduction is thought to be due to the shift towards smaller fractures specified in the fracture size distribution for the Elaborated Hydro-DFN compared to the SDM-Site Hydro-DFN used in the Hydrogeological base case. This implies less fracture connectivity, leading to more deposition holes that are not connected to the flow conducting network.

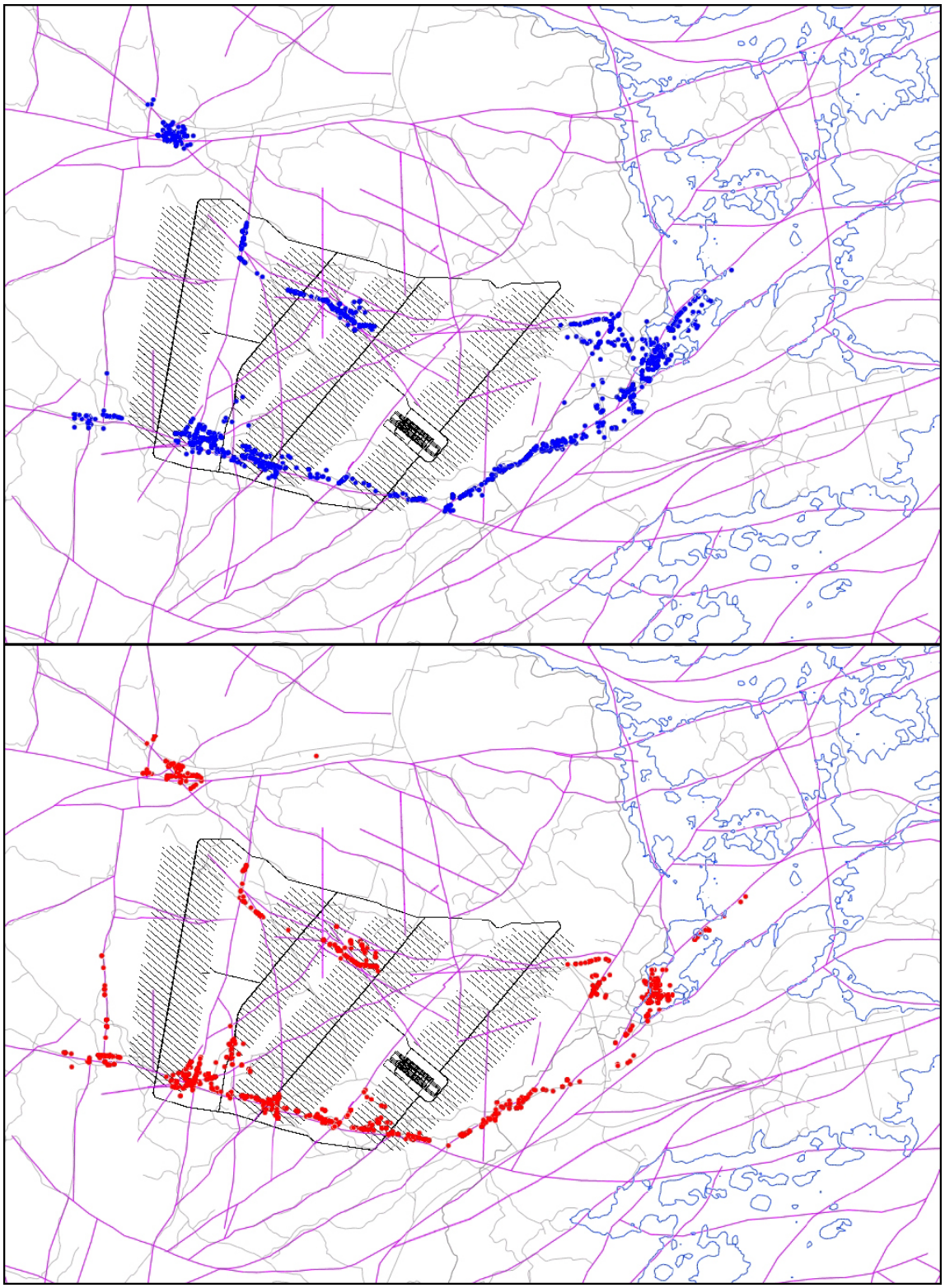

Figure 6-25. *Exit locations for the Q2 particles successfully reaching the top boundary of the Elaborated Hydro-DFN model (85%–87%), released at 2000 AD. Top: realisation r0 (dark blue). Bottom: realisation r2 (red). Also shown are the deformation zones at z = –50 m (purple), surface features (grey) and the shoreline at 2000 AD (blue).*

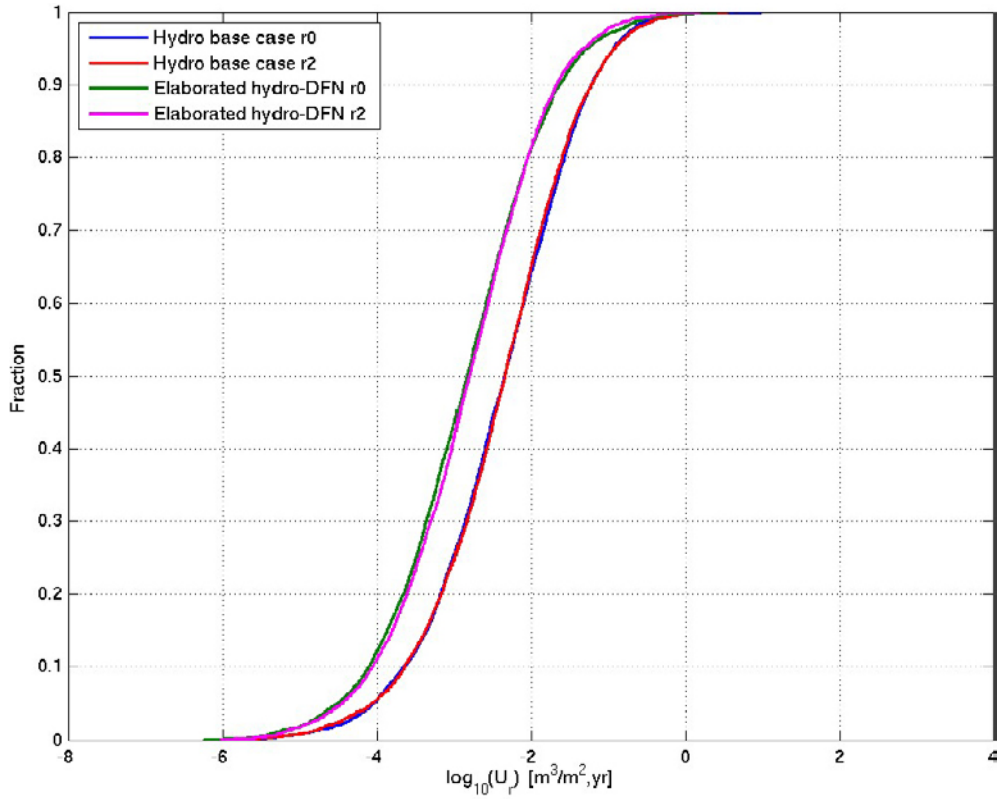

Figure 6-26. *Normalised CDF plots of U_r in the Hydrogeological base case model and the Elaborated Hydro-DFN model, including one additional realisation of each, for the Q1 particles successfully reaching the model top boundary (60%–69%) released at 2000 AD.*

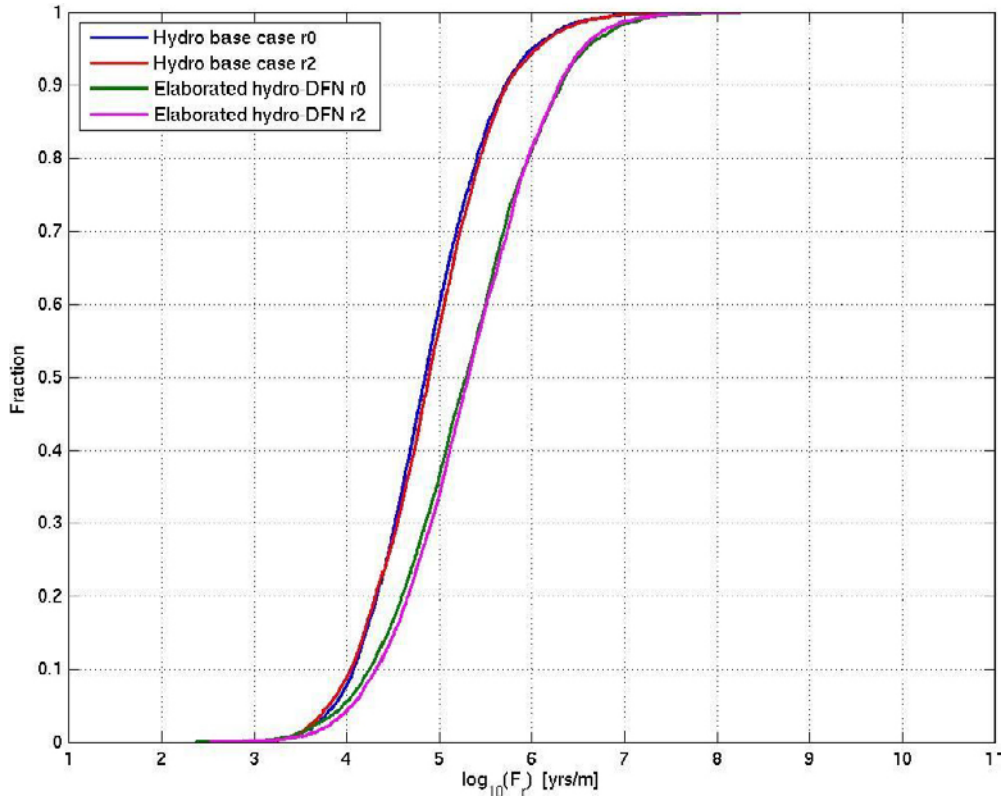

Figure 6-27. *Normalised CDF plots of F_r in the Hydrogeological base case model and the Elaborated Hydro-DFN model, including one additional realisation of each, for the Q1 particles successfully reaching the model top boundary (60%–69%) released at 2000 AD.*

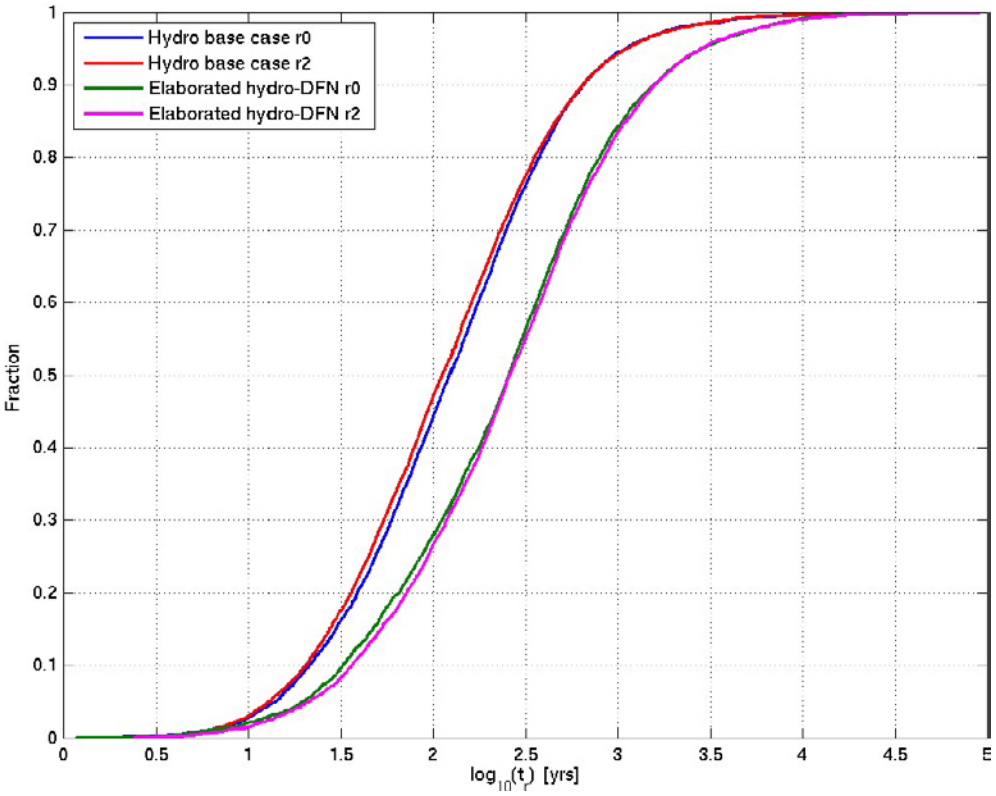

Figure 6-28. *Normalised CDF plots of t_r in the Hydrogeological base case model and the Elaborated Hydro-DFN model, including one additional realisation of each, for the Q1 particles successfully reaching the model top boundary (60%–69%) released at 2000 AD.*

The median values of U_r calculated by the Elaborated Hydro-DFN models are around a factor of three lower than those calculated by the Hydrogeological base case, with a value of approximately 0.001 m/y. The 90 percentile value is also approximately a factor of three lower, with a value of approximately 0.03 m/y.

The median values of F_r calculated by the Elaborated Hydro-DFN models are around a factor of two higher than those calculated by the Hydrogeological base case, with a value of approximately 200,000 y/m. The 10 percentile value is also approximately a factor of two higher, with a value of approximately 20,000 y/m.

The median values of t_r calculated by the Elaborated Hydro-DFN models are around a factor of 2.5 higher than those calculated by the Hydrogeological base case, with a value of approximately 250 years.

The changes to U_r, F_r and t_r can be understood in terms of the reductions to the effective (ECPM) conductivity associated with the Elaborated Hydro-DFN compared to the SDM-Site Hydro-DFN used in the Hydrogeological base case, as discussed in subsection 5.1.3.

The cumulative distribution functions of U_r and F_r for Q1 release locations in each of HRD_C, HRD_EW007 and HRD_W are shown in Figure 6-29 and Figure 6-30. These figures suggest that Q1 release locations in HRD_EW007 are associated with higher U_r values and lower F_r values than Q1 release locations in HRD_C or HRD_W. Of the total number of available deposition holes, approximately 60% are in HRD_C, 30% are in HRD_W and 10% are in HRD_EW007. Note that compared to the corresponding plots in Figure 6-17 and Figure 6-18 for the Hydrogeological base case, HRD_C has now the lowest U_r values and the highest F_r values. However, HRD_W has a lower proportion of particles that start due to the sparsity of the fracture network in that domain, but a greater variability in transmissivities. So although HRD_W can have some high transmissivities due to high variability, this is offset by a reduction in connectivity to the deposition holes due to the fracture network sparsity. This leads to HRD_W not having the lowest U_r values or the highest F_r values in the Elaborated Hydro-DFN model.

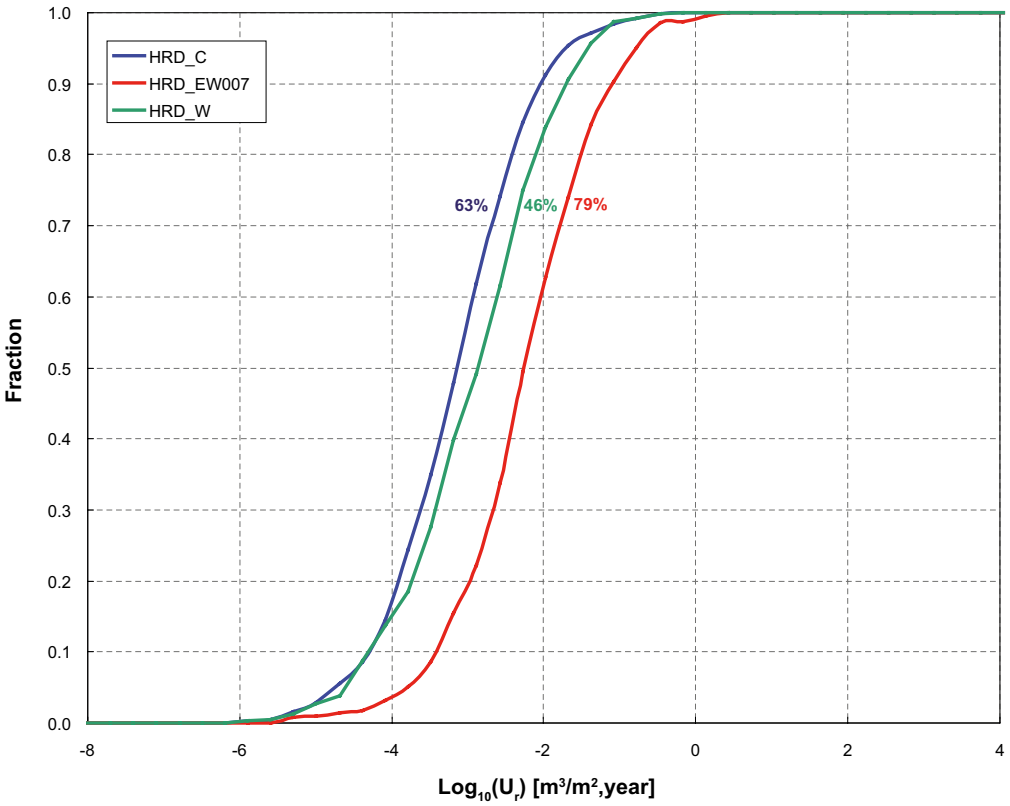

Figure 6-29. *Normalised CDF plots of U_r for Q1 release locations in each local HRD of the Elaborated Hydro-DFN model, for the particles successfully reaching the model top boundary (indicated by the percentage shown next to each curve), released at 2000 AD.*

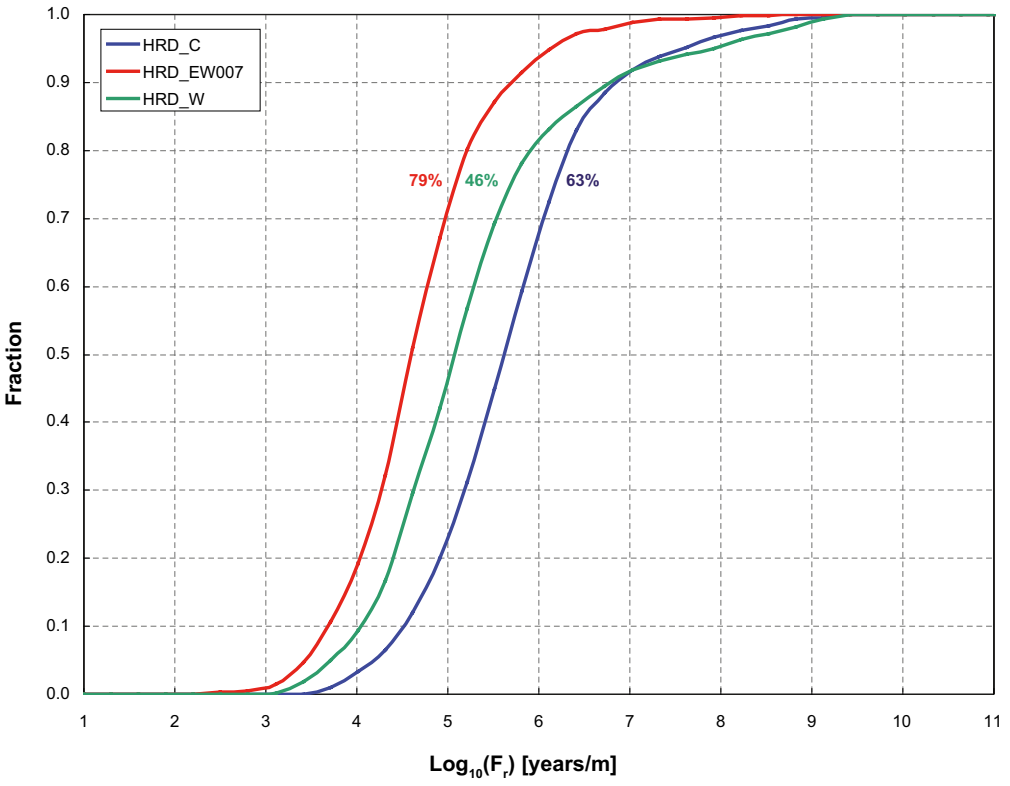

Figure 6-30. *Normalised CDF plots of F_r for Q1 release locations in each local HRD of the Elaborated Hydro-DFN model, for the Q1 particles successfully reaching the model top boundary (indicated by the percentage shown next to each curve), released at 2000 AD.*

6.4 The Elaborated Hydro-DFN model with no Minor Deformation Zones results

Particle discharge locations for the Elaborated Hydro-DFN model with no minor deformation zones for Q2 particles released at 2000 AD are shown in Figure 6-31. Normalised CDF plots of performance measures for Q1 particles are shown in Figure 6-32 to Figure 6-33. The CDF plots also show results for both realisations of the Elaborated Hydro-DFN for comparison. The figures suggest that the minor deformation zones have little effect on the particle discharge locations or the performance measures at 2000 AD.

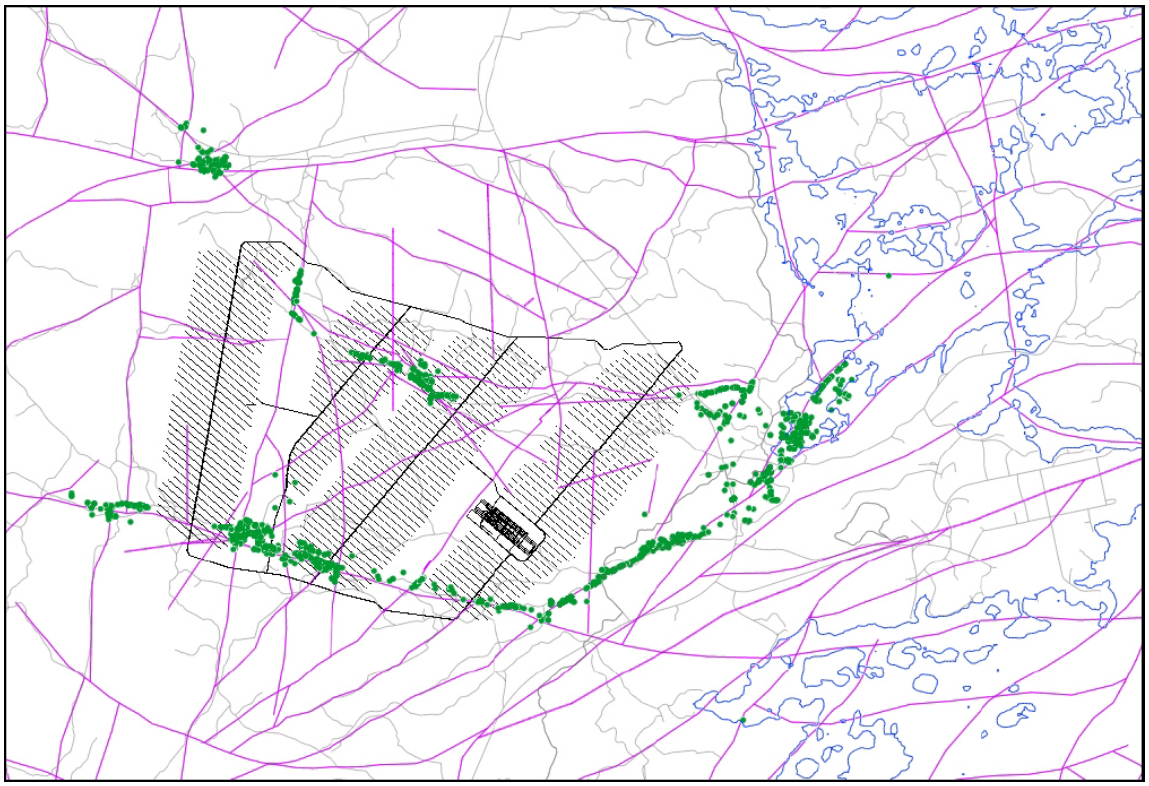

Figure 6-31. *Exit locations for the Q2 particles successfully reaching the top boundary of the Elaborated Hydro-DFN model with No MDZs (85%), released at 2000 AD. Also shown are the deformation zones at z = –50 m (purple), surface features (grey) and the shoreline at 2000 AD (blue).*

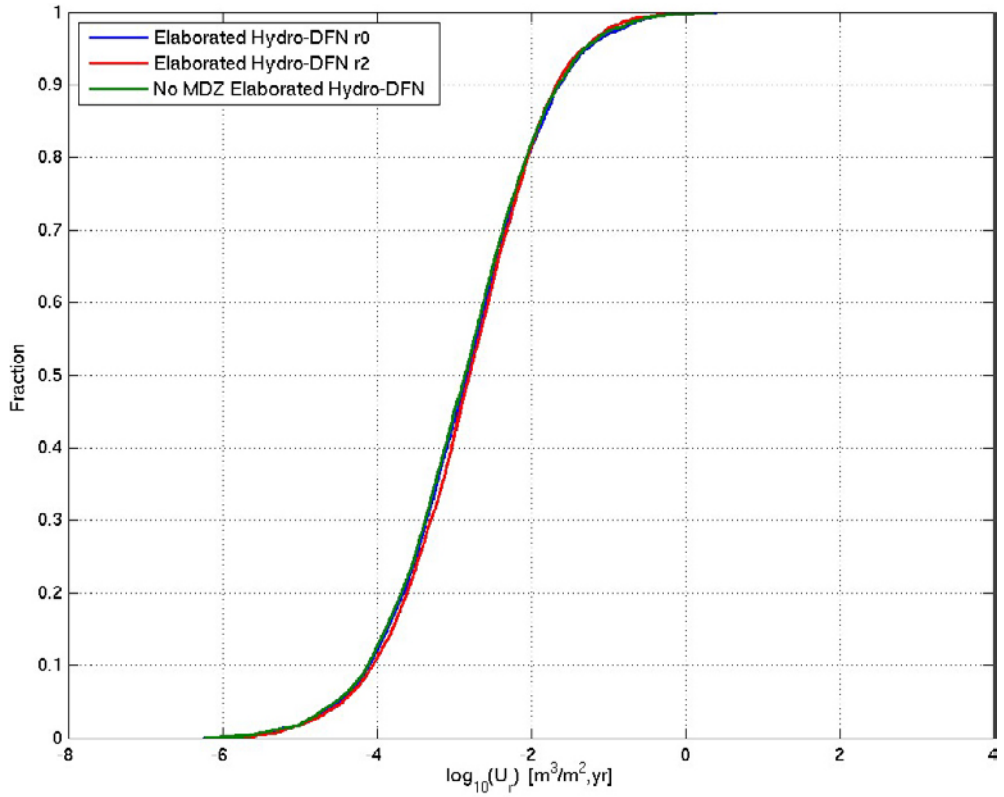

Figure 6-32. *Normalised CDF plots of U_r in the Elaborated Hydro-DFN model, including one additional realisation and the case with no MDZs, for the Q1 particles successfully reaching the model top boundary (59%–61%), released at 2000 AD.*

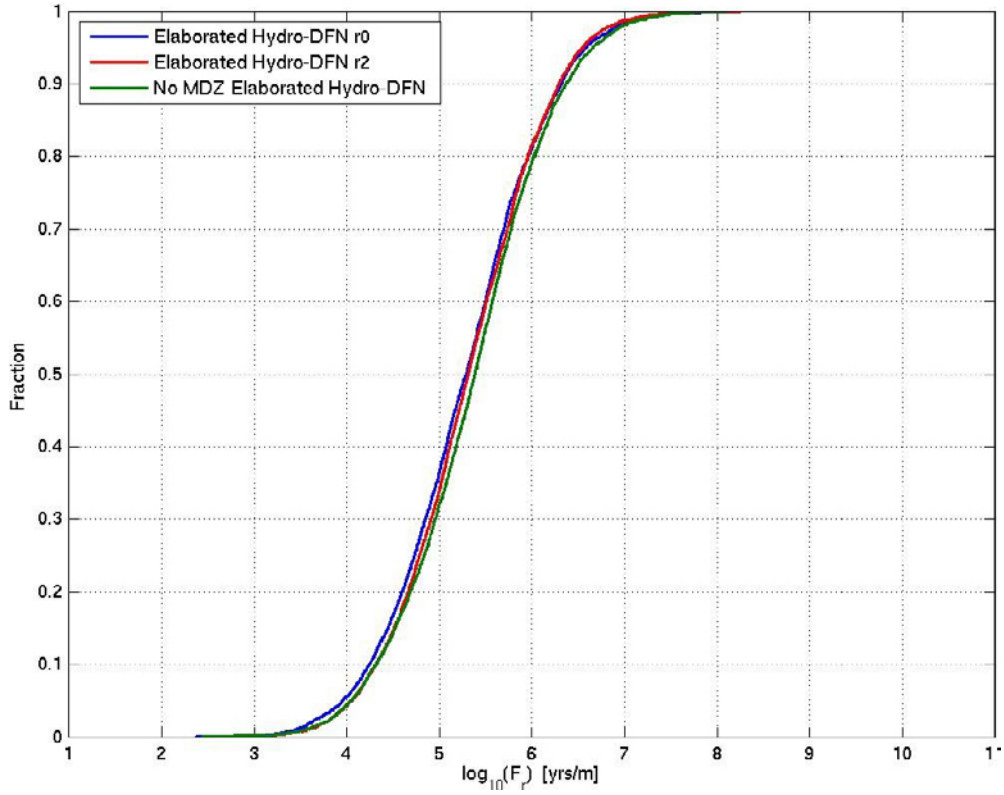

Figure 6-33. *Normalised CDF plots of F_r in the Elaborated Hydro-DFN model, including one additional realisation and the case with no MDZs, for the Q1 particles successfully reaching the model top boundary (59%–61%), released at 2000 AD.*

6.5 Stochastic continuum model results

Plots of the discharge locations of particles released from the Q2 locations in the repository are shown, for various release times, model scales and realisations of the HRD and HCD, in Figure 6-34 to Figure 6-36. The particles tend to either discharge through deformation zones situated locally around the repository or along the shoreline. There is a large variation in the discharge locations with time for those particles that exit on the shoreline. The particles that discharge through outcropping deformation zones northeast of the repository at 2000 AD are also significantly influenced by the receding shoreline and at 15,000 AD many of these particles discharge along the shoreline instead. These results differ from the Elaborated Hydro-DFN model where the discharge locations are more localised around the repository and vary little with release time.

The effect of different scales of spatial variability and realisations of the HRD and HCD is not very pronounced. The 20 m scale gives a slightly larger spread of particles away from the repository. In general, however, the discharge locations are still strongly influenced by the locations of outcropping deformation zones, as for the other cases.

The differences in discharge locations between the Stochastic continuum model and the Elaborated Hydro-DFN model, can be understood in terms of the different model concepts. The discrete fracture network of the Elaborated Hydro-DFN with a limited connectivity horizontally gives more localised discharge and shorter paths, while the Stochastic continuum model allows flow over a larger area because there is always horizontal connectivity between the elements even if the hydraulic conductivity varies.

In Figure 6-37 and Figure 6-38, performance measures of particles released from the Q1 locations in the repository at release times 2000 AD and 15,000 AD on two scales, 20 m and 100 m, of the Stochastic continuum model using the homogeneous HCD and realisation 1 of the HRD (denoted r0), are shown. The figures also show results for realisation r0 of the Elaborated Hydro-DFN model at release time 2000 AD for comparison. Non-normalised CDF plots were chosen to allow a more meaningful comparison between the two cases given the differences in the proportions of particles starting.

For the Stochastic continuum model nearly all particles released from the Q1 location start. The cut-off criteria is set to an initial Darcy flux of $1 \cdot 10^{-6}$ m/y, below which the particles are removed from the statistics. The corresponding proportion of particles successfully entering a fracture with a significant flow from a Q1 release location for the Elaborated Hydro-DFN model is ~70%. This reduction reflects the differences between a CPM model approach, where practically all particles start, and a DFN model approach, where many particles can fail to enter a fracture due to a sparse flow conducting network with low connectivity to the repository.

Performance measures of particles released at 2000 AD from the Q1 locations in the repository for two realisations of the HCD and HRD and two scales, 20 m and 100 m, of the Stochastic continuum model are shown in non-normalised CDF plots in Figure 6-39 and Figure 6-40, together with two realisations of the Elaborated Hydro-DFN model for comparison.

It should be noted that in these CDF plots for the Elaborated Hydro-DFN model, the contribution to F_r from the ECPM part of the model has been added. This was done in order to make the comparison with the Stochastic continuum model more equivalent since the Stochastic continuum model accounts for the full path of the particles, apart from within the HSD, when calculating the performance measures.

The figures show that there is no significant difference in performance measures for the Stochastic continuum model between the different release times at 2000 AD and 15,000 AD or between the two realisations considered. Further, there are only small differences between the two Stochastic continuum spatial variability scales, 20 m and 100 m. A greater difference in performance measures between the two scales might be expected given that the mean hydraulic conductivity values at repository depth are up to about 1.5 orders of magnitude lower for the 20 m scale than for the 100 m scale. However, the differences are much less for HRD_C and HRD_EW007 and the standard deviations are higher for HRD_W, giving less difference in the two models over all.

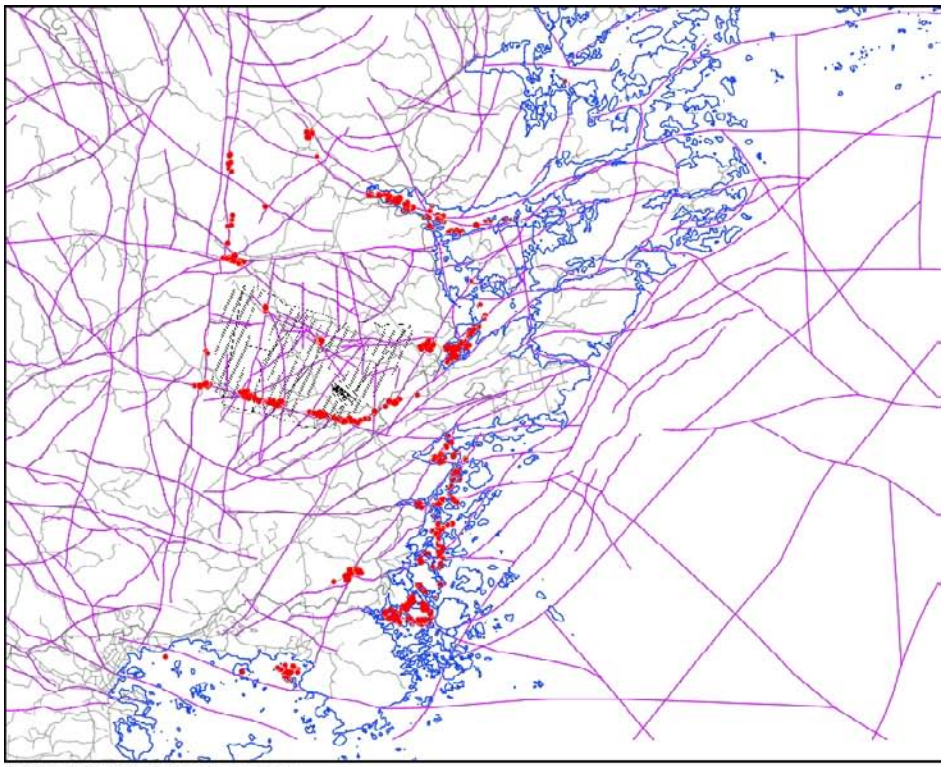

2000 AD (r0, 100 m scale)

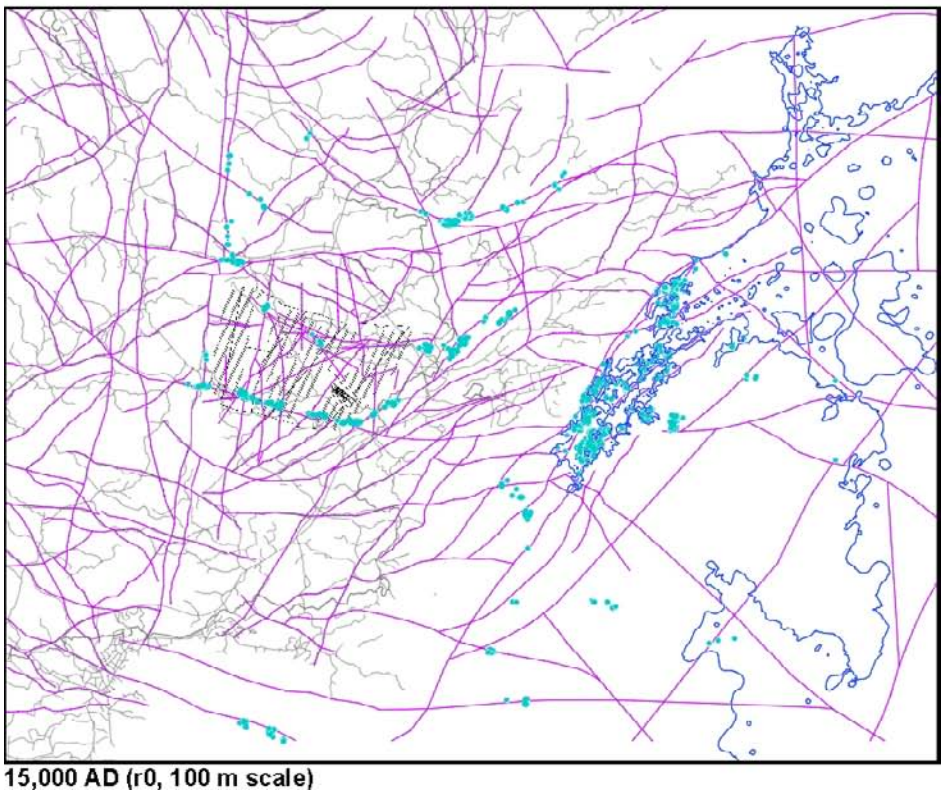

15,000 AD (r0, 100 m scale)

Figure 6-34. *Exit locations for the Q2 particles successfully reaching the top boundary of the Stochastic continuum 100 m site-scale models for the homogeneous HCD and realisation 1 of the HRD, with the shoreline at each time shown in blue. Individual plots presented are for releases at 2000 AD (red) and 15,000 AD (light blue). The deformation zones at z = –50 m (purple), surface features (grey) and the repository structures (black) are also shown.*

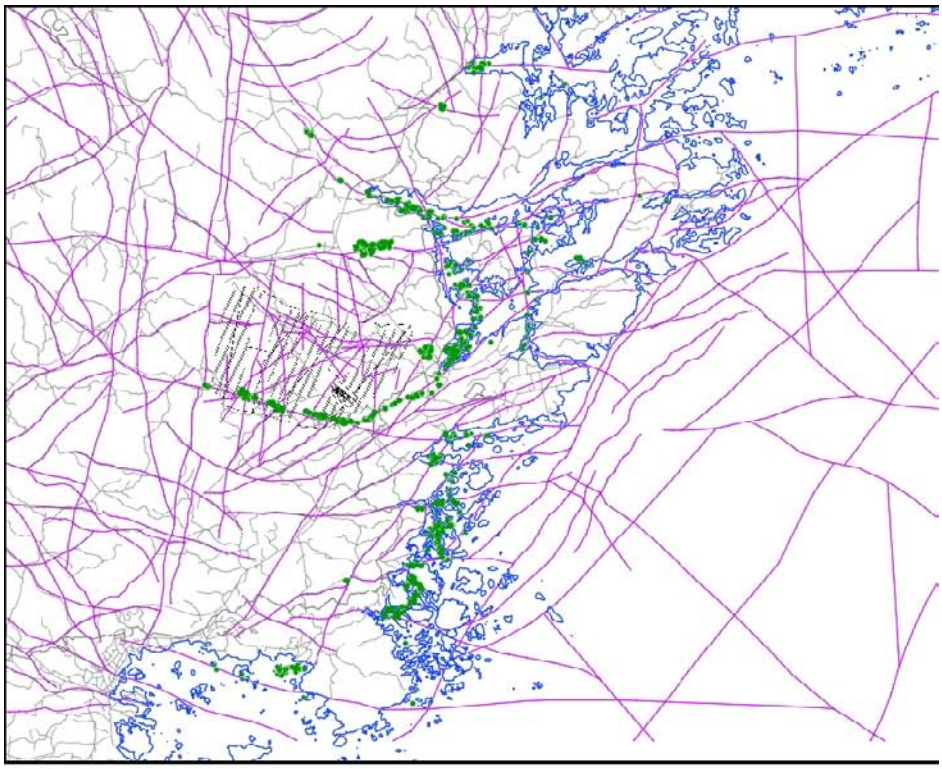

2000 AD (r0, 20 m scale)

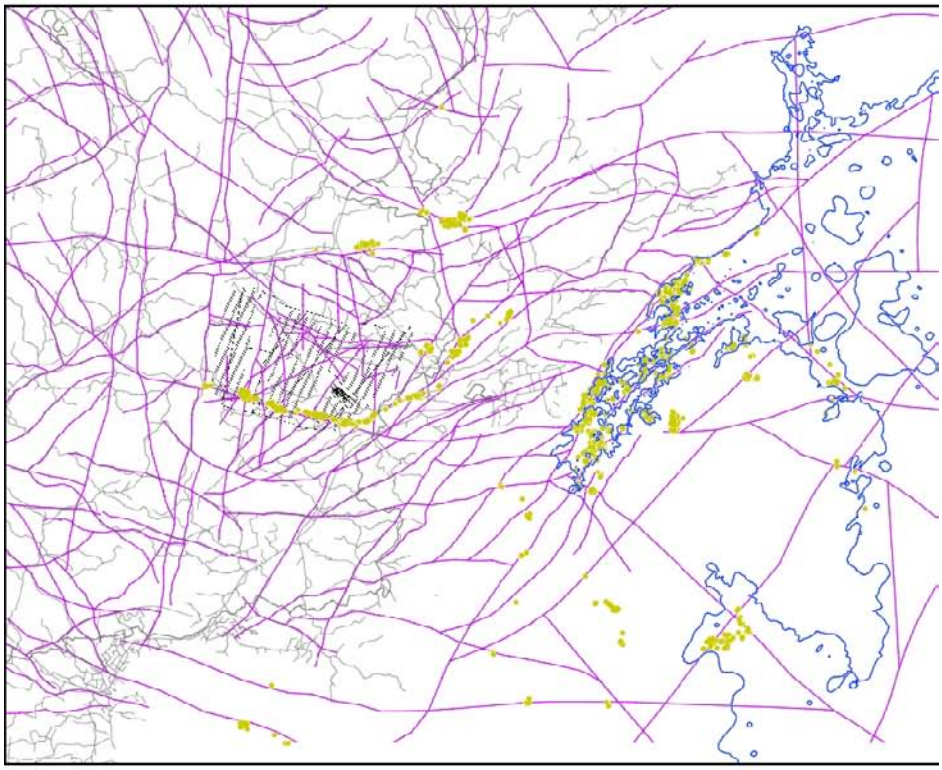

15,000 AD (r0, 20 m scale)

Figure 6-35. *Exit locations for the Q2 particles successfully reaching the top boundary of the Stochastic continuum 20 m site-scale models for the homogeneous HCD and realisation 1 of the HRD, with the shoreline at each time shown in blue. Individual plots presented are for releases at 2000 AD (green) and 15,000 AD (brown). The deformation zones at z = –50 m (purple), surface features (grey) and the repository structures (black) are also shown.*

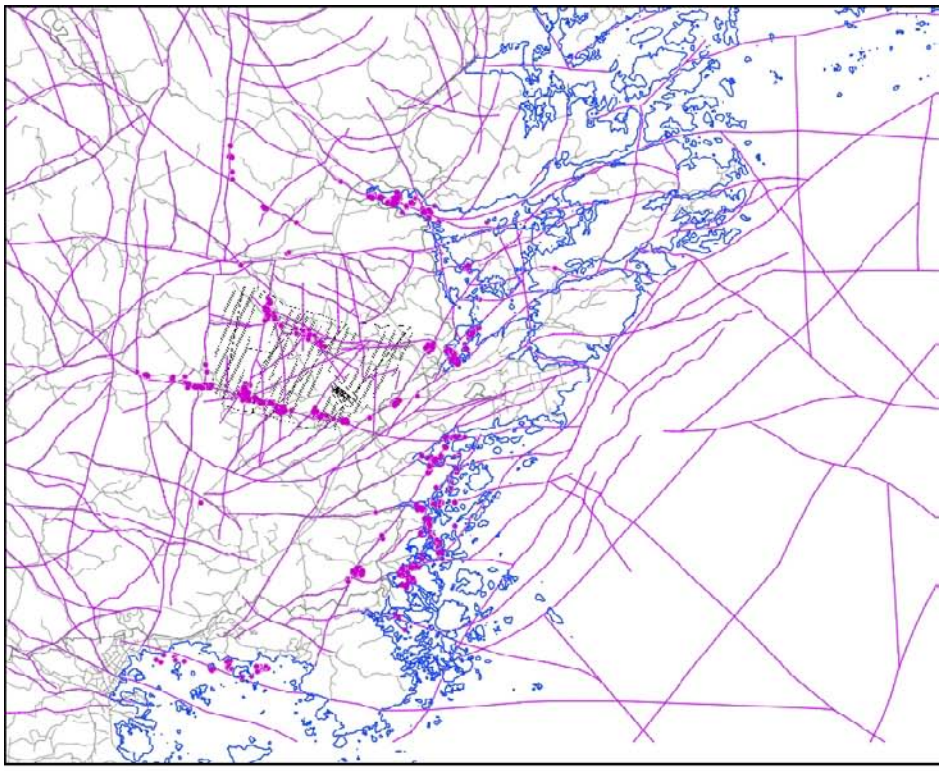

2000 AD (r2, 100 m scale)

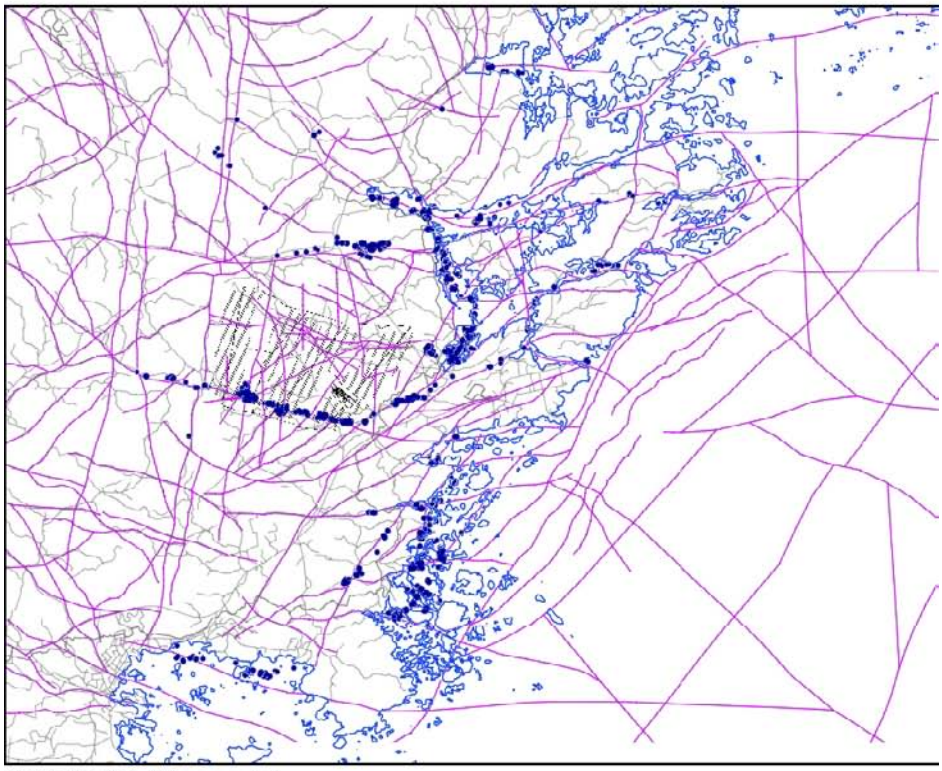

2000 AD (r2, 20 m scale)

Figure 6-36. *Exit locations for the Q2 particles successfully reaching the top boundary of the nested Stochastic continuum site-scale models for realisation 2 of the HCD and HRD, with the shoreline at each time shown in blue. Individual plots presented are for releases at 2000 AD, 100 m scale (top) and 20 m scale (bottom). The deformation zones at z = –50 m (purple), surface features (grey) and the repository structures (black) are also shown.*

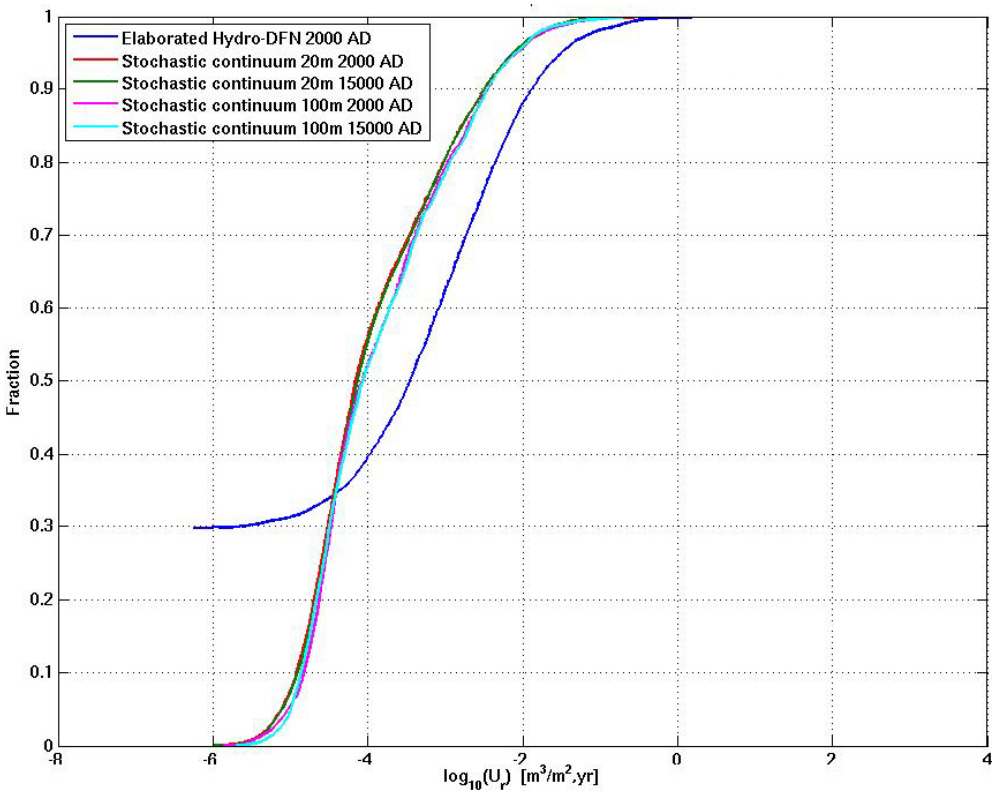

Figure 6-37. *Non-normalised CDF plots of U_r in a comparison of the Elaborated Hydro-DFN model and the Stochastic continuum models on 20 m and 100 m scales using the homogeneous HCD and realisation 1 of the HRD for the 8,031 Q1 particles released at the given times.*

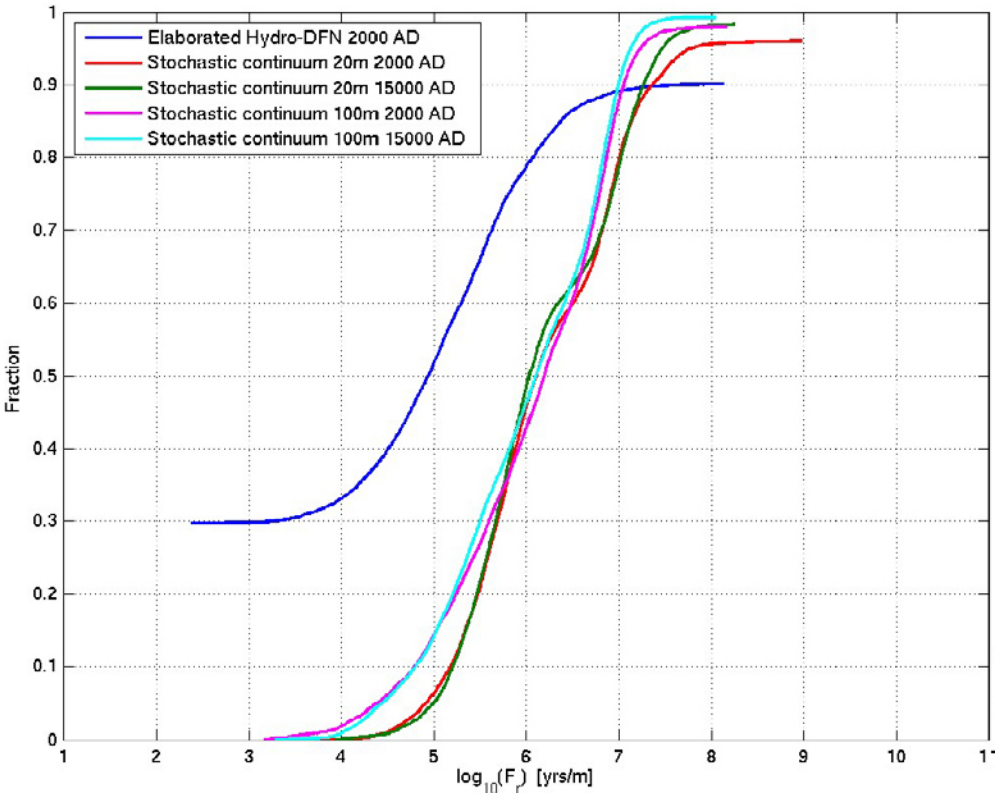

Figure 6-38. *Non-normalised CDF plots of F_r in a comparison of the Elaborated Hydro-DFN model and the Stochastic continuum models on 20 m and 100 m scales using the homogeneous HCD and realisation 1 of the HRD for the 8,031 Q1 particles released at the given times.*

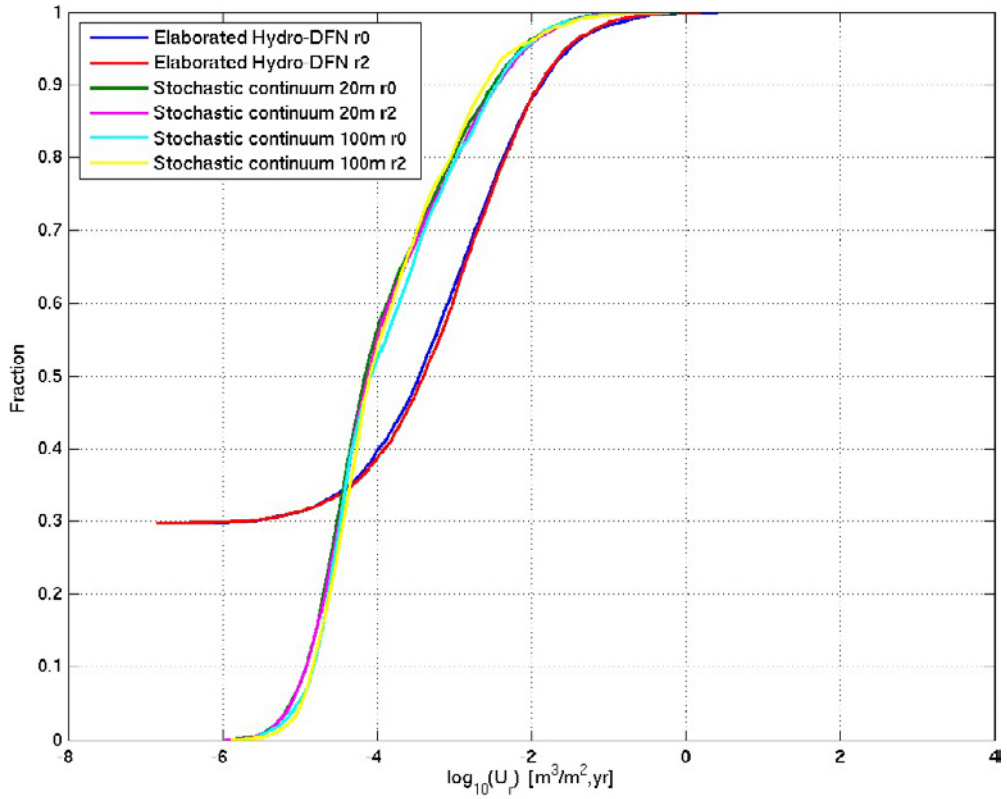

Figure 6-39. *Non-normalised CDF plots of U_r in a comparison of two realisations of the Elaborated Hydro-DFN model and the Stochastic continuum models on 20 m and 100 m scales for the 8,031 Q1 particles released at 2000 AD.*

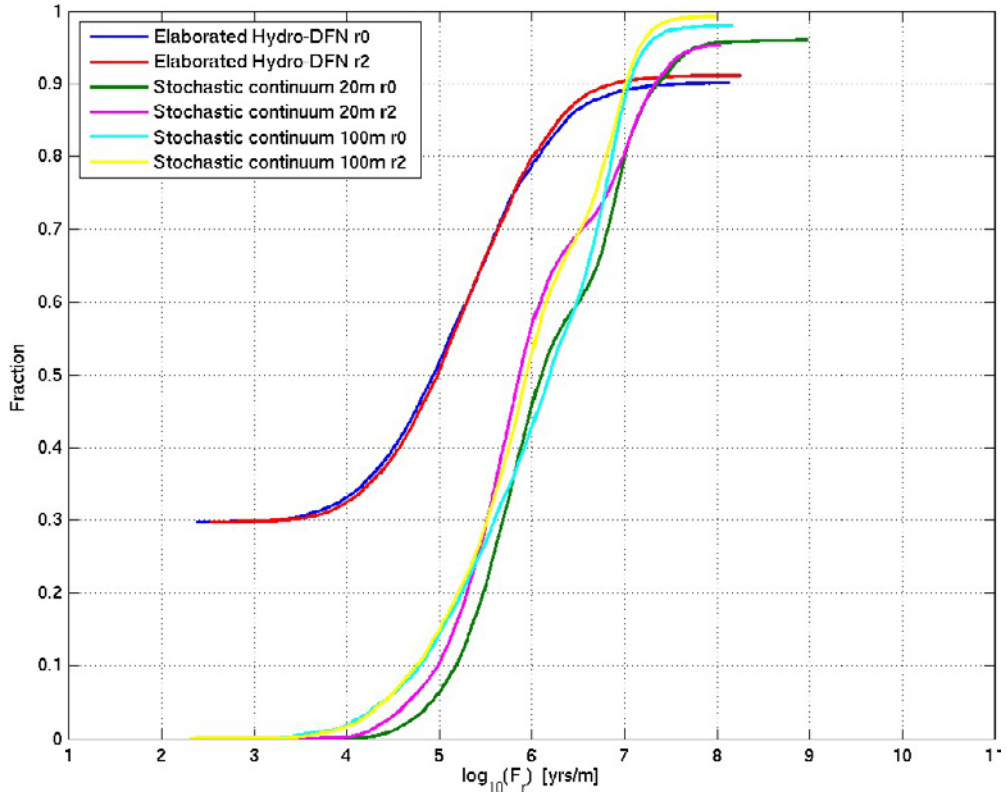

Figure 6-40. *Non-normalised CDF plots of F_r in a comparison of two realisations of the Elaborated Hydro-DFN model and the Stochastic continuum models on 20 m and 100 m scales for the 8,031 Q1 particles, released at 2000 AD.*

There are significant differences between the distributions of the performance measures calculated for the Stochastic continuum model compared to the Elaborated Hydro-DFN model. The median values of U_r calculated by the Stochastic continuum models are around a factor of ten lower than those calculated by the Elaborated Hydro-DFN model, with a value of approximately $1 \cdot 10^{-4}$ m/y. The 90 percentile value for the Stochastic continuum model is also around a factor of ten lower, with a value of approximately $3 \cdot 10^{-3}$ m/y. The median U_r value for the Stochastic continuum 100 m scale model is slightly higher compared to the 20 m scale.

The differences in U_r values for particles released from the Q1 locations in the repository for the Stochastic continuum model and the Elaborated Hydro-DFN model may be explained by differences in the two modelling concepts. The parameterisation of the Hydro-DFN depends on a calibration against the distribution of specific flow capacity for individual fractures, the total flow within each sub-domain and the geometric mean of 100 m PSS data. In contrast, the local properties of the stochastic continuum are only conditioned on the geometric mean of the PSS data. The calibration of the DFN model on the total flow within a sub-domain requires the model to reproduce both the geometric mean and arithmetic mean flow characteristics of the sub-domain, the latter being typically one to two orders of magnitude higher. This typically requires the introduction of relatively large, high transmissivity features. This is reflected by the hydraulic conductivity values calculated at repository depth (Section C.4.4), where the Elaborated Hydro-DFN case has values of up to a factor of two or three higher than the Stochastic continuum case. Also, the DFN model considers flow on the whole fracture when calculating U_r, whereas the Stochastic continuum model calculates the flow local to the deposition holes. In the case of a large fracture in a DFN model tessellated to 40 m in size, the flow being considered could be between fracture intersections a significant distance from the deposition hole and may be higher than that seen closer to the deposition hole. Finally, about 30% of the particles in the Elaborated Hydro-DFN model are discarded due to no fracture being present with a significant flow. In the Stochastic continuum model nearly all the particles start, even in low hydraulic conductivity elements (provided that the Darcy flux is greater than $1 \cdot 10^{-6}$ m/y), and this will tend to produce a greater proportion of particles with low U_r values.

The median values of F_r calculated by the Stochastic continuum models are around a factor of ten higher than those calculated by the Elaborated Hydro-DFN model, with a value of approximately $1 \cdot 10^{6}$ y/m. The 10 percentile value is approximately $1 \cdot 10^{5}$ y/m. The CDF plot of F_r for the Stochastic continuum model shows a bi-modal behaviour. The explanation for this behaviour may be explained by the plots showing the exit locations, Figure 6-34 to Figure 6-36. There clearly are two major groups of exit locations, one in outcropping deformation zones around the repository and one along the shoreline further away from the repository, giving higher F_r values. The Stochastic continuum 100 m scale model shows a slightly higher median F_r value compared to the 20 m scale whereas the 10 percentile is somewhat lower for the 100 m scale model. Comparing the two different realisations of the Stochastic continuum model shows that realisation 2 of the HCD and HRD differs in median F_r values by les than a factor of 2 compared to the first realisation of the Stochastic continuum model for both scales.

One explanation for the differences in F_r, between the two cases is that in the Elaborated Hydro-DFN model many of the discharge locations are found in the deformation zones close to the repository, while in the Stochastic continuum model many particles discharge at the shoreline and therefore have longer paths and hence increased F_r values. Also there is an assumption in the CPM models that flows see all the surface area within a cell, not just the most transmissive fracture, which also leads to higher F_r values.

7 Discussion and conclusions

Three main cases are presented in this report, the Hydrogeological base case, the Elaborated Hydro-DFN case and the Stochastic continuum case. The Hydrogeological base case takes the SDM-Site base case model, with minor modifications made to reflect an updated understanding or to address issues of concern for a safety assessment, and uses it to calculate a set of hydrochemistry results and performance measures for a series of time slices. The parameterisation of the Elaborated Hydro-DFN case builds on the methodology used for SDM-Site and produces a more developed DFN that takes in to account the location and effect of deformation zones and the actual locations and inclinations of real boreholes and that is better able to reproduce the measured PFL-f and PSS inflow data, measured head data and hydrochemistry data. The Stochastic continuum model provides an alternative model concept and uses the site data in a different way to explore the sensitivity of the results to the model representation and to scope the corresponding range of performance measures that can be obtained. All three cases are able to provide a reasonable match to the site hydrochemistry measurements at 2000 AD, which provides some confidence in their validity, but is partly due to a shared representation and parameterisation of rock matrix diffusion (RMD), which plays a key role in the evolution of solute distribution within the models. However, the Stochastic continuum model is unlikely to be able to accurately model the structural characteristics of a fractured bedrock site, particularly in relation to detailed particle flow pathways and the ability to capture the tails in the performance measure distributions.

Performance measures and particle exit locations do not show significant variation with release time for the Hydrogeological base case. The deformation zones appear to be the main influence on exit locations, with shoreline position having a lesser influence. As discussed in Section 6.2.2, the particle exit locations largely correspond to discharge areas in the SDM-Site regional modelling, which are in accordance with measured heads and the distribution of surface water. There was also little variation in the distributions of the performance measures for the one additional realisation considered. In summary, the following performance measure results were obtained for the Hydrogeological base case:

- The median value of the equivalent flux, U_r, at the release point is calculated to be approximately 0.003 m/y, with the 90 percentile value calculated to be approximately 0.1 m/y.
- The median value of the flow-related transport resistance, F_r, is calculated to be approximately 100,000 y/m, with the 10 percentile value calculated to be approximately 10,000 y/m.
- The median value of the advective travel time, t_r, is calculated to be approximately 100 years, with the 10 percentile value calculated to be approximately 20 years.

High flows in fractures that intersect deposition holes are undesirable in the repository as they have implications for buffer erosion and canister corrosion, as well as particle transport. However, it seems that the FPC and EFPC could be effective at removing the deposition holes that would be most affected by high flows. The criteria seem to be less effective at removing deposition holes that would lead to low F_r values, since F_r is a quantity that is integrated over the whole pathway. In the latter case, proximity to highly transmissive deformation zones could be more influential.

The Elaborated Hydro-DFN is sufficiently different to the SDM-Site Hydro-DFN used to define the Hydrogeological base case to cause important differences in the performance measure distributions. The differences can be explained in terms of an increase in the proportion of small fractures. Smaller fractures have lower transmissivities and less connectivity to other flowing features, leading to lower flow rates. The Elaborated Hydro-DFN also results in ECPM models which are approximately a factor of three less conductive below –150 m than the SDM-Site Hydro-DFN. The methodology changes applied in the calibration of the Hydro-DFN for the Elaborated Hydro-DFN are:

- Representative boreholes were modelled explicitly and deformation zones were included in the models of fracturing around boreholes used in the calibration.
- Particular care was taken with the fracture size to transmissivity relationship assigned to the WNW set in DZ3.
- Particular care was taken to calibrate the fracture sets individually.
- A maximum Terzaghi correction of 100 was used in the calibration, compared to a value of 7 used in the SDM-Site Hydro-DFN calibration /Rhén et al. 2008/.

Application of the Elaborated Hydro-DFN to modelling particle pathways in the temperate period led to the following differences in the results:

- The number of particles successfully entering a fracture from a Q1 location is ~70% for the Elaborated Hydro-DFN compared to ~76% for the Hydrogeological base case model. The reduction is thought to be due to the shift towards smaller fractures specified in the fracture size distribution for the Elaborated Hydro-DFN compared to the SDM-Site Hydro-DFN used in the Hydrogeological base case. Hence there is a reduction in the number of fractures with significant flow intersecting deposition holes.
- The median values of U_r calculated by the Elaborated Hydro-DFN models are around a factor of three lower than those calculated by the Hydrogeological base case, with a value of approximately 0.001 m/y. The 90 percentile value is also approximately a factor of three lower than that of the Hydrogeological base case model, with a value of approximately 0.03 m/y.
- The median values of F_r calculated by the Elaborated Hydro-DFN models are around a factor of two higher than those calculated by the Hydrogeological base case, with a value of approximately 200,000 y/m. The 10 percentile value is also approximately a factor of two higher than that of the Hydrogeological base case model, with a value of approximately 20,000 y/m.
- The median values of t_r calculated by the Elaborated Hydro-DFN models are around a factor of 2.5 higher than those calculated by the Hydrogeological base case, with a value of approximately 250 years.

For both the Hydrogeological base case and the Elaborated Hydro-DFN models, the results suggest that Q1 release locations in HRD_EW007 are associated with higher U_r values and lower F_r values than Q1 release location in HRD_C or HRD_W. The difference amounts to approximately a factor of three in the median value of U_r and F_r compared to HRD_C or HRD_W in the Hydrogeological base case and a factor of ten in the Elaborated Hydro-DFN case. Of the total number of available deposition holes, approximately 60% are in HRD_C, 30% are in HRD_W and 10% are in HRD_EW007. However, HRD_W has a lower proportion of particles that start due to the sparsity of the fracture network in that domain, but a greater variability in transmissivities. So although HRD_W can have some high transmissivities due to high variability, this is offset by a reduction in connectivity to the deposition holes due to the fracture network sparsity. This leads to HRD_W not having the lowest U_r values or the highest F_r values in the Elaborated Hydro-DFN model.

Calculations for the Elaborated Hydro-DFN model with no MDZs suggest that the MDZs have little effect on performance measures or discharge locations.

One of the main conclusions of this report is that HRD_EW007 has an adverse effect on performance measures relative to the other local HRDs. Certainly the palaeohydrogeological model for the Elaborated Hydro-DFN was least satisfactory for HRD_EW007, with the model struggling to reproduce the retention of glacial water in the fractures between –200 m and –400 m elevation. This may be a reflection of a genuinely more fractured environment in reality or may be due to unrepresentative data caused by the borehole drilling focusing on areas to support the structural model of ZSMEW007.

The discharge locations of the released particles in the Stochastic continuum model vary significantly for different release times. The group of particles that exit along the shoreline are most affected as the shoreline recedes. These results are different to the Hydrogeological base case and the Elaborated Hydro-DFN case, where the discharge locations are more localised around the repository area and do not vary significantly with release time. The effect of different model scales and realisations of the HRD and HCD is not very pronounced. The 20 m scale gives a slightly larger spread of particles away from the repository. In general, however, the discharge locations are still strongly influenced by the locations of outcropping deformation zones, as for the other cases.

There is little difference in performance measures between the two realisations of each of the Stochastic continuum models, between the two model scales (20 m and 100 m), or with release time (2000 AD and 15000 AD). The median U_r value for the Stochastic continuum 100 m scale model is slightly higher than for the 20 m scale model. The Stochastic continuum 100 m scale model shows a slightly higher median F_r value compared to the 20 m scale model.

There are significant differences between the distributions of the performance measures for the Q1 release locations calculated for the Stochastic continuum models and for the Elaborated Hydro-DFN model. The median values of U_r calculated by the Stochastic continuum models are around a factor of ten lower than those calculated by the Elaborated Hydro-DFN model. The median values of F_r calculated by the Stochastic continuum models are around a factor of ten higher than those calculated by the Elaborated Hydro-DFN model. An explanation for the changes to F_r, could be that in the Elaborated Hydro-DFN model many of the discharge locations are found in the deformation zones close to the repository while in the Stochastic continuum model many particles discharge at the shoreline and therefore have longer paths and hence increased F_r values. Also there is an assumption in the CPM models that flows see all the surface area within a cell, not just the most transmissive fracture, which also leads to higher F_r values.

The differences in performance measures of particles released from the Q1 locations in the repository for the Stochastic continuum model and the Elaborated Hydro-DFN model may be explained by differences in the two modelling concepts, as discussed in Chapter 6. Firstly, the way the DFN in the Elaborated Hydro-DFN model is calibrated to total flows means that higher transmissivity values are needed to match the higher measured flows. This will be reflected in higher U_r values and lower F_r values. Also, the DFN model considers flow on the whole fracture when calculating U_r rather than the flow local to the deposition holes and in some cases this could lead to higher values. Finally, about 30% of the particles in the Elaborated Hydro-DFN model are discarded due to there being no fracture present with a significant flow. In the Stochastic continuum model nearly all the particles start, even in low hydraulic conductivity elements (provided that the Darcy flux is greater than $1 \cdot 10^{-6}$ m/y), and this will tend to produce a greater proportion of particles with low U_r values.

A comparison of open repository tunnel inflows calculated by ConnectFlow and DarcyTools is presented in Appendix G. These calculations show that the two software packages are in good agreement when carrying out calculations of equivalent models, even when using a different methodology and rock concept. The ConnectFlow calculations again show that HRD_EW007 is responsible for the majority of the calculated flow in the repository area.

Considering the land uplift at the site (Figure 4-27 in /Rhen et al. 2009/), the land at Laxemar rose from the sea between about 6000 BC to 4000 BC. Hence, the bedrock has been subject to potential flushing by meteoric water for about 6,000 to 8,000 years. Analysis of hydrochemical data (Chapter 6 of /Laaksoharju et al. 2009/) interprets that fresh, recharge water penetrates to about –100 m to –250 m elevation during this time period. Hence, likely times for significant dilution by fresh recharge waters at a repository depth of about –500 m can be estimated as being some tens of thousands of years. This is consistent with estimates made on analyses of transport parameters for the recharge to the repository presented in Appendix H. This gives additional confidence in the models and the numerical results.

8 References

Carrera J, Sánchez-Vila X, Benet I, Medina A, Galarza G, Guímerà J, 1998. On matrix diffusion: formulations, solution methods and quantitative effects. Hydrogeology Journal, 6, pp 178–190.

Follin S, 2008. Bedrock hydrogeology Forsmark. Site descriptive modelling, SDM-Site Forsmark. SKB R-08-95, Svensk Kärnbränslehantering AB.

Follin S, Stigsson M, Berglund S, Svensson U, 2004. Variable-density groundwater flow simulations and particle tracking – numerical modelling using DarcyTools. Preliminary site description of the Simpevarp area – version 1.1. SKB R-04-65, Svensk Kärnbränslehantering AB.

Follin S, Stigsson M, Svensson U, 2005. Variable-density groundwater flow simulations and particle tracking – numerical modelling using DarcyTools. Preliminary site description Simpevarp subarea – version 1.2. SKB R-05-11, Svensk Kärnbränslehantering AB.

Follin S, Stigsson M, Svensson U, 2006. Hydrogeological DFN modelling using structural and hydraulic data from KLX04. Preliminary site description, Laxemar subarea – version 1.2. SKB R-06-24, Svensk Kärnbränslehantering AB.

Fredén C (ed), 2002. Sveriges nationalatlas. Berg och Jord (in Swedish). Stockholm: SNA publishing.

Hartley L, Worth D, Gylling B, Marsic N, Holmén J, 2004. Preliminary site description: Groundwater flow simulations. Simpevarp area (version 1.1) modelled with CONNECTFLOW. SKB R-04-63, Svensk Kärnbränslehantering AB.

Hartley L, Hoch A, Hunter F, Jackson P, Marsic N, 2005. Regional hydrogeological simulations – numerical modelling using CONNECTFLOW. Preliminary site description. Simpevarp subarea – version 1.2. SKB R-05-12, Svensk Kärnbränslehantering AB.

Hartley L, Hunter F, Jackson P, McCarthy R, Gylling B, Marsic N, 2006a. Regional hydrogeological simulations using CONNECTFLOW. Preliminary site description Laxemar subarea – version 1.2. SKB R-06-23, Svensk Kärnbränslehantering AB.

Hartley L, Hoch A, Jackson P, Joyce S, McCarthy R, Rodwell W, Swift B, and Marsic N, 2006b. Groundwater flow and transport modelling during the temperate period for the SR-Can assessment. Forsmark area – version 1.2. SKB R-06-98, Svensk Kärnbränslehantering AB.

Hartley L, Hoch A, Jackson P, Joyce S, McCarthy R, Swift B, Gylling B, Marsic N, 2006c. Groundwater flow and transport modelling during the temperate period for the SR-Can assessment. Laxemar subarea – version 1.2. SKB R-06-99, Svensk Kärnbränslehantering AB.

Hartley L, Jackson P, Joyce S, Roberts D, Shevelan J, Swift B, Gylling B, Marsic N, Hermanson J, Öhman J, 2007. Hydrogeological pre-modelling exercises. Assessment of impact of the Äspö Hard Rock Laboratory. Sensitivities of palaeo-hydrogeology. Development of a local near-surface Hydro-DFN for KLX09B–F. Site descriptive modelling, SDM-Site Laxemar SKB R-07-57, Svensk Kärnbränslehantering AB.

Hoch A R, Jackson C P, 2004. Rock-matrix diffusion in transport of salinity. Implementation in CONNECTFLOW. SKB R-04-78, Svensk Kärnbränslehantering AB.

Holmén J G, 2008. Premodelling of the importance of the location of the upstream hydraulic boundary of a regional flow model of the Laxemar-Simpevarp area. Site descriptive modelling, SDM-Site Laxemar. SKB R-08-60, Svensk Kärnbränslehantering AB.

Jackson C P, Hoch A R, Todman S, 2000. Self-consistency of a heterogeneous continuum porous medium representation of a fractured medium. Water Resources. Research, 36, pp 189–202.

Joyce S, Simpson T, Hartley L, Applegate D, Hoek J, Jackson P, Swan D, Marsic M, Follin S, 2010. Groundwater flow modelling of periods with temperate climate conditions – Forsmark. SKB R-09-20, Svensk Kärnbränslehantering AB.

Laaksoharju M, Smellie J, Tullborg E-L, Wallin B, Drake H, Gascoyne M, Gimeno M, Gurban I, Hallbeck L, Molinero J, Nilsson A-C, Waber N, 2009. Bedrock hydrogeochemistry Laxemar. Site descriptive modelling, SDM-Site Laxemar. SKB R-08-93, Svensk Kärnbränslehantering AB.

Larsson-McCann S, Karlsson A, Nord M, Sjögren J, Johansson L, Ivarsson M, Kindell S, 2002. Meteorological, hydrological and oceanographical data for the site investigation program in the community of Oskarshamn. SKB TR-02-03, Svensk Kärnbränslehantering AB.

Marsic N, Hartley L, Jackson P, Poole M, Morvik A, 2001. Development of hydrogeological modelling tools based on NAMMU. SKB R-01-49, Svensk Kärnbränslehantering AB.

Moreno L, Gylling B, 1998. Equivalent flow rate concept used in near field transport model COMP23 – Proposed values for SR 97. SKB R-98-53, Svensk Kärnbränslehantering AB.

Neretnieks I, 1979. Transport mechanism and rates of transport of radionuclides in the geosphere as related to the Swedish KBS concept. In: Proceedings of a symposium on the underground disposal of radioactive wastes, Otaniemi, Finland, 2–6 July 1979. Vienna: International Atomic Energy Agency, Vol II, pp 315–339.

Nyman H, Sohlenius G, Strömgren M, Brydsten L, 2008. Depth and stratigraphy of regolith. Site descriptive modelling, SDM-Site Laxemar. SKB R-08-06, Svensk Kärnbränslehantering AB.

Rhén I, Hartley L, 2009. Bedrock hydrogeology Laxemar, Site descriptive modelling, SDM-Site Laxemar. SKB R-08-92, Svensk Kärnbränslehantering AB.

Rhén I (ed), Gustafson G, Stanfors R, Wikberg P 1997. Äspö HRL – Geoscientific evaluation 1997/5. Models based on site characterization 1986–1995. SKB TR 97-06, Svensk Kärnbränslehantering AB.

Rhén I, Follin S, Hermanson J, 2003. Hydrological Site Descriptive Model – a strategy for its development during Site Investigations. SKB R-03-08, Svensk Kärnbärnslehantering AB.

Rhén I, Forsmark T, Forssman I, Zetterlund M, 2006a. Hydrogeological single-hole interpretation of KSH01, KSH02, KSH03, KAV01 and HSH01–03, Preliminary site description, Simpevarp subarea – version 1.2, SKB R-06-20, Svensk Kärnbränslehantering AB.

Rhén I, Forsmark T, Forssman I, Zetterlund M, 2006b. Hydrogeological single-hole interpretation of KLX02, KLX03, KLX04, KAV04A and B, HAV09–10 and 9 HLXxx boreholes. Laxemar subarea – version 1.2. SKB R-06-21, Svensk Kärnbränslehantering AB.

Rhén I, Forsmark T, Forssman I, Zetterlund M, 2006c. Evaluation of hydrogeological properties for Hydraulic Conductor Domains (HCD) and Hydraulic Rock Domains (HRD). Laxemar subarea – version 1.2. SKB R-06-22, Svensk Kärnbränslehantering AB.

Rhén I, Forsmark T, Hartley L, Jackson C P, Roberts D, Swan D, Gylling B, 2008. Hydrogeological conceptualisation and parameterisation. Site descriptive modelling, SDM-Site Laxemar. SKB R-08-78, Svensk Kärnbränslehantering AB.

Rhén I, Forsmark T, Hartley L, Joyce S, Roberts D, Gylling B, Marsic N, 2009. Bedrock hydrogeology. Model testing and synthesis. Site descriptive modelling, SDM-Site Laxemar. SKB R-08-91, Svensk Kärnbränslehantering AB.

Serco, 2010a. CONNECTFLOW Release 10.0 Technical Summary Document SA/ENV/CONNECTFLOW/15, Serco Assurance, UK.

Serco, 2010b. NAMMU Release 10.0 Technical Summary Document SA/ENV/CONNECTFLOW/8, Serco Assurance, UK.

Serco, 2010c. NAPSAC Release 10.0 Technical Summary Document SA/ENV/CONNECTFLOW/12, Serco Assurance, UK.

SKB, 2002. Simpevarp – site descriptive model version 0. SKB R-02-35, Svensk Kärnbränslehantering AB.

SKB, 2004. Preliminary site description Simpevarp area – version 1.1. SKB R-04-25, Svensk Kärnbränslehantering AB.

SKB, 2005. Preliminary site description. Simpevarp subarea – version 1.2. SKB R-05-08, Svensk Kärnbränslehantering AB.

SKB, 2006a. Preliminary site description. Laxemar subarea – version 1.2. SKB R-06-10, Svensk Kärnbränslehantering AB.

SKB, 2006b. Preliminary site description Laxemar stage 2.1. Feedback for completion of the site investigation including input from safety assessment and repository engineering. SKB R-06-110, Svensk Kärnbränslehantering AB.

SKB, 2006c. Data report for the safety assessment SR-Can. SKB TR-06-25, Svensk Kärnbränslehantering AB.

SKB, 2007. Final repository facility. Underground design premises/D2. SKB R-07-33, Svensk Kärnbränslehantering AB.

SKB, 2008a. Site description of Forsmark at completion of the site investigation phase. SDM-Site Forsmark. SKB TR-08-05, Svensk Kärnbränslehantering AB.

SKB, 2009a. Site description of Laxemar at completion of the site investigation phase. SDM-Site Laxemar. SKB TR-09-01, Svensk Kärnbränslehantering AB.

SKB, 2009b. Confidence assessment. Site descriptive modelling, SDM-Site Laxemar. SKB R-08-101, Svensk Kärnbränslehantering AB.

SKB, 2010a. Data report for the safety assessment SR-Site. SKB TR-10-52, Svensk Kärnbränslehantering AB.

SKB, 2010b. Climate and climate-related issues for the safety assessment SR-Site. SKB TR-10-49, Svensk Kärnbränslehantering AB.

Sohlenius G, Hedenström A, 2008. Description of regolith at Laxemar-Simpevarp. Site descriptive modelling, SDM-Site Laxemar. SKB R-08-05, Svensk Kärnbränslehantering AB.

Svensson U, Rhén I, 2010. Groundwater flow modelling of the excavation and operation phases – Laxemar. SKB R-09-23, Svensk Kärnbränslehantering AB.

Söderbäck B (ed), 2008. Geological evolution, palaeoclimate and historical development of the Forsmark and Laxemar-Simpevarp areas. Site descriptive modelling, SDM-Site. SKB R-08-19, Svensk Kärnbränslehantering AB.

Vidstrand P, Rhén I, Zugec N, 2010. Groundwater flow modelling of periods with periglacial and glacial climate conditions – Laxemar. SKB R-09-25, Svensk Kärnbränslehantering AB.

Wahlgren C-H, Curtis P, Hermanson J, Forssberg O, Öhman J, Fox A, La Pointe P, Drake H, Triumf C-A, Mattsson H, Thunehed H, Juhlin C, 2008. Geology Laxemar. Site descriptive modelling, SDM-Site Laxemar. SKB-R-08-54, Svensk Kärnbränslehantering AB.

Werner K, Öhman J, Holgersson B, Rönnback K, Marelius F, 2008. Meteorological, hydrological and hydrogeological monitoring data and near-surface hydrogeological properties data from Laxemar-Simpevarp. Site descriptive modelling, SDM-Site Laxemar. SKB R-08-73, Svensk Kärnbränslehantering AB.

Westman P, Wastegård S, Schoning K, Gustafsson B, Omstedt A. 1999. Salinity change in the Baltic Sea during the last 8,500 years: evidence, causes and models. SKB TR-99-38, Svensk Kärnbränslehantering AB.

Appendix A

Glossary of abbreviations and symbols

Abbreviations and notation used are:

a_r	Flow wetted fracture surface area per unit volume of rock (2·P32) (m^2m^{-3}), used for particle transport
CDF	Cumulative distribution function
CPM	Continuous porous medium
DFN	Discrete fracture network
DZ	Deformation zone
DZ1	Depth zone 1 (–150 m to 0 m elevation)
DZ2	Depth zone 2 (–400 m to –150 m elevation)
DZ3	Depth zone 3 (–650 m to –400 m elevation)
DZ4	Depth zone 4 (–1,000 m to –650 m elevation)
ECPM	Equivalent continuous porous medium
EDZ	Excavation damaged zone
EFPC	Extended full perimeter criteria
e_t	Fracture transport aperture (m)
F_r	Flow-related transport resistance in the rock (y m^{-1})
FPC	Full perimeter criteria
HCD	Hydraulic conductor domain
HRD	Hydraulic rock mass domain
HSD	Hydraulic soil domain
IFZ	Implicit fracture zone
K	Hydraulic conductivity (m s^{-1})
KLX	Cored borehole at Laxemar
k_r	Shape parameter in the power-law fracture size-intensity distribution
L_{EDZ}	Path-length in the EDZ (m)
L_r	Path-length in the rock (m)
L_t	Path-length in the tunnel (m)
MDZ	Minor deformation zone
OPO	Open and partly open fractures
P10	Linear fracture intensity: number of fractures per metre along a borehole (m^{-1})
$P10_c$	Linear fracture intensity of connected open fractures: number of connected fractures per metre along a borehole (m^{-1})
$P10_{corr}$	Terzaghi corrected linear fracture intensity: 'true' number of fractures per metre along a borehole corrected for the bias introduced by the angle the borehole made with fractures (m^{-1})
$P10_{PFL}$	Linear fracture intensity of PFL-anomalies: number of PFL anomalies per metre along a borehole (m^{-1})
$P10_{PFL,corr}$	Terzaghi corrected Linear fracture intensity of PFL-anomalies (m^{-1})
P21	Areal fracture intensity: total fracture trace lengths per square metre of outcrop (m m^{-2})

P32	Volumetric fracture intensity: total fracture surface area per cubic metre of rock ($m^2\ m^{-3}$)
$P32_c$	Volumetric fracture intensity of connected fractures: total connected fracture surface area per cubic metre of rock ($m^2\ m^{-3}$)
PA	Performance assessment
PDF	Probability distribution function
PFL	Posiva flow-log
ϕ	Kinematic porosity
PM	Performance measure
PSS	Pipe-string system
Q	Groundwater flow rate ($m^3\ s^{-1}$ or $m^3\ y^{-1}$)
Q_{eqr}	Equivalent flow rate in the rock ($m^3\ s^{-1}$ or $m^3\ y^{-1}$)
q	Darcy flux ($m\ s^{-1}$ or $m\ y^{-1}$)
q_f	Flow rate per unit width in a fracture ($m^2\ s^{-1}$ or $m^2\ y^{-1}$)
RMD	Rock matrix diffusion
r_0	Location parameter in the power-law fracture size-intensity distribution (m)
r_{min}	Minimum fracture radius used in DFN simulations (m)
RHB 70	Shoreline datum level of year 1970
SDM	Site descriptive modelling or model
s	Drawdown (m)
σ	Standard deviation, or the fracture surface area per unit volume ($m^2\ m^{-3}$) for solute transport (depending on context)
SMOW	Standard Mean Ocean Water
STP	Standard temperature and pressure
T	Fracture transmissivity ($m^2\ s^{-1}$)
t_{EDZ}	Advective travel-time in the EDZ (y)
t_r	Advective travel-time in the rock (y)
t_t	Advective travel-time in the tunnel (y)
Θ	Temperature (K)
TDS	Total dissolved solids ($g\ L^{-1}$)
U_r	Initial equivalent flux in the rock ($m\ y^{-1}$)
z	Elevation (m)

Appendix B

File Formats

B.1 PTABLE File Format

The PTABLE file format is used to export summary information on each pathline from a ConnectFlow particle tracking simulation. In the format that follows, text in bold indicates a literal entry in the file, text in italics between <> indicate an entry that is replaced by a number in the file, and other text is descriptive.

Header lines:

 # PARAMETER TABLE FILE FROM CONNECTFLOW

#

 # NUMBER OF COLUMNS DEFINED

<number of columns>

 # NUMBER OF TIMES THEY ARE USED

<number of rows> *<number of rows>* *<number of rows>*

 # HOW MANY TIMES THEY COULD BE USED

<number of rows> *<number of rows>* *<number of rows>*

 # THE PARAMETER TABLE:

Column header:

 # POINT XS YS ZS XE YE ZE OKFLAG T0 U0 QEQ TW F L TRAPP TW_TUN L_TUN TW_EDZ L_EDZ UR QEQR LR_TUN TR_TUN

Followed by one line per path each with the following space separated entries:

Entry	Description
POINT	Path number
XS	X-coordinate of start point.
YS	Y-coordinate of start point.
ZS	Z-coordinate of start point.
XE	X-coordinate of end point.
YE	Y-coordinate of end point.
ZE	Z-coordinate of end point.
OKFLAG	Indicates whether or not a particle reached the model boundary: • 0 = reached the top boundary. • 1 = failed to start due to no fracture (Q1 or Q2) or low initial flow (Q1, Q2 and Q3), as defined in Section 3.2.6. • 2 = ran out of time steps. • 3 = stuck. • 4 = oscillating between DFN and CPM. • 5 = reached a side boundary or the bottom boundary.
T0	Release time (y).
U0	Initial equivalent flux (m/y) for Q1 (U_{r1} in equation *(3-8)*) and Q2 (U_{r2} in equation (3-10)). For Q3 this is just the initial Darcy flux (m/y) and UR should be used for radionuclide transport.
QEQ	Equivalent groundwater flow rate (m^3/y) for Q1 (equation (3-7)) and Q2 (equation (3-9)). QEQR is used for Q3 instead.
TW	Travel time (y) in the rock, i.e. the DFN for embedded models.
F	Flow-related transport resistance (y/m) for the rock, i.e. the DFN for embedded models.
L	Path length (m) in the rock, i.e. the DFN for embedded models.

TRAPP	Initial transport aperture (m) in the first fracture for Q1 or Q2, or the porosity for Q3.
TW_TUN	Travel time (y) in the tunnels.
L_TUN	Path length (m) in the tunnels.
TW_EDZ	Travel time (y) in the EDZ.
L_EDZ	Path length (m) in the EDZ.
UR	Initial equivalent flux (m/y) in the first fracture for Q3 (equation (3-12)), zero for Q1 or Q2.
LR_TUN	Path length (m) to the first fracture for Q3, zero for Q1 or Q2.
TW_CPM	Travel time (y) in the ECPM or CPM, i.e. not in the DFN for embedded models.
L_CPM	Path length (m) in the ECPM or CPM, i.e. not in the DFN for embedded models.
F_CPM	Flow-related transport resistance (y/m) for the ECPM or CPM, i.e. not in the DFN for embedded models.
TR_TUN	Travel time (y) to the first fracture for Q3, zero for Q1 or Q2.
QEQR	Equivalent groundwater flow rate (m^3/y) in the first fracture for Q3 (equation (3-11)), zero for Q1 or Q2.
FPC	Whether or not the path is associated with a deposition hole that would be excluded if the FPC (Section 3.2.7) were applied: • 0 = would not be excluded. • 1 = excluded due to background fracture. • 2 = excluded due to deformation zone fracture.
EFPC	The largest number of adjacent deposition holes (including this deposition hole) fully intersected by a fracture that fully intersects this deposition hole. A value of 5 or greater means that the hole would be excluded if the EFPC (Section 3.2.7) were applied.
FLEN	The length (m) of the largest fracture intersecting the deposition hole. This is set at 1,000.0 m for a deformation zone fracture.

Appendix C

Peformance Measure Plots

C.1 Hydrogeological base case model

C.1.1 Evolution of exit locations with time

The discharge locations of particles released from Q2 locations in the repository are shown, for various discharge times, in Figure C-1 to Figure C-3. There is some variation in the discharge locations with time, as the shoreline recedes to the east, however the influence of the shoreline displacement is less than that of the deformation zones.

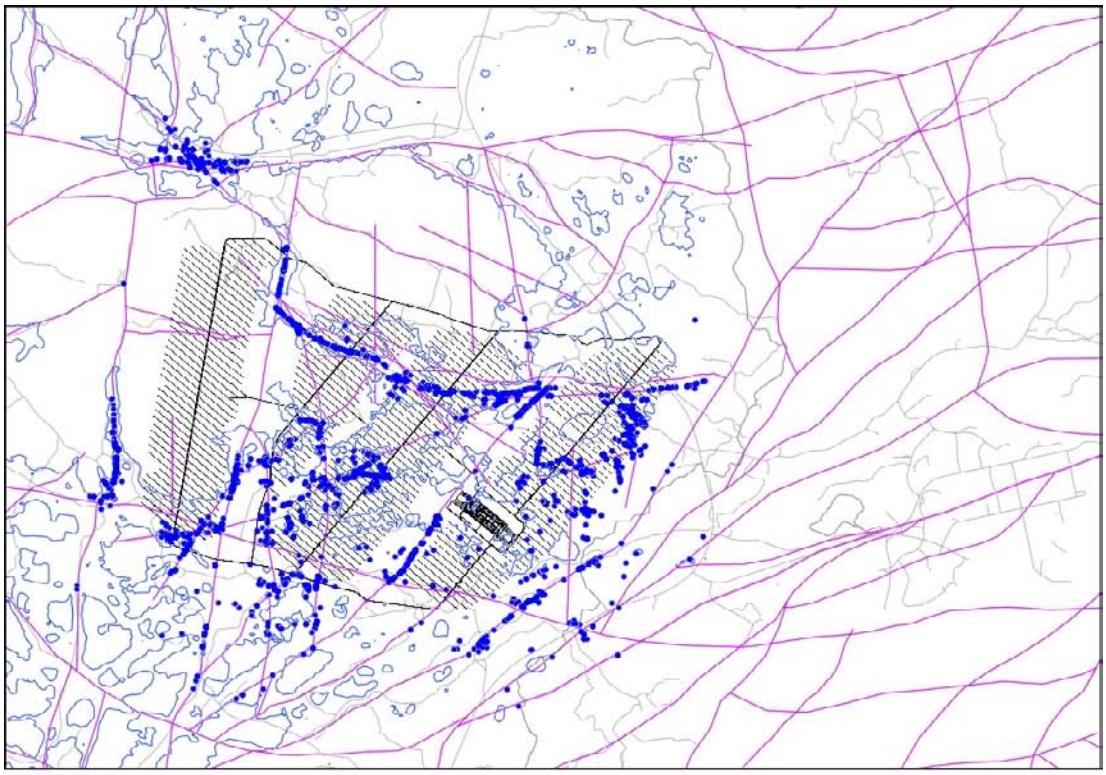

5000 BC

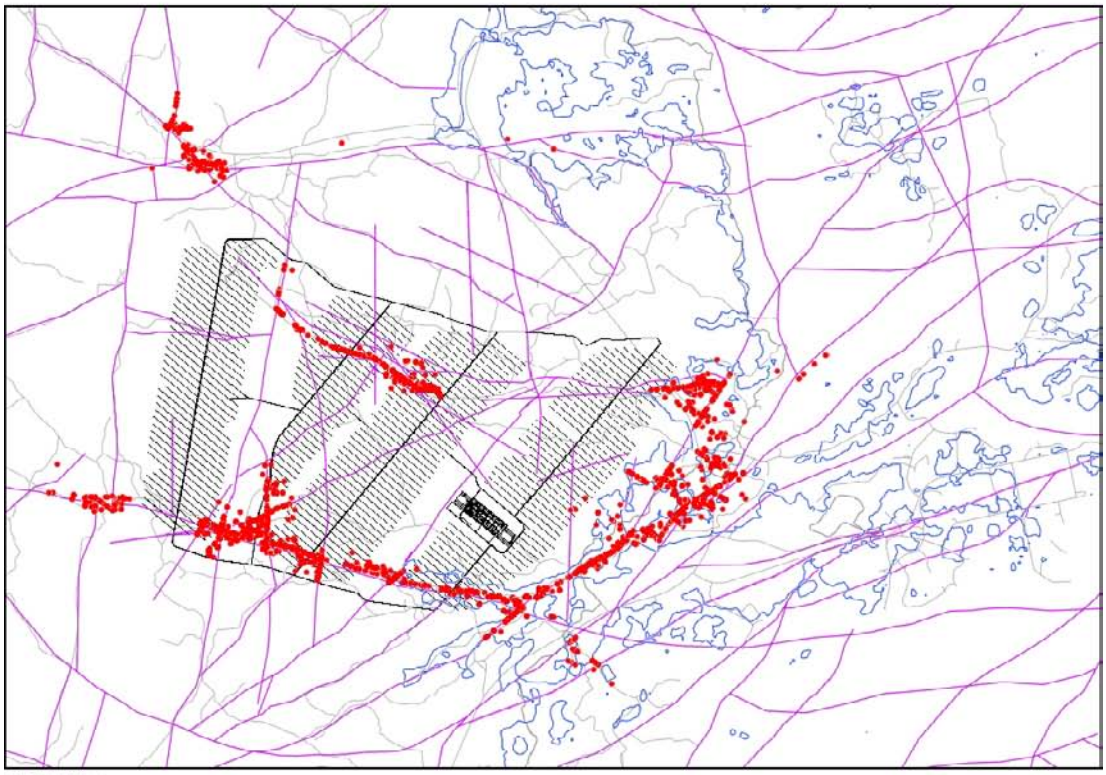

2000 BC

Figure C-1. *Exit locations for the Q2 particles successfully reaching the top boundary of the site-scale Hydrogeological base case model (96%–98%) for releases at 5000 BC (dark blue) and 2000 BC (red). The shoreline at each time is shown in blue, repository structures in black and surface features in grey.*

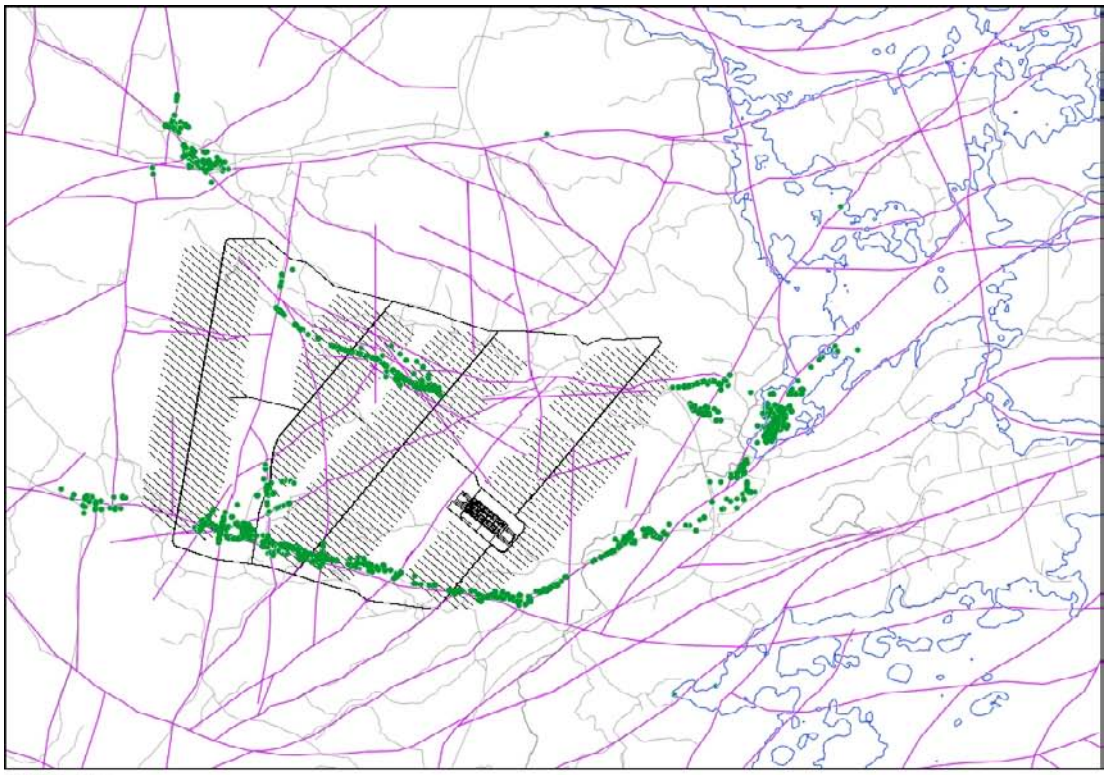

2000 AD

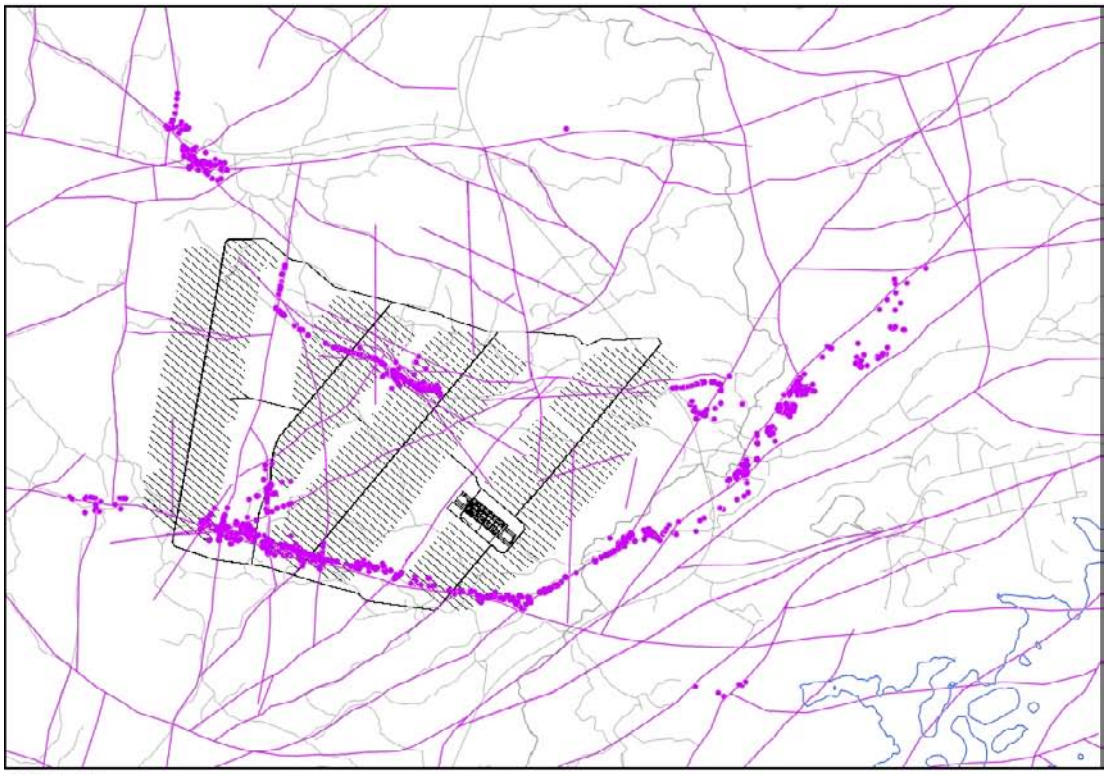

5000 AD

Figure C-2. *Exit locations for the Q2 particles successfully reaching the top boundary of the site-scale Hydrogeological base case model (96%–98%) for releases at 2000 AD (green) and 5000 AD (purple). The shoreline at each time is shown in blue, repository structures in black and surface features in grey.*

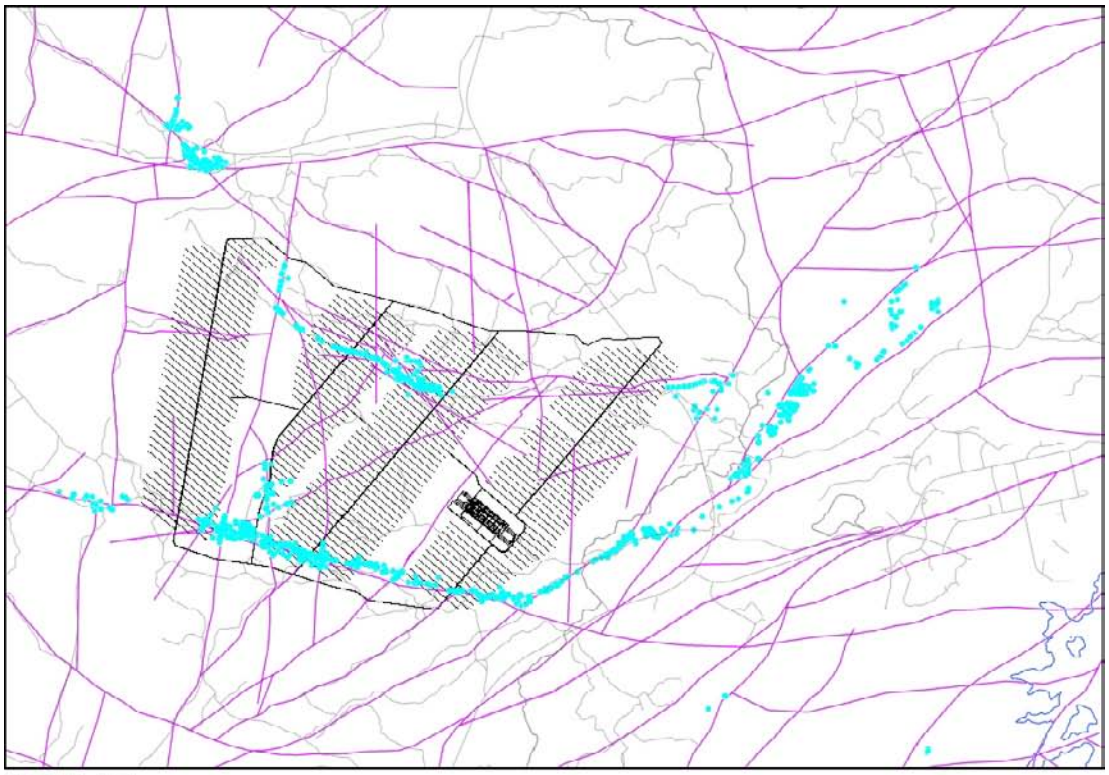

10,000 AD

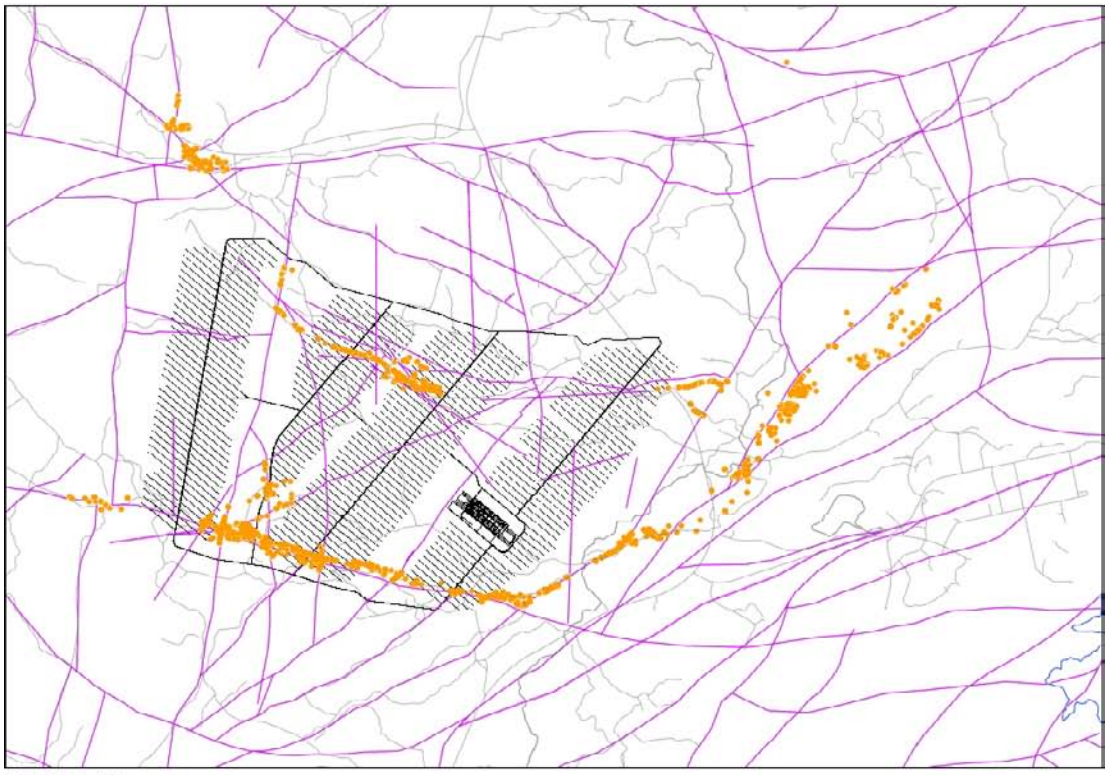

15,000 AD

Figure C-3. *Exit locations for the Q2 particles successfully reaching the top boundary of the site-scale Hydrogeological base case model (96%–98%) for releases at 10,000 AD (light blue) and 15,000 AD (orange). The shoreline at each time is shown in blue, repository structures in black and surface features in grey.*

C.1.2 Evolution of performance measures with time

Figure C-4 to Figure C-12 show the normalised cumulative distribution function (CDF) plots for the U_r, F_r and Q_{eqr} performance measures for the Q1, Q2 and Q3 release locations at each of the release times. There is very little variation in any of the performance measures in the rock with release time. This is because the particle pathways are dominated by the deformation zones rather than the location of the retreating shoreline. Also, the contribution from the ECPM to the performance measures is not included, which is likely to be a more significant component for later times as some particle pathways become longer and more horizontal.

The median value of U_r at the release point is approximately 0.003 m/y, with the 90 percentile value approximately 0.1 m/y.

The median value of F_r is approximately 100,000 y/m, with the 10 percentile value approximately 10,000 y/m.

The non-normalised CDF plots of U_r and F_r in Figure C-13 to Figure C-18 show that around 23% of all released particles fail to start for Q1 and around 2% for Q2 and Q3 release locations. Around 9% of all released particles fail to reach the model boundary. These percentages show little variation with release time.

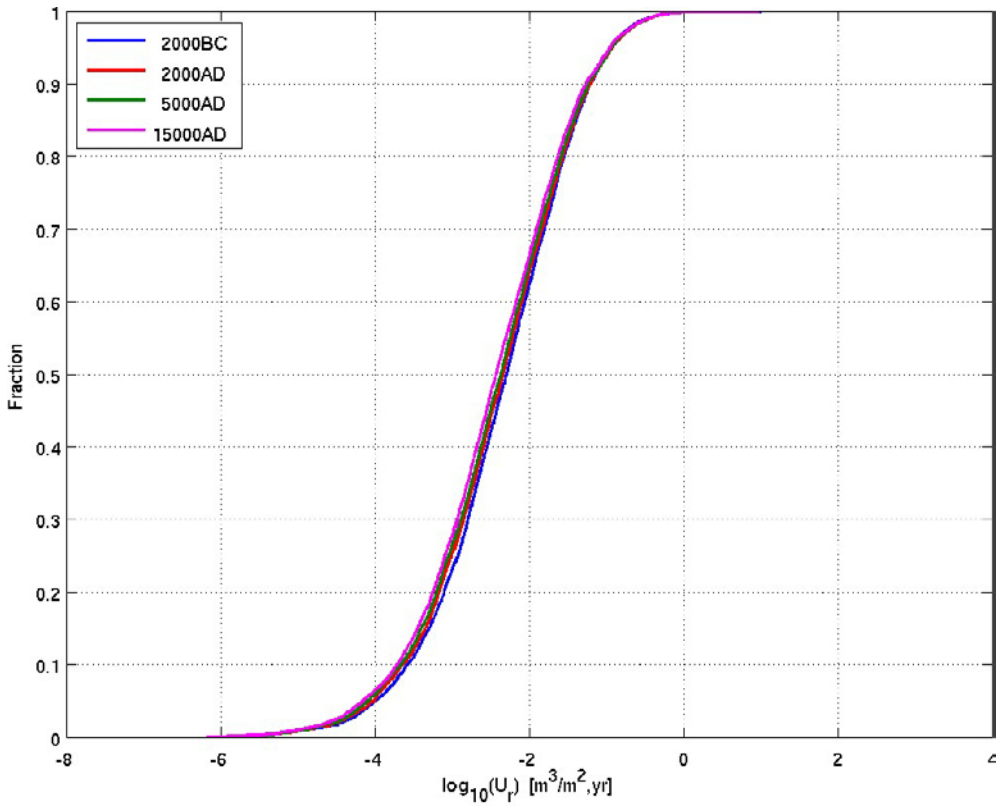

Figure C-4. *Normalised CDF plots of U_r in the Hydrogeological base case model for the Q1 particles successfully reaching the model top boundary (~69%), released at the given times.*

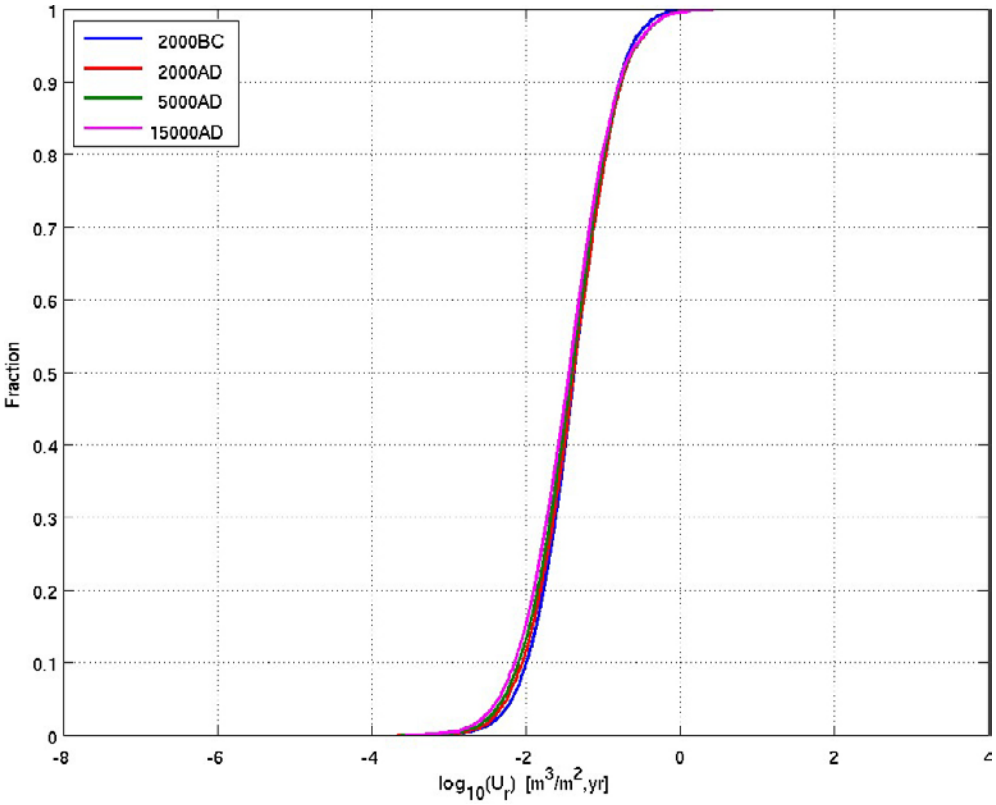

Figure C-5. *Normalised CDF plots of U_r in the Hydrogeological base case model for the Q2 particles successfully reaching the model top boundary (~90%), released at the given times.*

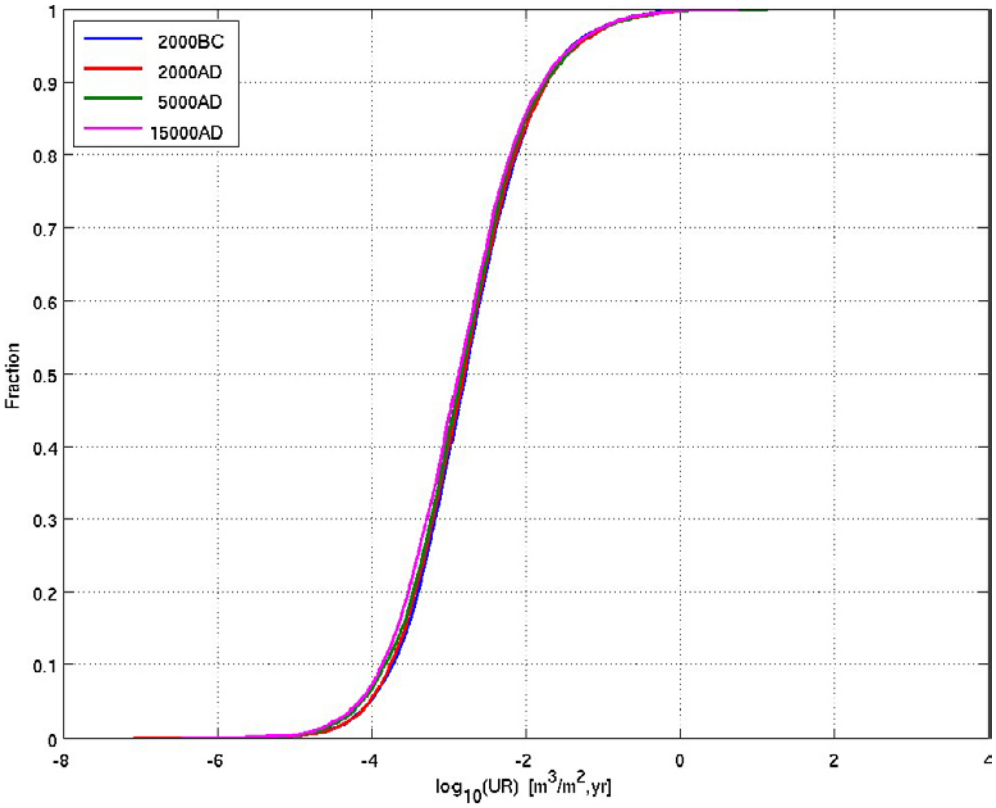

Figure C-6. *Normalised CDF plots of U_r in the Hydrogeological base case model for the Q3 particles successfully reaching the model top boundary (~89%), released at the given times. The UR axis corresponds to U_r for the Q3 release locations.*

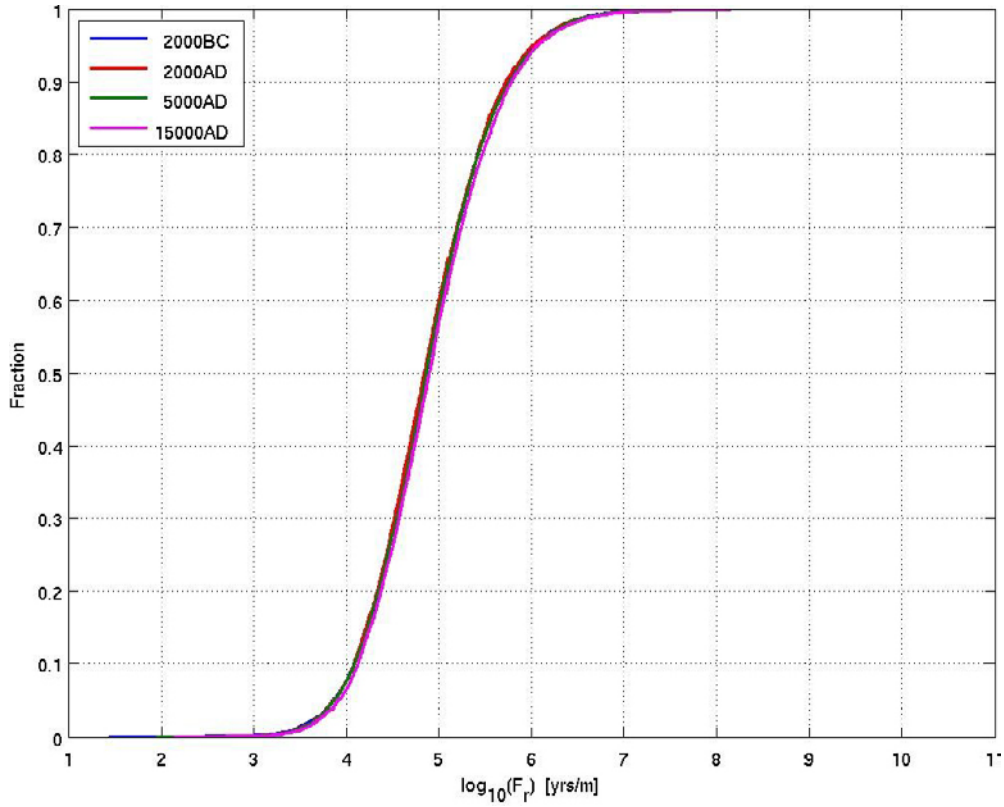

Figure C-7. *Normalised CDF plots of F_r in the Hydrogeological base case model for the Q1 particles successfully reaching the model top boundary (~69%), released at the given times.*

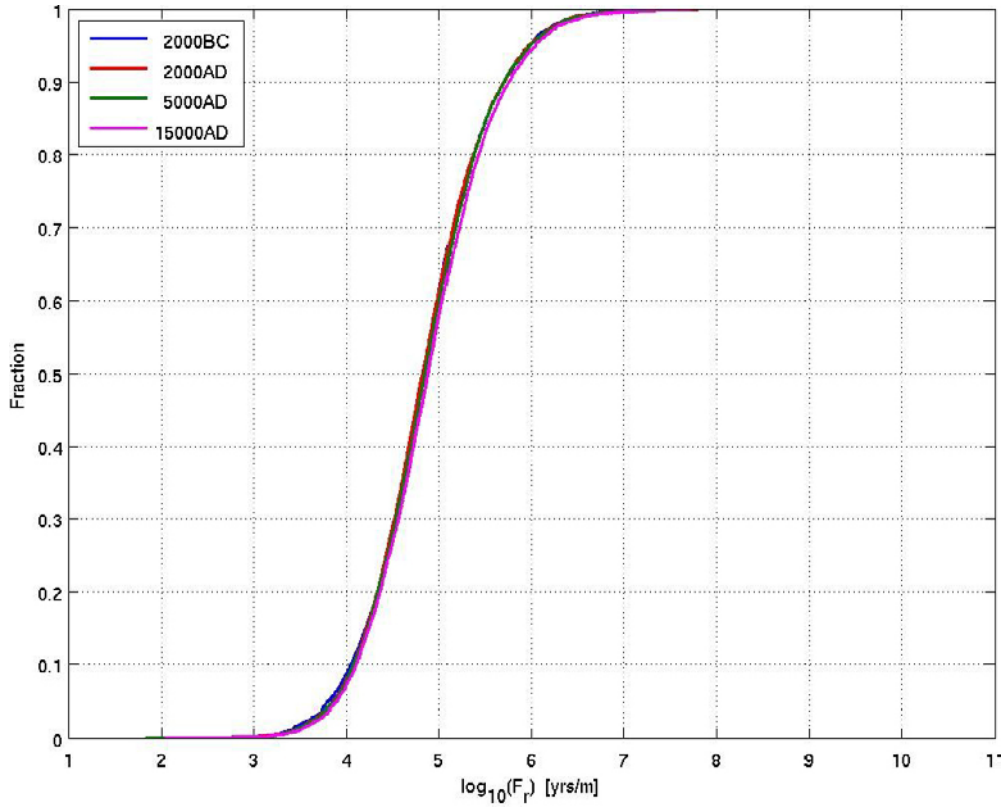

Figure C-8. *Normalised CDF plots of F_r in the Hydrogeological base case model for the Q2 particles successfully reaching the model top boundary (~90%), released at the given times.*

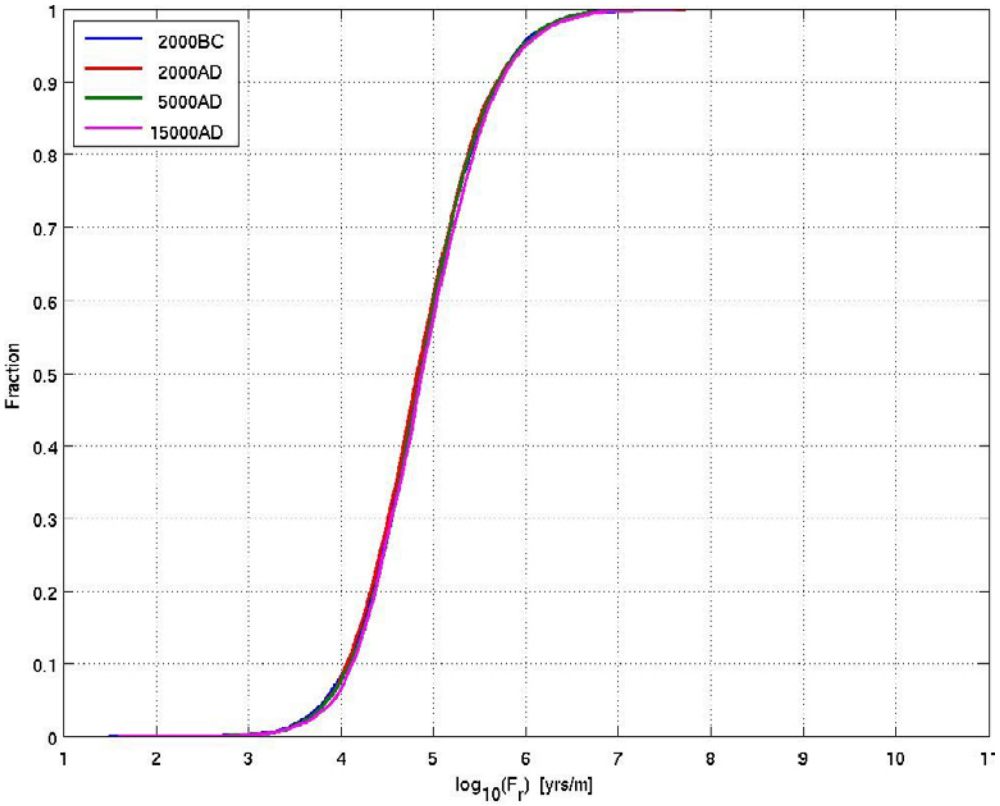

Figure C-9. *Normalised CDF plots of F_r in the Hydrogeological base case model for the Q3 particles successfully reaching the model top boundary (~89%), released at the given times.*

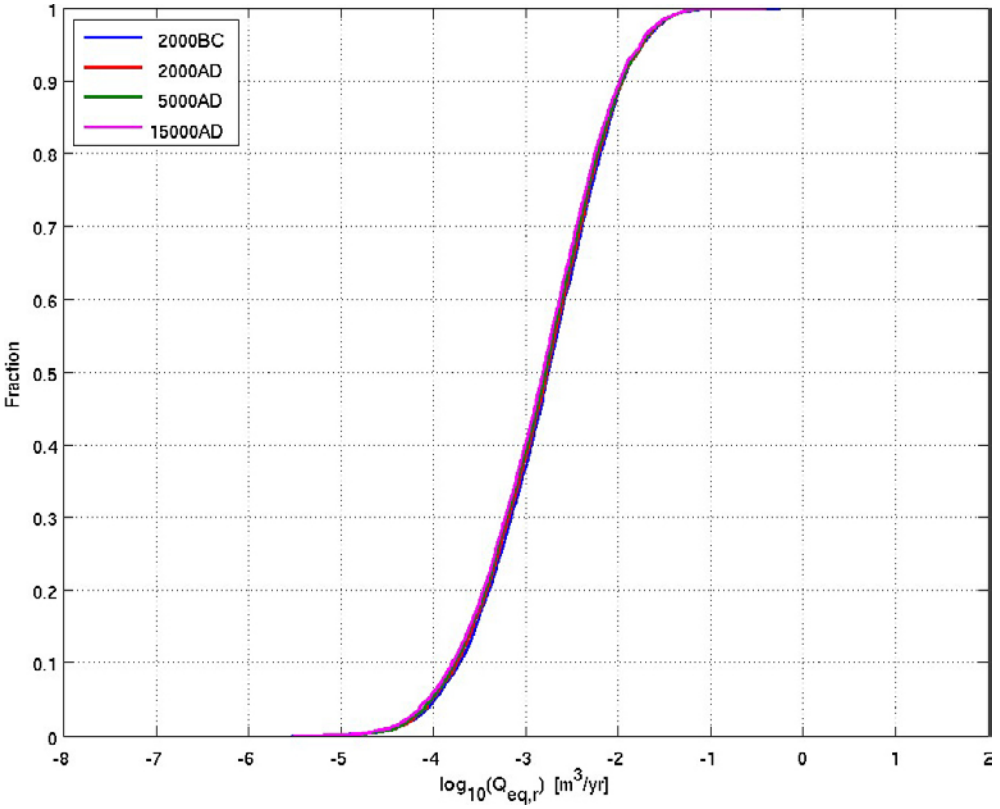

Figure C-10. *Normalised CDF plots of Q_{eqr} in the Hydrogeological base case model for the Q1 particles successfully reaching the model top boundary (~69%), released at the given times.*

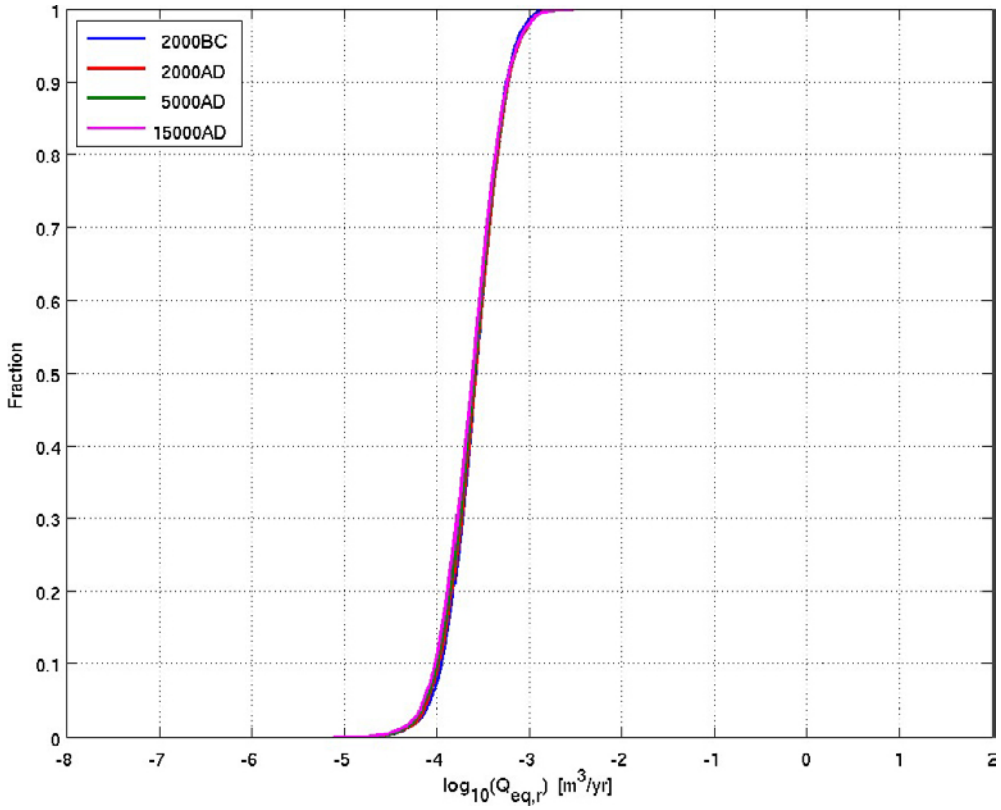

Figure C-11. *Normalised CDF plots of Q_{eqr} in the Hydrogeological base case model for the Q2 particles successfully reaching the model top boundary (~90%), released at the given times.*

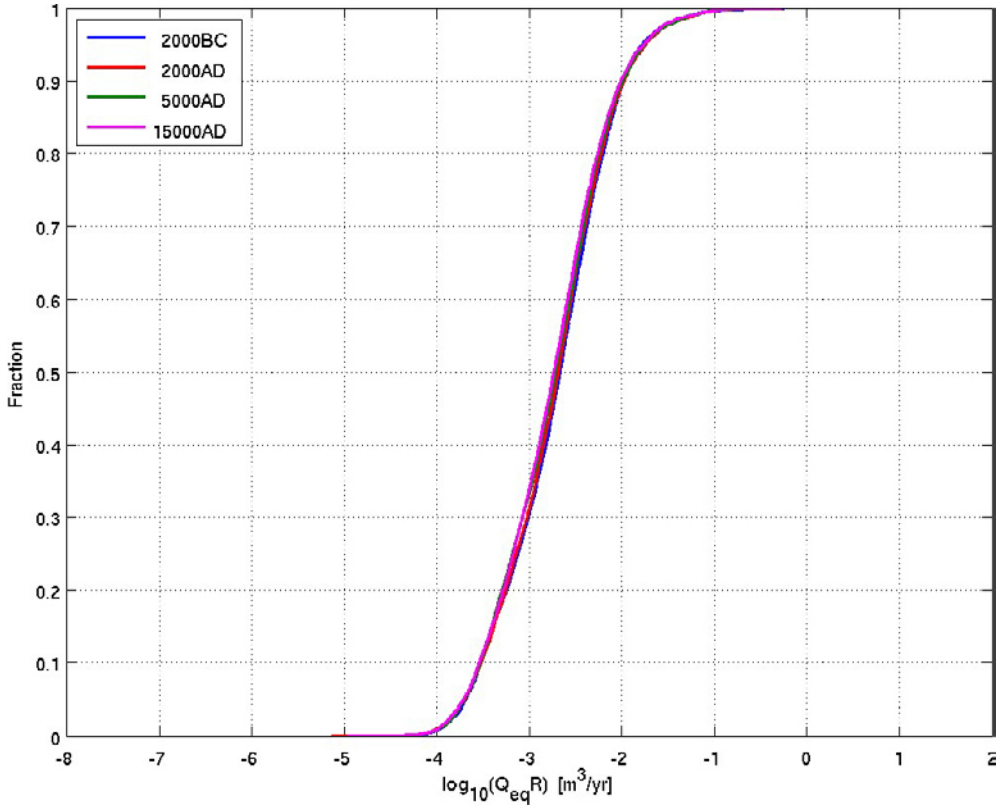

Figure C-12. *Normalised CDF plots of Q_{eqr} in the Hydrogeological base case model for the Q3 particles successfully reaching the model top boundary (~89%), released at the given times. The $Q_{eq}R$ axis corresponds to Q_{eqr} for the Q3 release locations.*

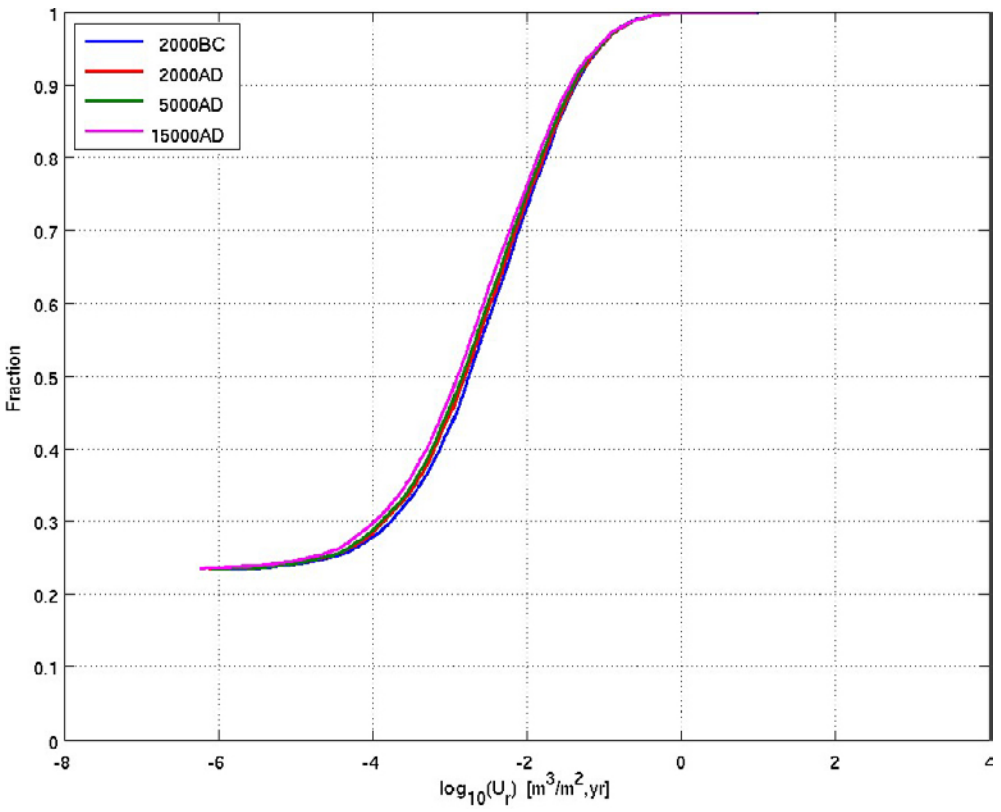

Figure C-13. *Non-normalised CDF plots of U_r in the Hydrogeological base case model for the 8,031 Q1 particles released at the given times.*

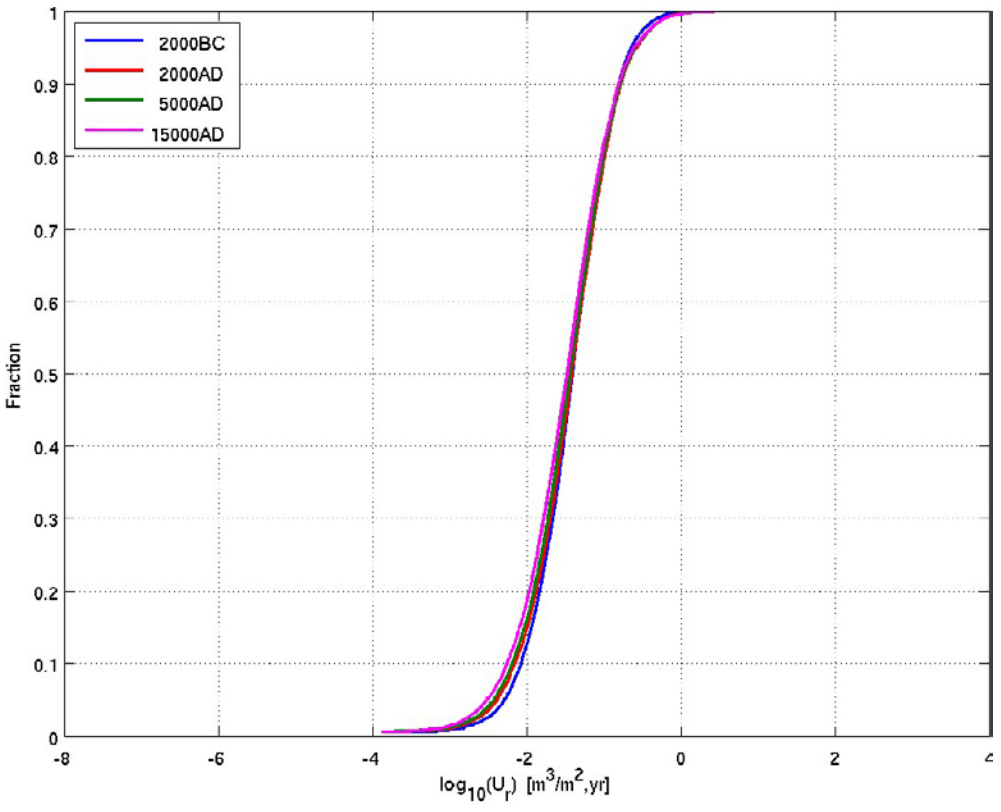

Figure C-14. *Non-normalised CDF plots of U_r in the Hydrogeological base case model for the 8,031 Q2 particles released at the given times.*

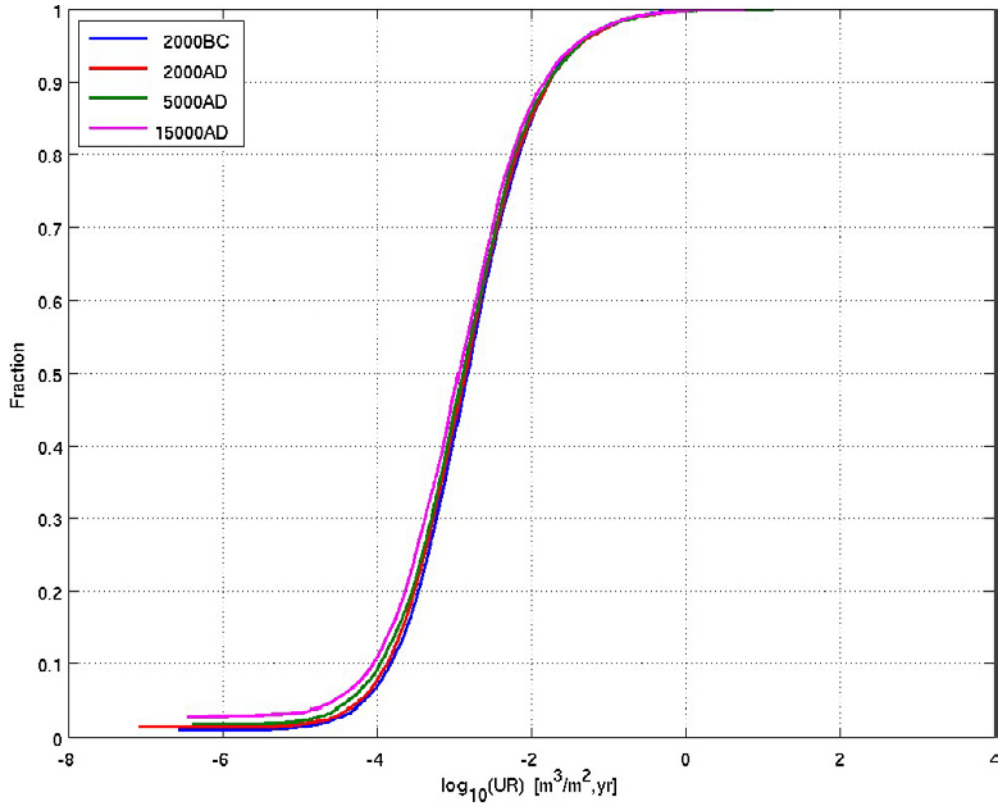

Figure C-15. *Non-normalised CDF plots of U_r in the Hydrogeological base case model for the 8,031 Q3 particles released at the given times. The UR axis corresponds to U_r for the Q3 release locations.*

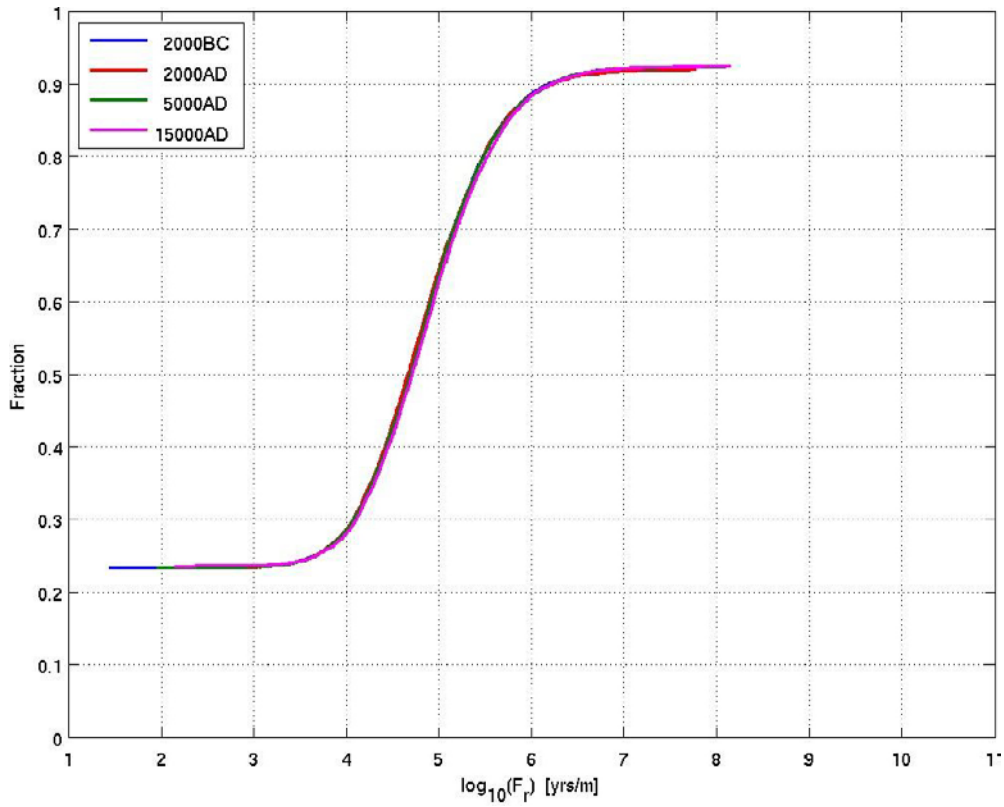

Figure C-16. *Non-normalised CDF plots of F_r in the Hydrogeological base case model for the 8,031 Q1 particles released at the given times.*

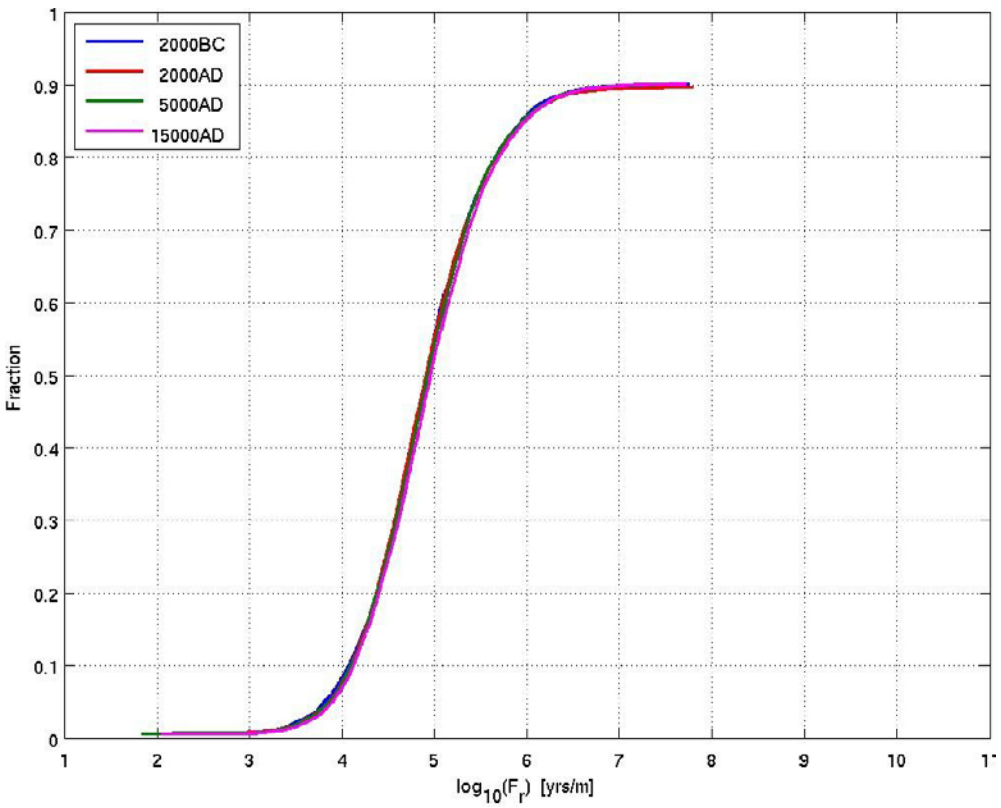

Figure C-17. *Non-normalised CDF plots of F_r in the Hydrogeological base case model for the 8,031 Q2 particles released at the given times.*

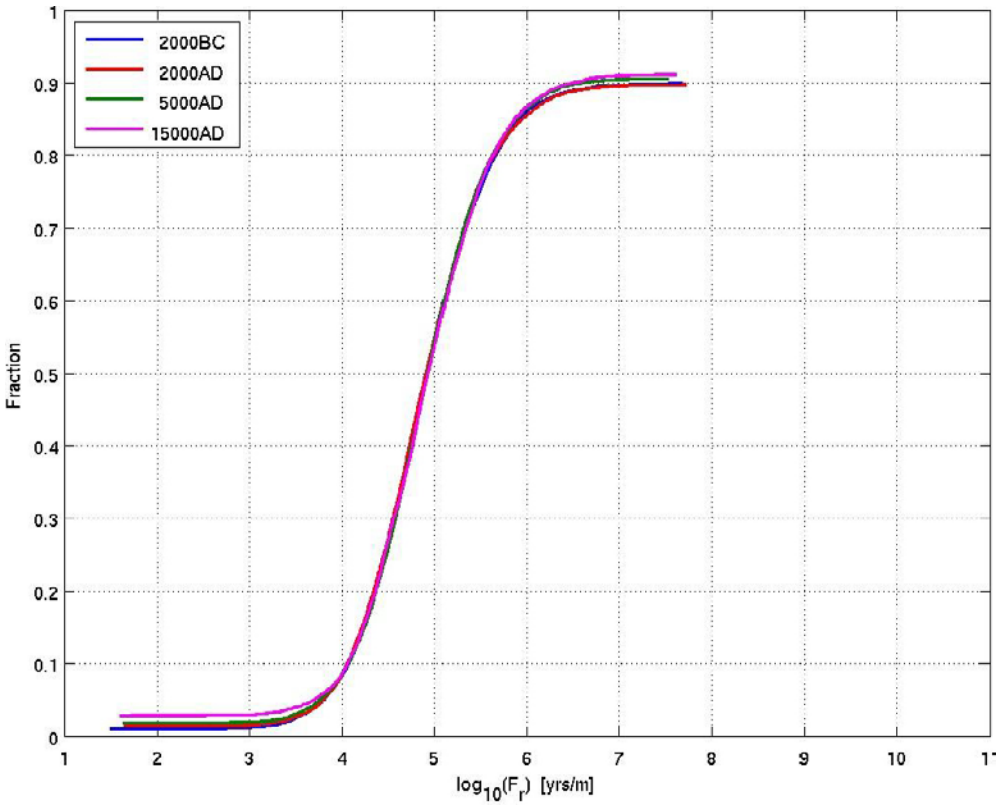

Figure C-18. *Non-normalised CDF plots of F_r in the Hydrogeological base case model for the 8,031 Q3 particles released at the given times.*

C.1.3 Spatial distribution of performance measures

Figure C-19 and Figure C-20 show the release locations of successful particles (those reaching the model boundaries) coloured by U_r and F_r respectively, for the 2000 AD release time. The U_r and F_r values calculated by the model vary across the repository.

The U_r plot shows that there are several of locations within the repository with relatively high fluxes, most notably within HRD_EW007. These correspond to locations near to deformation zones, suggesting that the U_r values can be strongly influenced by the proximity of major conducting features The converse, namely that locations near to deformation zones necessarily have relatively high fluxes is not apparent from the figure.

The F_r plots show that there are several of locations within the repository with relatively low flow-related transport resistance, most notably within HRD_EW007. They also correspond to locations near to deformation zones. This suggests that the F_r values are potentially strongly influenced by the proximity of major conducting features. The converse, namely that locations near to deformation zones necessarily have relatively low flow-related transport resistance is not apparent from the figure. There is little difference in the distribution of F_r values for the different release location types (Q1, Q2, Q3).

Plots showing discharge locations coloured by F_r is shown in Figure C-21 for the Q1, Q2 and Q3 release locations. This figure does not suggest any discharge regions are particularly associated with low F_r values.

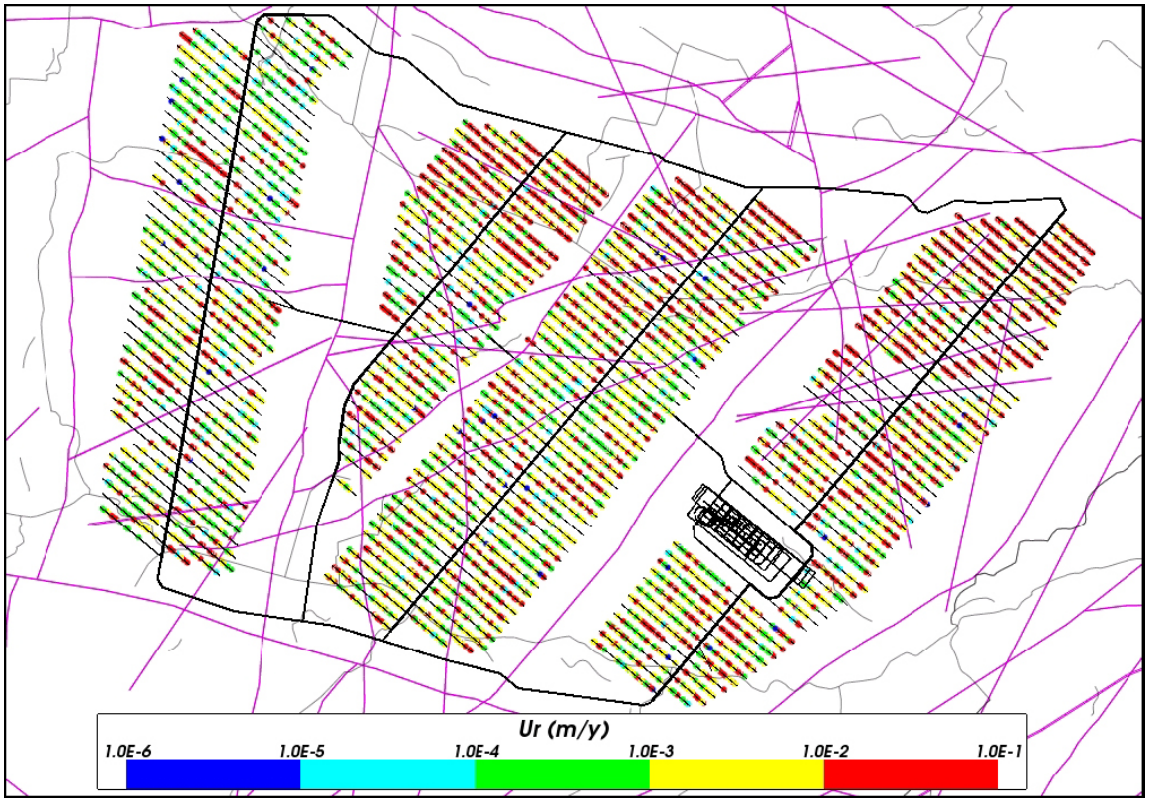

Figure C-19. *Starting locations coloured by $\log_{10}(U_r)$ for Q1 particles released at 2000 AD and successfully reaching the top boundary of the Hydrogeological base case model (69%). The deformation zones at z = –510m (purple), repository structures (black) and surface features (grey) are also shown.*

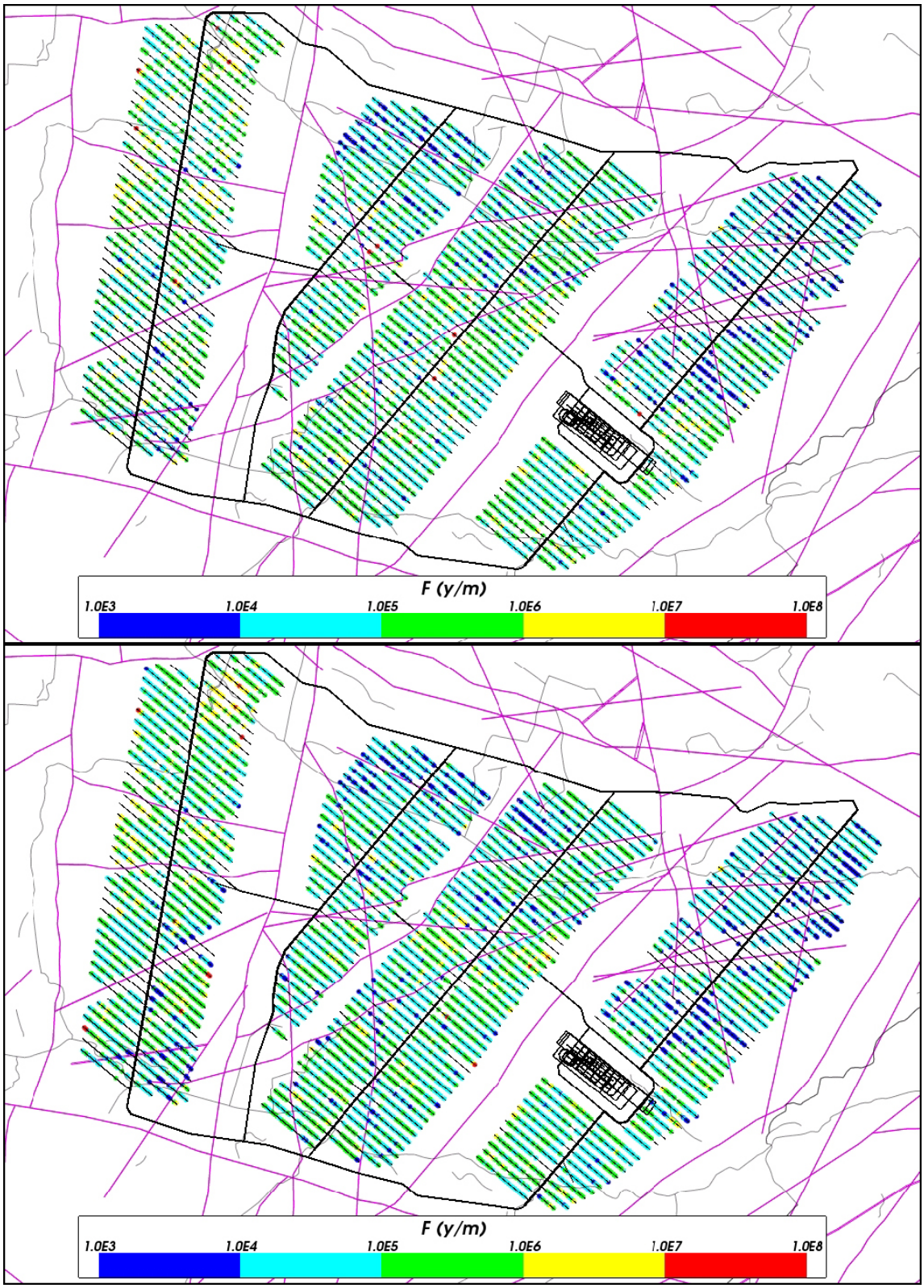
F (y/m)
1.0E3
1.0E4
1.0E5
1.0E6
1.0E7
1.0E8
F (y/m)
1.0E3
1.0E4
1.0E5
1.0E6
1.0E7
1.0E8

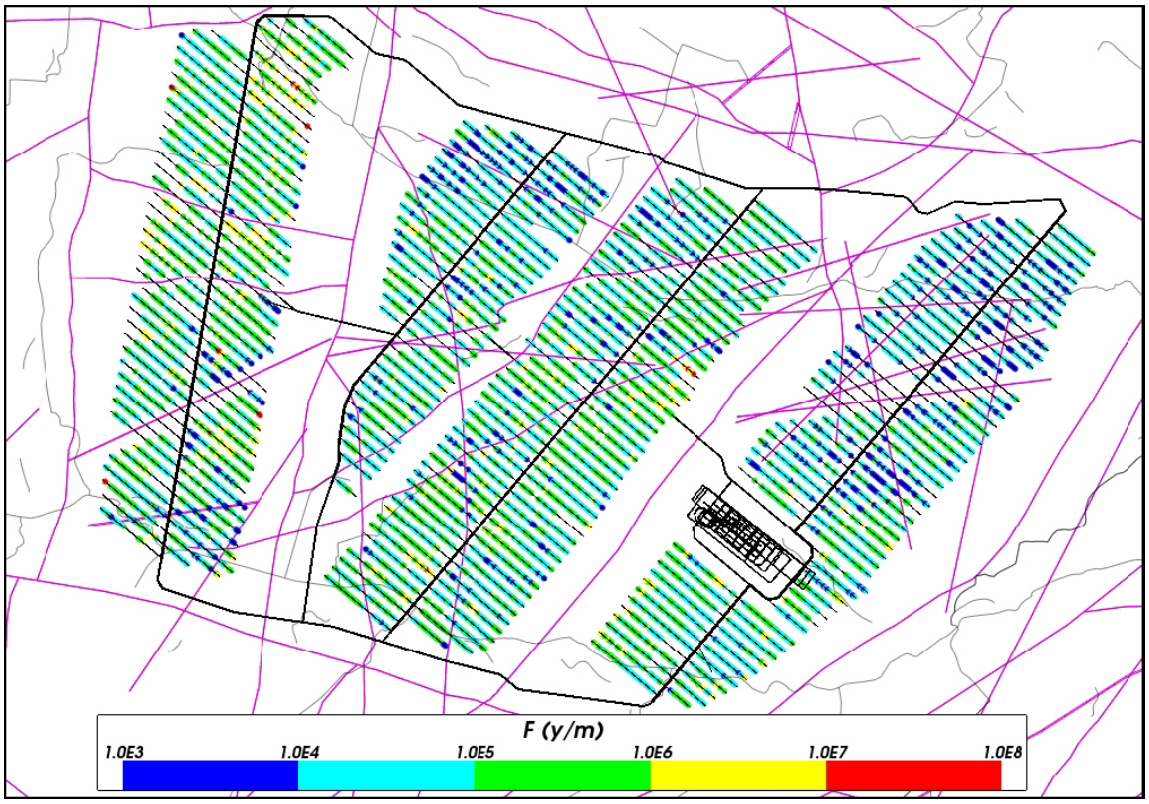

Figure C-20. *Starting locations coloured by $\log_{10}(F_r)$ for particles released at 2000 AD and successfully reaching the top boundary of the Hydrogeological base case model. From the top: Q1 (69%), Q2 (89%) and Q3 (88%) release locations. The deformation zones at z = –510 m (purple), repository structures (black) and surface features (grey) are also shown.*

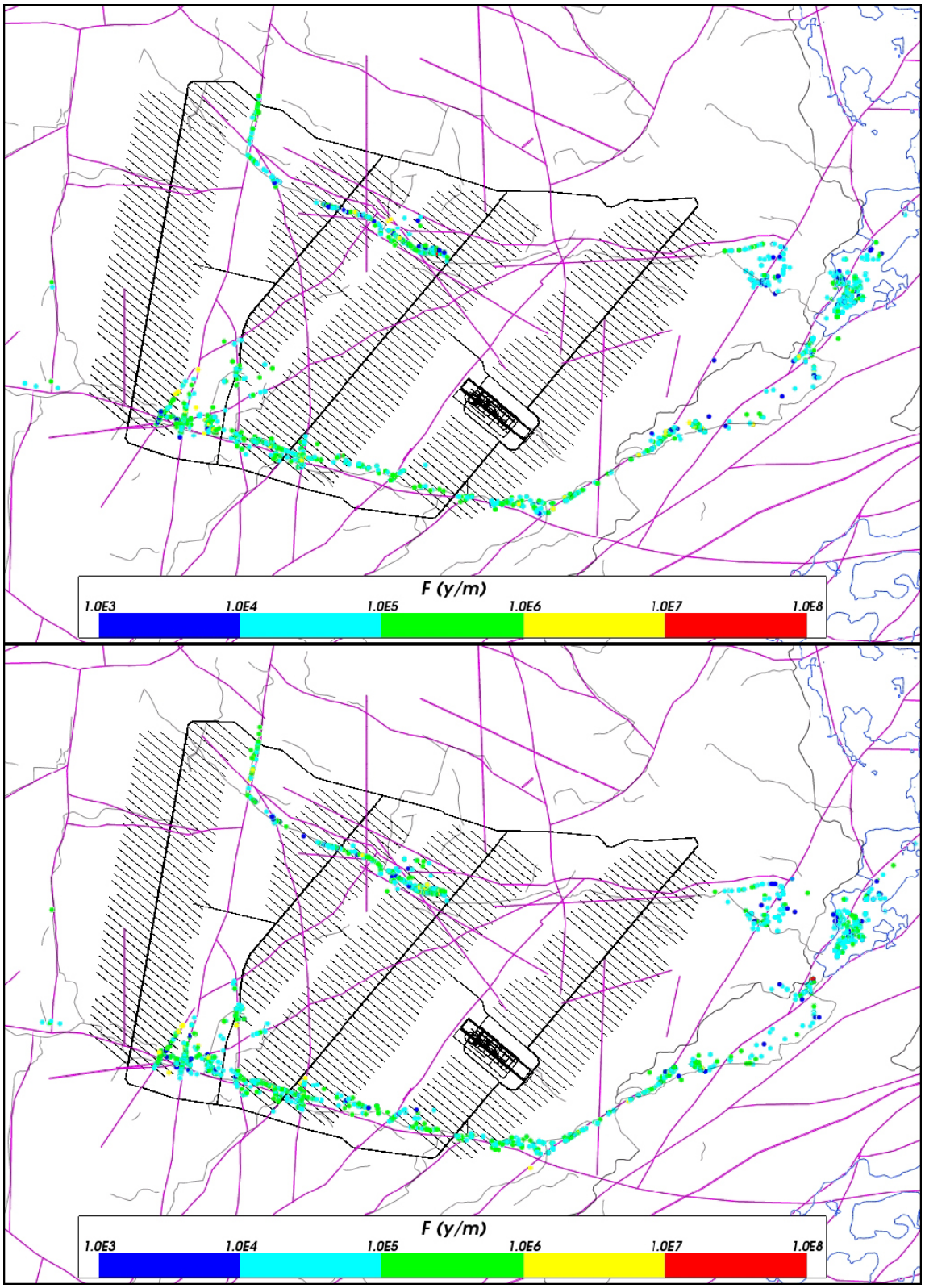
F (y/m)
1.0E3
1.0E4
1.0E5
1.0E6
1.0E7
1.0E8
F (y/m)
1.0E3
1.0E4
1.0E5
1.0E6
1.0E7
1.0E8

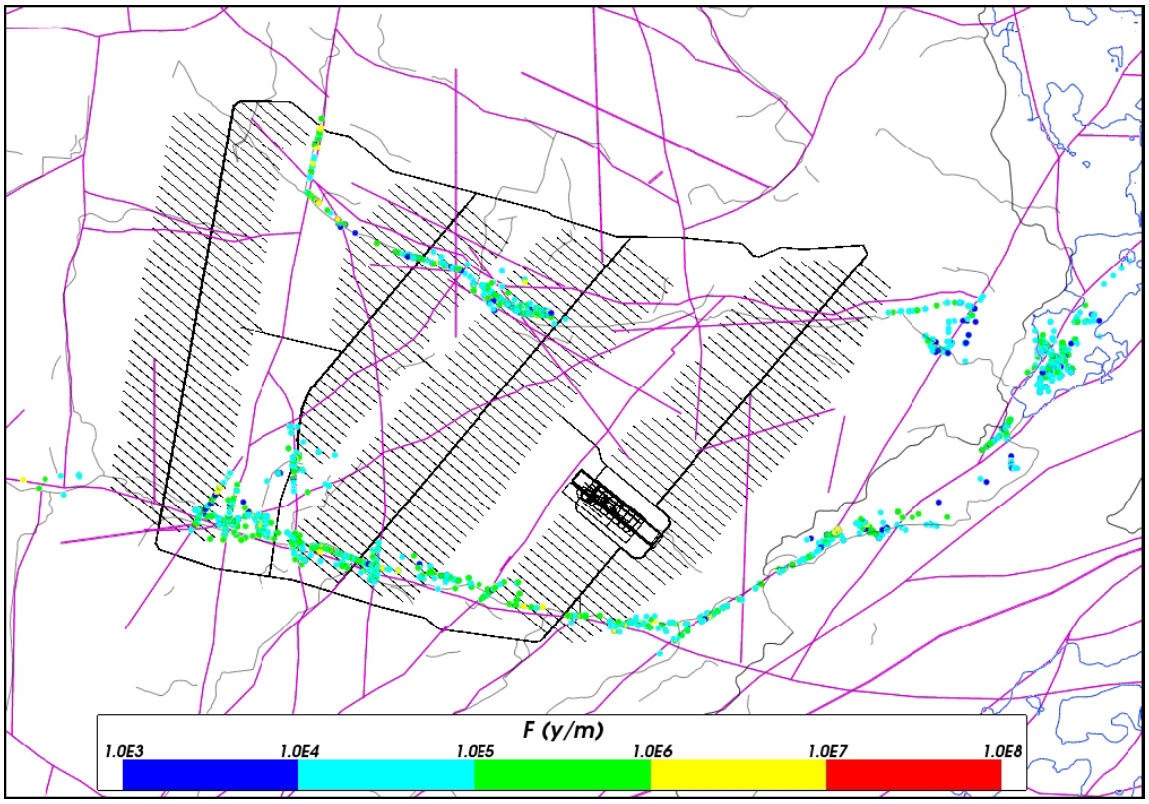

Figure C-21. *Exit locations coloured by $\log_{10}(F_r)$ for particles released at 2000 AD and successfully reaching the top boundary of the Hydrogeological base case model. From the top: Q1 (68%), Q2 (89%) and Q3 (88%) release locations. The deformation zones at z = –50 m (purple), shoreline at 2000 AD (blue) and surface features (grey) are also shown.*

C.1.4 Additional realisation

The distributions of U_r and F_r for an additional realisation of the Hydrogeological base case model are shown in Figure C-22 to Figure C-27. The results suggest that the distributions of both performance measures do not change significantly between the two stochastic realisations of the HRD. It also suggests that introducing heterogeneity to the HCD does not have a significant impact on performance measures.

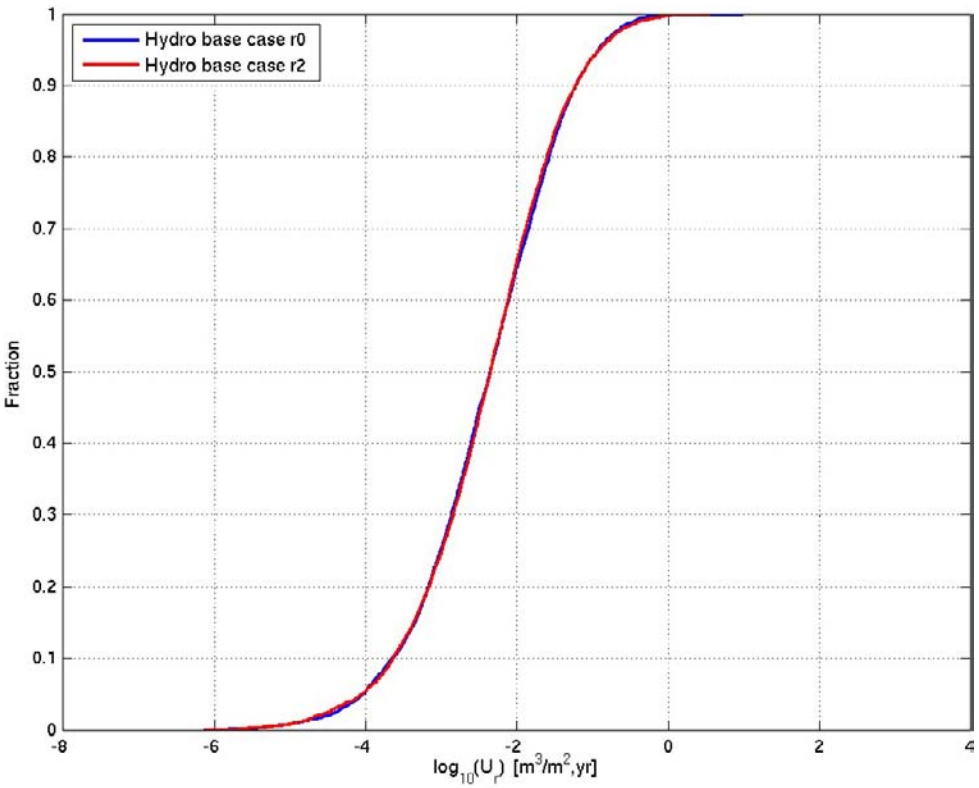

Figure C-22. *Normalised CDF plots of U_r in the Hydrogeological base case model (r0) and one additional stochastic realisation of the HCD and HRD (r2) for the Q1 particles successfully reaching the model top boundary (~69%).*

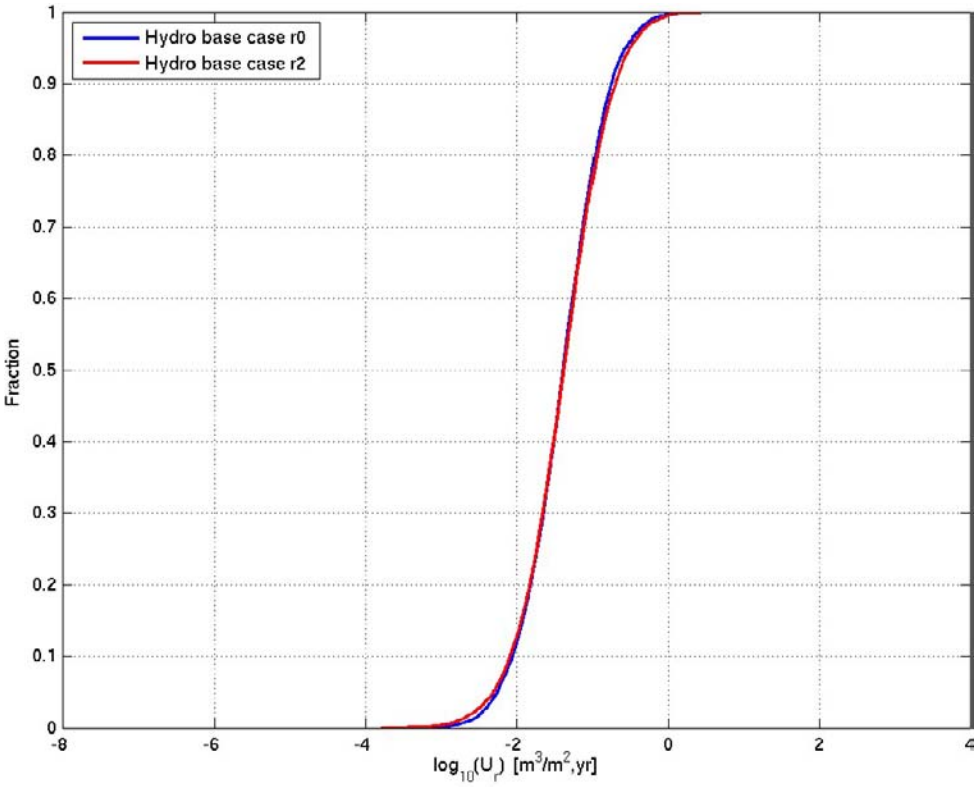

Figure C-23. *Normalised CDF plots of U_r in the Hydrogeological base case model (r0) and one additional stochastic realisation of the HCD and HRD (r2) for the Q2 particles successfully reaching the model top boundary (~89%).*

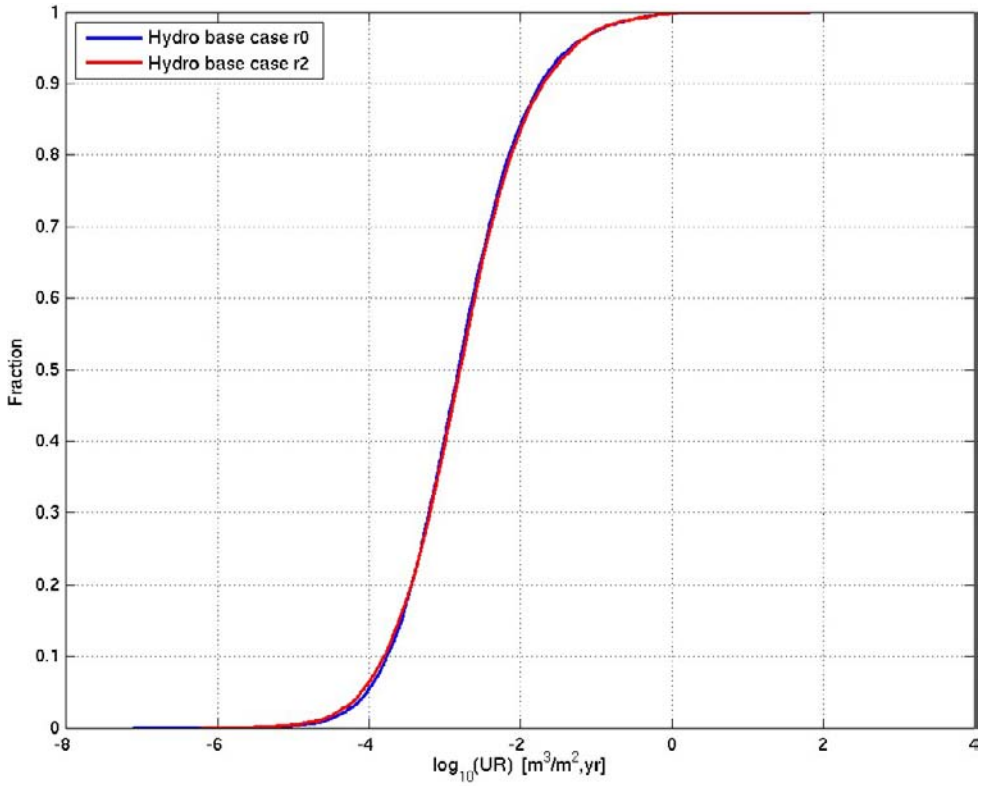

Figure C-24. *Normalised CDF plots of U_r in the Hydrogeological base case model (r0) and one additional stochastic realisation of the HCD and HRD (r2) for the Q3 particles successfully reaching the model top boundary (~88%). The UR axis corresponds to U_r for the Q3 release locations.*

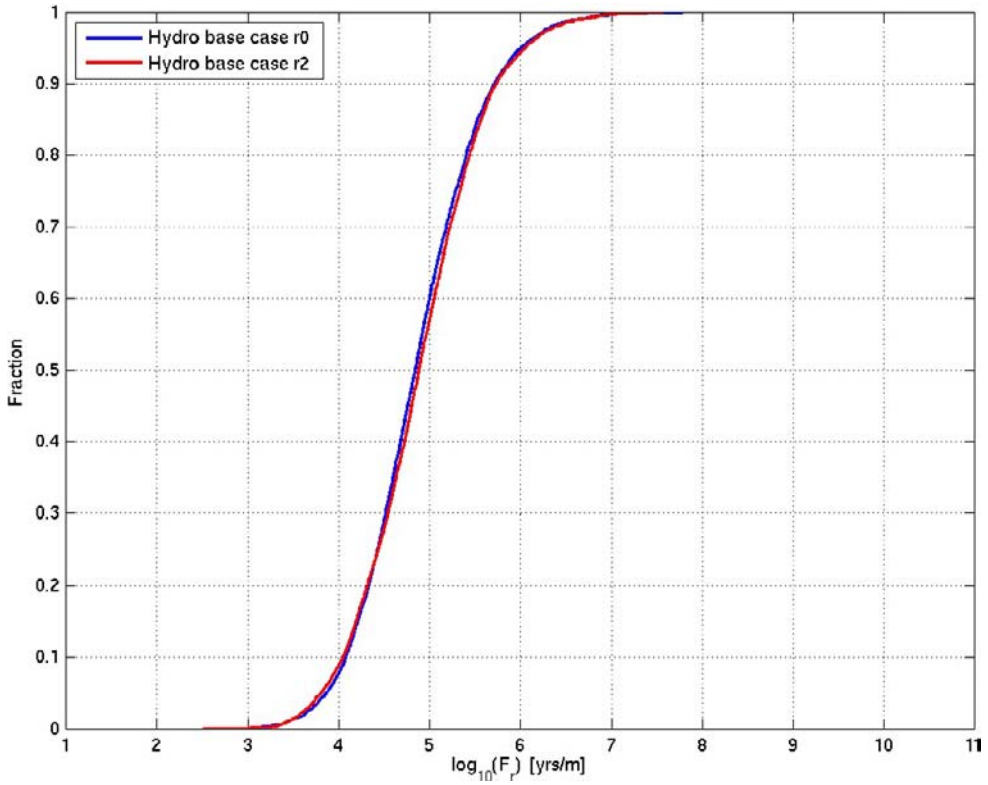

Figure C-25. *Normalised CDF plots of F_r in the Hydrogeological base case model (r0) and one additional stochastic realisation of the HCD and HRD (r2) for the Q1 particles successfully reaching the model top boundary (~69%).*

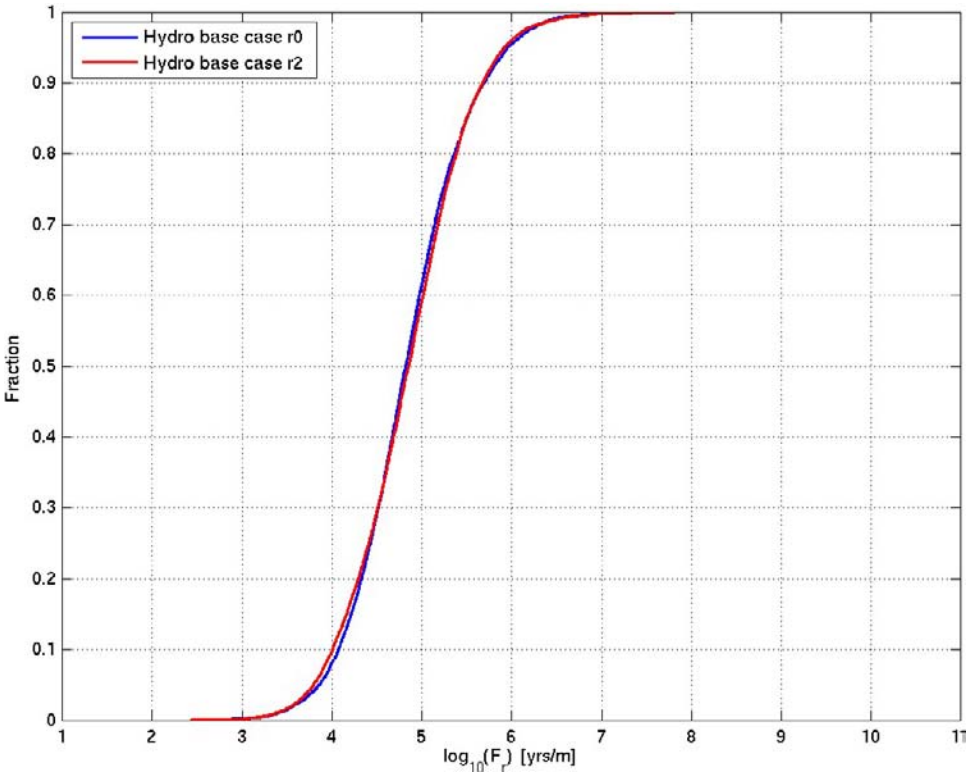

Figure C-26. *Normalised CDF plots of F_r in the Hydrogeological base case model (r0) and one additional stochastic realisation of the HCD and HRD (r2) for the Q2 particles successfully reaching the model top boundary (~89%).*

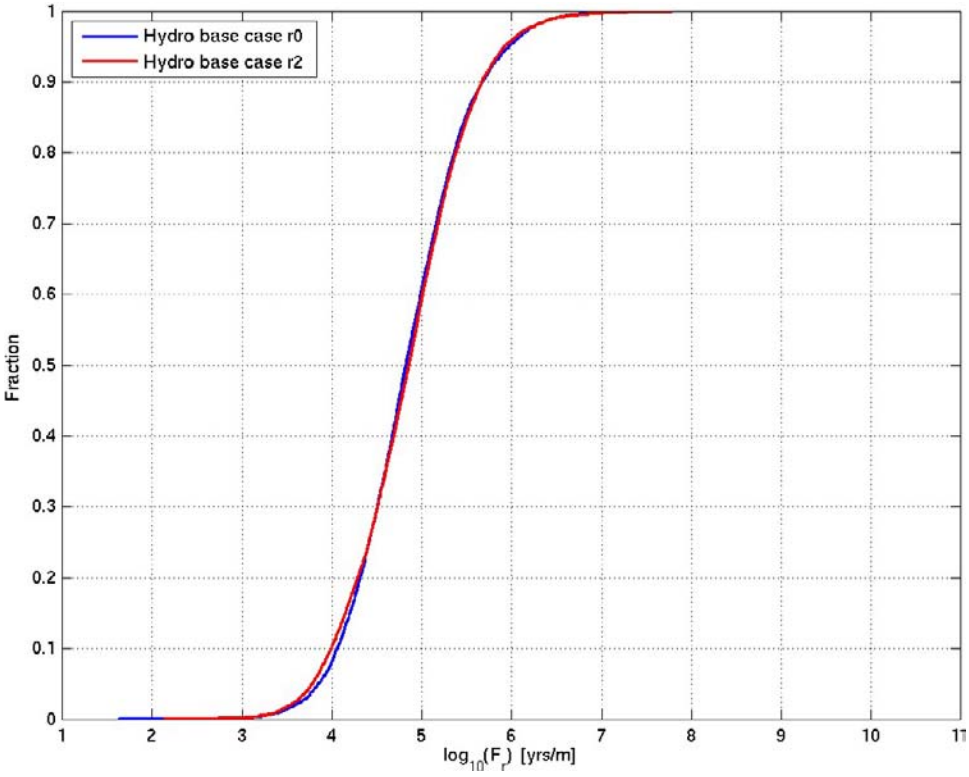

Figure C-27. *Normalised CDF plots of F_r in the Hydrogeological base case model (r0) and one additional stochastic realisation of the HCD and HRD (r2) for the Q3 particles successfully reaching the model top boundary (~88%).*

C.2 Elaborated Hydro-DFN model

Maps of discharge locations for Q2 releases are shown in Figure C-28 for both realisations of the model, for a release at 2000 AD. These figures show that the discharge locations are similar between realisations, and similar to the results calculated by the Hydrogeological base case. The discharge locations are strongly influenced by the locations of outcropping deformation zones, which are the same for the two cases.

Performance measures for two realisations of the Elaborated Hydro-DFN are shown in Figure C-29 to Figure C-37. These figures also show results for both realisations of the Hydrogeological base case for comparison.

The figures suggest that there is no significant difference between the two realisations of the Elaborated Hydro-DFN in terms of the distributions of U_r, F_r, or Q_{eqr}. There are, however, significant differences between the distributions of the performance measures calculated by the Elaborated Hydro-DFN compared to the Hydrogeological base case. There are also differences between the different release location types (Q1, Q2, Q3) for both cases.

The median values of U_r calculated by the Elaborated Hydro-DFN models are around a factor of three lower than those calculated by the Hydrogeological base case, with a value of approximately 0.001 m/y for the Q1 locations. The 90 percentile value is also approximately a factor of three lower, with a value of approximately 0.03 m/y for the Q1 locations. The differences between cases for the Q2 release locations are less and the U_r values are higher than for Q1, due to a relatively high and continuous EDZ transmissivity of $1 \cdot 10^{-8}$ m^2/s which is the same for both cases. The Q3 release locations show a tail with high U_r values for both cases, which is more likely to be a feature of the Q3 pathways because particles travel along a tunnel until the advective flow carries them in to a fracture, which is likely to be a significant flowing structure.

The median values of F_r calculated by the Elaborated Hydro-DFN models are around a factor of two higher than those calculated by the Hydrogeological base case, with a value of approximately 200,000 y/m for all release location types. The 10 percentile value is approximately a factor of two higher, with a value of approximately 20,000 y/m. The difference between the cases is greatest for the higher F_r values. The Q3 paths for both cases seem to have a tail with some very low F_r values. Again this is more likely to be a feature of Q3 pathways as particles tend to exit the tunnel into larger fractures with good connectivity to the surface.

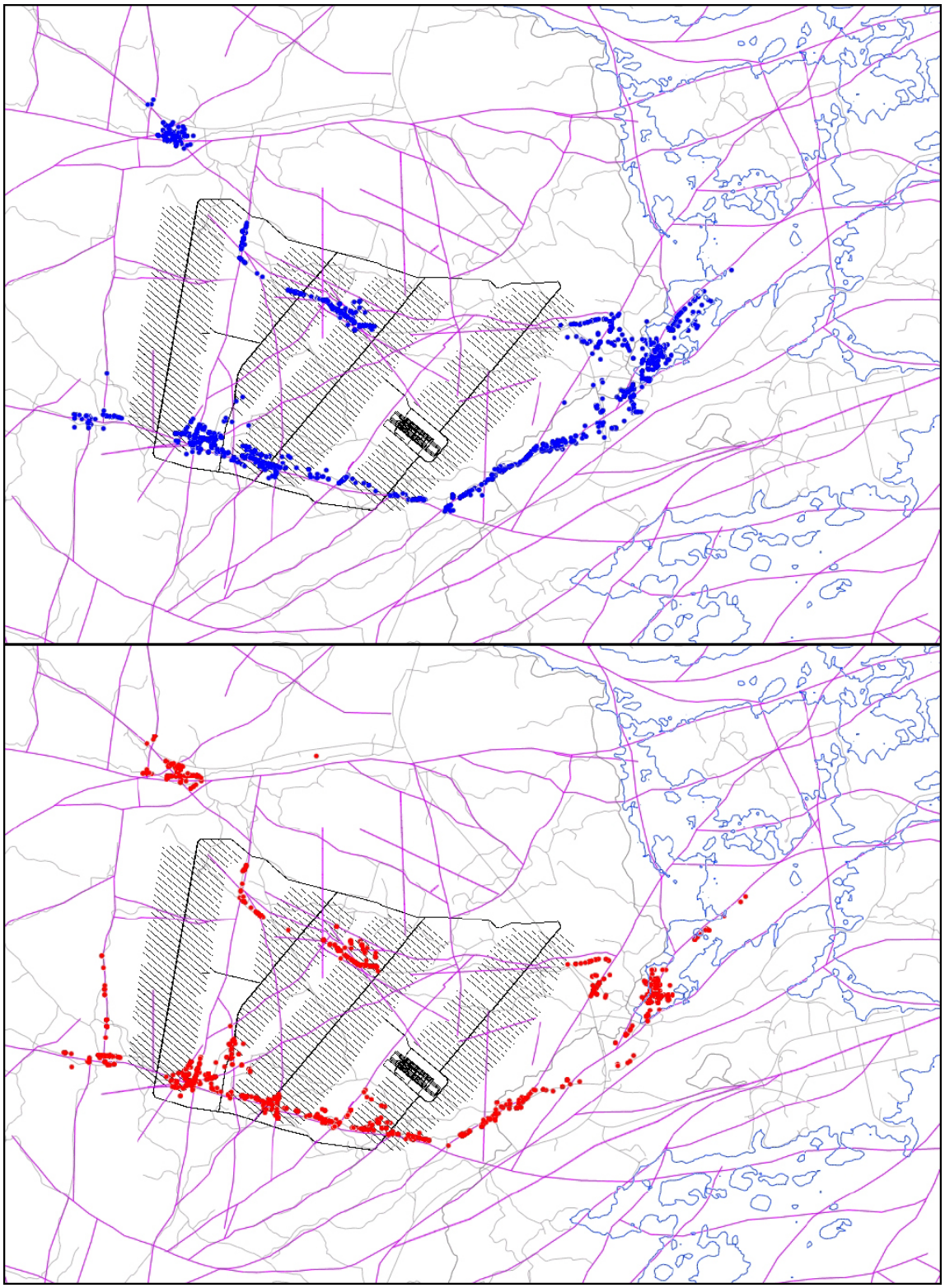

Figure C-28. *Exit locations for the Q2 particles successfully reaching the top boundary of the Elaborated Hydro-DFN model (85%–87%), released at 2000 AD. Top: realisation r0 (dark blue). Bottom: realisation r2 (red). Also shown are the deformation zones at z = –50 m (purple), surface features (grey) and the shoreline at 2000 AD (blue).*

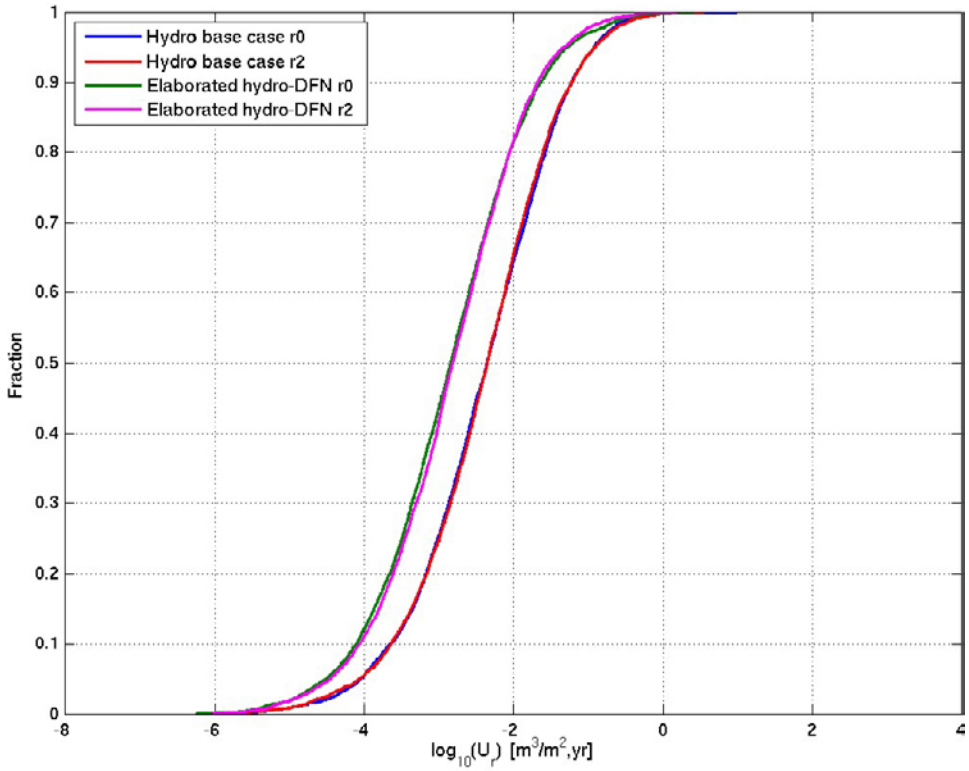

Figure C-29. *Normalised CDF plots of U_r in the Hydrogeological base case model and the Elaborated Hydro-DFN model, including one additional realisation of each, for the Q1 particles successfully reaching the model top boundary (60%–69%) released at 2000 AD.*

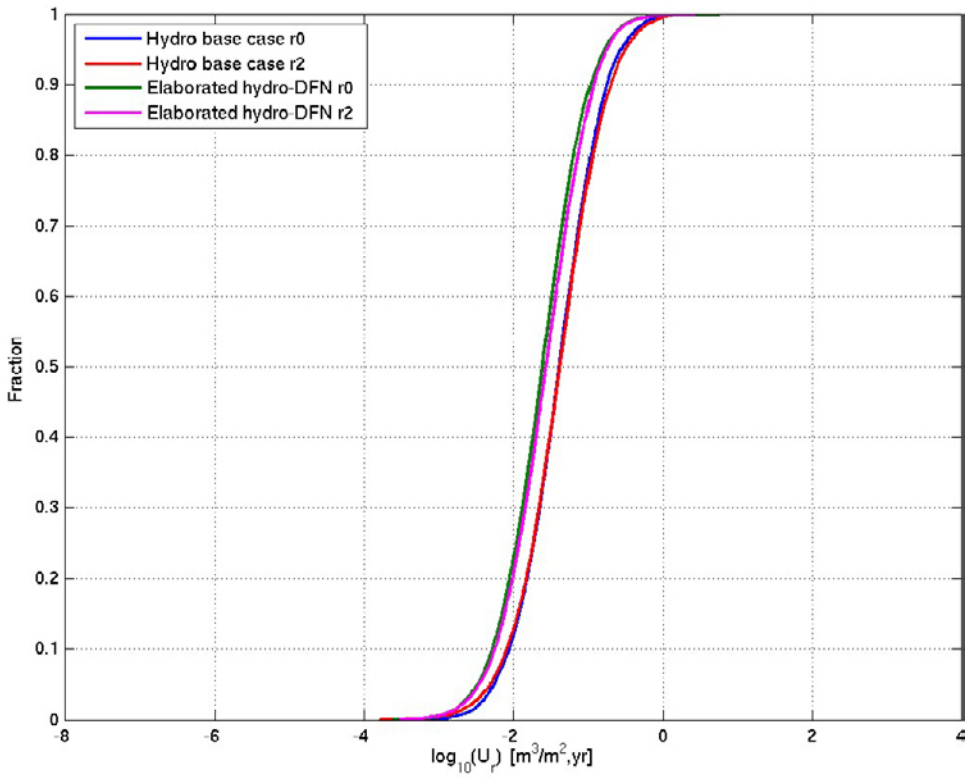

Figure C-30. *Normalised CDF plots of U_r in the Hydrogeological base case model and the Elaborated Hydro-DFN model, including one additional realisation of each, for the Q2 particles successfully reaching the model top boundary (86%–89%) released at 2000 AD.*

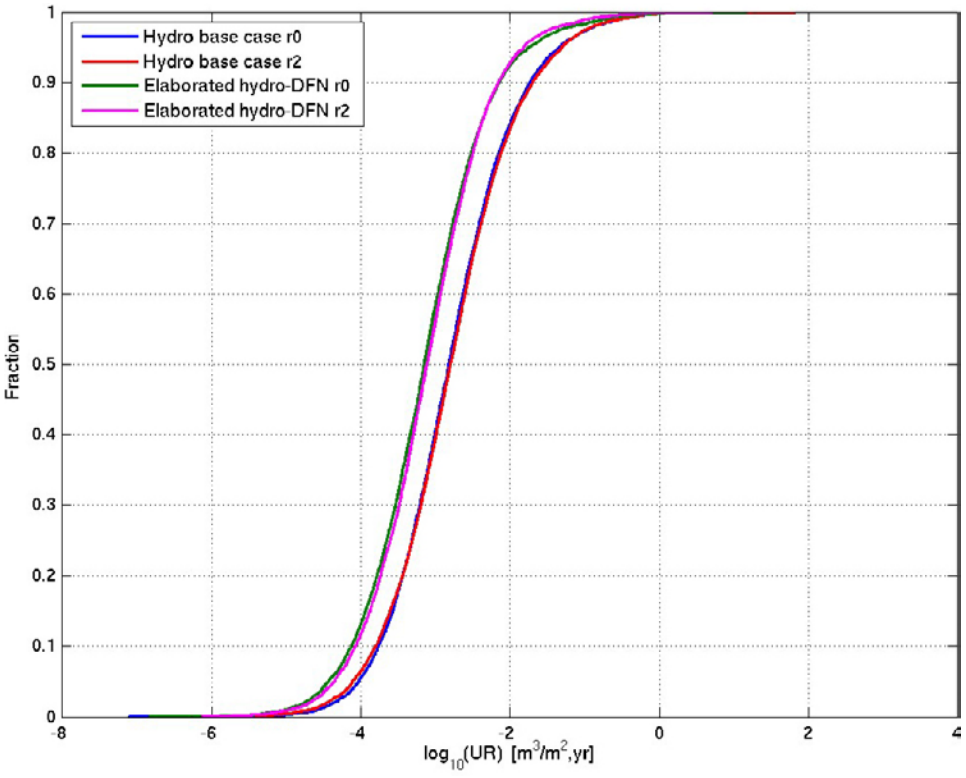

Figure C-31. *Normalised CDF plots of U_r in the Hydrogeological base case model and the Elaborated Hydro-DFN model, including one additional realisation of each, for the Q3 particles successfully reaching the model top boundary (85%–88%) released at 2000 AD. The UR axis corresponds to U_r for the Q3 release locations.*

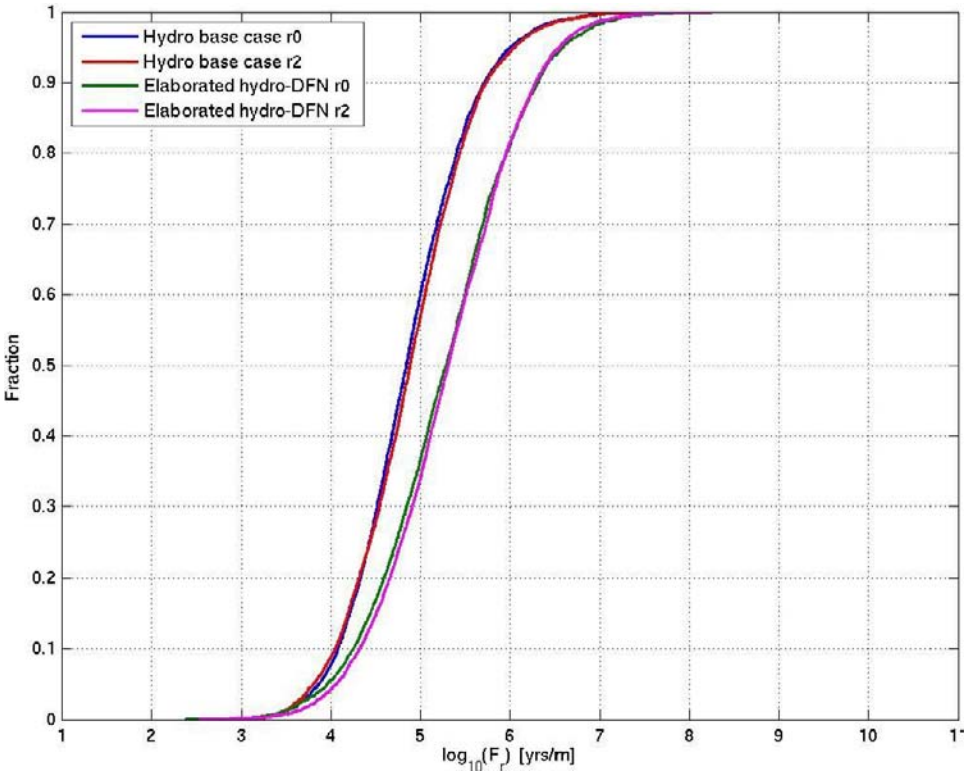

Figure C-32. *Normalised CDF plots of F_r in the Hydrogeological base case model and the Elaborated Hydro-DFN model, including one additional realisation of each, for the Q1 particles successfully reaching the model top boundary (60%–69%) released at 2000 AD.*

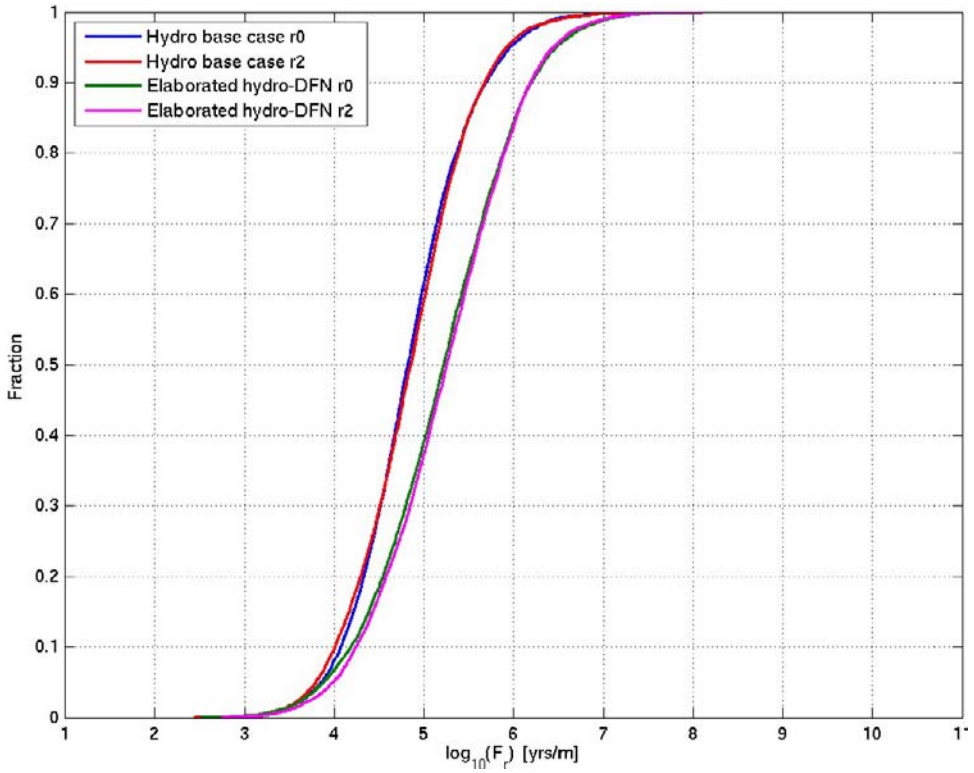

Figure C-33. *Normalised CDF plots of F_r in the Hydrogeological base case model and the Elaborated Hydro-DFN model, including one additional realisation of each, for the Q2 particles successfully reaching the model top boundary (86%–89%) released at 2000 AD.*

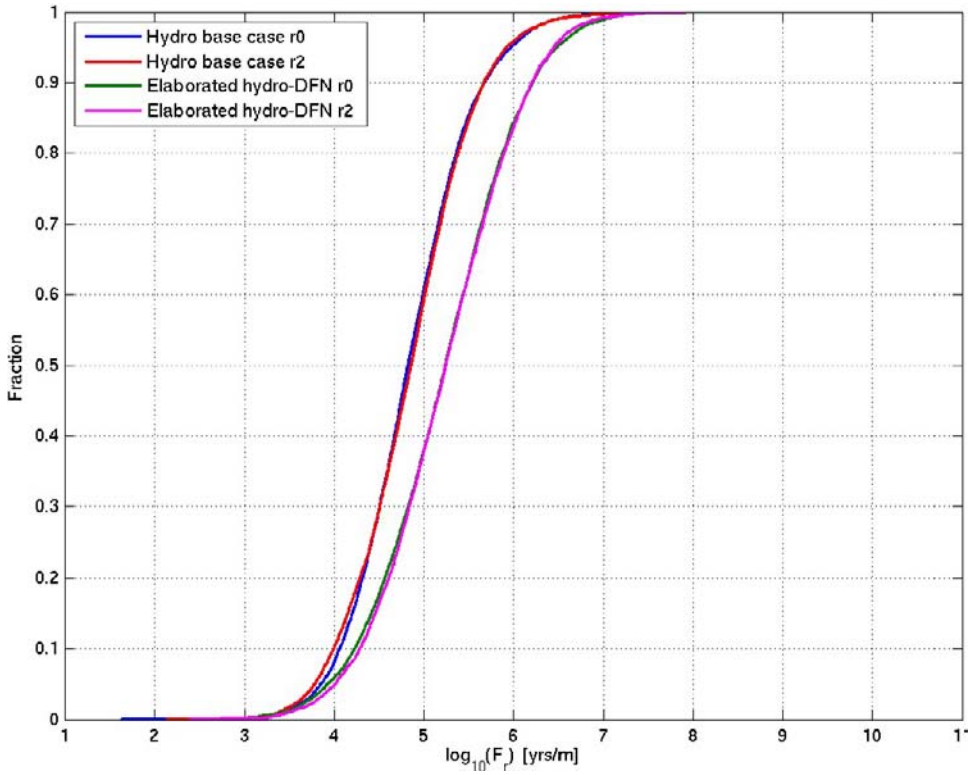

Figure C-34. *Normalised CDF plots of F_r in the Hydrogeological base case model and the Elaborated Hydro-DFN model, including one additional realisation of each, for the Q3 particles successfully reaching the model top boundary (85%–88%) released at 2000 AD.*

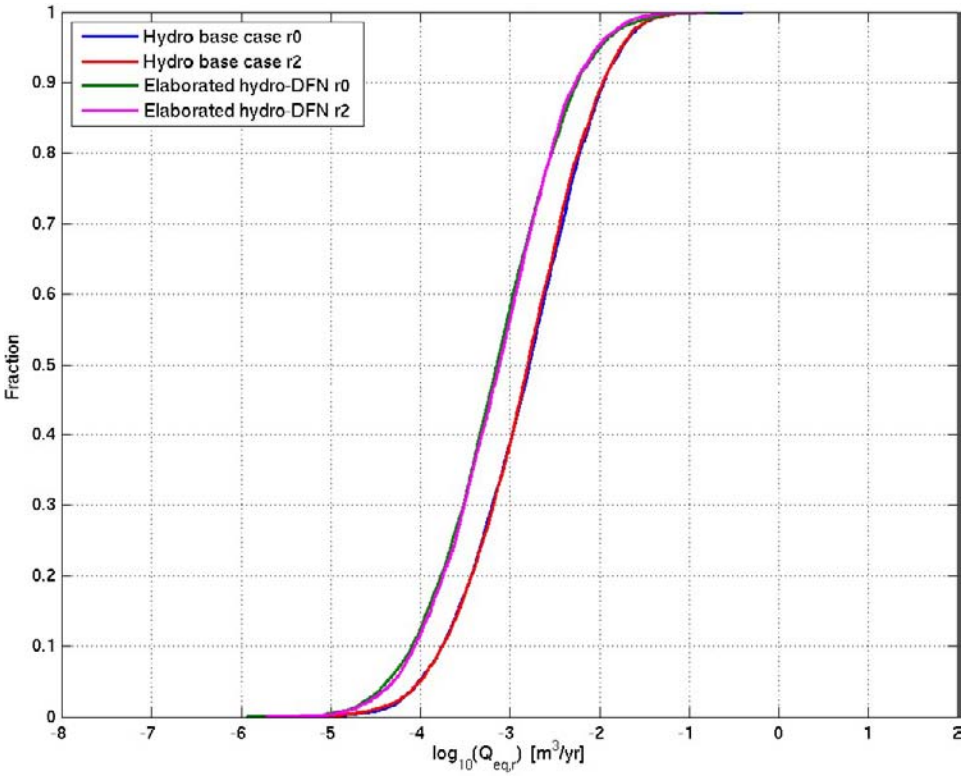

Figure C-35. *Normalised CDF plots of Q_{eqr} in the Hydrogeological base case model and the Elaborated Hydro-DFN model, including one additional realisation of each, for the Q1 particles successfully reaching the model top boundary (60%–69%) released at 2000 AD.*

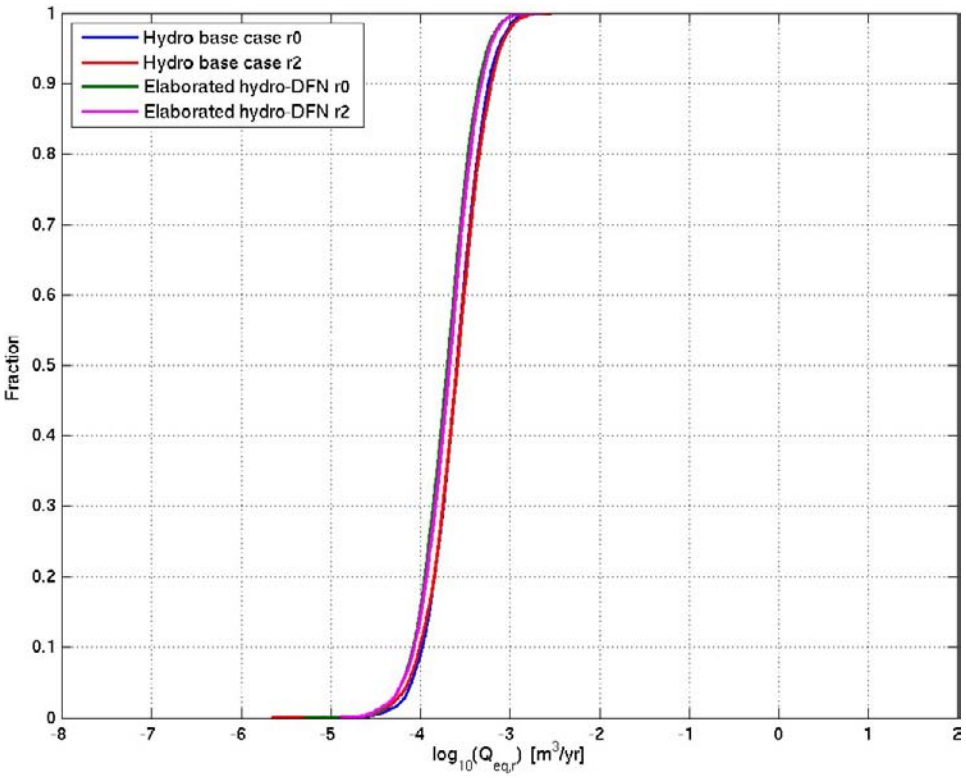

Figure C-36. *Normalised CDF plots of Q_{eqr} in the Hydrogeological base case model and the Elaborated Hydro-DFN model, including one additional realisation of each, for the Q2 particles successfully reaching the model top boundary (86%–89%) released at 2000 AD.*

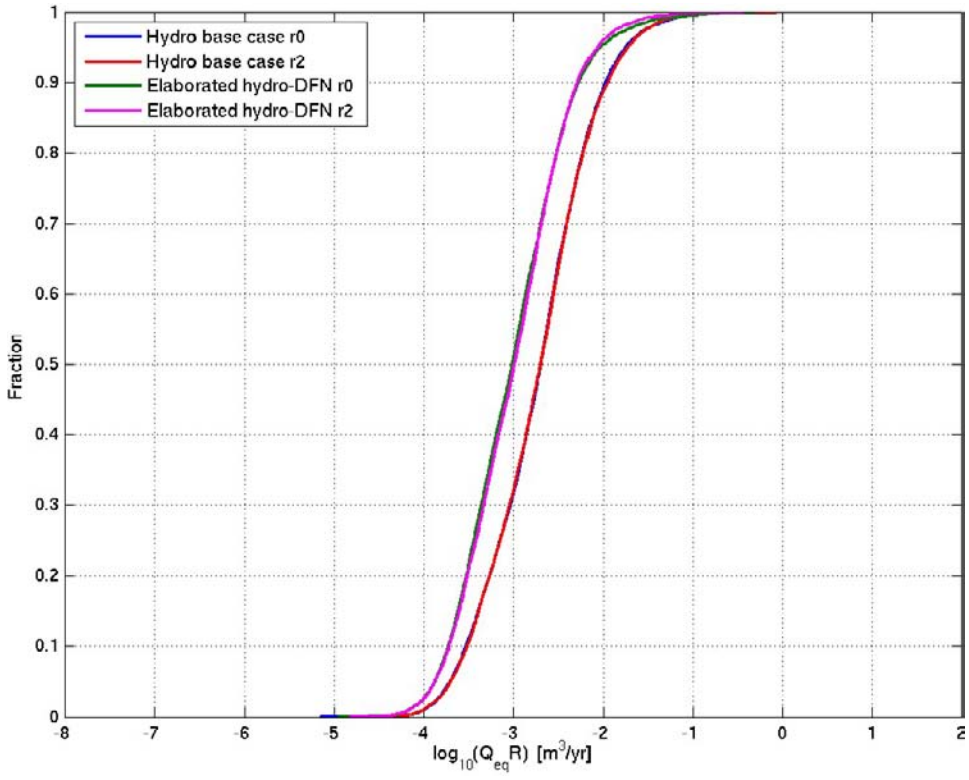

Figure C-37. *Normalised CDF plots of Q_{eqr} in the Hydrogeological base case model and the Elaborated Hydro-DFN model, including one additional realisation of each, for the Q3 particles successfully reaching the model top boundary (85%–88%) released at 2000 AD. The $Q_{eq}R$ axis corresponds to Q_{eqr} for the Q3 release locations.*

C.3 Elaborated Hydro-DFN model with no minor deformation zones model

Particle discharge locations for the Elaborated Hydro-DFN model with no minor deformation zones for Q2 particles released at 2000 AD are shown in Figure C-38. Normalised CDF plots of performance measures are shown in Figure C-39 to Figure C-44. The CDF plots also show results for both realisations of the Elaborated Hydro-DFN for comparison. The figures suggest that the minor deformation zones have little effect on the particle discharge locations or the performance measures at 2000 AD.

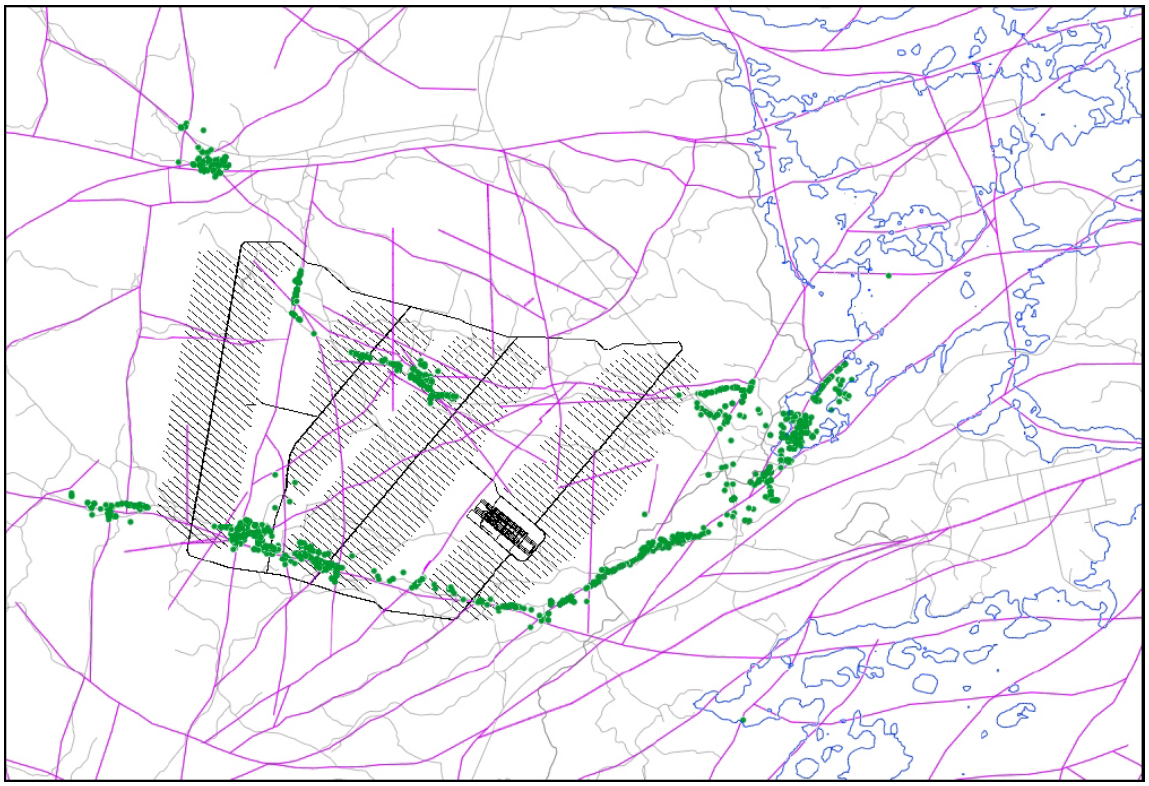

Figure C-38. *Exit locations for the Q2 particles successfully reaching the top boundary of the Elaborated Hydro-DFN model with No MDZs (85%), released at 2000 AD. Also shown are the deformation zones at z = –50 m (purple), surface features (grey) and the shoreline at 2000 AD (blue).*

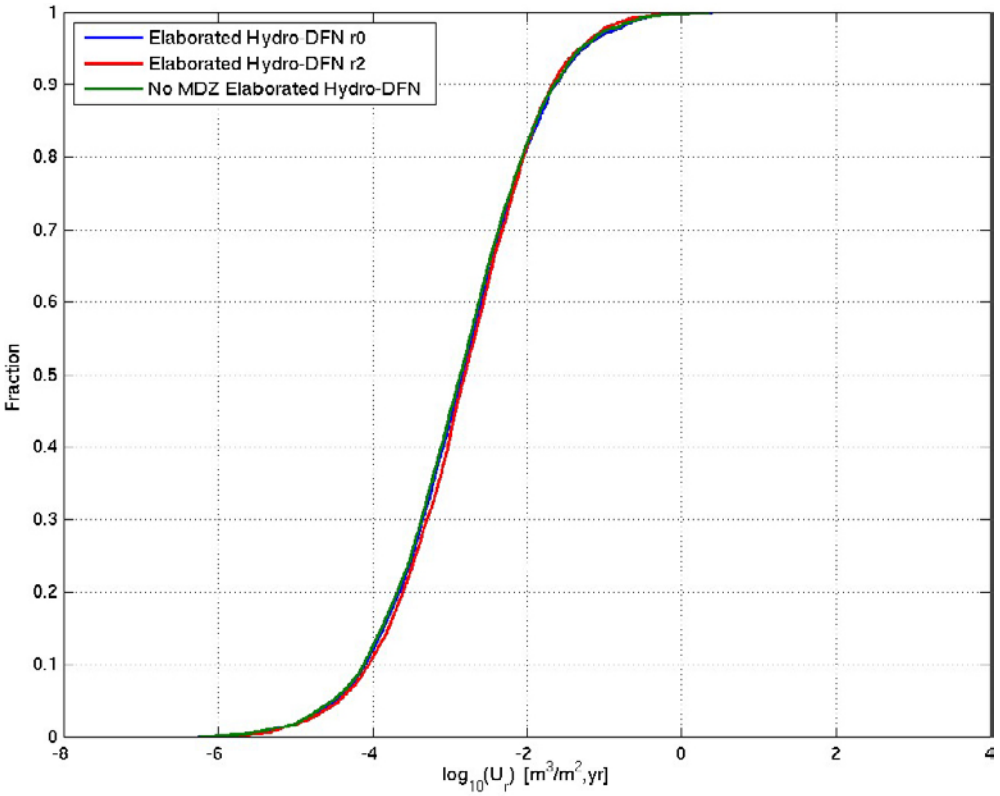

Figure C-39. *Normalised CDF plots of U_r in the Elaborated Hydro-DFN model, including one additional realisation and the case with no MDZs, for the Q1 particles successfully reaching the model top boundary (59%–61%), released at 2000 AD.*

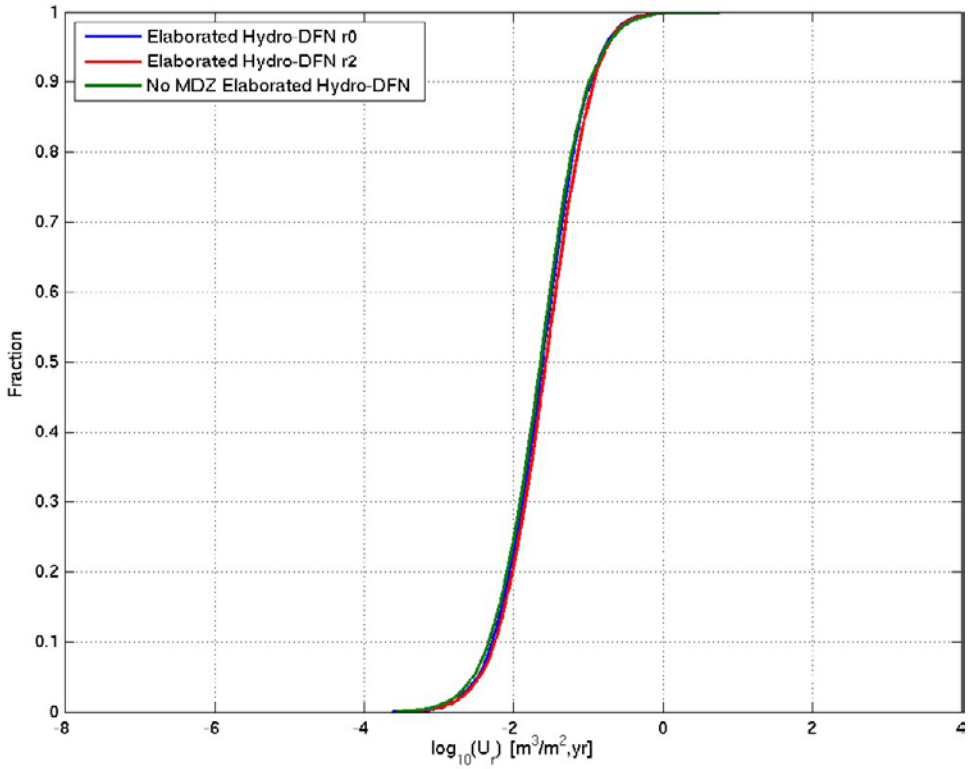

Figure C-40. *Normalised CDF plots of U_r in the Elaborated Hydro-DFN model, including one additional realisation and the case with no MDZs, for the Q2 particles successfully reaching the model top boundary (85%–87%), released at 2000 AD.*

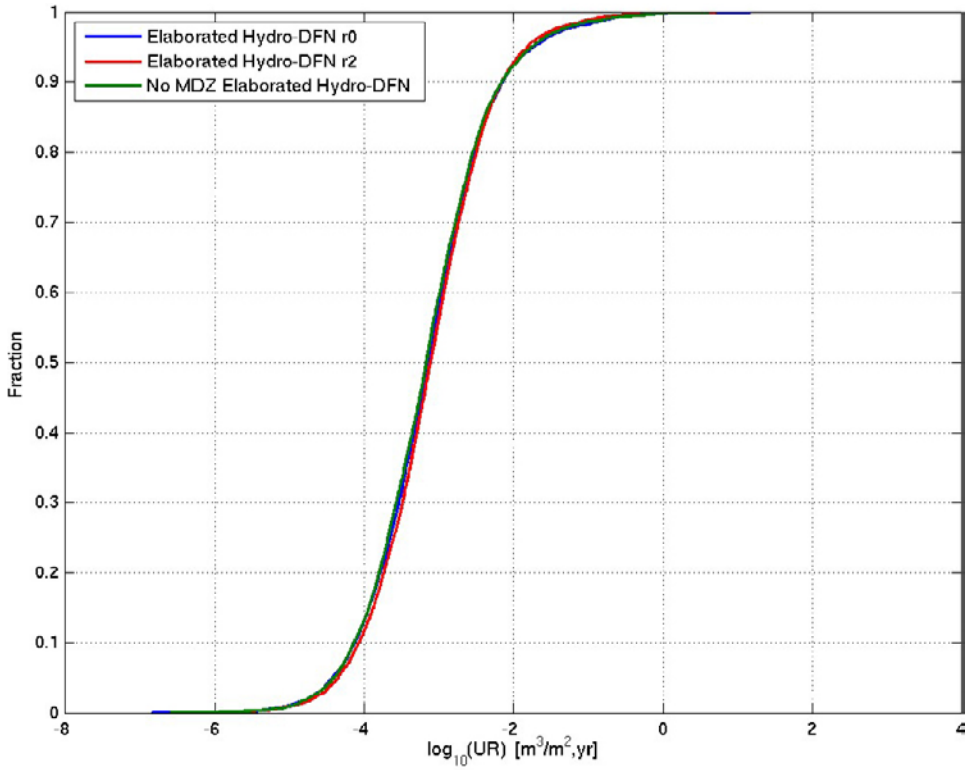

Figure C-41. *Normalised CDF plots of U_r in the Elaborated Hydro-DFN model, including one additional realisation and the case with no MDZs, for the Q3 particles successfully reaching the model top boundary (83%–86%), released at 2000 AD. The UR axis corresponds to U_r for the Q3 release locations.*

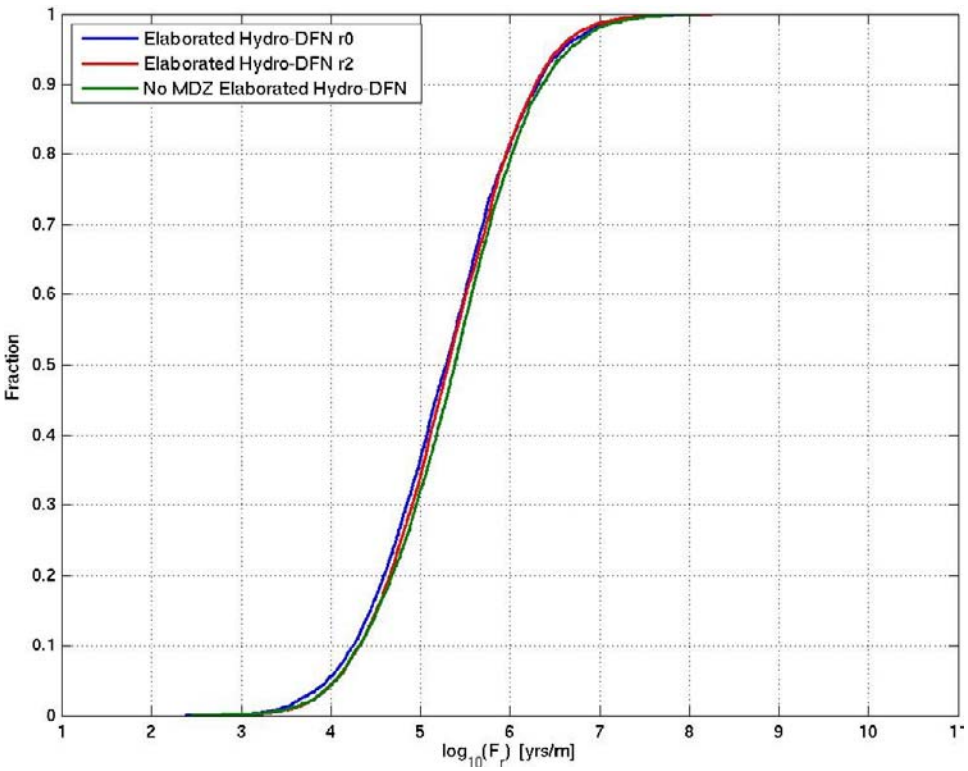

Figure C-42. *Normalised CDF plots of F_r in the Elaborated Hydro-DFN model, including one additional realisation and the case with no MDZs, for the Q1 particles successfully reaching the model top boundary (59%–61%), released at 2000 AD.*

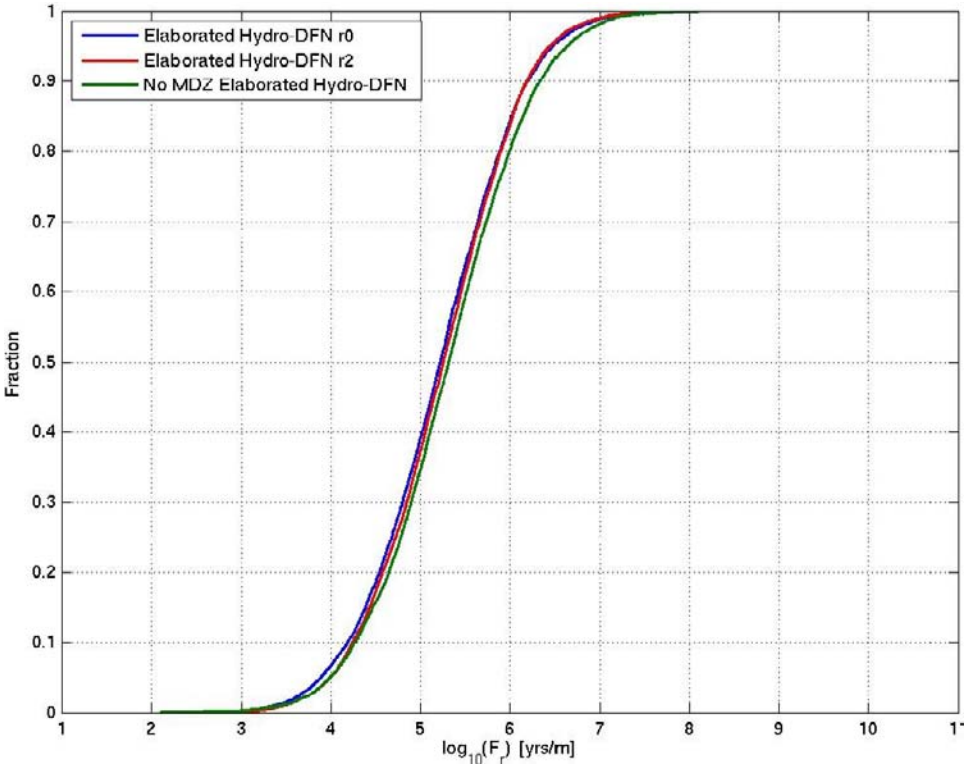

Figure C-43. *Normalised CDF plots of F_r in the Elaborated Hydro-DFN model, including one additional realisation and the case with no MDZs, for the Q2 particles successfully reaching the model top boundary (85%–87%), released at 2000 AD.*

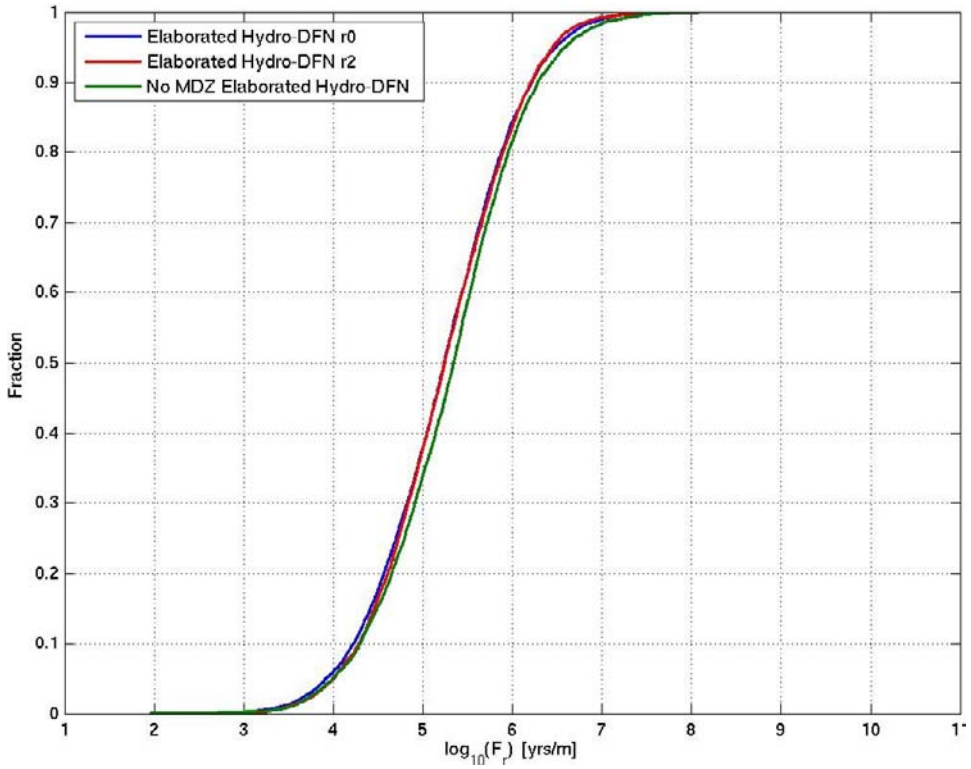

Figure C-44. *Normalised CDF plots of F_r in the Elaborated Hydro-DFN model, including one additional realisation and the case with no MDZs, for the Q3 particles successfully reaching the model top boundary (83%–86%), released at 2000 AD.*

C.4 Stochastic continuum model

C.4.1 Evolution of exit locations with time

Maps of the discharge locations of particles released from the Q2 locations in the repository are shown, for various release times, scales and realisations of the HRD and HCD, in Figure C-45 to Figure C-47. The particles tend to either discharge through deformation zones situated locally around the repository or along the shoreline. There is a large variation in the discharge locations with time for those particles that exit on the shoreline. The particles that discharge through outcropping deformation zones northeast of the repository at 2000 AD are also significantly influenced by the receding shoreline and at 15,000 AD many of these particles discharge along the shoreline instead. These results differ from the Elaborated Hydro-DFN model where the discharge locations are more localised around the repository area and vary little with release time.

The effect of different scales of spatial variability and realisations of the HRD and HCD on exit locations is not very pronounced.

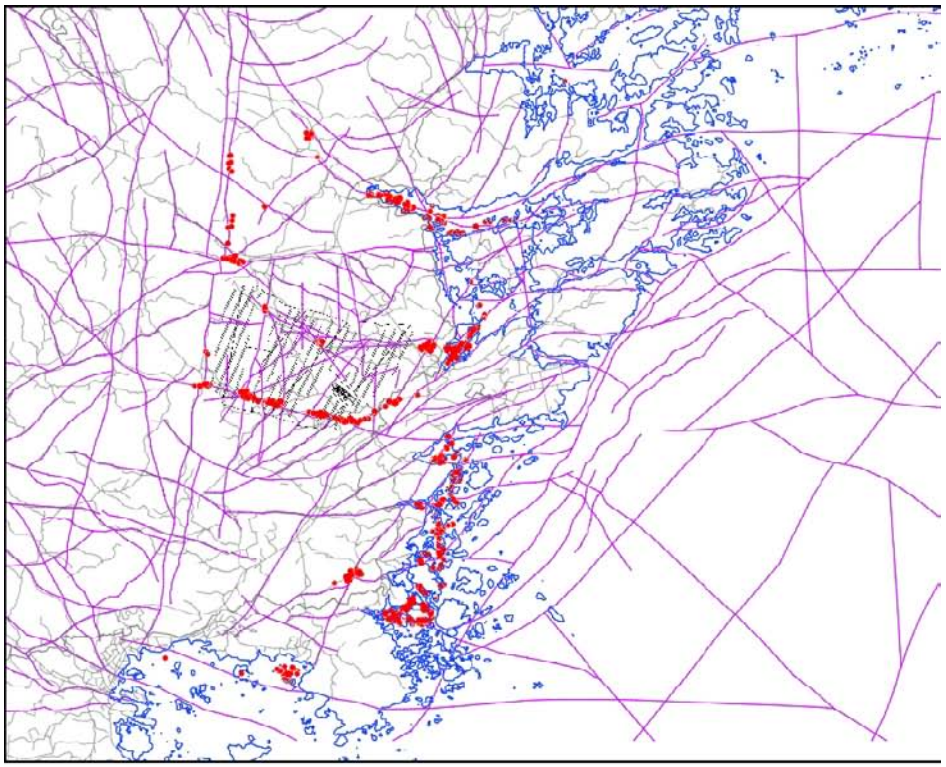

2000 AD (r0, 100 m scale)

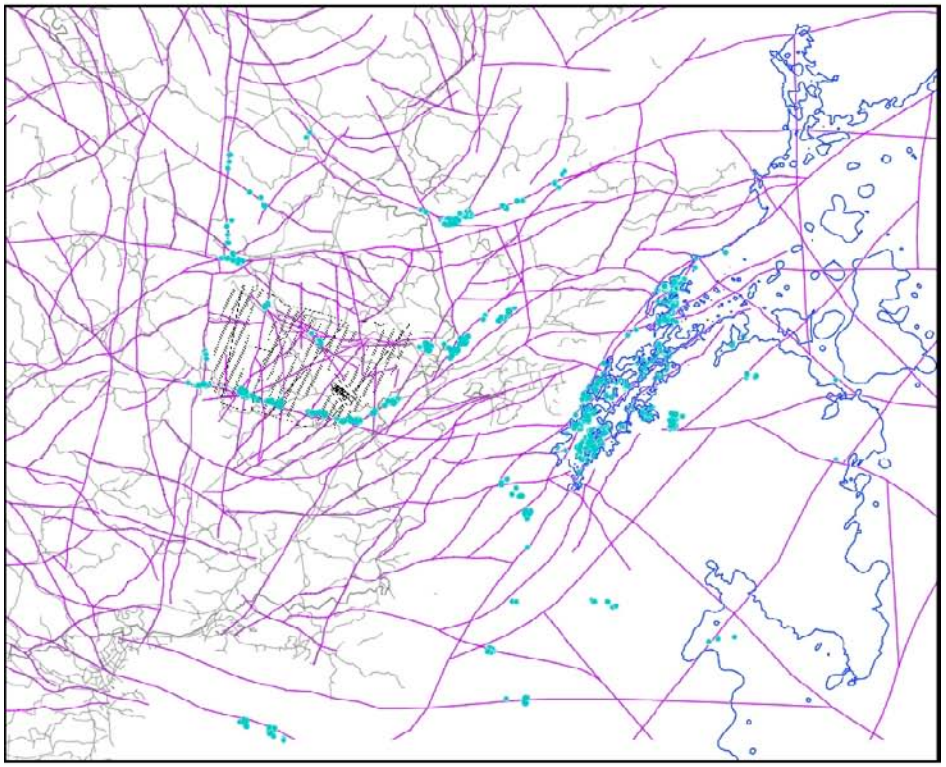

15,000 AD (r0, 100 m scale)

Figure C-45. *Exit locations for the Q2 particles successfully reaching the top boundary of the Stochastic continuum 100 m site-scale models for the homogeneous HCD and realisation 1 of the HRD, with the shoreline at each time shown in blue. Individual plots presented are for releases at 2000 AD (red) and 15,000 AD (light blue). The deformation zones at z = –50 m (purple), surface features (grey) and the repository structures (black) are also shown.*

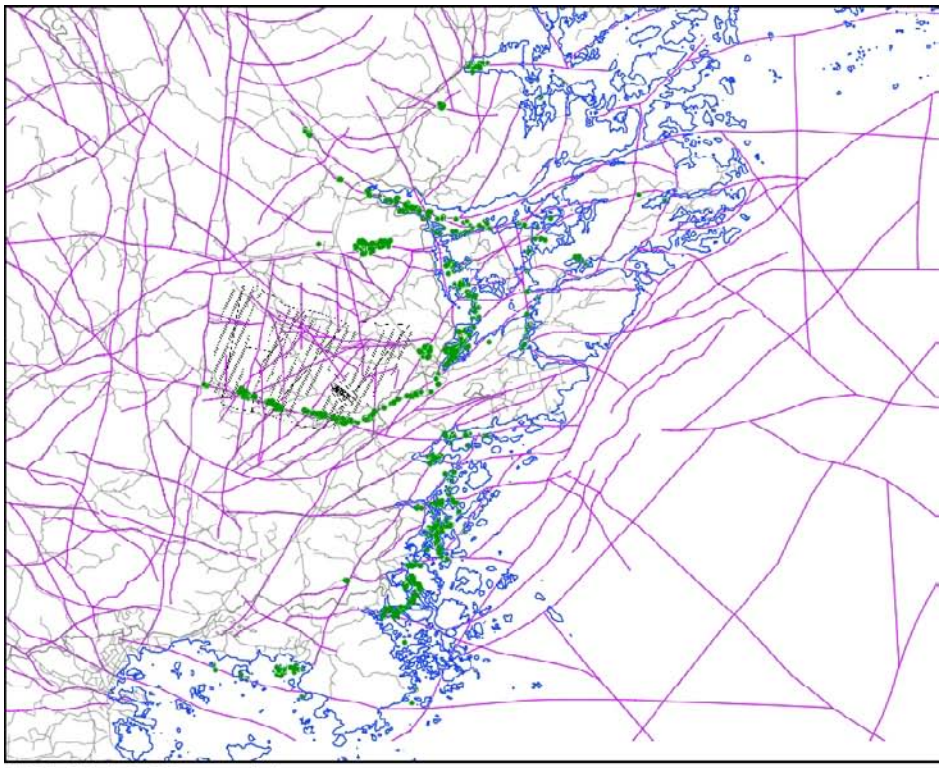

2000 AD (r0, 20 m scale)

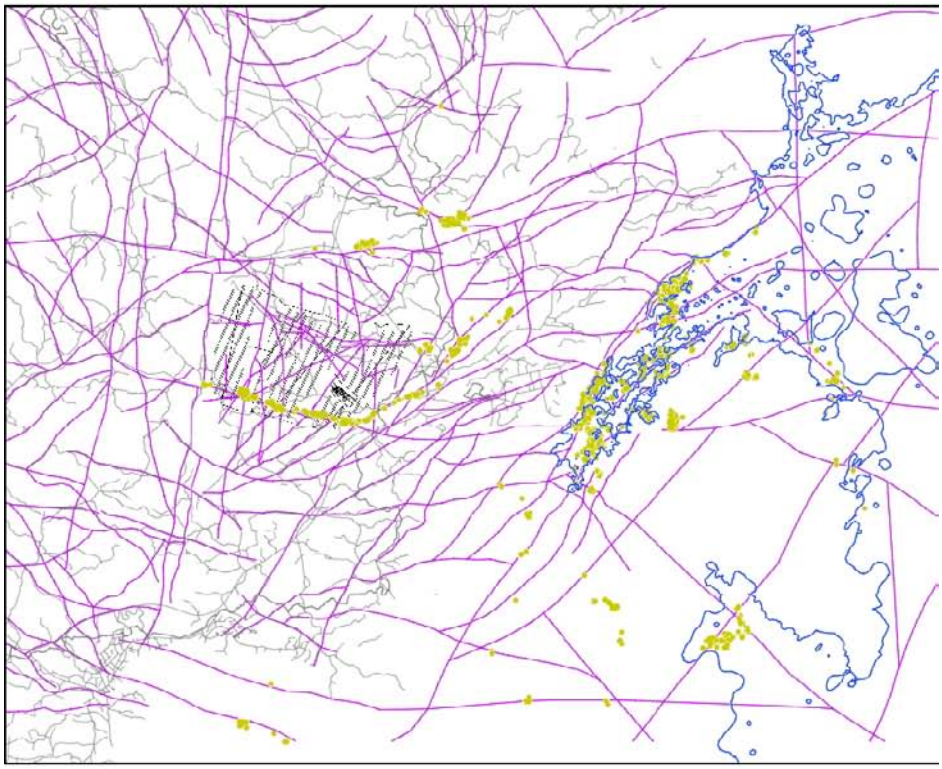

15,000 AD (r0, 20 m scale)

Figure C-46. *Exit locations for the Q2 particles successfully reaching the top boundary of the Stochastic continuum 20 m site-scale models for the homogeneous HCD and realisation 1 of the HRD, with the shoreline at each time shown in blue. Individual plots presented are for releases at 2000 AD (green) and 15,000 AD (brown). The deformation zones at z = –50 m (purple), surface features (grey) and the repository structures (black) are also shown.*

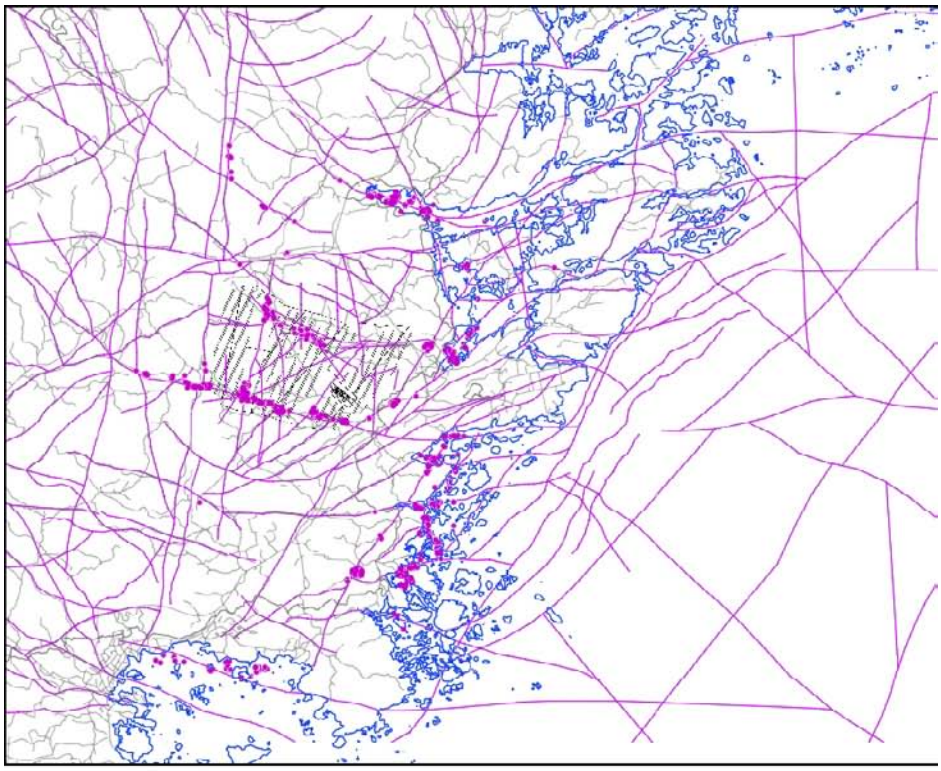

2000 AD (r2, 100 m scale)

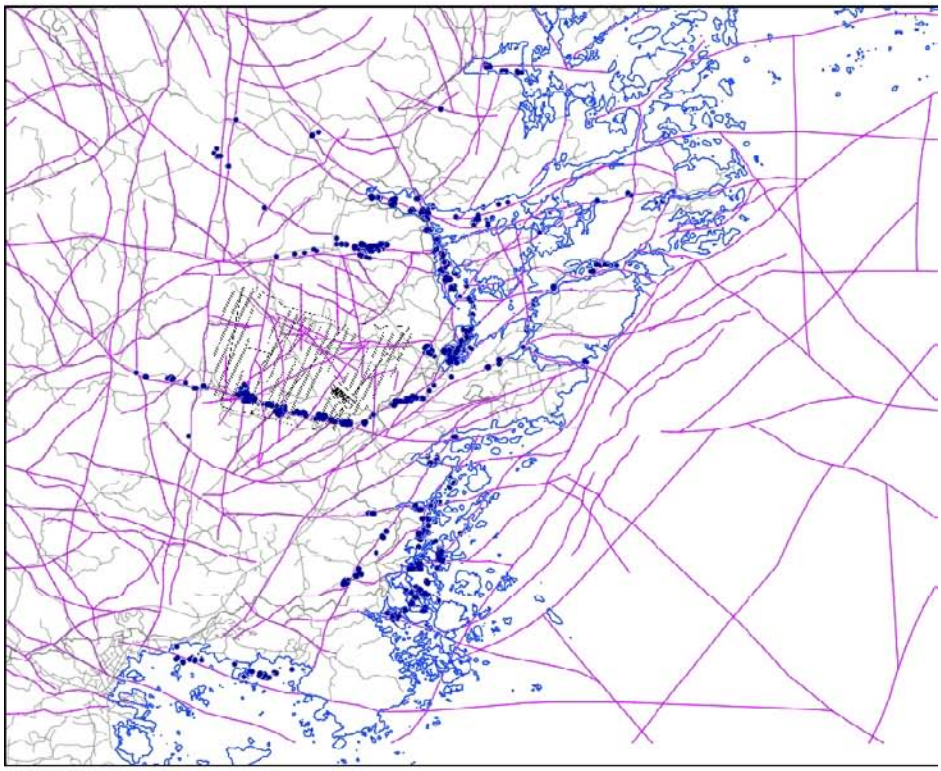

2000 AD (r2, 20 m scale)

Figure C-47. *Exit locations for the Q2 particles successfully reaching the top boundary of the nested Stochastic continuum site-scale models for realisation 2 of the HCD and HRD, with the shoreline at each time shown in blue. Individual plots presented are for releases at 2000 AD, 100 m scale (top) and 20 m scale (bottom). The deformation zones at z = –50 m (purple), surface features (grey) and the repository structures (black) are also shown.*

C.4.2 Evolution of performance measures with time

Figure C-48 to Figure C-53 show the non-normalised CDF plots for the U_r and F_r performance measures for the Q1, Q2 and Q3 release locations at the release times 2000 AD and 15,000 AD. In each of the figures a comparison of the results of the Elaborated Hydro-DFN model and the Stochastic continuum models on 20 m and 100 m scales is shown. All compared models use a homogeneous HCD and realisation 1 of the HRD (denoted r0). Non-normalised CDF plots were chosen to allow a more meaningful comparison between the two cases given the differences in the number of particles starting.

It should be noted that in these CDF plots for the Elaborated Hydro-DFN case, the contribution to F_r from the ECPM part of the model has been added. This was done in order to make the comparison with the Stochastic continuum model relevant since the Stochastic continuum model accounts for the full path of the particles, apart from within the HSD, when calculating the performance measures.

The figures show that there is no significant difference in performance measures between the different release times at 2000 AD and 15,000 AD. Further, there are only small differences between the two Stochastic continuum model scales. However, there are significant differences between the distributions of the performance measures calculated by the Stochastic continuum model compared to the Elaborated Hydro-DFN model.

The median values of U_r at the Q1 release locations calculated by the Stochastic continuum models are around a factor of ten lower than those calculated by the Elaborated Hydro-DFN model, with a value of approximately $1 \cdot 10^{-4}$ m/y. For Q1, the 90 percentile value for the Stochastic continuum model is around a factor of ten lower, with a value of approximately $3 \cdot 10^{-3}$ m/y.The median values of U_r at the Q2 release locations for the Stochastic continuum models are around a factor of five lower than those calculated by the Elaborated Hydro-DFN model, with a value of approximately $5 \cdot 10^{-3}$ m/y. For Q2, the 90 percentile value is about a factor of six lower than for the Elaborated Hydro-DFN model, at about $2 \cdot 10^{-2}$ m/y. The median U_r value for the Stochastic continuum 100 m scale model is slightly higher than for the 20 m scale model. For the Q3 release locations the median values of U_r for the Stochastic continuum models are about a factor of three higher than the for Elaborated Hydro-DFN model.

For the Stochastic continuum model, nearly all particles released from the Q1 location start. The cut-off criteria is set to an initial Darcy Flux of $1 \cdot 10^{-6}$ m/y, below which the particles are removed from the statistics. The corresponding proportion of particles successfully entering a fracture with significant flow from a Q1 release location for the Elaborated Hydro-DFN model is ~70%. For the Q2 and Q3 release locations nearly all particles start for both models.

The median value of F_r at the Q1 release locations is approximately a factor of ten higher for both scales of the Stochastic continuum model compared to the Elaborated Hydro-DFN model, with a value of approximately $1 \cdot 10^{6}$ y/m. The difference for the Q2 and Q3 release locations is a little less. For the Stochastic continuum model, the Q1 F_r 10 percentile value is approximately $1 \cdot 10^{5}$ y/m. The CDF plot of F_r for the Stochastic continuum model shows a bi-modal behaviour.

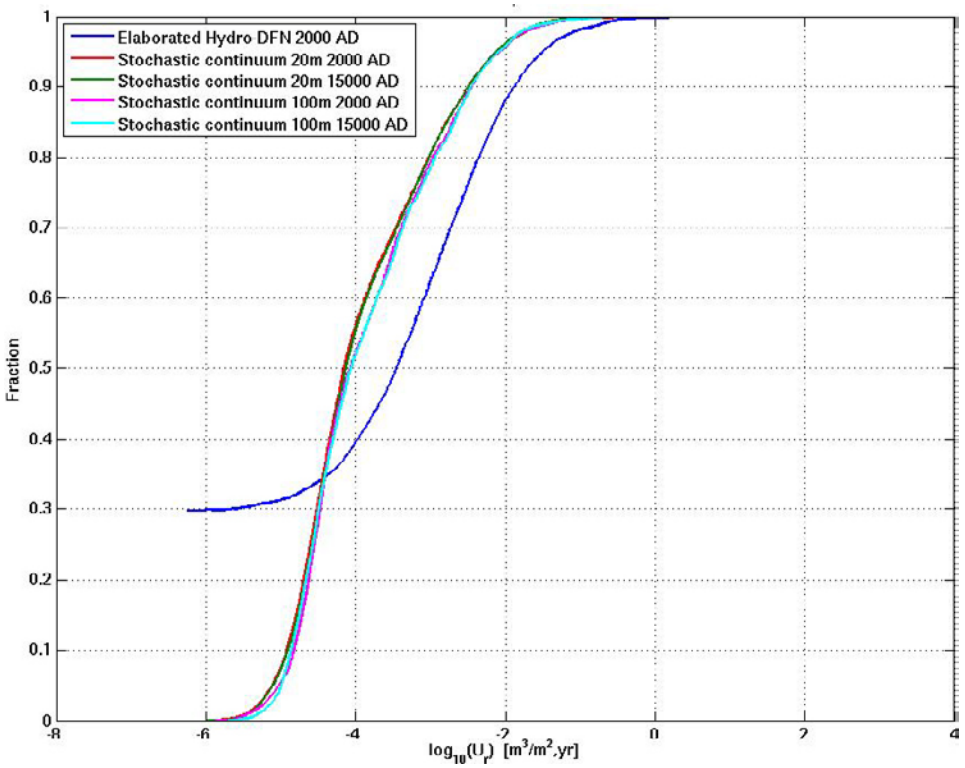

Figure C-48. *Non-normalised CDF plots of U_r in a comparison of the Elaborated Hydro-DFN model and the Stochastic continuum models on 20 m and 100 m scales for the 8,031 Q1 particles released at the given times.*

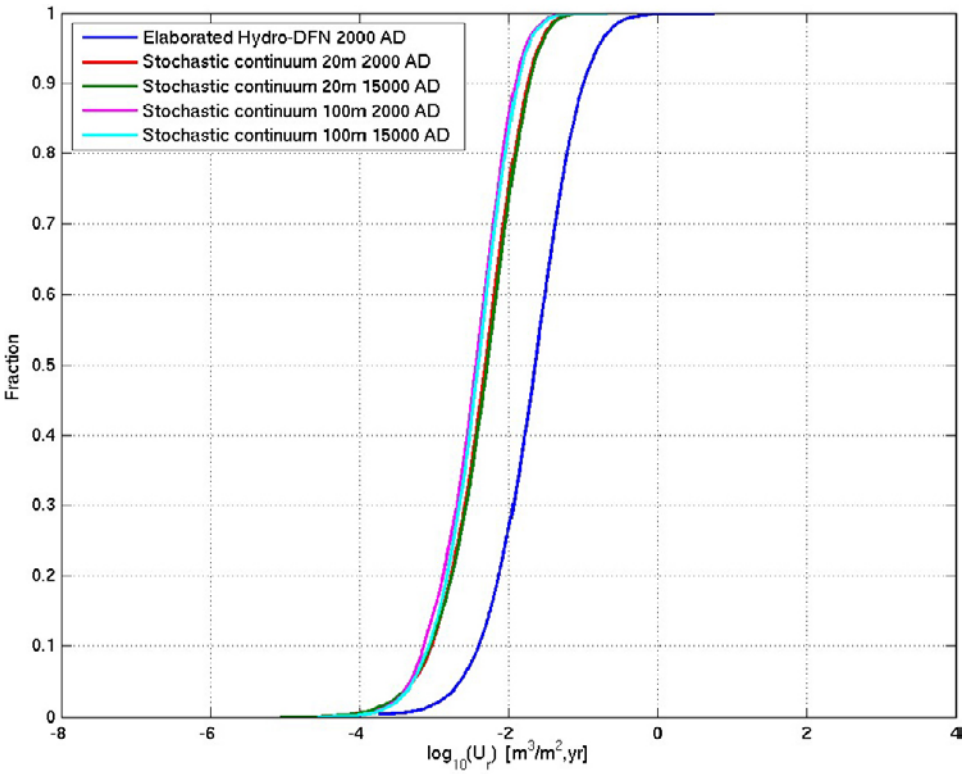

Figure C-49. *Non-normalised CDF plots of U_r in a comparison of the Elaborated Hydro-DFN model and the Stochastic continuum models on 20 m and 100 m scales for the 8,031 Q2 particles released at the given times.*

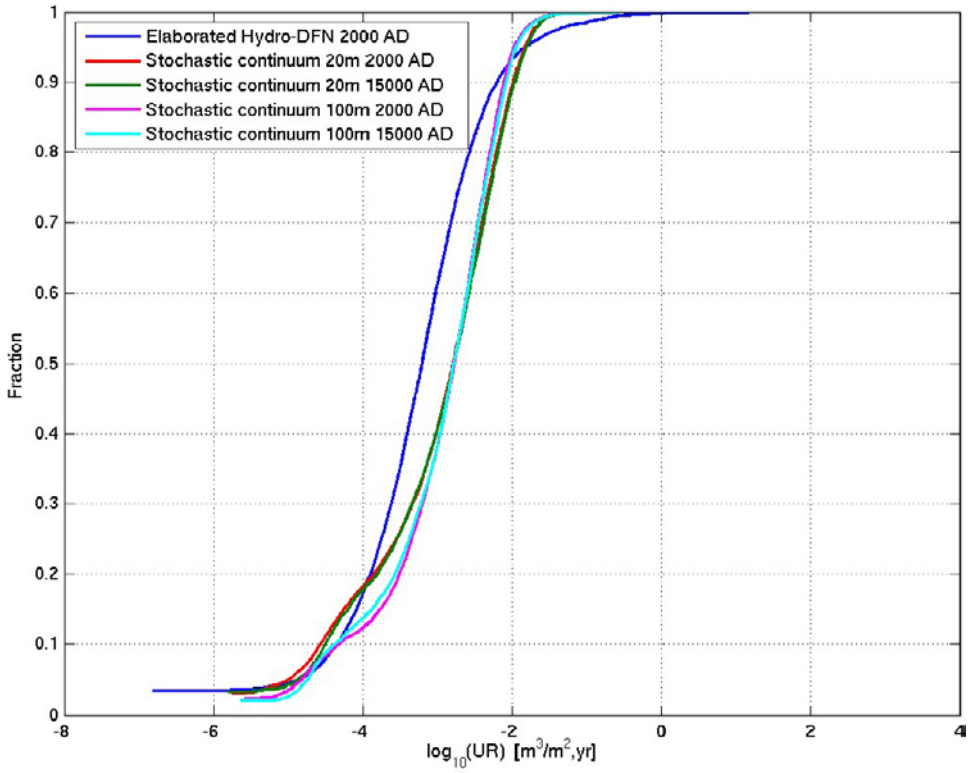

Figure C-50. *Non-normalised CDF plots of U_r in a comparison of the Elaborated Hydro-DFN model and the Stochastic continuum models on 20 m and 100 m scales for the 8,031 Q3 particles released at the given times. The UR axis corresponds to U_r for the Q3 release locations.*

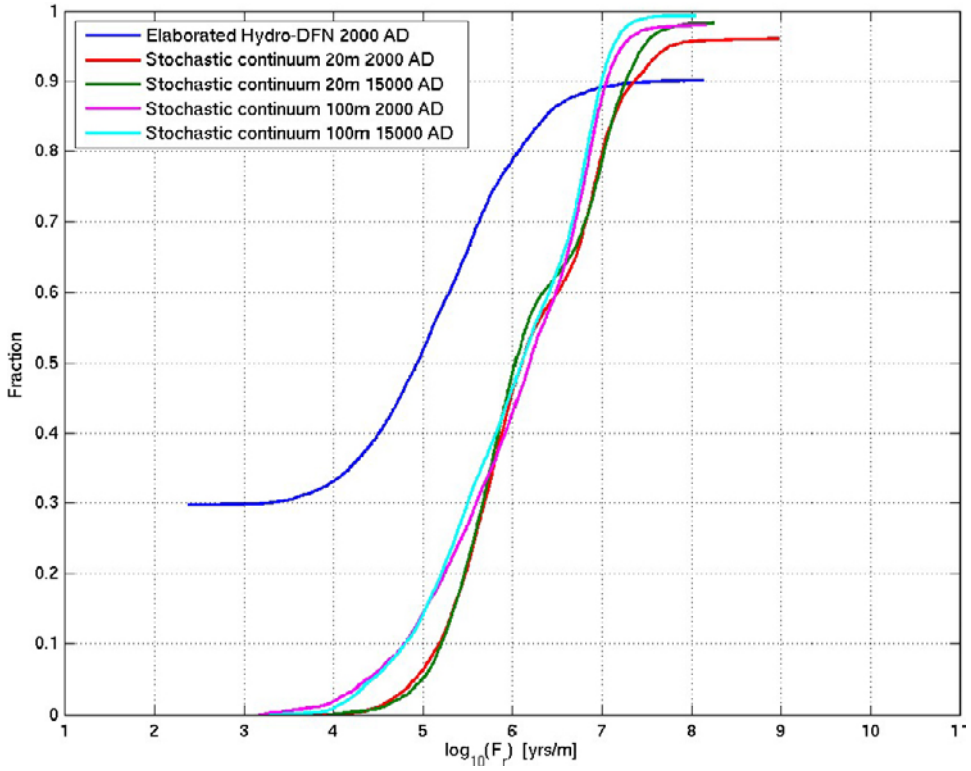

Figure C-51. *Non-normalised CDF plots of F_r in a comparison of the Elaborated Hydro-DFN model and the Stochastic continuum models on 20 m and 100 m scales for the 8,031 Q1 particles released at the given times.*

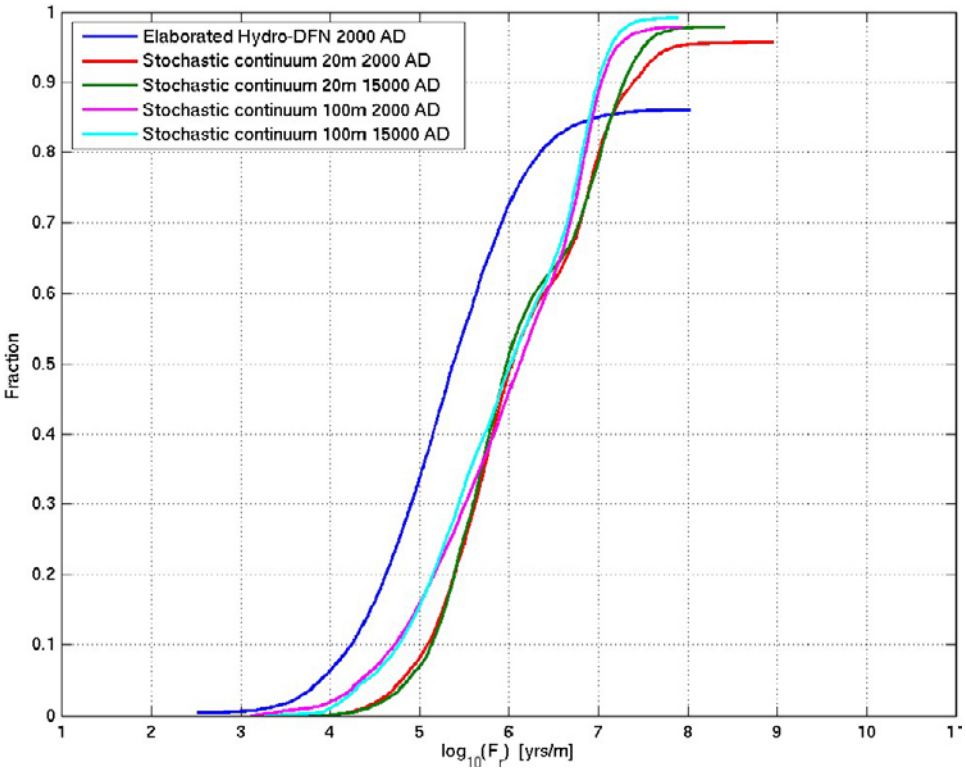

Figure C-52. *Non-normalised CDF plots of F_r in a comparison of the Elaborated Hydro-DFN model and the Stochastic continuum models on 20 m and 100 m scales for the 8,031 Q2 particles released at the given times.*

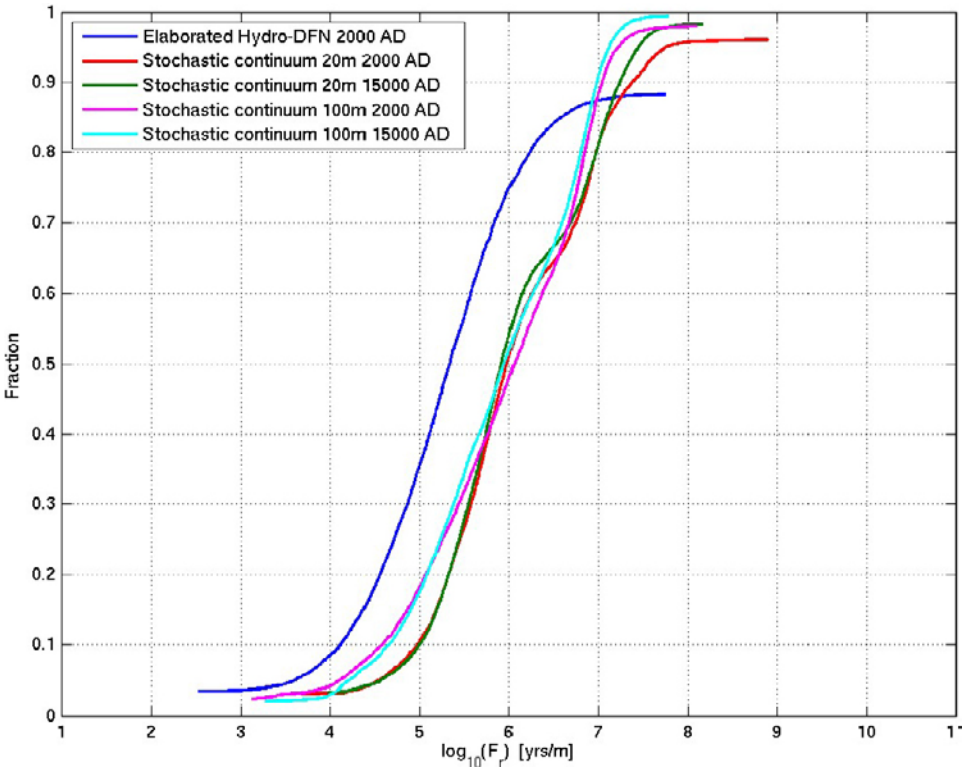

Figure C-53. *Non-normalised CDF plots of F_r in a comparison of the Elaborated Hydro-DFN model and the Stochastic continuum models on 20 m and 100 m scales for the 8,031 Q3 particles released at the given times.*

C.4.3 Additional realisation

Figure C-54 to Figure C-59 show the non-normalised CDF plots for the U_r and F_r performance measures for the Q1, Q2 and Q3 release locations at the release time 2000 AD. In each of the figures a comparison of the results from the two realisations of the Elaborated Hydro-DFN model and the Stochastic continuum models on 20 m and 100 m scales is shown.

It should be noted that in these CDF plots for the Elaborated Hydro-DFN model, contribution to F_r from the ECPM part of the model has been added. This was done in order to make the comparison with the Stochastic continuum model relevant, since the Stochastic continuum model accounts for the full path of the particles, apart from within the HSD, when calculating the performance measures.

For all compared cases, the results suggest that there is very little variation between the two different realisations of the HRD and the HCD in any of the performance measures in the rock. The results also suggests that introducing heterogeneity to the HCD does not have a significant impact on these performance measures.

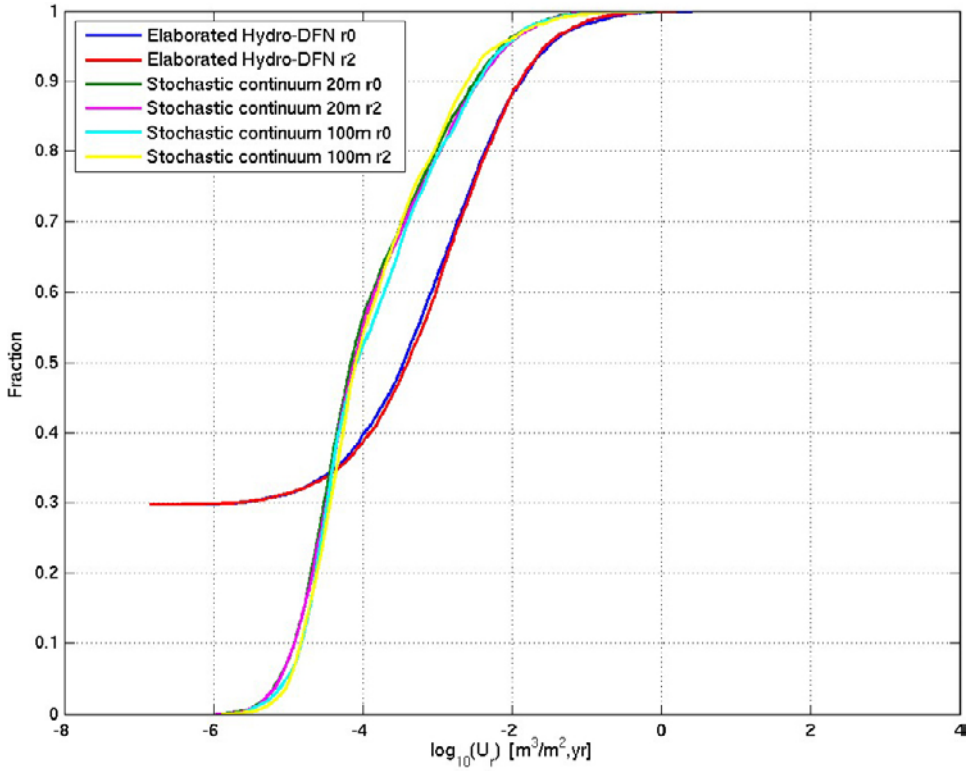

Figure C-54. *Non-normalised CDF plots of U_r in a comparison of two realisations of the Elaborated Hydro-DFN model and the Stochastic continuum models on 20 m and 100 m scales for the 8,031 Q1 particles released at 2000 AD.*

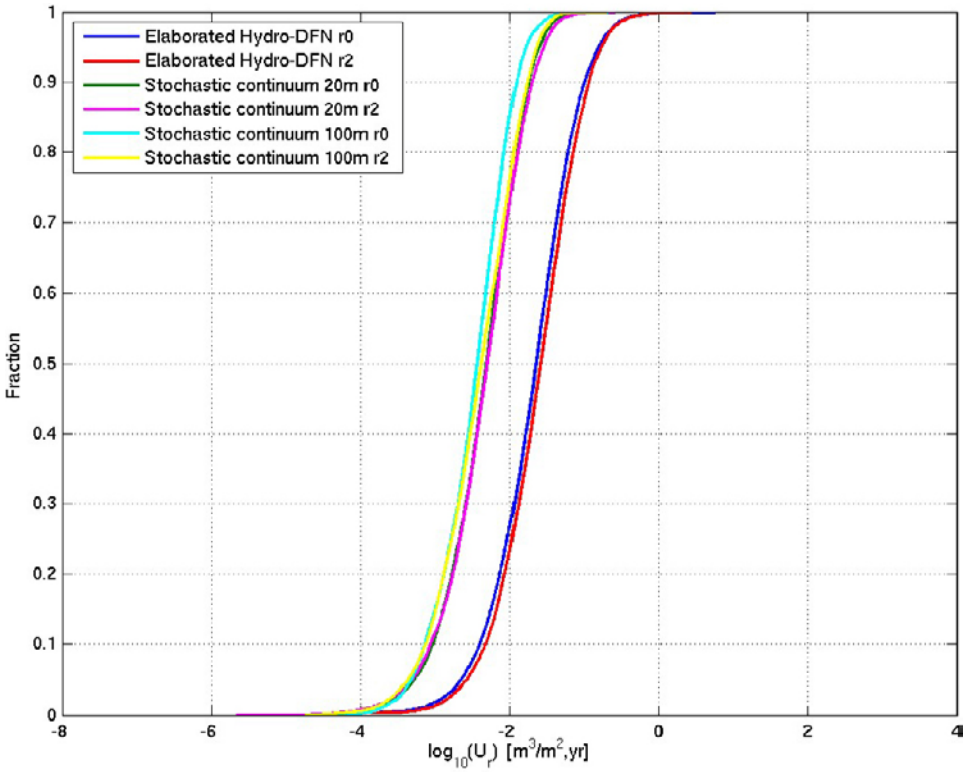

Figure C-55. *Non-normalised CDF plots of U_r in a comparison of two realisations of the Elaborated Hydro-DFN model and the Stochastic continuum models on 20 m and 100 m scales for the 8,031 Q2 particles released at 2000 AD.*

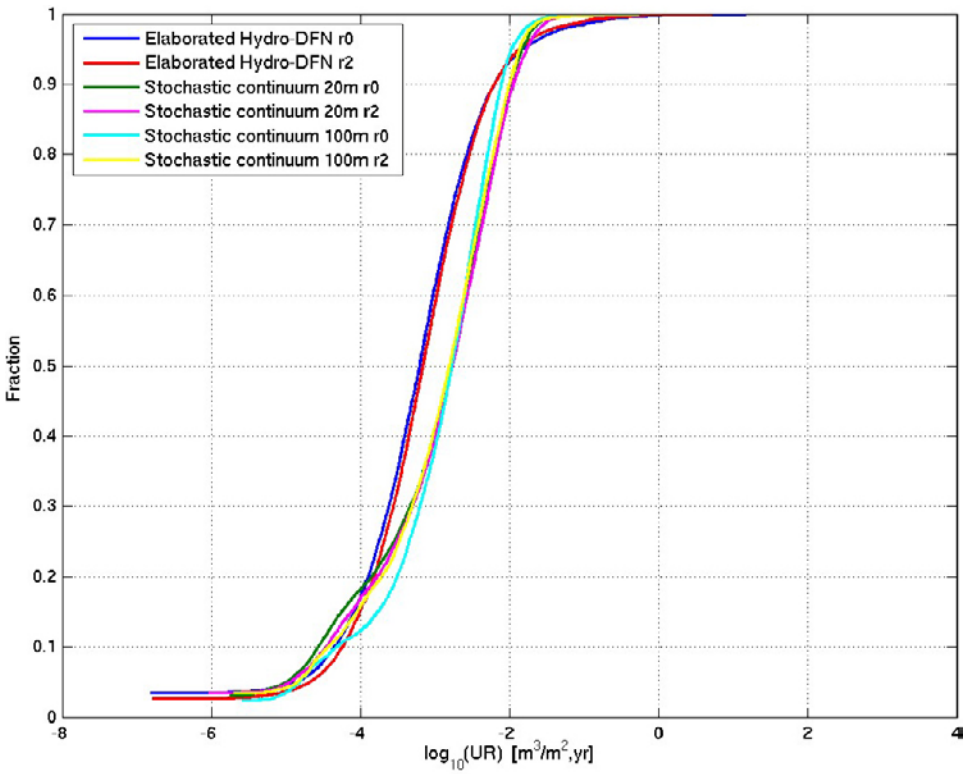

Figure C-56. *Non-normalised CDF plots of U_r in a comparison of two realisations of the Elaborated Hydro-DFN model and the Stochastic continuum models on 20 m and 100 m scales for the 8,031 Q3 particles released at 2000 AD. The UR axis corresponds to U_r for the Q3 release locations.*

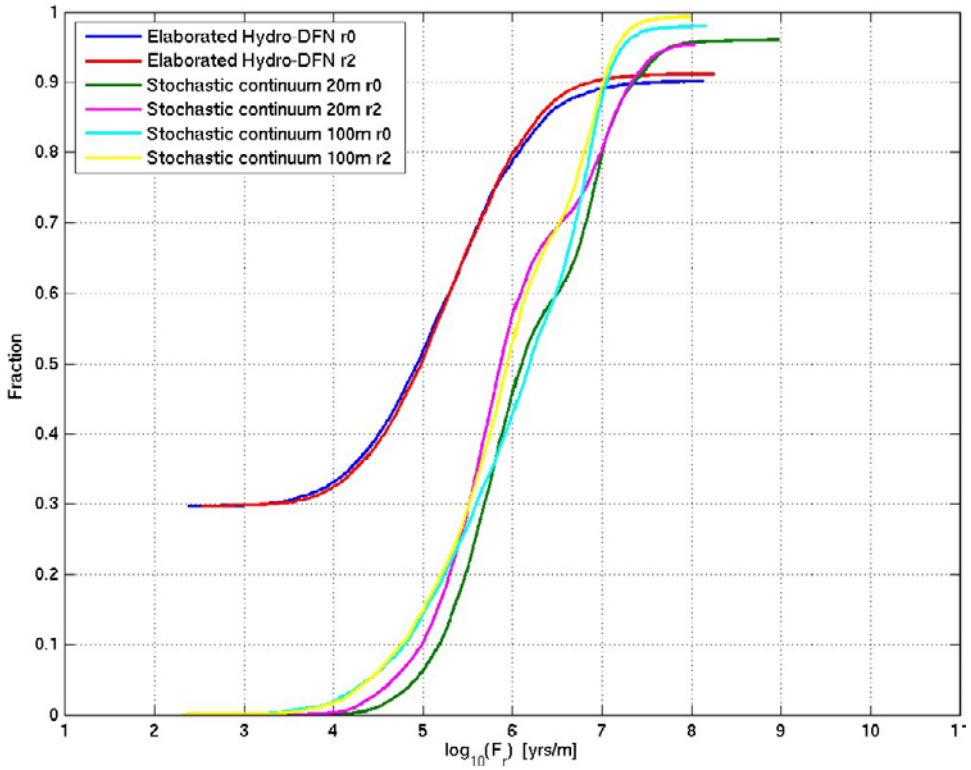

Figure C-57. *Non-normalised CDF plots of F_r in a comparison of two realisations of the Elaborated Hydro-DFN model and the Stochastic continuum models on 20 m and 100 m scales for the 8,031 Q1 particles released at 2000 AD.*

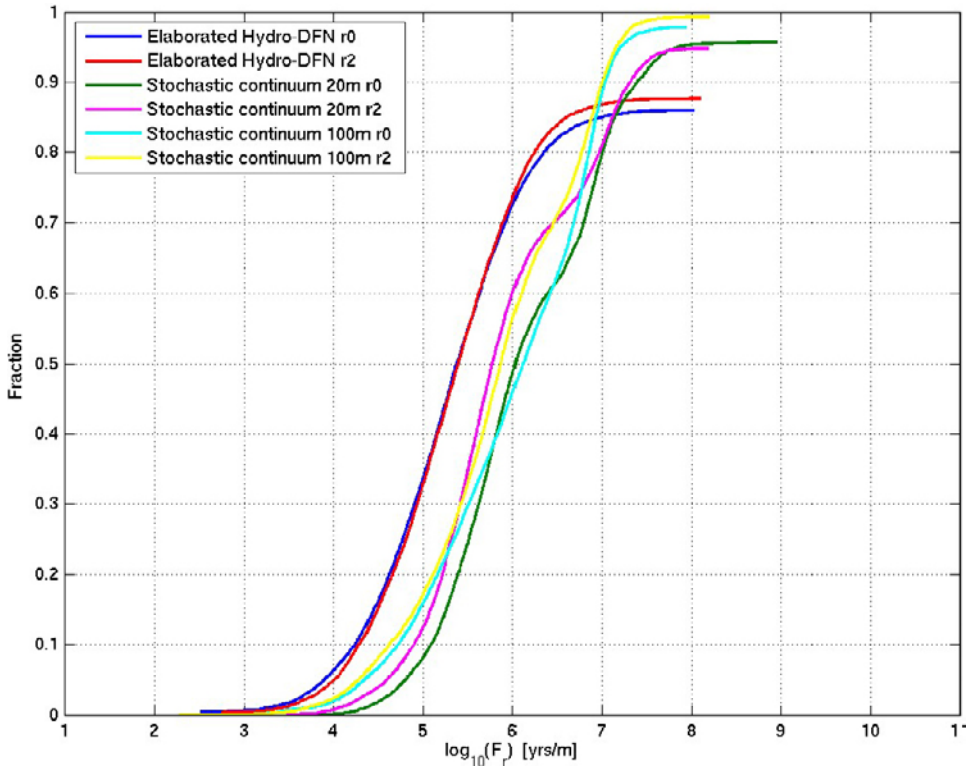

Figure C-58. *Non-normalised CDF plots of F_r in a comparison of two realisations of the Elaborated Hydro-DFN model and the Stochastic continuum models on 20 m and 100 m scales for the 8,031 Q2 particles released at 2000 AD.*

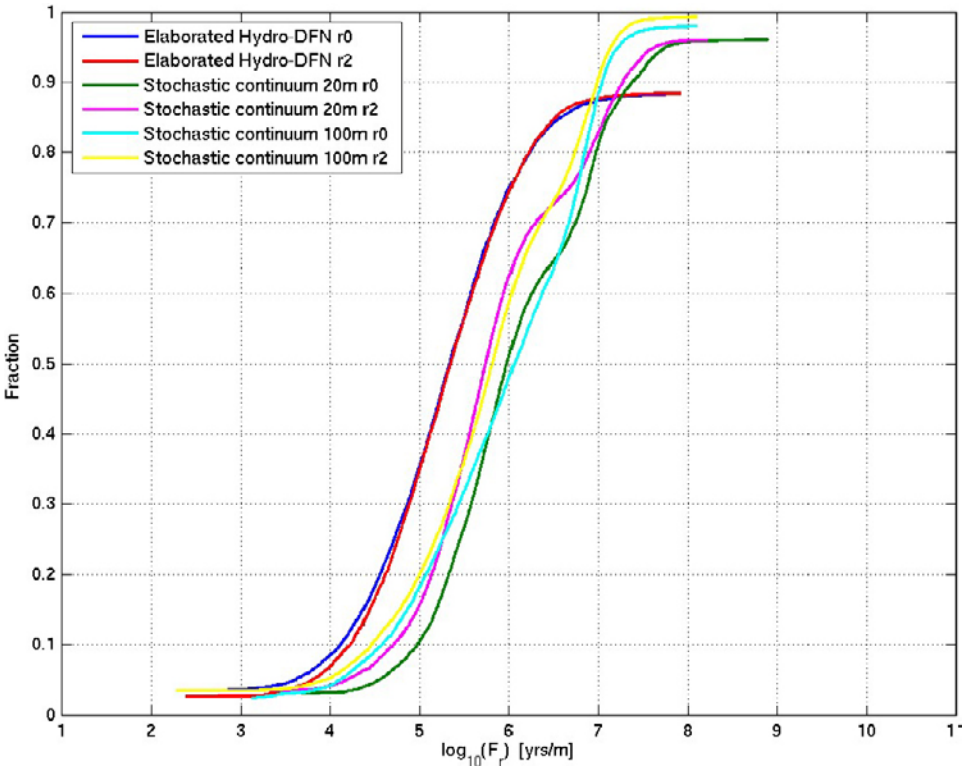

Figure C-59. *Non-normalised CDF plots of F_r in a comparison of two realisations of the Elaborated Hydro-DFN model and the Stochastic continuum models on 20 m and 100 m scales for the 8,031 Q3 particles released at 2000 AD.*

C.4.4 Bulk properties

Block hydraulic conductivity statistics at 20 m and 100 m scales (corresponding to two of the borehole interval scales used for PSS measurements) were calculated for the Stochastic continuum case and compared to the corresponding values for the upscaled Elaborated Hydro-DFN and the upscaled SDM-Site Hydro-DFN. These values are given in Table C-1 to Table C-6, along with the corresponding PSS values for information, although these are not strictly comparable to the other values due to the truncation of high and low hydraulic conductivities used in the modelling cases.

The mean hydraulic conductivity values are broadly similar for the Stochastic continuum and Elaborated Hydro-DFN cases. For the 20 m scale in depth zone 3 (containing the repository depth), the mean hydraulic conductivity values for the Stochastic continuum case are a factor of 2.2 lower for HRD_W, a factor of 1.3 lower for HRD_C and a factor of 3.0 lower for HRD_EW007. For the 100 m scale in depth zone 3, the mean hydraulic conductivity values for the Stochastic continuum case are a factor of 2.0 higher for HRD_W, a factor of 1.4 lower for HRD_C and a factor of 1.5 higher for HRD_EW007.

Vertical flows through a number of horizontal planes at different depths in the Stochastic continuum models and Elaborated Hydro-DFN ECPM model were calculated under freshwater steady state conditions to compare the bulk flow properties of the models. Each plane was 4,200 m by 4,200 m in size and located in the local area above the repository. The HCD and repository structures were not included in the calculations. The calculated upward flows through the planes are given in Table C-7. The results agree to within a factor of four or less for all depths, which is reasonable agreement given the differences in the models discussed in Section 6.5.

Table C-1. Hydraulic conductivity statistics at a 20 m scale for HRD_W.

Depth Zone	Case	Log_{10}(K) [m/s]	
		Mean	Standard deviation
DZ1	Stochastic continuum	–8.11	1.67
	Elaborated Hydro-DFN	–7.07	0.78
	SDM-Site	–6.81	0.98
	PSS	–8.36	2.08
DZ2	Stochastic continuum	–9.13	1.39
	Elaborated Hydro-DFN	–9.32	1.31
	SDM-Site	–8.05	1.17
	PSS	–10.41	2.65
DZ3	Stochastic continuum	–9.44	1.10
	Elaborated Hydro-DFN	–9.09	0.90
	SDM-Site	–8.78	1.26
	PSS	–11.10	2.55

Table C-2. Hydraulic conductivity statistics at a 20 m scale for HRD_C.

Depth Zone	Case	Log_{10}(K) [m/s]	
		Mean	Standard deviation
DZ1	Stochastic continuum	–7.30	1.31
	Elaborated Hydro-DFN	–6.93	0.95
	SDM-Site	–7.05	0.86
	PSS	–7.31	1.34
DZ2	Stochastic continuum	–9.06	1.19
	Elaborated Hydro-DFN	–9.05	1.03
	SDM-Site	–8.41	1.09
	PSS	–9.61	1.82
DZ3	Stochastic continuum	–9.55	0.82
	Elaborated Hydro-DFN	–9.42	0.89
	SDM-Site	–8.89	1.04
	PSS	–10.57	1.75
DZ4	Stochastic continuum	–9.81	0.51
	Elaborated Hydro-DFN	–9.00	1.00
	SDM-Site	N/A	N/A
	PSS	–11.40	1.67

Table C-3. Hydraulic conductivity statistics at a 20 m scale for HRD_EW007.

Depth Zone	Case	Log_{10}(K) [m/s]	
		Mean	Standard deviation
DZ1	Stochastic continuum	–6.70	1.09
	Elaborated Hydro-DFN	–7.02	0.56
	SDM-Site	–6.92	0.58
	PSS	–6.71	1.09
DZ2	Stochastic continuum	–7.71	1.68
	Elaborated Hydro-DFN	–7.10	0.93
	SDM-Site	–7.31	0.92
	PSS	–7.83	1.93
DZ3	Stochastic continuum	–8.58	1.25
	Elaborated Hydro-DFN	–8.10	0.95
	SDM-Site	–7.89	0.83
	PSS	–8.75	1.51

Table C-4. Hydraulic conductivity statistics at a 100 m scale for HRD_W.

Depth Zone	Case	Log_{10}(K) [m/s]	
		Mean	Standard deviation
DZ1	Stochastic continuum	–6.71	0.62
	Elaborated Hydro-DFN	–6.87	0.42
	SDM-Site	–6.79	0.39
	PSS	–6.67	0.59
DZ2	Stochastic continuum	–8.29	1.91
	Elaborated Hydro-DFN	–9.43	1.37
	SDM-Site	–8.29	1.03
	PSS	–9.05	3.00
DZ3	Stochastic continuum	–9.13	1.05
	Elaborated Hydro-DFN	–9.44	1.12
	SDM-Site	–8.79	1.03
	PSS	–9.63	1.64

Table C-5. Hydraulic conductivity statistics at a 100 m scale for HRD_C.

Depth Zone	Case	Log_{10}(K) [m/s]	
		Mean	Standard deviation
DZ1	Stochastic continuum	–6.90	0.94
	Elaborated Hydro-DFN	–6.69	0.47
	SDM-Site	–6.99	0.36
	PSS	–6.94	1.02
DZ2	Stochastic continuum	–8.75	1.01
	Elaborated Hydro-DFN	–8.78	0.69
	SDM-Site	–7.85	1.29
	PSS	–8.92	1.18
DZ3	Stochastic continuum	–9.30	0.93
	Elaborated	–9.16	0.80
	SDM-Site	–8.70	0.70
	PSS	–9.82	1.47
DZ4	Stochastic continuum	–9.64	0.65
	Elaborated Hydro-DFN	–8.86	0.93
	SDM-Site	–9.65	1.45
	PSS	–10.52	1.40

Table C-6. Hydraulic conductivity statistics at a 100 m scale for HRD_EW007.

Depth Zone	Case	Log_{10}(K) [m/s]	
		Mean	Standard deviation
DZ1	Stochastic continuum	–6.62	0.97
	Elaborated Hydro-DFN	–7.04	0.26
	SDM-Site	–7.15	0.24
	PSS	–6.69	1.04
DZ2	Stochastic continuum	–6.44	1.14
	Elaborated Hydro-DFN	–7.32	0.31
	SDM-Site	–7.37	0.36
	PSS	–6.45	1.15
DZ3	Stochastic continuum	–8.34	1.18
	Elaborated Hydro-DFN	–8.53	0.52
	SDM-Site	–8.12	0.29
	PSS	–8.40	1.35

Table C-7. Upward flows through a series of horizontal planes in the local area of the Elaborated Hydro-DFN ECPM model and Stochastic continuum models under steady state freshwater conditions without HCD and repository structures.

Elevation [m]	Case	Upward flow [m^3/s]
-110	Elaborated Hydro-DFN	$1.1 \cdot 10^{-2}$
	Stochastic continuum 20 m	$4.7 \cdot 10^{-2}$
	Stochastic continuum 100 m	$1.1 \cdot 10^{-2}$
-210	Elaborated Hydro-DFN	$2.8 \cdot 10^{-3}$
	Stochastic continuum 20 m	$7.6 \cdot 10^{-3}$
	Stochastic continuum 100 m	$6.1 \cdot 10^{-3}$
-310	Elaborated Hydro-DFN	$1.4 \cdot 10^{-3}$
	Stochastic continuum 20 m	$5.0 \cdot 10^{-3}$
	Stochastic continuum 100 m	$4.0 \cdot 10^{-3}$
-410	Elaborated Hydro-DFN	$6.1 \cdot 10^{-4}$
	Stochastic continuum 20 m	$1.8 \cdot 10^{-3}$
	Stochastic continuum 100 m	$2.4 \cdot 10^{-3}$
-510	Elaborated Hydro-DFN	$2.1 \cdot 10^{-4}$
	Stochastic continuum 20 m	$1.1 \cdot 10^{-4}$
	Stochastic continuum 100 m	$4.1 \cdot 10^{-4}$
-610	Elaborated Hydro-DFN	$6.4 \cdot 10^{-5}$
	Stochastic continuum 20 m	$5.1 \cdot 10^{-5}$
	Stochastic continuum 100 m	$9.7 \cdot 10^{-5}$

C.4.5 Palaeohydrogeology

The results of the palaeohydrogeology calculations at 2000 AD compared to measured hydrochemical data are given in Figure C-60 to Figure C-71. On the left in each figure are the results from the Stochastic continuum model using the 20 m scale, homogeneous HCD and realisation 1 of the HRD and on the right are the results for the Elaborated Hydro-DFN. There is a reasonable match to the hydrochemistry data and the results are generally comparable to those obtained for the Elaborated Hydro-DFN model. The similarity in hydrochemistry results between the two models may seem surprising, but the hydrochemistry depends not just on the hydraulic conductivity of the HRD, but also on other properties that are shared by the two cases, such as the HCD properties, diffusion parameters (fracture surface area, porosity, diffusivity), boundary conditions and initial conditions. The results for the Stochastic continuum model using the 100 m scale are very similar to those for the 20 m scale.

Again there seems to be too much flushing of glacial water in KLX04 and KLX08 in HRD_EW007, which may be suggestive of HRD_EW007 hydraulic data from boreholes not being representative samples of conditions in these boreholes or the domain as a whole.

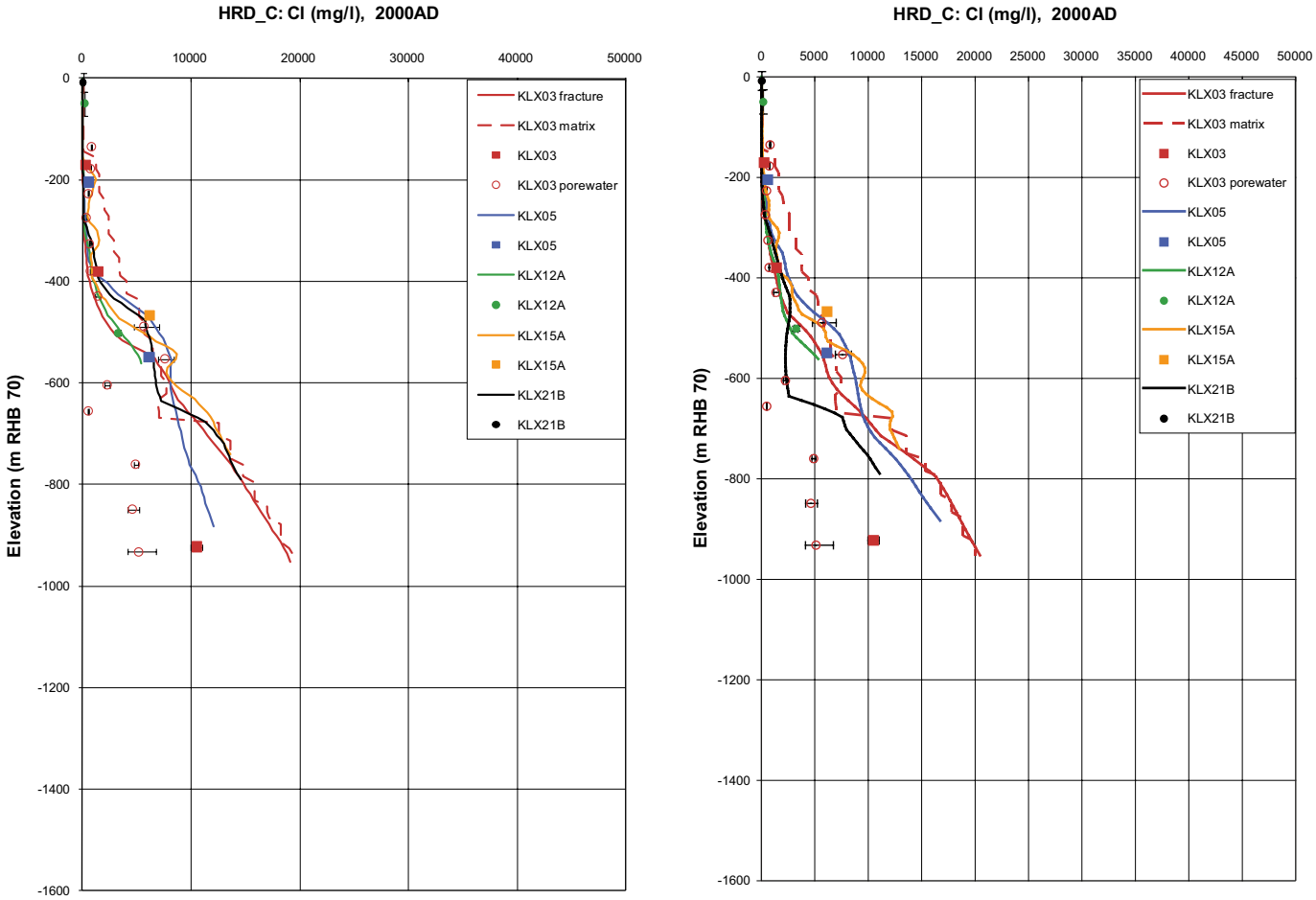

Figure C-60. *A comparison of the modelled and measured Cl concentrations in the fracture system for boreholes in HRD_C for the Stochastic continuum model (left) and the Elaborated Hydro-DFN (right). Square symbols are used for category 1–3 data, circles are used for the pore water data, and small diamond symbols are used for category 4 data. The error bars on the data indicate the laboratory analytical error. The solid lines show the distribution in the borehole simulated in the fracture system, and the dashed lines are for the matrix.*

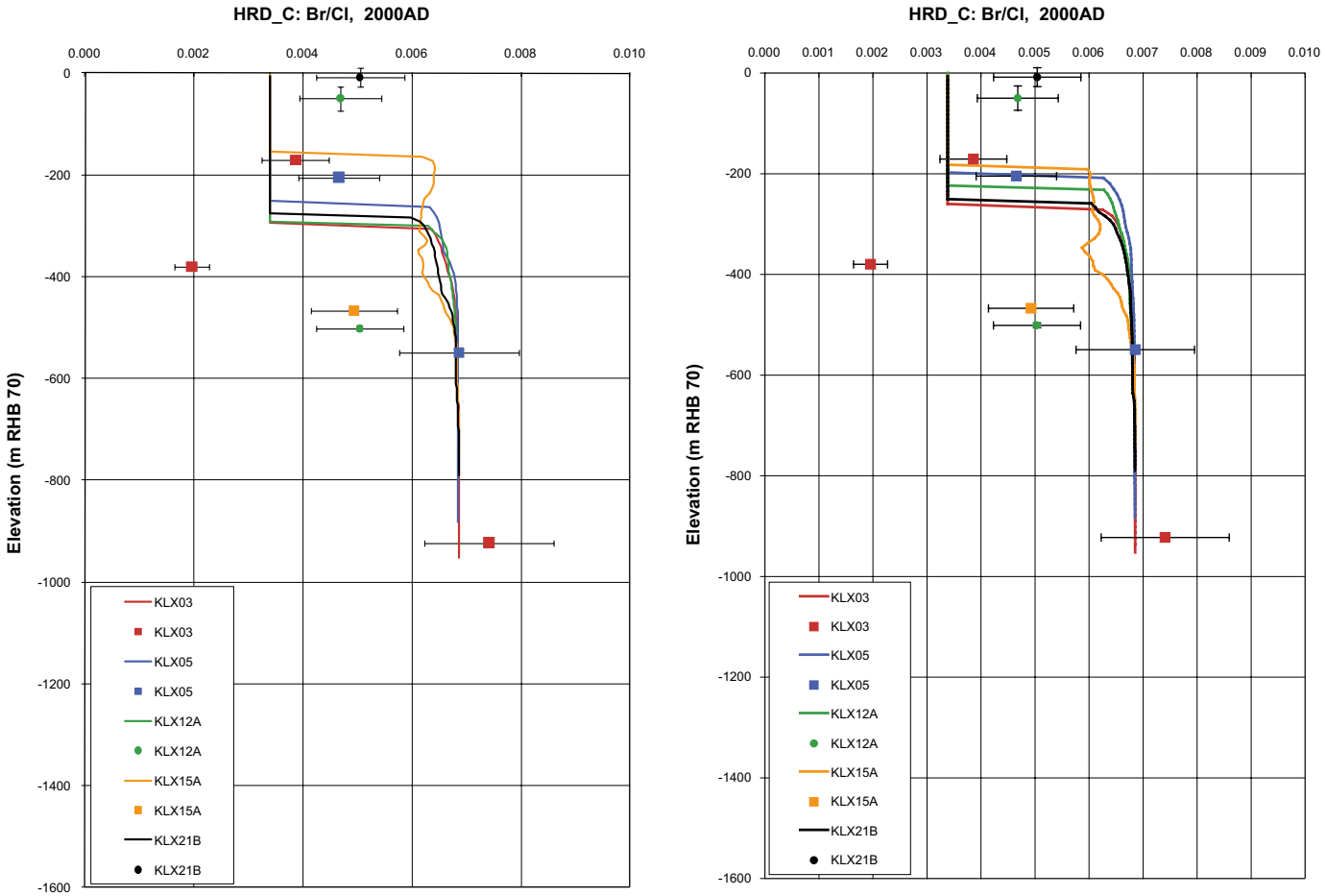

Figure C-61. *A comparison of the modelled and measured Br/Cl concentrations in the fracture system for boreholes in HRD_C for the Stochastic continuum model (left) and the Elaborated Hydro-DFN (right). Square symbols are used for category 1–3 data, circles are used for the pore water data, and small diamond symbols are used for category 4 data. The error bars on the data indicate the laboratory analytical error. The solid lines show the distribution in the borehole simulated in the fracture system, and the dashed lines are for the matrix.*

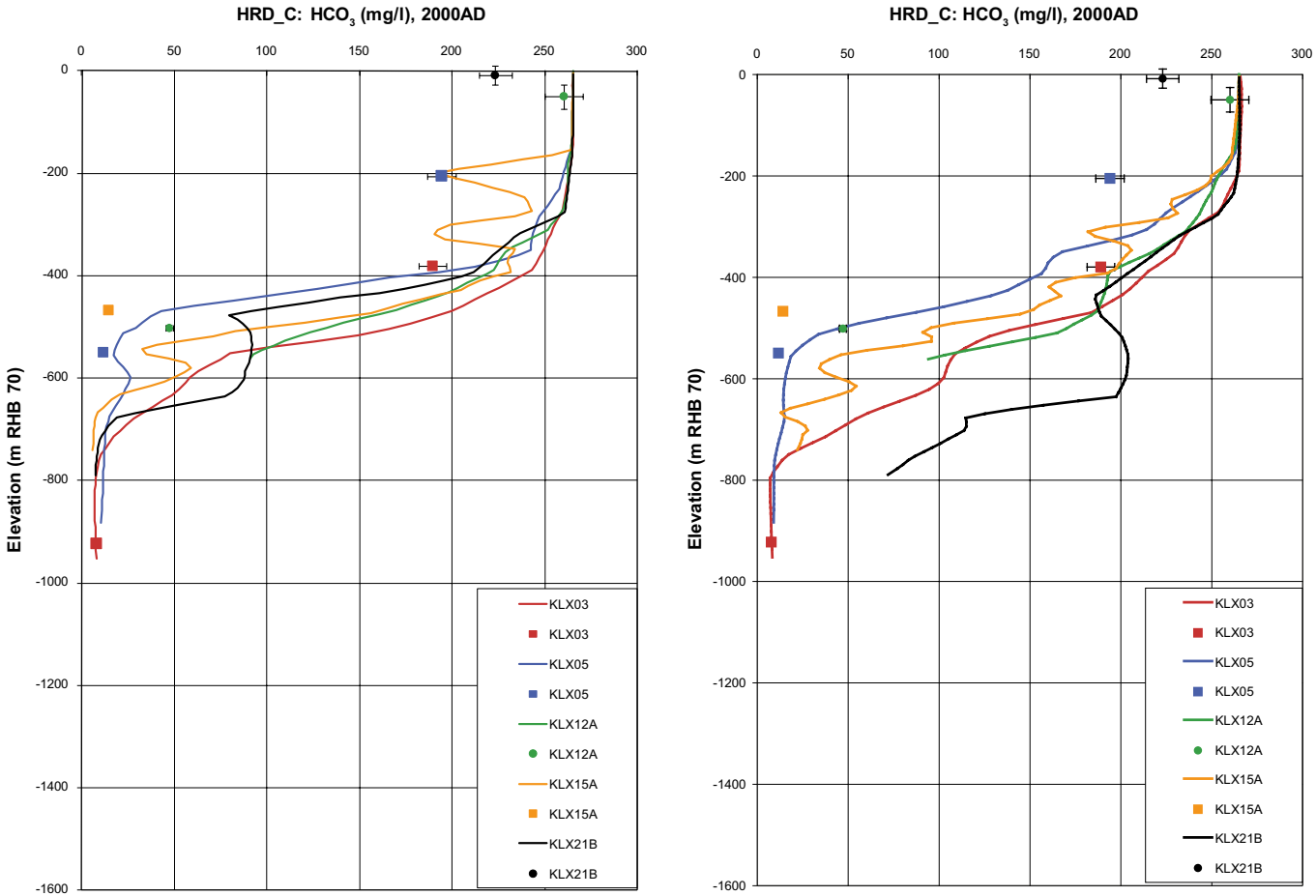

Figure C-62. *A comparison of the modelled and measured HCO_3 concentrations in the fracture system for boreholes in HRD_C for the Stochastic continuum model (left) and the Elaborated Hydro-DFN (right). Square symbols are used for category 1–3 data, circles are used for the pore water data, and small diamond symbols are used for category 4 data. The error bars on the data indicate the laboratory analytical error. The solid lines show the distribution in the borehole simulated in the fracture system, and the dashed lines are for the matrix.*

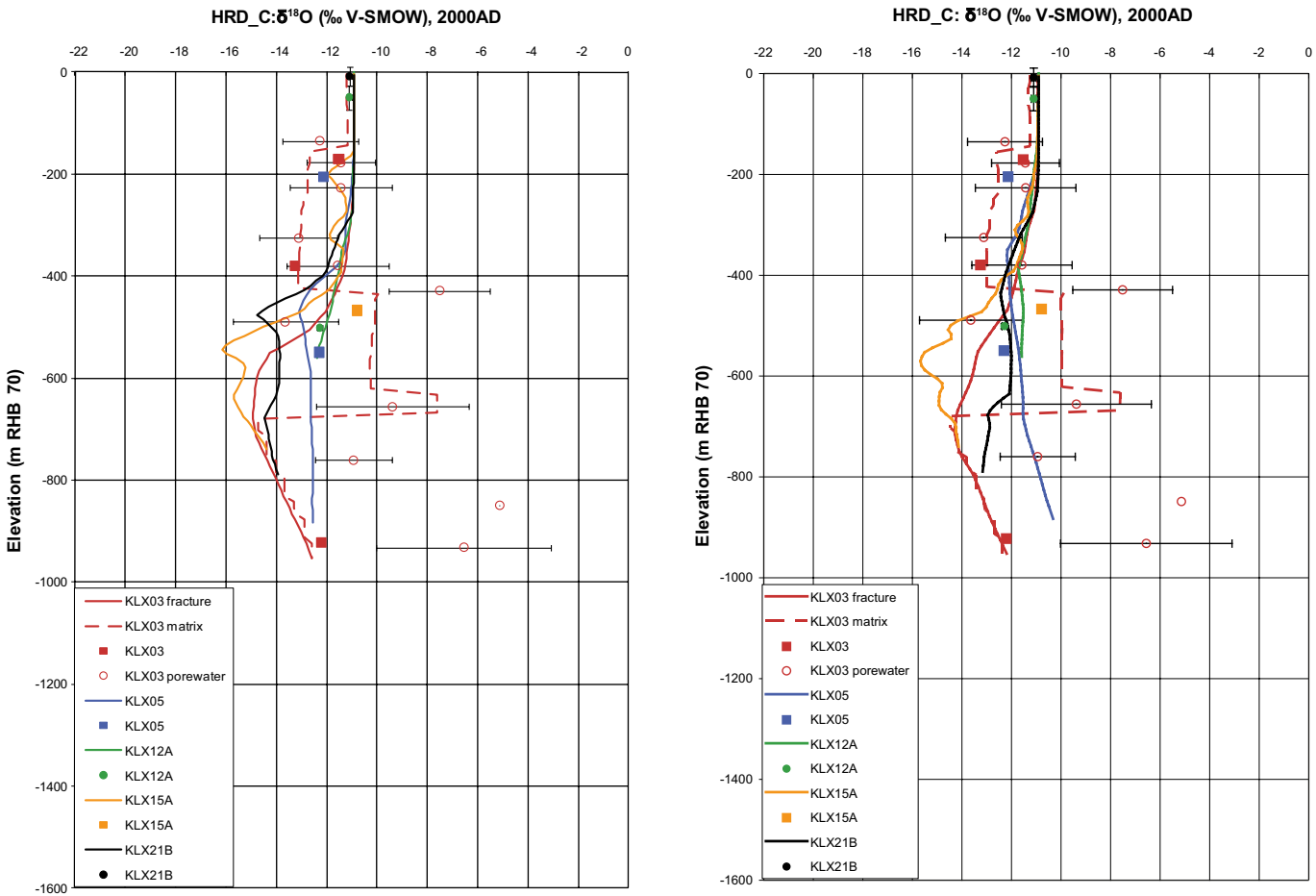

Figure C-63. *A comparison of the modelled and measured $\delta^{18}O$ concentrations in the fracture system for boreholes in HRD_C for the Stochastic continuum model (left) and the Elaborated Hydro-DFN (right). Square symbols are used for category 1–3 data, circles are used for the pore water data, and small diamond symbols are used for category 4 data. The error bars on the data indicate the laboratory analytical error. The solid lines show the distribution in the borehole simulated in the fracture system, and the dashed lines are for the matrix.*

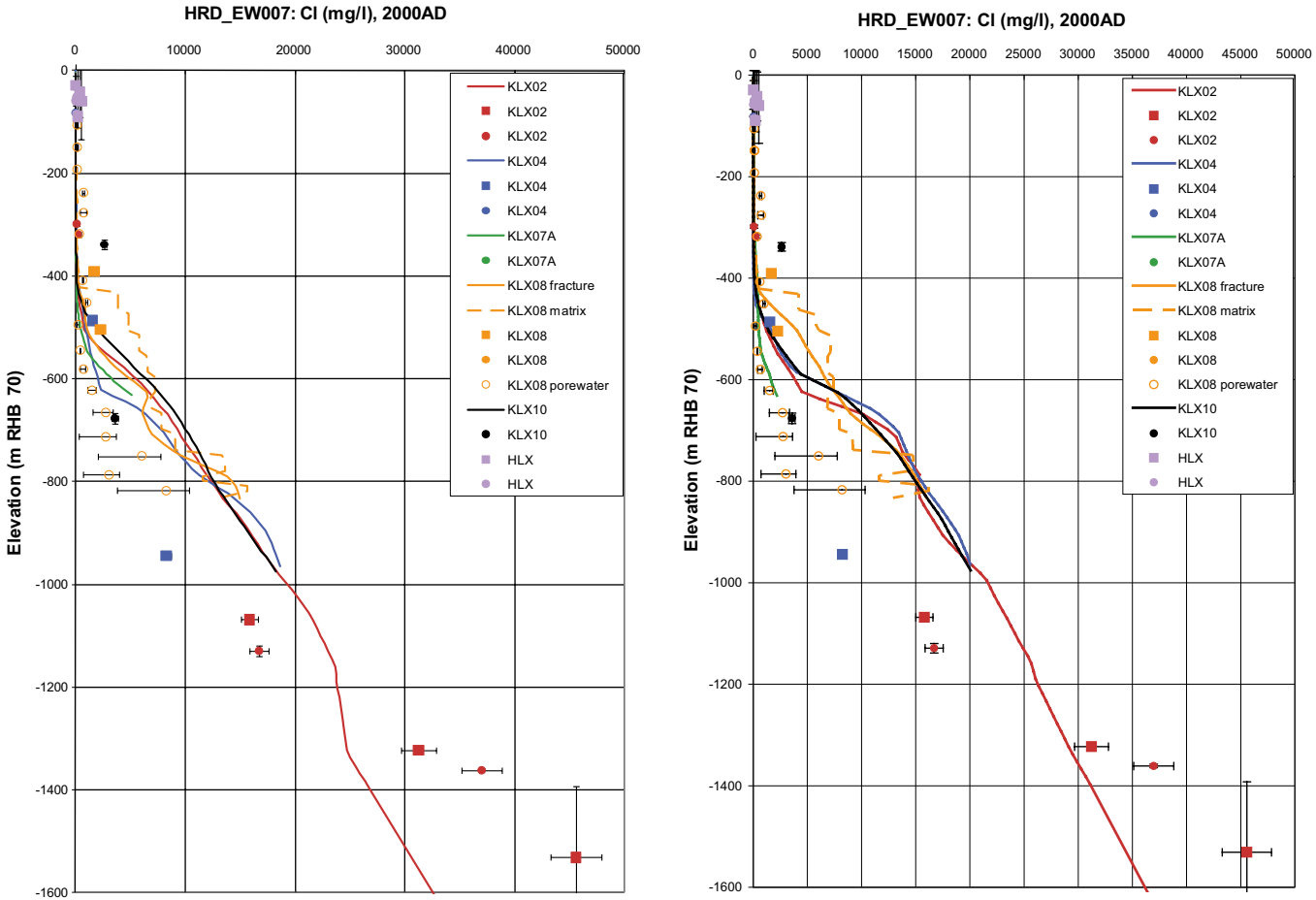

Figure C-64. *A comparison of the modelled and measured Cl concentrations in the fracture system for boreholes in HRD_EW007 for the Stochastic continuum model (left) and the Elaborated Hydro-DFN (right). Square symbols are used for category 1–3 data, circles are used for the pore water data, and small diamond symbols are used for category 4 data. The error bars on the data indicate the laboratory analytical error. The solid lines show the distribution in the borehole simulated in the fracture system, and the dashed lines are for the matrix.*

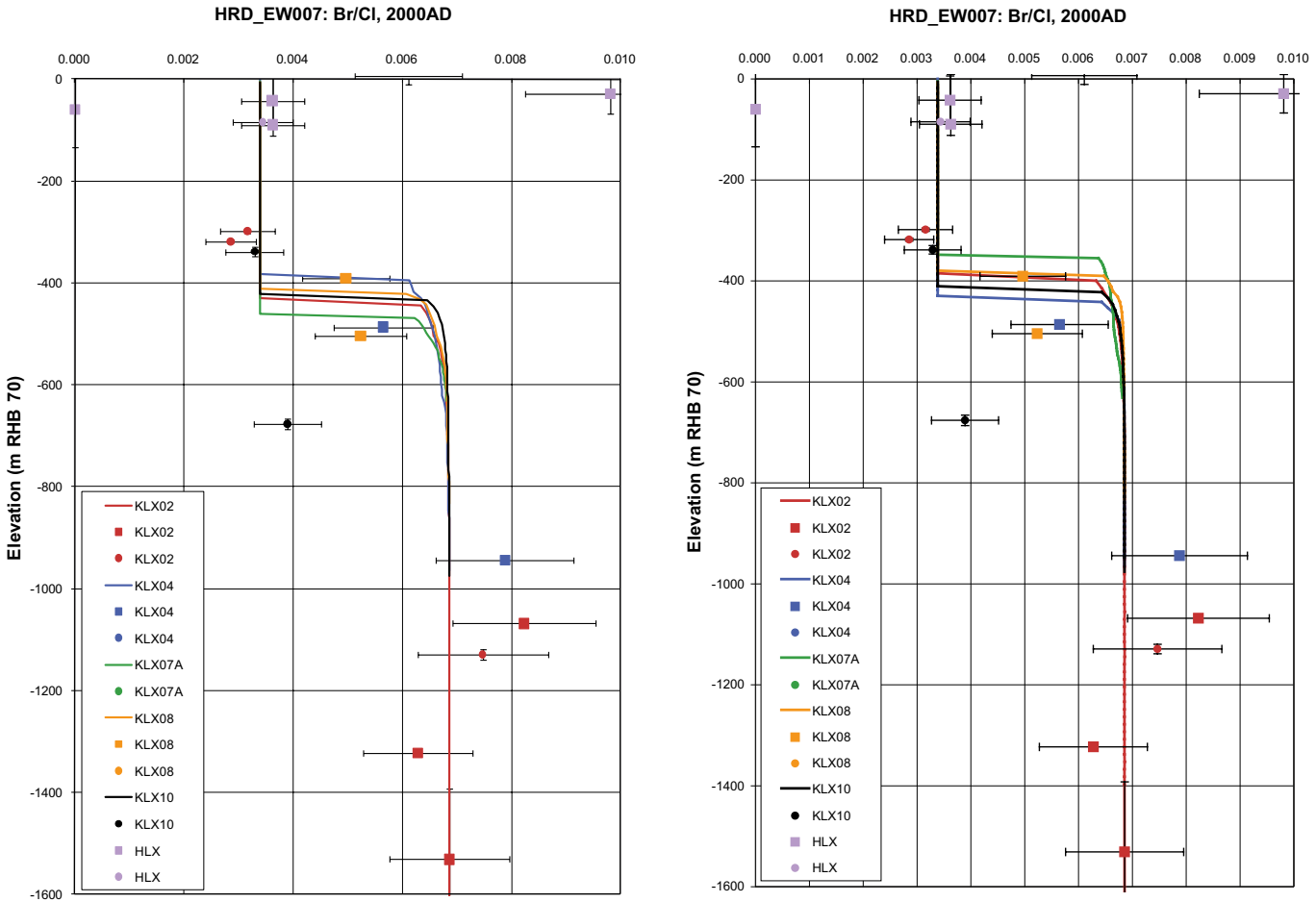

Figure C-65. *A comparison of the modelled and measured Br/Cl concentrations in the fracture system for boreholes in HRD_EW007 for the Stochastic continuum model (left) and the Elaborated Hydro-DFN (right). Square symbols are used for category 1–3 data, circles are used for the pore water data, and small diamond symbols are used for category 4 data. The error bars on the data indicate the laboratory analytical error. The solid lines show the distribution in the borehole simulated in the fracture system, and the dashed lines are for the matrix.*

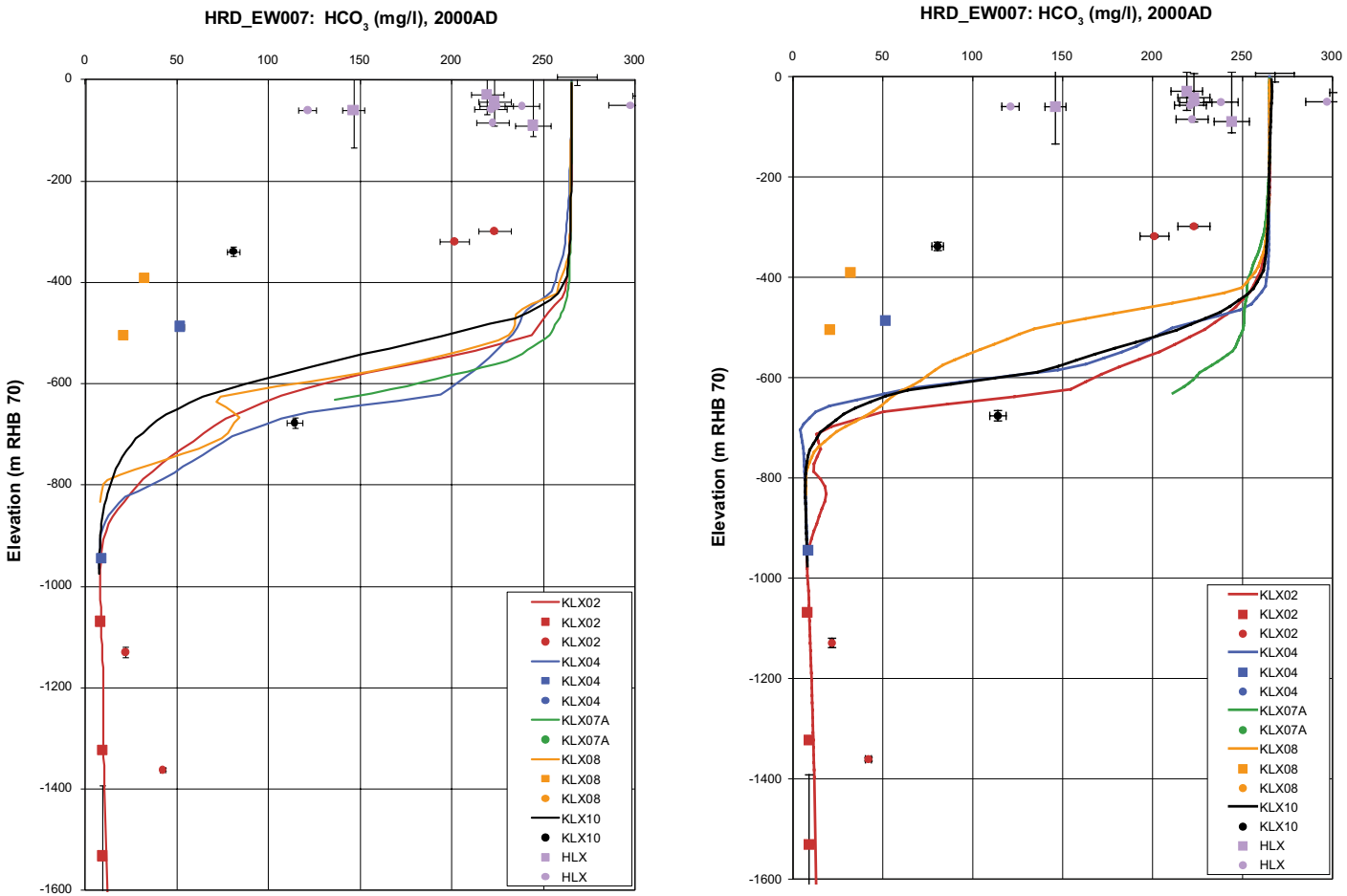

Figure C-66. *A comparison of the modelled and measured HCO_3 concentrations in the fracture system for boreholes in HRD_EW007 for the Stochastic continuum model (left) and the Elaborated Hydro-DFN (right). Square symbols are used for category 1–3 data, circles are used for the pore water data, and small diamond symbols are used for category 4 data. The error bars on the data indicate the laboratory analytical error. The solid lines show the distribution in the borehole simulated in the fracture system, and the dashed lines are for the matrix.*

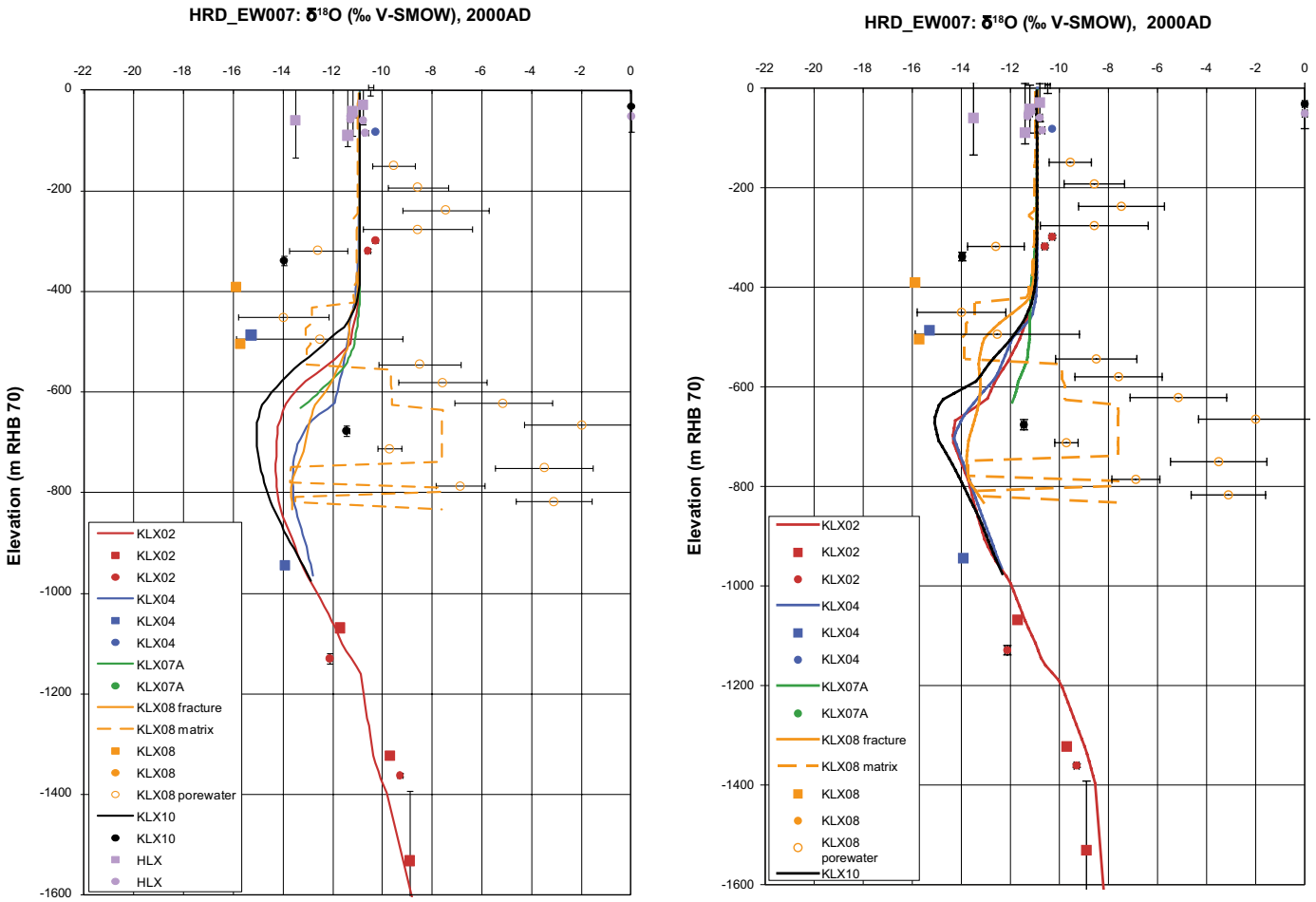

Figure C-67. *A comparison of the modelled and measured $\delta^{18}O$ concentrations in the fracture system for boreholes in HRD_EW007 for the Stochastic continuum model (left) and the Elaborated Hydro-DFN (right). Square symbols are used for category 1–3 data, circles are used for the pore water data, and small diamond symbols are used for category 4 data. The error bars on the data indicate the laboratory analytical error. The solid lines show the distribution in the borehole simulated in the fracture system, and the dashed lines are for the matrix.*

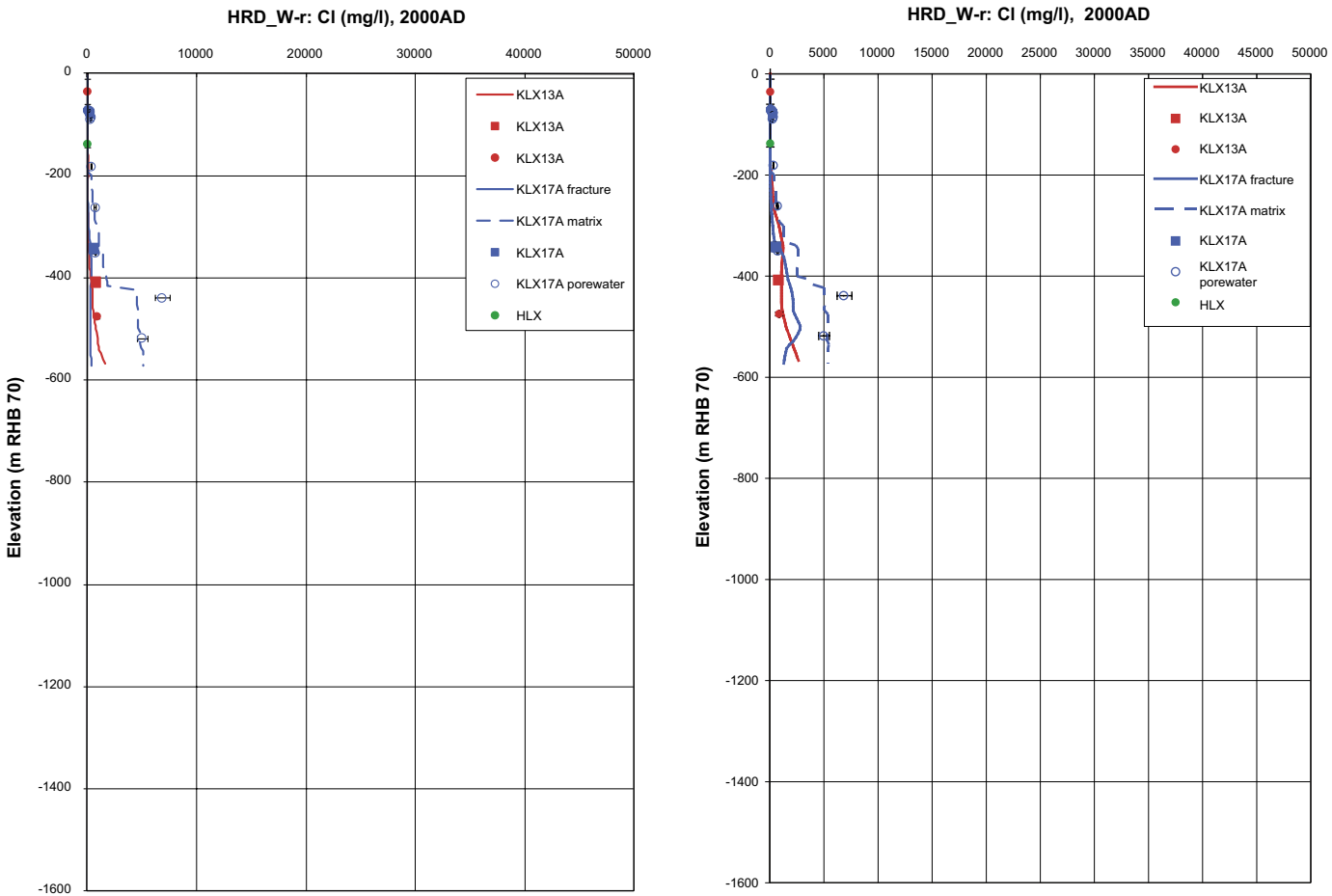

Figure C-68. *A comparison of the modelled and measured Cl concentrations in the fracture system for boreholes in HRD_W-recharge for the Stochastic continuum model (left) and the Elaborated Hydro-DFN (right). Square symbols are used for category 1–3 data, circles are used for the pore water data, and small diamond symbols are used for category 4 data. The error bars on the data indicate the laboratory analytical error. The solid lines show the distribution in the borehole simulated in the fracture system, and the dashed lines are for the matrix.*

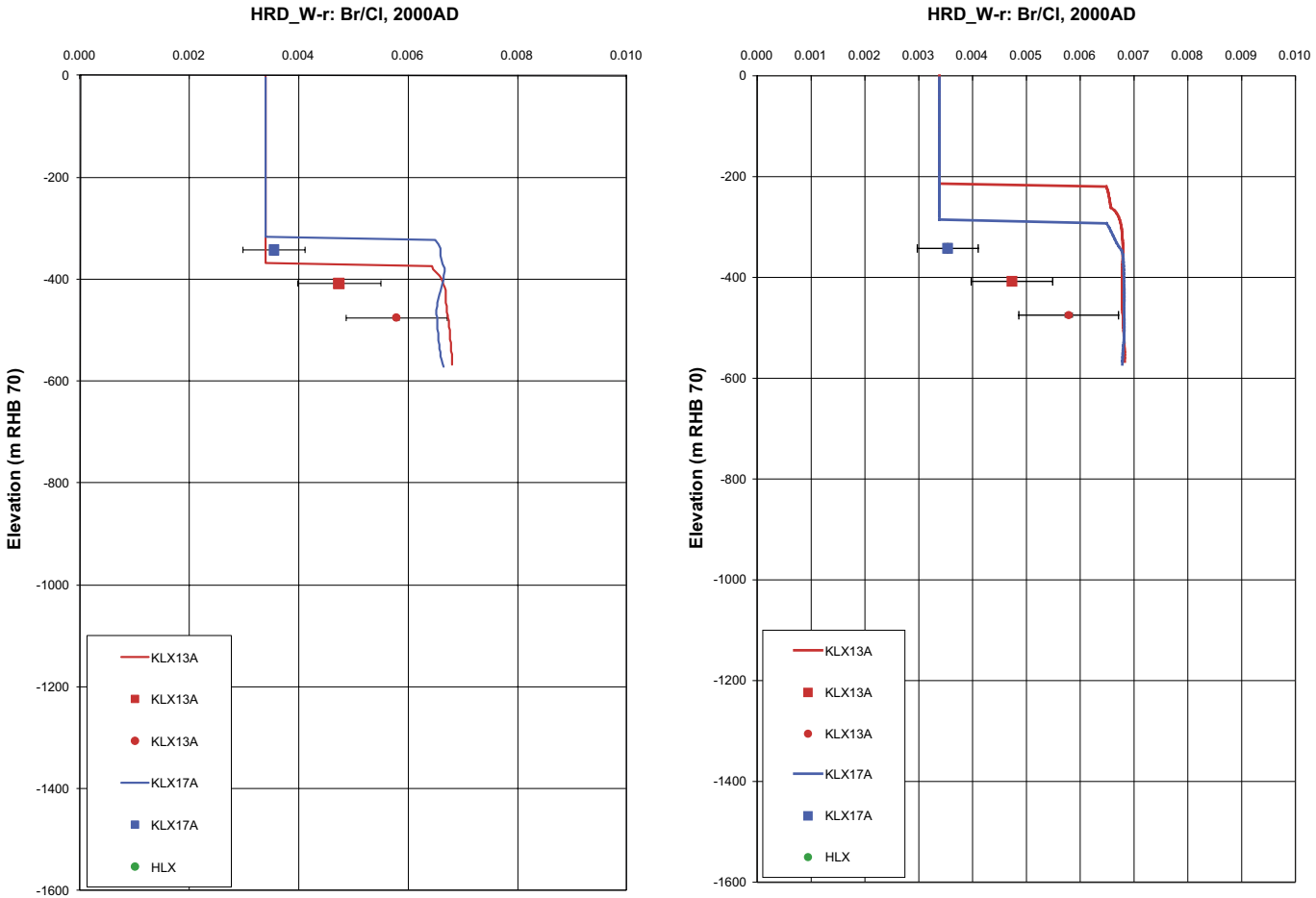

Figure C-69. *A comparison of the modelled and measured Br/Cl concentrations in the fracture system for boreholes in HRD_W-recharge for the Stochastic continuum model (left) and the Elaborated Hydro-DFN (right). Square symbols are used for category 1–3 data, circles are used for the pore water data, and small diamond symbols are used for category 4 data. The error bars on the data indicate the laboratory analytical error. The solid lines show the distribution in the borehole simulated in the fracture system, and the dashed lines are for the matrix.*

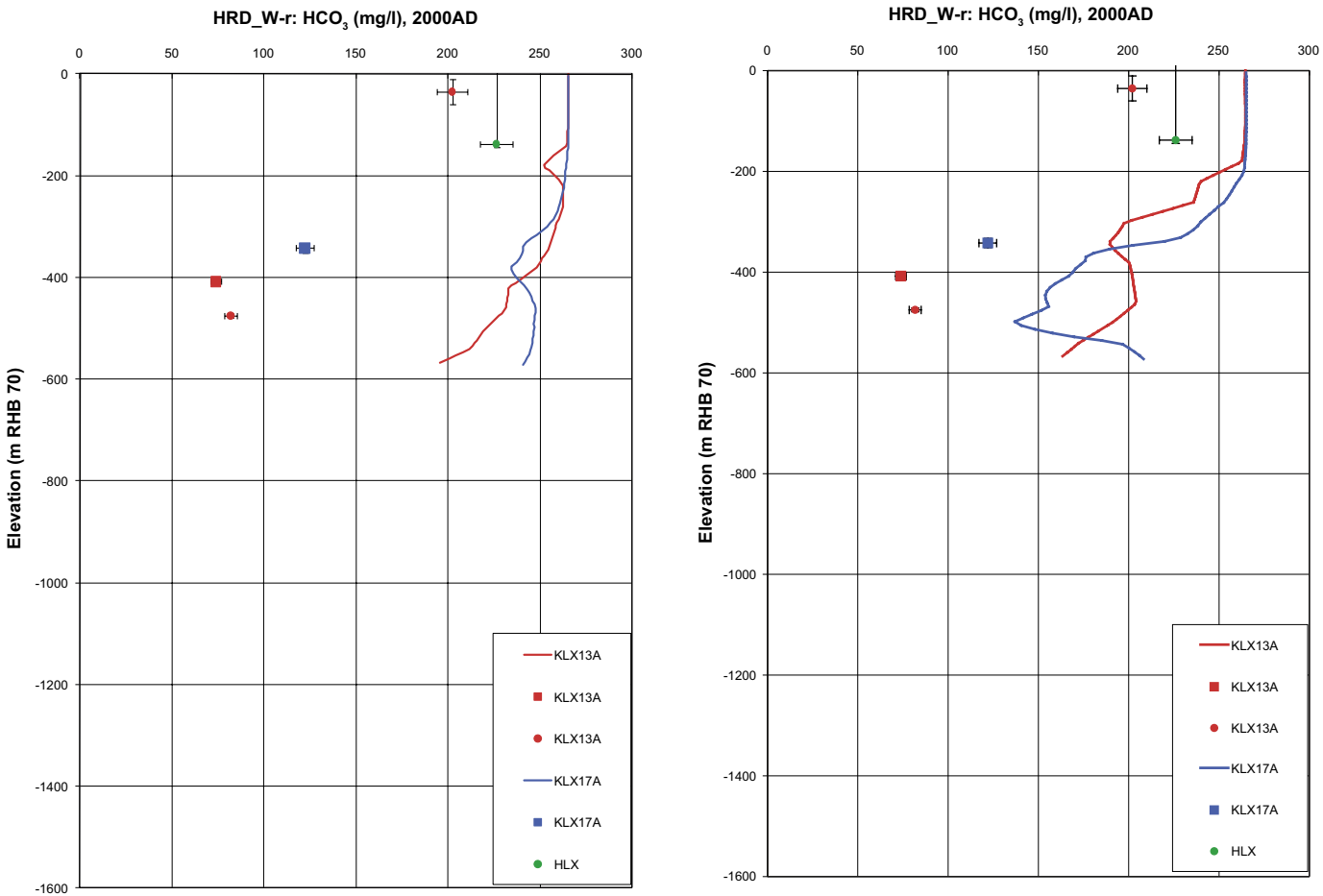

Figure C-70. *A comparison of the modelled and measured HCO_3 concentrations in the fracture system for boreholes in HRD_W-recharge for the Stochastic continuum model (left) and the Elaborated Hydro-DFN (right). Square symbols are used for category 1–3 data, circles are used for the pore water data, and small diamond symbols are used for category 4 data. The error bars on the data indicate the laboratory analytical error. The solid lines show the distribution in the borehole simulated in the fracture system, and the dashed lines are for the matrix.*

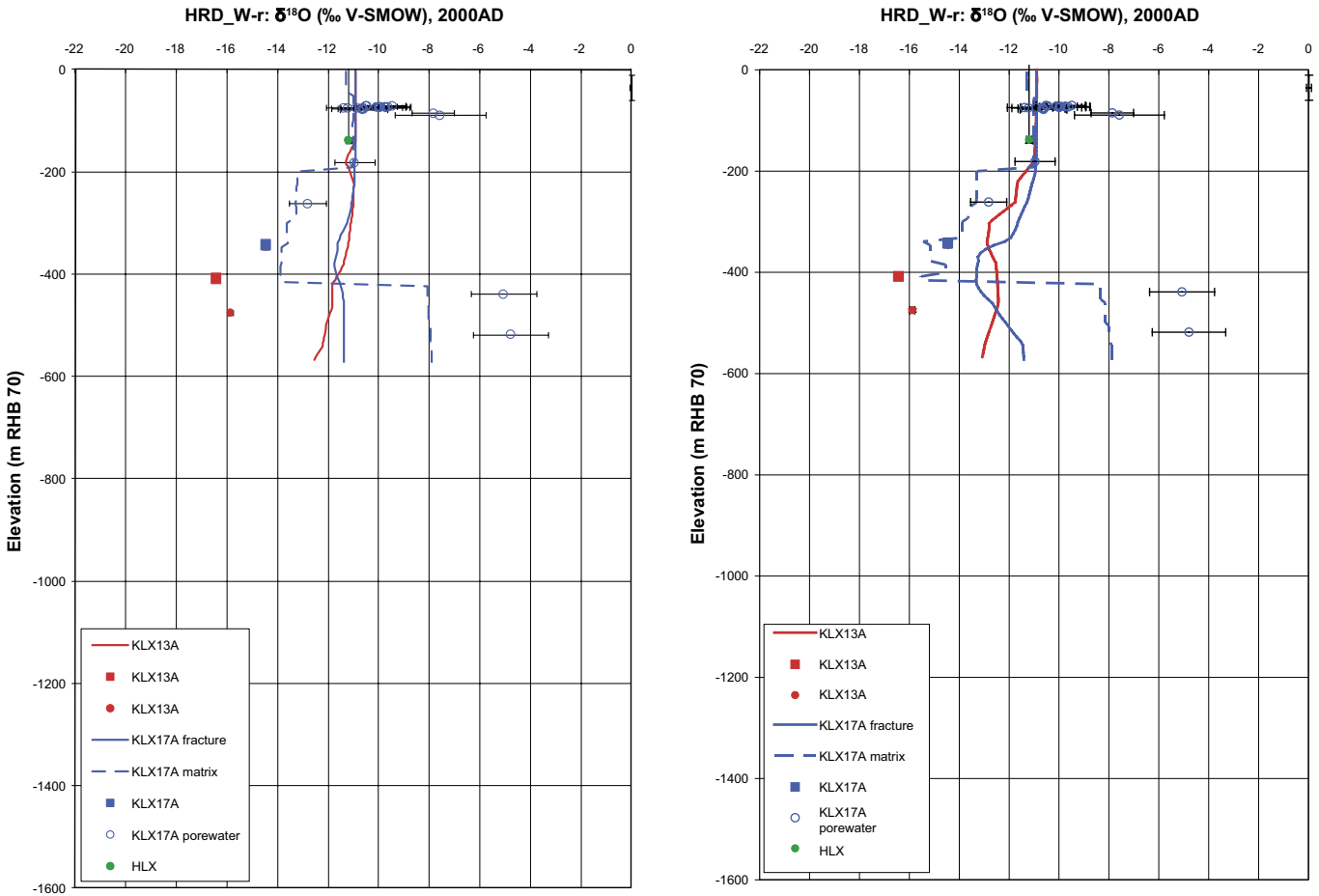

Figure C-71. *A comparison of the modelled and measured $\delta^{18}O$ concentrations in the fracture system for boreholes in HRD_W-recharge for the Stochastic continuum model (left) and the Elaborated Hydro-DFN (right). Square symbols are used for category 1–3 data, circles are used for the pore water data, and small diamond symbols are used for category 4 data. The error bars on the data indicate the laboratory analytical error. The solid lines show the distribution in the borehole simulated in the fracture system, and the dashed lines are for the matrix.*

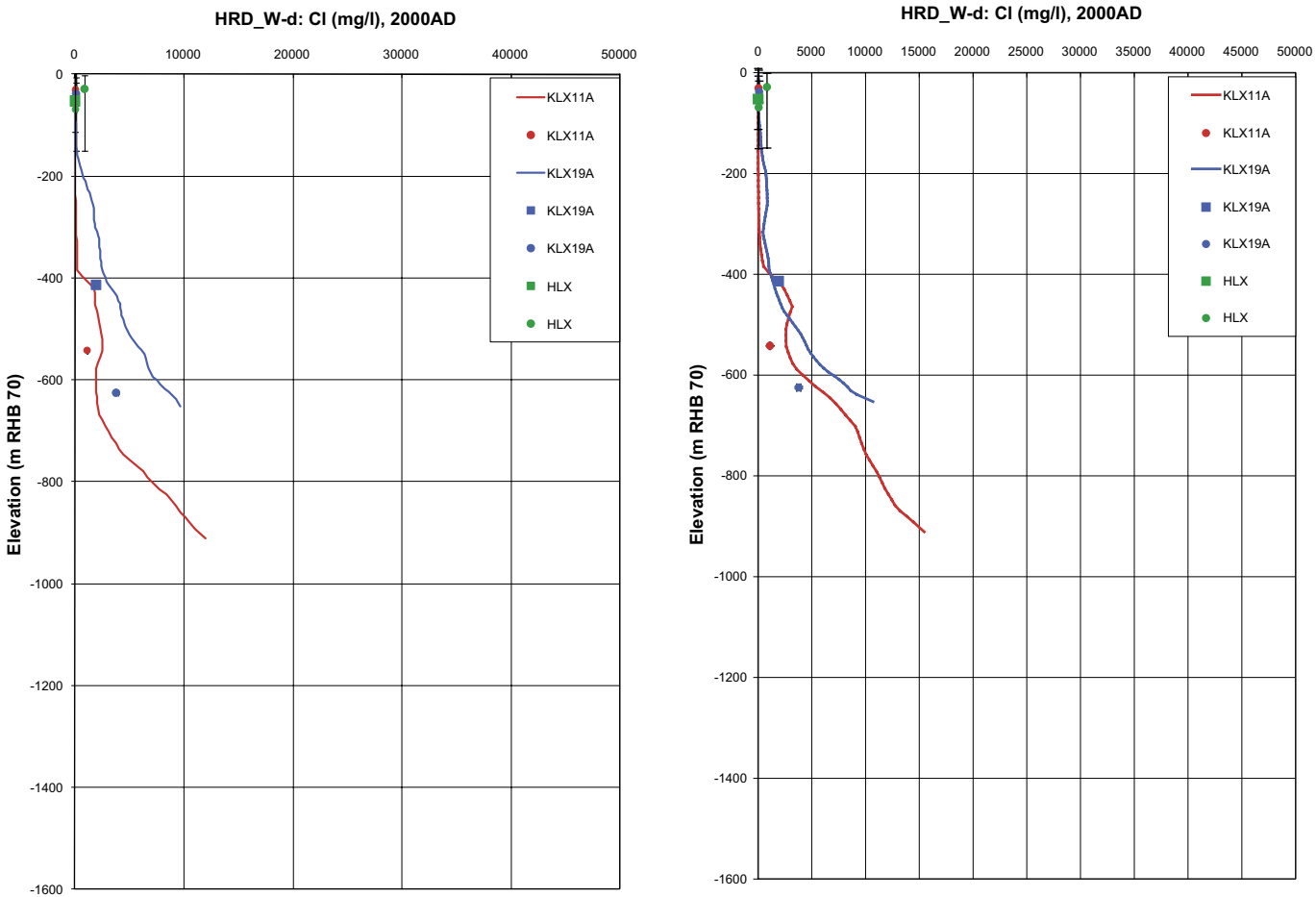

Figure C-72. *A comparison of the modelled and measured Cl concentrations in the fracture system for boreholes in HRD_W-discharge for the Stochastic continuum model (left) and the Elaborated Hydro-DFN (right). Square symbols are used for category 1–3 data, circles are used for the pore water data, and small diamond symbols are used for category 4 data. The error bars on the data indicate the laboratory analytical error. The solid lines show the distribution in the borehole simulated in the fracture system, and the dashed lines are for the matrix.*

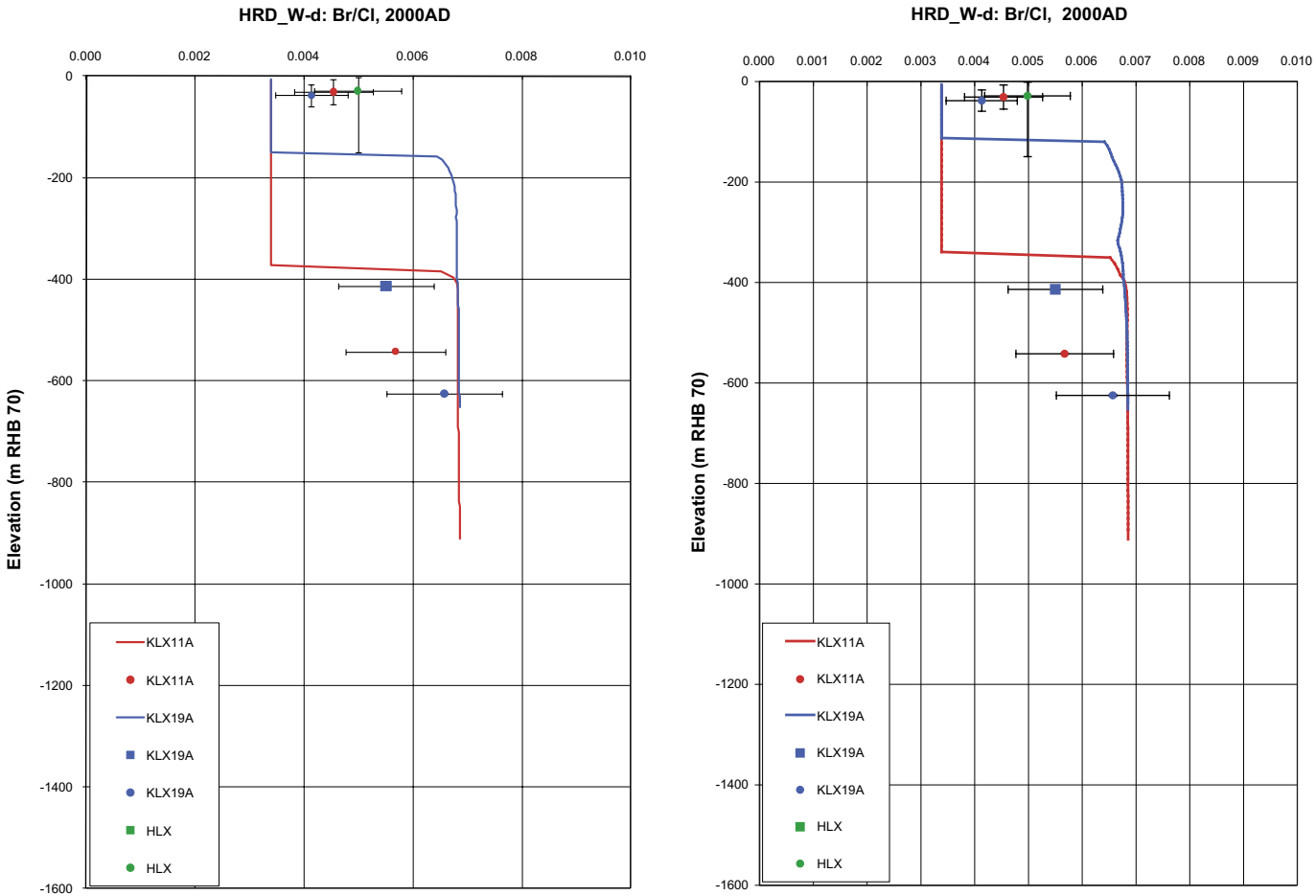

Figure C-73. *A comparison of the modelled and measured Br/Cl concentrations in the fracture system for boreholes in HRD_W-discharge for the Stochastic continuum model (left) and the Elaborated Hydro-DFN (right). Square symbols are used for category 1–3 data, circles are used for the pore water data, and small diamond symbols are used for category 4 data. The error bars on the data indicate the laboratory analytical error. The solid lines show the distribution in the borehole simulated in the fracture system, and the dashed lines are for the matrix.*

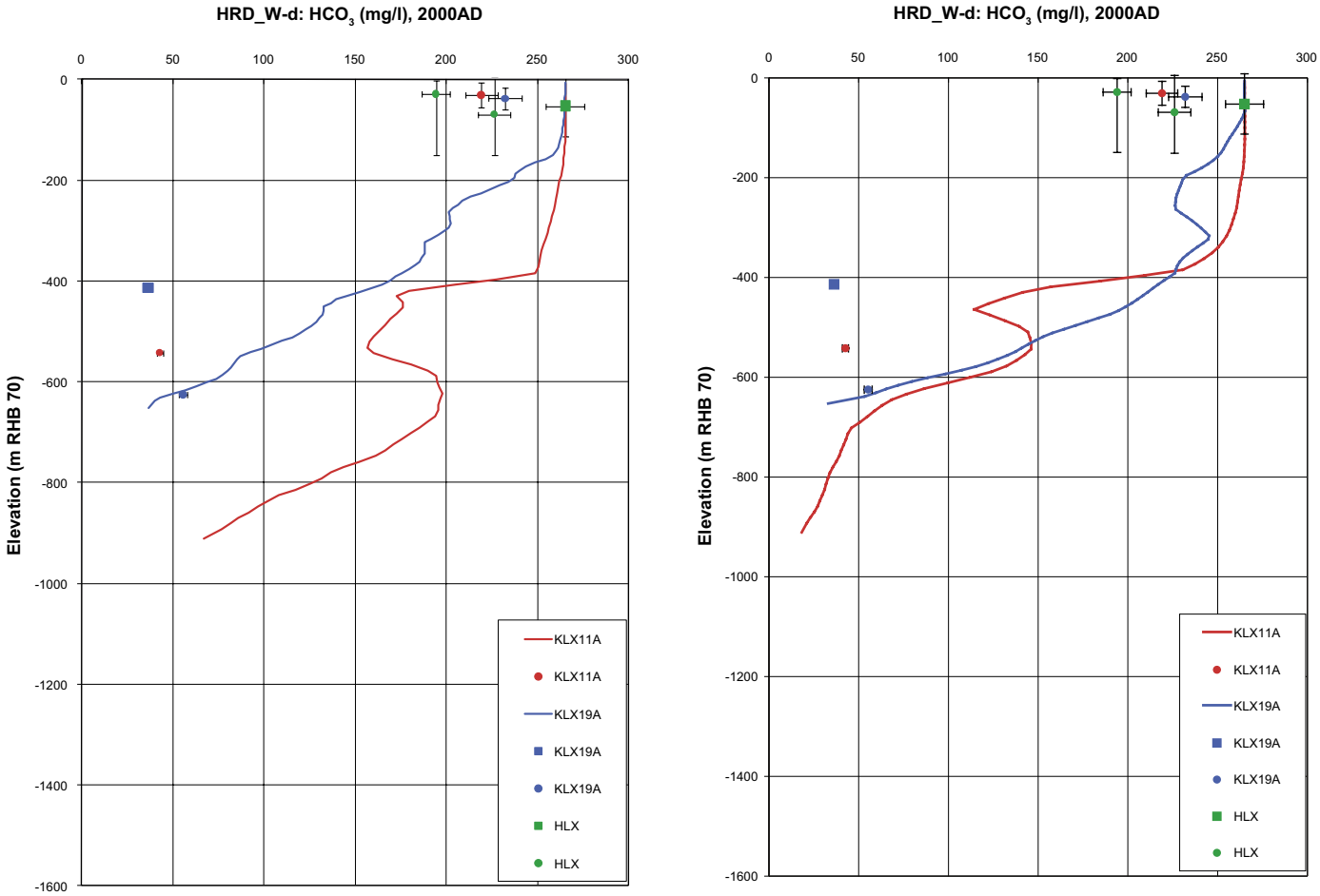

Figure C-74. *A comparison of the modelled and measured HCO_3 concentrations in the fracture system for boreholes in HRD_W-discharge for the Stochastic continuum model (left) and the Elaborated Hydro-DFN (right). Square symbols are used for category 1–3 data, circles are used for the pore water data, and small diamond symbols are used for category 4 data. The error bars on the data indicate the laboratory analytical error. The solid lines show the distribution in the borehole simulated in the fracture system, and the dashed lines are for the matrix.*

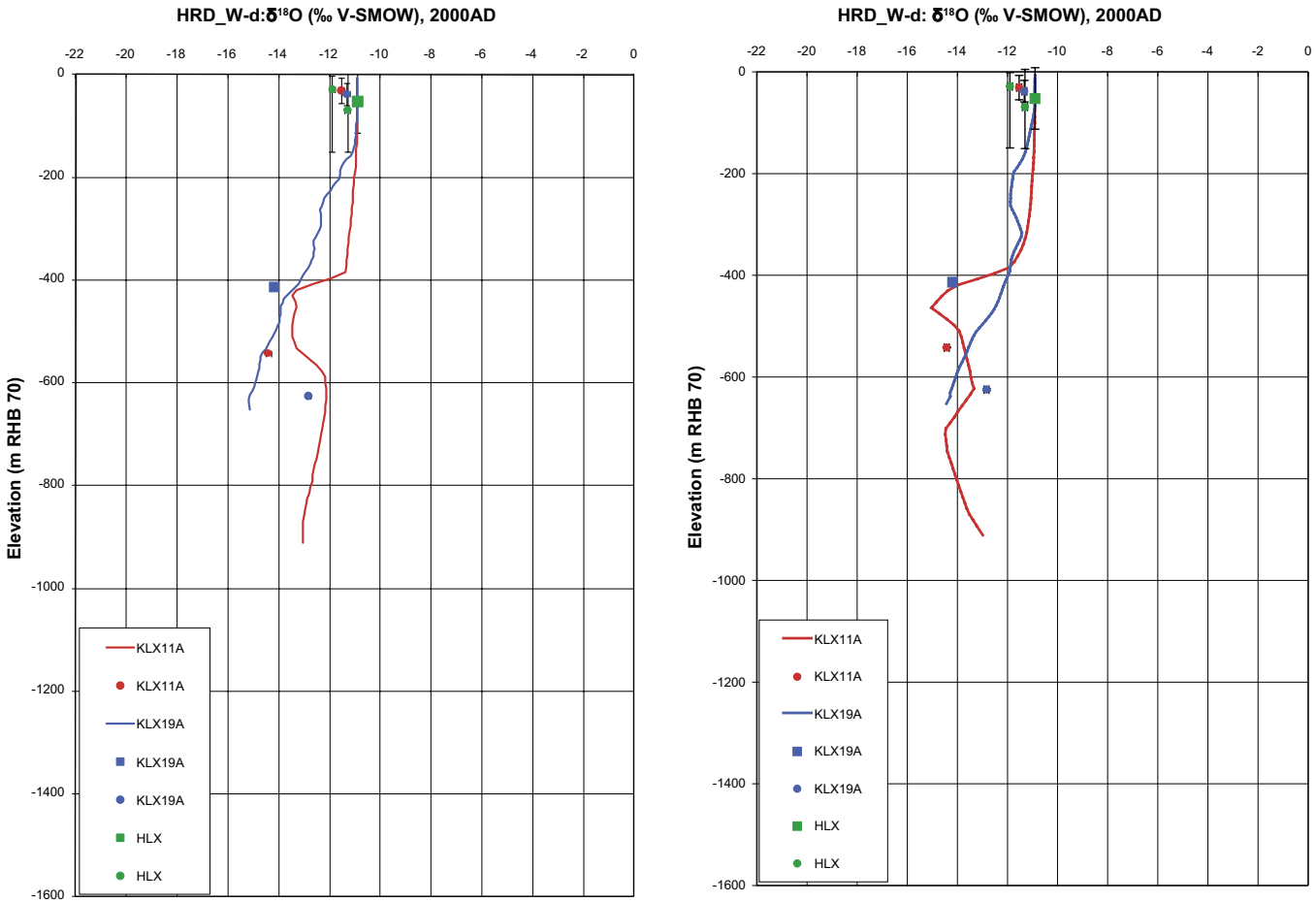

Figure C-75. *A comparison of the modelled and measured $\delta^{18}O$ concentrations in the fracture system for boreholes in HRD_W-discharge for the Stochastic continuum model (left) and the Elaborated Hydro-DFN (right). Square symbols are used for category 1–3 data, circles are used for the pore water data, and small diamond symbols are used for category 4 data. The error bars on the data indicate the laboratory analytical error. The solid lines show the distribution in the borehole simulated in the fracture system, and the dashed lines are for the matrix.*

Appendix D

Derivation of Performance Measure Equations

In COMP23 analytic solutions are used in several cases to give good representations of radionuclide migration in regions with small dimensions without incurring the computational costs of a finely discretised numerical model. One such case is that of radionuclide migration from a bentonite-filled deposition hole or tunnel into a fracture carrying flow that intersects the deposition hole or tunnel. This is represented in terms of the following analytic solution.

Radionuclide migration is considered for constant uniform flow u parallel to the x-axis in the region

$0 \leq x \leq L_f$

$0 \leq y \leq e_f$

$0 \leq z \leq \infty$

shown in Figure D-1, which represents a parallel-sided fracture with aperture e_f, with the concentration held at some value c_0 on $z = 0$, which represents the interface between the bentonite-filled deposition hole or tunnel, where there is no flow and the water flowing in the fracture.

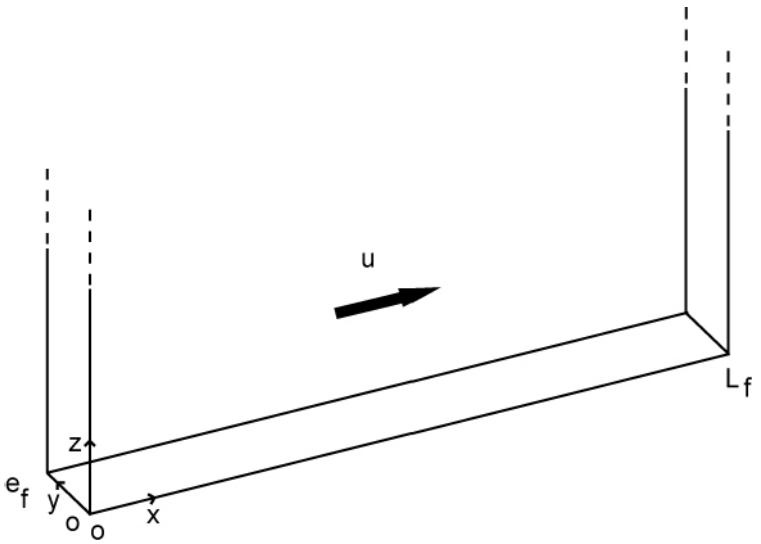

Figure D-1. *Domain for analytic solution.*

The equation that represents advection and diffusion of a solute migrating in the domain is

$$\frac{\partial c}{\partial t} + u\frac{\partial c}{\partial x} = D_w\left(\frac{\partial^2 c}{\partial x^2} + \frac{\partial^2 c}{\partial y^2} + \frac{\partial^2 c}{\partial z^2}\right) \quad \text{(D-1)}$$

where

- u is flow.
- c is concentration.
- t is time.
- D_w is the diffusion coefficient for the solute.

In the case of interest, the first term on the right-hand side is relatively small and can be neglected and the second term on the right-hand side is zero. Then, for steady state, the equation reduces to

$$u\frac{\partial c}{\partial x} = D_w\frac{\partial^2 c}{\partial z^2} \quad \text{(D-2)}$$

which is essentially the 1D diffusion equation with x/u taking the role of time. The solution to this for the case of interest is well known and is

$$c = c_0 erfc\left(\frac{z}{2\sqrt{D_w x/u}}\right) \quad \text{(D-3)}$$

where

$$erfc(\xi) = 1 - \frac{2}{\sqrt{\pi}}\int_0^{\xi} e^{-\zeta^2} d\zeta$$

is the complementary error function.

The total amount of solute in the water at $x = L_f$ is

$$\int_0^{\infty} dz e_f c_0 erfc\left(\frac{z}{2\sqrt{D_w L_f/u}}\right) \quad \text{(D-4)}$$

On changing variables to

$$\xi = \frac{z}{2\sqrt{D_w L_f/u}}$$

and integrating by parts, this can be written as

$$\left[e_f c_0 2\sqrt{D_w L_f/u}\,\xi erfc(\xi)\right]_0^{\infty} + e_f c_0 2\sqrt{D_w L_f/u}\int_0^{\infty} d\xi\xi\frac{2}{\sqrt{\pi}}e^{-\xi^2} = e_f c_0 2\sqrt{\frac{D_w L_f/u}{\pi}} \quad \text{(D-5)}$$

Hence the flux of solute out of the domain can be expressed as

$Q_{eq}c_0$

where

$$Q_{eq} = u e_f\sqrt{\frac{4D_w L_f/u}{\pi}} \quad \text{(D-6)}$$

Various approximations have been made in this. Firstly, the flow has been taken to be independent of y. In reality, there would be a parabolic variation of the flow with y within a fracture. It can be shown that, asymptotically, diffusion in such a flow field approximates to diffusion in the constant flow field with an enhanced diffusion coefficient (this is so-called Taylor dispersion). The flow field has also been taken to be 1D and unaffected by the presence of the deposition hole. The 1D approximation is reasonable provided that the radius of the deposition hole is large compared to the effective distance over which the solute diffuses.

The representation described above has been used for several cases, which are discussed below.

D.1 Qeq for release into fractured rock from a deposition hole (path Q1) for a repository-scale model

The first case is that of path Q1 (in the notation of section 3.2.6) in which several fractures intersect a deposition hole containing a waste package surrounded by bentonite, see Figure D-2. In this case, the approximation is made that the concentration on the interface between the bentonite and the water flowing in the fracture is the same for all fractures. Taking the fractures to be square, with uniform flow aligned with one of the axes, the flow velocity in a fracture is given by

$$u_f = \frac{Q_f}{e_f \sqrt{a_f}} \tag{D-7}$$

where

- Q_f is the water flux in the fracture [m^3/y].
- a_f is the area of the fracture (and so $\sqrt{a_f}$ is the length of a side) [m^2].
- e_f is the aperture of the fracture [m].

Then, using the analysis derived above, the total flux of solute into the fractures is given by $Q_{eq}c_0$ where

$$Q_{eq1} = \sum_f \frac{Q_f}{\sqrt{a_f}} \sqrt{\frac{4D_w t_f}{\pi}} \tag{D-8}$$

where

$$t_f = \frac{L_f e_f}{Q_f / \sqrt{a_f}}.$$

where L_f is the length of the intersection of the deposition hole with the fracture.

The equivalent Darcy flux in the vicinity of the deposition hole is given by

$$U_{r1} = \frac{1}{w_c} \sum_f \frac{Q_f}{\sqrt{a_f}} \tag{D-9}$$

where w_c is the height of the deposition hole.

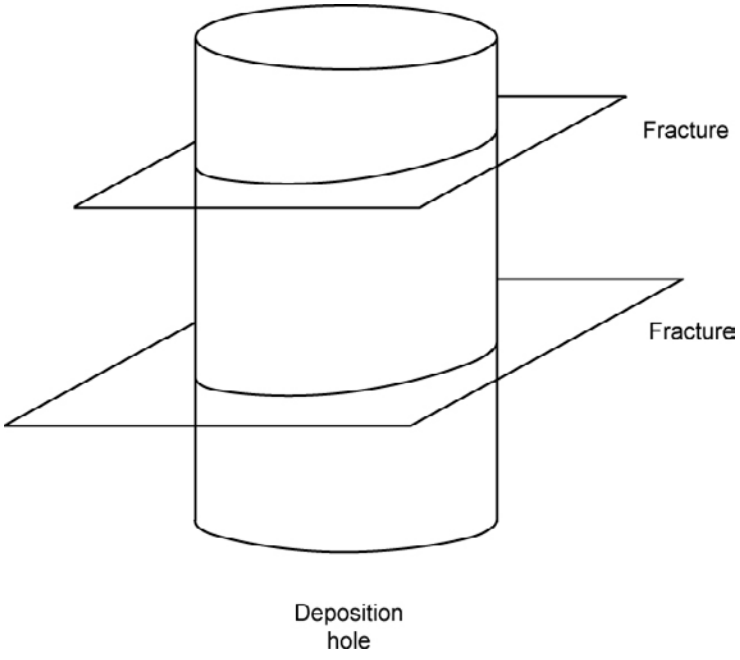

Figure D-2. *Fractures intersecting a deposition hole.*

D.2 Qeq for release into the EDZ from a deposition hole (path Q2) for a repository-scale model

The second case to be considered is that of migration of solute into fractures in the EDZ at the top of a deposition hole, path Q2 (in the notation of section 3.2.6), see Figure D-3. The analysis for this is essentially the same as that for the previous case, leading to

$$Q_{eq2} = \sum_E \frac{Q_E}{\sqrt{a_E}} \sqrt{\frac{4 D_w t_E}{\pi}} \qquad \text{(D-10)}$$

where

- Q_E is the water flux in a fracture in the EDZ intersecting the deposition hole [m³/y].
- a_E is the area of the fracture (and so $\sqrt{a_E}$ is the length of a side) [m²].
- e_E is the aperture of the fracture [m].

and

$$t_E = \frac{L_E e_E}{Q_E / \sqrt{a_E}} .$$

where L_E is the length of the intersection of the fracture in the EDZ with the deposition hole.

The equivalent Darcy flux in the EDZ in the vicinity of the deposition hole is given by

$$U_{r2} = \frac{1}{w_E} \sum_E \frac{Q_E}{\sqrt{a_E}} \qquad \text{(D-11)}$$

where

- w_E is the thickness of the EDZ [m].

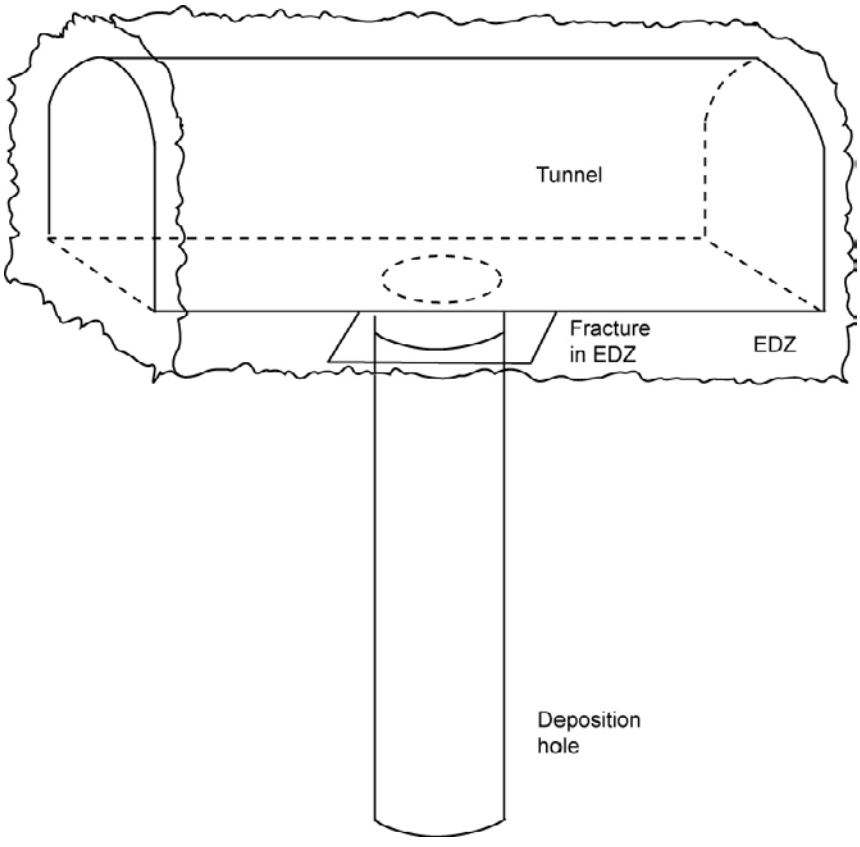

Figure D-3. *Fracture in EDZ intersecting deposition hole.*

D.3 Qeq for release into a fracture from a tunnel (path Q3) for a repository-scale model

The third case of interest is that of solute migration into a fracture intersecting a tunnel, path Q3 (in the notation of section 3.2.6), see Figure D-4. In this case, the fracture is taken to be larger than the tunnel diameter and so the flow in the fracture splits around the intersection with the tunnel. Solutes can then migrate into the flow on both sides. Taking this into account, a similar analysis to that for the previous two cases leads to

$$Q_{eq3} = 2\frac{Q_{f3}}{\sqrt{a_{f3}}}\sqrt{\frac{4D_w t_{f3}}{\pi}} \qquad \text{(D-12)}$$

where

- Q_{f3} is the water flux in the fracture intersecting the tunnel [m³/y].
- a_{f3} is the area of the fracture (and so $\sqrt{a_E}$ is the length of a side) [m²].
- e_{f3} is the aperture of the fracture [m].

and

$$t_{f3} = \frac{L_{f3} e_{f3}}{Q_{f3} / \sqrt{a_{f3}}}.$$

where L_{f3} is half the circumference of the tunnel, assuming the fracture is normal to the tunnel. The factor 2 indicates that flow can be around either side of the tunnel. For Q1 and Q2 in the repository-scale model, the factor 2 is not necessary as the flows through intersections with each face of the deposition hole are explicitly summed.

The equivalent Darcy flux in the vicinity of the tunnel is given by

$$U_{r3} = \frac{1}{w_{f3}}\frac{Q_{f3}}{\sqrt{a_{f3}}} \qquad \text{(D-13)}$$

where

- w_{f3} is the length of the tunnel associated with the fracture in some sense [m].
- Q_{f3} is the volumetric flow rate in the fracture intersecting the tunnel [m³/y].

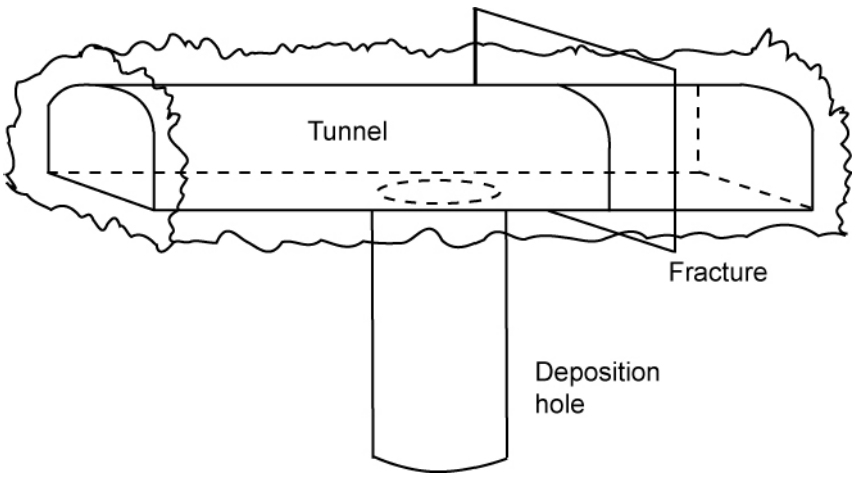

Figure D-4. *Fracture intersecting a tunnel.*

D.4 Qeq for release into a fracture (paths Q1, Q2 and Q3) for a site-scale model

For the site-scale model, the repository structures are represented by equivalent fractures rather than as CPM. Therefore, particles are released directly into fractures for Q1, Q2 and Q3. Since the tunnels and deposition holes are not represented with a 3D volume, it is not appropriate to sum over all fractures intersecting the deposition hole or tunnel. Therefore, the Q_{eq} and U_r values are only calculated for the single fracture that the particle enters when it leaves the deposition hole or tunnel. The equivalent groundwater flow-rate, Q_{eq123}, is calculated from the flow in the starting fracture for each released particle. Allowing for the flow being on either side of a deposition hole or tunnel, Q_{eq123} can be written as:

$$Q_{eq123} = 2\sqrt{\frac{4D_w L e_{tf} U_{T0}}{\pi}} \qquad \text{(D-14)}$$

The factor 2 indicates that flow can be around either side of the tunnel or deposition hole. For Q1 and Q2 in the repository-scale model, the factor 2 is not necessary as the flows through intersections with each face of the deposition hole are explicitly summed. An equivalent flux can be determined from

$$U_{123} = \frac{U_{T0}}{w}$$

where

- L is half the circumference of the deposition hole for paths Q1 and Q2 and half the circumference of the tunnel for path Q3.
- U_{T0} is the flow rate per unit width in the fracture [m^2/y].
- e_{tf} is the transport aperture of the fracture [m].
- w is the height of the deposition hole or fracture [m].

Appendix E

Elaborated Hydro-DFN model

E.1 Introduction

This section presents details of the Elaborated Hydro-DFN model described in Section 5.1. In particular:

- The details of the methodology are given.
- The full Hydro-DFN parameterisation is tabulated.
- The overall match to calibration targets presented.
- The results of all upscaling calculations are listed.
- The predictions of palaeochemical modelling are compared to measured values of various hydrochemical data.

E.2 Methodology

For SDM-Site, the Hydro-DFN models were set up by using artificial model domains with generic 1,000 m long vertical boreholes rather than specific boreholes. For the Elaborated Hydro-DFN method, geolocated data and deterministic HCD features are included to alter the connectivity in the system and thereby obtain an alternative fracture size distribution. The following general steps are followed:

- Select representative boreholes for each rock domain. The following boreholes were modelled: KLX11A, KLX17A and KLX19A in HRD_W; KLX03, KLX05, KLX15A and KLX21B in HRD_C; and KLX07A and KLX08 in HRD_EW007 (shown in Figure 5-1).
- Create a geolocated model for each of the selected boreholes, using a deterministic HCD, site coordinates (centred on the borehole) and real borehole coordinates (approximated by straight lines, starting from –50 m.a.s.l to simulate the borehole casing). The model volume for each borehole is about 400x400x1,200 m, but the depth varied according to borehole length. The model followed the inclination of the simplified borehole (see, for example, Figure 5-2).
- Use the same four depth zones as for SDM-Site:
  - DZ1 –150 to 0 m.a.s.l.
  - DZ2 –400 to –150 m.a.s.l.
  - DZ3 –650 to –400 m.a.s.l.
  - DZ4 –1,000 to –650 m.a.s.l.
- Simulate connectivity and flow for 12 realisations of the model in the same way as for SDM-Site.
- Compare the ensemble results of 12 model realisations to the ensemble of the measured data for all the selected boreholes within a given rock domain. Consider all sets individually, but the main focus is on the WNW set.
  - Start by matching the PFL-f intensity based on connectivity by using $P_{10,corr}$, with a maximum Terzaghi correction of 100.
  - Then match the flow distribution using semi-correlated transmissivity-size relationships.
  - Normalise the statistics to the thickness of each depth zone. This needs to be done for both simulations and data.
  - Normalize the simulation data to the lengths within each depth zone. The deformation zones have to be removed, and the lengths are different for each borehole.

E.3 Calibration

The calibrated Hydro-DFN parameters from this study are shown in Table E-1 to Table E-3. There is a shift to a slightly larger fracture size slope parameter, k_r, compared to the SDM-Site Hydro-DFN /Rhén et al. 2008/ (cf. Table 2-5). The match to the calibration data is summarised for each HRD in Figure E-1 to Figure E-18. These are in good agreement, generally as good as or better than SDM-Site. In particular, there is an improved match for individual sets, as shown in the bar and whisker plots. The agreement in the shape of the distributions of Q/s was also quantified by calculating the correlation coefficient between the numbers of PFL-f features across the histogram bins (half-order of magnitude in flow-rate) as given in Table E-4. The table also shows a comparison with the corresponding correlation coefficients obtained for SDM-Site. The Elaborated Hydro-DFN has higher correlation coefficients than SDM-Site for all rock domains and all depth zones, except for HRD_EW007 at elevations between –650 m and –400 m (DZ3) where the SDM-Site value is slightly higher. The improvement is particularly apparent for HRD_W. These results give a high degree of confidence that the DFN model is sound and reproduces measured data well.

Table E-1. Description of the Elaborated Hydro-DFN input parameters for HRD_C with fixed r_0 = 0.038 m and intensity of open fractures based on OPO.

Depth zone (m.a.s.l.)	Set	Orientation set pole: (trend, plunge), conc.	Fracture radius model power-law (k_r, r_0)	Intensity P_{32} (m^2/m^3) of open fractures	Transmissivity model T (m^2/s) (a, b, σ)
–150 to 0 (DZ1)	ENE	(155.1,3.4), 9.6	(2.70, 0.038)	0.52	SC: ($2\cdot10^{-7}$, 0.7, 0.4)
	WNW	(204,1.6), 12	(2.49, 0.038)	0.95	SC: ($2\cdot10^{-7}$, 0.9, 0.6)
	N-S	(270.2,8.4), 7.8	(2.80, 0.038)	0.54	SC: ($8\cdot10^{-8}$, 0.5, 0.4)
	SubH	(46.3,84.7), 12	(2.59, 0.038)	1.20	SC: ($6\cdot10^{-8}$, 0.7, 0.5)
–400 to –150 (DZ2)	ENE	(155.1,3.4), 9.6	(3.00, 0.038)	0.47	SC: ($6\cdot10^{-7}$, 0.7, 0.9)
	WNW	(204,1.6), 12	(2.44, 0.038)	0.55	SC: ($1\cdot10^{-8}$, 0.5, 0.7)
	N-S	(270.2,8.4), 7.8	(2.91, 0.038)	0.63	SC: ($1\cdot10^{-8}$, 0.7, 0.2)
	SubH	(46.3,84.7), 12	(2.87, 0.038)	0.71	SC: ($3.5\cdot10^{-8}$, 1.2, 0.9)
–650 to –400 (DZ3)	ENE	(155.1,3.4), 9.6	(2.87, 0.038)	0.38	SC: ($8\cdot10^{-8}$, 0.8, 0.6)
	WNW	(204,1.6), 12	(2.54, 0.038)	0.74	SC: ($3\cdot10^{-9}$, 0.8, 0.6)
	N-S	(270.2,8.4), 7.8	(2.87, 0.038)	0.47	SC: ($6\cdot10^{-9}$, 0.4, 0.4)
	SubH	(46.3,84.7), 12	(3.00, 0.038)	0.58	SC: ($2\cdot10^{-7}$, 0.8, 0.7)
–1,000 to –650 (DZ4)	ENE	(155.1,3.4), 9.6	(2.96, 0.038)	0.46	SC: ($1\cdot10^{-8}$, 0.7, 0.4)
	WNW	(204,1.6), 12	(3.00, 0.038)	0.73	SC: ($3\cdot10^{-7}$, 0.7, 0.4)
	N-S	(270.2,8.4), 7.8	(3.00, 0.038)	0.25	SC: ($1\cdot10^{-8}$, 0.7, 0.4)
	SubH	(46.3,84.7), 12	(2.97, 0.038)	0.35	SC: ($1\cdot10^{-7}$, 0.7, 0.4)

Table E-2. Description of the Elaborated Hydro-DFN input parameters for HRD_EW007 with fixed r_0 = 0.038 m and intensity of open fractures based on OPO.

Depth zone (m.a.s.l.)	Set	Orientation set pole: (trend, plunge), conc.	Fracture radius model power-law (k_r, r_0)	Intensity P_{32} (m^2/m^3) of open fractures	Transmissivity model T (m^2/s) (a, b, σ)
–150 to 0 (DZ1)	ENE	(162.8,1.4), 10.7	(2.77, 0.038)	0.55	SC: ($3\cdot10^{-8}$, 0.6, 0.4)
	WNW	(25.3,0.2), 16.4	(2.30, 0.050)	1.01	SC: ($3\cdot10^{-8}$, 0.6, 0.3)
	N-S	(88.9,3.9), 8.8	(2.53, 0.038)	0.33	SC: ($1\cdot10^{-7}$, 0.8, 0.3)
	SubH	(138.7,81.3), 9.7	(2.76, 0.038)	1.72	SC: ($2.3\cdot10^{-7}$,0.8,0.5)
–400 to –150 (DZ2)	ENE	(162.8,1.4), 10.7	(2.83, 0.038)	0.60	SC: ($2\cdot10^{-7}$, 0.6, 0.6)
	WNW	(25.3,0.2), 16.4	(2.41, 0.038)	1.15	SC: ($3\cdot10^{-8}$, 0.6, 0.4)
	N-S	(88.9,3.9), 8.8	(2.60, 0.038)	0.54	SC: ($3\cdot10^{-7}$,0.8, 0.4)
	SubH	(138.7,81.3), 9.7	(2.84, 0.038)	0.82	SC: ($5\cdot10^{-8}$, 0.8, 0.4)
–650 to –400 (DZ3)	ENE	(162.8,1.4), 10.7	(2.93, 0.038)	0.69	SC: ($1\cdot10^{-8}$, 0.5, 0.2)
	WNW	(25.3,0.2), 16.4	(2.62, 0.038)	1.43	SC: ($1.2\cdot10^{-7}$, 0.3, 0.2)
	N-S	(88.9,3.9), 8.8	(3.00, 0.038)	0.64	SC: ($8\cdot10^{-8}$, 0.4, 0.2)
	SubH	(138.7,81.3), 9.7	(2.99, 0.038)	0.92	SC: ($1.5\cdot10^{-7}$, 0.7, 0.3)
–1,000 to –650 (DZ4)	ENE	(162.8,1.4), 10.7	(2.96, 0.038)	0.33	SC: ($1\cdot10^{-8}$, 0.7, 0.4)
	WNW	(25.3,0.2), 16.4	(3.00, 0.038)	0.89	SC: ($3\cdot10^{-7}$, 0.7, 0.4)
	N-S	(88.9,3.9), 8.8	(3.00, 0.038)	0.21	SC: ($1\cdot10^{-8}$, 0.7, 0.4)
	SubH	(138.7,81.3), 9.7	(2.97, 0.038)	0.80	SC: ($1\cdot10^{-7}$, 0.7, 0.4)

Table E-3. Description of the Elaborated Hydro-DFN input parameters for HRD_W with fixed r_0 = 0.038 m and intensity of open fractures based on OPO.

Depth zone (m.a.s.l.)	Set	Orientation set pole: (trend, plunge), conc.	Fracture radius model power-law (k_r, r_0)	Intensity P_{32} (m^2/m^3) of open fractures	Transmissivity model T (m^2/s) (a, b, σ)
–150 to 0 (DZ1)	ENE	(340.3,1.2), 15	(2.59, 0.038)	0.44	SC: ($2.1\cdot10^{-8}$, 0.7, 0.6)
	WNW	(208.9,2.2), 10.9	(2.54, 0.038)	0.61	SC: ($7\cdot10^{-8}$, 0.8, 1.0)
	N-S	(272.8,12), 11.5	(2.52, 0.038)	0.54	SC: ($4\cdot10^{-8}$, 0.7, 0.8)
	SubH	(277.1,84.3), 11.1	(2.50, 0.038)	1.03	SC: ($8\cdot10^{-8}$, 0.7, 0.7)
–400 to –150 (DZ2)	ENE	(340.3,1.2), 15	(2.54, 0.038)	0.28	SC: ($2.2\cdot10^{-9}$, 0.5, 0.4)
	WNW	(208.9,2.2), 10.9	(2.65, 0.038)	0.38	SC: ($1.5\cdot10^{-8}$, 0.5, 1.2)
	N-S	(272.8,12), 11.5	(3.00, 0.038)	0.40	SC: ($5\cdot10^{-9}$, 0.4, 0.3)
	SubH	(277.1,84.3), 11.1	(2.72, 0.038)	0.50	SC: ($1.2\cdot10^{-7}$, 0.7, 1.2)
–650 to –400 (DZ3)	ENE	(340.3,1.2), 15	(3.00, 0.038)	0.17	SC: ($3\cdot10^{-9}$, 0.6, 0.4)
	WNW	(208.9,2.2), 10.9	(2.61, 0.038)	0.33	SC: ($1.5\cdot10^{-8}$, 0.5, 0.3)
	N-S	(272.8,12), 11.5	(2.53, 0.038)	0.30	SC: ($5\cdot10^{-8}$, 0.2, 0.2)
	SubH	(277.1,84.3), 11.1	(2.72, 0.038)	0.38	SC: ($2\cdot10^{-7}$, 0.8, 0.8)
–1,000 to –650 (DZ4)	ENE	(155.1,3.4), 9.6	(3.00, 0.038)	0.12	SC: ($1\cdot10^{-8}$, 0.7, 0.4)
	WNW	(208.9,2.2), 10.9	(3.00, 0.038)	0.09	SC: ($3\cdot10^{-8}$, 0.7, 0.4)
	N-S	(272.8,12), 11.5	(2.53, 0.038)	0.14	SC: ($1\cdot10^{-8}$, 0.7, 0.4)
	SubH	(277.1,84.3), 11.1	(3.00, 0.038)	0.65	SC: ($3\cdot10^{-8}$, 0.7, 0.4)

Table E-4. Correlation coefficients for the distribution of Q/s between model and PFL-f data for the semi-correlated transmissivity model with fixed r_0 = 0.038 m and intensity of open fractures based on OPO. Elaborated Hydro-DFN compared to SDM-Site Hydro-DFN /Rhén et al. 2008/.

Depth zone (m.a.s.l.)	HRD	Correlation coefficient for distribution of Q/s between model and PFL-f data	
		Elaborated Hydro-DFN	SDM-Site
–150 to 0 (DZ1)	HRD_C	0.96	0.92
	HRD_EW007	0.90	0.80
	HRD_W	0.99	0.91
–400 to –150 (DZ2)	HRD_C	0.85	0.82
	HRD_EW007	0.93	0.96
	HRD_W	0.79	0.64
–650 to –400 (DZ3)	HRD_C	0.78	0.77
	HRD_EW007	0.93	0.99
	HRD_W	0.80	0.58
–1,000 to –650 (DZ4)	HRD_C	0.45	0.18
	HRD_EW007	---	---
	HRD_W	---	---

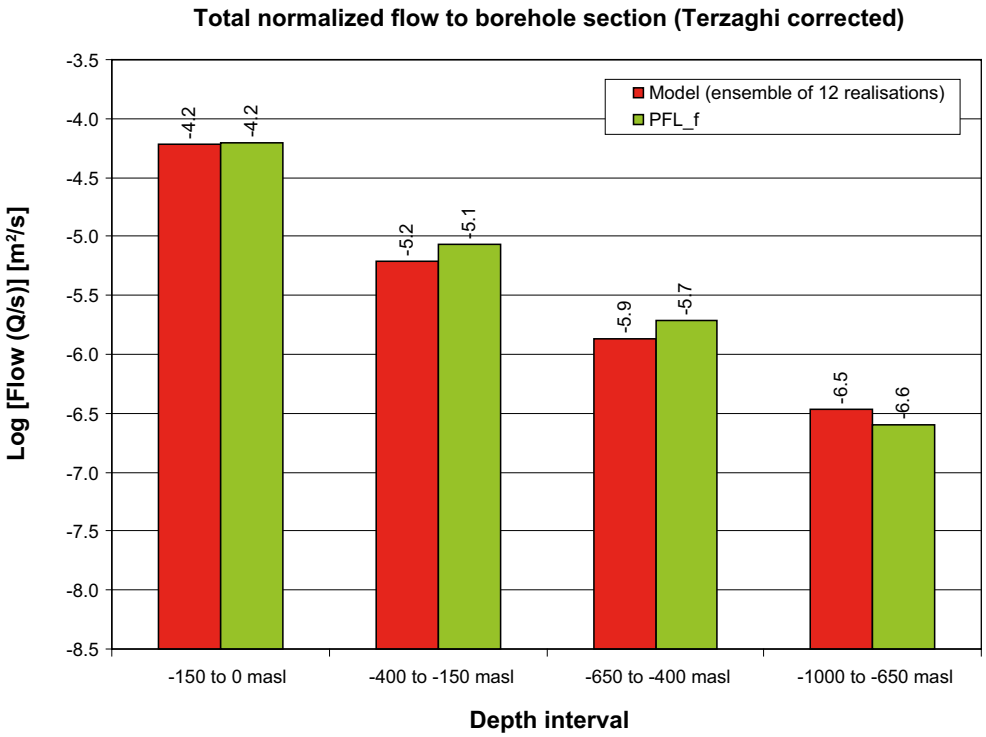

Figure E-1. *Comparison of the sum of individual inflows divided by drawdown, Q/s, for the PFL-f data from borehole sections within HRD_C against the Elaborated Hydro-DFN model. For the model, the arithmetic mean is taken over 12 realisations. The flows are Terzaghi weighted and normalised to the borehole length indicated by the range on the horizontal axis.*

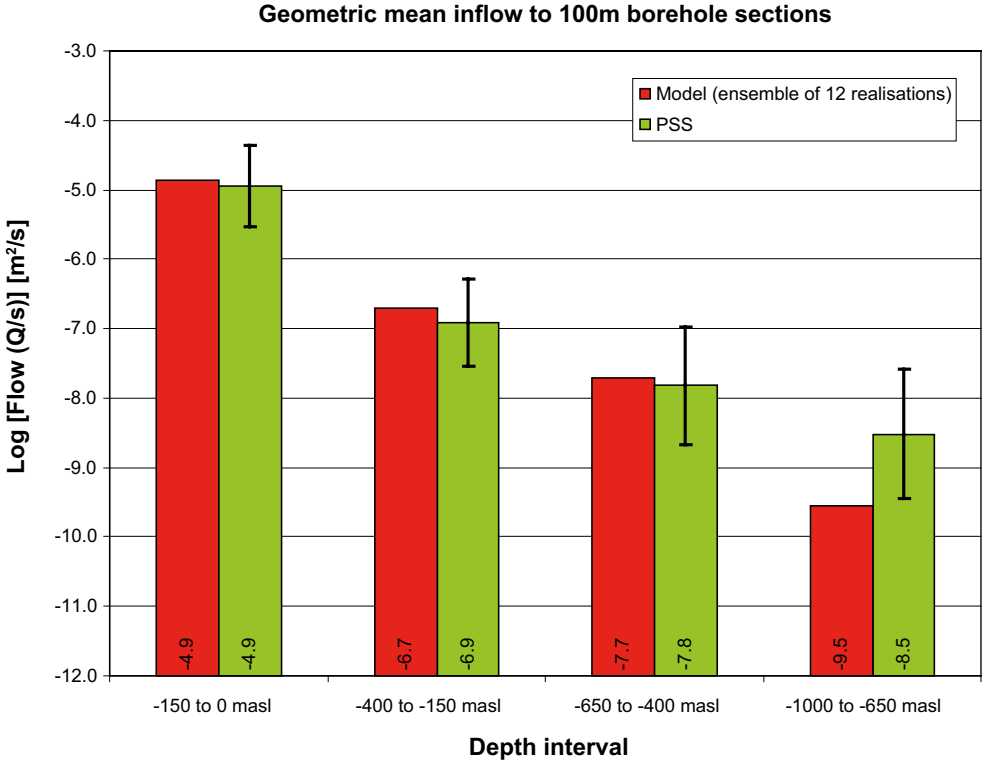

Figure E-2. *Comparison of the geometric mean of total inflows divided by drawdown, Q/s, to 100 m borehole intervals for the PSS data from borehole sections within HRD_C against the Elaborated Hydro-DFN model. For the data, the geometric mean is shown as well as the 95% confidence interval in the mean. For the model, the mean value of total flow is taken over 12 realisation.*

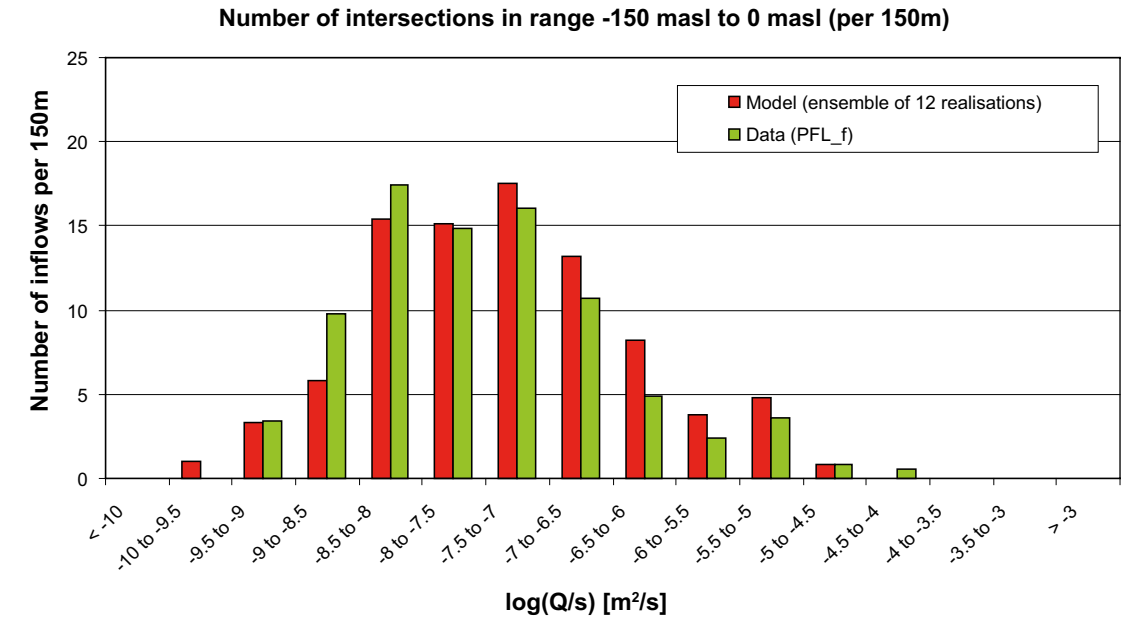

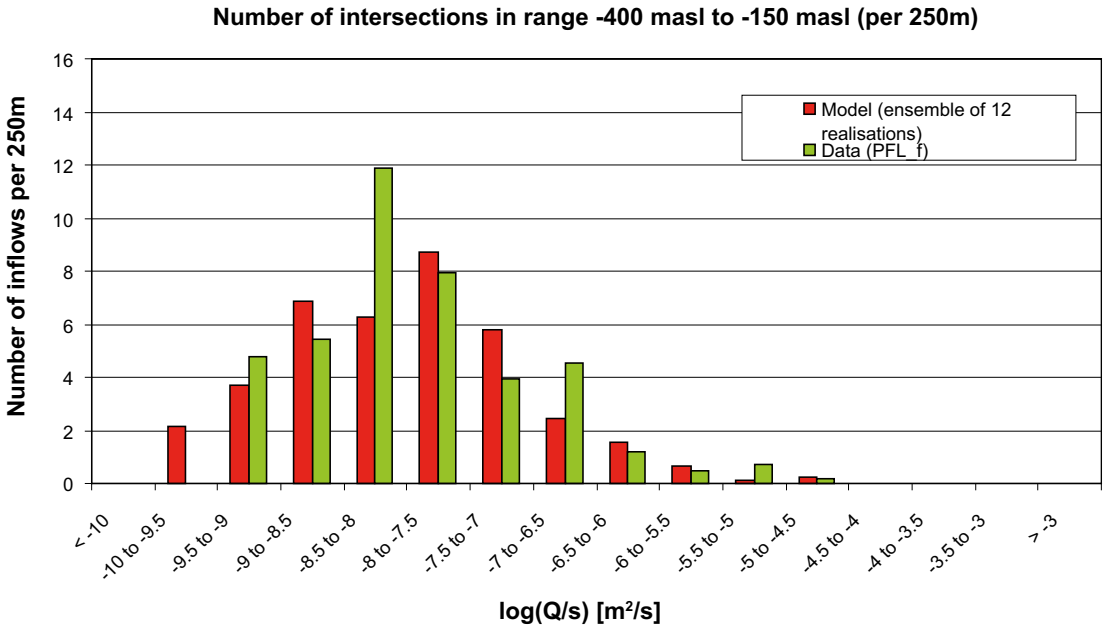

Figure E-3. *Histograms comparing the distribution of the magnitude of inflows divided by drawdown, Q/s, at abstraction boreholes in HRD_C (top DZ1, bottom DZ2). The PFL-f measurements are treated as ensembles over all boreholes sections within HRD_C. The simulations represent the combined results of 12 realisations of the Elaborated Hydro-DFN model. The numbers of intersections are Terzaghi weighted and normalised to the length of borehole which is provided in the heading of each graph.*

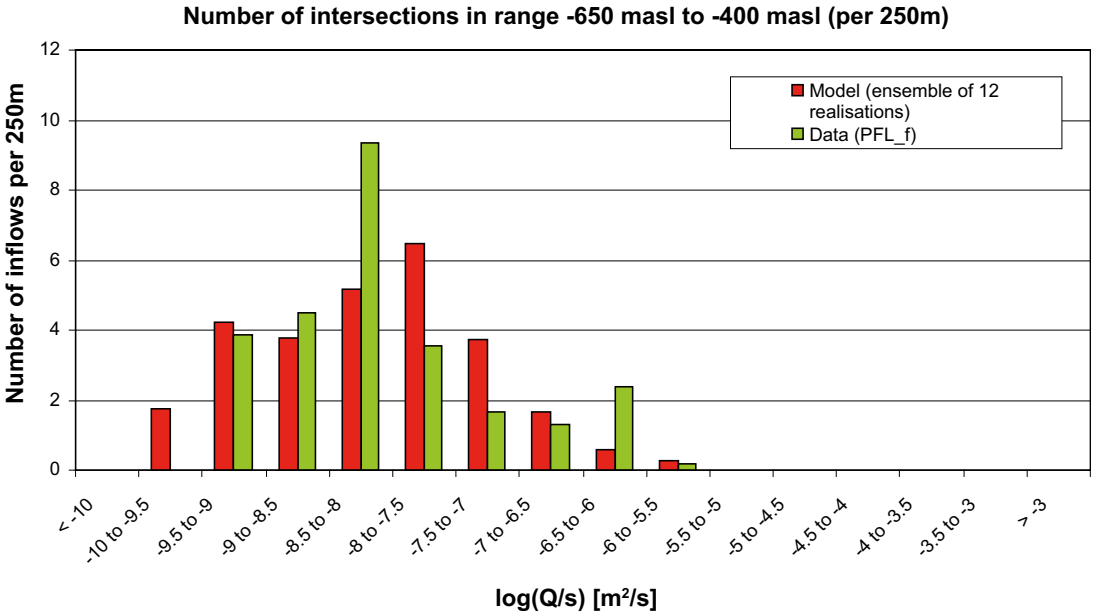

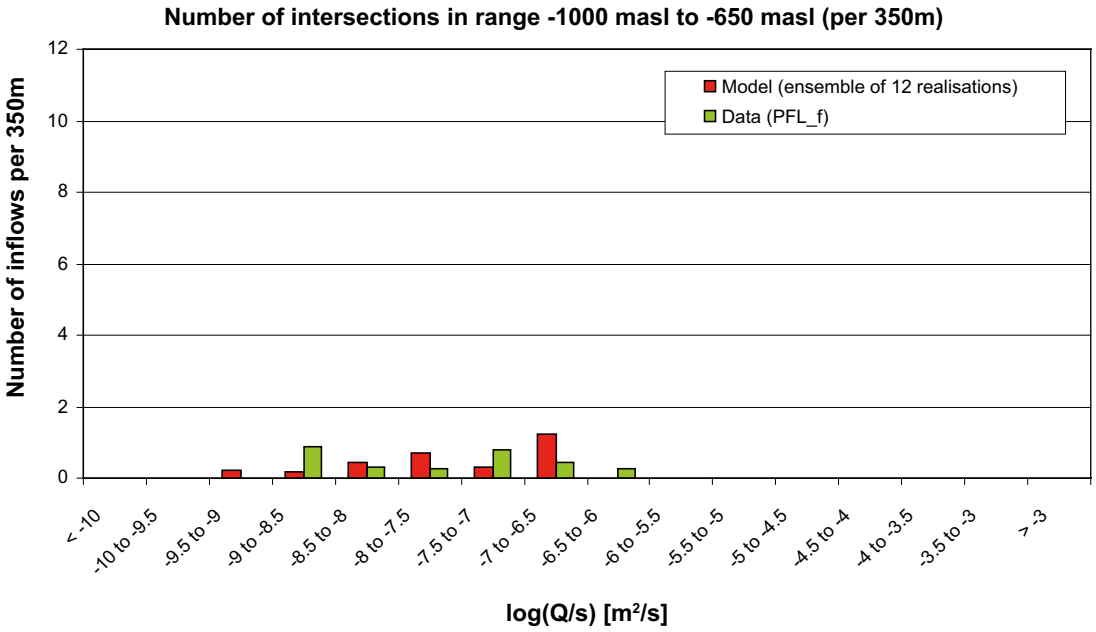

Figure E-4. *Histograms comparing the distribution of the magnitude of inflows divided by drawdown, Q/s, at abstraction boreholes in HRD_C (top DZ3, bottom DZ4). The PFL-f measurements are treated as ensembles over all boreholes sections within HRD_C. The simulations represent the combined results of 12 realisations of the Elaborated Hydro-DFN model. The numbers of intersections are Terzaghi weighted and normalised to the length of borehole which is provided in the heading of each graph.*

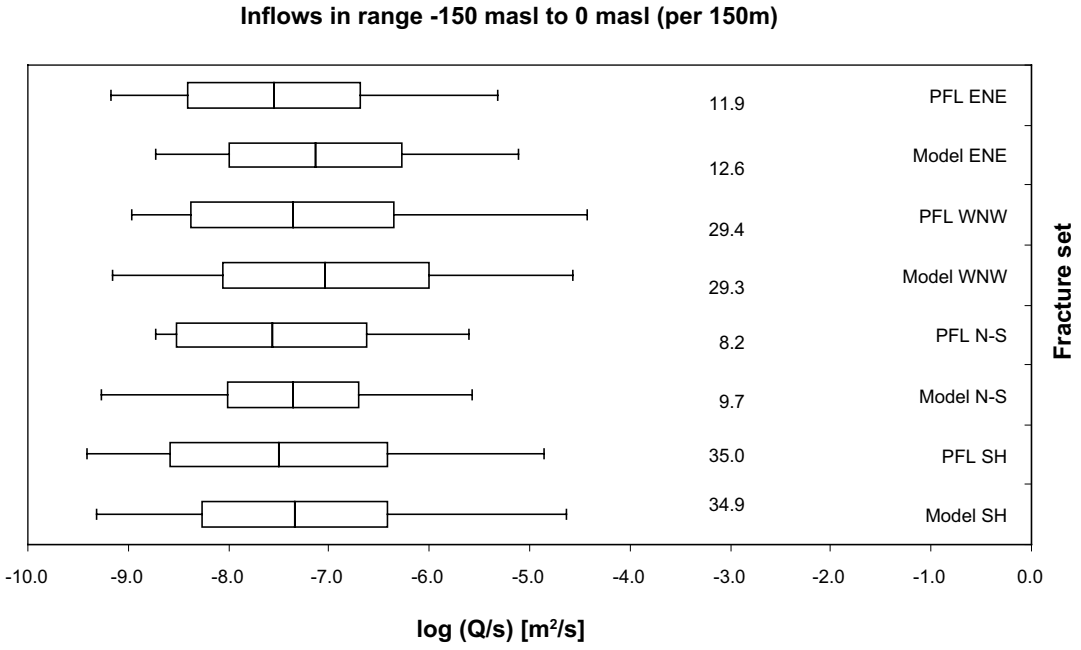

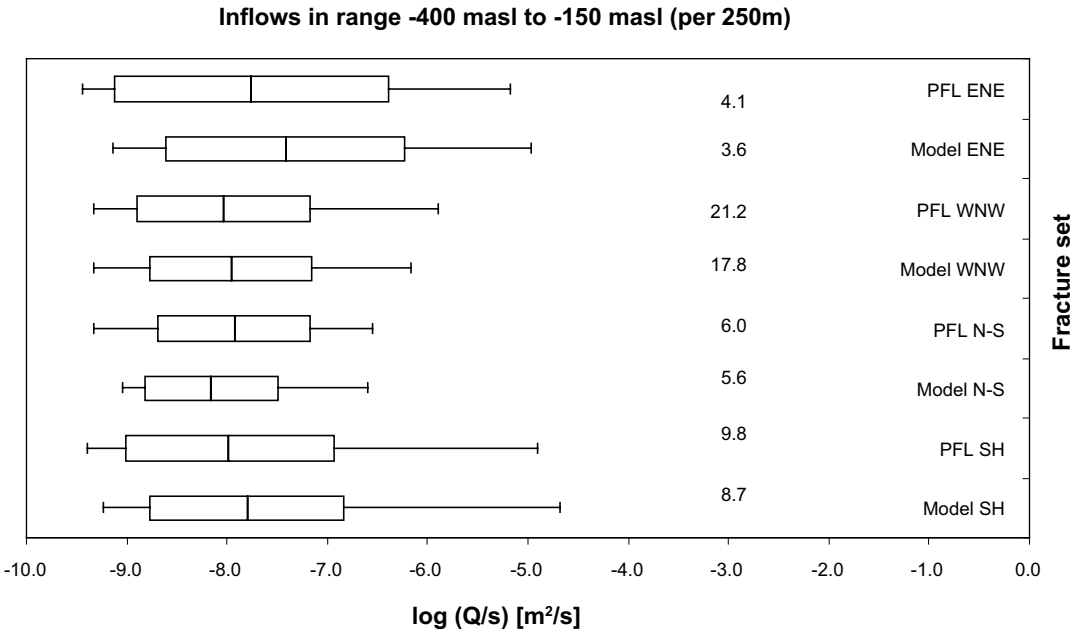

Figure E-5. *Bar and whisker plots comparing the statistics taken over each fracture set for the individual inflows divided by drawdown, Q/s, for the PFL-f data from borehole sections within in HRD_C (top DZ1, bottom DZ2). The PFL-f measurements are treated as ensembles over all boreholes sections within HRD_C. The simulations represent the combined results of 12 realisations of the Elaborated Hydro-DFN model. The centre of the bar indicates the mean value, the ends of the bar indicate ±1 standard deviation, the error bars indicate the minimum and maximum values and the value is the number of flowing features above the PFL-f detection limit per borehole section. For the data, statistics are taken over the identified flow-features within each set. For the model, statistics are taken over the fractures generated within each set and over 12 realisations. The numbers of fractures are Terzaghi weighted and normalised to the length specified in the respective plot heading.*

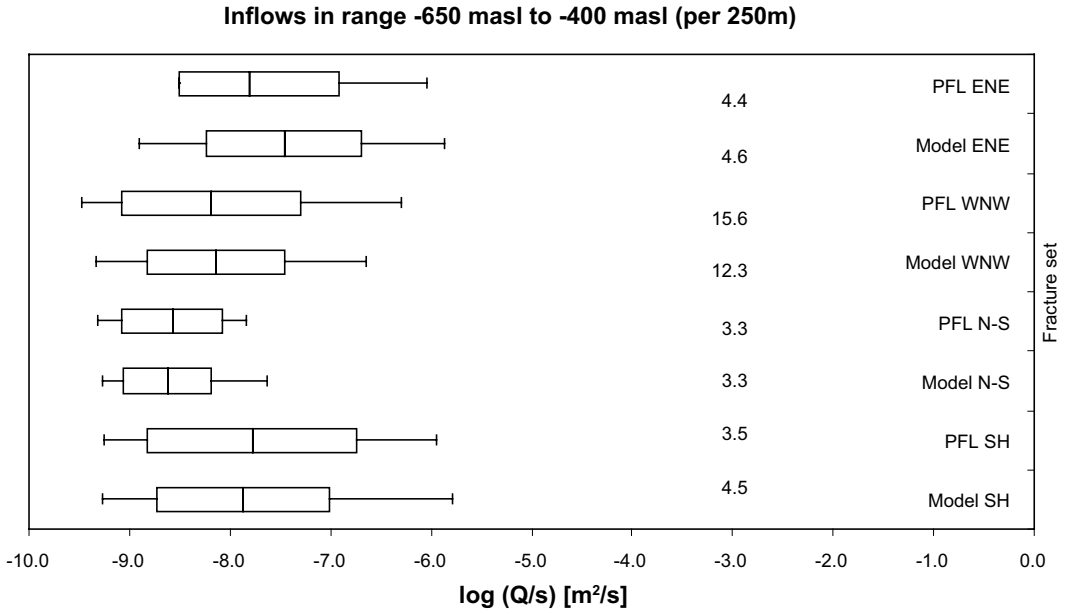

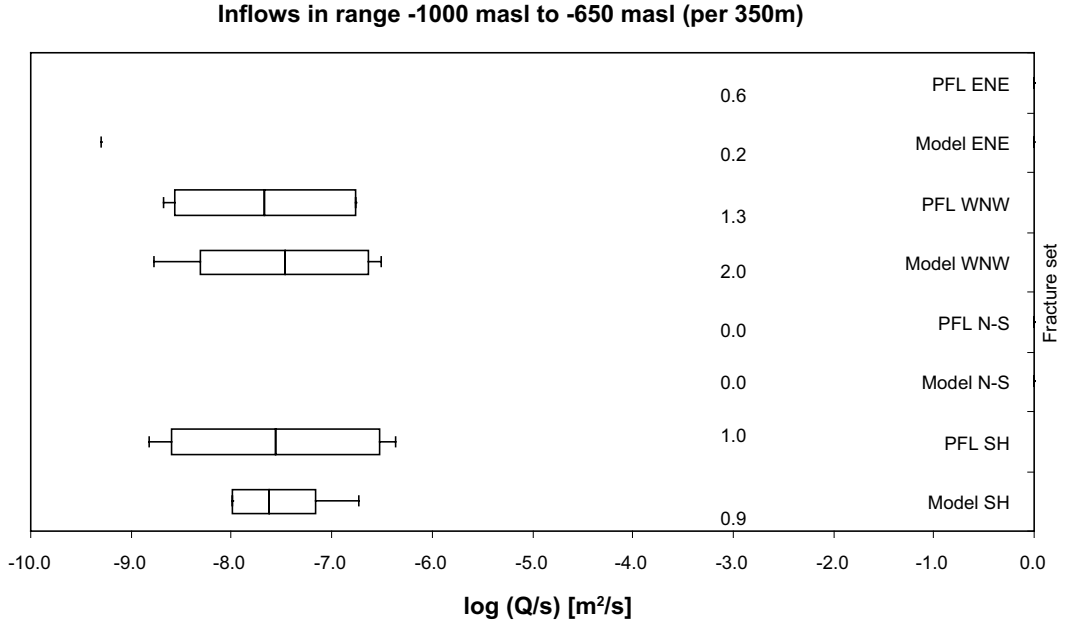

Figure E-6. *Bar and whisker plots comparing the statistics taken over each fracture set for the individual inflows divided by drawdown, Q/s, for the PFL-f data from borehole sections within in HRD_C (top DZ3, bottom DZ4). The PFL-f measurements are treated as ensembles over all boreholes sections within HRD_C. The simulations represent the combined results of 12 realisations of the Elaborated Hydro-DFN model. The centre of the bar indicates the mean value, the ends of the bar indicate ±1 standard deviation, the error bars indicate the minimum and maximum values and the value is the number of flowing features above the PFL-f detection limit per borehole section. For the data, statistics are taken over the identified flow-features within each set. For the model, statistics are taken over the fractures generated within each set and over 12 realisations. The numbers of fractures are Terzaghi weighted and normalised to the length specified in the respective plot heading.*

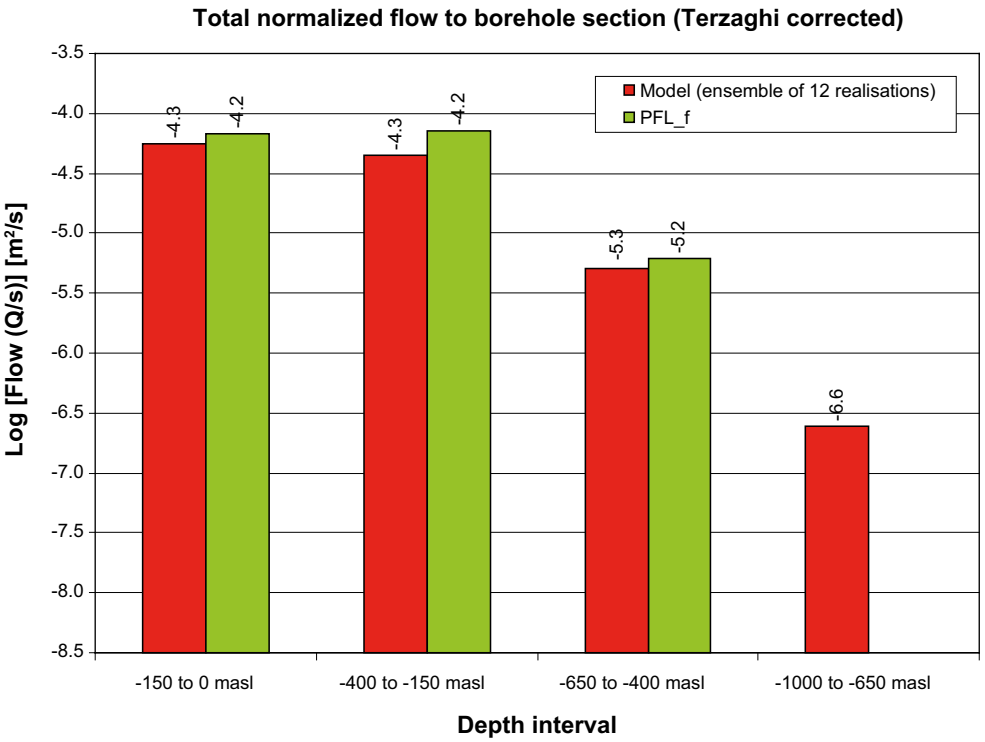

Figure E-7. *Comparison of the sum of individual inflows divided by drawdown, Q/s, for the PFL-f data from borehole sections within HRD_EW007 against the Elaborated Hydro-DFN model. For the model, the arithmetic mean is taken over 12 realisations. The flows are Terzaghi weighted and normalised to the borehole length indicated by the range on the horizontal axis.*

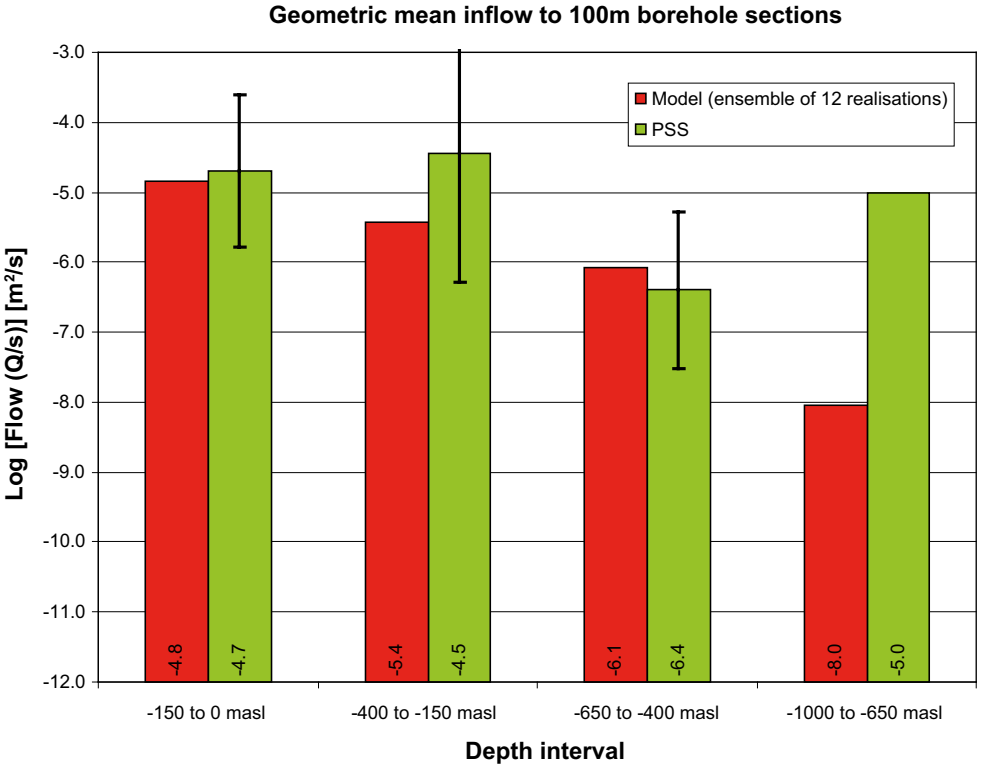

Figure E-8. *Comparison of the geometric mean of total inflows divided by drawdown, Q/s, to 100 m borehole intervals for the PSS data from borehole sections within HRD_EW007 against the Elaborated Hydro-DFN model. For the data, the geometric mean is shown as well as the 95% confidence interval in the mean. For the model, the mean value of total flow is taken over 12 realisation.*

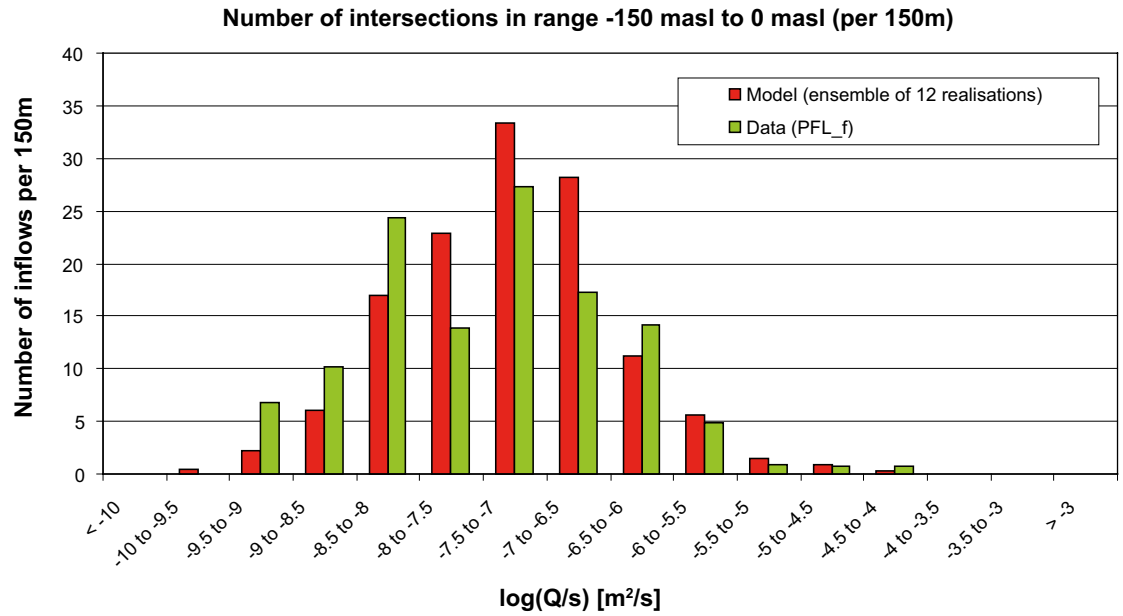

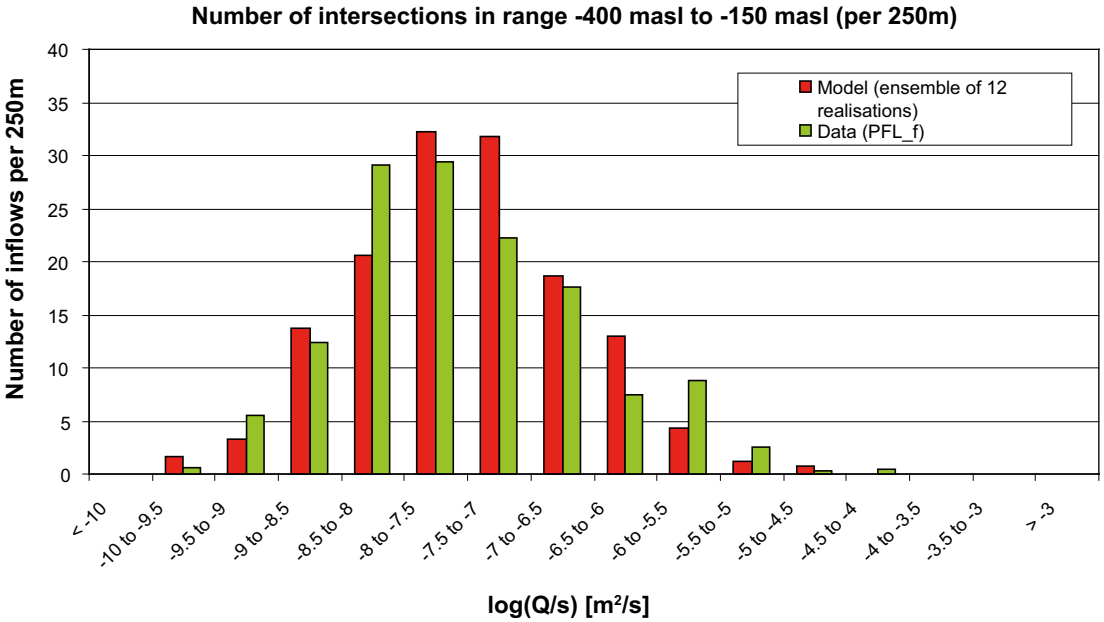

Figure E-9. *Histograms comparing the distribution of the magnitude of inflows divided by drawdown, Q/s, at abstraction boreholes in HRD_EW007 (top DZ1, bottom DZ2). The PFL-f measurements are treated as ensembles over all boreholes sections within HRD_EW007. The simulations represent the combined results of 12 realisations of the Elaborated Hydro-DFN model. The numbers of intersections are Terzaghi weighted and normalised to the length of borehole which is provided in the heading of each graph.*

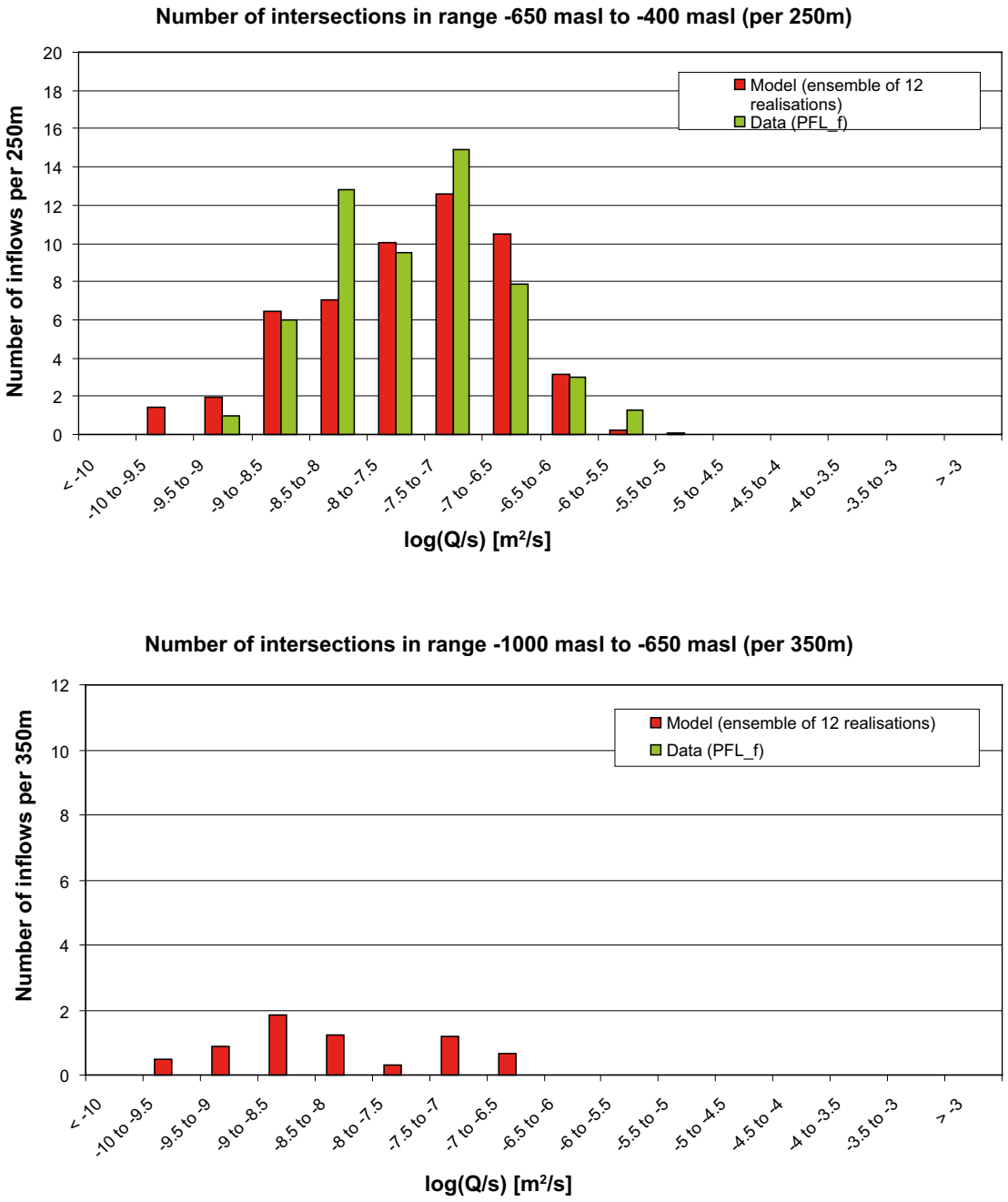

Figure E-10. *Histograms comparing the distribution of the magnitude of inflows divided by drawdown, Q/s, at abstraction boreholes in HRD_EW007 (top DZ3, bottom DZ4). The PFL-f measurements are treated as ensembles over all boreholes sections within HRD_EW007. The simulations represent the combined results of 12 realisations of the Elaborated Hydro-DFN model. The numbers of intersections are Terzaghi weighted and normalised to the length of borehole which is provided in the heading of each graph.*

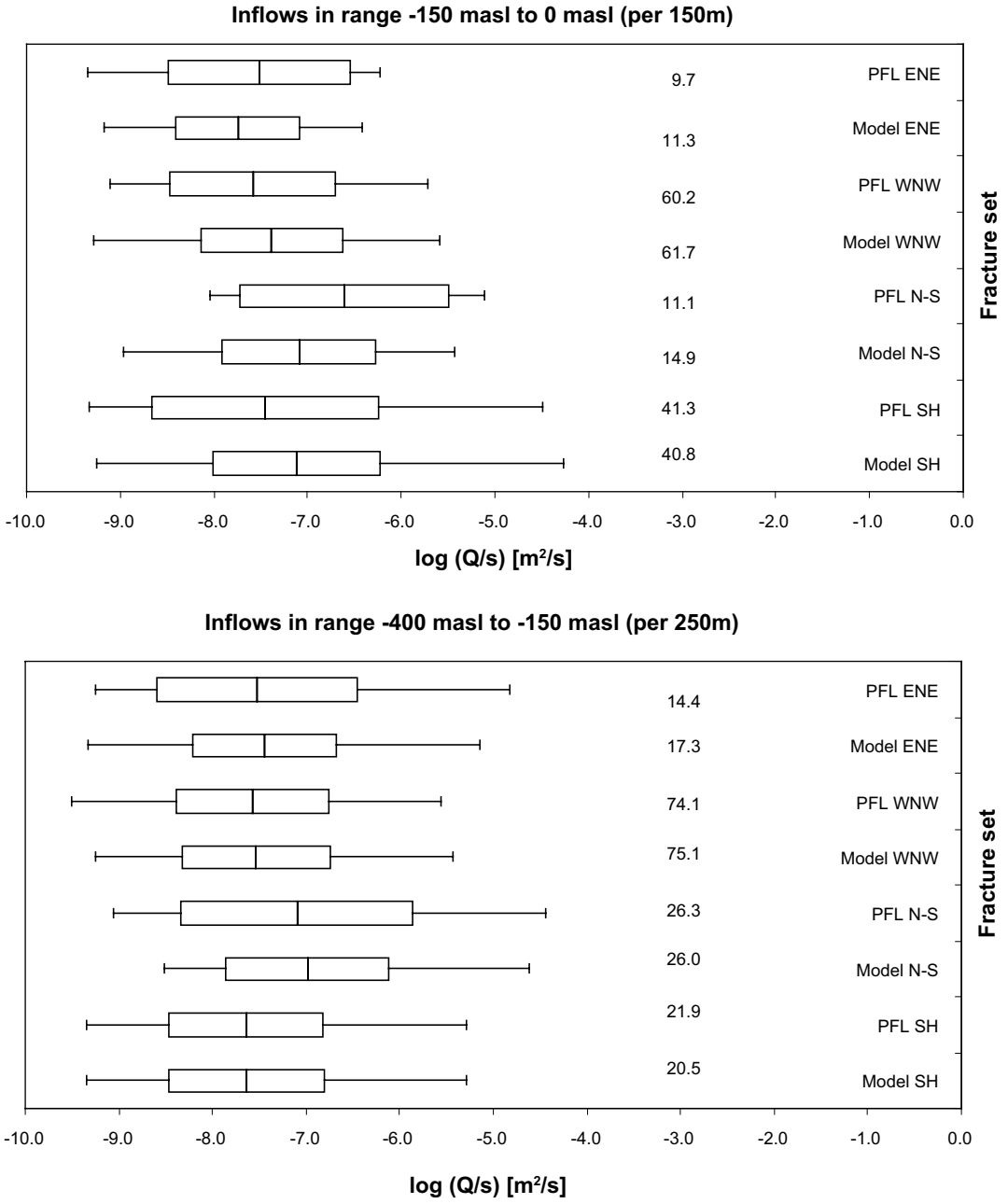

Figure E-11. *Bar and whisker plots comparing the statistics taken over each fracture set for the individual inflows divided by drawdown, Q/s, for the PFL-f data from borehole sections within in HRD_EW007 (top DZ1, bottom DZ2). The PFL-f measurements are treated as ensembles over all boreholes sections within HRD_EW007. The simulations represent the combined results of 12 realisations of the Elaborated Hydro-DFN model. The centre of the bar indicates the mean value, the ends of the bar indicate ±1 standard deviation, the error bars indicate the minimum and maximum values and the value is the number of flowing features above the PFL-f detection limit per borehole section. For the data, statistics are taken over the identified flow-features within each set. For the model, statistics are taken over the fractures generated within each set and over 12 realisations. The numbers of fractures are Terzaghi weighted and normalised to the length specified in the respective plot heading.*

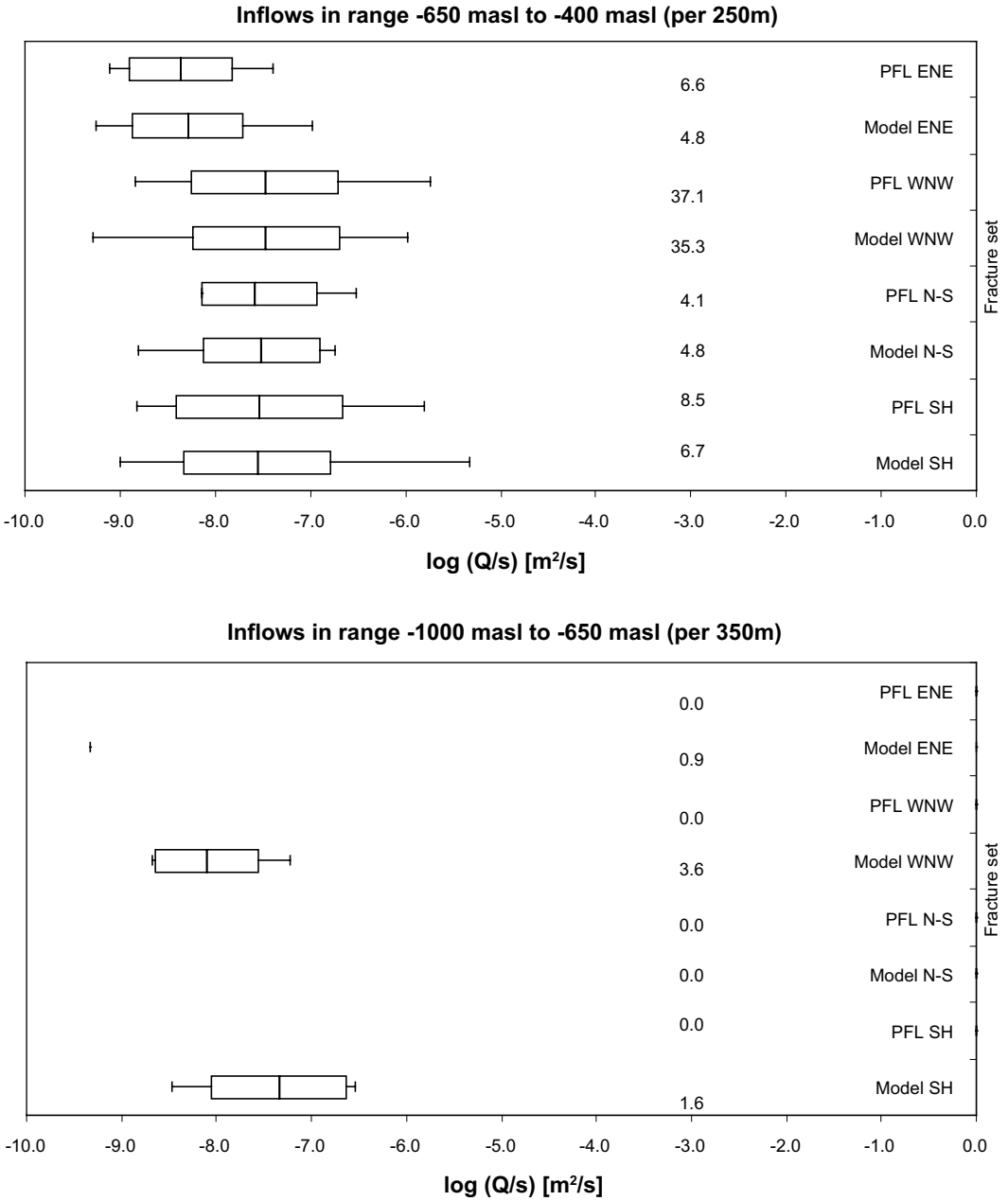

Figure E-12. *Bar and whisker plots comparing the statistics taken over each fracture set for the individual inflows divided by drawdown, Q/s, for the PFL-f data from borehole sections within in HRD_EW007 (top DZ3, bottom DZ4). The PFL-f measurements are treated as ensembles over all boreholes sections within HRD_EW007. The simulations represent the combined results of 12 realisations of the Elaborated Hydro-DFN model. The centre of the bar indicates the mean value, the ends of the bar indicate ±1 standard deviation, the error bars indicate the minimum and maximum values and the value is the number of flowing features above the PFL-f detection limit per borehole section. For the data, statistics are taken over the identified flow-features within each set. For the model, statistics are taken over the fractures generated within each set and over 12 realisations. The numbers of fractures are Terzaghi weighted and normalised to the length specified in the respective plot heading.*

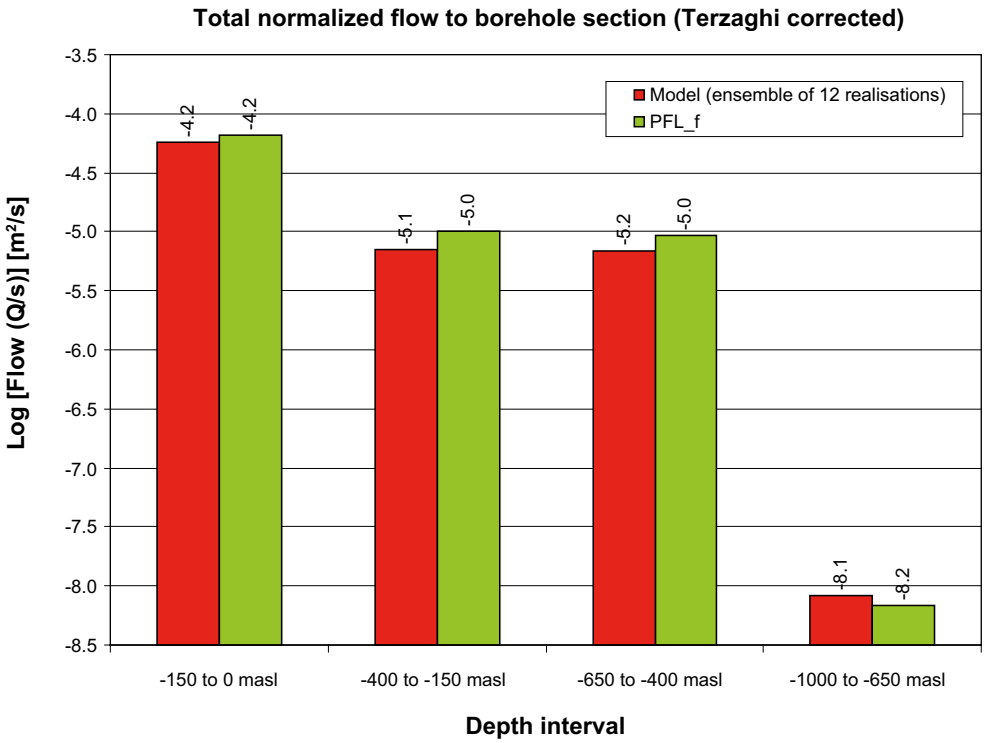

Figure E-13. *Comparison of the sum of individual inflows divided by drawdown, Q/s, for the PFL-f data from borehole sections within HRD_W against the Elaborated Hydro-DFN model. For the model, the arithmetic mean is taken over 12 realisations. The flows are Terzaghi weighted and normalised to the borehole length indicated by the range on the horizontal axis.*

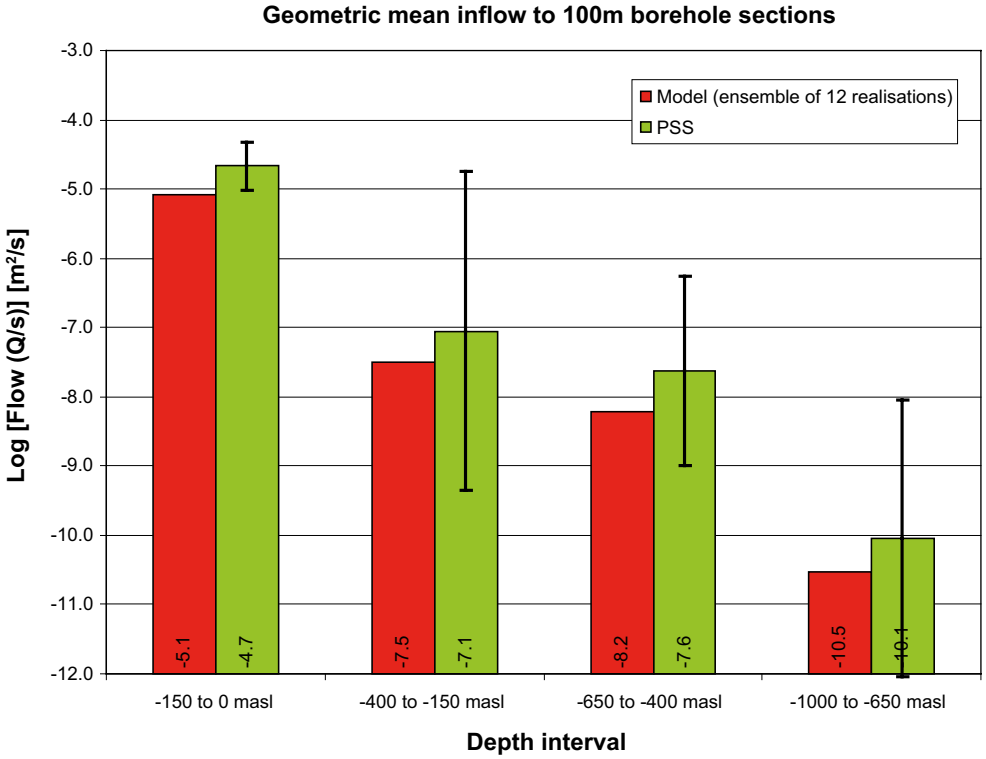

Figure E-14. *Comparison of the geometric mean of total inflows divided by drawdown, Q/s, to 100 m borehole intervals for the PSS data from borehole sections within HRD_W against the Elaborated Hydro-DFN model. For the data, the geometric mean is shown as well as the 95% confidence interval in the mean. For the model, the mean value of total flow is taken over 12 realisation.*

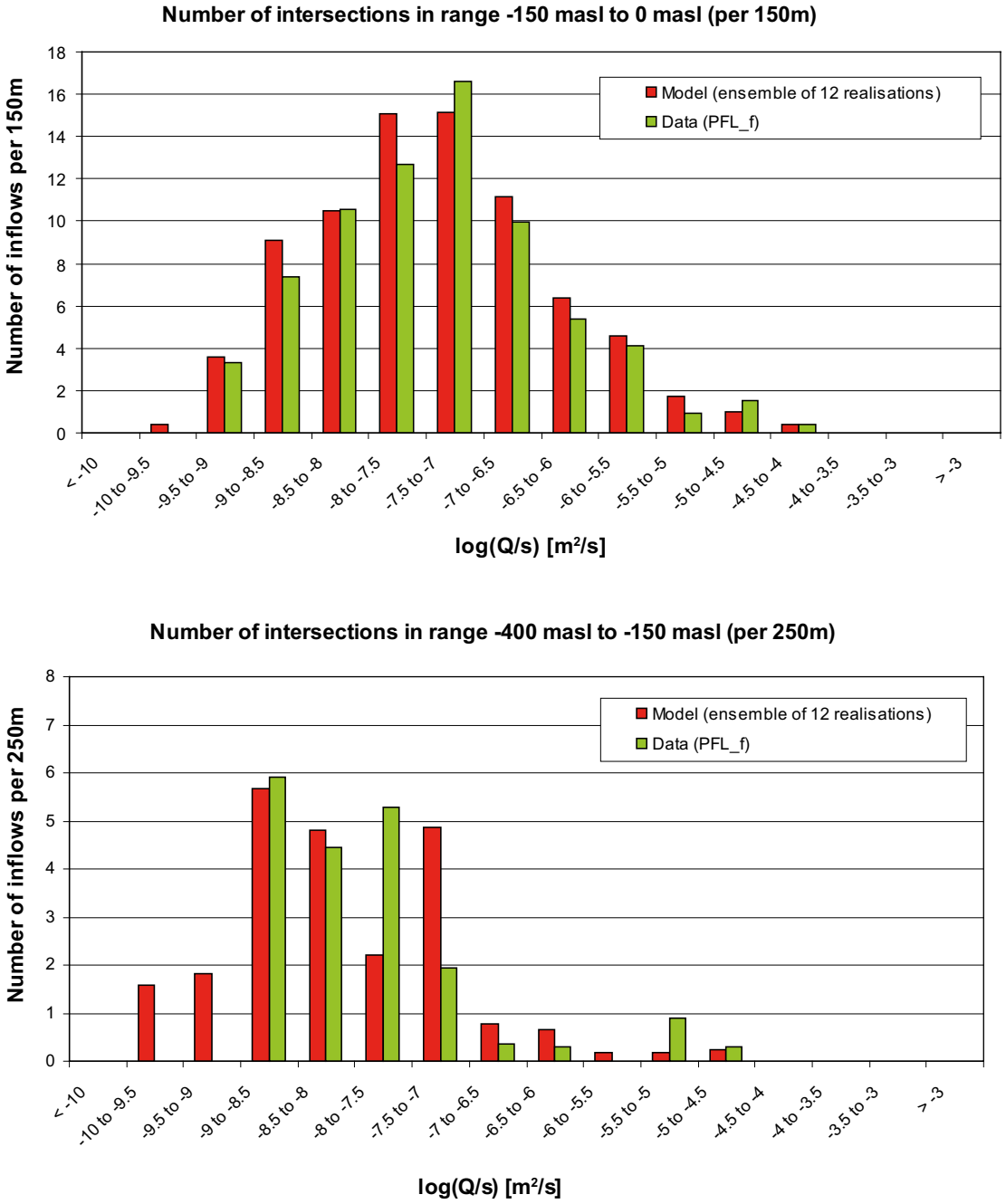

Figure E-15. *Histograms comparing the distribution of the magnitude of inflows divided by drawdown, Q/s, at abstraction boreholes in HRD_W (top DZ1, bottom DZ2). The PFL-f measurements are treated as ensembles over all boreholes sections within HRD_W. The simulations represent the combined results of 12 realisations of the Elaborated Hydro-DFN model. The numbers of intersections are Terzaghi weighted and normalised to the length of borehole which is provided in the heading of each graph.*

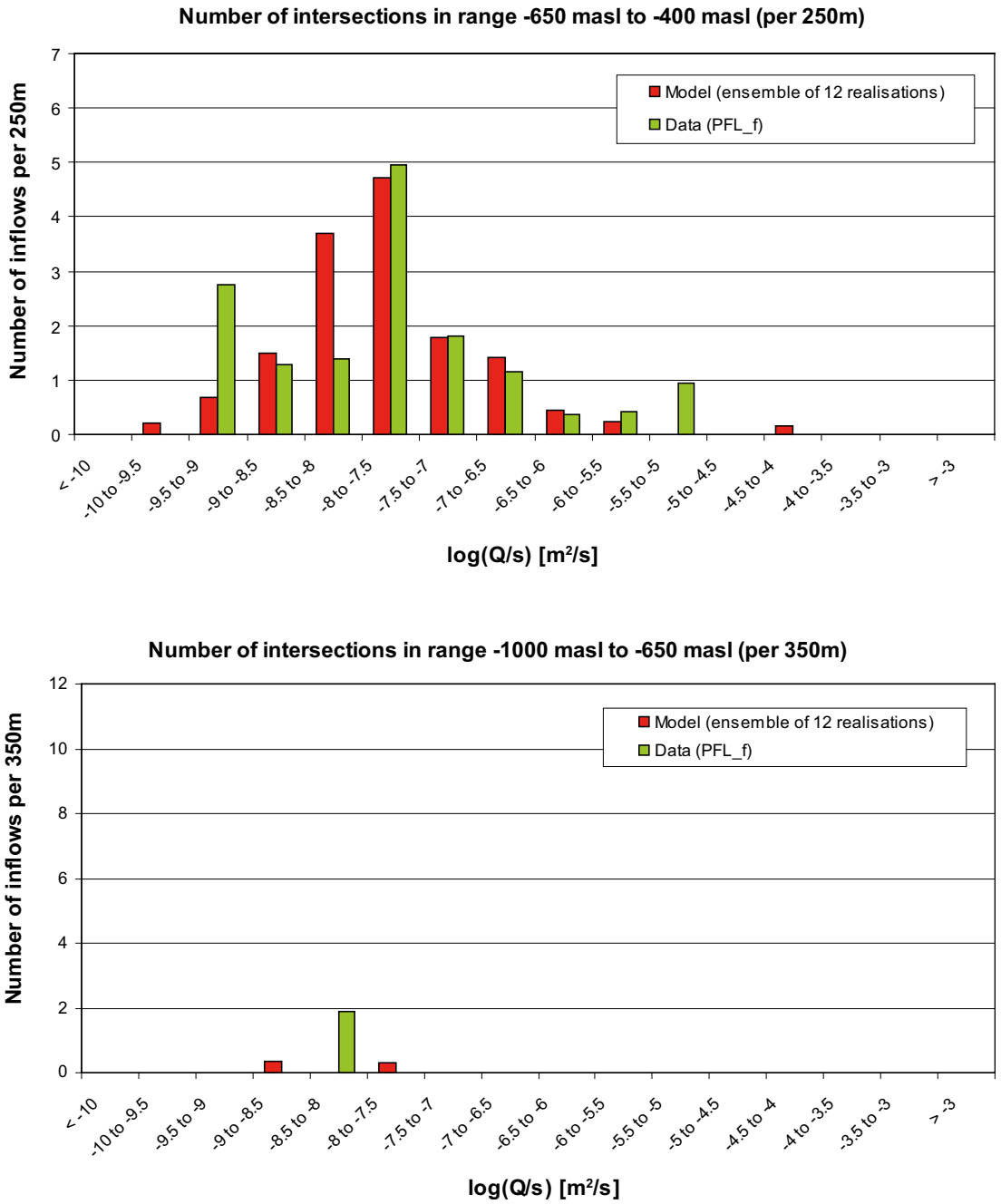

Figure E-16. *Histograms comparing the distribution of the magnitude of inflows divided by drawdown, Q/s, at abstraction boreholes in HRD_W (top DZ3, bottom DZ4). The PFL-f measurements are treated as ensembles over all boreholes sections within HRD_W. The simulations represent the combined results of 12 realisations of the Elaborated Hydro-DFN model. The numbers of intersections are Terzaghi weighted and normalised to the length of borehole which is provided in the heading of each graph.*

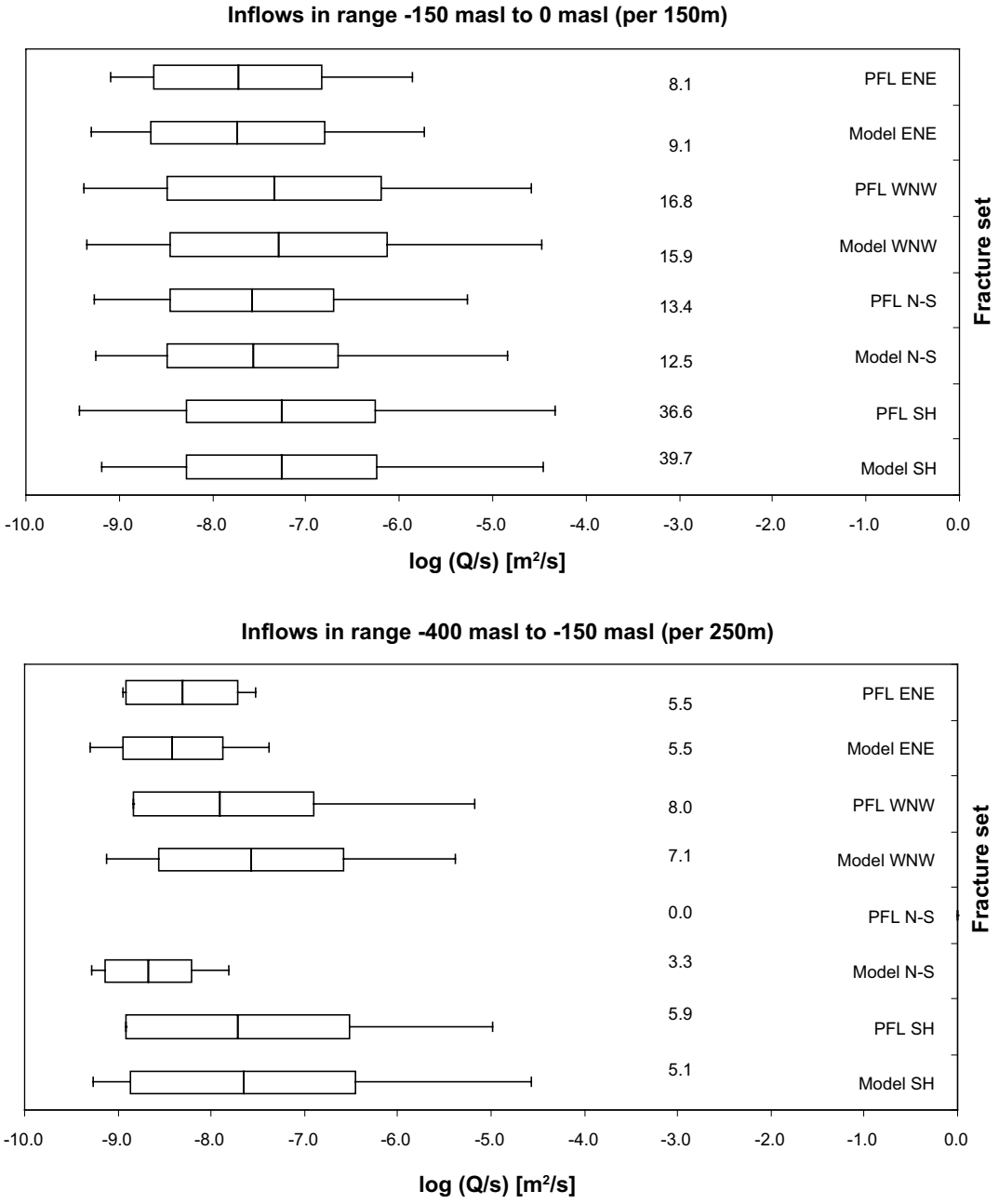

Figure E-17. *Bar and whisker plots comparing the statistics taken over each fracture set for the individual inflows divided by drawdown, Q/s, for the PFL-f data from borehole sections within in HRD_W (top DZ1, bottom DZ2). The PFL-f measurements are treated as ensembles over all boreholes sections within HRD_W. The simulations represent the combined results of 12 realisations of the Elaborated Hydro-DFN model. The centre of the bar indicates the mean value, the ends of the bar indicate ±1 standard deviation, the error bars indicate the minimum and maximum values and the value is the number of flowing features above the PFL-f detection limit per borehole section. For the data, statistics are taken over the identified flow-features within each set. For the model, statistics are taken over the fractures generated within each set and over 12 realisations. The numbers of fractures are Terzaghi weighted and normalised to the length specified in the respective plot heading.*

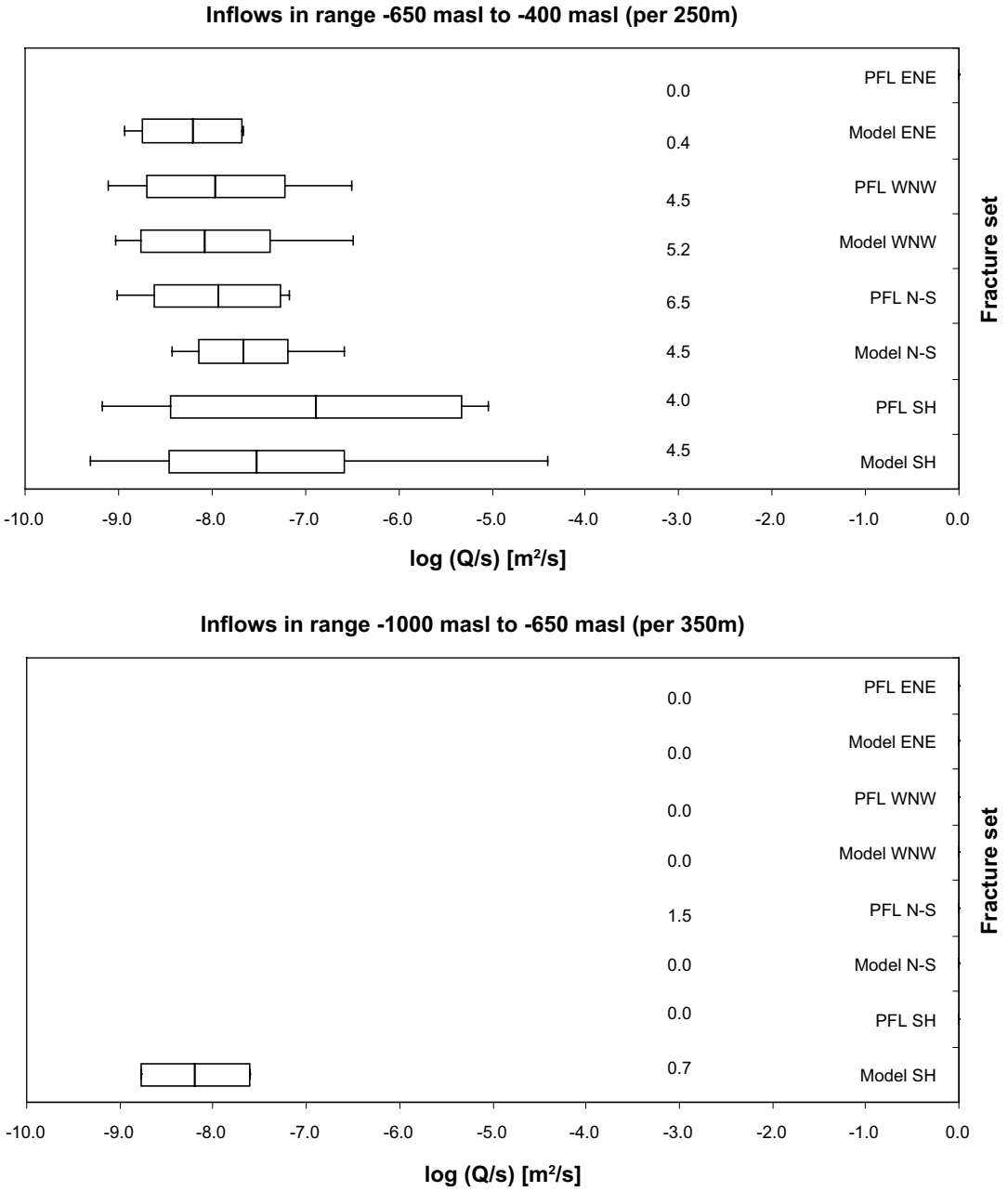

Figure E-18. *Bar and whisker plots comparing the statistics taken over each fracture set for the individual inflows divided by drawdown, Q/s, for the PFL-f data from borehole sections within in HRD_W (top DZ3, bottom DZ4). The PFL-f measurements are treated as ensembles over all boreholes sections within HRD_W. The simulations represent the combined results of 12 realisations of the Elaborated Hydro-DFN model. The centre of the bar indicates the mean value, the ends of the bar indicate ±1 standard deviation, the error bars indicate the minimum and maximum values and the value is the number of flowing features above the PFL-f detection limit per borehole section. For the data, statistics are taken over the identified flow-features within each set. For the model, statistics are taken over the fractures generated within each set and over 12 realisations. The numbers of fractures are Terzaghi weighted and normalised to the length specified in the respective plot heading.*

E.3 Block scale properties

As for SDM-Site /Rhén et al. 2008/, upscaling was used to calculate block properties at 5 m, 20 m and 100 m scales (corresponding to the borehole interval scales used for PSS measurements). The block scale properties calculated for the Elaborated Hydro-DFN are compared to the SDM-Site properties in Table E-5 to Table E-10. At repository depth (DZ3), the Elaborated Hydro-DFN calculates mean hydraulic conductivities that are about one-third of those calculated by SDM-Site for HRD_C, one-half for HRD_EW007 and about one-quarter for HRD_W.

Figure E-20 to Figure E-30 show CDF plots of hydraulic conductivity and plots of the strike of maximum horizontal hydraulic conductivity plotted as a frequency for each rock domain.

Table E-5. Results of upscaling calculations for the Elaborated Hydro-DFN, for HRD_C.

Depth Zone	Scale (m)	r_{min} (m)	% active	Log10(K_{eff}) [m/s]			Log10(phi) [–]	
				Mean	Median	Standard deviation	Mean	Standard deviation
DZ1	5	0.11	98%	–7.93	–7.72	0.95	–2.73	0.04
DZ1	20	2.3	100%	–6.93	–6.88	0.72	–3.05	0.09
DZ1	100	5.7	100%	–6.69	–6.68	0.47	–3.33	0.06
DZ2	5	0.11	56%	–9.30	–10.42	1.20	–3.11	0.03
DZ2	20	2.3	70%	–9.05	–9.38	1.03	–3.77	0.12
DZ2	100	5.7	99%	–8.78	–8.75	0.69	–3.91	0.06
DZ3	5	0.11	42%	–9.39	–12.72	1.21	–3.25	0.05
DZ3	20	2.3	64%	–9.42	–9.93	0.89	–3.96	0.08
DZ3	100	5.7	97%	–9.16	–9.08	0.80	–4.09	0.06
DZ4	5	0.11	14%	–8.97	N/A	1.53	–3.26	0.04
DZ4	20	2.3	3%	–9.00	N/A	1.00	–4.25	0.10
DZ4	100	5.7	5%	–8.86	N/A	0.93	–4.49	0.06

Table E-6. Results of upscaling calculations for the SDM-Site Hydro-DFN, for HRD_C.

Depth Zone	Scale (m)	r_{min} (m)	% active	Log10(K_{eff}) [m/s]			Log10(phi) [–]	
				Mean	Median	Standard deviation	Mean	Standard deviation
DZ1	5	0.11	98%	–7.72	–7.65	1.08	–2.64	0.04
DZ1	20	2.3	100%	–7.05	–7.07	0.86	–3.06	0.15
DZ1	100	5.7	100%	–6.99	–7.03	0.36	–3.33	0.04
DZ2	5	0.11	44%	–9.65	–12.11	1.52	–2.87	0.02
DZ2	20	2.3	76%	–8.41	–8.51	1.09	–3.52	0.10
DZ2	100	5.7	100%	–7.85	–8.32	1.29	–3.48	0.09
DZ3	5	0.11	66%	–9.27	–9.55	1.41	–3.01	0.02
DZ3	20	2.3	67%	–8.89	–9.21	1.04	–3.74	0.08
DZ3	100	5.7	99%	–8.70	–8.61	0.70	–3.91	0.05
DZ4	5	0.11	N/A	N/A	N/A	N/A	N/A	N/A
DZ4	20	2.3	N/A	N/A	N/A	N/A	N/A	N/A
DZ4	100	5.7	32%	–9.65	N/A	1.45	–4.45	0.08

Table E-7. Results of upscaling calculations for the Elaborated Hydro-DFN, for HRD_EW007.

Depth Zone	Scale (m)	r_{min} (m)	% active	Log10(K_{eff}) [m/s]			Log10(phi) [–]	
				Mean	Median	Standard deviation	Mean	Standard deviation
DZ1	5	0.11	99%	–7.88	–7.87	0.97	–2.71	0.06
DZ1	20	2.3	100%	–7.02	–7.13	0.56	–3.08	0.07
DZ1	100	5.7	100%	–7.04	–7.07	0.26	–3.38	0.04
DZ2	5	0.11	94%	–8.64	–8.53	0.87	–2.86	0.02
DZ2	20	2.3	100%	–7.10	–7.29	0.93	–3.16	0.12
DZ2	100	5.7	100%	–7.32	–7.33	0.31	–3.44	0.04
DZ3	5	0.11	72%	–8.86	–9.14	1.23	–2.84	0.02
DZ3	20	2.3	90%	–8.10	–8.12	0.95	–3.47	0.13
DZ3	100	5.7	100%	–8.53	–8.42	0.52	–3.82	0.03

Table E-8. Results of upscaling calculations for the SDM-Site Hydro-DFN, for HRD_EW007.

Depth Zone	Scale (m)	r_{min} (m)	% active	Log10(K_{eff}) [m/s]			Log10(phi) [–]	
				Mean	Median	Standard deviation	Mean	Standard deviation
DZ1	5	0.11	99%	–7.62	–7.49	0.66	–2.58	0.02
DZ1	20	2.3	100%	–6.92	–6.99	0.58	–3.05	0.06
DZ1	100	5.7	100%	–7.15	–7.15	0.24	–3.46	0.04
DZ2	5	0.11	95%	–8.57	–8.43	1.04	–2.87	0.04
DZ2	20	2.3	100%	–7.31	–7.52	0.92	–3.20	0.12
DZ2	100	5.7	100%	–7.37	–7.39	0.36	–3.58	0.05
DZ3	5	0.11	88%	–8.89	–8.69	1.09	–2.82	0.02
DZ3	20	2.3	99%	–7.89	–7.86	0.83	–3.41	0.07
DZ3	100	5.7	100%	–8.12	–8.07	0.29	–3.69	0.03

Table E-9. Results of upscaling calculations for the Elaborated Hydro-DFN, for HRD_W.

Depth Zone	Scale (m)	r_{min} (m)	% active	Log10(K_{eff}) [m/s]			Log10(phi) [–]	
				Mean	Median	Standard deviation	Mean	Standard deviation
DZ1	5	0.11	97%	–7.85	–7.86	1.11	–2.81	0.05
DZ1	20	2.3	100%	–7.07	–7.10	0.78	–3.10	0.11
DZ1	100	5.7	100%	–6.87	–6.92	0.42	–3.38	0.05
DZ2	5	0.11	21%	–9.57	N/A	1.29	–3.25	0.04
DZ2	20	2.3	43%	–9.32	N/A	1.31	–3.87	0.17
DZ2	100	5.7	84%	–9.43	–9.80	1.37	–3.99	0.09
DZ3	5	0.11	21%	–9.44	N/A	1.27	–3.32	0.05
DZ3	20	2.3	41%	–9.09	N/A	0.90	–3.96	0.10
DZ3	100	5.7	80%	–9.44	–9.69	1.12	–4.07	0.10

Table E-10. Results of upscaling calculations for the SDM-Site Hydro-DFN, for HRD_W.

Depth Zone	Scale (m)	r_{min} (m)	% active	Log10(K_{eff}) [m/s]			Log10(phi) [–]	
				Mean	Median	Standard deviation	Mean	Standard deviation
DZ1	5	0.11	94%	–7.85	–7.92	1.40	–2.72	0.06
DZ1	20	2.3	100%	–6.81	–6.83	0.98	–3.00	0.14
DZ1	100	5.7	100%	–6.79	–6.80	0.39	–3.26	0.04
DZ2	5	0.11	32%	–9.59	N/A	1.34	–3.08	0.03
DZ2	20	2.3	59%	–8.05	–8.95	1.17	–3.59	0.12
DZ2	100	5.7	97%	–8.29	–8.19	1.03	–3.75	0.06
DZ3	5	0.11	14%	–10.25	N/A	1.11	–3.15	0.03
DZ3	20	2.3	51%	–8.78	–10.67	1.26	–3.75	0.13
DZ3	100	5.7	97%	–8.79	–8.84	1.03	–3.89	0.08

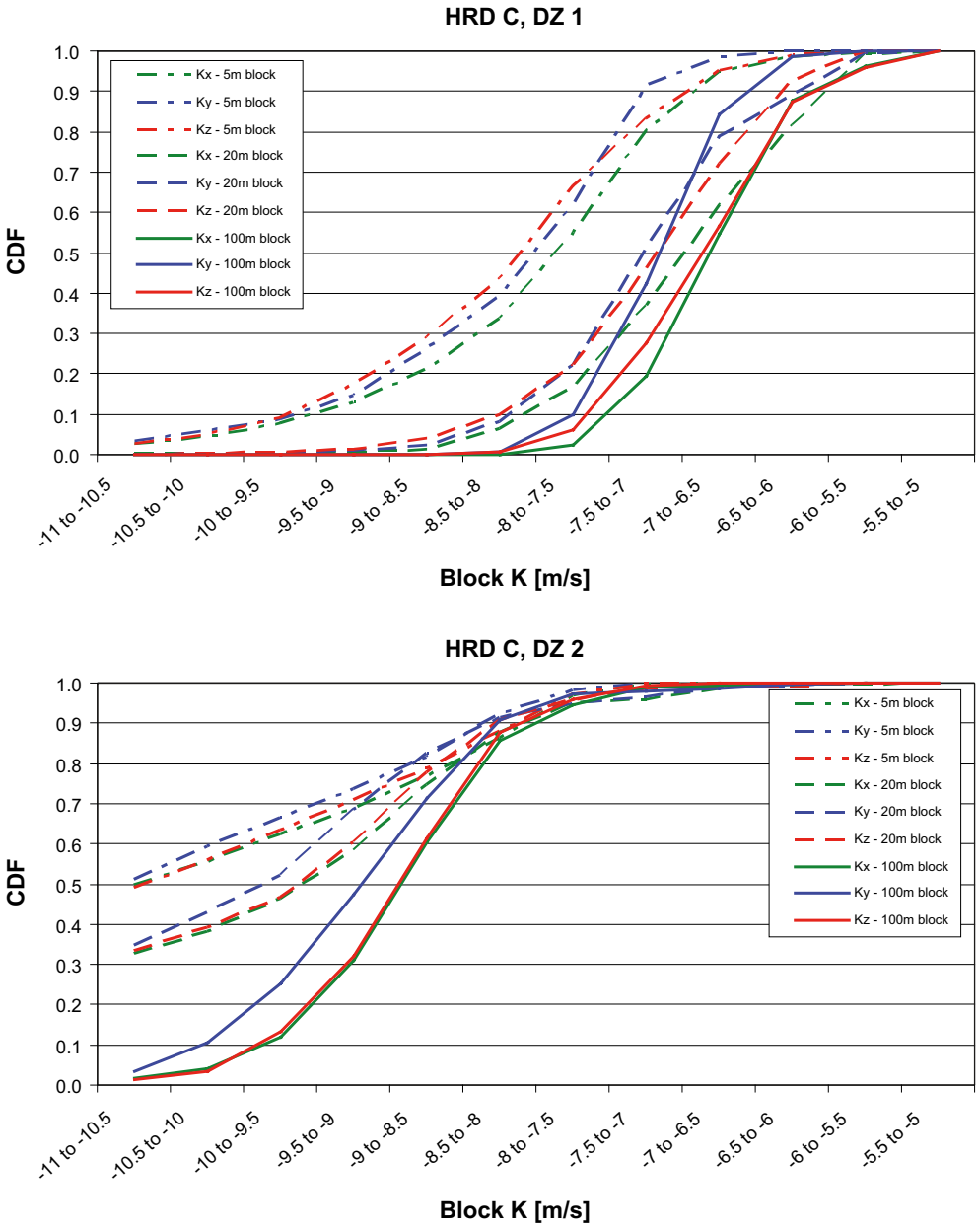

Figure E-19. *Cumulative distribution of calculated block scale Kx, Ky and Kz values for HRD_C (top DZ1, bottom DZ2).*

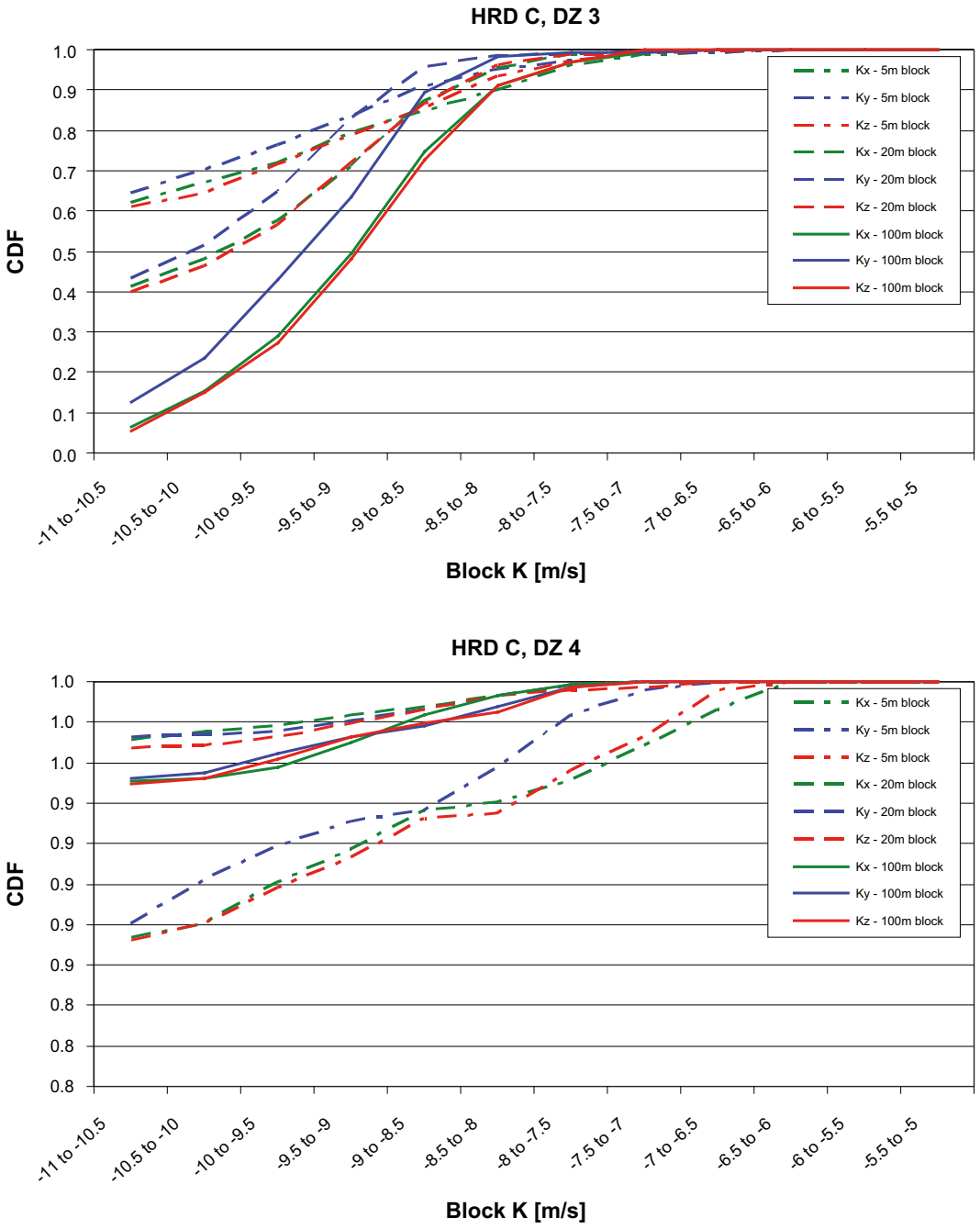

Figure E-20. *Cumulative distribution of calculated block scale Kx, Ky and Kz values for HRD_C (top DZ3, bottom DZ4).*

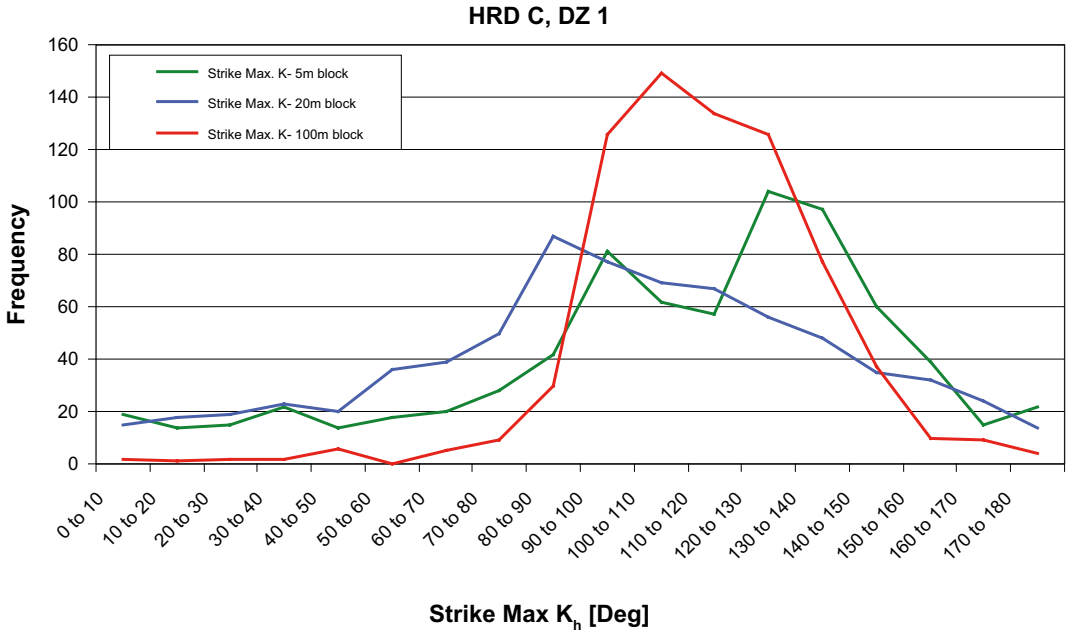

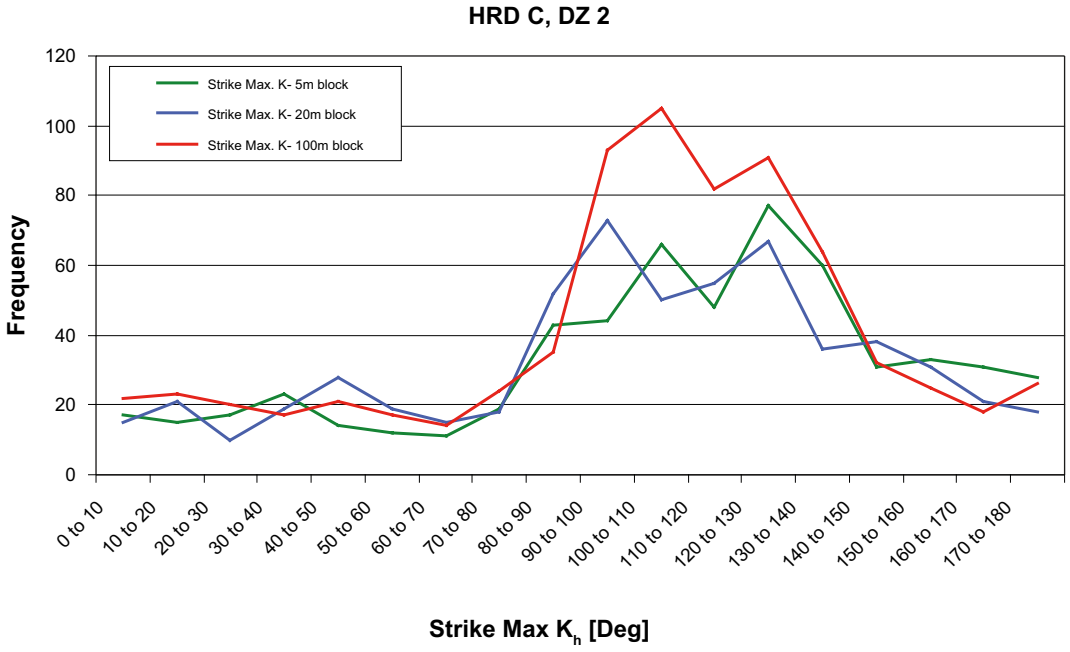

Figure E-21. *A comparison of the strike of maximum horizontal hydraulic conductivity for block scales of 5 m, 20 m and 100 m, for HRD_C (top DZ1, bottom DZ2).*

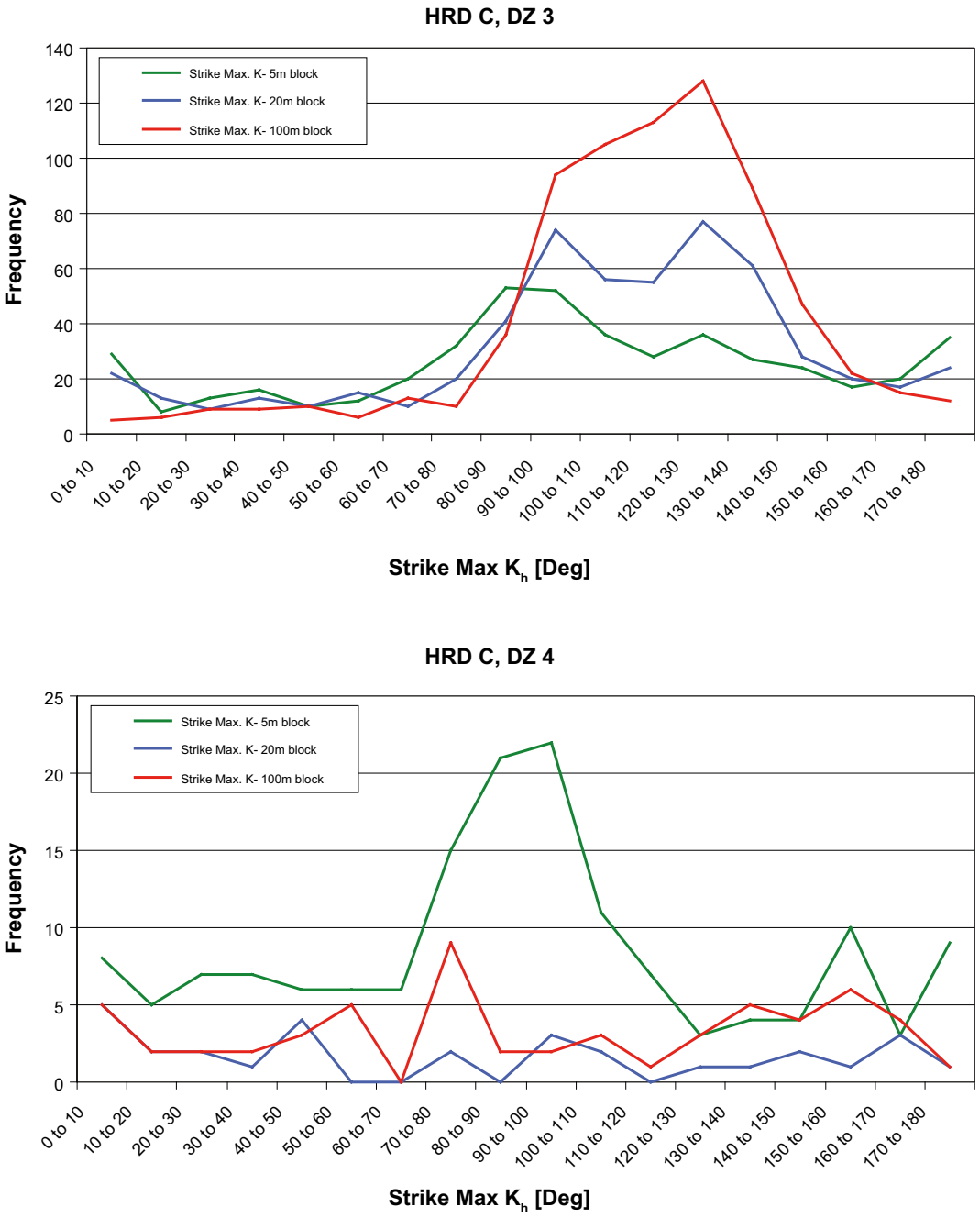

Figure E-22. *A comparison of the strike of maximum horizontal hydraulic conductivity for block scales of 5 m, 20 m and 100 m, for HRD_C (top DZ3, bottom DZ4).*

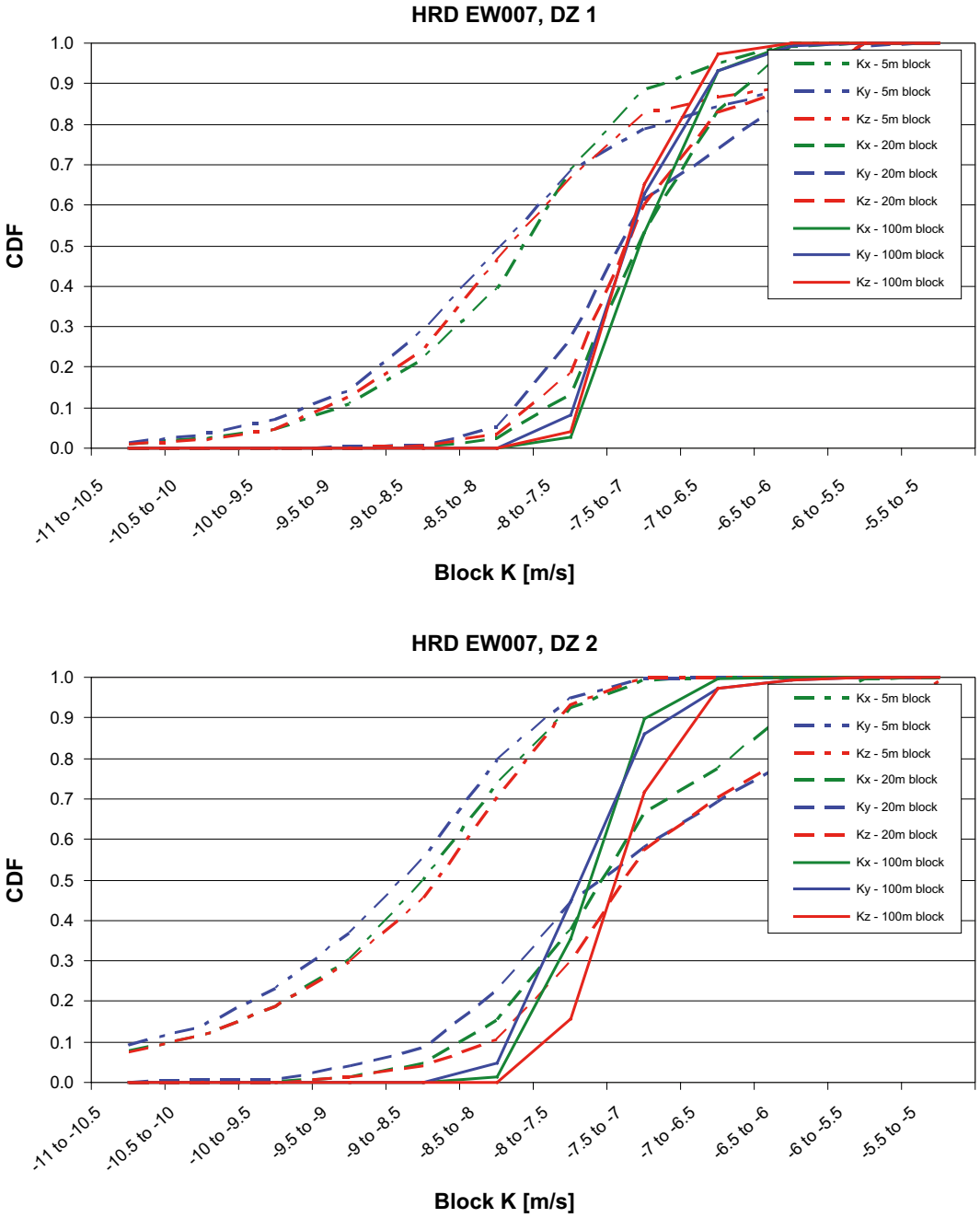

Figure E-23. *Cumulative distribution of calculated block scale Kx, Ky and Kz values for HRD_EW007 (top DZ1, bottom DZ2).*

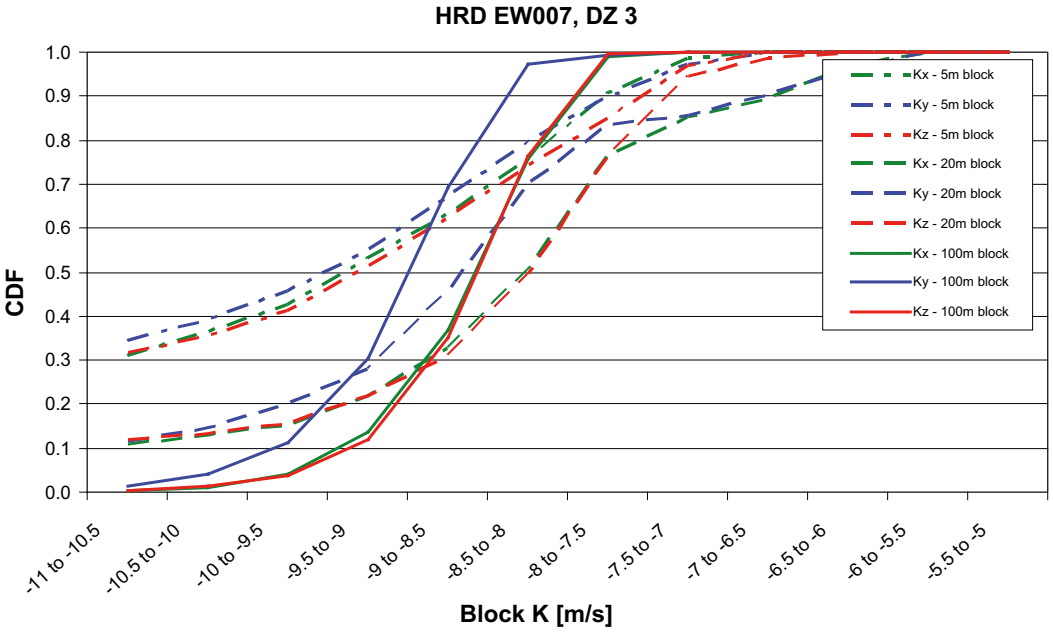

Figure E-24. *Cumulative distribution of calculated block scale Kx, Ky and Kz values for HRD_EW007 (DZ3).*

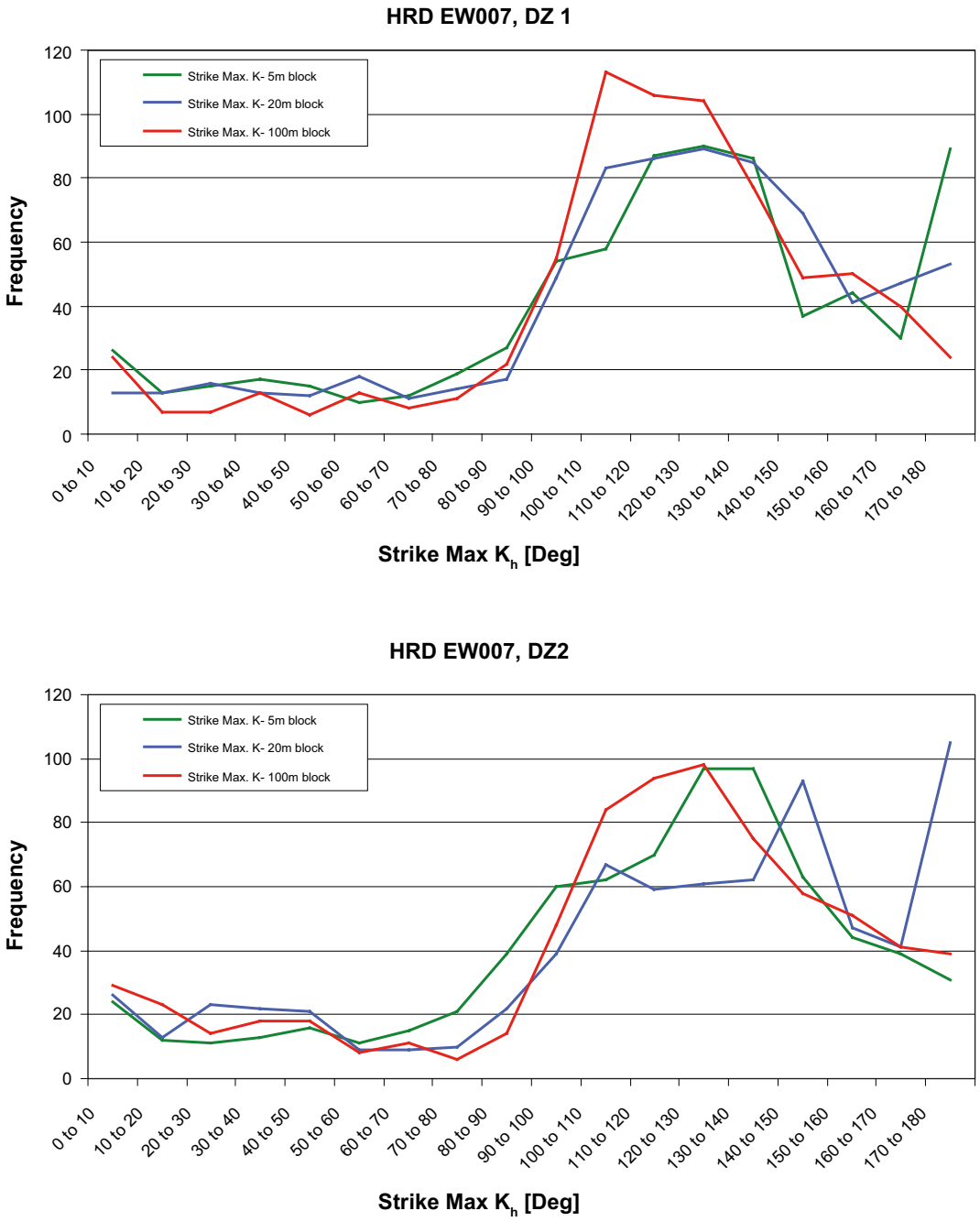

Figure E-25. *A comparison of the strike of maximum horizontal hydraulic conductivity for block scales of 5 m, 20 m and 100 m, for HRD_EW007 (top DZ1, bottom DZ2).*

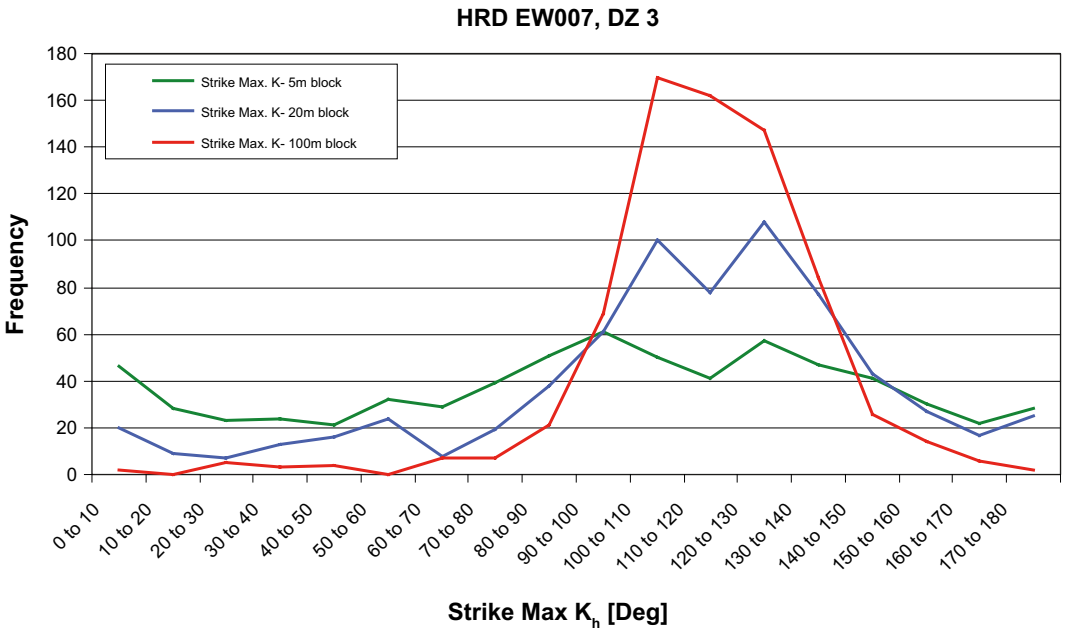

Figure E-26. *A comparison of the strike of maximum horizontal hydraulic conductivity for block scales of 5 m, 20 m and 100 m, for HRD_EW007 (DZ3).*

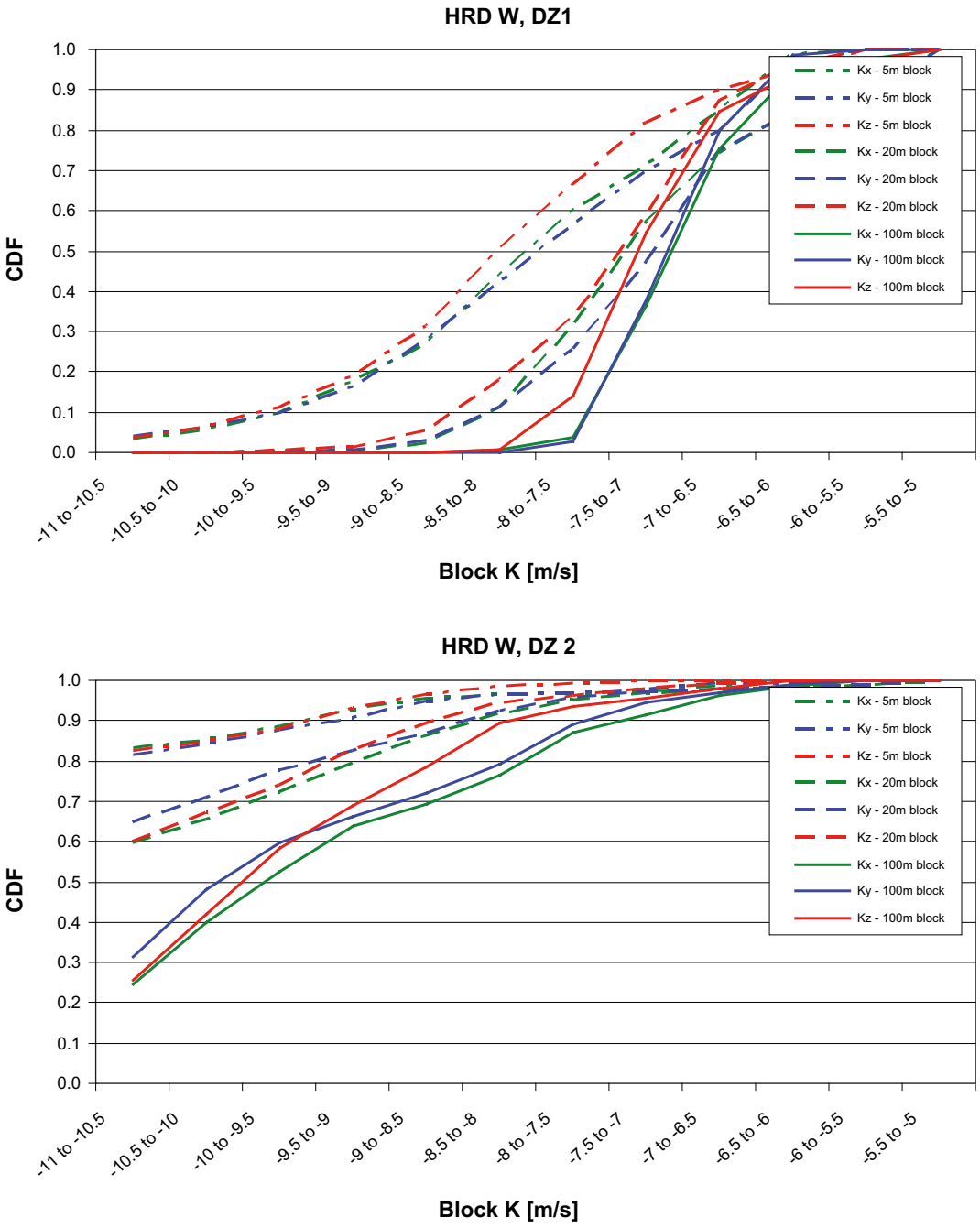

Figure E-27. *Cumulative distribution of calculated block scale Kx, Ky and Kz values for HRD_W (top DZ1, bottom DZ2).*

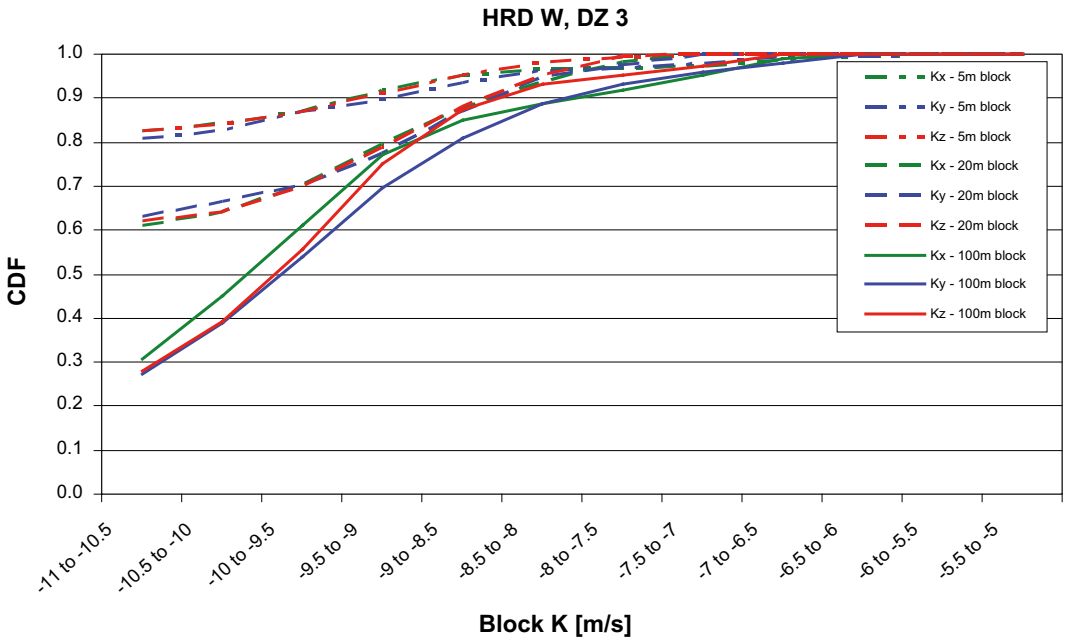

Figure E-28. *Cumulative distribution of calculated block scale Kx, Ky and Kz values for HRD_W (DZ3).*

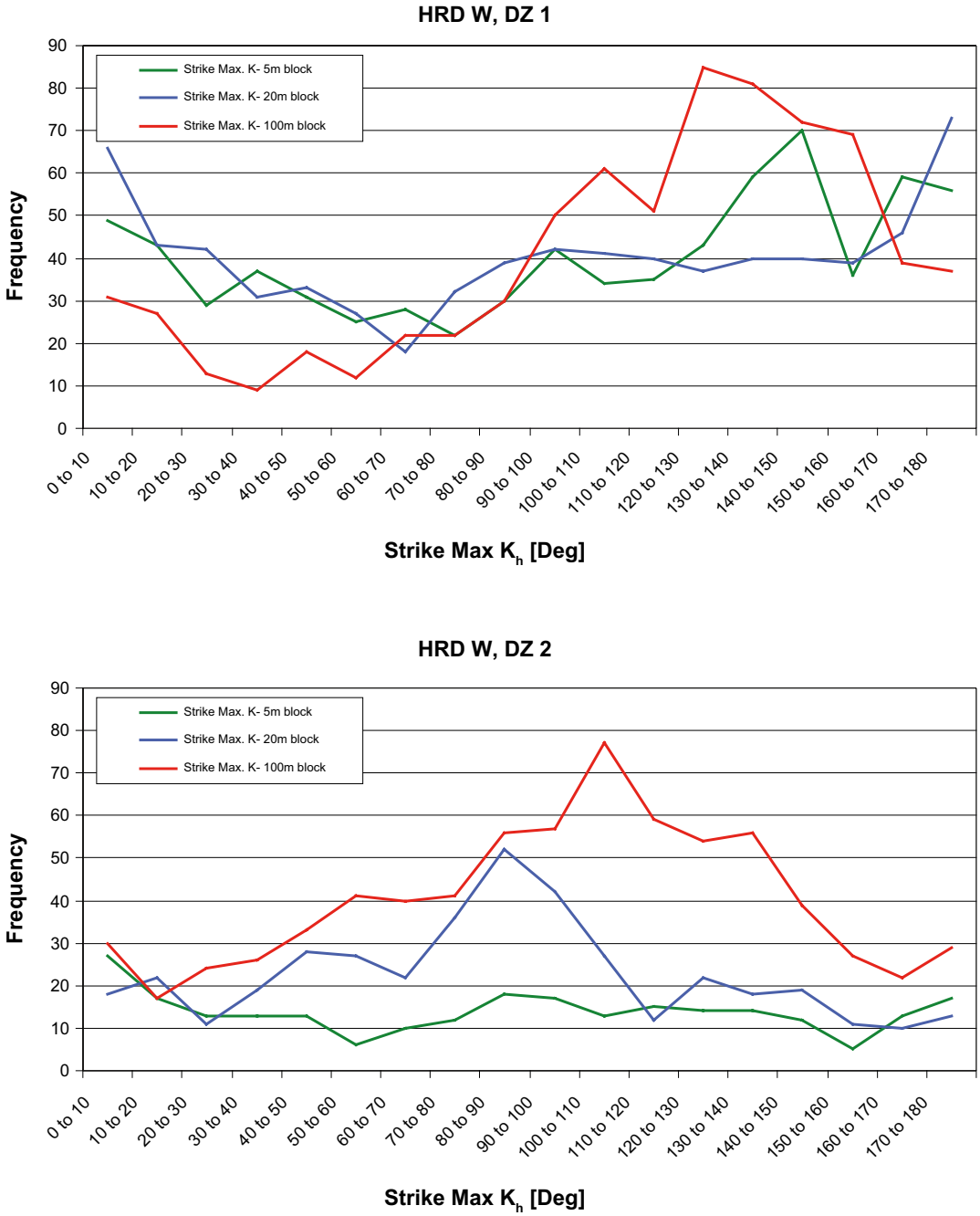

Figure E-29. *A comparison of the strike of maximum horizontal hydraulic conductivity for block scales of 5 m, 20 m and 100 m, for HRD_W (top DZ1, bottom DZ2).*

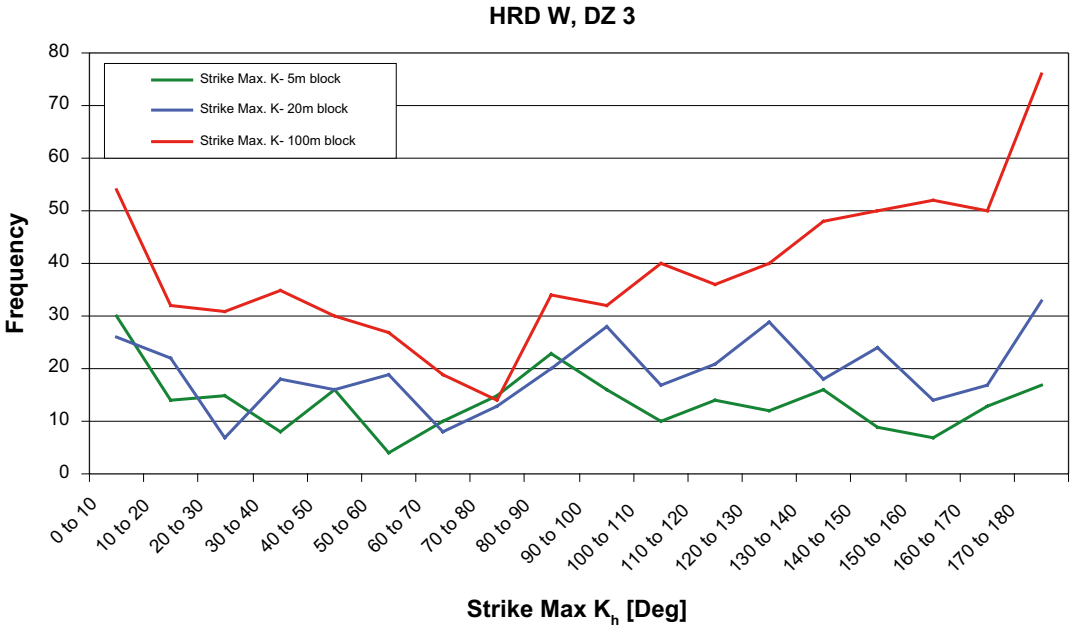

Figure E-30. *A comparison of the strike of maximum horizontal hydraulic conductivity for block scales of 5 m, 20 m and 100 m, for HRD_W (DZ3).*

E.4 Regional-scale calibration

The results of head calculations for the Elaborated Hydro-DFN regional-scale model at 2000 AD compared to example measured data are given in Figure E-31 to Figure E-35. Included for comparison are the results for the SDM-Site Hydro-DFN /Rhén et al. 2009/. An example of the matching of the point water heads is shown for HLX boreholes in Figure E-31 and for SSM boreholes in Figure E-32. Lines indicating the elevation of the topographic surface and the elevation of the soil/bedrock contact are shown for reference. In each case, the upper plot is for the SDM-Site base case and the lower plot is for the Elaborated Hydro-DFN case.

Some examples of comparisons between simulated and measured environmental heads in core drilled boreholes are given in Figure E-33 through Figure E-35. In each case, the left plot is for the SDM-Site base case and the right plot is for the Elaborated Hydro-DFN case.

There is a reasonable match to the head data and the results are generally comparable to those obtained for SDM-Site, but without the need to use the hydraulic conductivity scaling factor of one-third below –150 m elevation. Interference test simulations were not re-run for this model as they relate to HRD_A, which was not modified relative to the SDM-Site base case.

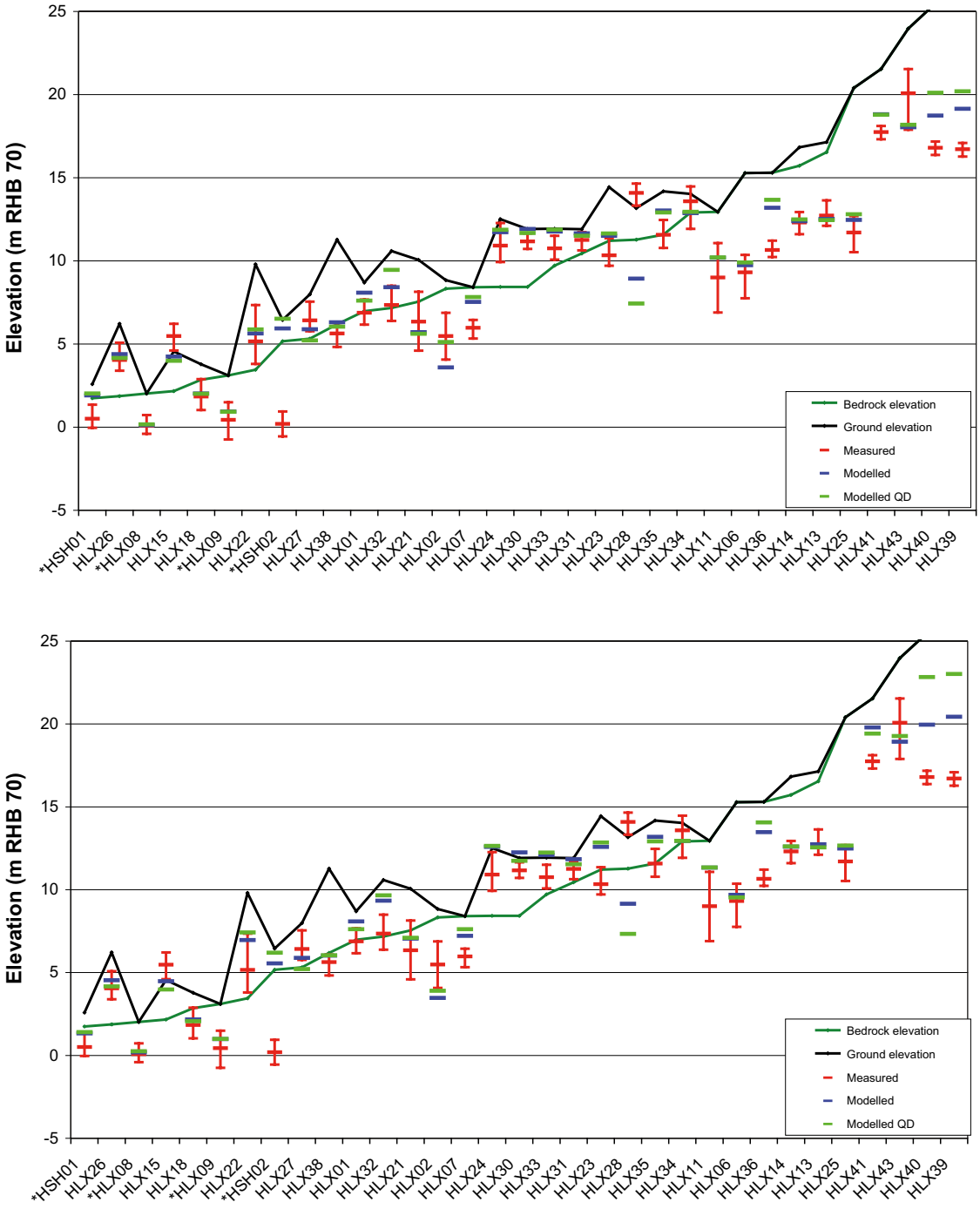

Figure E-31. *Comparison of measured heads in percussion drilled boreholes (HLX) with results of the SDM-Site base case model (top) and the Elaborated Hydro-DFN model (bottom). For the models, values are given for the QD and at the mid elevation of the borehole section in the bedrock. The field data are plotted as mean point water heads in the bedrock with error bars to show the range of values at different measurement times. Boreholes marked by a * are outside the local model area.*

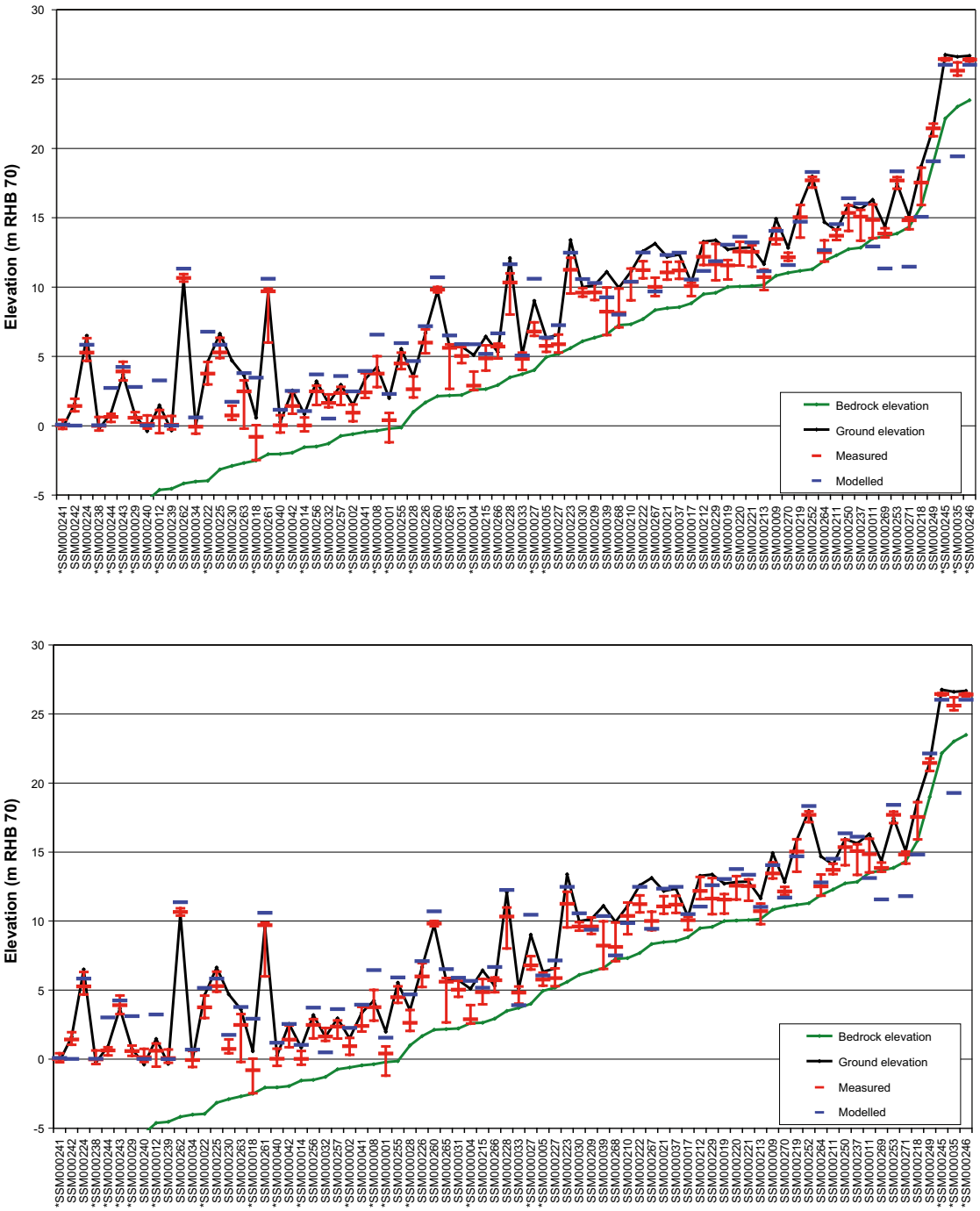

Figure E-32. *Comparison of measured heads in groundwater monitoring wells (SSM) with the results of the SDM-Site base case model and the Elaborated Hydro-DFN model (bottom). For the models, values are given for the QD only. The field data are plotted as mean point water heads in the soil with error bars to show the range of values at different measurement times. Boreholes are ordered by bedrock elevation at the borehole collar. Boreholes marked by a * are outside the Laxemar local model area.*

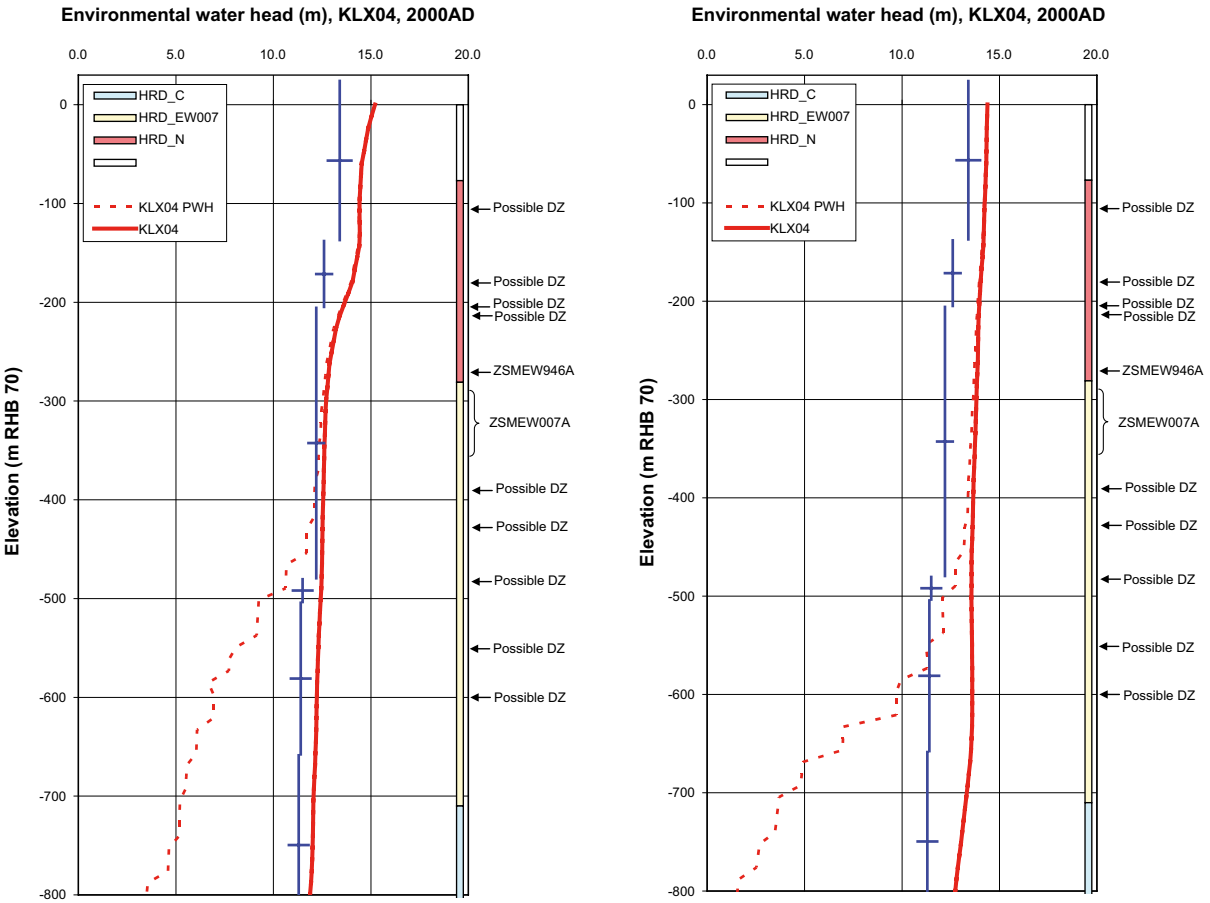

Figure E-33. *Examples of modelled environmental-water head (solid red line) and point-water head (dotted red line) in KLX04 for the SDM-Site base case (left) and Elaborated Hydro-DFN (right) compared with environmental-water heads (blue crossed lines, centre showing midpoint of the section, vertical line showing the extent of the section and horizontal line showing the temporal variation of the measured head) calculated from measured point-water head data in sections along the borehole. At the right hand side, the prevailing hydraulic rock domains are shown as coloured bars along the borehole. Detected deformation zones are indicated at the intersection depth in the borehole.*

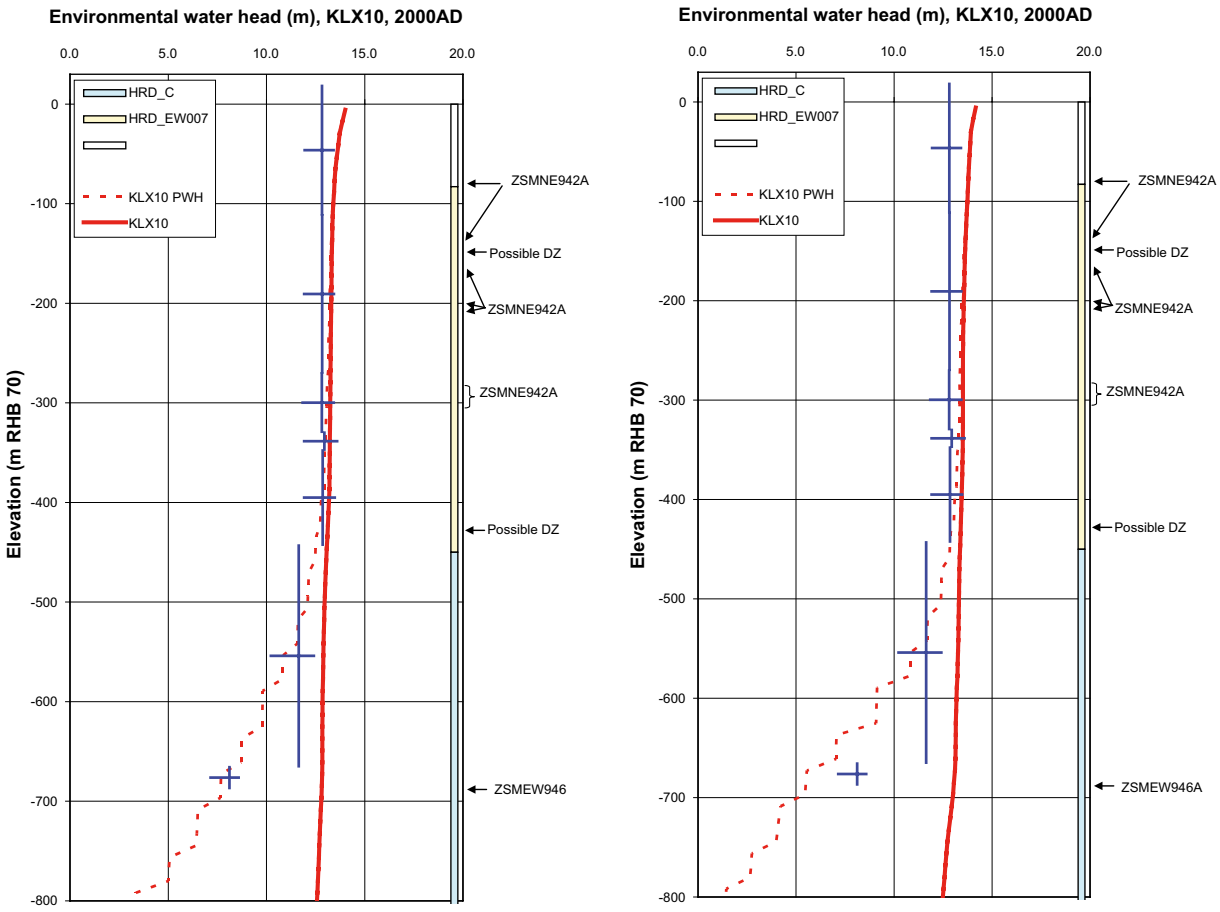

Figure E-34. *Examples of modelled environmental-water head (solid red line) and point-water head (dotted red line) in KLX10 in HRD_C for the SDM-Site base case (left) and Elaborated Hydro-DFN (right) compared with environmental-water heads (blue crossed lines, centre showing midpoint of the section, vertical line showing the extent of the section and horizontal line showing the temporal variation of the measured head) calculated from measured point-water head data in sections along the borehole. At the right hand side, the prevailing hydraulic rock domains are shown as coloured bars along the borehole. Detected deformation zones are indicated at the intersection depth in the borehole.*

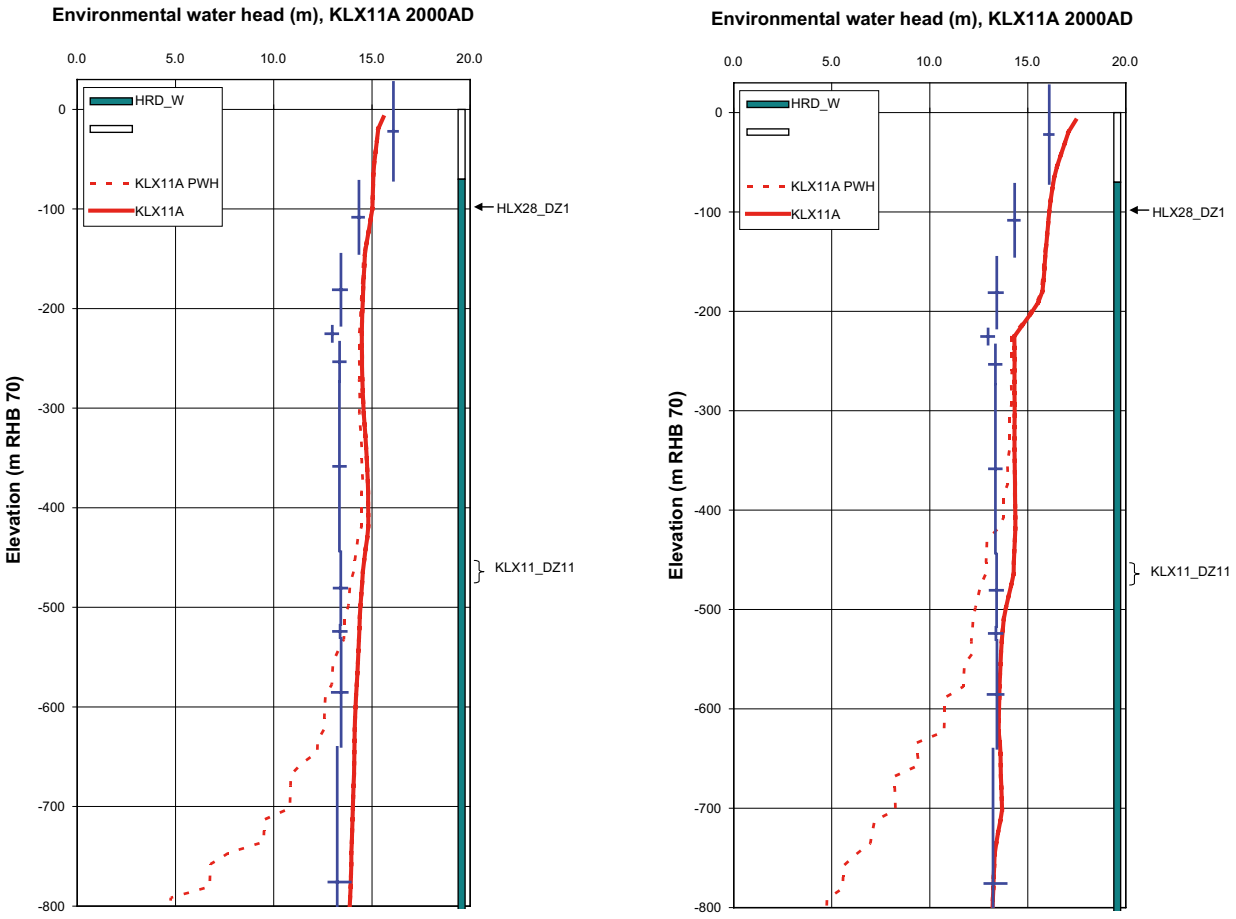

Figure E-35. *Examples of modelled environmental-water head (solid red line) and point-water head (dotted red line) in KLX11A in HRD_W for the SDM-Site base case (left) and Elaborated Hydro-DFN (right) compared with environmental-water heads (blue crossed lines, centre showing midpoint of the section, vertical line showing the extent of the section and horizontal line showing the temporal variation of the measured head) calculated from measured point-water head data in sections along the borehole. At the right hand side, the prevailing hydraulic rock domains are shown as coloured bars along the borehole. Detected deformation zones are indicated at the intersection depth in the borehole.*

E.5 Palaeohydrogeology

The results of the regional-scale palaeohydrogeology calculations at 2000 AD compared to measured hydrochemical data are given in Figure E-36 to Figure E-51. On the left in each figure are the results from the Elaborated Hydro-DFN and on the right are the results for the SDM-Site Hydro-DFN /Rhén et al. 2008/. There is a reasonable match to the hydrochemistry data and the results are at least as good as those obtained for SDM-Site, but without the need to use the hydraulic conductivity scaling factor of one-third below –150 m elevation.

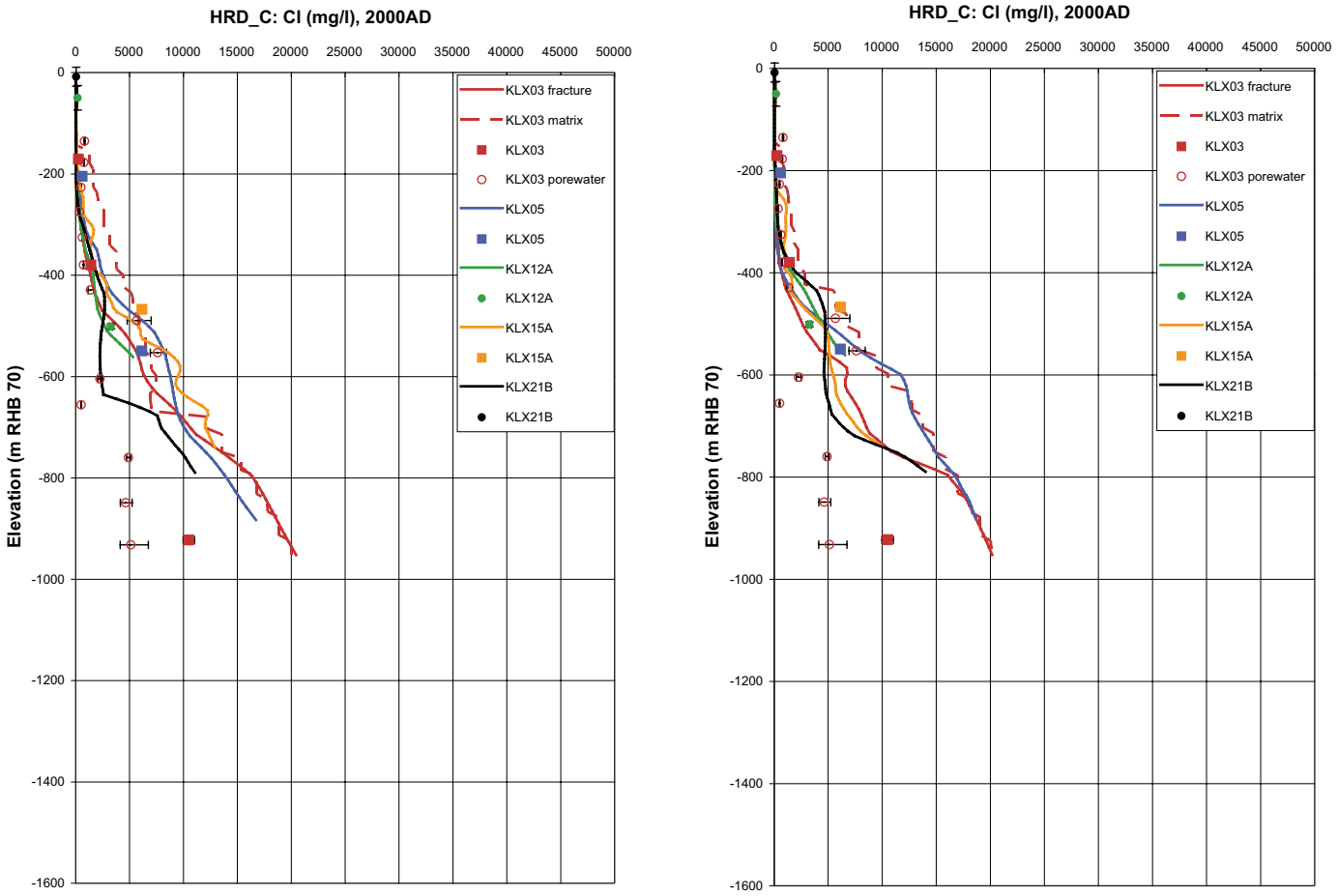

Figure E-36. *A comparison of the modelled and measured Cl concentrations in the fracture system for boreholes in HRD_C for the Elaborated Hydro-DFN (left) and the SDM-Site Hydro-DFN (right). Square symbols are used for category 1–3 data, circles are used for the pore water data, and small diamond symbols are used for category 4 data. The error bars on the data indicate the laboratory analytical error. The solid lines show the distribution in the borehole simulated in the fracture system, and the dashed lines are for the matrix.*

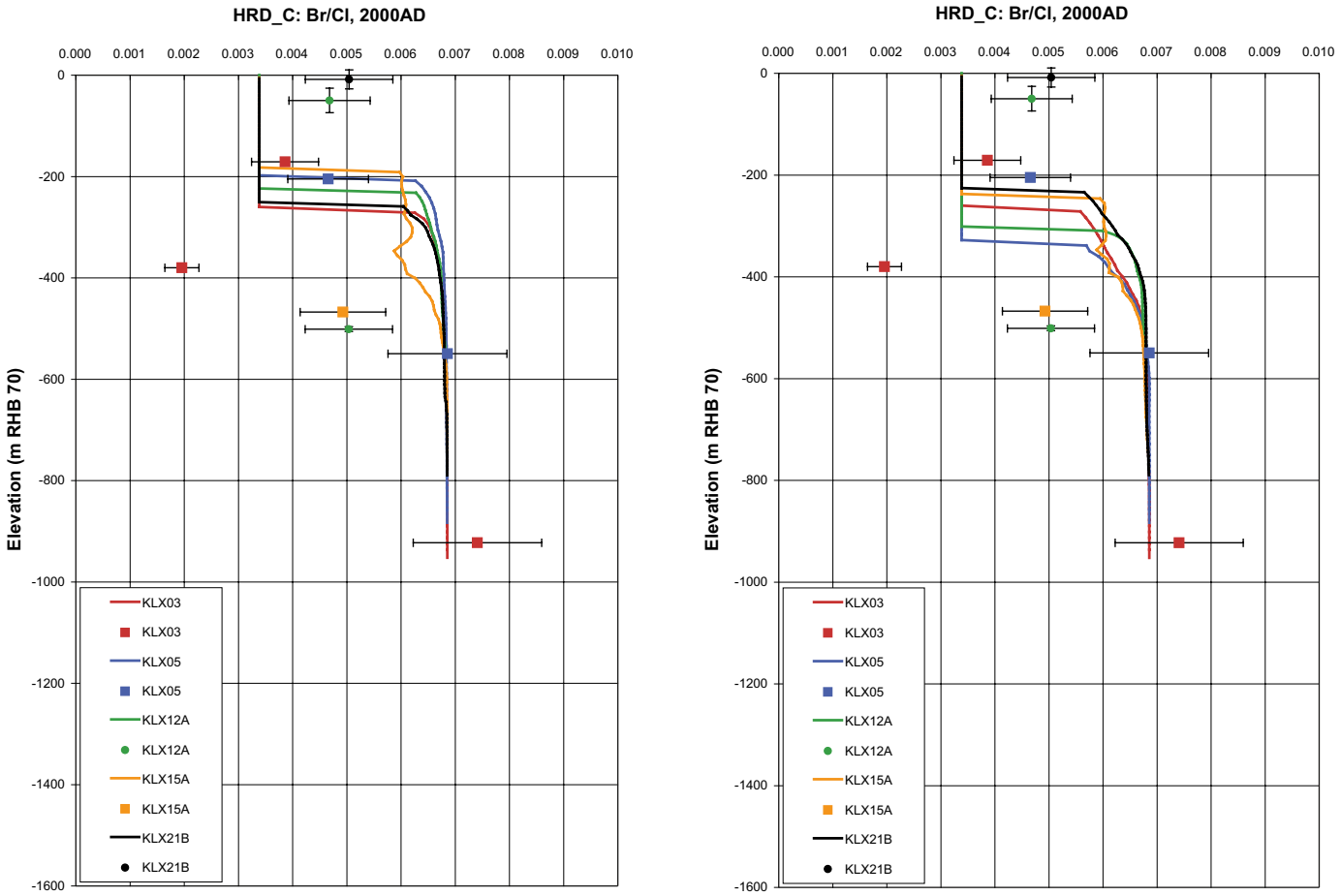

Figure E-37. *A comparison of the modelled and measured Br/Cl concentrations in the fracture system for boreholes in HRD_C for the Elaborated Hydro-DFN (left) and the SDM-Site Hydro-DFN (right). Square symbols are used for category 1–3 data, circles are used for the pore water data, and small diamond symbols are used for category 4 data. The error bars on the data indicate the laboratory analytical error. The solid lines show the distribution in the borehole simulated in the fracture system, and the dashed lines are for the matrix.*

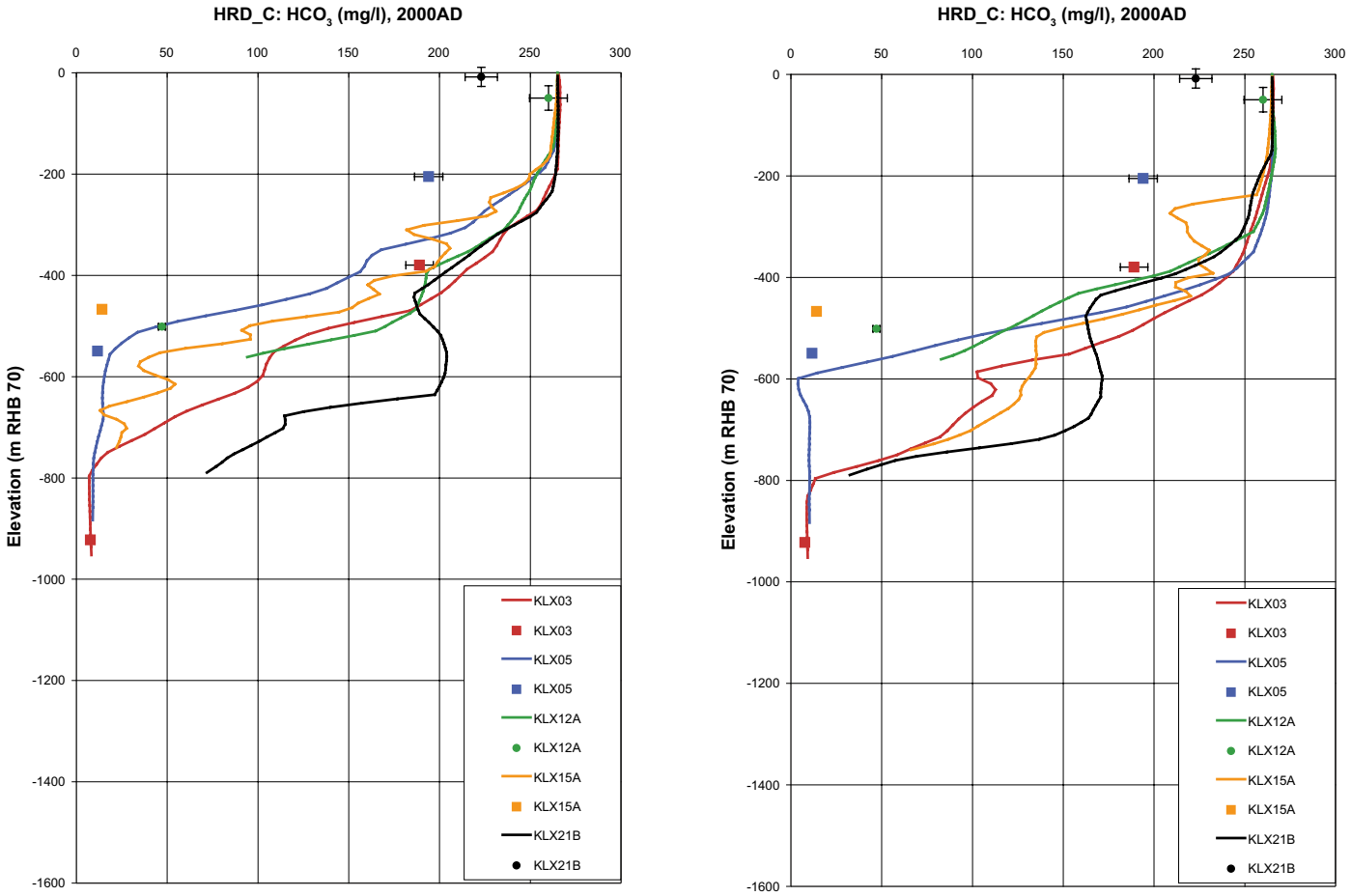

Figure E-38. *A comparison of the modelled and measured HCO_3 concentrations in the fracture system for boreholes in HRD_C for the Elaborated Hydro-DFN (left) and the SDM-Site Hydro-DFN (right). Square symbols are used for category 1–3 data, circles are used for the pore water data, and small diamond symbols are used for category 4 data. The error bars on the data indicate the laboratory analytical error. The solid lines show the distribution in the borehole simulated in the fracture system, and the dashed lines are for the matrix.*

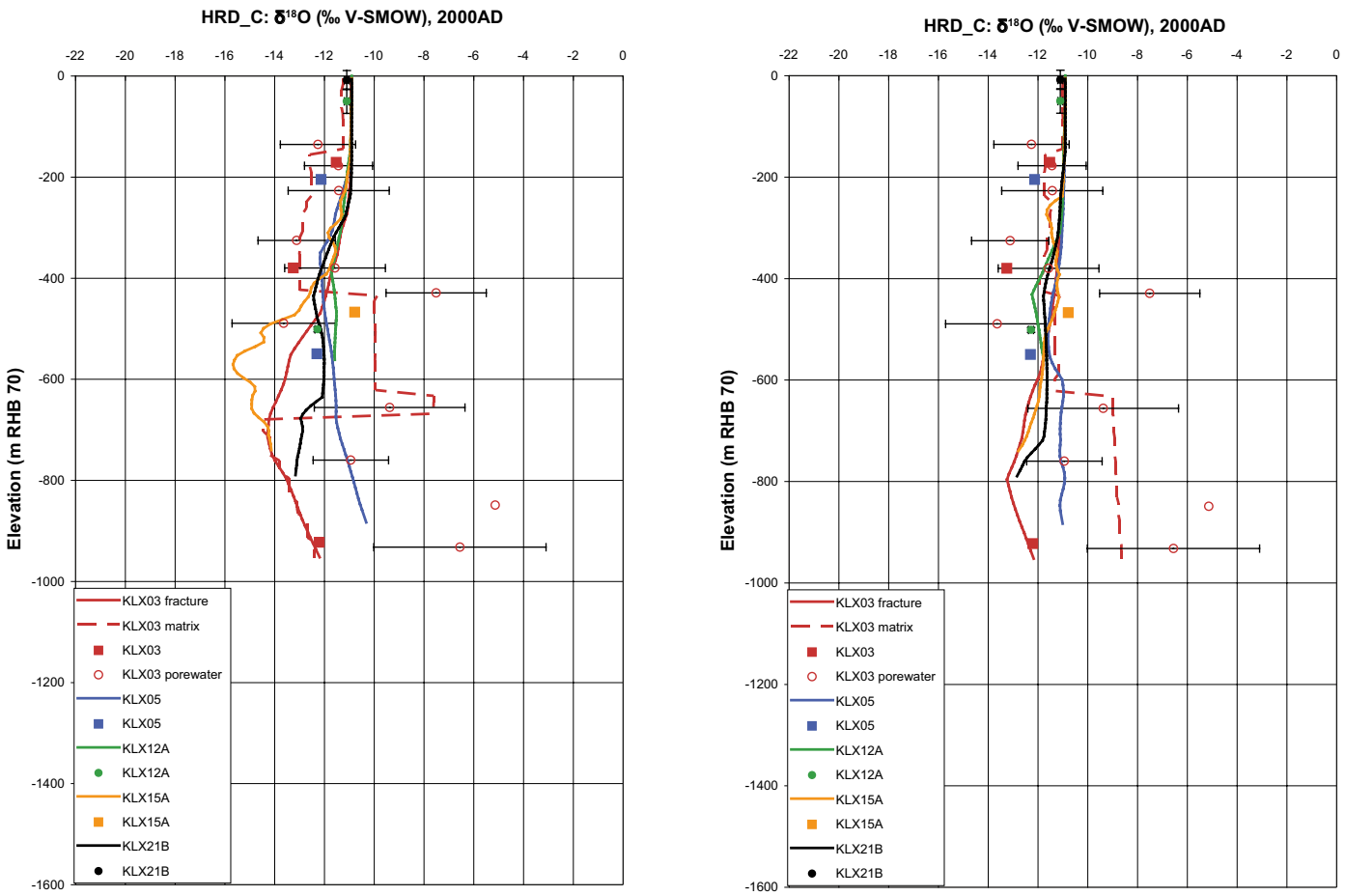

Figure E-39. *A comparison of the modelled and measured $\delta^{18}O$ concentrations in the fracture system for boreholes in HRD_C for the Elaborated Hydro-DFN (left) and the SDM-Site Hydro-DFN (right). Square symbols are used for category 1–3 data, circles are used for the pore water data, and small diamond symbols are used for category 4 data. The error bars on the data indicate the laboratory analytical error. The solid lines show the distribution in the borehole simulated in the fracture system, and the dashed lines are for the matrix.*

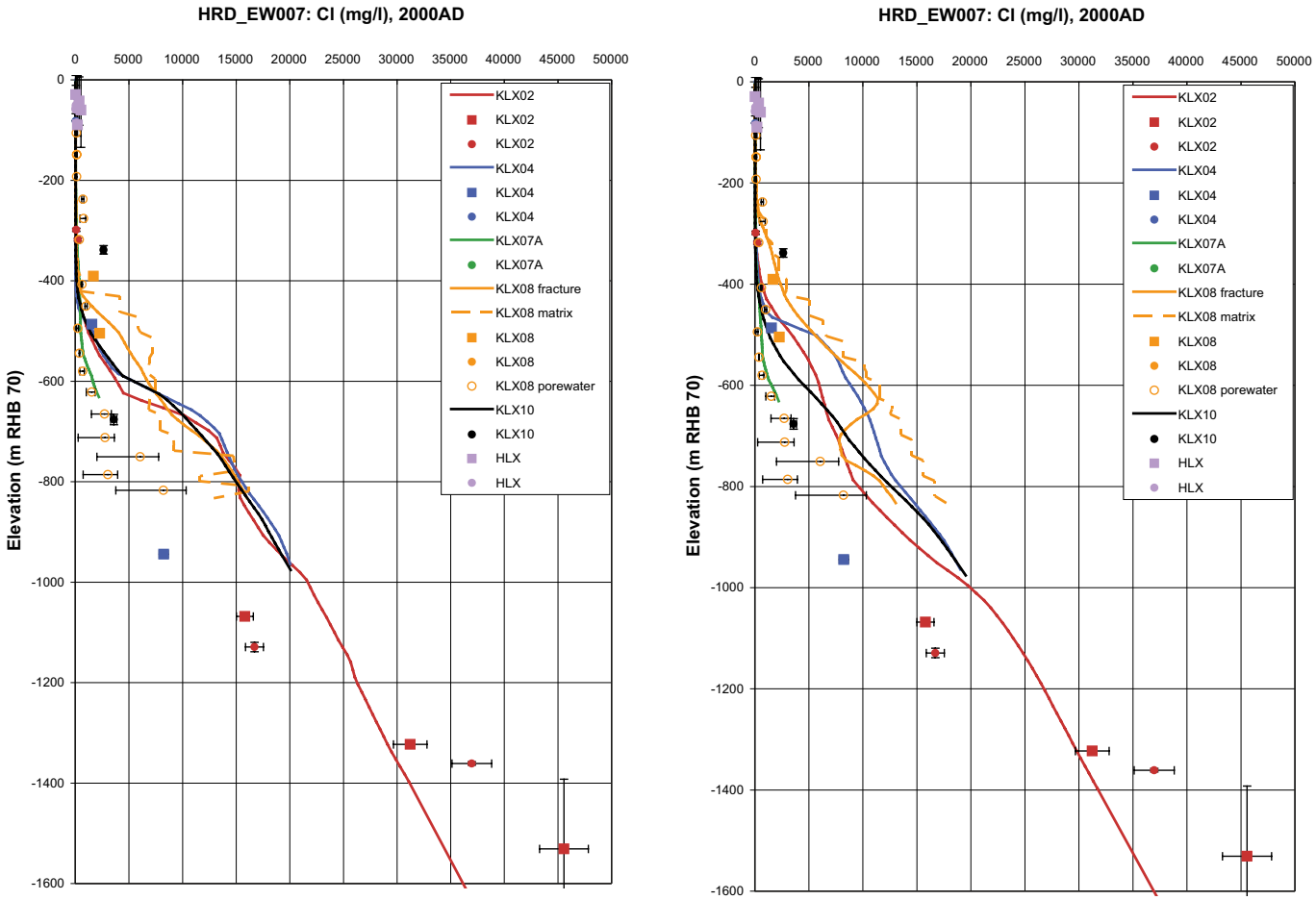

Figure E-40. *A comparison of the modelled and measured Cl concentrations in the fracture system for boreholes in HRD_EW007 for the Elaborated Hydro-DFN (left) and the SDM-Site Hydro-DFN (right). Square symbols are used for category 1–3 data, circles are used for the pore water data, and small diamond symbols are used for category 4 data. The error bars on the data indicate the laboratory analytical error. The solid lines show the distribution in the borehole simulated in the fracture system, and the dashed lines are for the matrix.*

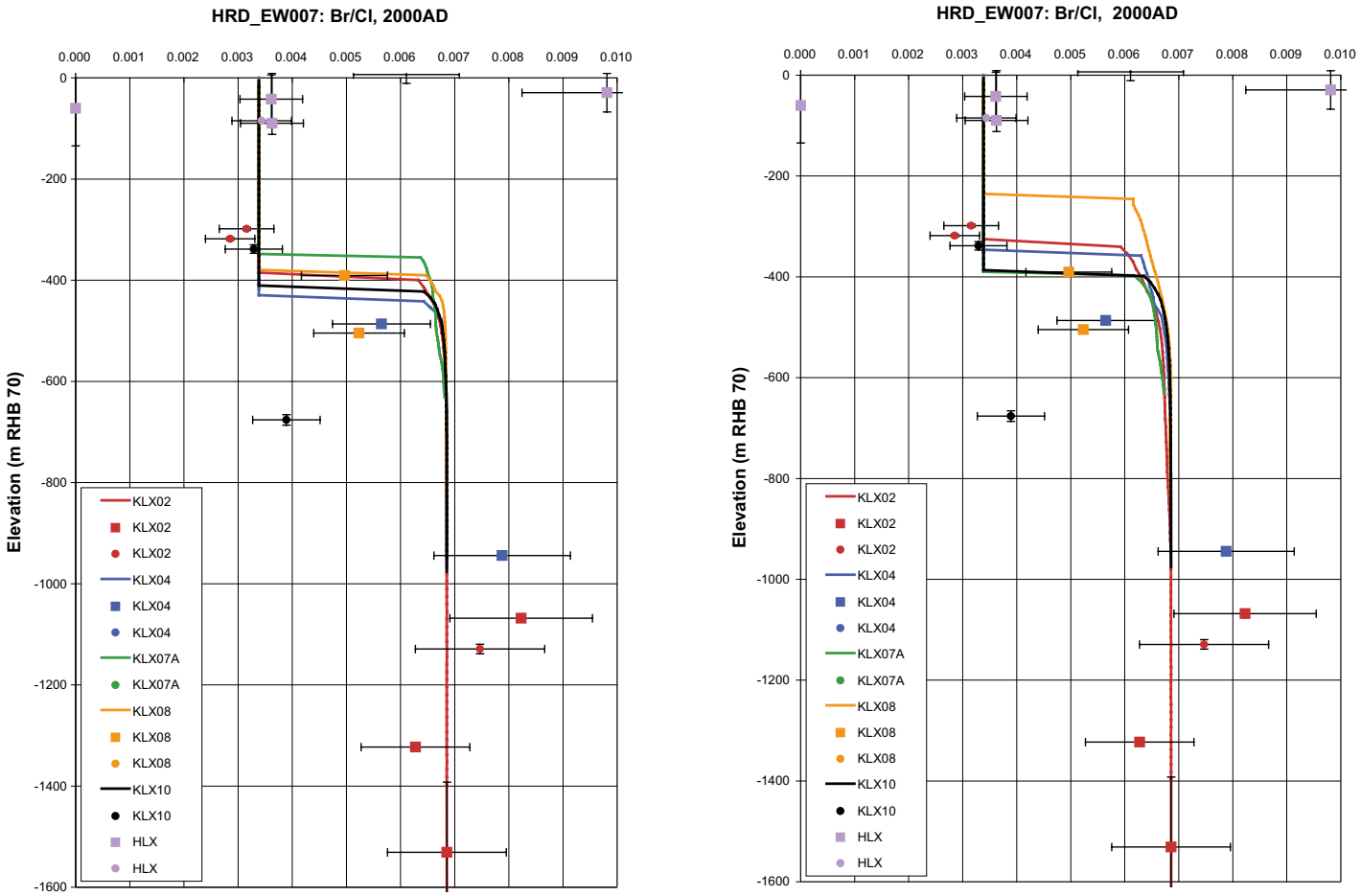

Figure E-41. *A comparison of the modelled and measured Br/Cl concentrations in the fracture system for boreholes in HRD_EW007 for the Elaborated Hydro-DFN (left) and the SDM-Site Hydro-DFN (right). Square symbols are used for category 1–3 data, circles are used for the pore water data, and small diamond symbols are used for category 4 data. The error bars on the data indicate the laboratory analytical error. The solid lines show the distribution in the borehole simulated in the fracture system, and the dashed lines are for the matrix.*

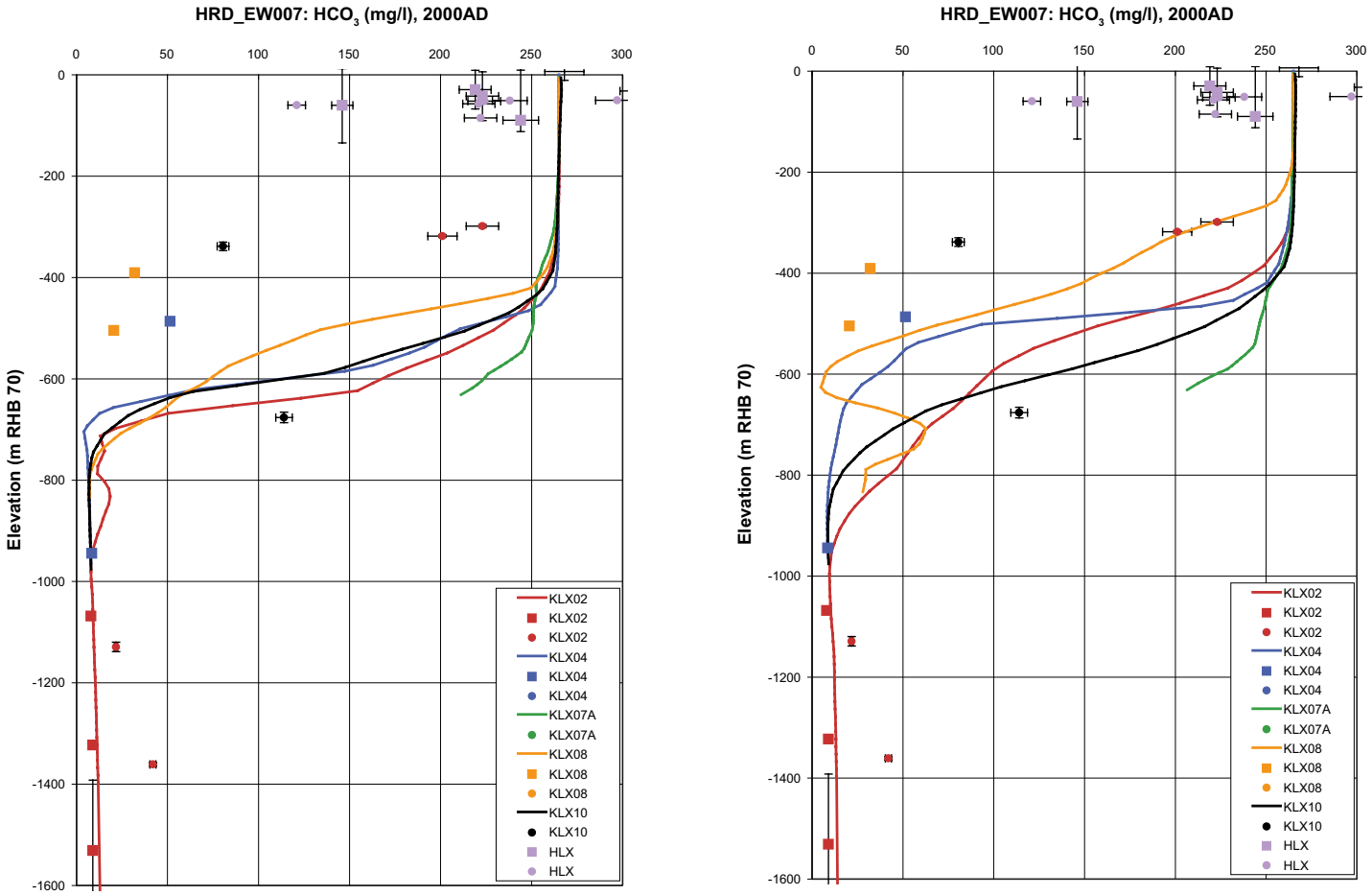

Figure E-42. *A comparison of the modelled and measured HCO_3 concentrations in the fracture system for boreholes in HRD_EW007 for the Elaborated Hydro-DFN (left) and the SDM-Site Hydro-DFN (right). Square symbols are used for category 1–3 data, circles are used for the pore water data, and small diamond symbols are used for category 4 data. The error bars on the data indicate the laboratory analytical error. The solid lines show the distribution in the borehole simulated in the fracture system, and the dashed lines are for the matrix.*

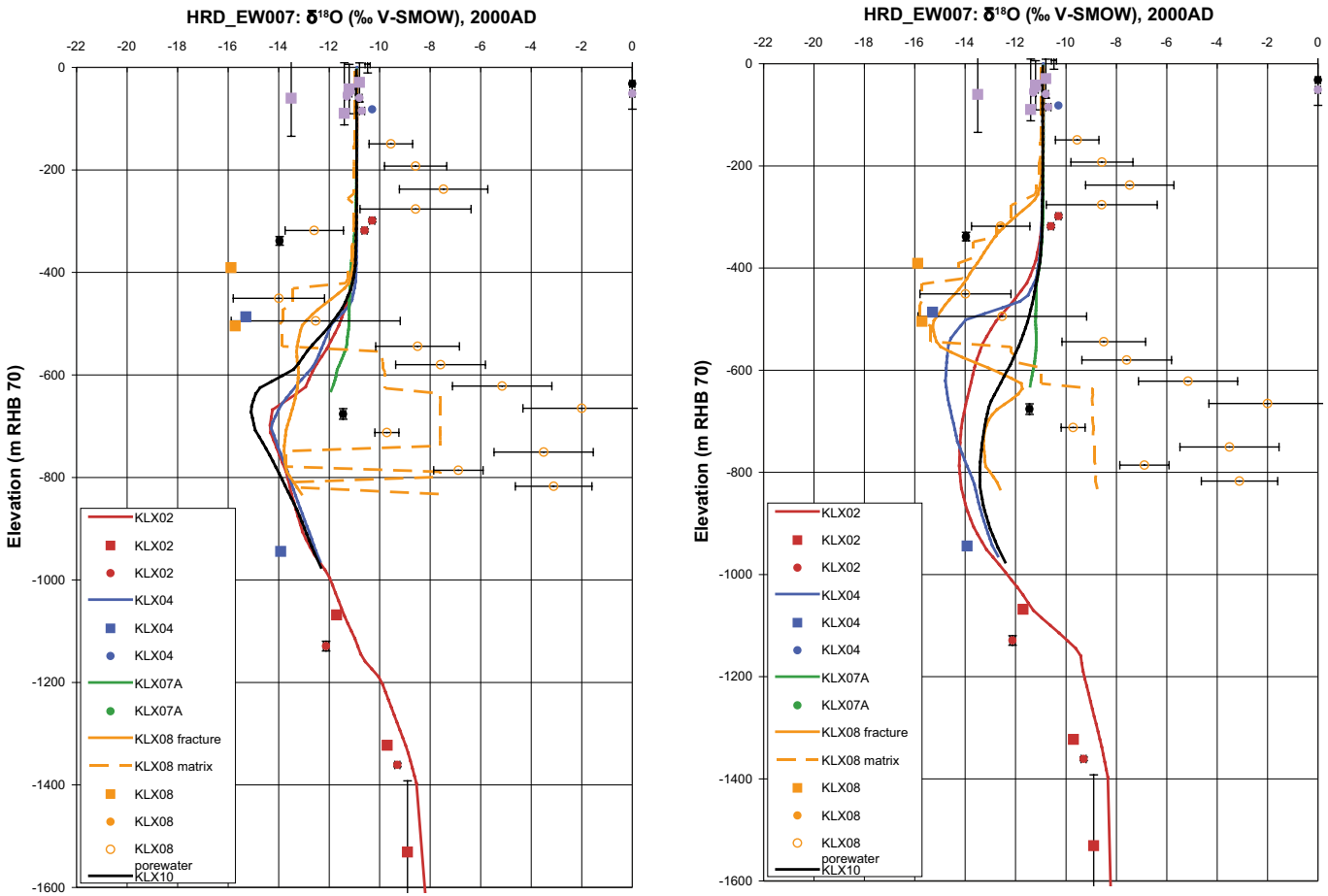

Figure E-43. *A comparison of the modelled and measured $\delta^{18}O$ concentrations in the fracture system for boreholes in HRD_EW007 for the Elaborated Hydro-DFN (left) and the SDM-Site Hydro-DFN (right). Square symbols are used for category 1–3 data, circles are used for the pore water data, and small diamond symbols are used for category 4 data. The error bars on the data indicate the laboratory analytical error. The solid lines show the distribution in the borehole simulated in the fracture system, and the dashed lines are for the matrix.*

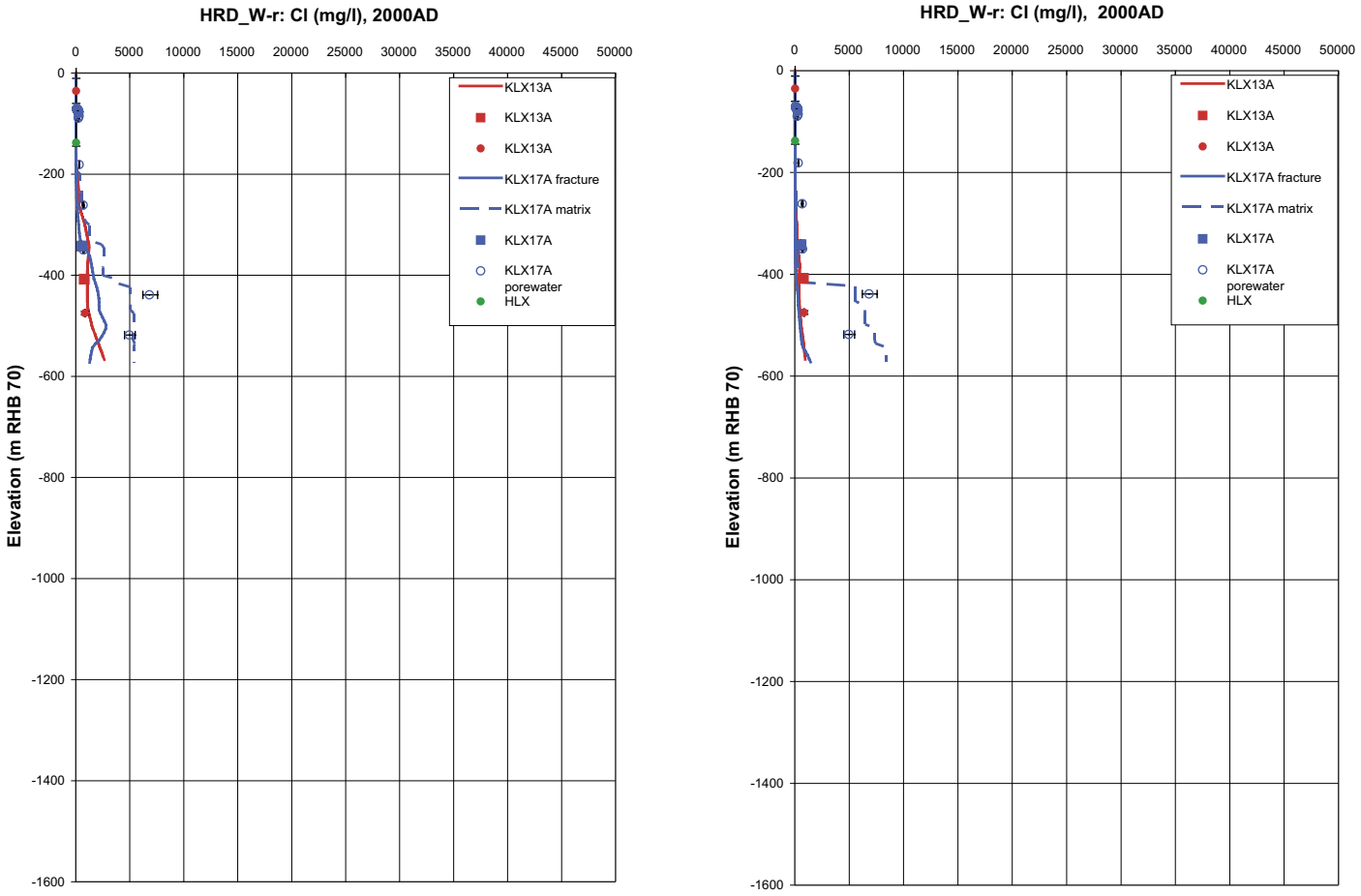

Figure E-44. *A comparison of the modelled and measured Cl concentrations in the fracture system for boreholes in HRD_W-recharge for the Elaborated Hydro-DFN (left) and the SDM-Site Hydro-DFN (right). Square symbols are used for category 1–3 data, circles are used for the pore water data, and small diamond symbols are used for category 4 data. The error bars on the data indicate the laboratory analytical error. The solid lines show the distribution in the borehole simulated in the fracture system, and the dashed lines are for the matrix.*

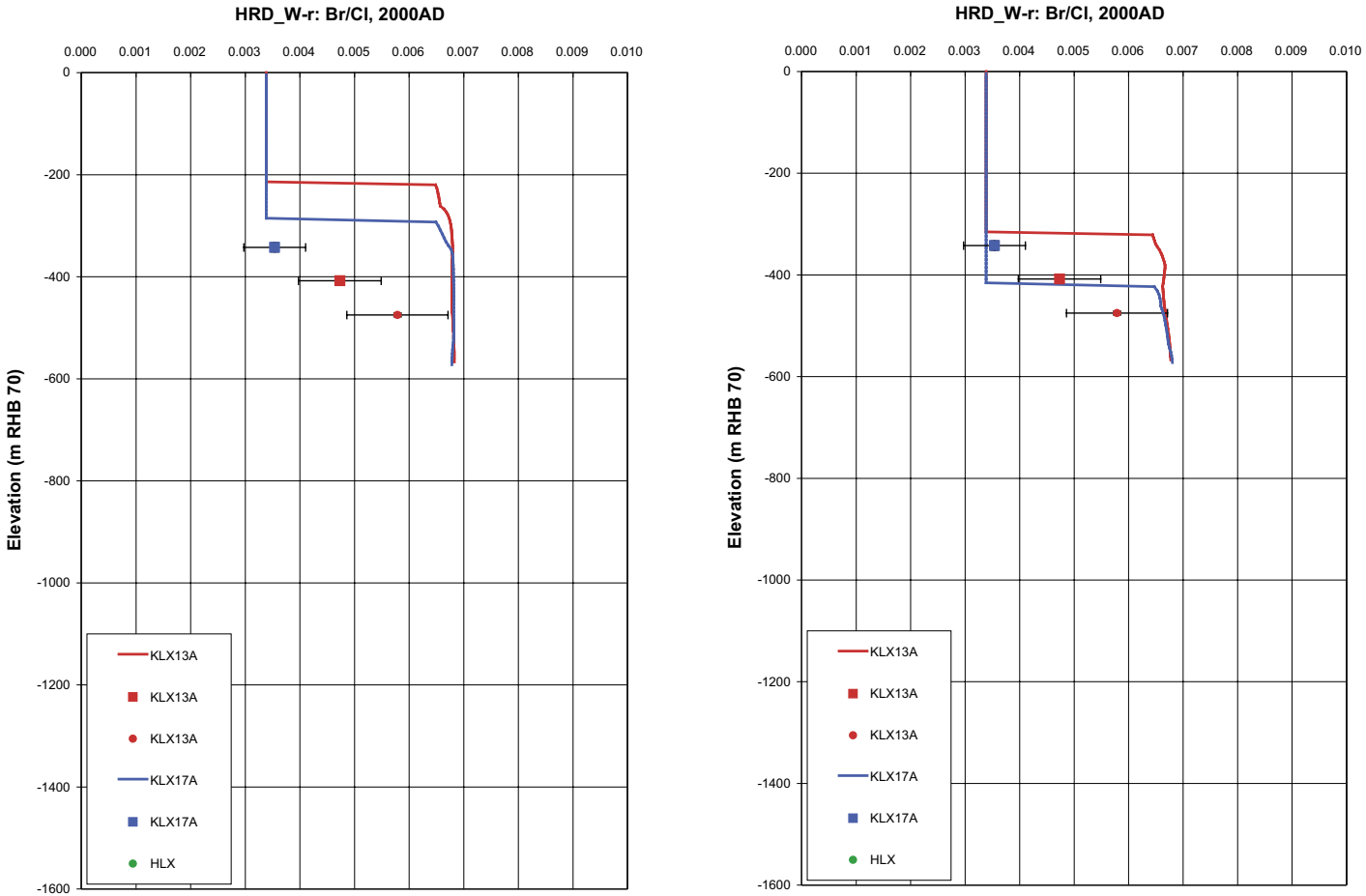

Figure E-45. *A comparison of the modelled and measured Br/Cl concentrations in the fracture system for boreholes in HRD_W-recharge for the Elaborated Hydro-DFN (left) and the SDM-Site Hydro-DFN (right). Square symbols are used for category 1–3 data, circles are used for the pore water data, and small diamond symbols are used for category 4 data. The error bars on the data indicate the laboratory analytical error. The solid lines show the distribution in the borehole simulated in the fracture system, and the dashed lines are for the matrix.*

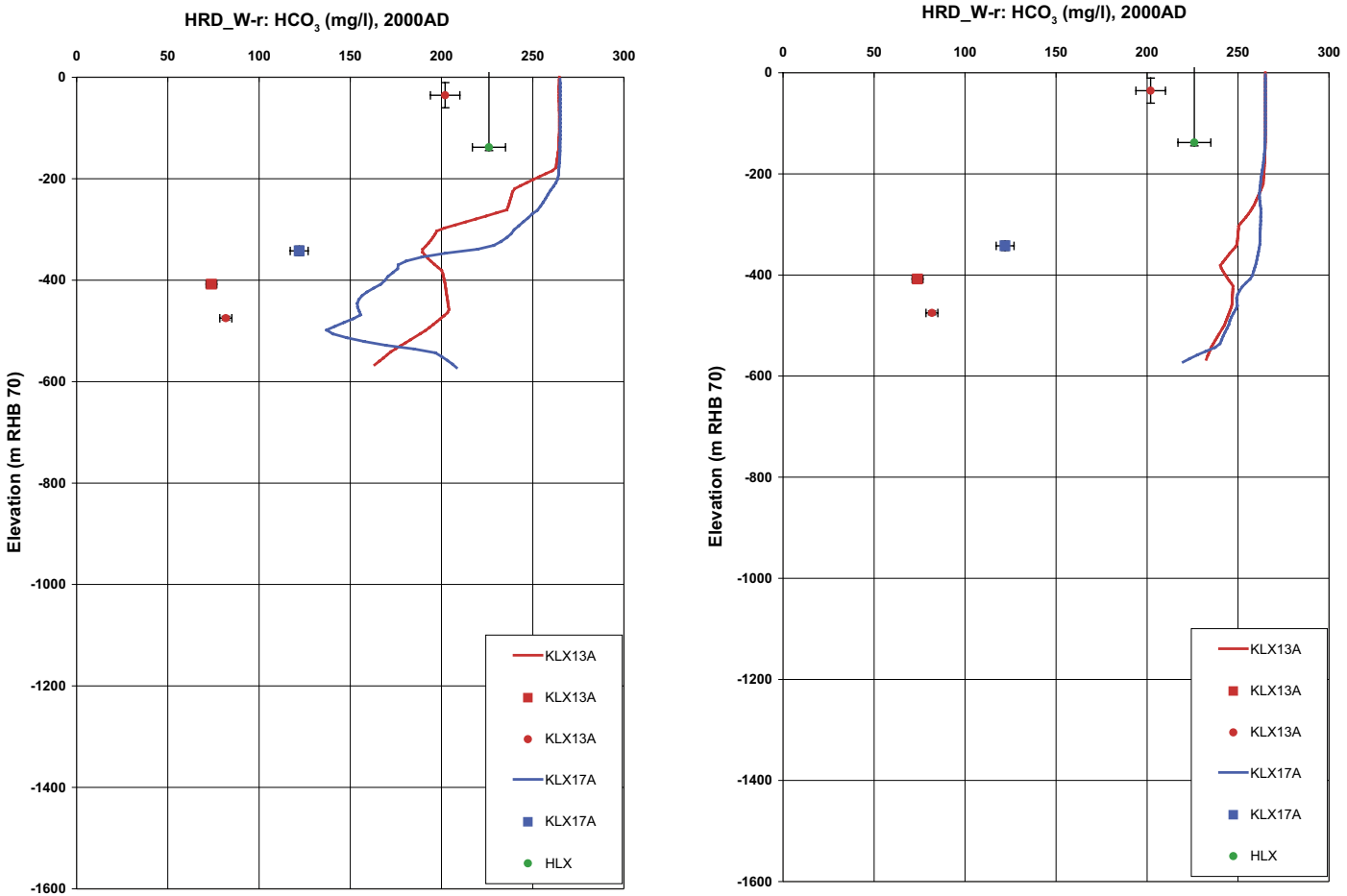

Figure E-46. *A comparison of the modelled and measured HCO_3 concentrations in the fracture system for boreholes in HRD_W-recharge for the Elaborated Hydro-DFN (left) and the SDM-Site Hydro-DFN (right). Square symbols are used for category 1–3 data, circles are used for the pore water data, and small diamond symbols are used for category 4 data. The error bars on the data indicate the laboratory analytical error. The solid lines show the distribution in the borehole simulated in the fracture system, and the dashed lines are for the matrix.*

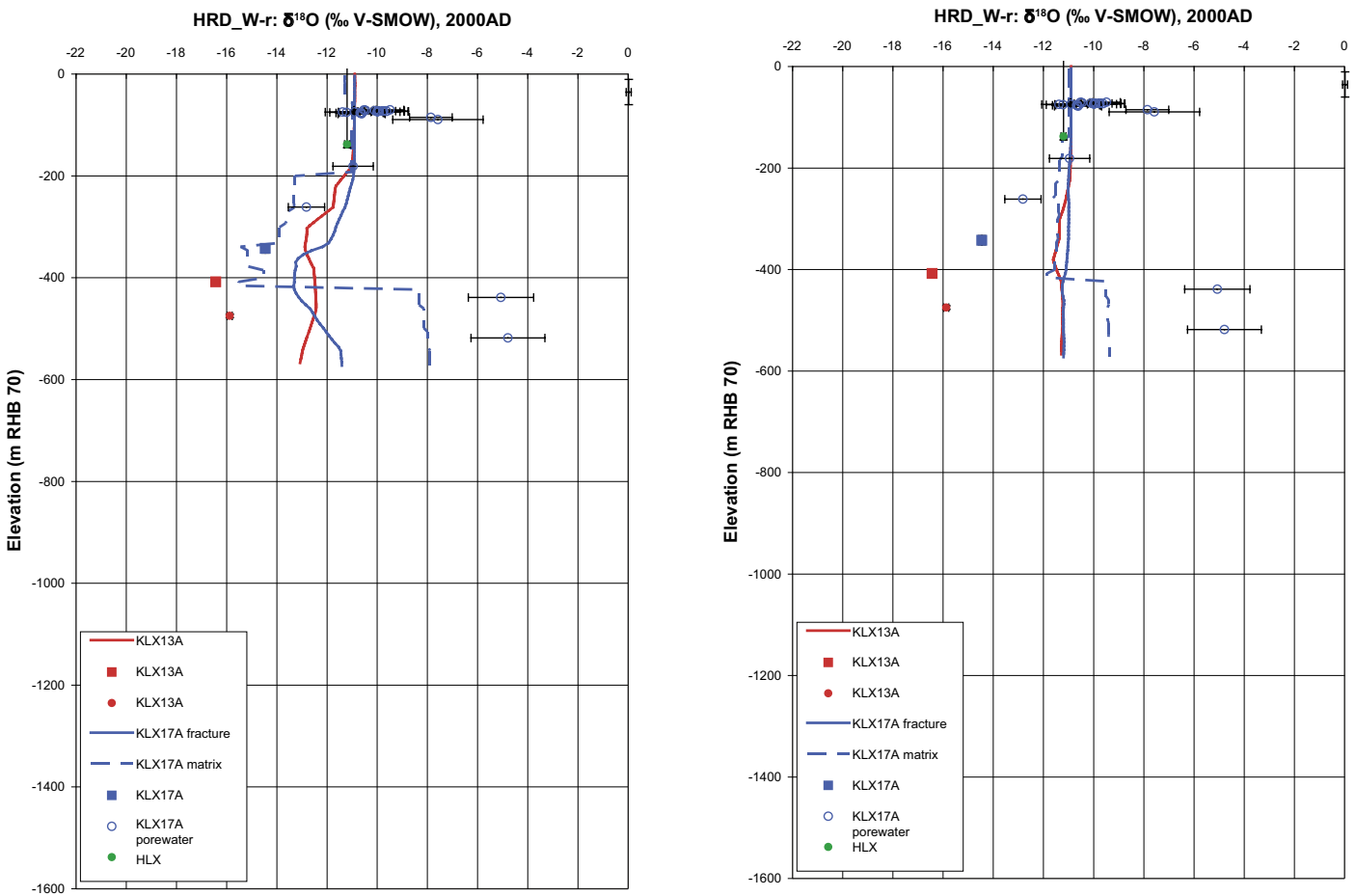

Figure E-47. *A comparison of the modelled and measured $\delta^{18}O$ concentrations in the fracture system for boreholes in HRD_W-recharge for the Elaborated Hydro-DFN (left) and the SDM-Site Hydro-DFN (right). Square symbols are used for category 1–3 data, circles are used for the pore water data, and small diamond symbols are used for category 4 data. The error bars on the data indicate the laboratory analytical error. The solid lines show the distribution in the borehole simulated in the fracture system, and the dashed lines are for the matrix.*

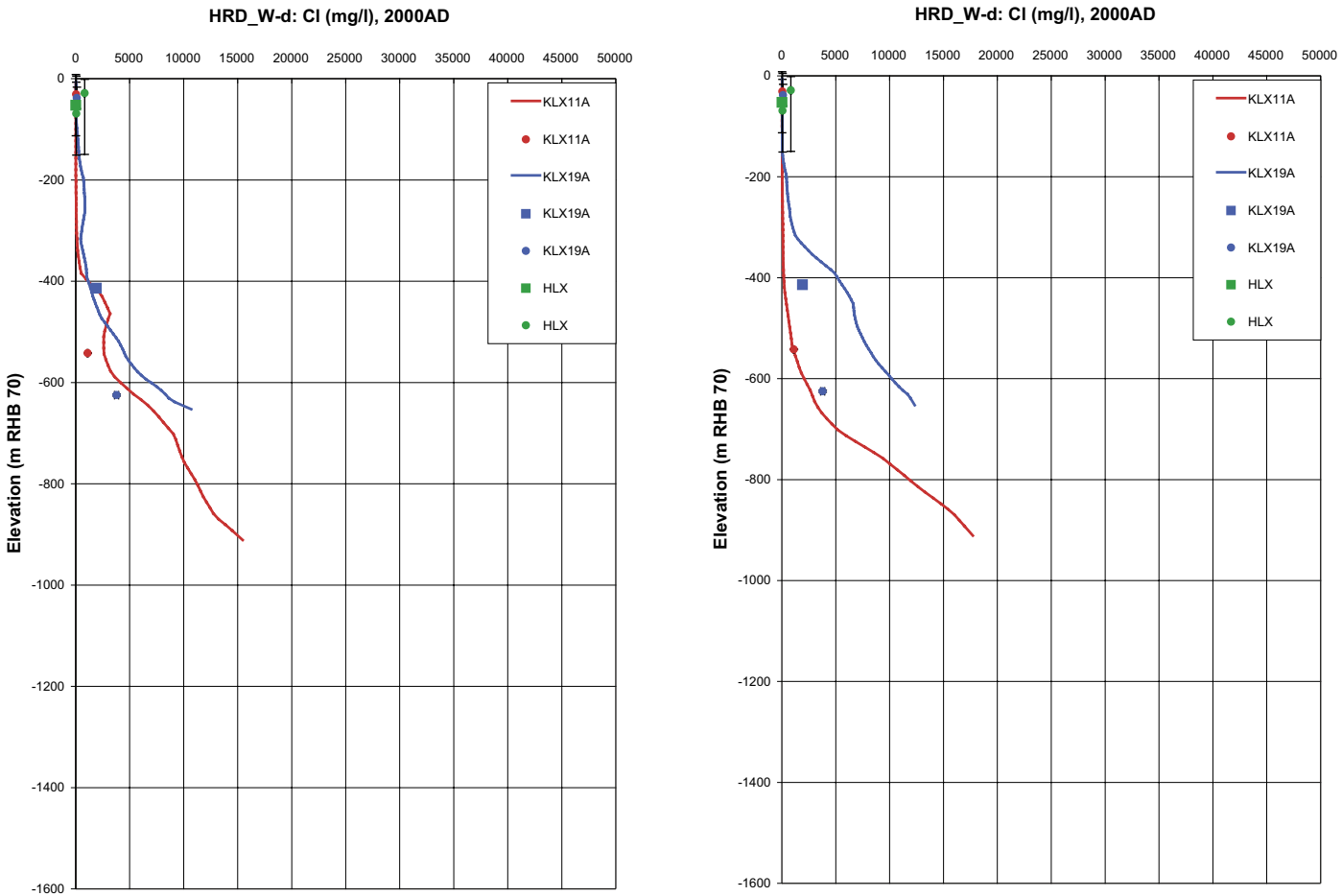

Figure E-48. *A comparison of the modelled and measured Cl concentrations in the fracture system for boreholes in HRD_W-discharge for the Elaborated Hydro-DFN (left) and the SDM-Site Hydro-DFN (right). Square symbols are used for category 1–3 data, circles are used for the pore water data, and small diamond symbols are used for category 4 data. The error bars on the data indicate the laboratory analytical error. The solid lines show the distribution in the borehole simulated in the fracture system, and the dashed lines are for the matrix.*

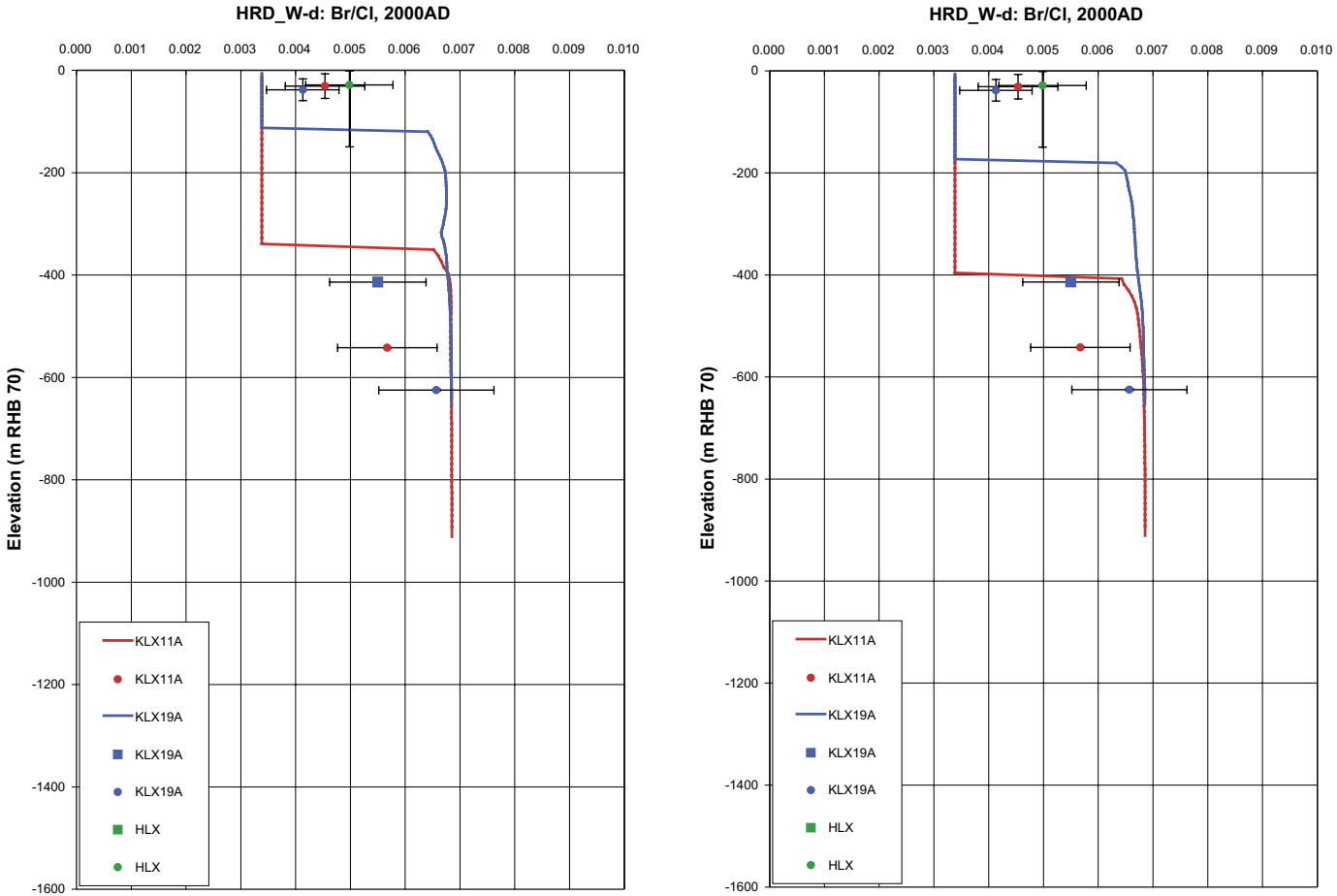

Figure E-49. *A comparison of the modelled and measured Br/Cl concentrations in the fracture system for boreholes in HRD_W-discharge for the Elaborated Hydro-DFN (left) and the SDM-Site Hydro-DFN (right). Square symbols are used for category 1–3 data, circles are used for the pore water data, and small diamond symbols are used for category 4 data. The error bars on the data indicate the laboratory analytical error. The solid lines show the distribution in the borehole simulated in the fracture system, and the dashed lines are for the matrix.*

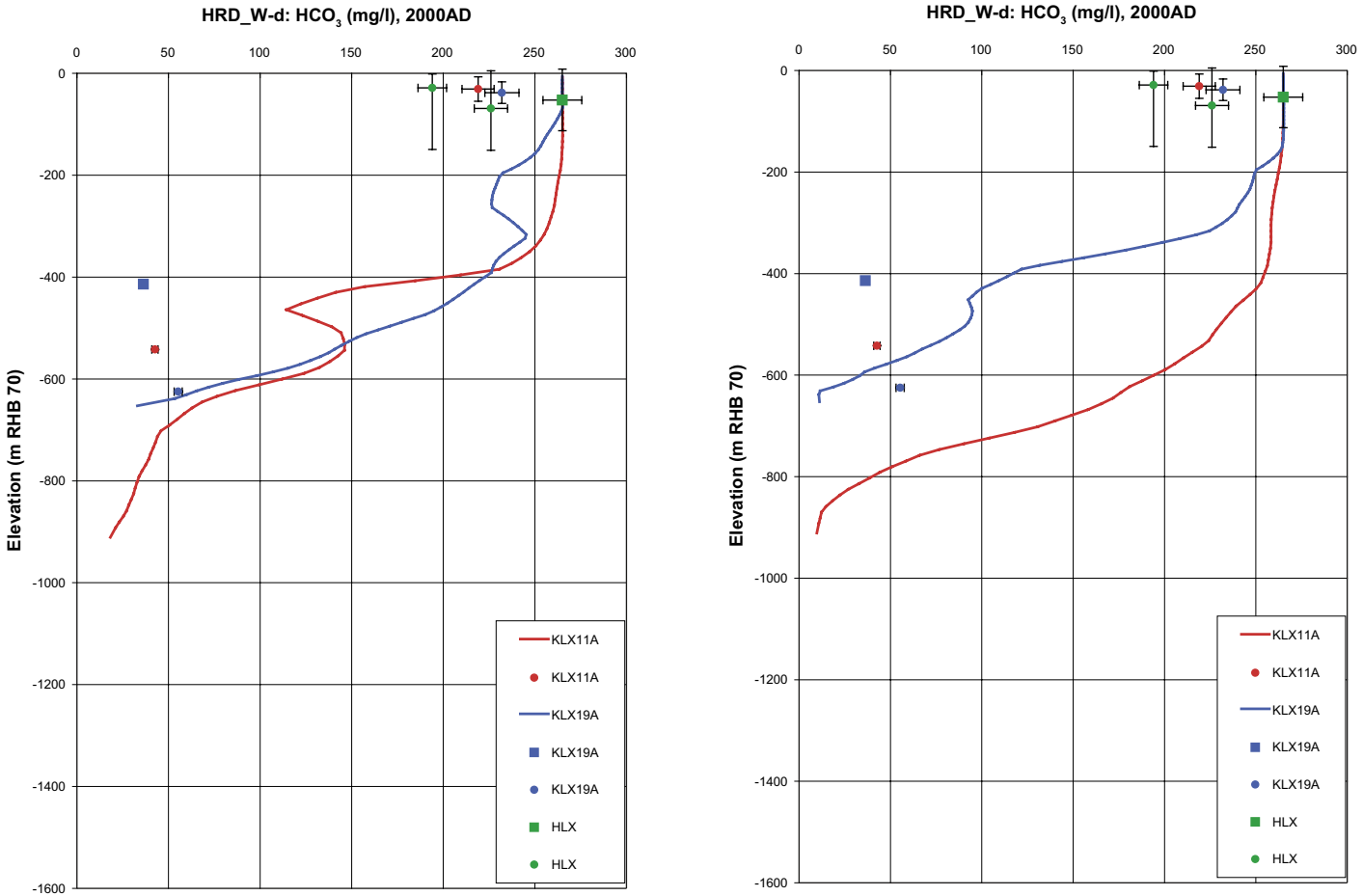

Figure E-50. *A comparison of the modelled and measured HCO_3 concentrations in the fracture system for boreholes in HRD_W-discharge for the Elaborated Hydro-DFN (left) and the SDM-Site Hydro-DFN (right). Square symbols are used for category 1–3 data, circles are used for the pore water data, and small diamond symbols are used for category 4 data. The error bars on the data indicate the laboratory analytical error. The solid lines show the distribution in the borehole simulated in the fracture system, and the dashed lines are for the matrix.*

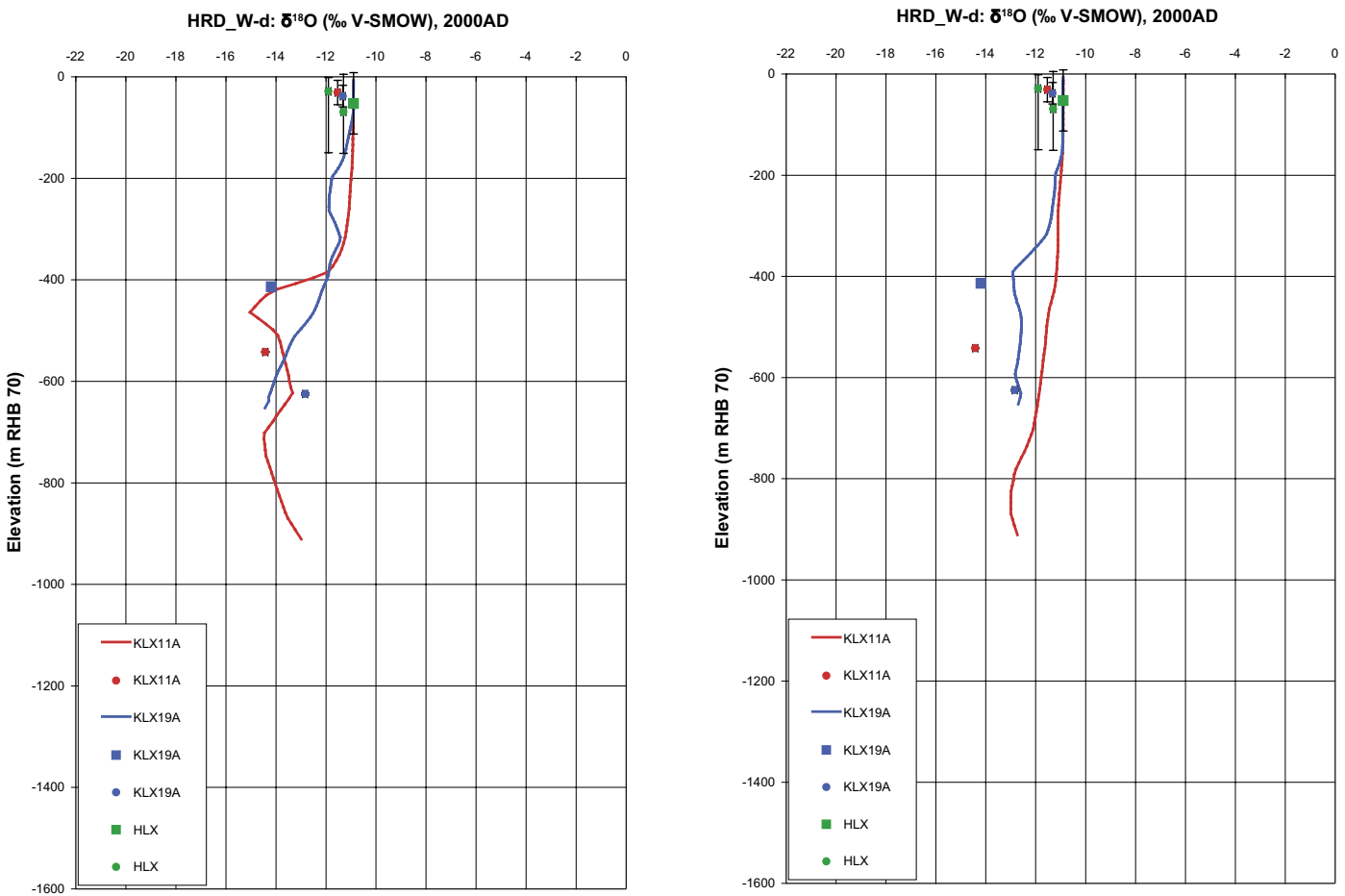

Figure E-51. *A comparison of the modelled and measured $\delta^{18}O$ concentrations in the fracture system for boreholes in HRD_W-discharge for the Elaborated Hydro-DFN (left) and the SDM-Site Hydro-DFN (right). Square symbols are used for category 1–3 data, circles are used for the pore water data, and small diamond symbols are used for category 4 data. The error bars on the data indicate the laboratory analytical error. The solid lines show the distribution in the borehole simulated in the fracture system, and the dashed lines are for the matrix.*

Appendix F

Differences between Hydrogeological base case and SDM-Site Laxemar models

F.1 Background

The regional-scale Hydrogeological base case model used for this study was derived from the SDM-Site base case model /Rhén et al. 2009/, but with the following modifications:

- Shoreline displacement curve updated.
- Revision of the effective diffusivity, D_e, from $1.5 \cdot 10^{-13}$ m^2/s to $5 \cdot 10^{-14}$ m^2/s.
- Changes to fracture network generation.
- The composition of the Inter-glacial Porewater reference water.
- Factor 3 higher transmissivity for 3 zones in HRD_W based on HLX28 interference tests.
- Increase in fracture surface area per unit volume, σ, in HCD volumes for salt transport.

These modifications combined a "best case" recommended model from SDM-Site with new data provided for this study.

F.2 Shoreline displacement curve

Updated shoreline displacement data was used for this study. The differences between the curve used for SDM-Site and that used for this study are shown in Figure F-1. SDM-Site specified more shoreline depression before 2000 AD and less depression afterwards, i.e. a slightly higher rate of land rise, however the differences in depression are no more than 5 m before 2000 AD and no more than 1 m afterwards. However, SDM-Site did not consider future shorelines.

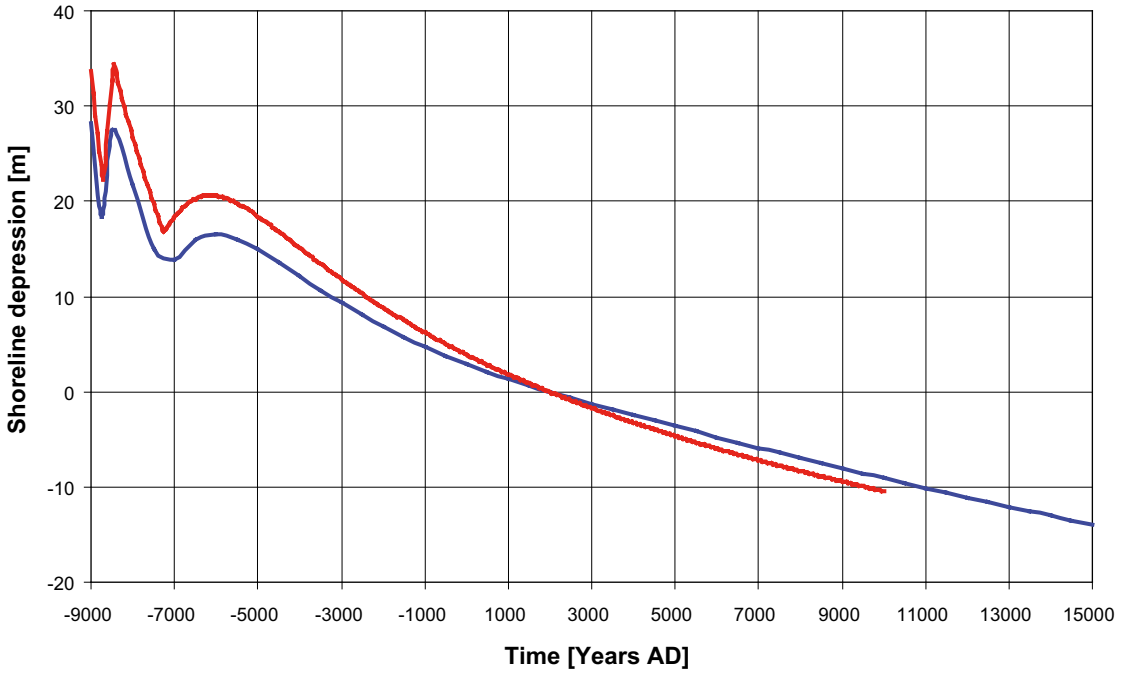

Figure F-1. *Plot showing shoreline depression against time in years for SDM-Site (red) and this study (blue).*

F.3 Revision of the effective diffusivity

In SKB's programme, *in situ* effective diffusivity, D_e, is usually formulated in terms of the formation factor, F_f, and the diffusivity in free-water, D_w,

$$D_e = F_f D_w \quad \text{(F-1)}$$

Although strictly a geometrical parameter, measurement of the formation factor is influenced by other non-geometrical artefacts such as surface diffusion and anion exclusion effects. The formation factor is calculated using electrical resistivity measurements or through-diffusion experiments /Crawford 2008/. Mainly these are laboratory measurements, although electrical resistivity can also be measured *in situ*. From the formation factor, approximate effective diffusivities can be calculated for all solutes. The D_w is about 10^{-9} m^2/s and laboratory measurements of formation factor are around 10^{-4}, and hence a calibrated value of $1.5 \cdot 10^{-13}$ m^2/s was used for D_e as a typical value of effective diffusivity into the matrix in SDM-Site Laxemar /Rhén et al. 2009/.

In the SR-Can Data report /SKB 2006c/, the formation factor and diffusivity in free solution for Na^+ and Cl^- are given in Tables A-41 and A-40, respectively. The mean value of the formation factor is given as $\log_{10}(F_f) = -4.74$, corresponding to a formation factor of $1.8 \cdot 10^{-5}$. The D_w of Cl^- and Na^+ at 25°C is given as $2.0 \cdot 10^{-9}$ m^2/s and $1.3 \cdot 10^{-9}$ m^2/s, respectively. For the in situ temperature at repository depth, which is presently around 12°C, the diffusivities should be reduced by a factor of about 1.5, compared to 25°C (/SKB 2010a, section 6.8.5 and Appendix A/). Furthermore, an anion exclusion reduction factor of 10 is suggested in the SR-Can Data report /SKB 2006c, p 193/. Accordingly, the diffusivity of chloride should be reduced by a factor of 10.

When modelling matrix diffusion of salt, the diffusivity of the ion-pair is needed. This requires the use of the harmonic mean of the ions' individual diffusivities (equations in /SKB 2010a, Appendix A/). If doing this, using the F_f and the D_w of the ion-pair based on the data presented above, the effective diffusivity D_e becomes $4 \cdot 10^{-15}$ m^2/s, which was the value used for the SR-Site Forsmark temperate modelling /Joyce et al. 2010/.

It should be noted that in SR-Site generally, the data are modified, predominantly on two accounts. Firstly, the best estimate F_f of $1.8 \cdot 10^{-5}$ for the undisturbed rock and $7.2 \cdot 10^{-5}$ for the fractured rock surrounding flow paths are suggested (/SKB 2010a, section 6.8.10 and Appendix A/). Secondly, the anion exclusion reduction factor of $\sqrt{10}$ is suggested, as compared to 10 in SR-Can. Based on this, the effective diffusivity for salt transport is in SR-Site suggested to be within the range of $1 \cdot 10^{-14} - 1 \cdot 10^{-13}$ m^2/s, with the best estimate at $4 \cdot 10^{-14}$ m^2/s (cf. justification in /SKB 2010a, Appendix A/). The calibrated D_e value used in this study is $5 \cdot 10^{-14}$ m^2/s.

F.4 Changes to fracture network generation

The palaeo-hydrogeological modelling is performed using an equivalent continuous porous medium (ECPM) approach to describe the hydraulic and transport properties of the bedrock. The description of the hydraulic rock mass domains (HRD) is based on an underlying hydrogeological discrete fracture network (Hydro-DFN) model which is upscaled to the scale of the finite-element regional-scale grid. The steps are as follows:

1. Generate a realisation of the Hydro-DFN on the regional-scale.
2. Perform a connectivity analysis of the regional-scale Hydro-DFN to identify and remove isolated fractures and dead-end fractures.
3. Perform upscaling of the Hydro-DFN to provide ECPM properties for each finite-element in the regional grid.
4. Perform palaeo-hydrogeological simulations using these ECPM properties.

In SDM-Site Laxemar, steps 1–3 were performed with only the stochastic fractures present and no representation of repository features, a representation of the HCD only being introduced in step 4 to modify the properties of elements crossed by one or more deformation zones. In this study, the approach was enhanced to include both the HCD and repository structures, represented as equivalent fractures, in the connectivity analysis of step 2. This was to account for a potentially enhanced connectivity around the tunnels. Fractures connected to two or more repository structure surfaces were not removed, even if they were not connected to any other fractures. After identifying the connected fractures in step 2, the HCD and repository structures were removed prior to the upscaling calculation of step 3 so as to provide ECPM properties for the HRD separately and then include the hydraulic effects of the HCD in step 4, as for SDM-Site Laxemar. The potential change in hydraulic properties resulting from flows along the repository structures were not included in the palaeo-hydrogeological simulations, although the enhanced connectivity around the tunnels was included as it may have an indirect effect on the equivalent hydraulic conductivity of the fracture network in the vicinity of the repository.

In addition, smaller scale fractures down to a radius of $r = 0.4$ m were generated in a volume surrounding the repository, while fractures $r > 5.6$ m were created over the whole volume of the model. Only the stochastic fractures $r > 5.6$ m were generated in the SDM-Site Laxemar work.

F.5 The composition of the Inter-glacial Porewater

Two reference water compositions representing the 'Inter-glacial Porewater' were suggested for palaeohydrogeological and future evolution simulations and are referred to in Table F-1 as Case 1 and Case 2. The initial definition (Case 1) was provided in time for the base case modelling in SDM-Site Laxemar and as site investigations progressed the updated definition was provided and found to be a more representative match for deep porewater. It was therefore suggested that Case 2 be used for the deeper bedrock (depths of about 500–600 m) in the simulations for this study.

Table F-1. Composition of the reference waters selected for the mixing calculations in the Laxemar area. Data provided for hydrochemistry data delivery for SDM-Site Laxemar. All concentrations are in mg/L.

	Deep Saline water	Littorina sea water	Altered Meteoric water	Glacial melt water	Inter-glacial Porewater	
					Case 1	Case 2
pH	8	7.6	8.17			8
HCO_3	14.1	92.5	265.0	0.12	265.0	10
Cl	47,200	6,500	23.0	0.5	23.0	5,000
SO_4^{2-}	906.0	890	35.8	0.5	35.8	375
Br	323.66	22.2	–0.2		–0.2	34
Ca	19,300	151	11.2	0.18	11.2	1,585
Mg	2.12	448	3.6	0.1	3.6	2
Na	8,500	3,674	110.0	0.17	110.0	1,440
K	45.5	134	3.0	0.4	3.0	4
Si	2.9	3.94	7.0	----	---	–
Fe^{2+}	----	0.002 (Fe tot)	0.08		---	–
S^{2-}	----	-----	-----		----	–
δ^2H (‰)	–44.9	–37.8	–76.5	–158.0	–50	–50
$\delta^{18}O$ (‰)	–8.9	–4.7	–10.9	–21.0	–5	–5

F.6 The increase in transmissivity for 3 zones in HRD_W based on HLX28 interference tests

The HLX28 interference tests were made in the spring of 2007 (see Appendix 1 of /Rhén et al. 2009/) and the results provided after the initial base case simulation for SDM-Site. These interference test calculations were integrated into the Hydrogeological base case model since the affected zones are in the repository area. The zones affected are HLX28_DZ1, which had its transmissivity subsequently increased by a factor of four in the Hydrogeological base case model and zones ZSMNW042A-west and ZSMNS059A, which were increased individually by a factor of three. These deformation zones are shown in Figure F-2.

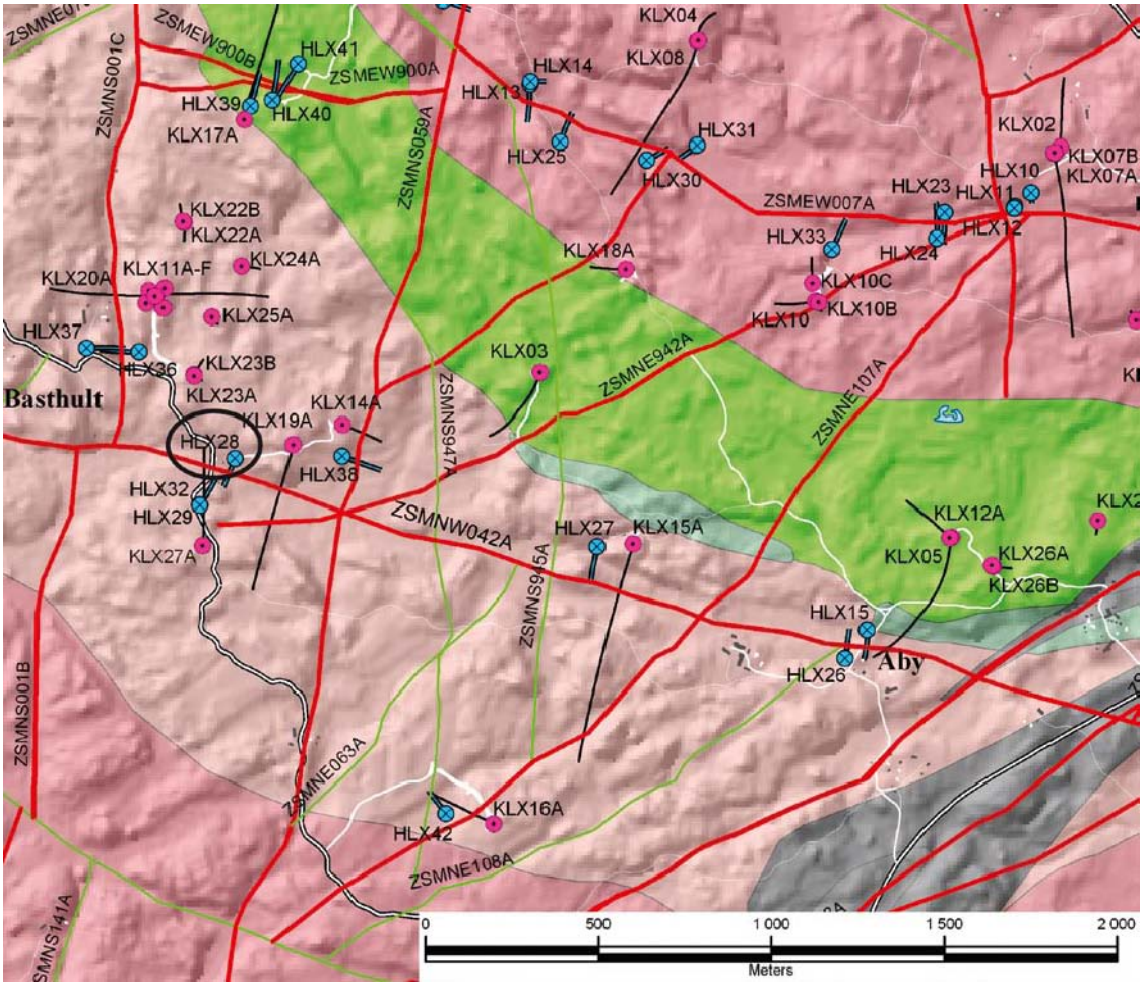

Figure F-2. *Borehole map. Test in April 2007 with HLX28 as pumping borehole. KLX20A intersects ZSMNS01, KLX14A intersects ZSM059A and KLX19A, HLX27A and others intersects ZSMNW042A (Figure A1-6 from /Rhén et al. 2009/).*

F.7 Increase in fracture surface area per unit volume in HCD volumes for salt transport

An observed characteristic of the rock is a higher fracture intensity in the HCD. SDM-Site considered a variant model with the fracture surface area per unit volume for rock matrix diffusion of solutes, σ, increased by a factor of three in the HCD /Rhén et al. 2009, Section 9.1.4/. This variant gave the best results overall, especially for boreholes intersecting major deformation zones, since the increased fracture surface area in the HCD retarded the mixing from where advection was greatest. Since there was an improvement to the palaeohydrogeology calibration, this change was incorporated in to the Hydrogeological base case.

Appendix G

A comparison of inflows to tunnels under open repository conditions between ConnectFlow and DarcyTools

G.1 Introduction

The open repository modelling described in /Svensson and Rhén 2010/ uses the DarcyTools software to calculate inflows to repository tunnels during particular construction and operational phases and with different levels of grouting. As with the regional-scale modelling described in this report, an ECPM concept is used to describe the properties of the surrounding bedrock. Indeed, in both studies the same underlying Hydro-DFN data is used as an input to the upscaling process used to generate the ECPM for the HRD. The same HCD data was also used. However, in the case of ConnectFlow, a combined ECPM/DFN concept was used for the site-scale and repository-scale models. Also, DarcyTools has a different upscaling method from ConnectFlow. In order to build confidence that the two software packages would produce consistent results for a given set of data and model description, even when using different modelling concepts, a series of inflow calculations were carried out and the results compared.

G.2 Model description

As far as possible, equivalent models were set up for the ConnectFlow and Darcy Tools calculations as follows:

- Specified pressure top boundary.
- No grouting.
- Fresh water, i.e. no density affects due to salinity.
- Steady-state flow solution.
- Repository represented by main tunnels, transport tunnels, deposition tunnels and deposition holes at atmospheric pressure.
- The ramp, shafts, central area and EDZ were not included.
- Realisation 1 of the HRD with the deterministic HCD for the Hydrogeological base case.

For the ConnectFlow calculations, the repository-scale model was used. Since the transport tunnels were represented as equivalent fractures in this model it was not possible to apply an atmospheric preassure boundary condition to them. Therefore, the transport tunnels were represented as high conductivity (0.1 m/s) fractures. The assumption was that inflows to the transport tunnels would be carried to the main tunnels and accumulated into the total inflows. External boundary conditions were imported from a site-scale DFN model of the open repository model. In this site-scale model, the main tunnels and deposition tunnels were represented by shafts with atmospheric pressure boundary conditions and the transport tunnels as high conductivity (0.1 m/s) fractures. The boundary conditions for the site-scale model were the same as for the Hydrogeological base case. Flows were calculated under steady-state fresh water conditions at both scales.

For the DarcyTools calculations, a single regional-scale ECPM model was used with fine grid refinement around the tunnels. A fixed head top surface boundary condition was used and a fresh water steady-state flow calculation carried out.

G.3 Results

In the ConnectFlow results given in Table G-1, a breakdown by repository-scale block and rock domain is provided. The percentages in each hydraulic rock domain are based on the number of deposition holes in that domain rather than length of tunnel.

For DarcyTools, it was not possible to provide a breakdown of the inflows by rock domain. The total inflow calculated to the repository tunnels was 1.085 m^3/s.

Table G-1. Open repository inflows calculated by ConnectFlow, summarised by repository-scale block and rock domain. The approximate percentage volume of the repository structures within each rock domain is also given.

Block	1 (East main tunnel)	2 (Central 2 main tunnels)	3 (West main tunnel)	All
Inflow HRD_EW007 (m^3/s)	0.0844	0.545	0.0052	0.635
Inflow HRD_C (m^3/s)	0.0737	0.122	---	0.204
Inflow HRD_W (m^3/s)	---	---	0.0446	0.0446
Total Inflow (m^3/s)	0.158	0.667	0.0498	0.875
% volume HRD_EW007	30	32	5	21
% volume HRD_C	70	68	---	50
% volume HRD_W	---	---	95	29

G.4 Discussion

The total repository inflow of 0.875 m^3/s calculated by ConnectFlow compares very well with the value of 1.085 m^3/s calculated by DarcyTools, especially given the differences in model concepts used. This gives confidence that the two software packages and the two modelling approaches give consistent results for the equivalent model conditions.

It is of interest to note from the ConnectFlow calculations that HRD_EW007 is responsible for 71% of the inflow even though it represents roughly 21% of the repository. HRD_W accounts for only 5% of the inflow for 29% of the repository volume. This is consistent with other results in this report (Section 6.2.3) that suggests that HRD_EW007 has high fracture intensities and high flows relative to the other rock domains in the repository area.

Appendix H

Using analytic expressions to estimate time for fresh water penetration to repository depths

Here, the issue is of how many canisters may be affected by infiltration of dilute groundwater from ground surface driven by evolutions in climate through temperate and glacial cycles.

H.1 Analytical models

H.1.1 Rock matrix diffusion into an infinite matrix

A constant inlet of a non-decaying and non-sorbing solute (like Cl-35) of concentration *C(t)* at time *t* into a system with zero initial concentration yields, for an infinite matrix and when neglecting hydrodynamic dispersion, a release according to

$$C(t) = C_0 \operatorname{erfc}\left(\frac{t_w}{2A_R\sqrt{t-t_w}}\right) \qquad t > t_w\ , \tag{H-1}$$

where

$$A_R = \frac{t_w}{F\sqrt{\varepsilon_p D_e}}\ . \tag{H-2}$$

In this expression t_w is the advective travel time, F is the flow-related transport resistance, ε_p is the kinematic porosity and D_e is the effective diffusivity. The same expression can be used for the case of an inlet of fresh water into a system with initial fracture and matrix concentrations C_0, yielding the release

$$C(t) = C_0\ \operatorname{erf}\left(\frac{t_w}{2A_R\sqrt{t-t_w}}\right) \qquad t > t_w\ , \tag{H-3}$$

so that

$$C(t) = C_0\ \operatorname{erf}\left(\frac{F\sqrt{\varepsilon_p D_e}}{2\sqrt{t-t_w}}\right) \qquad t > t_w\ . \tag{H-4}$$

The concentration is hence reduced to a fraction $\alpha = C/C_0$ of the initial concentration when

$$\frac{F\sqrt{\varepsilon_p D_e}}{2\sqrt{t-t_w}} = \operatorname{erf}^{-1}(\alpha)\ , \tag{H-5}$$

or in terms of time

$$t = t_w + \frac{F^2\varepsilon_p D_e}{4\left(\operatorname{erf}^{-1}(\alpha)\right)^2}\ . \tag{H-6}$$

Values for the inverse error function for relevant reductions in concentrations are tabulated in Table H-1.

Table H-1. Tabulated values of the inverse of the error function for relevant values of *α*.

α	$\operatorname{erf}^{-1}(\alpha)$
0.1	0.088856
0.01	0.008863
0.001	0.000886
0.0001	0.000089

H.1.2 Equilibrium transport conditions for a finite matrix

Alternatively, the effects of retardation by rock matrix diffusion into a finite matrix can be considered. Assuming advection is sufficiently slow to allow equilibrium transport conditions to apply then the retardation factor for the advance of a mixing front can be written as

$$t = t_w + \varepsilon_p \delta_m F, \tag{H-7}$$

where δ_m is the average half size of matrix blocks, i.e. half the flowing fracture spacing.

Combining these two formulae an estimate of the breakthrough of dilute groundwater to a canister location can then be estimated as

$$t = t_w + \min\left(\frac{F^2 \varepsilon_p D_e}{4\left(\text{erf}^{-1}(\alpha)\right)^2}, \varepsilon_p \delta_m F \right). \tag{H-8}$$

Equation (H-6) gives the smaller retardation times for low values of F less than about $3 \cdot 10^5$ y/m, and Equation (H-7) gives the smaller retardation times at larger F values when the assumption of a finite matrix becomes important.

H.2 Application to transport of dilute surface water to repository depth

The above formulae can be used to estimate the timescale for dilute groundwater to penetrate from ground surface to repository depth for each deposition hole given the advective travel time and F for the pathway between the top surface and the deposition hole. These can be calculated by performing backward particle tracking (i.e. following the upstream trajectory rather than usual downstream trajectory) with a particle released into any fractures surrounding the deposition hole. The details of the temperate climate situation are given in Table H-2, where two durations are given depending on whether or not a global warming scenario is considered. Dilute groundwater is judged to have reached the repository if the transport time predicted by Equation (H-8) is less than the duration for which the temperate climate conditions persist.

In summary, the approach used is as follows:

- Calculate steady-state flow for a fixed but spatially variable-density field.
- Calculate backward (recharge) particle tracks to identify t_w and F for the recharge pathway to each canister.
- Calculate forward (discharge) particle tracks to calculate t_w and F for discharge paths.
- Calculate retardation times for dilute groundwater based on Equation (H-8) using t_w and F for backward pathways, and compare these times with the duration of the temperate climate situation.
- Consider F for the forward (discharge) pathways from those locations with dilute water break-through times less than the epoch duration.

Table H-2. Climate situations considered during which dilute groundwaters may penetrate to repository depth.

Climate situation	Duration	Comments
Temperate	10,000 to 60,000 y	60,000 y is a global warming scenario. Use situation at 2,000 AD. Injection of meteoric water of zero salinity.

Other notes:

- The Elaborated Hydro-DFN case (as specified in Section 5.1) is used to determine recharge/discharge pathways.
- The Elaborated Hydro-DFN case is used to derive t_w, F, FPC, and EFPC for each deposition hole.
- The calculated travel times and F used are for transport within rock domains that are represented by an explicit DFN model. Travel time and retention in the ECPM outside of this have not been included. Also, to be conservative, no retardation in tunnels is included, although this could be large.

H.2.1 Groundwater flows during the temperate climate situation

Figure H-1, Figure H-2 and Figure H-3 show Elaborated Hydro-DFN case simulations of regional flow paths under temperate climate conditions. Most paths recharge and discharge just above the site, with some recharging from the higher elevations to the west. The repository area flow paths reach elevations of down to around –1,000 m, whereas the longer paths from the west reach elevations down to around –2,000 m.

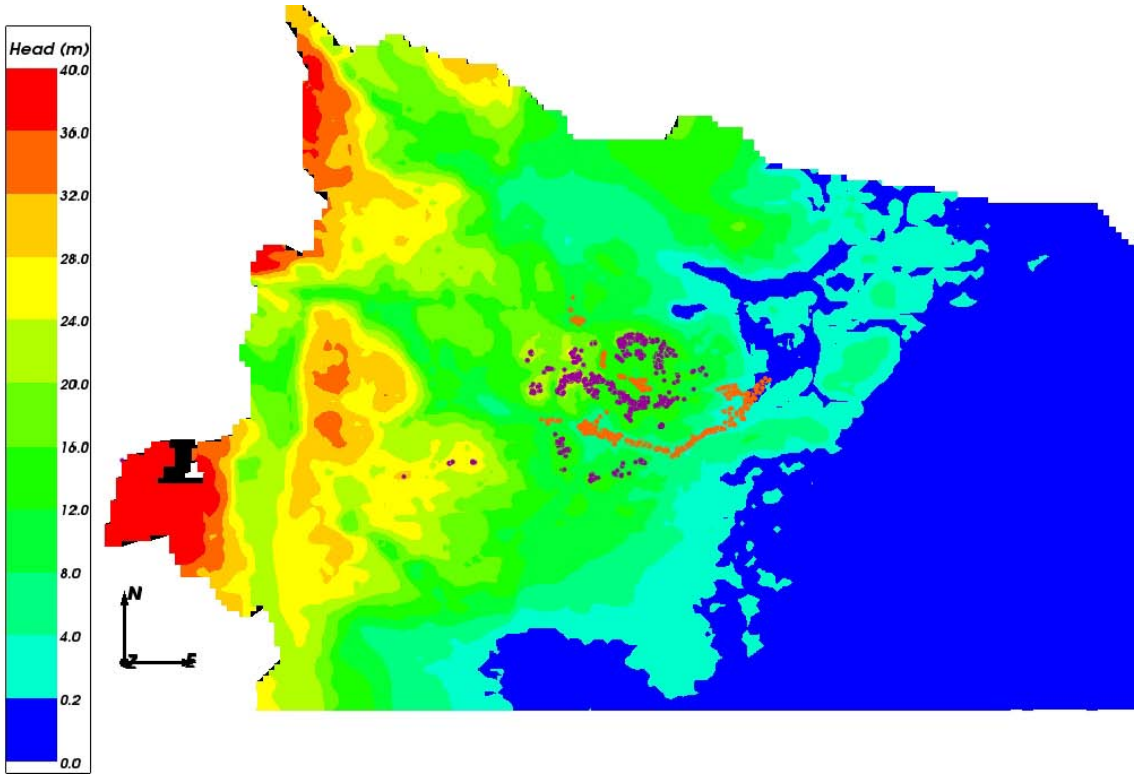

Figure H-1. *Simulations of discharge points (orange) and recharge points (purple) for Q1 paths successfully reaching the top boundary of the Elaborated Hydro-DFN model (60% discharge, 43% recharge) in the flow field under temperate climate conditions at 2000 AD.*

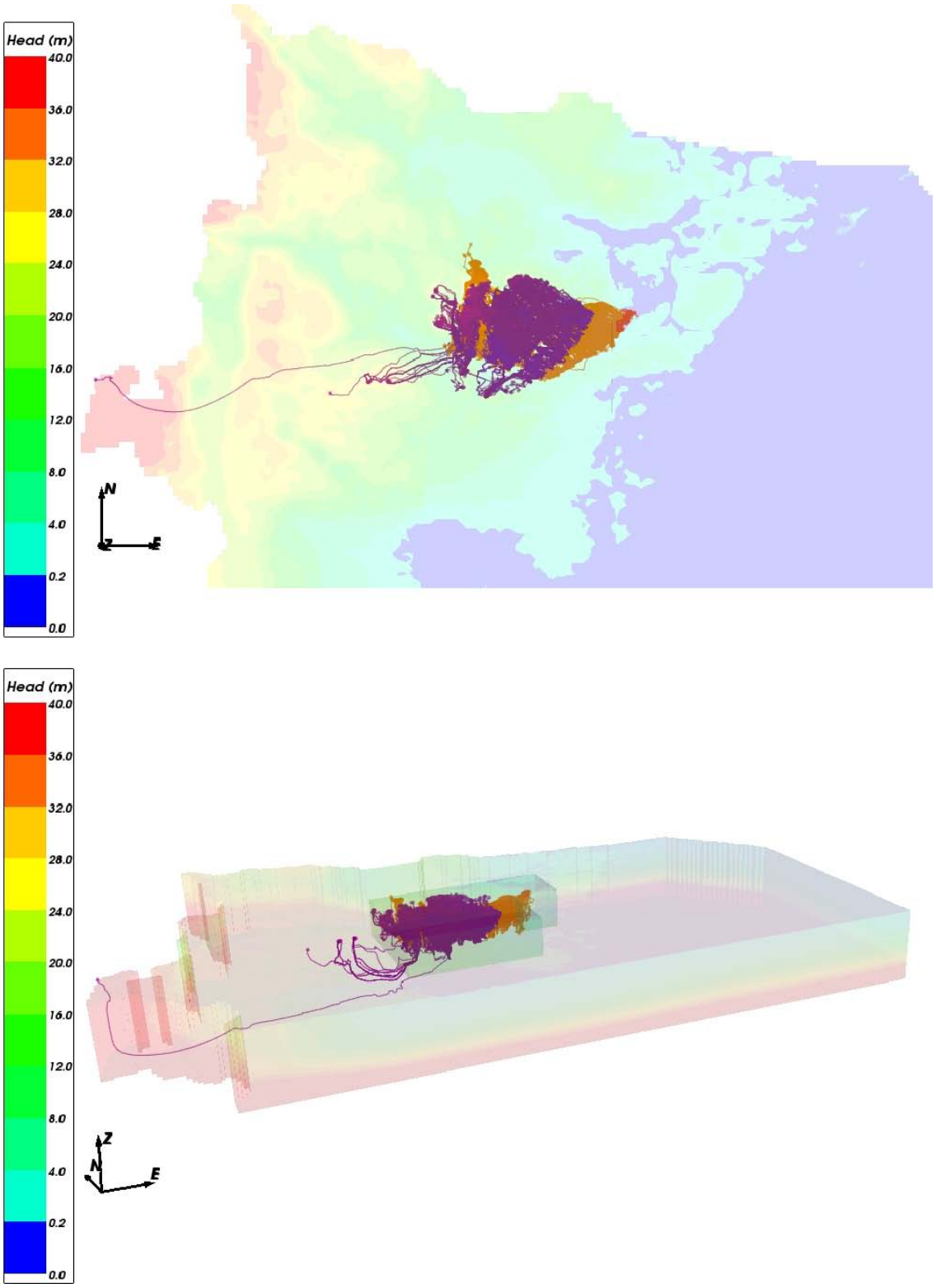

Figure H-2. *Simulations of discharge pathways (orange) and recharge pathways (purple) for Q1 paths successfully reaching the top boundary of the Elaborated Hydro-DFN model (60% discharge, 43% recharge) in the flow field under temperate climate conditions at 2000 AD. Top: map view; Bottom: oblique view from the south west.*

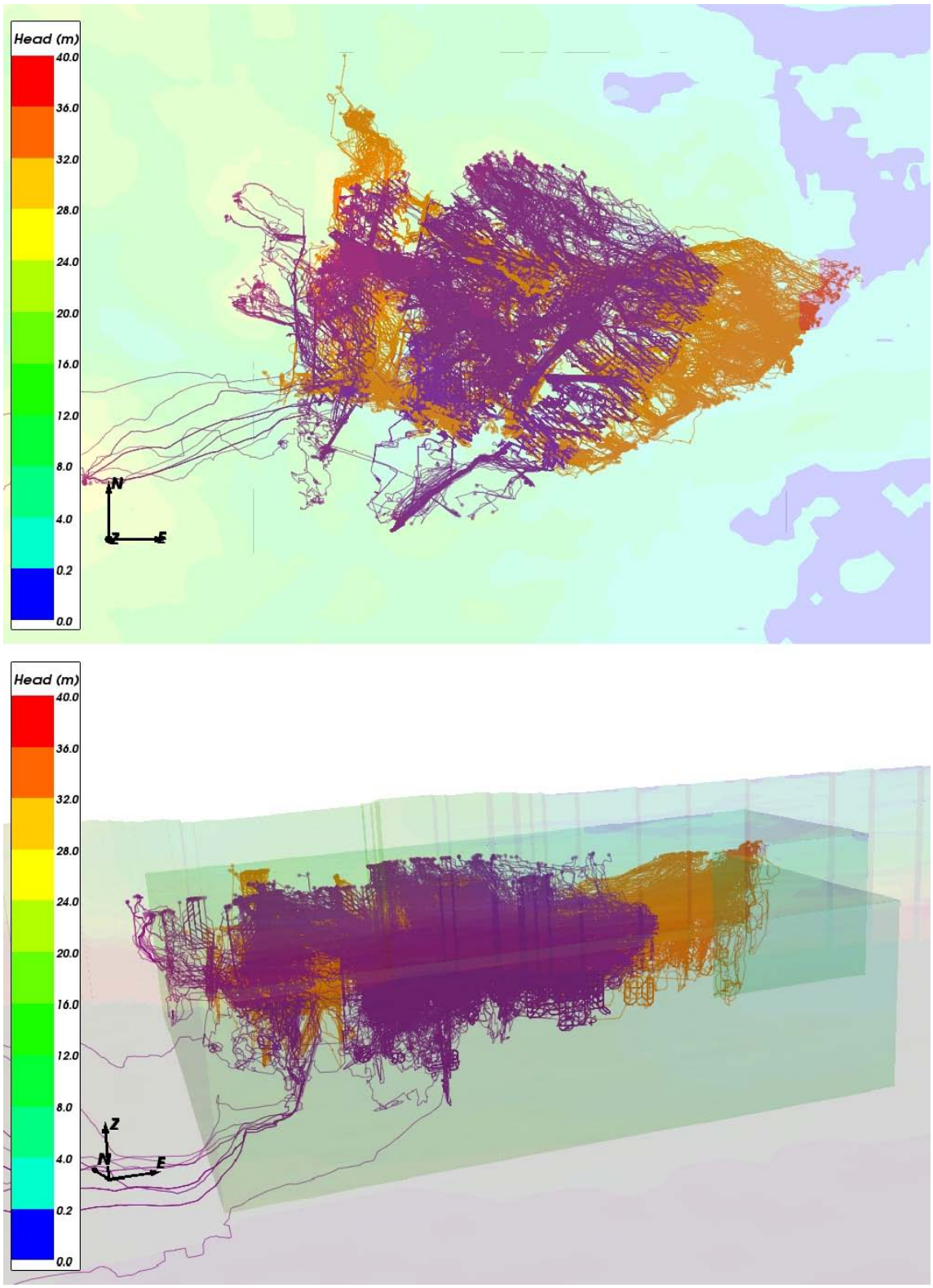

Figure H-3. *Simulations of discharge pathways (orange) and recharge pathways (purple) for Q1 paths successfully reaching the top boundary of the Elaborated Hydro-DFN model (60% discharge, 43% recharge) in the flow field under temperate climate conditions at 2000 AD. Top: repository area map view; Bottom: Oblique view of repository area from the south west.*

H.2.2 Evaluation of dilute groundwater mixing times

The following lists the parameters used to estimate the time for groundwater to dilute the deposition holes.

General parameters

- $D_e = 5 \cdot 10^{-14}$ m²/s ($1.58 \cdot 10^{-6}$ m²/y), as used in the palaeo-hydrogeology simulations.
- $\varepsilon_p = 8.0 \cdot 10^{-3}$, as used in the palaeo-hydrogeology simulations.
- $\delta_m = 3.05$ m, the approximate spacing of PFLs (Based on Terzaghi corrected spacing of flowing features $0.5/P10_{PFL,corr}$ from Table 4-1 /Rhén et al. 2009/ for HRD_C for elevations between –150 m and –400 m).
- $\text{erf}^{-1}(0.1) = 0.089$, i.e. $\alpha = 0.1$.

where α represents the dilution factor. The salinity criterion for buffer erosion is 0.3 g/L, which represents the dilute conditions with the potential for buffer erosion to occur. The present day salinity (TDS) at repository depth is about 10 g/L. As an illustration, an α of 0.1 would give a dilution to about 1 g/L TDS at repository depth for the temperate period, which is above the criterion of 0.3 g/L and so could be viewed as a conservative estimate.

To summarise the specific assumptions made in the analysis:

- Use Elaborated Hydro-DFN case model.
- Only use backward paths with OKFLAG = 0 (complete path).
- Eliminate FPC+EFPC positions.
- 2,960 positions remain for backward paths.
- c.f. 4,167 positions remaining for forward paths.

Results

Table H-3 gives estimates of the numbers of deposition holes that become critically diluted by the end of the temperate period. The sensitivity to the duration of the temperate period is quantified.

Figure H-4 shows the cumulative distribution of transport times for dilute water to reach the canister positions under temperate climate conditions. If this epoch lasts only 10,000 years then 1,659 positions are effected. If the epoch lasts 60,000 years, then 2,650 positions are effected. The question then is whether these positions correlate with low F values for discharge pathways. This is evaluated in Figure H-5 as a cross-plot of F values for forward and backward paths. Of these locations, 965 have F values below 10^5 y/m, and 126 have F values below 10^4 y/m.

The positions of deposition holes at risk from dilute groundwater are shown in Figure H-6. The highest concentrations of holes affected in the first 10,000 years (coloured blue) seem to be located in the HRD_EW007 domain.

Table H-3. Estimates of numbers of deposition holes that become critically diluted by the end the temperate period. Sensitivities to the duration of the climate situation are considered.

	Duration	Dilution factor = 0.1
Temperate	10,000 y	1,659
	60,000 y	2,650

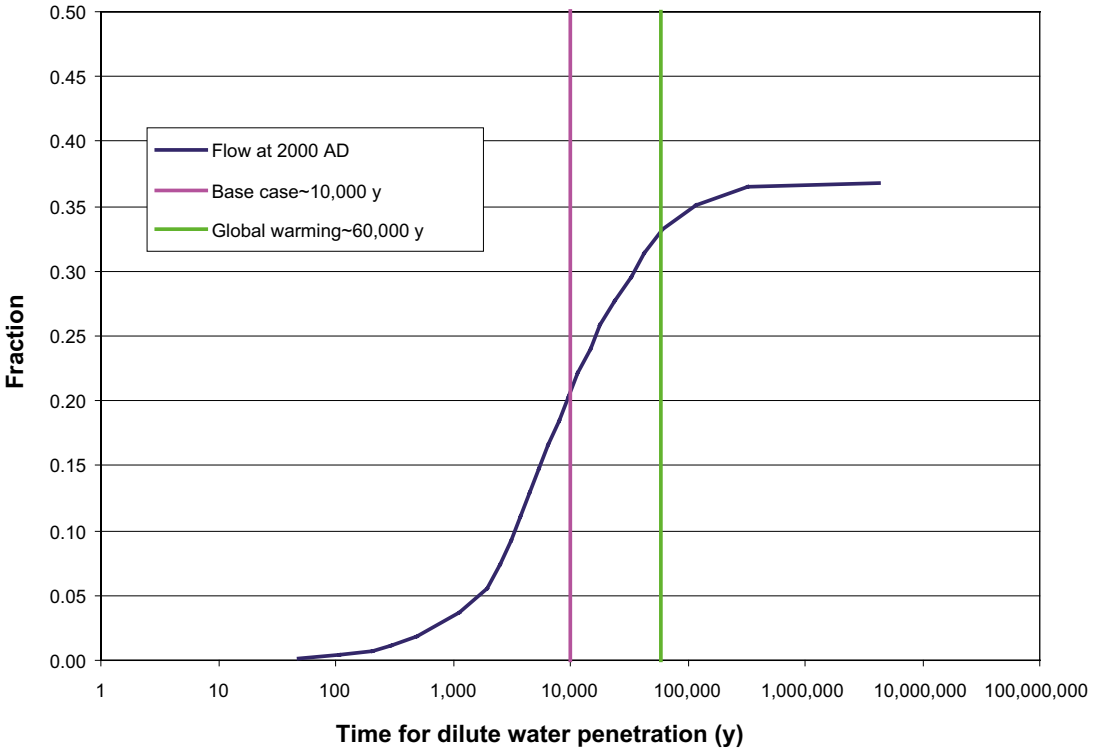

Figure H-4. *Estimates of time for penetration of dilute groundwater under temperate climate conditions based on Equation (F-8) for backward paths. The vertical lines indicate the duration of the initial temperate period: Base case ~10,000 years (purple), Global warming variant ~60,000 years (green).*

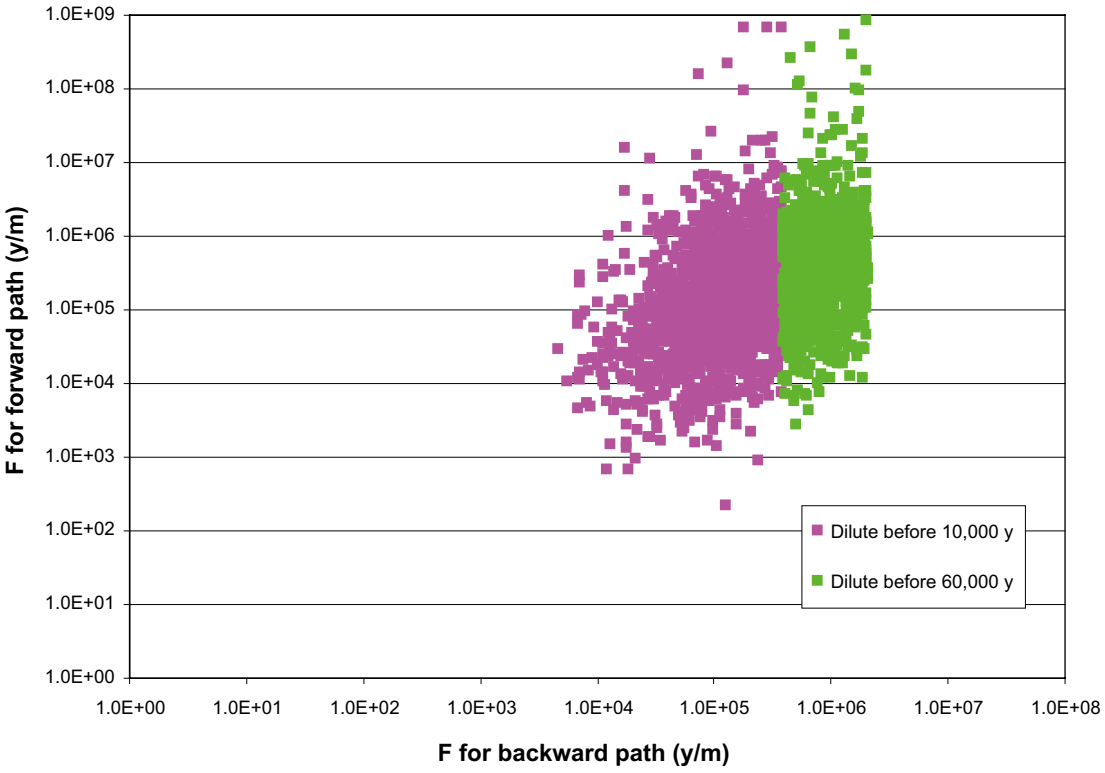

Figure H-5. *Cross-plot of F for the forward (discharge) pathway and backward (recharge) pathway under temperate climate conditions for canister positions with times to dilution less than the epoch duration.*

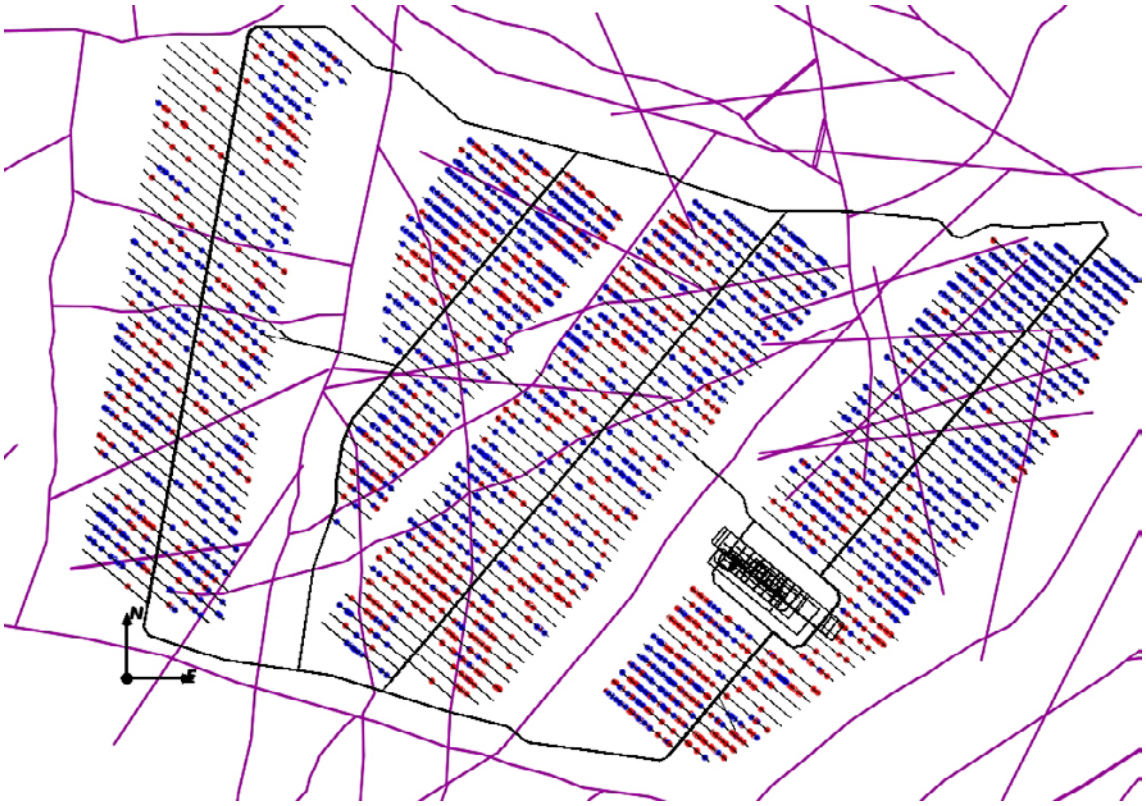

Figure H-6. *Deposition holes at risk from dilute groundwater infiltration. Holes at risk during the first 10,000 years of the temperate period are coloured blue; holes at risk during the next 50,000 years are coloured red. The deformation zones at –510 m are shown in purple and the repository structures are shown in black.*

H.3 Conclusions

During the temperate period between 21% and 33% of canister locations might be recharged by dilute groundwater, depending on duration. The locations where times for dilute recharge are short do not necessarily correlate with locations of very low F for the discharge pathways, although they are concentrated more within HRD_EW007.

Appendix I

Compilation of input files

Identifier	Date	Name of file at delivery
HCD		
Regional zones	2008-06-02	DZ_LX_REG_v23.xml
Local zones	2008-04-14	DZ_LX_LOC_v23.xml
Disks	2008-08-27	ADD_DZ_LX_LOC_V23-new-clip-hydro_080827.xml
NW042 divided into east and west, hlx28	2008-08-27	ADD_DZ_LX_LOC_V23-new-clip-hydro_080828.xml
New disks	2009-01-08	Hydro_090108_xml_2.xml
Conditioning	2008-05-08	Lx2.3_Bh_T_cond_3.csv
Borehole trajectories	2008-08-11	Lx2.3_H_K_boreholes.csv
HCD properties	2009-03-27	Hydro_DZ_summary table_080430x_CF_1.xls
SHORE LEVEL		
Shore level displacement	2009-04-29	SR-Site_Lx_Shorelevel_displacement_090427.xls
SALINITY		
Baltic Sea salinity at Laxemar	2009-04-22	Salinity_developm_Laxemar_SRSite.xls
DEM		
Topography	2008-03-26	SDM_L23_dem_sjobat.xyz
REPOSITORY LAYOUT		
Repository layout files	2009-02-03	Laxemar_layout_090228.zip
Deposition hole coordinates for section D	2009-03-09	LX_DD.xls
ROCK DOMAINS		
FSM_C-20m-Local.txt	2008-04-01	FSM_C-20m-Local.txt
FSM_EW007-20m-Local.txt	2008-04-01	FSM_EW007-20m-Local.txt
FSM_N-20m-Local.txt	2008-04-01	FSM_N-20m-Local.txt
FSM_NE005-20m-Local.txt	2008-04-01	FSM_NE005-20m-Local.txt
FSM_S-20m-Local.txt	2008-04-01	FSM_S-20m-Local.txt
FSM_W-20m-Local.txt	2008-04-01	FSM_W-20m-Local.txt
RSMA01-100m-Regional.txt	2008-04-01	RSMA01-100m-Regional.txt
RSMA02-100m-Regional.txt	2008-04-01	RSMA02-100m-Regional.txt
RSMB01-100m-Regional.txt	2008-04-01	RSMB01-100m-Regional.txt
RSMB03-100m-Regional.txt	2008-04-01	RSMB03-100m-Regional.txt
RSMB05-100m-Regional.txt	2008-04-01	RSMB05-100m-Regional.txt
RSMB06-100m-Regional.txt	2008-04-01	RSMB06-100m-Regional.txt
RSMBA03-100m-Regional.txt	2008-04-01	RSMBA03-100m-Regional.txt
RSMC01-100m-Regional.txt	2008-04-01	RSMC01-100m-Regional.txt
RSMC02-100m-Regional.txt	2008-04-01	RSMC02-100m-Regional.txt
RSMD01-100m-Regional.txt	2008-04-01	RSMD01-100m-Regional.txt
RSMD02-100m-Regional.txt	2008-04-01	RSMD02-100m-Regional.txt
RSMD03-100m-Regional.txt	2008-04-01	RSMD03-100m-Regional.txt
RSMD04-100m-Regional.txt	2008-04-01	RSMD04-100m-Regional.txt
RSMD05-100m-Regional.txt	2008-04-01	RSMD05-100m-Regional.txt
RSMD06-100m-Regional.txt	2008-04-01	RSMD06-100m-Regional.txt
RSMD07-100m-Regional.txt	2008-04-01	RSMD07-100m-Regional.txt
RSME01-100m-Regional.txt	2008-04-01	RSME01-100m-Regional.txt
RSME11-100m-Regional.txt	2008-04-01	RSME11-100m-Regional.txt
RSME12-100m-Regional.txt	2008-04-01	RSME12-100m-Regional.txt
RSME13-100m-Regional.txt	2008-04-01	RSME13-100m-Regional.txt
RSME14-100m-Regional.txt	2008-04-01	RSME14-100m-Regional.txt
RSME15-100m-Regional.txt	2008-04-01	RSME15-100m-Regional.txt
RSME16-100m-Regional.txt	2008-04-01	RSME16-100m-Regional.txt
RSME17-100m-Regional.txt	2008-04-01	RSME17-100m-Regional.txt
RSME18-100m-Regional.txt	2008-04-01	RSME18-100m-Regional.txt

Identifier	Date	Name of file at delivery
RSMF01-100m-Regional.txt	2008-04-01	RSMF01-100m-Regional.txt
RSMF02-100m-Regional.txt	2008-04-01	RSMF02-100m-Regional.txt
RSMF03-100m-Regional.txt	2008-04-01	RSMF03-100m-Regional.txt
RSMG01-100m-Regional.txt	2008-04-01	RSMG01-100m-Regional.txt
RSMG02-100m-Regional.txt	2008-04-01	RSMG02-100m-Regional.txt
RSMM01-100m-Regional.txt	2008-04-01	RSMM01-100m-Regional.txt
RSMP01-100m-Regional.txt	2008-04-01	RSMP01-100m-Regional.txt
RSMP02-100m-Regional.txt	2008-04-01	RSMP02-100m-Regional.txt
REGIONAL BOUNDARY		
Outer boundary	2008-04-01	Outer_boundary_trim5.txt
Bottom boundary	2008-04-11	bottom.xyz
HSD		
z1.cnv	2008-04-03	z1.cnv
z2.cnv	2008-04-03	z2.cnv
z3.cnv	2008-04-03	z3.cnv
z4.cnv	2008-04-03	z4.cnv
z5.cnv	2008-04-03	z5.cnv
z6.cnv	2008-04-13	z6.cnv
L23_soil_thickness.dat	2008-04-22	L23_soil_thickness.dat
z1_qdcode.asc	2008-05-01	z1_qdcode.asc
z3_qdcode.asc	2008-05-01	z3_qdcode.asc
z4_qdcode.asc	2008-05-01	z4_qdcode.asc
z6_qdcode.asc	2008-05-01	z6_qdcode.asc

A list of all input files above, including storage location, is for traceability documented in the SKB data base SKBdoc under ID number 1271537.